Multidimensional magnetotelluric studies of the Precambrian Alberta basement

by

Enci Wang

A thesis submitted in partial fulfillment of the requirements for the degree of

Doctor of Philosophy

in

Geophysics

Department of Physics
University of Alberta

Abstract

The Alberta basement is part of the North American craton, which has been stable since Proterozoic and is also known as Laurentia. Geophysical and geology studies in Alberta have revealed that the basement rocks of Alberta have been assembled by complex tectonic events, such as subduction, arc-continent and continent-continent collisions accompanied by magmatism, metamorphism, metasomatism, and strike-slip deformation. Study of the Alberta basement provides information on how tectonic processes operated in the past and how they affect the current crustal and lithospheric structure. The magnetotelluric method has been used to study lithospheric structure in many areas of the world. This thesis describes the first detailed 3-D study of the Alberta basement using MT. The thesis has been divided into two projects. In Project 1, broadband magnetotelluric data were collected in northwest Alberta and were used to generate a 2-D electrical resistivity model of the crust across the Hay River Fault. In Project 2, long-period MT data collected in central Alberta were combined with legacy long-period MT data and were used to generate the first 3-D electrical resistivity model of the crust and upper mantle beneath Alberta. In Project 1, The Western Canada Sedimentary Basin was imaged as a low resistivity layer above the resistive crystalline basement. Four crustal basement conductors were defined: (1) the Kiskatinaw conductor, (2) a conductor on the boundary of the Ksituan and Chinchaga domains, (3) a conductor on the boundary of the Chinchaga and Buffalo Head domains and (4) a conductor near the Hay River Fault. Both (1) and (2) correspond to areas of high seismic reflectivity. The low resistivity can be explained by the presence of

interconnected grain boundary graphite, or sulfide minerals, deposited by metamorphic fluid migration. In Project 2, The Western Canada Sedimentary Basin was imaged as a low resistivity layer. A number of crustal and upper mantle conductors were imaged and include: (1) the Red Deer conductor, (2) the Kiskatinaw conductor, (3) a conductor coincident with the Kimiwan oxygen isotope anomaly, (4) the southern Alberta – British Columbia conductor, (5) the Loverna block conductor, (6) a conductor beneath the Birch Mountain kimberlite field. All these conductors can be related to past tectonic events suggested by previous studies. The lithosphere-asthenosphere depth across Alberta was defined from the electrical resistivity structure, and varies from 150 – 300 km. The Snowbird tectonic zone in Alberta is characterized by a deep and resistive lithosphere which indicates that it is highly depleted in incompatible elements. The diamondiferous Buffalo Head Hills kimberlite field is believed to be underlain by the most depleted lithosphere in Alberta.

Preface

Chapter 6 of this thesis has been published as E. Wang, M. J. Unsworth, and T. Chacko, "Geoelectric structure of the Great Slave Lake shear zone in northwest Alberta: implications for structure and tectonic history," *Canadian Journal of Earth Sciences*, vol. 55, issue 3,295-307. I was involved in the data collection and was responsible for the data analysis as well as the manuscript composition. M. J. Unsworth was my supervisor and responsible for the data collection and was involved with concept formation and manuscript composition. Thomas Chacko assisted with manuscript edits.

Acknowledgements

I would like to thank my supervisor, Dr. Martyn Unsworth, for his patience and help throughout my studies. His guidance in research and writing has been invaluable to me. I would also like to thank the members of my committee (Thomas Chacko and Jeff Gu) for their comments and conversations during this research.

I have learnt and enjoyed discussions with my colleagues at the University of Alberta, including: Greg Nieuwenhuis, Benjamin Lee, Darcy Cordell, Matthew Comeau, Juliane Huebert, Mitch Liddell, Cedar Hanneson, Sean Bettac, Theron Finley, Lijuan Liu, Gaofeng Ye, Shan Xu, Yaotian Yin, Zeyi Dong, Feng Jiang, Zhiguo An, Yan Zhan. Field help from Benjamin Lee, Greg Nieuwenhuis, Juliane Huebert, Mitch Liddell, Michael Cote and Feng Jiang is greatly appreciated. Proofreading of my thesis by Darcy Cordell, Benjamin Lee, Sean Bettac, and Cedar Hanneson is appreciated.

Luke Ootes is acknowledged for sharing his geological database. Greg Nieuwenhuis and Jacek Majorowicz are thanked for providing the temperature database of Alberta. Jeff Gu and Yunfeng Chen are thanked for sharing their seismic model of Alberta. Xuewei Bao and Andrew Schaeffer are thanked for sharing their seismic model of western Canada.

We thank Alan Jones and Gary McNeice for providing their tensor decomposition program. Weerachai Siripunvaraporn, Anna Kelbert, Gary Egbert are thanked for sharing their 3-D MT inversion algorithm. Randi Mackie is thanked for the use of the 2-D MT inversion software.

This research was financially supported by research grants from NSERC and Helmholtz-Alberta Initiative (HAI). Three-dimensional MT inversions were run using computational resources from WestGrid (Compute Canada). I would like to acknowledge the financial support from China Scholarship Council (CSC).

At lastly, I would like to thank my family for their encouragement and support during my study.

Table of Contents

List of Tables

List of Figures

[1] Martyn Unsworth, Home Page. Updated December, 2013. https://sites.ualberta.ca/~unsworth/MT/MT.html.
[2] Figure from https://sites.ualberta.ca/~unsworth/MT/MT.html

[3] Image from *http://www.phoenix-geophysics.com*
[4] Image from *http://ngf.oregonstate.edu*

Data from Geomatics Canada (2017). The black rectangle in (a) and (c) shows the location of (b) and (d). The gray lines mark the Precambrian terrane boundaries from Pilkington et al. (2000). Broadband MT stations are shown by triangles. The white triangles in (b) represent stations not used in the 2-D inversion due to low data quality. The two white rectangles in (b) mark the stations with typical data shown in Figure S2 in the Supplementary Material[5]. The black circles mark the locations of nearby towns. The dashed line indicates the location of the trace of the Kiskatinaw conductor according to Boerner et al. (2000). H, Hottah; N, Nova; Kw, Kiskatinaw; Ks, Ksituan; Ch, Chinchaga; BHH, Buffalo Head High; BHU, Buffalo Head Uricuma; FS, Fort Simpson; GSLSZ, Great Slave Lake shear zone; HRF, Hay River fault; GB, Great Bear; T, Taltson; RLK, Rainbow Lake; HL, High Level.

Figure 6.3: Interpreted seismic data of lines 11-12 from Peace River Arch Industry Seismic Experiment (PRAISE). Figure adapted from Figure 5 in Ross and Eaton (2002). The location of this profile is shown in Figure 6.1. WCSB, Western Canada Sedimentary Basin.

Figure 6.4: Temperature map at 1.5 km depth in Alberta (left) and the study area (right). The gray contour lines with numbers show the depth of the basement rocks. Temperature is not extrapolated in the basement rocks because there is little well control under the Western Canada Sedimentary Basin (WCSB, Nieuwenhuis et al. 2015). The black triangles represent the MT stations. The thickness of the WCSB is plotted according to the isopach map from Wright et al. (1994).

[5] Listed as Appendix in this thesis.

represents valid data at the specific period and the MT station. When there is only a red dot, it means that the MT station has no data at the specific period.

Figure 7.3: The inversion models of central Alberta using ModEM (figure (d), (e), (f)) and WSINV3DMT (figure (a), (b), (c)) algorithms shown as horizontal slices. The MT dataset (with 102 LMT stations) and initial model (100 Ωm half space) were the same for both inversions. The gray lines mark the boundaries of the basement terranes (Pilkington et al., 2000).

Figure 7.4: The r.m.s. misfit of the central Alberta inversion models computed using the WSINV3DMT (figure a, b, c) and ModEM (figure d, e, f) algorithms. The same dataset with 102 LMT stations was used for both methods. The black lines on the maps represent the geological boundaries (Pilkington et al., 2000). The diamonds show the locations of MT stations with color-filling to show the r.m.s. misfit. Figure (g) shows the convergence history of these two inversions.

Figure 7.5: Typical fit of the response of the central Alberta inversion model (solid lines) to the measured MT data (circles with error bars). The MT station aba950 was chosen to show this. The top panel (a) shows the fit of the ModEM central Alberta inversion model and the bottom panel (b) shows the fit of the WSINV3DMT central Alberta inversion model. Note that the reversed signs of the imaginary components of tippers were due to the sign convention difference in the two inversion schemes.

Figure 7.6: The preferred ModEM inversion model using the 183-station dataset shown as horizontal slices at varies depths. The gray lines mark the boundaries of the basement terranes (Pilkington et al., 2000).

Figure 7.7: The fit of the ModEM inversion model of the 183-station dataset. (a) The r.m.s. misfit of impedance and tipper at each station shown as filling colors of the diamonds. (b)The r.m.s. misfit of each period (triangles) and the overall averaged r.m.s. misfit (blue line). (c) The comparison of the MT dataset with the model responses shown with the averaged apparent resistivity and phase of the *xy* and *yx* modes. The gray lines mark the boundaries of the basement terranes (Pilkington et al., 2000).

Figure 7.8: The comparison of data fit and convergence for ModEM inversions with the 183-station datasets using 31/16/10 periods in figure (a), (b), and (c), respectively. The r.m.s. misfit is the averaged value (averaged over all the periods and data components) for each station in the map. All of the inversions converged to a final r.m.s. misfit of ~2.3. The bottom right figure shows the r.m.s. reduction for the inversions as the inversion progressed in iterations. The grey lines mark the boundaries of the basement terranes (Pilkington et al., 2000).

Figure 7.9: The r.m.s. misfit maps of ModEM inversions that used datasets with impedance only (8 responses, figure (a)) or with impedance and tipper (12 responses, figure (b)). Figure (c) shows the r.m.s. reduction for the two inversions as the inversion progressed in iterations. (d): Horizontal slices of the ModEM inversion models with datasets of impedance only (top) and datasets of impedance and tipper (bottom). The black dots represent the locations of MT stations. The grey lines in (a), (b), and (d) mark the boundaries of the basement terranes (Pilkington et al., 2000).RDC, Red Deer conductor. SABC, Southern Alberta British Columbia conductor.

The change of the r.m.s. misfit of the modified model from the inverted model for each MT station (diamonds) is shown in the center. The change of the r.m.s. misfit of the modified model from the inverted model for each MT station at period = 1000 s is shown at the right side. The red color represents r.m.s. misfit increase after the model modification. The grey line represents the tectonic terrane boundaries (Pilkington et al., 2000).

Figure 8.8: The sensitivity test for the Loverna block conductor and the southern Alberta – British Columbia conductor (LC and SABC, respectively) Their boundaries are marked with red lines based on the whole Alberta resistivity model obtained using ModEM. The change of the r.m.s. misfit of the modified model from the inverted model for each MT station (diamonds) is shown also. The red color represents r.m.s. misfit increase after the model modification. The grey line represents the tectonic terrane boundaries (Pilkington et al., 2000).

Figure 8.9: The sensitivity test for the Birch Mountain conductor based on the whole Alberta resistivity model obtained using ModEM. The resistivity of the BMC was replaced with 3000 Ωm at depths 100-200 km and 1000 Ωm at depths 200-300 km as shown in the left-side figures. The change of the r.m.s. misfit of the modified model from the inverted model for each MT station (diamonds) is shown in the middle figure. The right-side figure shows the change of the r.m.s. misfit for each MT station of the corresponding period. The red color represents r.m.s. misfit increase after the model modification. The grey line represents the tectonic terrane boundaries (Pilkington et al., 2000).

Figure 8.10: The sensitivity test of the effective investigation depths based on the whole Alberta resistivity model obtained using ModEM. The resistivity of the inverted model was replaced with 3000 Ωm at depths greater than 300/350/400/450/500 km. The change in the r.m.s. misfit of the modified model from the inverted model for each MT station (diamonds) is shown in the figure. The red color represents r.m.s. misfit increase after the model modification. This shows that the effective investigation depth is probably 350 km for most of the MT stations. The grey line represents the tectonic terrane boundaries (Pilkington et al., 2000).

Figure 8.11: The r.m.s. misfit of the central Alberta inversion averaged over all the periods for each station (left) and over all the stations for each period (right). The gray lines in the map mark the boundaries of the basement terranes (Pilkington et al., 2000).

Figure 8.12: The comparison of the MT data and the resistivity model response at periods from 10-10000 s. The apparent resistivity and phase are calculated as an average from the XY and YX components. The grey lines represent the terrane boundaries (Pilkington et al., 2000).

Figure 8.13: The 3-D resistivity model of the central Alberta shown with horizontal slices. The algorithm used is ModEM. The gray and red lines mark the terrane boundaries and faults, respectively (Pilkington et al., 2000). The black dots represent the locations of MT stations used for the inversion. Abbreviations: WCSB, Western Canada sedimentary basin; RDC, Red Deer conductor; SABC, Southern Alberta – British Columbia conductor; LC, Loverna block conductor.

Figure 9.1: Depth slices of (a) the whole Alberta (WAB) inversion model and (b) the central Alberta (CAB) inversion model showing the Western Canada Sedimentary Basin conductor (WCSB). (c) shows the WCSB as defined in the seismic model – CRUST 1.0 (Laske et al., 2013). (d) shows the conductance in the depth range 0-5 km. The red box is the location of (e) which is marked with conductance values of the WCSB (from Boerner et al. (2000)). The thick black lines in figures (a-d) represent the location of the Cordillera deformation front (CDF). The black lines with numbers in (e) represent the depths of the WCSB. Shaded zones in (e) indicate Leduc Formation reef complexes. The grey lines are geological boundaries and the red lines are faults (Pilkington et al., 2000; Colpron and Nelson, 2011).

Figure 9.2: The Red Deer conductor (RDC) imaged in the CAB model in horizontal slice view at depths of 8/10/27 km (a/b/c) and profiles (A-E). Locations of profiles A-E are shown in the (a) with black solid lines. (d) shows the RDC parallel to the strike direction of the RDC. (e) shows the RDC as slices that are normal to the strike direction of the RDC on three profiles B, D, and E. (f) shows the RDC in a profile that is collocated with the 2-D magnetic model of Hope and Eaton, (2002). The grey lines in (a), (b), (c) mark the terrane boundaries (Pilkington et al., 2000; Colpron and Nelson, 2011). In panel (b), south and north segments of the RDC are marked with white and black dashed lines, respectively. Abbreviations: WCSB, Western Canada Sedimentary Basin; LC, Loverna block conductor; CDF, Cordillera deformation front; VE, vertical exaggeration.

Figure 9.3: Comparison of the CAB resistivity model with the CAT seismic reflection profiles (Ross, 2002). The bottom of the WCSB and the crust are defined from the seismic

CAB model. The red thick line represents the location of the profile shown in (c) as imaged in the WAB model. The red and gray lines are basement faults and terrane boundaries (Pilkington et al., 2000; Colpron and Nelson, 2011). (d) and (e) show the V_p- / V_s- velocity profiles from Chen et al. (2018). Abbreviations: BHH, Buffalo Head High; BHU, Buffalo Head Uricuma; BHT, Buffalo Head terrane (including BHH and BHU); WTR, Wabamun Thorsby Rimbey; La, Lacombe; LB, Loverna block; VS, Vulcan Structure; MHB, Medicine Hat block.

Figure 9.7: The analysis of water and melt content using the method of Rippe et al. (2013). (a): The resistivity profile imaged in the Alberta model beneath the MT station SAB225 (blue line; see the location of SAB225 in Figure 9.5) and the resistivity of dry olivine of model SEO3 (black line; Constable, 2006). The station SAB225 is located above the LC conductor. (b): simplified geotherm, as calculated in Appendix 9 (blue), dry peridotite solidus (red line; Hirschmann et al., 2009), and the 35 mW/m^2 geotherm defined by Pollack and Chapman (1976; dash black line). (c): water content calculated using the methods of Karato (1990, blue dashed line), Wang et al. (2006, magenta line) and Yoshino et al. (2009, green line). The black line (A) represents the hydrogen solubility (Lizarralde et al., 1995; Bell et al., 2003). The red line (B) shows the minimum amount of water required for hydrous melting. (d): the expected melt fraction using the methods of Karato (1990, blue dashed line), Wang et al. (2006, magenta line) and Yoshino et al. (2009, green line). The resistivity of melt used was 0.03 Ωm.

Figure 9.8: Plots of the Kimiwan conductor (KMC) as imaged in the WAB 3-D inversion model. (a): Horizontal slice of the WAB model at a depth of 22 km. The box with

dashed lines shows the location of the Kimiwan oxygen isotope anomaly (Burwash et al., 2000). The black solid lines are the locations of Lithoprobe seismic reflection profiles (Bouzidi et al., 2002). The black open and filled squares are the location of the normal and anomalous $\delta^{18}O$ samples around the Kimiwan O-isotope anomaly, respectively. The gray lines are terrane boundaries (Pilkington et al., 2000). The red solid lines show the location of profiles A and B chosen to show the vertical extent of the Kimiwan conductor in figure (b) and (c).

Figure 9.9: The Alberta 3-D inversion model compared with the Lithoprobe profiles 11-14 and 20. Black lines represent the major faults defined by (Ross and Eaton, 2002). Zone B and D were defined in Hope and Eaton (2002). D: a zone of disruption where the Winagami reflection sequence (WRS) is disturbed. B: a blank zone which may represent a plutonic body or a fault shadow zone. KMC represents the Kimiwan conductor.

Figure 9.10: Plots of the Kiskatinaw conductor (KC) imaged in the Alberta 3-D inversion model and the 2-D inversion model of Chapter 6. (a): Horizontal slice of the Alberta 3-D inversion model at the depth of 22 km. The location of long-period MT stations (LMT) used in the 3-D inversion is shown with black dots. The red line represents the closely located broadband MT stations (BBMT) used in the 2-D inversion. The location of the Rainbow Lake (RLK) profile is indicated with the white dashed line. PRAISE lines 11-12 that crossed the KC at the south are also shown with pink lines. A profile subtracted from the Alberta 3-D inversion model along lines 11-12 is shown in Figure 9.9. The gray lines are terrane boundaries (Pilkington et al., 2000). (b): 2-D resistivity model along the RLK profile using BBMT. WCSB, Western Canada

Sedimentary Basin; HC, Hottah conductor; KCC, Ksituan-Chinchaga conductor; CBHC, Chinchaga-Buffalo Head conductor. (c): Resistivity structure along the RLK profile subtracted from the Alberta 3-D inversion model using LMT.

Figure 9.11: Details of the WAB model around the Birch Mountain field conductor (BMC). (a) Horizontal slice at 189 km depth. Purple and white diamonds represents the occurrence kimberlite pipes/ultrabasic rocks (Open Data Portal – Alberta Geological Survey, 2018). Black dots are the locations of MT stations used in the WAB inversion. Thick red lines are the location of the two profiles shown in panels (b) and (c). The gray lines are basement terrane boundaries (Pilkington et al., 2000; Colpron and Nelson, 2011). Red thin lines show the location of faults in southeast British Columbia. Thick black dashed line represents the Cordillera deformation front (CDF). The star marks the location of the MT station LAB010 whose resistivity profile is used in Figure 9.12. (b) Profile along latitude of 57.5˚N. The purple bars in (b) and (c) are the basement terrane boundaries. (c) Profile along longitude of 113˚W. Triangles on top of the profiles show the location of kimberlite fields near to the profile. Figure (d), (e), (f) show the shear velocity model of Chen et al. (2018) at various depth-slices. The low velocity anomaly is at the same location as the BMC. Abbreviations: BHH, Buffalo Head Hills kimberlite field; BM, Birch Mountains kimberlite field; ML, Mountain Lake kimberlite field; CR, Cross kimberlite field; BBM, Black Butte Minette fields; BMC, Birch Mountain field conductor; STZ, Snowbird tectonic zone.

Figure 9.12: The analysis of water and melt content of the BMC using the method of Rippe et al. (2013). (a): The resistivity profile imaged in the Alberta model beneath the MT

station LAB010 (blue line) and the resistivity of dry olivine of model SEO3 (black line; Constable, 2006). The station LAB010 is located on the top of the BMC conductor (see its location in Figure 9.11). (b): simplified geotherm calculated (blue), dry peridotite solidus (red line; Hirschmann et al., 2009), the geotherm defined from xenolith studies (gray line; Aulbach et al., 2004), the 40 mW/m^2 geotherm defined by Pollack and Chapman (1976; dash black line).(c): water content calculated using the methods of Karato (1990, blue dashed line), Wang et al. (2006, magenta line) and Yoshino et al. (2009, green line). The black line (A) represents the hydrogen solubility (Lizarralde et al., 1995; Bell et al., 2003). The red line (B) shows the minimum amount of water required for hydrous melting. (d): the expected melt fraction using the methods of Karato (1990, blue dashed line), Wang et al. (2006, magenta line) and Yoshino et al. (2009, green line). The resistivity of melt used was 0.03 Ωm. (e)-(h): the same calculations except that the resistivity profile of station LAB010 is multiplied by 10.

Figure 9.13: The Snowbird tectonic zone (red dash line) and lithospheric structure imaged in the Alberta inversion model shown with horizontal slice at 189 km depth (a) and vertical profiles in (b), (c), (d), and (e). The white lines in (a) are the location of the vertical profiles. Red and grey lines in figure (a) represent geological boundaries and faults (Pilkington et al., 2000; Colpron and Nelson, 2011). The thick black dash line shows the location of the Cordillera deformation front (CDF). The black and white contour lines in (b), (c), (d), and (e) are corresponding to 1000 Ωm and 100 Ωm, respectively. The black and white dashed lines represent where the 100 Ωm contour line should not be considered as the lithosphere-asthenosphere boundary

(LAB). Abbreviations: BM, Birch Mountain kimberlite field; BHH, Buffalo Head Hills kimberlite field; ML, Mountain Lake kimberlite field; BBM, Black Butte Minette fields; SABC, Southern Alberta – British Columbia conductor; CR, Cross kimberlite field; KMC, Kimiwan conductor; LC, Loverna block conductor; KC, Kiskatinaw conductor.

Figure 9.14: North-south profiles of the WAB electrical resistivity model. White and black lines represent the contour of resistivity values of 100 and 1000 Ωm, respectively. Purple bars are the terrane boundaries defined from Pilkington et al. (2000). Red triangles show the location of kimberlite and ultramafic intrusions. Abbreviations: GB, Great Bear; TMZ, Taltson; BHH, Buffalo Head High; BHU, Buffalo Head Uricuma; Ch, Chinchaga; Wa, Wabamun; R, Rimbey; T, Thorsby; L, Lacombe; LVB, Loverna Block; MH, Matzhiwin high; EH, Eyehill high; VS, Vulcan structure; MHB, Medicine Hat Block; BM, Birch Mountain kimberlite field; BHH, Buffalo Head Hills kimberlite field; ML, Mountain Lake kimberlite field; BBM, Black Butte Minette fields; CR, Cross kimberlite field.

Figure 9.15: East-west profiles of the WAB 3-D electrical resistivity model. White and black lines represent resistivity contours of 100 and 1000 Ωm, respectively. Purple bars are the basement terrane boundaries (Pilkington et al., 2000). White dash lines represent the location of the Cordillera deformation front. Red dash lines represent the location of the Hay River Fault. Abbreviations: Ho, Hottah; GB, Great Bear; TMZ, Taltson; BHH, Buffalo Head High; BHU, Buffalo Head Uricuma; Ch, Chinchaga; Wa, Wabamun; R, Rimbey; T, Thorsby; L, Lacombe; LVB, Loverna Block; MH, Matzhiwin high; EH, Eyehill high; VS, Vulcan structure; MHB, Medicine Hat Block; Ks, Ksituan; MHB, Medicine Hat block; EH, Eyehill high; VS, Vulcan structure; BM, Birch Mountain

kimberlite field; BHH, Buffalo Head Hills kimberlite field; ML, Mountain Lake field; BBM, Black Butte Minette fields; CR, Cross kimberlite field.

Figure 9.16: Comparison of the CAB model with the SALT profiles. The interpreted profile 25 and 32 is from (Eaton et al., 1999). The seismic section of profiles 21-24 is from Bouzidi et al. (2002). LC, Loverna block conductor; SABC, Southern Alberta British Columbia conductor; MHBC, Medicine Hat block conductor.

Figure 9.17: (a): The CAB model compared with the SAREX (Southern Alberta Refraction Experiment and Deep Probe) result from Clowes et al. (2002) and Gorman et al. (2002). Thin solid lines are major reflectors observed including Moho. Thick solid lines named f1 and f2 are the mantle reflectors. The dashed line underneath LC is extended from f1. (b) and (c): The CAB model compared with the Vibroseis Augmented Listen Time (VAuLT) profile 34E and 32E (Eaton et al., 2000). Dashed lines are the imaged reflectors. Abbreviations: RDC, Red Deer conductor; LC, Loverna block conductor; SABC, Southern Alberta – British Columbia conductor; MHB, Medicine Hat block.

List of symbols and abbreviations

1-D	One Dimensional
2-D	Two Dimensional
3-D	Three Dimensional
ABT	Alberta Basement Transect
BBMT	Broadband Magnetotelluric
BHT	Buffalo Head terrane
BHHR	Buffalo Head Hills resistor
BMC	Birch Mountain Field Conductor
BT	Bostick Transform
CAB	Central Alberta
CBHC	Chinchaga-Buffalo-Head conductor
CDF	Cordillera Deformation Front
EGS	Enhanced Geothermal System
EM	Electromagnetic
FFT	Fast Fourier Transform
GSLSZ	Great Slave Lake Shear Zone
GFTZ	Great Fall Tectonic Zone
HL	High Level

HRF	Hay River Fault
HC	Hottah Conductor
KC	Kiskatinaw Conductor
KCC	Ksituan-Chinchaga Conductor
KIA	Kimiwan Isotopic Anomaly
KMC	Kimiwan Conductor
KSR	Ksituan Resistor
LAB	Lithosphere – Asthenosphere Boundary
LC	Loverna Block Conductor
LIMS	Long-period Intelligent Magnetotelluric system
LMT	Long-period Magnetotelluric
LVB	Loverna block
MHB	Medicine Hat Block
MT	Magnetotelluric
NAM	Nominally Anhydrous Minerals
NIMS	Narod Intelligent Magnetotelluric system
PRASE	Peace River Arch Seismic Experiment
PRAISE	Peace River Arch Industry Seismic Experiment
RDC	Red Deer Conductor

RDT	Red Deer Trend
RLK	Rainbow Lake
RMT	Rocky Mountain Trench
SABC	Southern Alberta and British Columbia conductor
SALT	Southern Alberta Lithospheric Transect
SAREX	Southern Alberta Refraction Experiment
STZ	Snowbird tectonic zone
STZR	Snowbird Tectonic zone resistor
TE	Transverse Electric
THO	Trans-Hudson Orogen
TM	Transverse magnetic
TMZ	Taltson Magmatic Zone
TTZ	Thelon Tectonic Zone
VauLT	Vibroseis Augmented Listen Time
VE	Vertical Exaggeration
VS	Vulcan Structure
WAB	Whole Alberta
WCSB	Western Canada Sedimentary Basin
WRS	Winagami Reflection Sequences

Chapter 1 : Introduction

The Earth has a bimodal crustal distribution with mafic oceanic crust and felsic continental crust. Oceanic crust is relatively young, since it is recycled / destroyed in subduction zones, with a maximum age of 300 Ma (Müller et al., 2008). In contrast, the lower density continental crust is difficult to destroy and geochronological dating of zircons has identified grains formed at ca. 4400 Ma (Stern and Bleeker, 1998; Bowring and Williams, 1999). The high degree of heterogeneity of the continental crust means that its structure and tectonic history is complex, and significant work is needed to determine both structure and history.

The basement rocks in Alberta are located beneath the western Canada sedimentary basin (WCSB) and are part of the Archean craton called Laurentia (Figure 1.1). This craton is one of the largest in the world and is relatively well studied (Hoffman, 1988). It is composed of a number of small Archean cratons that were sutured together, with or without the formation of an orogenic belt. The tectonic processes involved in the assembly of Laurentia included closure of ocean basins through subduction, arc-continent and continent-continent collisions. Arc magmatism, intra-plate magmatism, metamorphism and strike-slip motion are suggested to have accompanied these tectonic events (Ross, 2002; Chacko et al., 2000; Hoffman, 1989).

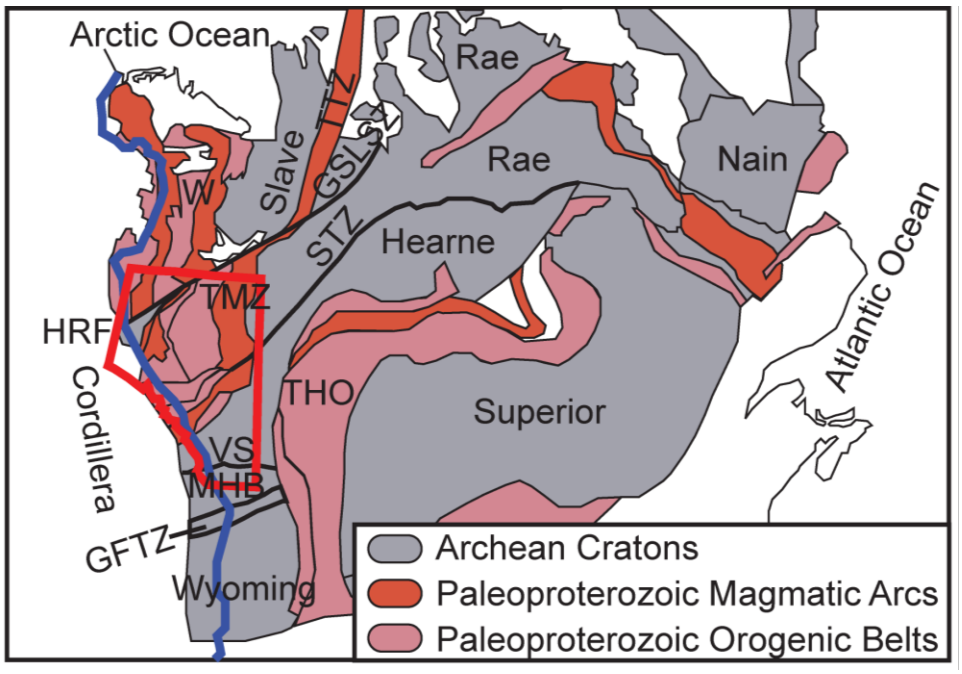

Figure 1.1: Tectonic map of the core of Laurentia (modified from Ross, 2002 and Hoffman, 1988). The blue line marks the deformation front of the Cordillera. Abbreviations: GFTZ, Great Fall Tectonic Zone; GSLSZ, Great Slave Lake Shear Zone; MHB, Medicine Hat Block; THO, Trans-Hudson Orogen; TMZ, Taltson Magmatic Zone; TTZ, Thelon Tectonic Zone; VS, Vulcan Structure; W, Wopmay Orogen; HRF, Hay River Fault.

Despite numerous studies, there are many aspects of the structure and formation of Laurentia that are poorly understood. This includes the parts of the craton beneath Alberta. Knowledge of the crustal and lithospheric structure in Alberta is important because:

1. It can help us determine how the crust of Alberta evolved.

2. It can give insights into present-day tectonic processes, which should be in similar style regardless of the speed, according to the theory of Uniformitarianism (Lyell, 1830).

3. This information can be used to investigate the distribution of resources such as geothermal energy and mineral deposits. There are occurrences of many kinds of

mineral deposits in Alberta, including sulfur, iron, zinc, lithium, uranium and diamonds (Olson et al., 2006).

Geological and geophysical studies are both needed to fully determine the structure of the crust and mantle. Geological mapping can determine the surface distribution of different rock types, and determine their ages through geochronology. In contrast geophysical methods can image the present-day subsurface structures. The Canadian Shield, which is the exposed part of Laurentia, has been well studied by geological mapping and geophysical methods because the Precambrian rocks are exposed at the surface. In contrast, in Alberta, the WCSB overlies the crystalline basement rocks, making geological mapping impossible and resulting in increased uncertainty about the basement structure. Geophysical methods must be used to study the basement of Alberta. Previous geological and geophysical studies of the Alberta basement include the following:

1. Tectonic basement terranes were delineated and identified on the basis of their aeromagnetic and gravity anomalies in combination with geochronology studies of drill core samples (Ross et al., 1991; Villeneuve et al., 1993; Pilkington et al., 2000).
2. Seismic reflection and refraction studies have imaged the crustal reflectivity features and have mapped the depth of Moho in Alberta (Zelt and Ellis 1989; Eaton and Cassidy, 1996; Hope et al., 1999; Eaton et al., 2000; Bouzidi et al., 2002; Clowes et al., 2002; Gorman et al., 2002; Ross, 2002; Ross and Eaton, 2002).
3. Teleseismic studies have revealed crustal and upper mantle velocity structure of Alberta and have imaged large variation of the depth of the lithosphere-asthenosphere boundary (LAB). The Hearne craton in Alberta has been imaged with a thick lithosphere

with the LAB at depth greater than 200 km (Shragge et al., 2002; Bao et al., 2014; Bao and Eaton, 2015; Chen et al., 2015; Gu and Shen, 2015; Chen et al., 2017; Chen et al., 2018; Gu et al., 2018).

4. Previous magnetotelluric (MT) and magnetovatiational studies have imaged several crustal and upper mantle conductors in Alberta that were interpreted to be closely related to the tectonic assembly history of Alberta (Reddy and Rankin, 1972; Gough, 1986; Wang 1988a&b; Boerner et al., 1995; Boerner et al., 1999; Boerner et al., 2000; Nieuwenhuis et al., 2014; Türkoğlu et al., 2009; Yin et al., 2015; Liddell et al., 2016).

All of these previous studies have contributed valuable information on the present-day geological structure and tectonic history of the Alberta basement. However, further investigations are needed because many of the aspects of the geological features observed in Alberta are not fully understood. A number of interesting features are listed below.

1. The Hay River Fault (HRF) is a crustal-scale right-lateral fault located in northwest Alberta recognized by the truncation of cross-cutting aeromagnetic features (Villeneuve et al., 1993). The structure and geological history of the Hay River Fault (HRF) are poorly defined. Together with the Great Slave Lake shear zone (GSLsz), it was proposed as a continental transform structure (Hoffman, 1987). It was considered as a later-stage brittle segment of the Great Slave Lake shear zone (Ross and Eaton, 2002). To date very few geophysical studies have imaged the subsurface structure of the HRF in Alberta.

2. The Snowbird tectonic zone (STZ) is located in central Alberta. It is marked by aeromagnetic and gravity anomalies that extend more than 2800 km from Hudson's Bay to the Foothills of the Rocky Mountains (Hoffman, 1988). The STZ separates (a) the

Hearne and Rae provinces in the Canadian Shield and (b) the Hearne province and the Proterozoic basement terranes in Alberta. Many hypotheses have been proposed for the formation and deformation of the STZ. For example, the STZ was described as a Paleoproterozoic intra-continental shear zone by Lewry et al. (1985), a mid-late Archean intra-continental deformation zone by Hanmer et al. (1995), a Neoarchean tectonic suture zone (Jones et al., 2002), a Paleoproterozoic intra-continental thrust and strike-slip shear zones (Mahan and Williams, 2005), a Paleoproterozoic suture zone (Berman et al., 2007), and a Paleoproterozoic subduction zone (Ross, 2002). However, no consensus has been reached to date.

3. The deformation in the Hearne province in Alberta was proposed to be extensive and it has been proposed to be related to Precambrian tectonic processes (Chen et al., 2018; Ross, 2002).

4. There are 56 occurrences of kimberlite and alkaline rocks in Alberta, some of which are diamondiferous (Eccles et al., 2004). MT study provides an opportunity to investigate the factors that influence the diamond content in kimberlites.

The research described in this thesis uses geophysical data to investigate the structure of the Alberta basement rocks. The magnetotelluric (MT) method is a useful tool to study crustal and upper mantle structures. It utilizes the natural occurring electromagnetic field and can image the electrical resistivity structure of the Earth laterally and vertically. The electrical resistivity of a rock depends on temperature and the composition, especially on the minor highly conductive constituents such as: saline fluids, melts, H+, and conducting phases such as graphite and sulfides. The application of MT to

the study of the Alberta basement rocks has been divided into two linked projects in this thesis.

Project 1. Strike-slip tectonics of the HRF in northwest Alberta. MT data in the frequency range of 0.001-1000 Hz were collected along a profile and 2-D inversions were systematically applied to the data.

Project 2. The lithospheric-scale electrical resistivity structure of the whole of Alberta. In Alberta, there are legacy MT data from previous studies such as Boerner et al. (2000). However, additional geophysical data are needed to fully understand the structure and tectonic history of Alberta. New MT data have been collected to obtain a uniformly spaced MT dataset and 3-D inversions have been applied to this dataset to determine a 3-D electrical resistivity model of the crust and upper mantle beneath Alberta.

In this thesis, the MT method is introduced in Chapter 2. In Chapters 3 and 4, the geological setting of Alberta and previous geophysical studies are reviewed. In Chapter 5, the MT data collection and processing techniques are introduced and the characteristics of the MT dataset used for Project 2 are described. In Chapter 6, a paper published on Project 1 is included (Wang et al., 2018) In Chapter 7, 3-D MT inversion tests based on the Alberta MT dataset are shown. In Chapter 8, the 3-D inversion models developed for the crust and upper mantle beneath Alberta are described. In Chapter 9, these electrical resistivity models of Alberta are interpreted in terms of the causes of the high and low resistivity features. This analysis is used to develop some preliminary tectonic interpretations regarding the present-day geological structure and tectonic history.

Chapter 2 : The Magnetotelluric method

2.1. Introduction

The electrical resistivity of the subsurface is a useful physical property to measure in order to study the properties of the Earth's interior. This is because the electrical resistivity of a rock is sensitive to both the temperature and the presence of conductive phases such as water, melt, sulfide minerals or graphite films. Electrical conductivity is the reciprocal of electrical resistivity (Chave and Jones, 2012).

Measurement of resistivity at depth within the Earth requires observations of how electromagnetic signals propagate within the Earth. These signals can be natural occurring or generated by a transmitter. The magnetotelluric method uses naturally electromagnetic (EM) signals in the frequency range 1000 - 0.0001 Hz. We will show in this chapter that for typical conductivity values, these low frequency signals can travel to a depth of several hundred kilometers. In contrast, the EM signals generated with a man-made transmitter are weaker than the natural signals. Therefore, controlled source electromagnetic exploration methods are primarily used for near surface exploration. Moreover, controlled source (CS) methods use signals of higher frequencies in the range from 0.1 Hz to 10,000 Hz. The MT and CS methods have a number of strengths and weaknesses.

MT exploration is logistically simpler than CS exploration because no transmitter is needed to generate signals. In areas where there is significant electromagnetic noise, the CS method has advantages because the user can control the signals and more effectively study near surface structure. CS methods also allow for rapid data collection, as the signal is

guaranteed to occur during a particular recording window. In practice, the MT method is widely used in deep and regional exploration and the CS method is used in detailed local imaging of shallow structures.

The MT method was independently discovered by Tikhonov (1950) and Cagniard (1953) who both described the theory of the MT method for the case when the resistivity of the Earth varies in 1-D only with depth. However, the electrical resistivity structure of the subsurface can be 2-D, which means that the electrical resistivity of the Earth varies in the vertical and one horizontal direction. In a 3-D structure resistivity varies in all three directions. Numerous improvements have been made since then in data analysis and 2-D/3-D MT inversion methods are now widely used. Additional details of the MT method can be found in the textbooks by Simpson and Bahr (2005) and Chave and Jones (2012).

In MT, the electric and magnetic field components are measured at the surface of the Earth (Figure 2.1). The electric fields are measured in two orthogonal directions (north-south and east-west) with non-polarizing electrodes. The magnetic fields are measured in three orthogonal directions (north-south, east-west, and vertical) and are recorded using induction coils or a three-component flux-gate magnetometer. By recording the natural electromagnetic signals over a wide range of frequencies, the MT method is capable of measuring the electrical resistivity of the subsurface from a depth of tens of meters to several hundred kilometers.

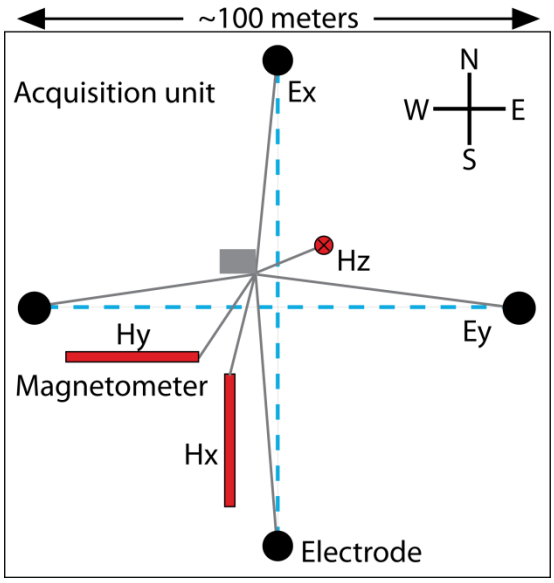

Figure 2.1: Typical layout of an MT site. E_x and E_y are horizontal electric fields measured in the north-south and east-west directions, respectively. H_x, H_y, and H_z are the magnetic field components in the north-south, east-west, and vertical directions.

2.2. Resistivity of rocks

The dry rocks in the upper crust of the Earth are generally characterized by a high resistivity because of the lack of charge carriers in these materials. Low resistivity regions are often associated with fluids such as saline water or partial melt (Figure 2.2). Low resistivity can also be due to solid, low resistivity materials such as sulfide minerals or graphite films. At mantle depths, hydrogen dissolved in olivine provides charge carriers and can permit a rock to conduct electricity (Karato, 1990). A concentration of few percent of these conducting phases can significantly reduce the overall resistivity of a rock. Because of these factors, the MT method is very sensitive to the presence of the conductive materials mentioned above.

Note that the overall resistivity of a rock often depends on a low resistivity phase that constitutes a relatively small volume fraction of the rock. This is in contrast to seismic velocity which is generally a volumetric average of the velocities of all phases present. These differing sensitivities to material properties allow MT data and seismic data to complement one another in exploration.

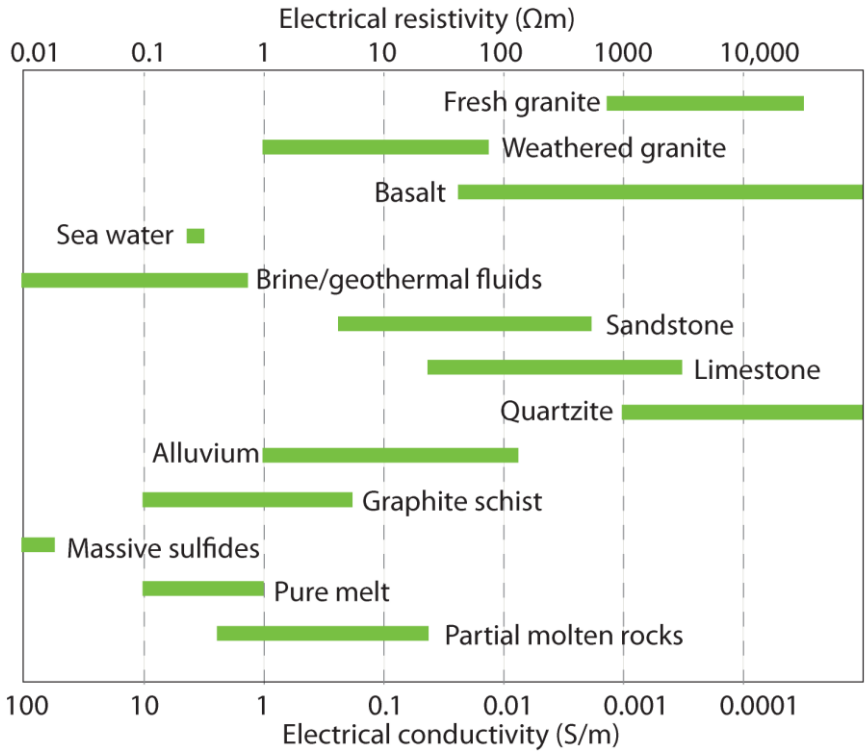

Figure 2.2: Electrical resistivities of materials found in the Earth[1].

[1] Martyn Unsworth, Home Page. Updated December, 2013. https://sites.ualberta.ca/~unsworth/MT/MT.html.

2.3. Governing equations

The goal of this section is to understand how electromagnetic fields travel in the Earth. This requires an understanding of how the propagation depends on the properties of the rock. The electrical properties of a rock are defined by three quantities:

(1) Electrical resistivity (ρ, in Ωm), which is the inverse of the electrical conductivity (σ, in S/m),

(2) Dielectric permittivity (ε, in F/m) and

(3) Magnetic permeability (μ, in H/m).

The constitutive relationships relate these properties (μ, ε, σ) to the magnetic field ($\boldsymbol{H}$, in A/m), the electric displacement ($\boldsymbol{D}$, in C/m^2), the current density ($\boldsymbol{J}$, in A/m^2), the electric field ($\boldsymbol{E}$, in V/m) and the magnetic flux density ($\boldsymbol{B}$, in T) are given by:

$$\boldsymbol{B} = \mu \boldsymbol{H} \tag{2.1}$$

$$\boldsymbol{J} = \sigma \boldsymbol{E} \tag{2.2}$$

$$\boldsymbol{D} = \varepsilon \boldsymbol{E} \tag{2.3}$$

In a general case, the three quantities (μ, ε, σ) will vary with position in the Earth. However, the MT method is insensitive to changes in the dielectric permittivity at the low frequencies used in exploration, since the displacement current is ignored. Therefore, the dielectric permittivity are assumed to be constant in MT and equal to the value of free space ($\varepsilon=\varepsilon_0=8.85\text{x}10^{-12}$ F/m). Moreover, the magnetic permeability is assumed to be equal to the value of free space as well ($\mu=\mu_0=4\pi\text{x}10^{-7}$ H/m). This is valid for most of the crustal and mantle rocks except certain metal ore (e.g., pure iron).

The MT method is based on the propagation of EM signals in a low resistivity Earth. The modern understanding of the electromagnetism has been developed from Maxwell's Equations (Maxwell, 1865):

$$\nabla \cdot \boldsymbol{E} = \rho/\varepsilon \tag{2.4}$$

$$\nabla \cdot \boldsymbol{B} = 0 \tag{2.5}$$

$$\nabla \times \boldsymbol{B} = \mu\left(\boldsymbol{J} + \varepsilon \frac{\partial \boldsymbol{E}}{\partial t}\right) \tag{2.6}$$

$$\nabla \times \boldsymbol{E} = -\frac{\partial \boldsymbol{B}}{\partial t} \tag{2.7}$$

Equation (2.4) is known as Gauss's Law in the differential form. It can be rewritten in the integral form:

$$\oint \boldsymbol{E} \cdot d\boldsymbol{A} = \frac{q}{\varepsilon} \tag{2.8}$$

where A is the surface area of a volume, q is the total electric charge inside the volume. Gauss's Law expresses the fact that the electric flux leaving a volume is proportional to the total electric charge inside the volume. Equation (2.5) is Gauss's Law for magnetism which states that magnetic monopoles do not occur in isolation. They always occur as pairs with positive and negative polarity as a dipole.

Equation (2.6) shows how magnetic fields are generated by electric currents. The first term on the right-hand side of Equation (2.6) was discovered by Ampère which shows the relationship between the electric current carried by a wire and the circulation of the magnetic field. This type of electric current is referred as conduction current and is caused by the flow of electrons or other charge carriers. It shows that the magnetic field generated

by a closed loop is proportional to the conduction current. Ampère's Law was generalized by Maxwell who added a term for a second type of electric current that he termed displacement current. Equation (2.7) is Faraday's law of induction that shows how the voltage induced in a closed circuit is proportional to the rate of change of the magnetic flux it encloses.

Maxwell's Equations can be used to derive equations that describe how electromagnetic signals will travel in the Earth. To do this, Ampère's Law can be rewritten using the constitutive relation in Equation (2.3) as

$$\nabla \times \boldsymbol{B} = \mu \left(\sigma \boldsymbol{E} + \varepsilon \frac{\partial \boldsymbol{E}}{\partial t} \right) \tag{2.9}$$

Taking the curl of Equation (2.7) we get:

$$\nabla \times (\nabla \times \boldsymbol{E}) = -\frac{\partial}{\partial t} (\nabla \times \boldsymbol{B}) \tag{2.10}$$

Using the vector identity for the left hand side of Equation (2.10) we get:

$$\nabla \times (\nabla \times \boldsymbol{E}) = \nabla(\nabla \cdot \boldsymbol{E}) - \nabla^2 \boldsymbol{E} = -\frac{\partial}{\partial t} (\nabla \times \boldsymbol{B}) \tag{2.11}$$

Substituting Equation (2.9) into (2.11) and assuming that $\mu=\mu_0$, it can be shown that Equation (2.10) can be rewritten as:

$$\nabla(\nabla \cdot \boldsymbol{E}) - \nabla^2 \boldsymbol{E} = -\mu\sigma \frac{\partial \boldsymbol{E}}{\partial t} - \mu\varepsilon \frac{\partial^2 E}{\partial t^2} \tag{2.12}$$

Where there is a boundary between regions of differing conductivity, electric charges may develop on this boundary. If we assume that currents only flow parallel to these boundaries (as in 1-D) then we can assume that there are no free electric charges, and Equation (2.4) can be simplified to:

$$\nabla \cdot \boldsymbol{E} = 0 \tag{2.13}$$

Using the assumptions listed above, Equation (2.12) can be simplified to:

$$\nabla^2 \boldsymbol{E}(\boldsymbol{t}) = \mu_0 \sigma \frac{\partial \boldsymbol{E}(\boldsymbol{t})}{\partial t} + \mu_0 \varepsilon \frac{\partial^2 \boldsymbol{E}(\boldsymbol{t})}{\partial t^2} \tag{2.14}$$

This equation describes arbitrary time variations in the electric field components. It can be simplified if the analysis is transferred into the frequency domain, by assuming that the EM fields have harmonic time dependence ($e^{-i\omega t}$) with angular frequency ω ($\omega=2\pi f$), Equation (2.14) can be rewritten as:

$$\nabla^2 \boldsymbol{E} = -i\omega\mu_0\sigma\boldsymbol{E} + \omega^2\mu_0\varepsilon\boldsymbol{E} \tag{2.15}$$

The first term on the right-hand side of Equation (2.15) represents the conduction current, and the second term represents the displacement current. The ratio of displacement current to conduction current is given by the ratio $R = \omega\varepsilon/\sigma$.

It is useful to consider which type of current will dominate in typical EM geophysics surveys. For the MT method the frequency is typically around 0.0001-10000 Hz. Using the Earth conductivity of 0.01 S/m, and the free space dielectric permittivity ($\varepsilon=\varepsilon_0=8.85\times10^{-12}$ F/m) it gives R in the range 5.56×10^{-5} – 5.56×10^{-12}. This shows that in MT surveys, the displacement current is much smaller than the conduction current. Therefore, the displacement current can be ignored in MT and Equation (2.15) can be simplified to

$$\nabla^2 \boldsymbol{E} = -i\omega\mu_0\sigma\boldsymbol{E} \tag{2.16}$$

A similar equation for the magnetic field can be derived as:

$$\nabla^2 \boldsymbol{B} = -i\omega\mu_0\sigma\boldsymbol{B} \tag{2.17}$$

Equation (2.16) and (2.17) are diffusion equations and they show that the EM signals propagate diffusively in the Earth.

2.4. Source of the EM signals used in MT

The EM signals used in MT originate in two distinct sources:

- high frequency (> 1Hz) EM signals from worldwide lightning activity and
- low frequency (< 1Hz) EM signals originate in the magnetosphere.

The high frequency EM signals in the range of 1-10000 Hz are caused by distant lightning activity. These EM signals propagate in a wave guide between the conductive Earth and the conductive ionosphere. The electrical conductivity of the ionosphere is anisotropic and the conductivity parallel to the layers of the ionosphere increases with height dramatically (Baker and Martyn, 1953).

The low frequency signals (0.0001-1 Hz) are generated by time variations in the solar wind (Vozoff, 1991). The plasmasphere (part of the magnetosphere) and the ionosphere are composed of regions of plasma and are electrically conductive (Baker and Martyn, 1953). The ionization is the result of the solar and cosmic radiation. Changes in the velocity of the solar wind can induce electric currents in the magnetosphere and ionosphere and cause variations in the electromagnetic field on the Earth.

Because of the wide range of frequencies present in the natural electromagnetic signal (typically 0.0001-10000 Hz), the MT method is the only electromagnetic exploration technique that can provide resistivity information about the subsurface from the surface to depths greater than 500 km (Chave and Jones, 2012).

In the initial formulation of MT, the EM waves were assumed to be planar and normally incident on the Earth's surface by Cagniard (1953). These assumptions simplified the data analysis of MT data, but were the subject of a debate (Wait, 1954; Price, 1962). Because the theory of MT is based on the plane wave assumption, it was argued that if the assumption was not valid, then the resistivity values derived from MT data could not be trusted. However, it was successfully proven that the planar wave assumption is sufficiently accurate for MT measurements to reliably image the interior resistivity structure of the Earth (Madden and Nelson, 1964). Furthermore, Dmitriev and Berdichevsky (1979) showed that the MT method is valid when the EM field at the study area varies linearly in a horizontal direction at the surface.

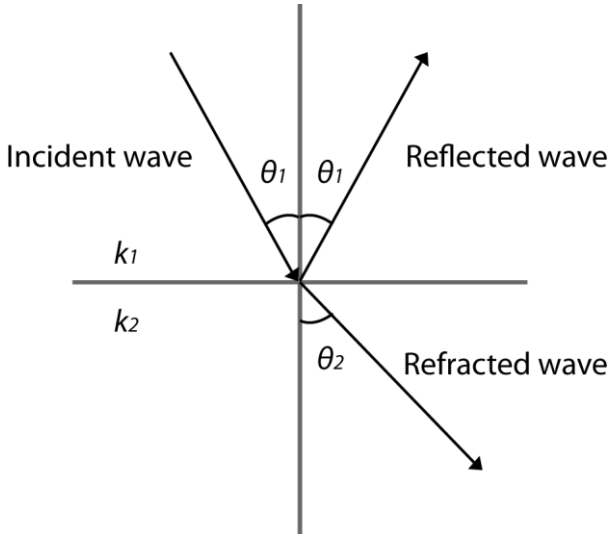

Figure 2.3: Transmission and reflection of an EM signal at the surface of the Earth illustrating Snell's Law.

When EM signals in the atmosphere enter the Earth, the transmission can be described using Snell's Law (Figure 2.3). The common definition of Snell's Law is given by:

$$k_1 sin\theta_1 = k_2 sin\theta_2, \tag{2.18}$$

where k_1 and k_2 are the wavenumbers of the incident wave and the refracted wave, respectively. θ_1 and θ_2 are the angles of the incident and the refracted waves, respectively.

Snell's Law can be applied to the diffusion of EM signals in the Earth by the use of complex wavenumbers. The wavenumber of an EM signal is dependent on the frequency of the wave. In the case of MT signals, because the frequency is relatively low, the displacement current is ignored and the EM signal propagates through diffusion in the Earth. In this case, the wavenumber, k_2, of the EM signal in the Earth can be approximated as

$$k_2 = \sqrt{-i\omega\mu\sigma}, \tag{2.19}$$

where ω is the angular frequency, μ is the magnetic permeability, σ is the electrical conductivity. Because the Earth is much more conductive than the air, the wavenumber of the incident wave is much smaller than that of the refracted wave ($k_1 \ll k_2$). As a result, θ_2 is a very small number and the refracted EM wave travels in the Earth in an almost vertical direction. Moreover, only a small fraction of the energy of the EM signal transmitted into the Earth. However, this is sufficient for the MT method to work.

2.5. Definitions of quantities used in MT

2.5.1 Skin depth

In working with MT data, it is essential to understand how deep the EM signals are travelling into the Earth. It has been demonstrated that the EM signals propagate diffusively in the Earth in section 2.3. In other words, the Earth is sampled volumetrically.

The part of the Earth that can be sampled is determined by the skin depth, which is defined as the depth at which the amplitude of the EM signal has decreased to *1/e* of the amplitude at the surface. For a homogenous earth with resistivity ρ, the skin depth is given by:

$$\delta(f) = \sqrt{\rho/\pi f \mu} \tag{2.20}$$

where f is the frequency, μ the magnetic permeability which is generally set to the free space value ($\mu_0 = 4\pi \times 10^{-7}$ H/m) in the absence of magnetic materials.

From Equation (2.20) it can be seen that the depth of penetration of electromagnetic signals decreases with increasing frequency (Figure 2.4). The way that EM signals propagate in the Earth is different from the seismic signals. The portion of the subsurface that can be imaged with MT method extends from the surface to a depth of one skin depth equation. In contrast, seismic signals propagate in the Earth as waves. Therefore, the seismic method is more sensitive to sharp interfaces than MT.

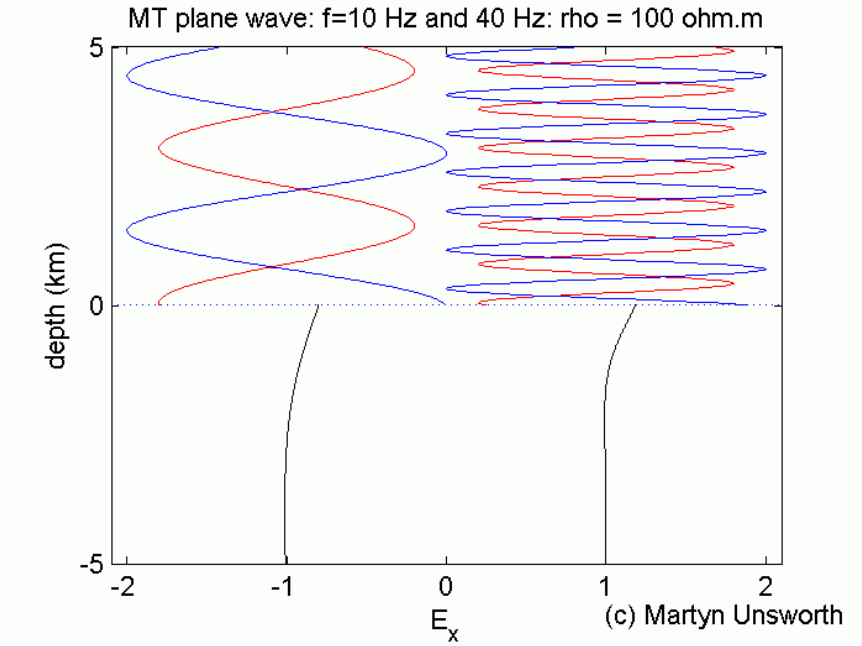

Figure 2.4: Illustration of the penetration of electromagnetic waves in the Earth with different frequencies[2]. The surface of the Earth is at depth of zero. The EM signals travel as plane waves in the air and diffuse in the Earth.

2.5.2 Magnetotelluric Impedance

In order to extract information about the electrical resistivity of the Earth from MT observations, we need to remove information about the absolute value of the incident electromagnetic field. This can be done through the calculation of the impedance. The impedance is a quantity that relates the electric field and magnetic field and contains information about the electrical resistivity of the Earth. It is defined as

$$Z_{xy}(\omega) = \frac{E_x(\omega)}{H_y(\omega)} \tag{2.21}$$

[2] Figure from https://sites.ualberta.ca/~unsworth/MT/MT.html

where $E_x(\omega)$ represents the electric field in the *x* direction, $H_y(\omega)$ represents the magnetic field in the *y* direction, and ω is the angle frequency. In MT, the *x* direction is defined as geographic north and the *y* direction is defined as the geographic east. Using the equations shown in section 2.3, the electromagnetic field at any time (t) and depth (z) can be shown with a wave number (k_1) and the electrical field at the earth's surface (E_s):

$$E_x(z,t,\omega) = E_s e^{-k_1 z} e^{-i\omega t}, \tag{2.22}$$

$$H_y(z,t,\omega) = \frac{1}{iw\mu_0} E_s(-k_1) e^{-k_1 z} e^{-i\omega t}, \tag{2.23}$$

where E_s is the amplitude of the electromagnetic signal at the surface of the Earth, ; μ_0 is the magnetic susceptibility in free space; k_1 is the wave number of the EM signal transmitted in the Earth. Wave number is a value that characterizes the damping of the EM signal. It is a real number when the EM signal is travelling in the air but a complex number when the EM signal for MT source propagates in the Earth by diffusion. It can be proved that:

$$k_1 = \sqrt{\frac{-i\omega\mu_0}{\rho_1}}, \tag{2.24}$$

There are many common terms in Equation 2.22 and 2.23; thus, the impedance can be rewritten as:

$$Z_{xy}(\omega) = \frac{E_x(\omega)}{H_y(\omega)} = \frac{-i\omega\mu_0}{k_1} = \sqrt{-i\omega\mu_0\rho_1}\,, \tag{2.25}$$

From the Equation 2.25, it can be seen that the impedance does not depend on the amplitude of the EM signal but only on the electrical resistivity of the subsurface (ρ_1). The impedance is a complex number since both $E_x(w)$ and $H_y(w)$ are complex numbers. In a general case (3-D), the electric and magnetic field has components in both *x* and *y*

directions. In this case the impedance has four components: $Z_{xx}(\omega)$, $Z_{xy}(\omega)$, $Z_{yx}(\omega)$, and $Z_{yy}(\omega)$, which are defined as :

$$\begin{pmatrix} E_x(\omega) \\ E_y(\omega) \end{pmatrix} = \begin{pmatrix} Z_{xx}(\omega) & Z_{xy}(\omega) \\ Z_{yx}(\omega) & Z_{yy}(\omega) \end{pmatrix} \begin{pmatrix} H_x(\omega) \\ H_y(\omega) \end{pmatrix} \tag{2.26}$$

Equation (2.26) can be expanded as

$$E_x(\omega) = Z_{xx}(\omega)H_x(\omega) + Z_{xy}(\omega)H_y(\omega) \tag{2.27}$$

$$E_y(\omega) = Z_{yx}(\omega)H_x(\omega) + Z_{yy}(\omega)H_y(\omega) \tag{2.28}$$

If the electrical resistivity structure of the Earth is 1-D, where the electrical resistivity changes only with depth, the electric and magnetic fields in the *x* and *y* directions should be same. Moreover, the impedance should have the same off-diagonal values $Z(\omega)$ and zero diagonal values (Chave and Jones, 2012). Equation (2.27) and (2.28) should be identical and Equation (2.26) can be written as

$$\begin{pmatrix} E(\omega) \\ E(\omega) \end{pmatrix} = \begin{pmatrix} Z(\omega) & 0 \\ 0 & -Z(\omega) \end{pmatrix} \begin{pmatrix} H(\omega) \\ H(\omega) \end{pmatrix} \tag{2.29}$$

In a 2-D case, the off-diagonal values will have different values. The diagonal values are zero only when the *x* or *y* direction is coincident with the strike of the subsurface electrical structure. In this case, Equations (2.27) and (2.28) can be rewritten as

$$\begin{pmatrix} E_x(\omega) \\ E_y(\omega) \end{pmatrix} = \begin{pmatrix} 0 & Z_{xy}(\omega) \\ Z_{yx}(\omega) & 0 \end{pmatrix} \begin{pmatrix} H_x(\omega) \\ H_y(\omega) \end{pmatrix} \tag{2.30}$$

Depending on the polarization of the EM field in the 2-D case, the components of the impedance tensor can be identified as either the TE (transverse electric) or TM (transverse magnetic) modes (Figure 2.5). The TE mode represents the component of the EM field in

which the electric current flow is parallel to the strike direction, whereas the electrical currents are perpendicular to the strike direction in the TM mode. Usually, the *xy* component is rotated to the strike direction and identified as the TE mode in 2-D MT. Similarly, the *yx* component is identified as the TM mode. For the convenience of analyses, sometimes the average of the two modes is calculated and the averaged impedance can be used to represent the subsurface electrical structure.

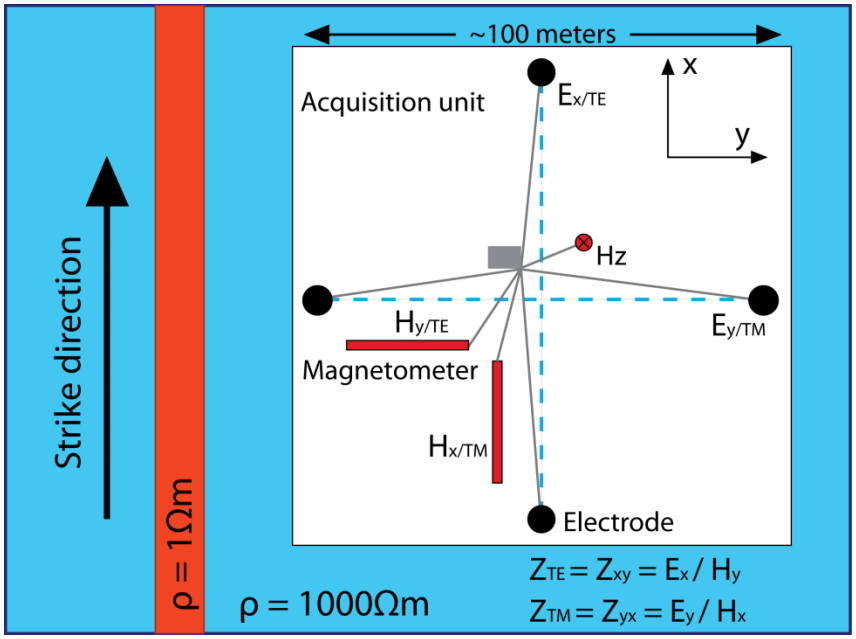

Figure 2.5: Illustration of the TE (transverse electric) mode and TM (transverse magnetic) mode field components in a 2-D scenario. The 2-D electrical resistivity model contains an infinitely long conductor located in a resistive background. The x direction is rotated to be same as the strike direction which is the same as the direction of the maximum current flow.

2.5.3 Apparent resistivity

It can be shown that the impedance contains information about the resistivity of the Earth (Chave and Jones, 2012). For a uniform half space Earth with resistivity ρ, the magnitude of the impedance $Z(\omega)$ can be expressed as:

$$|Z(\omega)|^2 = \omega\mu_0\rho(\omega) \tag{2.31}$$

where μ_0 is the permeability of free space ($4\pi\times10^{-7}$ H/m), ω is the angular frequency. It is clear from Equation (2.31) that the impedance is only dependent on the properties of the Earth. It should be noted that the EM fields sample the Earth volumetrically and attenuate the Earth with the length scale of the skin depth. Therefore, in a uniform half space Earth, a hemisphere of radius δ centered at the measuring point is sampled. In this case, the resistivity defined in Equation (2.31) is equal to the true resistivity of the Earth.

In the real world, however, the resistivity of the Earth is heterogeneous i.e. it varies with depth and or horizontal position. The region sampled by the EM signal will not be a perfect hemisphere and the resistivity in Equation (2.31) can be considered as an average value over the sampled volume. This average is defined as the apparent resistivity ρ_a as:

$$\rho_a(\omega) = \frac{1}{\omega\mu_0}|Z(\omega)|^2 = \frac{1}{\omega\mu_0}\left|\frac{E(\omega)}{H(\omega)}\right|^2 \tag{2.32}$$

The apparent resistivity changes with the angular frequency ω, which gives the depth resolution of MT method.

2.5.4 Impedance Phase

The MT phase (φ) is the phase of the impedance. For a uniform half space Earth, the phase of $Z\,(\omega)$ can be expressed as:

$$\varphi(\omega) = tan^{-1}[Z(\omega)] = tan^{-1}\left[\frac{E(\omega)}{H(\omega)}\right] \tag{2.33}$$

It can be shown that the phase of the impedance is the phase difference between the electric and magnetic field.

$$\varphi(\omega) = \varphi_E - \varphi_H \tag{2.34}$$

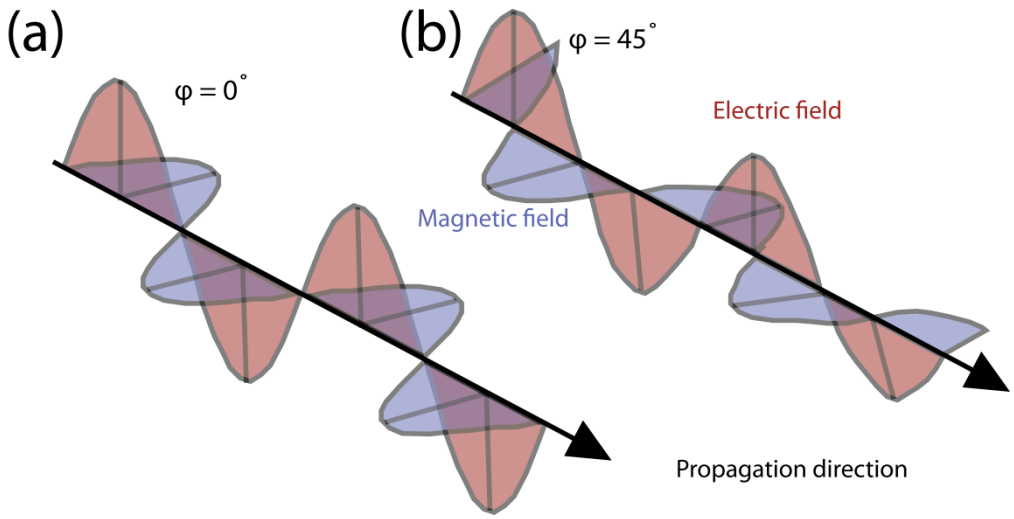

Figure 2.6: (a) The propagation of EM signal in the air as a wave (φ = 0°) and (b) in a uniform half space diffusively (φ = 45°) and the relationship of the electric and magnetic field. Not that the amplitude of the EM signal in a uniform half space (φ = 45°) get smaller because of attenuation.

For an EM wave travelling in free space, where the resistivity is infinitively high, the phase is zero (Figure 2.6). In a uniform conductive half space, the phase of the EM signals

will be *45°*. The phase can be related to the apparent resistivity through the approximate equation:

$$\varphi \approx \frac{\pi}{4}\left(1 - \frac{\partial \log \rho_a}{\partial \log T}\right) \tag{2.35}$$

From Equation (2.35), it is obvious that the phase should be larger than *45°* when the apparent resistivity decreases with period and vice versa. Moreover, in a 1-D or 2-D resistivity structure, it can be shown that the phases should lie in the first or the third quadrant ([0°, *90°*] or [*180°, 270°*]). This feature can be used to distinguish 1-D and 2-D structure from more complex 3-D or 2-D anisotropic structure, although near surface galvanic distortion and current channeling should also be considered.

2.5.5 Tipper and induction vector

The induction vectors are the plots of the tipper ($T_{zx}(\omega)$, $T_{zy}(\omega)$), which is a transfer function that relates the horizontal and vertical components of the magnetic field ($H_x(\omega)$, $H_y(\omega)$, and $H_z(\omega)$).

$$\mathrm{H_z}(\omega) = \mathrm{T_{zx}}(\omega)\mathrm{H_x}(\omega) + \mathrm{T_{zy}}(\omega)\mathrm{H_y}(\omega) \tag{2.36}$$

The vertical magnetic field is generated by the lateral variation of resistivity if the source is a plane wave. In this case, it is only non-zero when a 2-D or 3-D resistivity structure is present (Figure 2.10). A nonzero-tipper is a good indicator of lateral resistivity change. The real and imaginary components of the tipper can be projected to the *xy* plane separately and plotted as induction vectors.

$$\overrightarrow{T_{Real}(\omega)} = \left(Real\left(T_{zx}(\omega)\right), Real(T_{zy}(\omega))\right) \tag{2.37}$$

$$\overrightarrow{T_{Imag}(\omega)} = (Image(T_{zx}(\omega)), Image(T_{zy}(\omega))) \quad (2.38)$$

In this thesis, the induction vectors are the real components of the tipper and are plotted point away from conductors, according to the Wiese convention (Wiese, 1962).

2.5.6 Phase tensor

The phase tensor approach was developed by Caldwell et al. (2004) to extract information from the impedance that eliminated distortion by unresolvable near-surface small-scale structures (i.e., galvanic distortion, described in section 2.8). Another advantage of the phase tensor is that it is independent of the dimensionality of the structure because it is not based on the assumption of 1-D or 2-D structures. The phase tensor (Φ) is defined as:

$$\emptyset = X^{-1}Y \quad (2.39)$$

where *X* and *Y* represent the real and imaginary parts of the impedance tensor *Z*.

The phase tensor is usually displayed to demonstrate two pieces of information: (1) directionality as the phase tensor ellipses and (2) the β skew values as color fill(Figure 2.11). The phase tensor ellipses contain information about the strike direction in a 2-D case or the directions of the maximum and minimum inductive currents in a 3-D case. Furthermore, it was noted that the major axes of the phase tensor ellipse should be coincident with the induction vectors in a 2-D case (Caldwell et al. 2004). (1) In a 1-D scenario, the phase tensor ellipse should be a circle. (2) In a 2-D scenario, the phase tensor ellipse should be elongated with β skew values equal to zero in ideal MT data without

errors. (3) In a 3-D scenario, the phase tensor ellipse should be elongated with non-zero β skew values.

The skew values are related to the dimensionality of regional resistivity structure. Very small skew values (smaller than the error) are necessary to identify 1-D or 2-D resistive structure. Large skew values always indicate 3-D or 2-D anisotropic structure. It was suggested that a skew value smaller than 3˚ to be the acceptable upper limit for the justification of 2-D interpretation (Booker, 2013).

2.6. Synthetic examples

In order to illustrate these definitions, two synthetic models were built and analyzed. The first one (model A) contains a prism shaped conductor which represents a 2-D electrical resistivity structure (Figure 2.7a). The second one (model B) contains an L-shaped conductor which represents a 3-D electrical resistivity structure (Figure 2.7b).

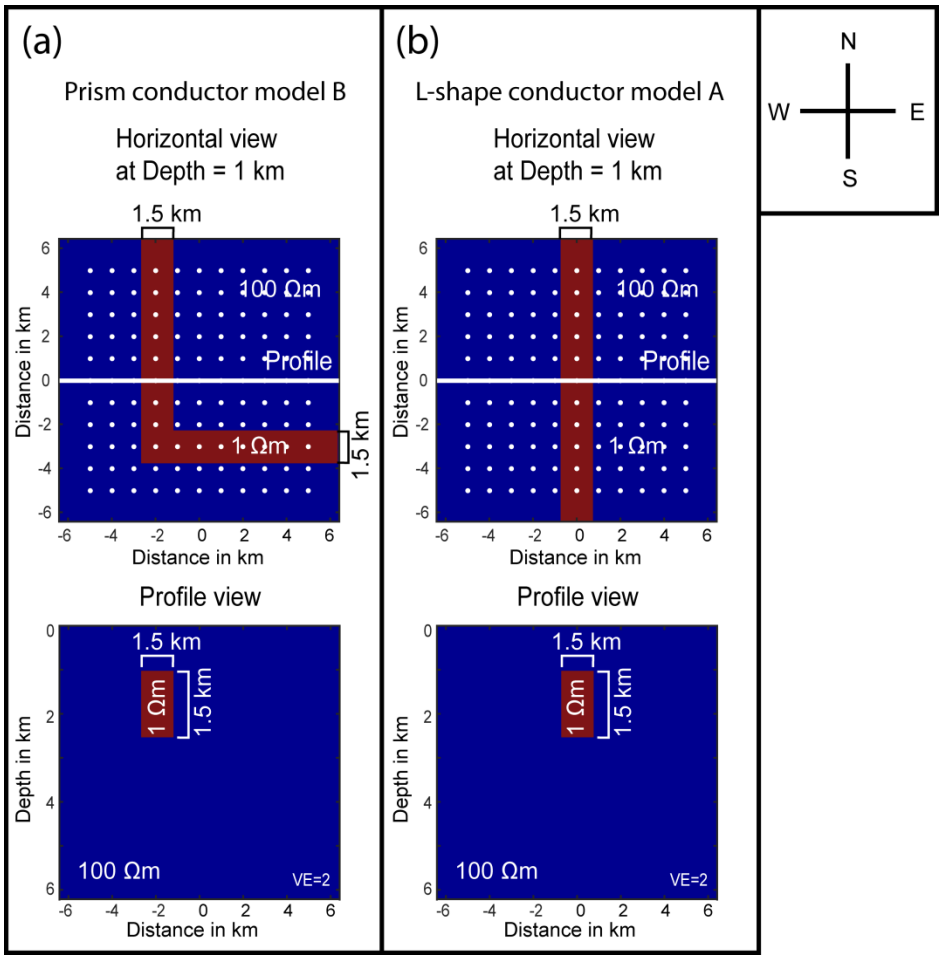

Figure 2.7: Synthetic models with a prism conductor (model A) and an L-shape conductor (model B). The geometry of the models is shown with horizontal view (top) and vertical profile view (bottom).

The conductor in the synthetic model A has a width of 1.5 km and a thickness of 1.5 km as well. Its upper boundary is at 1 km depth (Figure 2.7a). The background resistivity of the model was 100 Ωm, and the resistivity of the conductor is 1 Ωm. The L-shaped conductor in the synthetic model B has a width of 1.5 km in both horizontal directions and extends horizontally to the edges of the synthetic model (Figure 2.7b). The thickness of the conductor is 1.5 km. The top of the conductor is at 1 km depth. The background resistivity of the model is set to 100 Ωm, and the resistivity of the conductor is 1 Ωm.

2.6.1 Map views of apparent resistivity and phase

Map views of the averaged off-diagonal apparent resistivities and phase of model A and B at various frequencies are shown in Figure 2.8 and 2.9, respectively. The apparent resistivities and phases in the map views show the approximate location of the conductors in both models A and B, even though its shape is not correct. In the 2-D case (model A), the apparent resistivity and phase doesn't vary along the strike direction of the prism conductor. In the 3-D case (model B), the phases are very close to 45° at periods of 0.01s where the MT signals are not sensitive to the conductor and the sampled Earth are close to a half space. When the conductor is sensed, the phase values increase to >45°. This is in agreement to the relationship described in Equation 2.31. In the map views of the averaged resistivity and phase, the approximate location of the conductors can be identified but the shape of the anomaly is not the same as the original model. Moreover, the depth of the conductors cannot be determined by observing the map views of the apparent resistivity and phase. This shows that an inversion scheme is necessary to recover the subsurface structure.

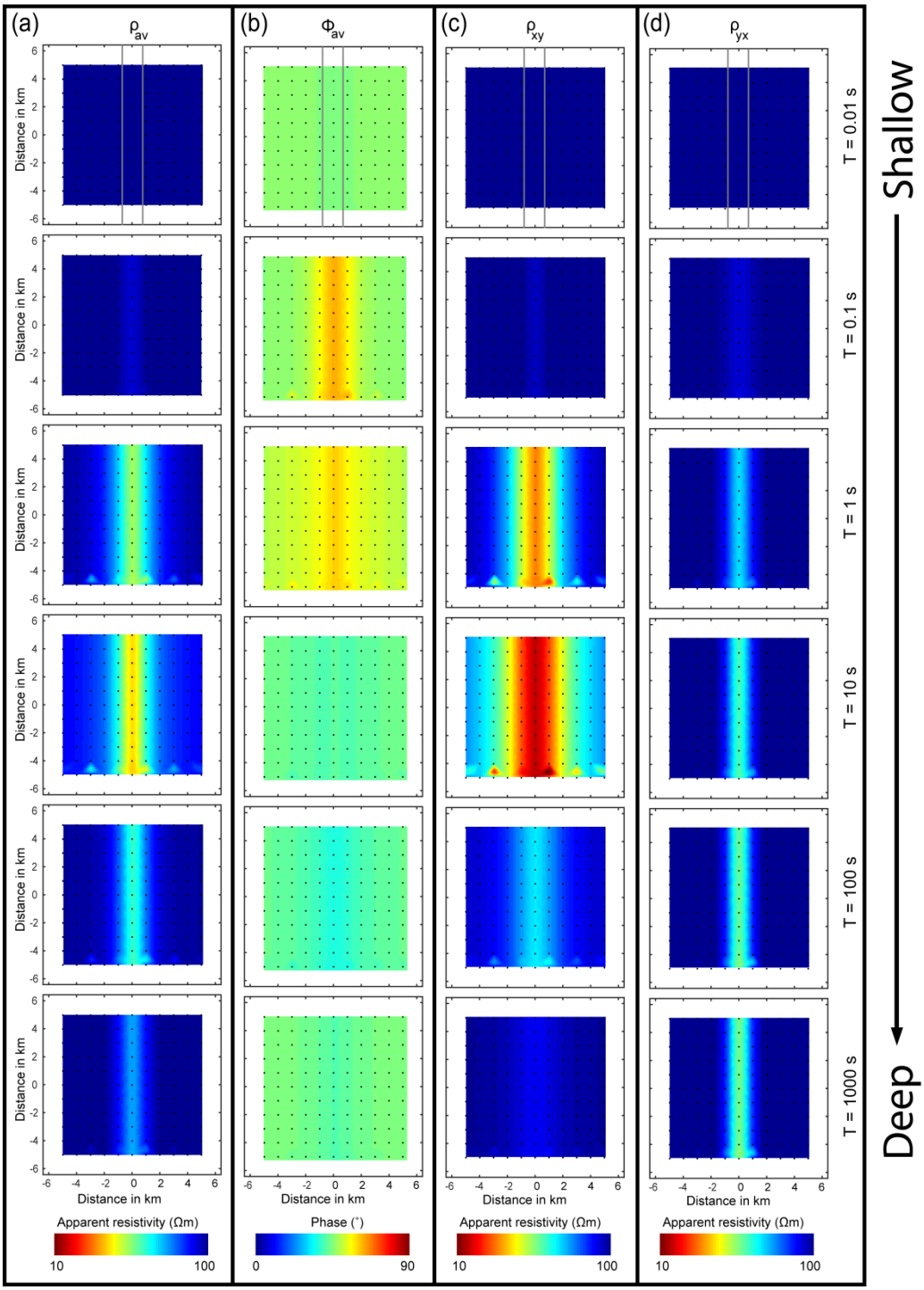

Figure 2.8: Plots of the apparent resistivity and phase of the response of the prism conductor model at period of 0.01-1000 s in map view. The grey lines mark the boundary of the conductor. The black dots represent the location of MT stations. Definitions: ρ_{xy}, the apparent resistivity of the xy component; ρ_{yx}, the apparent resistivity of the yx component; ρ_{av}, the averaged apparent resistivity of the xy and yx components; Φ_{av}, the averaged phase of the xy and yx components.

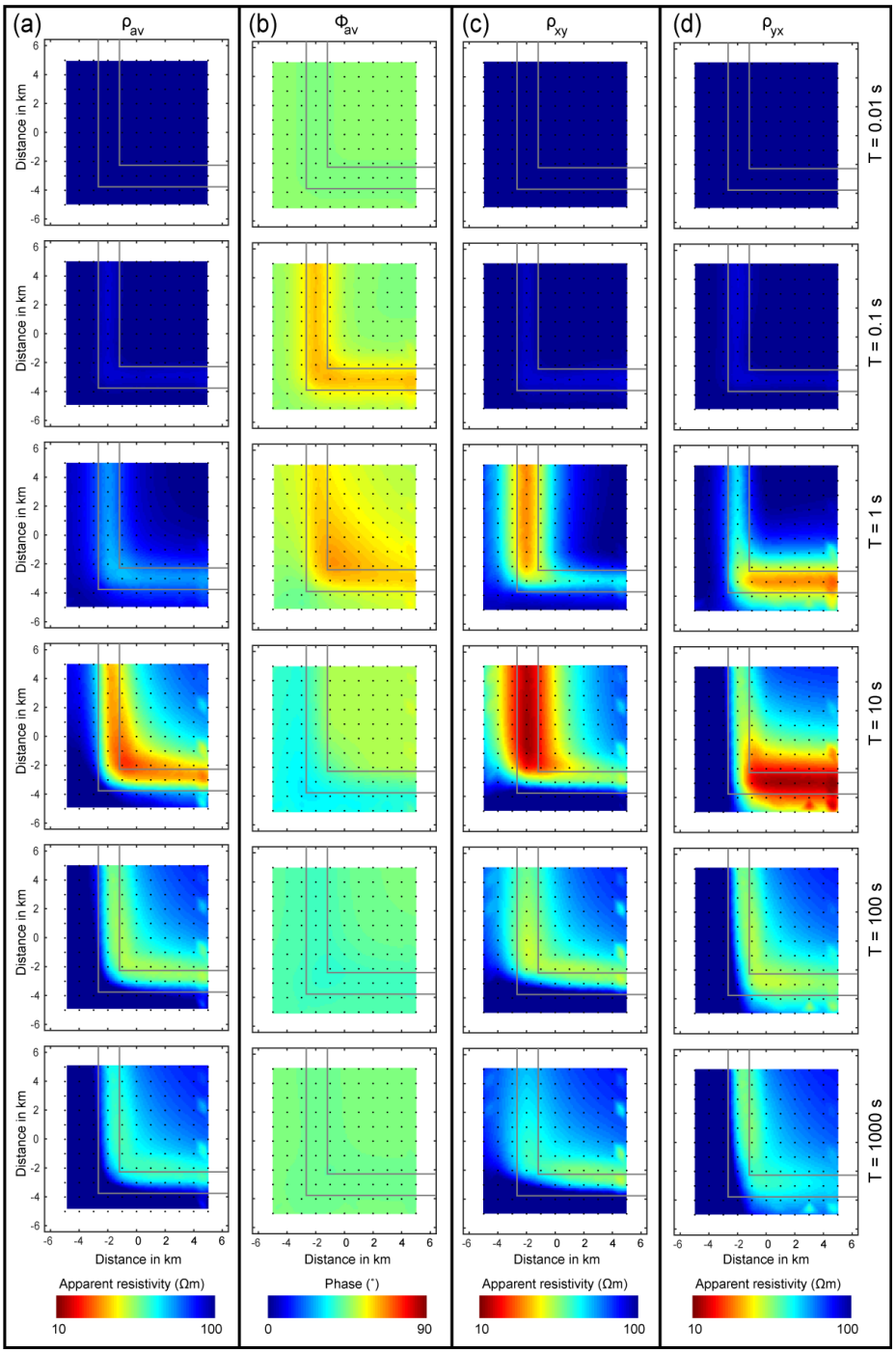

Figure 2.9: Plots of the apparent resistivity and phase of the response of the L-shape conductor model at period of 0.01-1000 s in map view. The grey lines mark the boundary of the conductor. The black dots represent the location of MT stations. Vertical exaggeration (VE) of the profile was set to 2. Definitions: ρ_{xy}, the apparent resistivity of the xy component; ρ_{yx}, the apparent resistivity of the yx component; ρ_{av}, the averaged apparent resistivity of the xy and yx components; Φ_{av}, the averaged phase of the xy and yx components.

2.6.2 Plots of induction vectors

Figure 2.10 is an example of tipper plots using the response of the two synthetic models. For the periods of 0.1/1000 s, the tippers are very small which indicates that the EM signal of these periods are not sensitive to the conductor. In contrast, for the periods of 1/10/100 s, the tippers show regional trends and are pointing away from the conductor. In the 2-D case with model A, the induction vectors are perpendicular to the boundary of the prism conductor which is not the case for the model B.

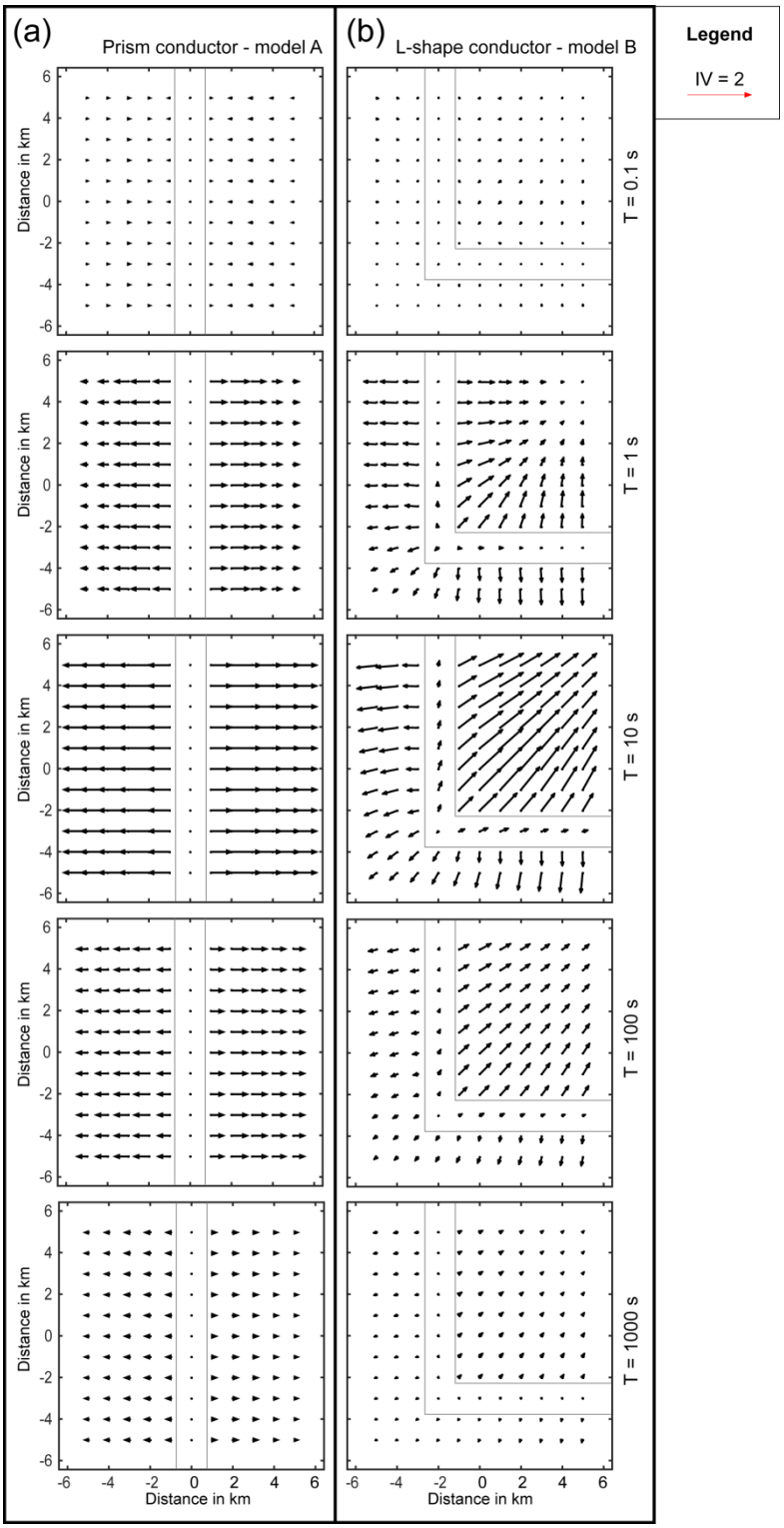

Figure 2.10: The real induction vectors for the two synthetic models. The model with a prism represents a 2-D structure (a) and the model with an L-shaped conductor represents a 3-D structure (b). The gray lines mark the boundaries of the conductors. The induction vectors point away from the conductor in Weise convention (Wiese, 1962).

2.6.3 Plots of pseudo-sections

In order to compare the change of the apparent resistivity, phase, and tipper with period of the two models, pseudo-sections of these along the profiles in Figure 2.7 are shown in Figure 2.11. It can be seen that the pseudo-sections of the 2-D prism model A is symmetrical with respect to the strike direction of the prism conductor. Moreover, the values of T_{zx} of the prism model A are zero. In contrast, the pseudo-sections of the 3-D L-shape conductor model are not symmetrical and the tippers values are not zero in either T_{zx} or T_{zy}.

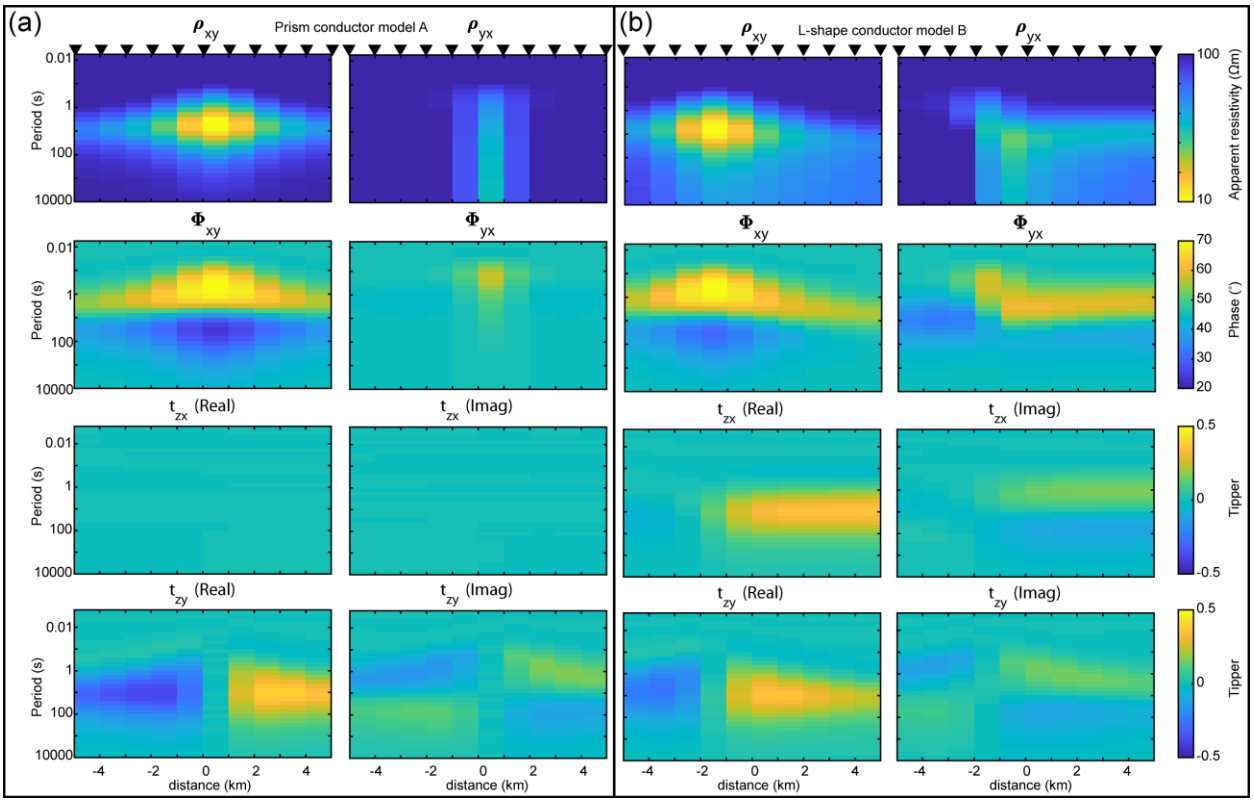

Figure 2.11: Pseudo-sections of apparent resistivity, phase, and tipper of the two synthetic models along the profiles shown in Figure 2.7. The model with a prism represents a 2-D structure (a) and the model with an L-shaped conductor represents a 3-D structure (b). Triangles mark the location of MT sites.

2.6.4 Plots of phase tensors

The phase tensors of the synthetic models are shown in Figure 2.12. Similar to the observation of the induction vectors at period of 0.1/1000 s for the two synthetic models, the phase tensors show 1-D feature because the signal at these periods are not sensitive to the conductor. In contrast, the phase tensors of the model B at periods of 1/10/100 s, show 2-D or 3-D features. The 3-D feature of model B is the most prominent at the period of 10 s and along the edges of the L-shape conductor. The phase tensors of the model A at periods of 1/10/100 s show 2-D features only because the skew angle values are zero. A zero skew angle value indicates 1-D or 2-D electrical resistivity structure only.

It is worth noting that the orientation of the major axis of the phase tensors changes from east-west to north-south in the period band 1-10 s. This change happens at the period of which the EM signal is sensitive to the upper boundary of the conductor. Possible reason may be the change of the direction of induction currents. At a period of 10 s, the major induction currents flow in the prism conductor and the long axis of the phase tensor ellipse may be the same as the major induction currents flow. In contrast, at the period of 0.1 and 1 s, the long axis of the phase tensor ellipses may be perpendicular to the prism.

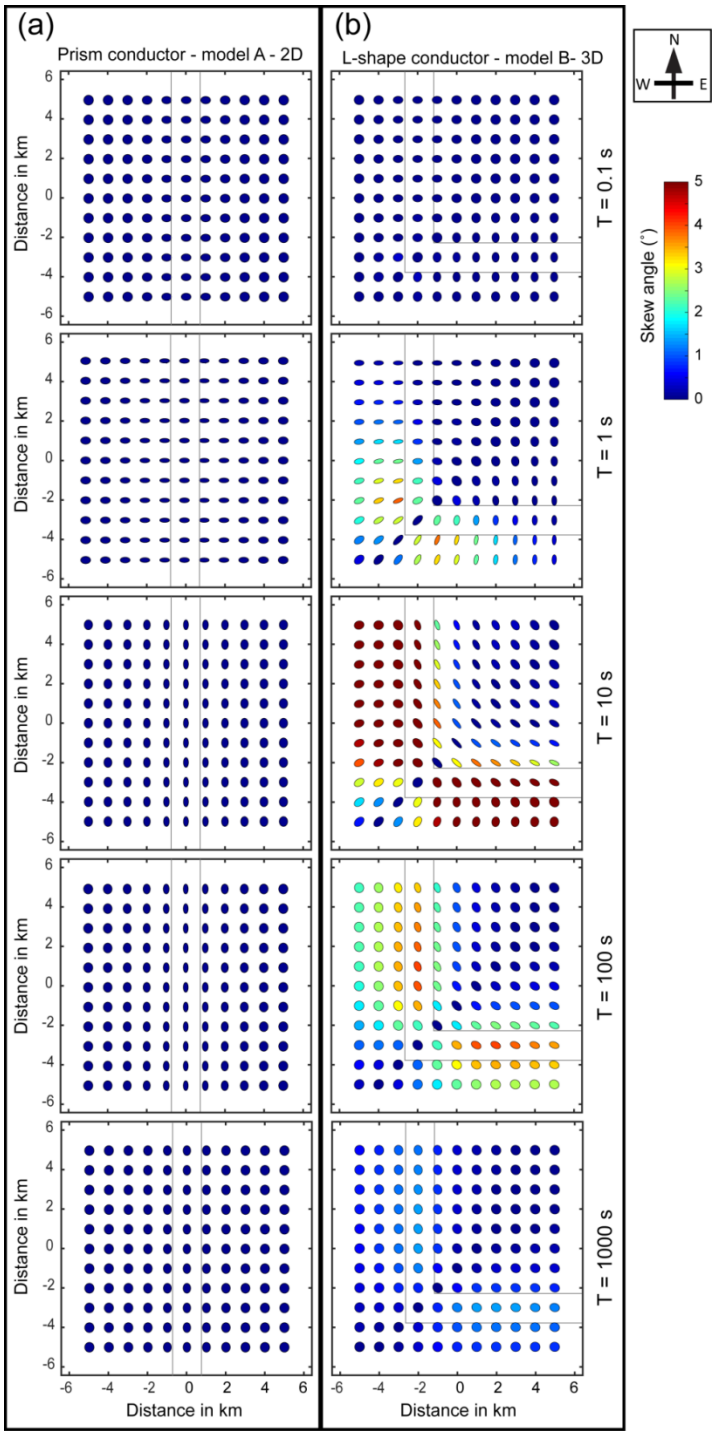

Figure 2.12: Phase tensors of the two synthetic models at periods from 0.1 s to 1000 s. The model with an L-shaped conductor represents a 3-D structure (a) and the model with a prism represents a 2-D structure (b). The gray lines mark the boundaries of the conductor. The shapes of the ellipses are indicative of the electrical strike information and the color fill of the ellipses is the skew angles.

2.7. Electrical anisotropy

In electrically anisotropic materials, the resistivity varies with the direction of electric current flow (Wannamaker, 2005). This is different from an electrically isotropic material where the resistivity is the same in all directions and can be represented by a scalar value of ρ_{iso}.

The resistivity values of an anisotropic material (ρ_{anis}) can be expressed in tensor form instead of a scalar for an isotropic material (Martí, 2014).

$$\rho_{anis}(x, y, z) = \begin{pmatrix} \rho_{xx} & \rho_{xy} & \rho_{xz} \\ \rho_{yx} & \rho_{yy} & \rho_{yz} \\ \rho_{zx} & \rho_{zy} & \rho_{zz} \end{pmatrix} \tag{2.40}$$

where *x, y, z* are defined in Cartesian coordinates with the origin at any point of the Earth, and *x* defined as north , *y* defined as east and *z* vertically downwards.

The non-diagonal components of the resistivity tensor represent the deviation of the anisotropic axes from the Cartesian axes. When the resistivity tensor is rotated to the anisotropic axes using Euler's elementary rotation, it can be represented with 6 unknowns that include the rotation angle for the three directions and $\rho_{x'x'}$, $\rho_{y'y'}$, $\rho_{z'z'}$.

$$\rho_{anis}(x', y', z') = \begin{pmatrix} \rho_{x'x'} & 0 & 0 \\ 0 & \rho_{y'y'} & 0 \\ 0 & 0 & \rho_{z'z'} \end{pmatrix} \tag{2.41}$$

Electrical anisotropy can be detected in measured MT data in several ways. However this can be a non-unique and complicated task.

(a) It was suggested that phase splits (difference of the impedance phase in the *xy* and *yx* components) observed over a large area can be indicative of electrical anisotropy (Heise and Pous, 2001).

(b) Phase tensor analysis can also be used to identify anisotropy (Liddell et al., 2016). Large skew values of the phase tensor were interpreted to be related with either 3-D or 2-D anisotropic structures. This occurs because anisotropic structures may deflect the current flow and result in large skew values.

(c) In a 2-D isotropic case, the induction vectors should be either parallel or perpendicular to the axis of the phase tensor. The axis of the phase tensor indicates the direction of major current flow. When the induction vectors are observed to deflect away from the axis of the phase tensor, a 3-D structure or anisotropic structure may be present. Therefore deflection of induction vectors from the axis of the phase tensors was another way to identify electrical anisotropy (Wannamaker, 2005).

(d) Out of quadrant phases can be another indicator of electrical anisotropy because of the deflection of currents due to anisotropy, which was discussed by Heise and Pous (2003) and Pek and Verner (1997).

Electrically anisotropic crustal structure was first proposed to exist in Alberta by Boerner et al. (2000). This is because the 2-D isotropic MT inversion model they obtained was characterized by many small conductive bodies located in the gaps between MT stations. Addition of extra MT stations resulted in the conductors moving into the new gaps. It was expected that a single large conductor should have been imaged. This phenomenon was discussed by Nieuwenhuis et al. (2014) using an MT dataset collected in southern

Alberta. It was shown that a 3-D isotropic model could equally fit the MT data collected by Boerner et al. (2000) and that electrical anisotropy was not necessary to interpret the MT data in central Alberta. In another study in the Fort McMurray region of northern Alberta, Liddell et al. (2016), showed that 2-D electrical anisotropy structure at 4-5 km depths was required to interpret the measured MT data. Therefore, researchers should be cautious when interpreting MT data because an electrically anisotropic structure can be difficult to distinguish from a 3-D isotropic structure.

2.8. Static shift and galvanic distortion

Static shift is a change in the amplitude of the electric field that produces a frequency independent shift in the apparent resistivity of MT data. The change in the electric field amplitude is caused by conductive or resistive bodies that are small in terms of skin depth and unresolvable inductively with the highest frequency MT data.

Galvanic distortion is a more general term and involves changes in both the direction and amplitude of the electric fields (Chave and Smith, 1994). It was demonstrated that the galvanic distortion could be described by a real distortion tensor, and only the amplitude of the MT impedance is affected (Bahr, 1988). Galvanic distortion makes it difficult to use the shifted apparent resistivity values for further analysis and interpretation. If the distortion is not removed from the impedance data, subsequent analysis and inversion can result in an unrealistic resistivity model.

A number of methods have been proposed to remove static shift from the apparent resistivity data. Jones (1988) proposed a statistical approach that can be applicable for regions with one homogenous layer which is recognized before the interpretation of MT

data. In this method, the modal value of the homogenous layer was considered as a criterion to remove static shift. Rodi and Mackie (2000) published a 2-D MT inversion scheme that estimated static shifts as part of the model. Many methods have been proposed to remove galvanic distortion and extract the undistorted data. The phase tensor analysis method developed by Caldwell et al. (2004) to extract information that was not influenced by the galvanic distortion. Groom and Bailey (1989) developed a tensor decomposition that recovered the principle axes of induction, and estimated the degree of distortion in terms of parameters with a physical meaning. Groom-Bailey (GB) method was further developed by McNeice and Jones (2000) to handle multiple stations and frequencies.

2.9. Current channeling

Current channeling is another type of distortion caused by regional large-scale conductivity discontinuities (Figure 2.13; Jones, 1983). Because of the high conductivity contrast across the electrical discontinuity, some currents on the more conductive side are deflected near the interface and electric charges can develop on the interface. Thus, the MT data recorded near the discontinuities can be distorted. It can cause problems when trying to interpret the distorted MT data with a 1-D or 2-D resistivity model. It was suggested that the effect of the current channeling could be ignored, only when the MT station is farther than the 'equilibrium distances' from the conductivity discontinuity (Jones, 1983). Therefore, it is important to collect MT data far enough from the discontinuity to permit a valid 2-D or 1-D interpretation. If it is impossible to get MT data farther than the 'equilibrium distances', then a 3-D method must be utilized to reliably interpret the MT data.

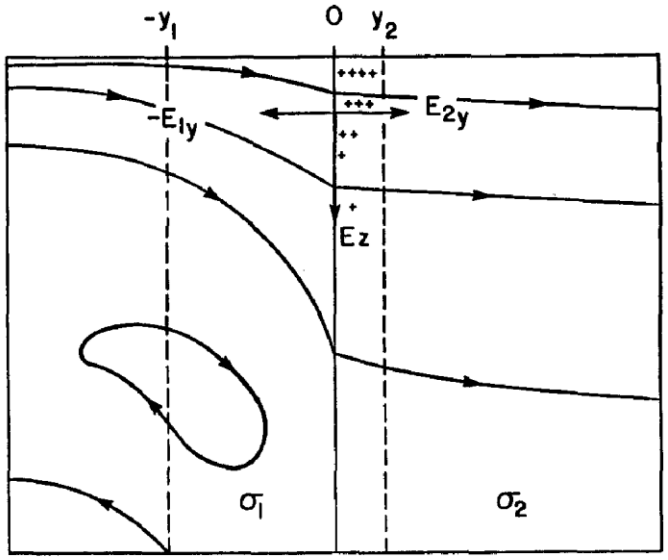

Figure 2.13: Illustration of electrical field (represented by current lines) and surface charge distributions across a vertical electrical boundary that separates materials with different conductivities ($\sigma_1 > \sigma_2$). Figure from Jones (1983).

A synthetic 3-D resistivity model was developed to illustrate the concept of current channeling and out-of-quadrant phases using the WinGLink software (Figure 2.14). The synthetic resistivity model has three features.

(1) The background resistivity is high (1000 Ωm).

(2) There is a large (16 km wide by 150 km long) and thin conductor (1 Ωm) at the surface (0-1 km) in the right-top corner.

(3) Another small conductor (1 Ωm) is located just below the surface conductor in the depth range 1-3 km.

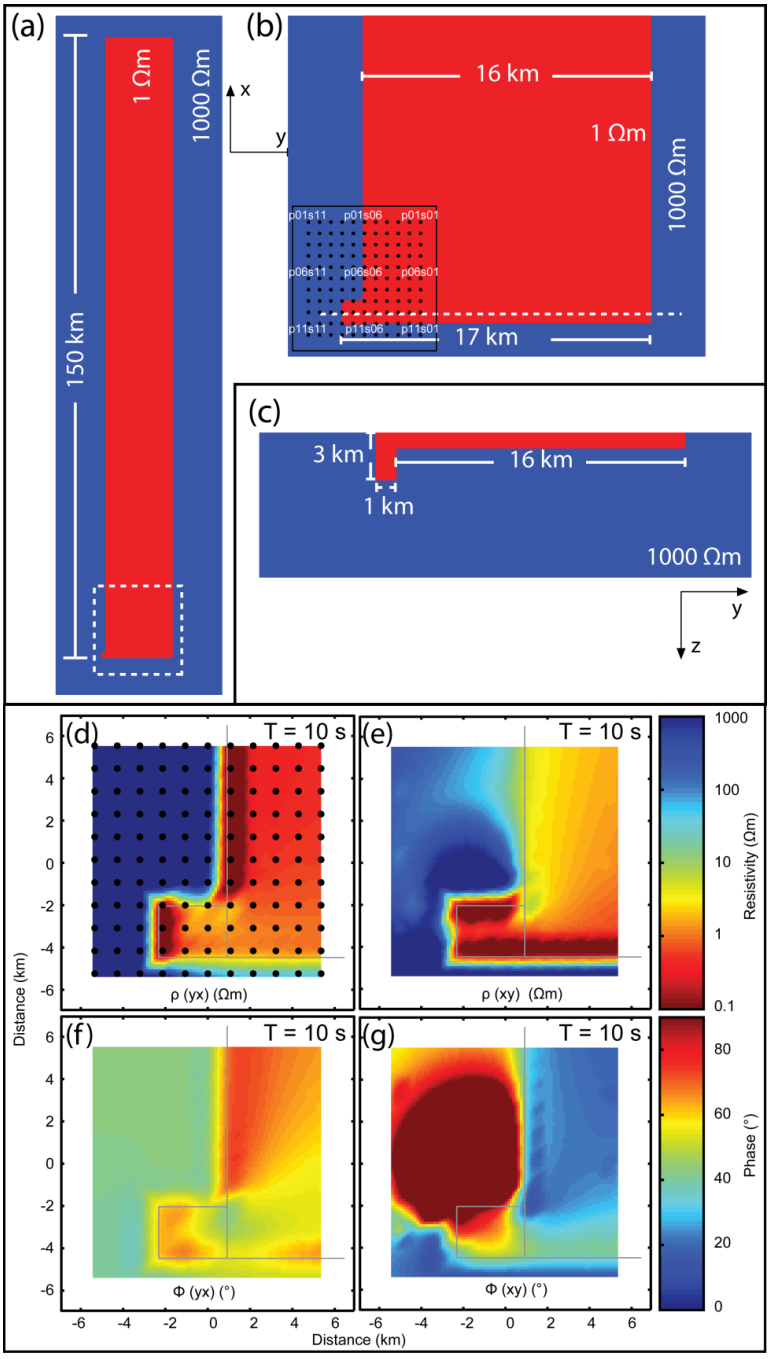

Figure 2.14: The synthetic model with a full view of the conductor (a), a detailed view at one end with a small conductor attached at one corner (b), and a profile view (c). This model generates out-of-quadrant phases as shown at the bottom. The box with dashed line represents the location of figure (b). The dashed line shows the location of the profile in figure (c). Figure (d) and (e) is the interpolated resistivity map at the period of 10 seconds. Figure (f) and (g) is the interpolated phase map at the period of 10 seconds. Black dots in figure (d) and (d) represents MT sites. It is obvious that out-of-quadrant phases (>90˚) are all distributed in the more resistive side of the model.

The map view of the phase (Figure 2.14) demonstrates that all the out-of-quadrant phases are within the more resistive side of the model and the inner corner of the two conductors. This is result of current channeling in the model. The typical resistivity and phase curves of two stations in the synthetic model are shown in Figure 2.15. The phases of the *xy* component near to the corner of the conductors are out of quadrant. Site p06s06 shows out-of-quadrant phases. The out-of-quadrant phases are caused by sudden and large increase of the phase values. This means the apparent resistivity deceases at this location according to Equation 2.35. Apparent resistivity is positively correlated with electrical field strength (Equation 2.32) which would imply that the electrical field is weak in this corner. In a 2-D case such as the prism synthetic model shown in section 2.6, there would be no out of quadrant phases even at the sharp boundary of the conductor. This leads to the speculation that 3-D effects are causing the out of quadrant phases in this synthetic study. It is possible that strong current flow in the x direction out of the small conductor cancels with the current flow out of the long conductor and a region of weak electrical field occurs in this scenario.

Interestingly, this feature is similar to what is observed in MT data collected in Alberta and southeast British Columbia. The WCSB is similar to the top conductor which is on the top of the resistive basement. Nearly all of the MT stations with out-of-quadrant phases used in this study are located out of the WCSB.

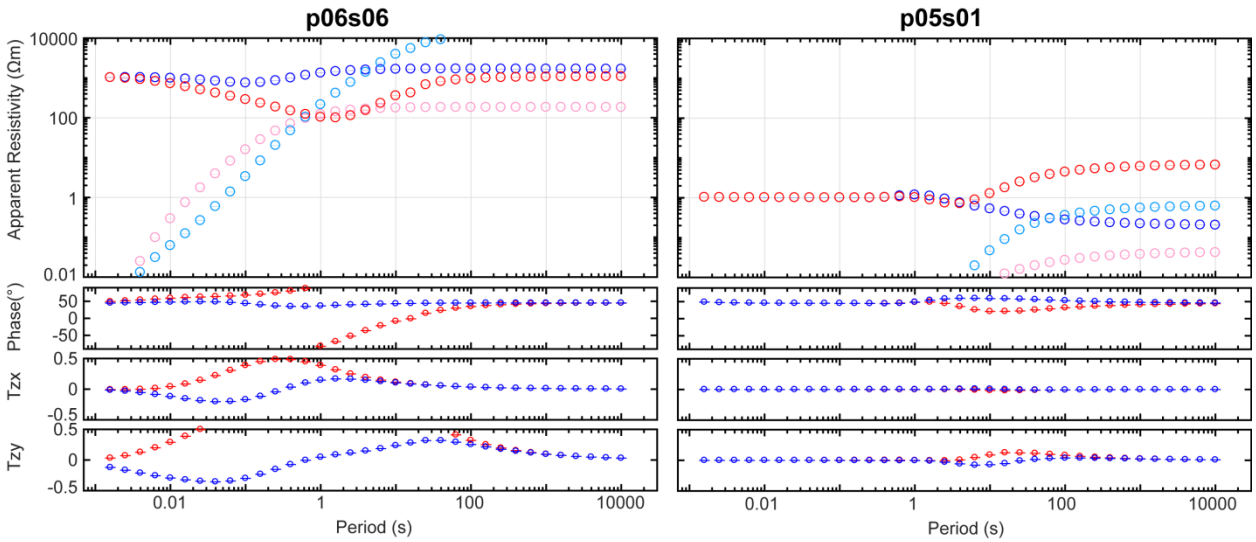

Figure 2.15: The apparent resistivity and phase and tipper of two typical stations (p06s06 and p05s01) from the synthetic model shown in Figure 2.14.

2.10. Strike and dimensionality analysis of MT data

It is important to carefully inspect measured MT data before the start of inversions and interpretation, because this type of data analysis can give important information about the general features of the data and indicate the complexity of the subsurface resistivity structure. Furthermore, because the 2-D inversion methods assume the geoelectric structure to be two dimensional, a specific geoelectric strike direction needs to be determined before the start of 2-D MT inversions.

Many methods have been proposed to determine the strike / dimensionality of MT data, including:

- induction vector analysis (Wiese, 1962; Parkinson, 1962),
- Swift skew (Swift, 1967),

- Bahr skew (Bahr, 1988),
- phase tensor analysis (Caldwell et al., 2004),
- and GB tensor decomposition (Groom and Bailey, 1989).

In this thesis, induction vectors, phase tensor analysis, and GB tensor decomposition are used.

2.10.1 Tensor decomposition

The tensor decomposition method used in this thesis was developed by McNeice and Jones (2000). This method is an extension of Groom and Bailey (1989) that is referred widely as GB decomposition. The GB decomposition is basically a factorization of the impedance tensor that recovers the principle axes of induction, and quantifies the degree of galvanic distortion (Groom and Bailey, 1989). In contrary, the conventional methods, such as the Swift skew which finds the strike direction by minimizing the diagonal elements of the measured impedance tensor, is invalid when there is galvanic distortion.

The GB decomposition assumes the regional structure is 2-D. The measured impedance is decomposed into a twist tensor, shear tensor, a scaled regional 2-D impedance tensor, and a rotation tensor in GB decomposition. The scaled regional 2-D impedance tensor represents the actual regional 2-D impedance tensor scaled by a site gain and an anisotropy tensor which are undeterminable in this method. The decomposition process is done by minimizing the least-squared misfit between the data and the decomposed model (McNeice and Jones, 2000). The principle axes of induction are the rotation angle contained in the rotation tensor. It should be note that there is an inherent

90° ambiguity in the strike angle, and other geophysical or geological results should be considered to decide the strike angle.

The conventional GB decomposition method has to be applied to the MT data frequency-by-frequency and site-by-site. Therefore, it is difficult to determine the suitable strike angle for all the sites and frequencies. McNeice and Jones (2000) presented a method to do the GB decomposition statistically with multiple stations and multiple frequencies. This is very useful to determine the regional strike direction for certain period ranges.

The tensor decomposition was applied to the synthetic model A and B mentioned above (Figure 2.7). The results of the prism model A is much simpler than the results of the model B. In the 2-D case of model A, the strike directions of the MT stations are consistent. The inherent 90° ambiguity is observed because the bars plotted are perpendicular to the strike direction of the prism conductor. The r.m.s. misfit, shear and twist values of model A are all zero.

In the result of model B, it is observed that the results are symmetric along the central axis of the L-shape conductor. High r.m.s. misfits are observed around the L-shapes and concentrated near the corner. High twist and shear values are observed also but they are not located at the same location. Because synthetic MT data are used, the ambiguity in the strike angle can be overcome and it should be the angles perpendicular to the short lines shown in the Figure 2.16 and 2.17.

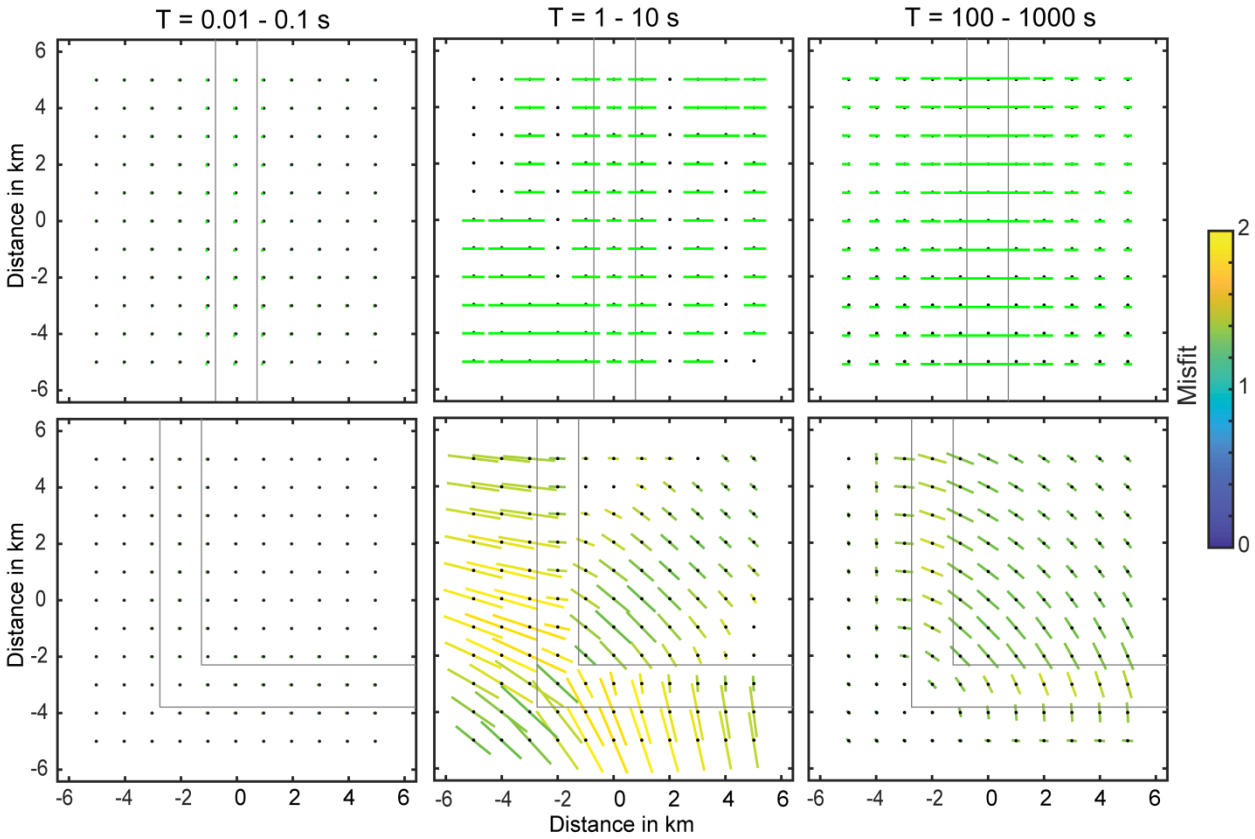

Figure 2.16: Tensor decomposition results of the two synthetic models' responses in map view at three period ranges: 0.01-0.1 s, 1-10 s, and 100-1000 s. The gray lines mark the boundaries of the conductor. The strike angles should be perpendicular to the short bars shown in the maps. The colors of the bars are r.m.s. misfit values of the tensor decomposition.

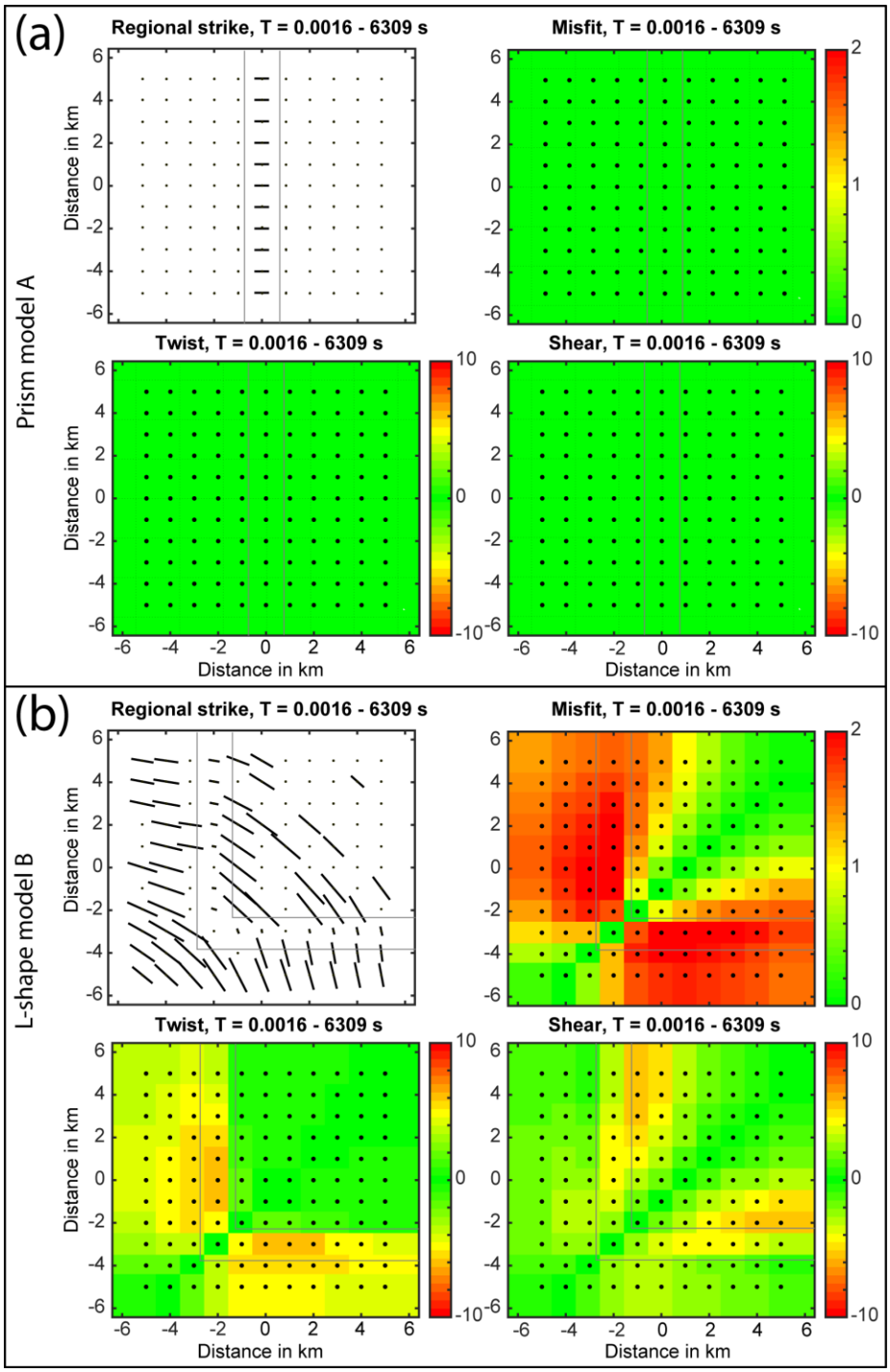

Figure 2.17: Tensor decomposition result of the two synthetic models' response in map view at periods from 0.0016 s to 6309 s. The gray lines mark the boundaries of the conductors.

2.11. Magnetotelluric modeling and inversion methods

A model of the subsurface resistivity is a straightforward way to interpret MT data. The resistivity model is expected to reproduce the observed MT data which also confirms the reliability of the model. Complicated computation needs to be done to find the best resistivity model. In MT, this process solves both forward modeling and inverse modeling iteratively.

2.11.1 Forward modeling

In MT, forward modeling is the calculation of the synthetic MT response d_s from a known resistivity model m. A forward operator F is needed to relate the predicted response (apparent resistivity, phase, impedance) to the resistivity model. The operator F is sought by solving Maxwell's Equations described in section 2.3 of this chapter.

$$d_s = F(m) \tag{2.42}$$

In the simplest case with a 1-D resistivity model, this problem can be solved using analytic expressions. Numerical methods, such as finite difference, finite element or integral equations, are needed to solve the forward problem when the resistivity model is 2-D or 3-D (Čuma et al., 2017).

2.11.2 Inverse modeling

Inverse modeling is the process of finding a resistivity model m from a set of observed data using the operator Equation (2.42). The goal is to find a resistivity model (m) that gives a statistically acceptable fit of the predicted data (d_s) to the measured data (d_m). Inverse modeling is ill-posed, i.e., the solution model is non-unique in MT inversions. To

overcome the non-uniqueness, a regularization method, which penalize between the overall r.m.s. misfit and the roughness of the inversion model, is used (Constable et al., 1987).

Mathematically this can be written as a minimization of the equation:

$$J = \|W_d(d_s - d_m)\|^2 + \tau\delta(m) \tag{2.43}$$

where W_d is the weighing matrix that weighs the data according to their standard errors; $\|W_d(d_s - d_m)\|^2$ is the least square misfit function; $\delta\ (m)$ is a parameter related to the model roughness; τ is the regularization parameter that controls the trade-off between the model misfit and the model roughness.

2.11.3 1-D MT inversion

The MT inverse problem is non-linear and requires more complicated schemes to solve than linear inverse problems. Linear problems are expressed in functions with no exponential greater than one, while non-linear problems are related to functions with exponential larger than one. To take advantage of the well-established linear inverse methods, researchers proposed some simplified linearized inversion algorithms to solve MT inverse problems. These included the 1-D solutions from Wu (1968) and Jupp and Vozoff (1975). These inversion methods begin with a starting model that is best guess to the structure. The model is updated through a series of iterations to reduce the r.m.s. misfit between the measured MT data and the predicted response of the inversion model. However these methods were often dependent on the starting model being close to the true model. In other cases extremely unrealistic rough models were obtained. For instance, Parker (1980) proved that all MT sounding curves could be fit with a model of many thin,

highly conductive layers embedded in highly resistive half-space. This problem is related to the non-uniqueness nature of MT inversions. Weidelt (1985) gave a good reason for the non-uniqueness, and showed that it is impossible to constrain the conductivity at a certain depth. The quantity that can be constrained is the conductance, which is a depth-integrated conductivity (inverse of the resistivity). Supposing there is a layer of constant resistivity ρ and thickness h, the conductance (c) of this layer can be calculated by equation

$$c = h/\rho. \tag{2.44}$$

A major step forward in MT inversion was proposed by Constable et al. (1987) who implemented regularized solutions for 1-D inversions, as described above in section 2.11.2. This method was referred to as OCCAM method, and a regularization method was used to obtain a smooth model with minimum structure. This method avoids over fitting of the MT data and produces more realistic resistivity models. A similar idea was demonstrated by Smith and Booker (1988) which showed minimum structure in the inversion model should be sought and equal fitting on all the frequency bands should be achieved.

2.11.4 Bostick transformation

The 1-D inversion methods mentioned above require some computational resources. In order to reduce the time / memory consumption of the 1-D inversions, some alternative methods were developed, such as the Niblett approximation (Niblett and Sayn-Wittgenstein, 1960), the Schmucker scheme (Schmucker, 1970), and the Bostick transformation (Bostick, 1977). These methods are not true inversion schemes but give the approximate resistivity-depth distribution using less computational resources. It was

demonstrated that the Bostick and Niblett schemes are essentially the same by Jones (1983).

The Bostick transformation (BT) was used by Jones et al. (2014) to produce continental-scale resistivity maps of Canada at depths corresponding to upper crust to the mantle. This was done by first calculating depth-resistivity curves at each MT sites. Then, the resistivity values of all stations at a certain depth were interpolated laterally. In this way, the resistivity map of the whole area at this selected depth was obtained. This approach has the advantage that it requires very little computational resources, and a large scale map could be obtained in a few minutes on a desktop computer. In contrast, it could take several weeks or months using a fully 3-D MT inversion algorithm. However, it should be noted that the resistivity maps are low-resolution because it is an approximate method and interpolation is applied.

The Bostick scheme transforms the apparent resistivity-period curve to a resistivity-depth distribution using the equations listed below.

$$\rho_B(h) = \rho_a(T)\frac{1+m(T)}{1-m(T)} \tag{2.45}$$

$$h = \sqrt{\frac{\rho_a(T)T}{2\pi\mu_0}} \tag{2.46}$$

$$m(T) = \frac{dlog(\rho_a(T))}{dlog(T)} \tag{2.47}$$

where ρ_a represents the apparent resistivity, T is the period, ρ_B is the transformed resistivity at the penetration depth h, m(T) is the gradient of the apparent resistivity curve on a log-log scale (Jones, 1983).

Some synthetic modeling was done in this study and one case is shown in Figure 2.18. A synthetic 1-D resistivity model is built firstly. Secondly, the response of the synthetic model is calculated analytically. Then the BT is applied to get a depth-resistivity distribution. Finally, the response of the BT result is calculated as in the second step. From the Figure 2.18, it can be seen that the responses of the BT results are close to the real responses of the synthetic model. The BT could image the low resistive layers better than the high resistive layers.

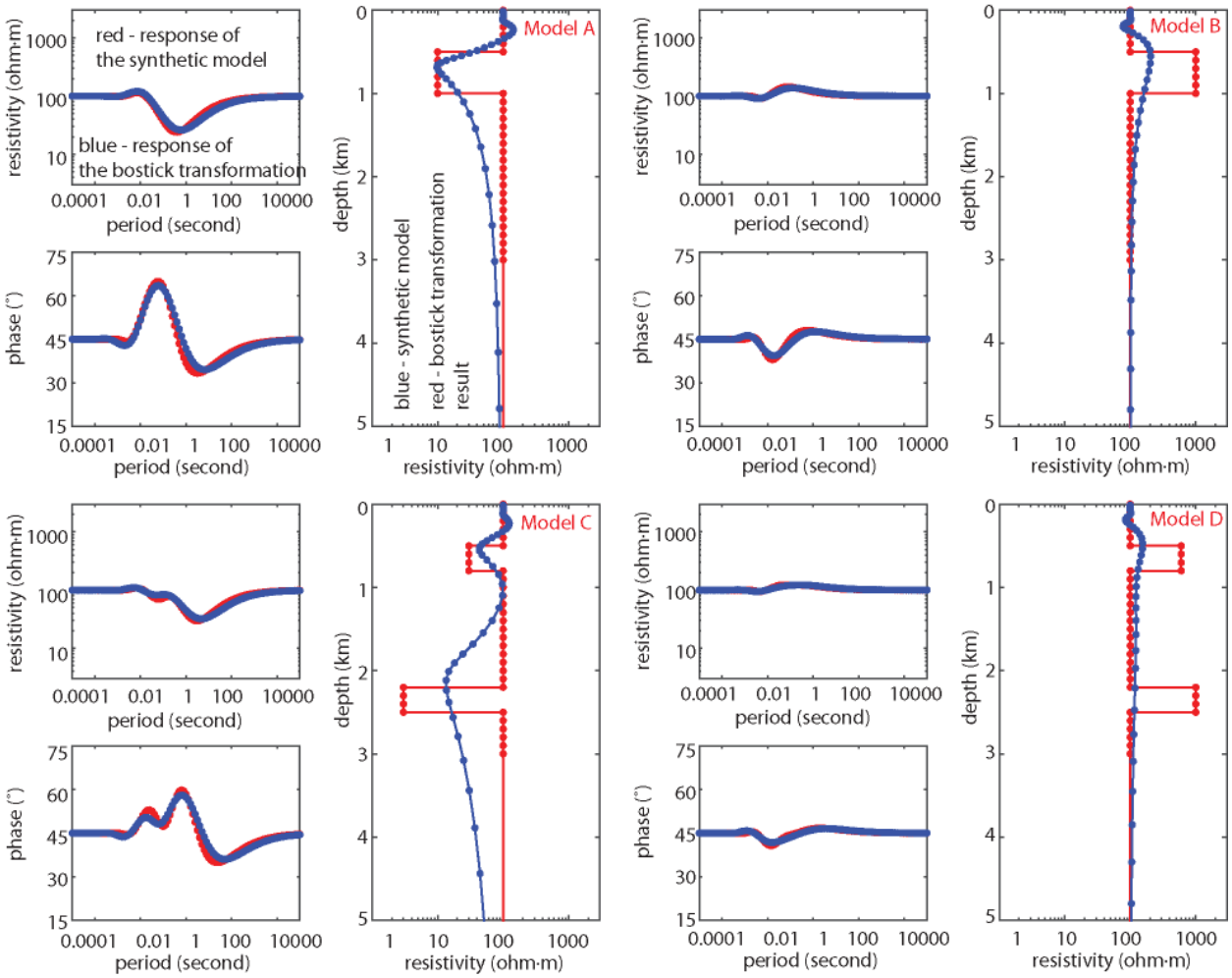

Figure 2.18: Comparison of synthetic 1-D models (red) and BT result (blue). Four different models are constructed. In all models, the background resistivity is 100 Ωm. Model A has one low resistive layer, model B has one high resistive layer, model C has two low resistive layers, and model D has two resistive layers.

2.11.5 2-D MT inversion

In 2-D MT inversions, similar algorithms used in 1-D MT inversion were applied, such as Jupp and Vozoff (1977), Jiracek et al. (1987), Madden and Mackie (1989), deGroot-Hedlin and Constable (1990, 2-D OCCAM), Smith and Booker (1991, 2-D RRI), Mackie et al. (1993).

Efforts have been made to improve the computing speed of 2-D inversions. The RRI method of Smith and Booker (1991) tried to speed the 2-D inversion process by using approximate sensitivities. Another major achievement was that Siripunvaraporn and Egbert (2000) proposed a method (referred to as REBOCC method) which transforms the matrix to be inverted from the model space to the data space. This transformation results in a smaller matrix to handle and reduces the computational requirement compared to the other methods. This transformation was further developed into 3-D MT inversion codes (Siripunvaraporn et al. 2005) that are widely used now.

Moreover, a nonlinear conjugate gradient (NLCG) algorithm for 2-D MT inversions was proposed by Rodi and Mackie (2000). An NLCG scheme was applied in this algorithm to find the regularized solution as mention above. This algorithm is superior to the methods based on linear inversion schemes because it requires less computational resources and converges faster. This algorithm also included static shift calculations along with inversion of the resistivity model.

Furthermore, a 2-D algorithm developed by Pek and Verner (1997) could model electrically anisotropic structures. It gives the resistivity values in a general tensor form. Another 2-D anisotropic algorithm is an extension of the Rodi and Mackie's (2000) 2-D inversion program (Baba, et al., 2005). The latter program gives a different form of resistivity than the general format. It resolves three resistivity images for the along-strike, cross-strike and vertical resistivity components (Wannamaker, 2005).

2.11.6 3-D MT inversion

The development of 3-D MT inversion was impeded by the limited computational resources even though many inversion algorithms were proposed (Mackie and Madden, 1993; Zhdanov and Hursan, 2000; Farquharson et al., 2002; Avdeev, 2005). Because the 3-D RRI method (Smith and Booker, 1991) approximates some of the calculation into 1-D circumstances to reduce the computational consumption, it was widely used before the more recent WSINV3DMT and ModEM algorithm became available.

Three-dimensional inversions started to be more practical in the last decade because the computers are faster and algorithms are more efficient. The algorithm (referred as WSINV3DMT in this thesis) developed by Siripunvaraporn et al. (2005) is based on the regularized OCCAM method and is popular worldwide. It transforms the inversion matrices from the model-space to data-space. Because the number of model parameters is always greater than the number of data matrices in MT, this transformation reduces the required computational resources by making the matrix to be stored smaller. Moreover, it reduces the computational time by over 70% because a relaxed convergence criterion is applied.

More recently, Kelbert et al. (2014) developed the ModEM software package for 3-D inversions. In ModEM, a modular system of computer codes is applied to solve the EM inversion problems more efficiently. This inversion algorithm is also based on the data-space inversion as used in the WSINV3DMT.

2.12. Summary

In summary, the MT method is based on Maxwell's Equations and several assumptions have been applied to simplify the calculation. These include: the planar wave assumption, displacement currents can be ignored, and the assumption of no free charge. However, these assumptions may not be true for some situations. For example, the assumption of no free charge is valid only in a 1-D and the TE mode of a 2-D case. Charges can develop in the TM mode of a 2-D and all 3-D cases. Therefore, caution should be kept in mind to verify the assumptions when using MT.

The MT data collection is relatively easy and environmentally friendly because no transmitter is needed, and natural source EM waves are used as signal. MT method is a useful tool to find the electrical resistivity of the Earth from the surface of the Earth to the upper mantle depths. The electrical resistivity is representative of conducting phases such as water, melt, graphite or sulfite minerals. The MT data interpretation should consider the possible distortions, strike and dimensionality analysis and 1-D, 2-D and 3-D resistivity models could be constructed to show the complex electrical structure of the subsurface.

Chapter 3 : Geological setting and tectonic history

3.1. Geological setting

The crystalline basement rocks of Alberta are part of the North American Craton, which is also known as Laurentia. The core of Laurentia is composed of Archean cratons and Proterozoic terranes that were assembled during the Paleoproterozoic to form the continent found today (Hoffman, 1988; Figure 1.1). These rocks record a long tectonic history and vital information on how tectonics operated in the past.

However, direct study of these Precambrian basement rocks in Alberta is difficult because they are largely covered by the sedimentary rocks of the Western Canada Sedimentary Basin (WCSB; Wright et al., 1994). The WCSB comprises the Williston Basin to the southeast, the Alberta Basin at the center, and the eastern Canadian Cordillera to the west. In Alberta, the WCSB comprises a southwest-deepening wedge of sedimentary rocks with its greatest thickness of 6-7 km near the Rocky Mountain foothills. At the northeast corner of Alberta, the basement rocks are exposed at the surface (Figure 3.1). The ages of the sedimentary strata range from Mesoproterozoic to Cenozoic (Wright et al., 1994).

The sedimentary rocks of WCSB have been studied extensively during hydrocarbon exploration. However, the structure and history of the Precambrian basement rocks that underlie the WCSB are not as well understood. Furthermore, because of the extensive coverage of the basement by the WCSB, little direct geological mapping has been possible and geological studies of the Alberta basement are limited to lithological and geochronology studies of drill-core samples (Villeneuve et al., 1993). The crustal terranes

mapped in Alberta were defined mainly on the basis of geophysical potential field data in combination combined with U-Pb zircon and monazite isotopic dating of drill core samples (Ross et al., 1991; Villeneuve et al., 1993; Pilkington et al., 2000; Figure 3.1).

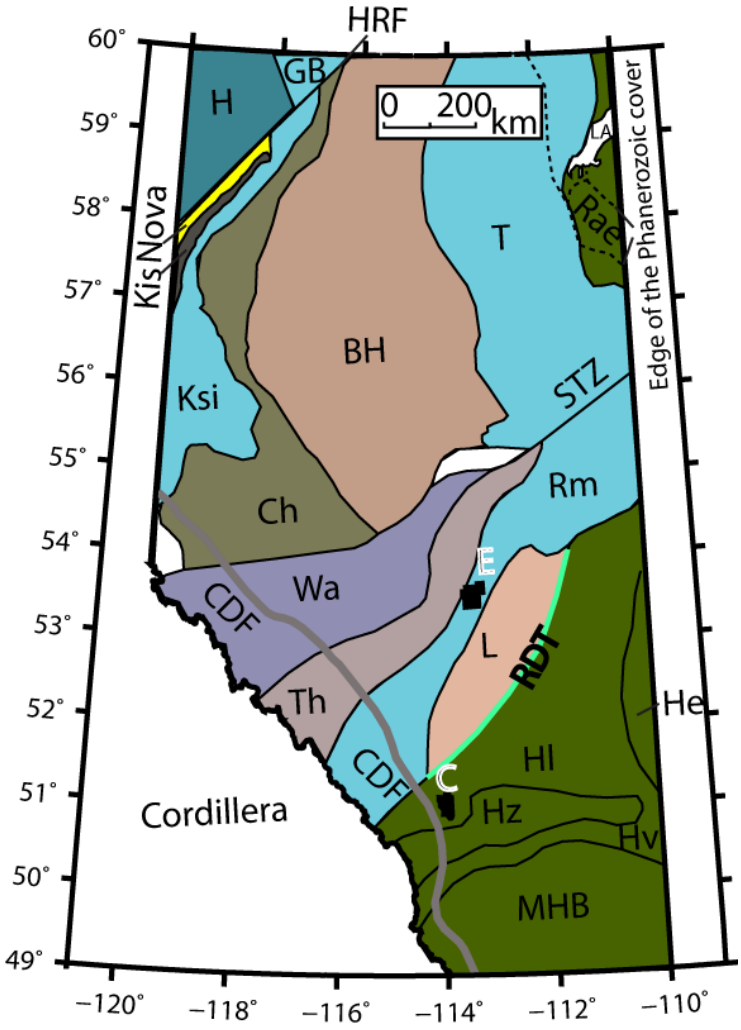

Figure 3.1: Tectonic map of the Precambrian terranes in Alberta basement (modified after Hoffman, 1988; Villeneuve et al., 1993; Ross et al., 1994; Pilkington et al., 2000). The thick gray line marks the Cordilleran deformation front. The dash line represents the edge of the Western Canada sedimentary basin. The two white characters mark the locations of Edmonton (E) and Calgary (C). Abbreviations: CDF, Cordillera Deformation Front; HRF, Hay River Fault; H, Hottah; GB, Great Bear; T, Taltson; Kis, Kiskatinaw; Ksi, Ksituan; BH, Buffalo Head; Ch, Chinchaga; Wa, Wabamun; Rm, Rimbey; STZ, Snowbird Tectonic Zone; Th, Thorsby; L, Lacombe; Hl, Loverna Block; Hz, Matzhiwin; He, Eyehill; Hv, Vulcan structure; MHB, Medicine Hat Block; RDT, Red Deer Trend; LA, Lake Athabasca.

3.1.1. Major tectonic features

Four transverse structural elements played an important role in the Proterozoic tectonic assembly of the Alberta basement (Figure 3.1). From the north to south these are: (1) the Great Slave Lake shear zone (GSLsz); (2) the Snowbird Tectonic Zone (STZ); (3) the Vulcan Structure (VS) and (4) the Great Falls Tectonic Zone (GFTZ). The GSLsz is a right-lateral fault associated with younger faults of the McDonald – Hay River fault (HRF) system. The STZ extends northeasterly from the Foothills of the Canadian Cordillera to Hudson's Bay and separates the Rae and Hearn provinces in the Canadian Shield. The STZ contains mylonitic rocks where it is exposed and, in Alberta, the Thorsby domain is considered to be an extension of the STZ which separates the Paleoproterozoic terranes in northwest Alberta from the Archean Hearn province (Ross, 2002). The basement terranes in central Alberta have clearly been influenced by the STZ (Villeneuve et al., 1993). The VS marks the northern structural boundary between the Medicine Hat block (MHB) and the Hearne craton and the GFTZ defines the boundary between the MHB and Wyoming Craton (Ross, 2002).

3.1.2. Tectonic terranes of the Alberta basement

The Alberta basement is composed of a number (17) of unique Precambrian tectonic terranes sutured together by past tectonic events (Figure 3.1). From the north to south, they are listed and described below.

(1) The Great Bear terrane is located to the north of the HRF. It is composed of calc-alkaline magmatic rocks and considered as a magmatic arc. Basement drill core samples

consist of granitic rocks and are dated as ca. 1.8 Ga but with large age uncertainties (Villeneuve et al., 1993).

(2) The Hottah terrane is located to the north of the HRF and west of the Great Bear terrane. It has ca. 1.9 Ga crust and is a major element of the Wopmay Orogen (Ootes et al., 2015). Drill core samples are mostly plutonic rocks and one calcsilicate gneiss with probable metasedimentary origin (Villeneuve et al., 1993).

(3) The Nova terrane is located next to the HRF and is believed to be composed of Archean age crust based on a mafic gneiss sample with an age of 2.80 Ga (Ross et al., 1991).

(4) The Ksituan terrane is located southeast of the Nova terrane and separated from the latter by the Kiskatinaw terrane. It is inferred to be a magmatic arc of 1.98-1.90 Ga age (Villeneuve et al., 1993).

(5) The Kiskatinaw terrane was identified as having the same age as the Ksituan terrane based on dating of granite samples. Considering the foliated and gneissic feature of the rocks from the Kiskatinaw terrane, the Kiskatinaw terrane was interpreted as being a deformed portion of the Ksituan magmatic arc (Villeneuve et al., 1993).

(6) The Buffalo Head terrane is located in central-northern Alberta and is a complex magmatic belt with metaplutonic and subordinate felsic metavolcanic rocks with crystallization ages of 2.0-2.32 Ga as determined by zircon geochronology. However, neodymium isotope data indicate that these Paleoproterozoic magmas were derived by reworking of pre-existing Archean crust that was extracted from the mantle at ca. 2.54-2.83 Ga (Villeneuve et al., 1993).

(7) The Taltson Magmatic Zone (TMZ) is located to the east of the Buffalo Head terrane and is composed of granitoids, metasedimentary gneisses, granitic basement gneisses, and

amphibolites. It is dominated by 1.99-1.93 Ga granitoid rocks (Chacko et al., 2000; McDonough et al., 2000).

(8) The Chinchaga domain separates the Ksituan and Buffalo Head terranes. It is composed of metaplutonic and metasedimentary gneisses dated between 2.09-2.18 Ga (Plint and Ross, 1993).

(9) The Wabamum domain is located at the southern boundary of the Chinchaga and Buffalo Head domains. The boundaries of the Wabamun domain were interpreted as fault zones. One drill core sample from the basement was dated with an age of 2.32 Ga (Villeneuve et al., 1993).

(10) The Thorsby domain is located south of the Wabamun and considered to be a splay of the STZ because of continuous aeromagnetic and gravity anomalies. Three drill core samples have been dated and yield an age of 1.9-2.4 Ga (Villeneuve et al., 1993).

(11) The Rimbey domain is located southeast of the STZ and interpreted as a magmatic belt (Villeneuve et al., 1993). The basement drill core samples are mostly biotite granite rocks that were dated between 1.85-1.78 Ga.

(12) The Red Deer Trend marks the southern boundary of the Lacombe Domain and corresponds to a narrow, positive aeromagnetic anomaly trending northeast. One red phyllite sample recovered from a drill core along the trend was dated with a maximum age of 2.30 Ga (Villeneuve et al., 1993).

(13) The Lacombe domain is located between the Red Deer Trend and the Rimbey domain. The zircon dating of the drill core sample was inconclusive (Villeneuve et al., 1993). The Lacombe domain is characterized by low-grade metavolcanic and metasedimentary rocks (Ross, 2002; Boerner et al., 2000).

(14) The Loverna Block does not have distinct features in the geophysical potential fields but is identified by the extent of the bordering domains. Core samples of the Loverna Block are mostly biotite granites with one sample of amphibolite and granitic gneiss. The Loverna block records both Archean (ca. 2.71 Ga) and Proterozoic (ca. 1.82 and 1.78 Ga) zircon and monazite magma crystallization ages but Nd isotope data indicate even the Proterozoic rocks have Archean crust formation ages (Villeneuve et al., 1993). The Loverna Block is considered as part of the Hearne province.

(15) The Eyehill High is located east of the Loverna Block and considered as another block within the Hearne province. The contact between the Eyehill High and the Loverna Block is inferred to be east-dipping (Ross, 2002). The basement intersections comprise Archean metaplutonic and gneissic rocks dated at 2.6-2.8 Ga.

(16) The Matzhiwin High is tentatively interpreted to be a magmatic belt. One single core sample from this domain is a biotite-hornblende granite which has a crystallization age of 2.6 Ga (Villeneuve et al., 1993).

(17) The Medicine Hat Block is the oldest domain of the Alberta basement with an U-Pb zircon age range of 2.6-3.3 Ga. It is separated from the Loverna Block and the Matzhiwin High to the north by the Vulcan Structure and from the Wyoming province to the south by the Great Falls tectonic zone. It is bounded by the Cordillera to the west and the Trans-Hudson Orogen to the east. Drill core samples are quartz diorite and granodiorite and yield neodymium crust formation ages of 2.86-3.48 Ga (Villeneuve et al., 1993).

3.2. Tectonic history of the Precambrian Alberta basement

Alberta is located in northwestern Laurentia (i.e. the North American craton), which has had a protracted Archean and post-Archean tectonic history (Hoffman, 1988; Ross, 2002). The oldest rocks on Earth are found in the Acasta gneiss complex of the Slave Craton, which date from the end of the Hadean Eon (>4 Ga; Stern and Bleeker, 1998; Bowring and Williams, 1999; Figure 1.1). The core of Laurentia, including the Alberta basement has survived the three supercontinent cycles that formed Columbia (ca. 1.8 Ga), Rodinia (ca. 1.0 Ga), and Pangea (ca. 0.3 Ga; Meert, 2012).

3.2.1. Archean cratons

The oldest elements of western Laurentia – the Slave, Rae, Hearn, Medicine Hat, and Wyoming cratons (Figure 1.1) were formed in the Archean Eon (4 - 2.5 Ga) based on geochronological data. They are considered as formerly independent microcontinents (Hoffman, 1988), even though their structure at the time of formation is not well known because younger Proterozoic tectonic events have largely overprinted structures (Ross, 2002). Typical Archean basement structures are observed in all of these provinces. They are composed of granite-greenstone terranes, or their high-grade equivalent, and covered by Early Proterozoic sedimentary rocks (Hoffman, 1988). These Archean provinces can be divided into two groups: (a) the Slave, Medicine Hat, and Wyoming provinces, which are intact crustal regions only marginally affected by Proterozoic assembly and; (b) the Hearne and Rae provinces, which have been modified significantly by subsequent tectonics (Ross, 2002; Schultz et al., 2007).

3.2.2. Paleoproterozoic terranes

Terranes that record Proterozoic (2.5-2.0 Ga) U-Pb ages include the Chinchaga, Buffalo Head, and Hottah terranes, etc (Figure 1.1). Most of these earliest Proterozoic terranes were built on Archean crust based on patterns of inheritance and Nd isotopic signatures (Ross, 2002), whereas the Hottah terrane is thought to have originated from juvenile Proterozoic crust (Bowring and Podosek, 1989). These crustal elements are mostly composed of magmatic rocks and their tectonic setting is generally unknown because they have been extensively overprinted by subsequent Proterozoic tectonic events (Ross, 2002).

3.2.3. Tectonic accretion history of Laurentia

It has been proposed that the northwestern part of Laurentia was affected by three major tectonic collisions between the Archean cratons and Proterozoic crustal domains during the Paleoproterozoic era (Figure 3.2). (1) The Slave-Rae collision (1.98-1.92 Ga) happened during the Thelon Orogeny, which continued into the Taltson Magmatic Zone - a suture marks the site of accretion (Bowring and Grotzinger, 1992). (2) The Hearn-Superior collision (1.85-1.78 Ga) is recorded by the Trans-Hudson Orogeny, which involved the closure of an ocean basin (Ansdell et al. 1995). (3) The Wopmay Orogeny is coeval with or younger than the Slave-Rae collision, and represents the accretion of Proterozoic crust along the western flank of the Slave province. The sedimentary rocks of the Wopmay Orogeny record the opening and closing of an ocean basin, which is known as a Wilson cycle (Monroe and Wicander, 2014).

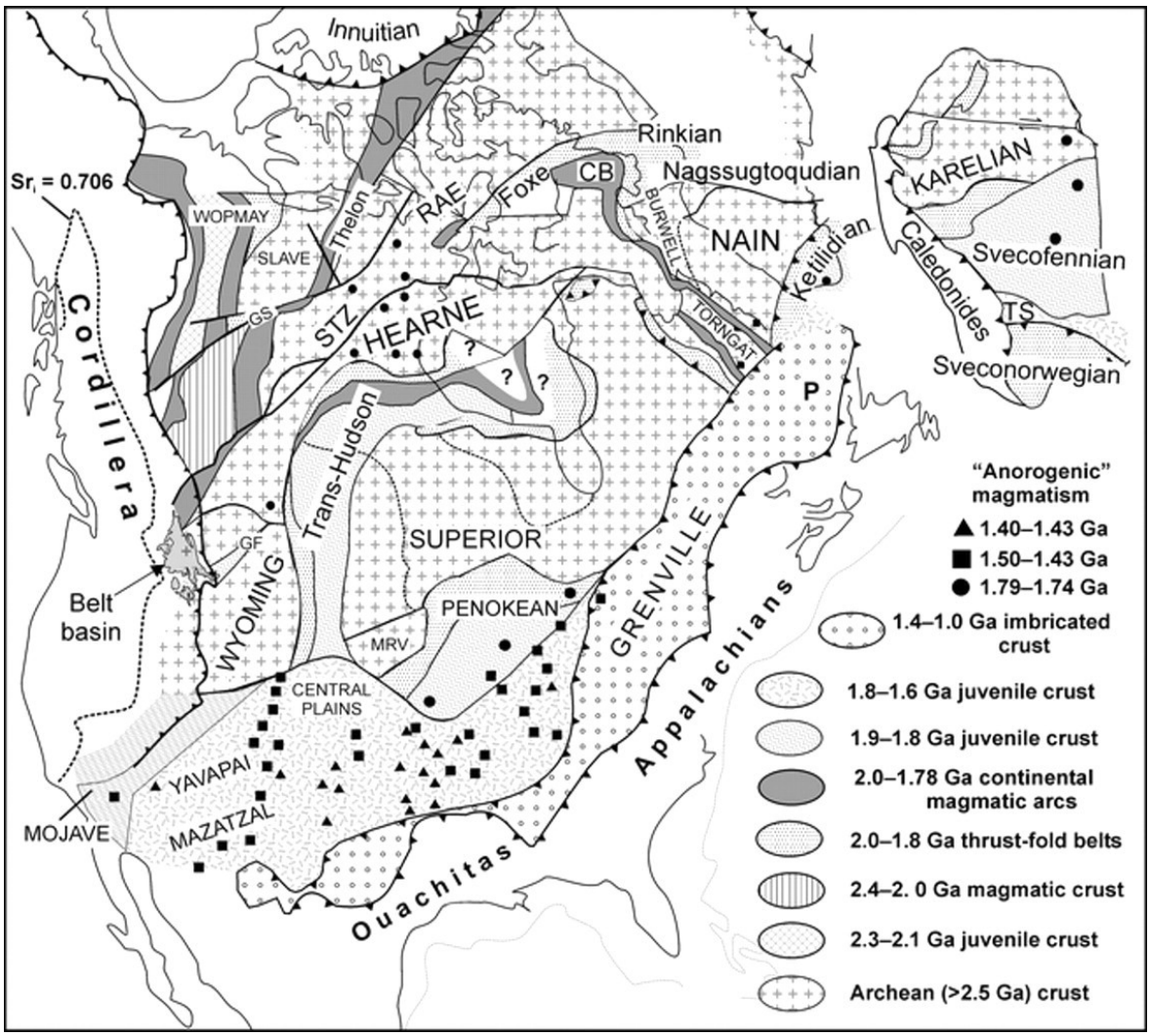

Figure 3.2: Tectonic map of the North American craton (From Hoffman, 1988; Ross and Villeneuve, 2003). The dashed lines are the extensions of the basement proposed by Ross and Villeneuve according to $^{87}Sr/^{86}Sr$ ratios (Sr_i) = 0.706. Abbreviations: GF, Great Falls tectonic zone; STZ, Snowbird Tectonic Zone; GS, Great Slave Lake shear zone; MRV, Minnesota River valley; CB, Cumberland batholith; P, Pinware terrane; TS, Trans-Scandinavian igneous belt.

Ross (2002) proposed that closure of oceanic basins was involved in the assembly process because of the common occurrence of calc-alkaline magmatic rocks (e.g. the Great Bear magmatic belt, Ksituan magmatic belt, and Taltson magmatic belt; Figure 3.1). Calc-alkaline magmatic rocks are commonly produced during the subduction of oceanic

lithosphere beneath continental lithosphere and characterized geophysically by positive aeromagnetic anomalies. Moreover, the final stages of the assembly also involved arc-continent and continent-continent collision and the boundaries of different Precambrian crustal domains are marked by suture zones (e.g. the Snowbird Tectonic Zone) or transform faults (e.g. the Hay River Fault and the Great Slave Lake shear zone; Ross, 2002). On the other hand, more extensive study of the magmatic rocks in the TMZ has shown that (1) the majority of the magmatic rocks in the TMZ are S-type granites and (2) only a few of the older magmatic rocks in the TMZ have weak calc-alkaline affinities. In fact, Chacko et al. (2000) and De et al. (2000) considered the rocks of (2) in detail and argued that they are petrologically, chemically or isotopically unlike Phanerozoic subduction-related granitoids. Based on these observations, Chacko et al. (2000) suggested the TMZ to be the product of intra-continental orogeny instead of subduction related.

After these collisions and/or intra-continental deformations had taken place, accretion occurred along Laurentia's southern margin from 1.8 Ga to 1.6 Ga and the Yavapai and Mazatzal Pecos orogenies occurred. The final Precambrian tectonic activity was associated with rifting at 1.3-1.0 Ga and the Grenville orogen and the granite-rhyolite province was also formed. These tectonic activities extended Laurentia to the southeast (Monroe and Wicander, 2014).

During the Phanerozoic Eon (540 Ma until present), North America continued to grow along its margins, with 25% of present area being accreted primarily along the eastern and western margins (Monroe and Wicander, 2014). Four mobile belts were formed at this time: the Franklin, Cordillera, Ouachita, and Appalachian mobile belts. In Alberta, the Canadian Cordillera marks the western boundary of the Precambrian rocks in

Alberta. The Cordillera mobile belt was formed through complex processes involving tectonic activity and major mountain-building activity in the Phanerozoic eon. The convergent process resulted from the continued westward movement of the North American plate as it overrode the subducting Farallon plate (Monroe and Wicander, 2014).

3.3. Proposed tectonic models

3.3.1. Snowbird Tectonic Zone

The Snowbird Tectonic Zone (STZ) is recognized as a series of linear potential field anomalies (both magnetic and gravity) that extend over a distance of ~2800 km from Hudson Bay to the Foothills of the Rocky Mountains in southwest Alberta. It was first identified by Hoffman (1988) and was interpreted as a Paleoproterozoic suture. It can be separated into three segments: the southwest segment is buried under the WCSB in central Alberta (Ross, 2002); the central segment with granulite-facies mylonites and high-pressure metamorphic complexes in Saskatchewan/Manitoba (Hanmer et al., 1995); and the northeast segment in Manitoba/NW Nunavut. The STZ marks the boundary between the Rae and Hearne provinces and its tectonic evolution is a key to understanding the assembly history of the northwestern Laurentia. Many hypotheses, based on different methodologies, have been proposed to explain the formation of the STZ. However, no consensus has emerged because of the differences in the nature of each segment of the STZ.

The earliest geological studies of the STZ were described by Lewry et al. (1985) who studied the central segment of the STZ and proposed that it was a Paleoproterozoic intra-continental shear zone related to the Hudsonian Orogeny. Later structural and

geochronological studies of the central exposed segments of the STZ (located in the northern Saskatchewan) were carried out by Hanmer et al. (1995).

Based on geochronological results it was concluded that the major deformation of the STZ occurred in a mid-late Archean intra-continental setting (Hanmer et al., 1995; Figure 3.3). Heterogeneity in the lithospheric strength was used to explain why the deformation was localized along the STZ rather than other locations. Paleoproterozoic reactivation of the STZ was proposed along the Virgin River shear zone, which is located at the south side of the central STZ (Figure 3.3). A pair of reentrants (Slave-Thelon and Virgin-Taltson) that collided with the Churchill western margin was proposed to initiate the Paleoproterozoic reactivations.

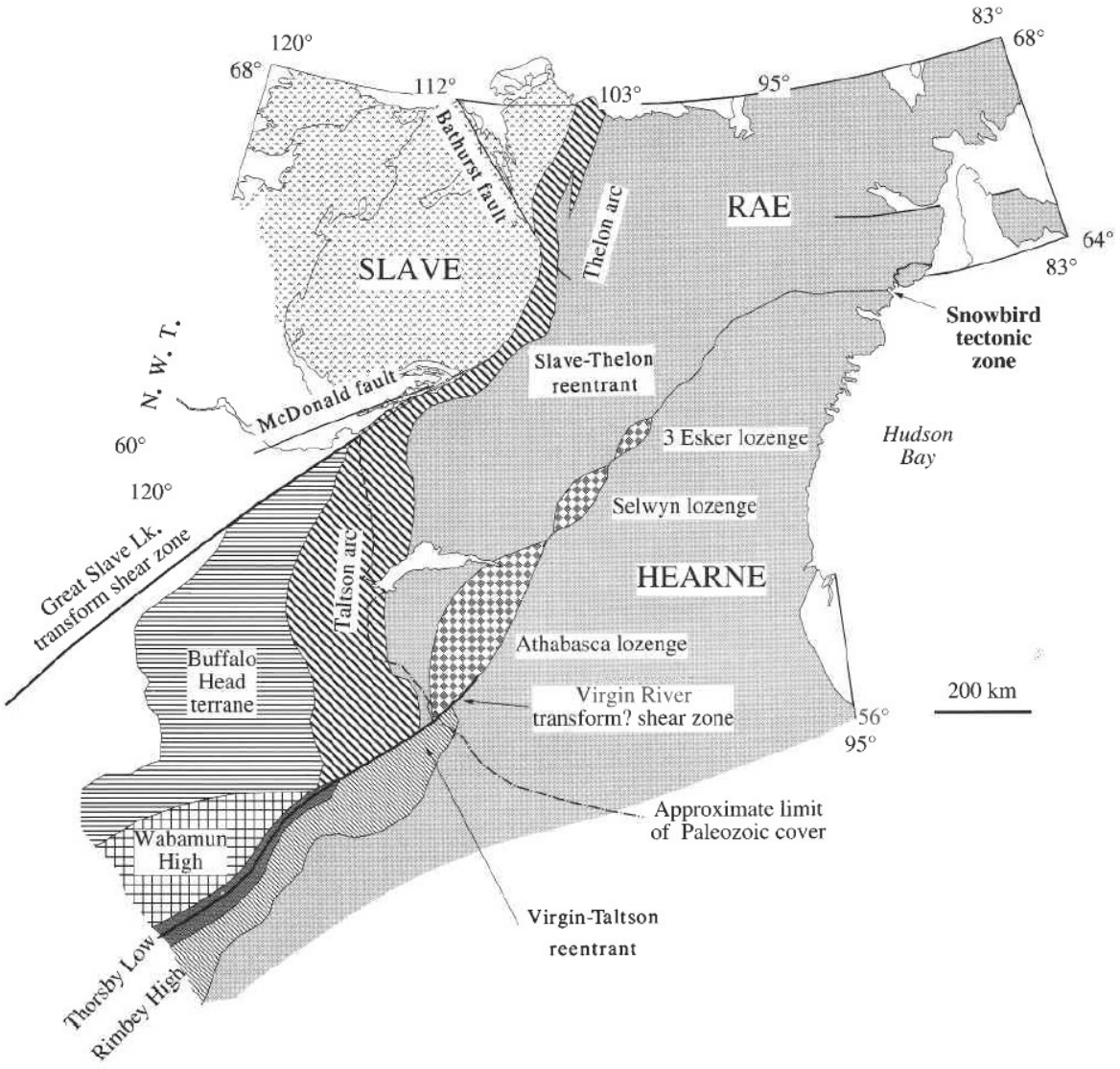

Figure 3.3: The tectonic map illustrating the jagged boundary of the Churchill province and the Proterozoic domains (from Hanmer et al., 1995).

Magnetotelluric (MT) and teleseismic studies of the northeast segment of the STZ in the Canadian Shield supported the idea that the STZ is a lithospheric boundary between the Rae and Hearne provinces (Jones et al., 2002; Figure 3.4). Contrasting electrical resistivity in the crust and mantle suggested that the Rae lithosphere has been thrusted beneath the Hearne craton by 150-200 km. They concluded that the STZ was a Neoarchean tectonic

suture that marks the juxtaposition of the Rae and Hearne cratons. This is in contrast with Hanmer et al. (1995), who stated that the STZ was an intra-continental shear zone. A suture is the result of convergence movement such as subduction, whereas a shear zone is caused by strike-slip (i.e., horizontal) motion. Reactivations of the STZ were also suggested by Jones et al. (2002) to explain observed crustal reworking and thermal events in the Paleoproterozoic era.

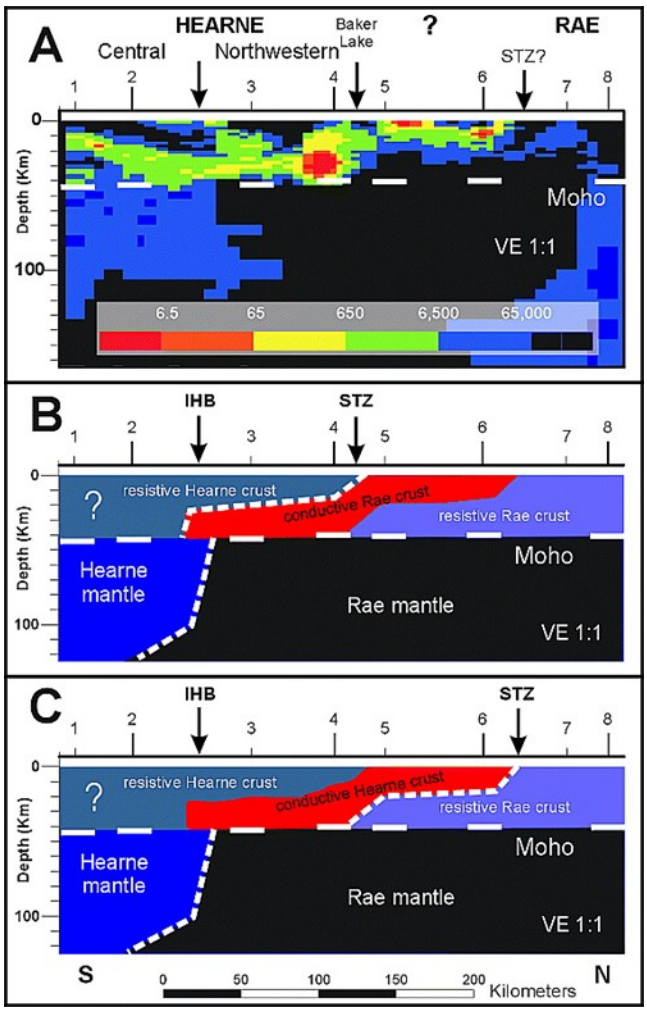

Figure 3.4: Proposed tectonic model of the northern STZ (B and C) according to the electric resistivity model (From Jones et al., 2002).

In contrast to the accretionary model suggested by Hoffman (1988) and Jones et al. (2002), Mahan and Williams (2005) interpreted the central STZ as Paleoproterozoic intra-continental thrust and strike-slip shear zones. It was suggested that the STZ was first a major zone of thrust-sense shearing with the Rae craton as the hanging wall, which is opposite to the model proposed by Jones et al. (2002). The thrust process was interpreted to be coeval with the collision between the Superior and western Churchill[3] cratons and accompanied by uplift of granulite-facies lower continental crust that is exposed now on the surface. Following the convergent event, further strike-slip movement was proposed to have happened along the STZ, which offsets the thrust zone (Mahan and Williams, 2005). Mahan and Williams (2005) also proposed that the STZ reflects a rather late stage (Paleoproterozoic) of deformation in the Churchill province that is not necessary related with the assembly of the Churchill province.

Petrological and geochronological studies by Berman et al. (2007; Figure 3.5) indicated that the northern STZ is a zone of medium- to high-pressure metamorphism dated to ca. 1.9 Ga. Combining other observations such as tectonic thickening, geological contrasts across the STZ, and subduction-related microdiamonds within the STZ, they argued that the STZ is a Paleoproterozoic suture zone that represents a pre-1.865 Ga phase of the Hudsonian orogeny. This is supported by Card (2016) who studied the Virgin River shear zone of the central STZ.

[3] Refers to Hearne and Rae provinces.

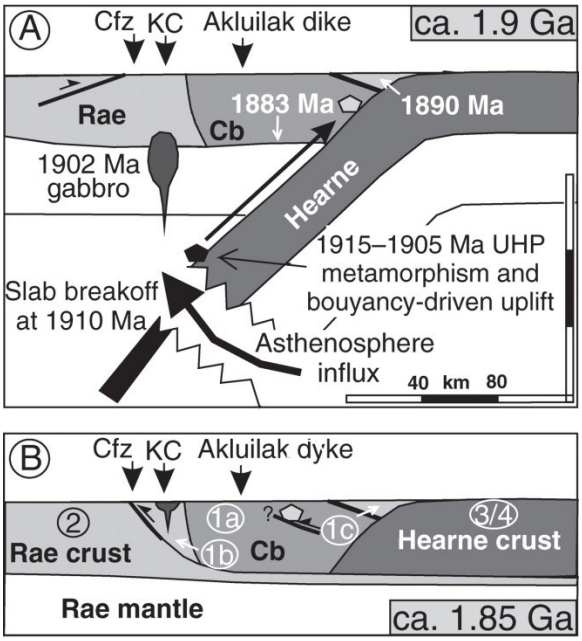

Figure 3.5: Proposed tectonic model of the northern STZ. Abbreviations: Cfz, Chesterfield fault zone; KC, Kramanituar; Cb, Cumberland Batholith; UHP, ultra-high pressure. Figure from Berman et al. (2007).

Ross (2002) studied the southwest segment of the STZ using seismic reflection data collected by the Central Alberta Transect (CAT) in 1992 (Figure 3.6). They interpreted the STZ as a Paleoproterozoic subduction zone bounded to the northwest of the Hearne province. Another coeval subduction zone – the Trans-Hudson Orogen was interpreted on the southeastern margin of the Hearne province. The Hearne province was proposed to be trapped in a tectonic "vice" between both subduction zones ca. 1.85-1.78 Ga in a collisional plateau setting.

It was proposed that the Thorsby domain was in an extensional setting in the Proterozoic while the central and northeast segments of the STZ were inactive (Ross, 2002). The opening of the Thorsby basin also accommodated the lateral escaped block from the

Taltson. This was followed by a convergence process of oceanic crust consumption and terminal collision of the Wabamun domain and the Hearne (Ross, 2002).

In this scenario, the Wabamun domain was proposed to have collided with and been thrust below the Hearne domain following the subduction of the oceanic crust of the intervening Thorsby basin. The present Thorsby domain is interpreted as a suture zone formed by subduction. The granitic rocks in the Rimbey domain were formed as near-trench magmatic arc rocks during the subduction of the oceanic crust beneath the Hearne province. Furthermore, delamination or convective erosion beneath the Hearne terrane was proposed to have follow the two coeval subduction events. The melt generated during the delamination was proposed to explain the emplacement of melts into the Hearne crust ca. 1830-1812 Ma (Ross, 2002).

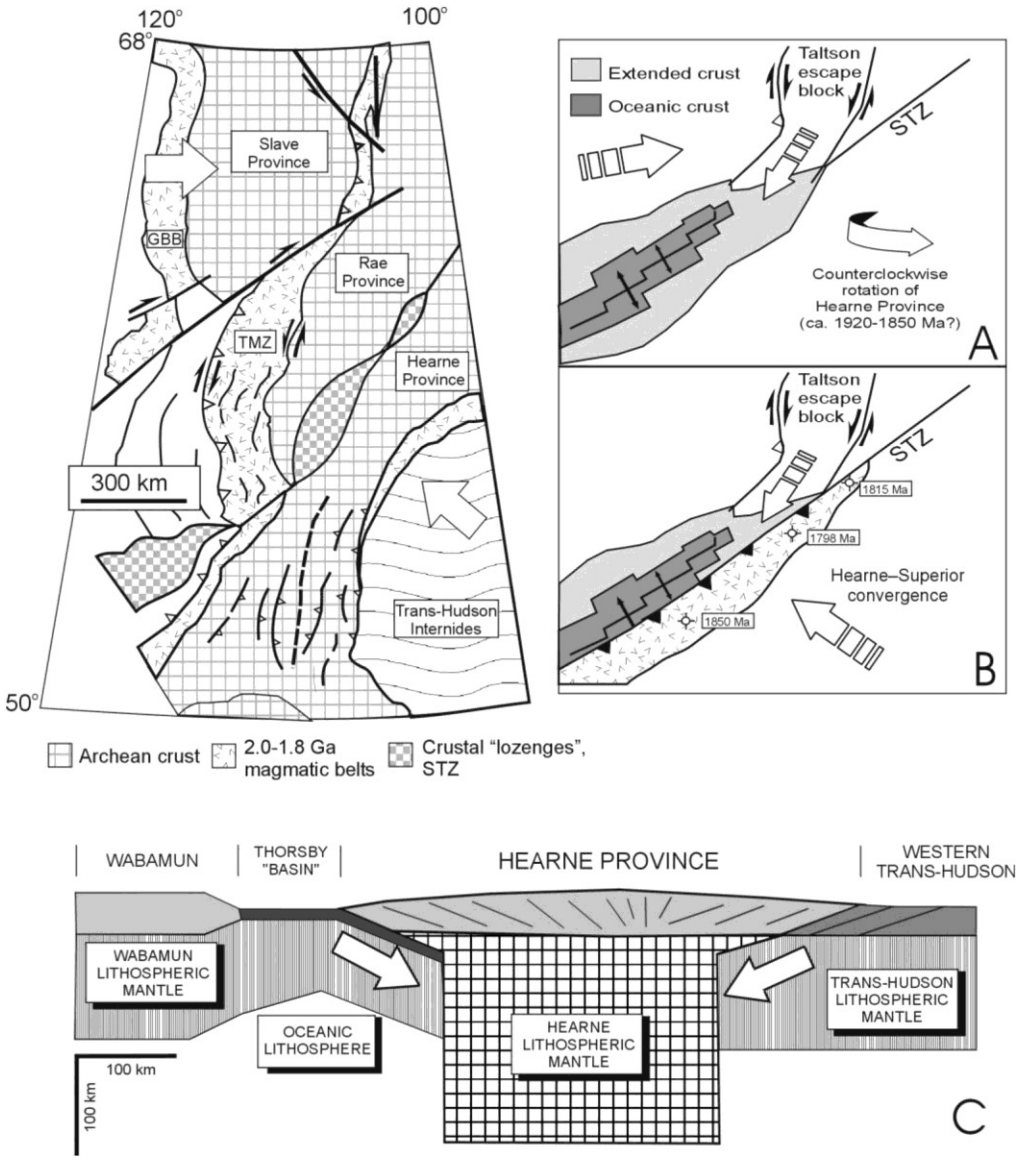

Figure 3.6: Cartoon illustrating the tectonic setting of western Canada ca. 1.84 Ga. GBB, Great Bear batholith; TMZ, Taltson Magmatic Zone; STZ, Snowbird Tectonic Zone. Figure from Ross (2002).

3.3.2. Hay River Fault

The Hay River Fault (HRF) is a major crustal-scale, right-lateral structure in northwest Alberta (Villeneuve et al., 1993) and is continuous with the Great Slave Lake

shear zone (GSLsz). Different tectonic models have been proposed to account for the history of the GSLsz and surrounding terranes.

Ross and Eaton (2002; Figure 3.7) proposed that the Nova terrane and the Chinchaga terrane were sutured together by a west-dipping subduction event and that the Ksituan terrane was generated as magmatic belt between them. This process was accompanied by the subduction of the Slave craton beneath the west boundary of the Rae craton. In this explanation, the Slave craton is similar to the Indian plate in the Indo-Asian collision.

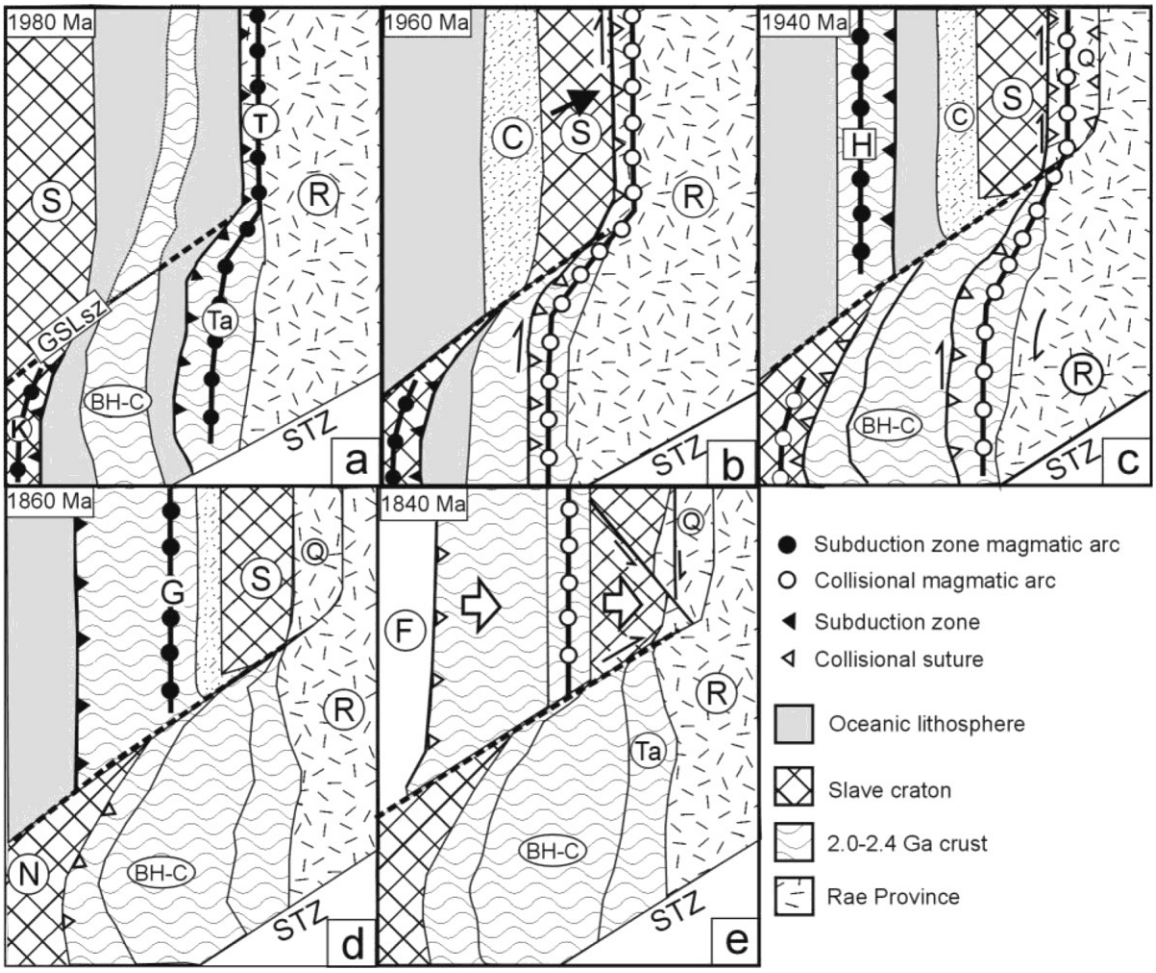

Figure 3.7: The tectonic model of the GSLsz and surrounding terranes during 1840-1980 Ma proposed by Ross (2002). Abbreviations: S, Slave craton; GSLsz, Great Slave Lake shear zone; K, Ksituan; BH-C, Buffalo Head and Chinchaga terranes; Ta, Taltson; T, Thelon; R, Rae craton; STZ, Snowbird Tectonic Zone; H, Hottah; Q, Queen Maud uplift; C, Coronation margin.

An alternative view is that no subduction occurred between the Slave and Rae cratons during ca. 1.95-2.0 Ga, according to the study of granitoids in the Taltson magmatic zone in eastern Alberta (Chacko et al., 2000; Figure 3.8). Any subduction event in northern Alberta coeval with the formation of the Taltson Magmatic zone (1.9-2.0 Ga) should have been east-dipping. Because the Ksituan terrane was found to be a ca. 1.9-1.98 Ga magmatic arc, the subduction between the Nova and Chinchaga terranes should also be east-dipping.

In this scenario, the Slave craton corresponds to the Tarim block and the Buffalo Head terrane to the Tibetan plateau in the Indo-Asian collisional system.

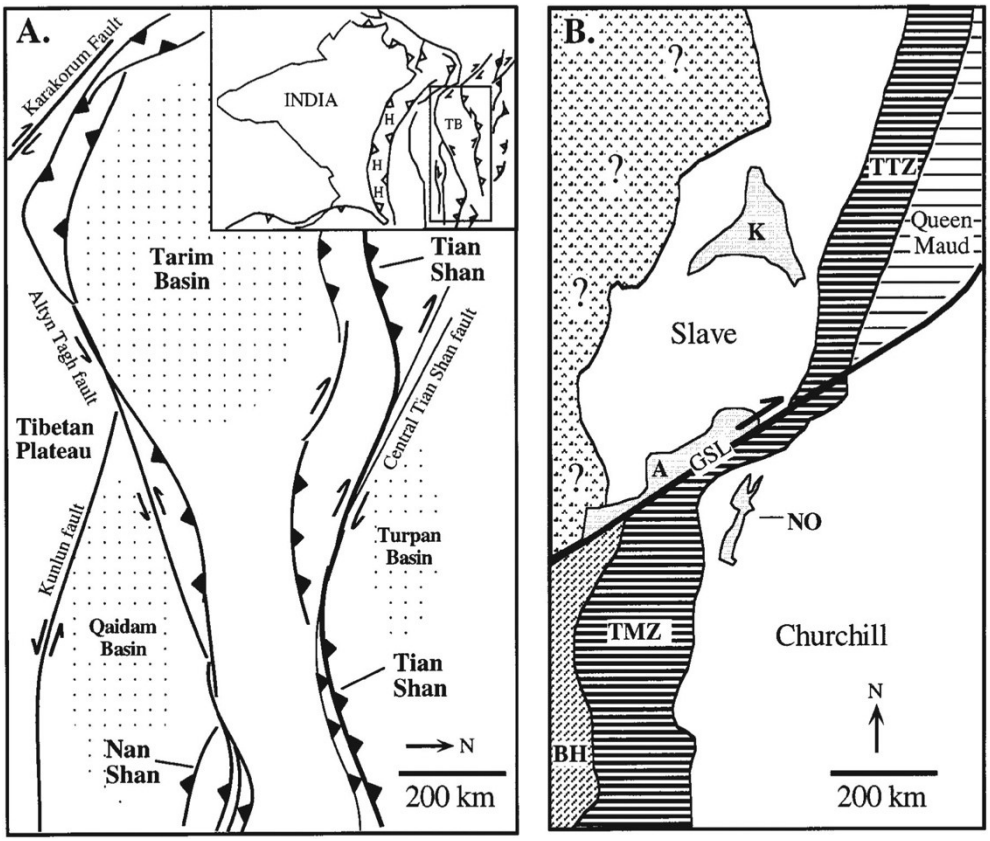

Figure 3.8: (A) Simplified tectonic map of the Indo-Asian collisional system in comparison with the tectonic model of northwest Laurentia during ca. 1.95-2.0 Ga. Figure from Chacko et al. (2000). Abbreviations: H, Himalayas; TB, Tarim Basin; TMZ, Taltson magmatic zone; TTZ, Thelon tectonic zone; BH, Buffalo Head; K, Kilohigok basin; A, Athapuscow basin; N, Nanacho basin.

3.3.3. Loverna Block, Vulcan structure and Medicine Hat Block

The Vulcan structure (VS) is located within the Hearne province. It is a 40-70 km wide and > 350 km long feature that is defined in the magnetic and gravity field data, and which separates the Medicine Hat Block (MHB) from the Loverna block (Eaton et al., 1999).

A number of hypotheses have been proposed for its formation. It was proposed to be a failed Precambrian rift by Kanasewich et al. (1969) based on seismic reflection and potential field studies. Hoffman (1988) interpreted the VS as a collisional suture between the Hearne and Wyoming cratons. In this scenario, the MHB was considered as a part of the Wyoming craton. This model was revised, and the VS was interpreted as an intra-continental collision zone within the Hearne craton (Hoffman, 1990). Ross et al. (1991) further proposed the VS to be either a northward subduction zone or an amagmatic shear zone based on potential field observations.

Eaton et al. (1999) studied seismic data from the Southern Alberta Lithospheric Transect program (SALT) and potential field data and reinterpreted the VS. They proposed that the VS was a relatively narrow axial zone of the continental collisional belt between the Hearne and Wyoming cratons. The linear potential field anomaly was interpreted as a mid-crustal pluton, and neighboring gravity highs to the north and east of the VS was interpreted as lower crustal material thrust to shallower depths during the collision. Seismic reflection results implied south-dipping subduction with crustal delamination of the Hearne craton. The time of the collision was proposed to be slightly older than the terminal collision in the Tran-Hudson Orogen. They also suggested that the location of the VS should include the southern part of the Matzhiwin high (Figure 3.9).

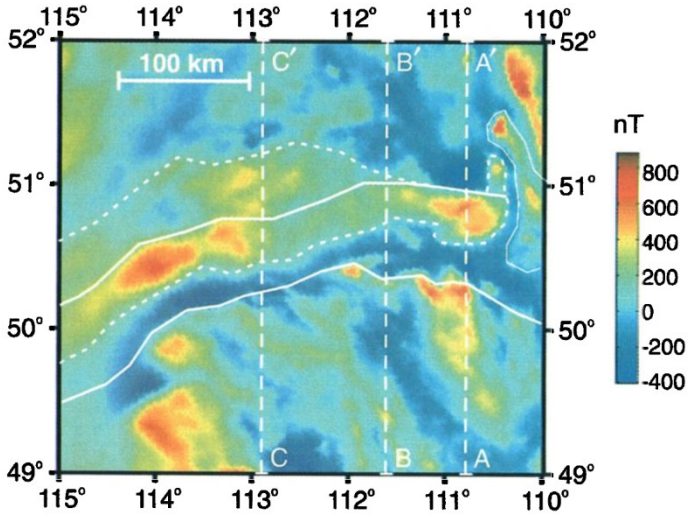

Figure 3.9: The aeromagnetic anomaly map of southern Alberta showing the extent of the Vulcan structure (solid thick white lines). Figure from Eaton et al. (1999). The dashed white line encompasses the Matzhiwin magmatic high.

Lemieux et al. (2000) expanded the interpretation of Eaton et al. (1999) and proposed a model to explain the observed west and southwest-dipping reflections and the layered lower crust (Figure 3.10) in the MHB. The dipping reflections were interpreted to be associated with Archean assembly of the western and eastern part of the MHB through subduction and continental collisions. The layered lower crust was interpreted to be delaminated Hearne craton that was the footwall of the terminal collision between the Hearne craton and MHB. Another source of the layered lower crust was proposed to be injection of mafic material during the early Proterozoic.

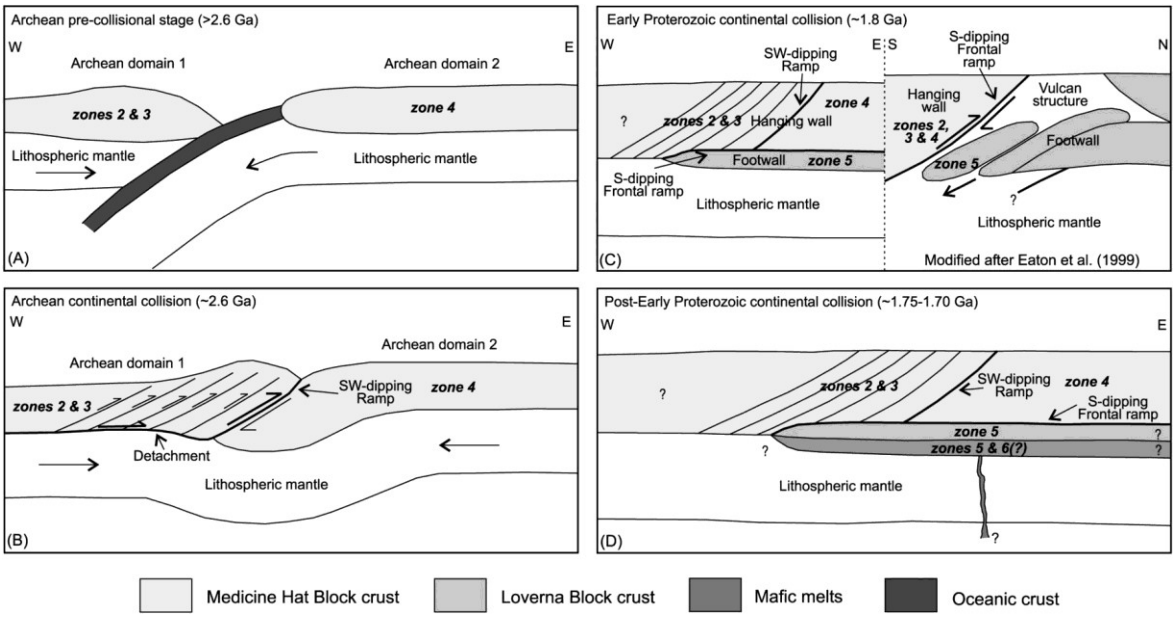

Figure 3.10: Tectonic model of the evolution of the MHB in the Precambrian (figure from Lemieux et al., 2000).

Gorman et al. (2002) analyzed the Southern Alberta Refraction Experiment and the Lithoprobe Deep Probe datasets and obtained a 2-D velocity model across southern Alberta to depths of ~150 km. Two northward-dipping reflectors were imaged in the subcrustal lithosphere underneath the MHB and VS (Figure 3.11). The two reflectors were interpreted as relic subduction zones associate with the accretion history of the Wyoming craton, MHB, and Hearne province. In other words, the Wyoming, MHB, and Hearne province are considered as Archean crustal blocks that formed independently. Gorman et al., (2002) proposed that the accretion of the Wyoming and MHB occurred through north-dipping subduction in the Late Archean. This was followed by subduction of the MHB below the Hearne province before the Paleoproterozoic Trans-Hudson Orogeny. Furthermore, a lower crustal layer (LCL) of high-velocity below the MHB and Wyoming craton was imaged and interpreted to be Proterozoic in age. Proterozoic magmatic underplating in a Pre-

Laurentia continental margin setting was proposed to explain this layer. The absence of an LCL under the Hearne province was explained by implying the Hearne was more to the center the continent.

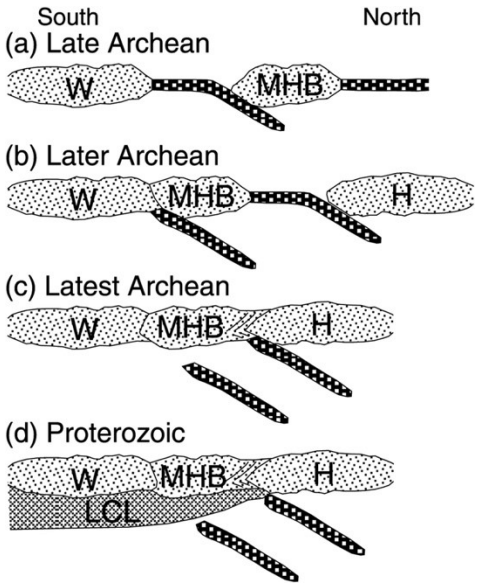

Figure 3.11: Proposed tectonic assemblage history of western Laurentia from Gorman et al. (2002). Abbreviations: W, Wyoming craton; MHB, Medicine Hat block; H, Hearne craton; LCL, lower crustal layer.

The tectonic models of Ross (2002), Gorman et al. (2002) and Lemieux et al. (2000) were summarized by Clowes et al. (2002) and a comprehensive model for the amalgamation of the western Laurentia was proposed (Figure 3.12).

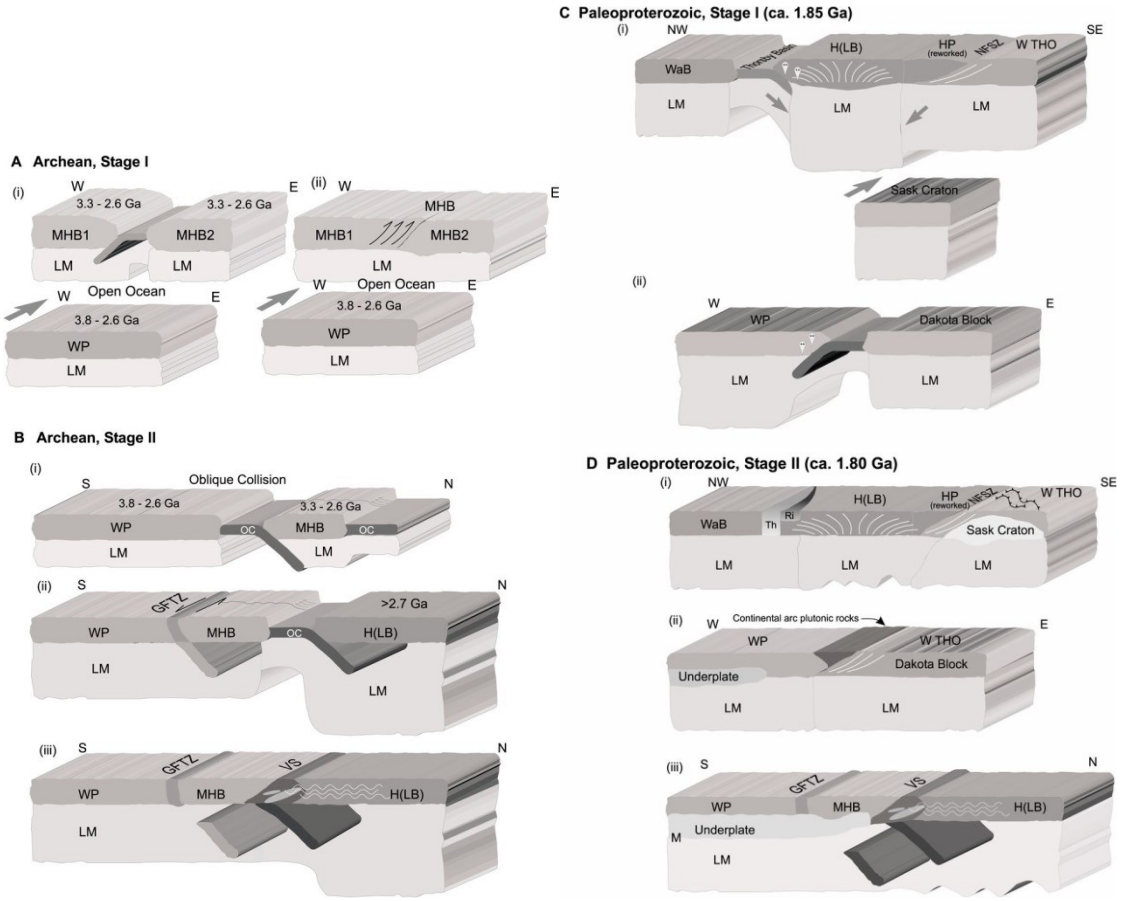

Figure 3.12: Tectonic model proposed for the assembly of western Laurentia during ca. 3.3-1.8 Ga. Figure from Clowes et al. (2002).

Contrary to the delamination interpretation of a thinned Hearne craton, Shragge et al. (2002) used teleseismic images to demonstrate that the lithosphere of the Hearne craton has remained intact and is exceptionally thick to depths of 200-250 km. The southern Hearne craton is associated with high velocities that are interpreted as deep-seated lithosphere structure.

A high-velocity root of the Hearne craton was also revealed by another teleseismic study (Chen et al. 2017, 2018). Moreover, low P- and S- velocities in the crust and shallow mantle of the Hearne craton were also observed that are coincident with high conductivity

(Nieuwenhuis et al., 2014). The thick lithosphere of the Hearne craton (~330 km) was proposed to represent an accreted, basalt-depleted oceanic plate during the amalgamation of the Hearne craton with the western Wabamun domain and the eastern Tran-Hudson Orogen (Figure 3.13). The lower velocities were interpreted as a result of metasomatism in the upper mantle induced by dehydration of fluids in the subducting slab. Connective erosion of the lithosphere of the terranes to the west of the Hearne craton was proposed to explain the thinner lithosphere (<200 km) observed in the Buffalo Head terrane (Chen et al. 2017, 2018).

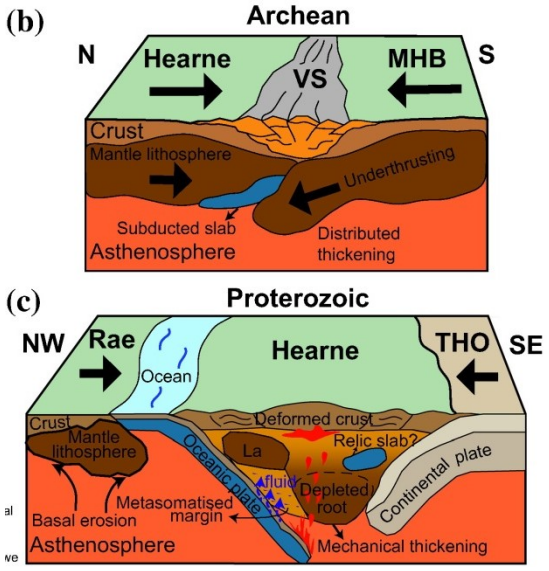

Figure 3.13: Proposed model for the Archean and Proterozoic tectonic process in southern Alberta. Figure from Chen et al. (2017). Abbreviations: VS, Vulcan structure; MHB, Medicine Hat block; THO, Tran-Hudson Orogen; La, Lacombe domain.

3.4. Diamondiferous kimberlites in Alberta

Diamond is one of the most popular gemstones in the world. Diamond is generally considered to be metasomatic mineral in the mantle, formed as a result of the cooling of C-

O-H fluids (Stachel and Luth, 2015). There is strong evidence that 99% of diamonds found at the surface originated in the sub-continental lithospheric mantle where the necessary pressure and temperature condition exists (Stachel and Luth, 2015). The average pressure and temperature of the peridotitic-suite diamond formation is from 5.3 +/- 0.8 GPa and 1130 +/- 120 ˚C (Stachel and Luth, 2015). The search for diamonds has been mostly based on surface till geochemistry and regional-scale geophysical methods such as magnetic and gravity surveys (Jones and Craven, 2004). Since diamonds are formed deep within the Earth, exploration for diamonds can be helped by deep geophysical surveys such as those provided by magnetotelluric and teleseismic methods. Jones and Craven (2004) used electrical resistivity models derived from MT data to explain diamond formation in the Slave and Superior cratons. It was observed that elevated mantle conductivity is sometimes associated with the diamond occurrences (Jones and Craven, 2004). Several fields of diamondiferous kimberlites have been discovered in Alberta, including the Buffalo Head Hills and Birch Mountains. Since electrical resistivity may be changed during metasomatic process and diamond formation is linked to metasomatism processes, it would be interesting to try to find the relationship between electrical resistivity and the location of diamondiferous kimberlites.

3.4.1. Characterization of ultramafic intrusions and kimberlite fields in Alberta

There are 56 occurrences of kimberlite and alkaline rocks found in four areas of Alberta: Mountain Lake, the Buffalo Head Hills, Birch Mountains and Black Butte Minette fields (Open Data Portal – Alberta Geological Survey, 2018). Different magmatic signatures

are observed in various fields. Moreover, multiple eruptions have been observed in every field according to palynology and geochronology studies (Eccles, 2011).

The Buffalo Head Hills field is located in the Buffalo Head domain. In total, 41 kimberlite intrusions have been discovered in the Buffalo Head Hills field to date. Moreover, it is the third largest known diamondiferous kimberlite field in Canada (Hauff et al., 2001). Various kimberlite volcanic facies are present in the Buffalo Head Hills field, including pyroclastic, volcaniclastic and re-sedimented volcaniclastic facies, which have been dated ca. 88-81 Ma (Eccles, 2011). Another major group of Buffalo Head Hill intrusions was defined as alkaline ultrabasic rocks dated ca. 60 Ma with low diamond content.

Alkaline basalt-type rocks are found at the Mountain Lake field, which is located within the Chinchaga domain. According to geochronology studies, they were proposed to have been emplaced during late Late Cretaceous (ca. 76-68 Ma; Eccles, 2011). The Mountain Lake alkaline rocks are of volcaniclastic origin and are not economic (Hauff et al., 2001).

The Birch Mountains kimberlite field is located in the southern Taltson Magmatic zone (TMZ). Both more evolved kimberlite and alkaline rock types are observed at the Birch Mountains field. Geochronological studies place kimberlite emplacement at ca. 100-70 Ma (Eccles, 2011). Both crater-facies pyroclastic kimberlite and resedimented volcaniclastic kimberlites are observed in the Birch Mountains field (Eccles, 2011).

The Black Butte Minette field is located within the Medicine Hat block and is part of the Sweet Grass Intrusive suite (Hauff et al., 2001). The emplacement age is Eocene.

3.4.2. Petrogenesis studies

According to petrogenetic studies of the northern Alberta kimberlites, the mantle of the kimberlite fields is thought to be heterogeneous and contain zones dominated by carbonate-rich lherzolite that were formed by metasomatic alteration (Eccles, 2011). Furthermore, the sub-continental mantle of the Buffalo Head Hills is characterized by higher levels of melt depletion than beneath the other kimberlite fields in Alberta. It was also noted that the more primitive kimberlite samples from the Buffalo Head Hills contain less carbonate than the samples from the Birch Mountains (Eccles et al., 2004).

The formation depths of the Buffalo Head Hills diamonds were suggested to range from the top of the diamond-stable lithosphere to the sublithospheric mantle. A sublithospheric source of the diamond formation indicates that tectonic events, such as deep subduction and slab break-off, were possibly involved (Banas et al., 2007).

Two distinct ancient metasomatic events of the Buffalo Head Hills lithosphere were described by Aulbach et al. (2004). An earlier silicate melt metasomatism was suggested to dominate the deep lithosphere. Another volatile-rich (such as carbonatite) metasomatism was proposed to impact the shallower lithosphere in a later event. Sulfides in spinel lherzolites were analyzed and were suggested to indicate metasomatic origin. The lithosphere-asthenosphere boundary was constrained to ca. 180 km at the Buffalo Head Hills (Aulbach et al., 2004).

3.5. Questions for investigation

1) What is the structure and history of the Hay River Fault? Was it formed by ductile or brittle deformation? The Hay River Fault and Great Slave Lake shear zone appear to be continuous features on the aeromagnetic map, yet it is not fully known how they are structurally related.
2) The assembly history of the terranes located between the Hay River Fault and the Snowbird tectonic zone is debated and the polarity of subduction (i.e. east-dipping versus west-dipping) is not resolved.
3) How the Snowbird tectonic zone developed remains uncertain. The Snowbird tectonic zone has been interpreted as both a suture zone (Hoffman 1989, Jones et al. 2002) and an Archean or Paleoproterozoic intra-continental shear zone (Berman et al. 2007; Hanmer et al. 1995). In contrast, there is evidence that the Snowbird tectonic zone was formed by subduction in central Alberta (Ross, 2002). The reason for the contrasting structures of different segments of Snowbird tectonic zone is of interest.
4) The Vulcan structure has been proposed as south- or north-dipping suture zone. More investigation is needed to verify different models.
5) The structures of the eastern and western Medicine Hat block were observed to be different. It was proposed to be two Archean blocks suture together by subduction and continental collision. These observations are based on seismic imaging of the crustal structure. MT imaging of the electrical structure of the Medicine Hat block could be useful to verify this hypothesis.

6) The Hearne craton was proposed to have experienced extensive Proterozoic metasomatism and deformation. The electrical properties of the rocks in the Hearne craton could reflect this metasomatism and deformation.
7) It has been suggested that the locations of diamondiferous kimberlites are related to regions with elevated carbon concentrations, where the lithosphere is thick and old (Jones and Craven, 2004). Both of these factors influence electrical resistivity and can be studied with MT. Since there are several clusters of diamondiferous kimberlites in Alberta, it provides an opportunity to investigate this hypothesis.

Chapter 4 : Previous geophysical studies in Alberta

Geophysical exploration measures the physical properties of the Earth (electrical resistivity, seismic velocity, density, magnetic susceptibility, temperature, etc.), from which the structure and rock properties of the subsurface can be interpreted. Several types of geophysical studies have been carried out in Alberta and are described below, including magnetic studies, gravity surveys, geothermic, seismic, and magnetotelluric studies.

4.1. Magnetic studies

Magnetic studies measure the strength of the geomagnetic field at or above the surface using magnetometers. The difference between the observed magnetic field and that predicted by the International Geomagnetic Reference Field (IGRF) is defined as a magnetic anomaly. Geological structures can be mapped from magnetic anomalies.

4.1.1. Magnetic anomalies

Magnetic anomalies are related to both the remnant magnetization and induced magnetization of crustal rocks. The amplitude of induced magnetization depends on the magnetic susceptibility of crustal rocks. Induced magnetization depends on the present day magnetic field and has the same direction as the current magnetic field (Lowrie, 2007). Remnant magnetization is more complicated and only significant in case of mafic or ultramafic rocks. It is acquired by ferrimagnetic minerals during their formation or some later-stage metamorphic alteration. It preserves the direction of the ancient magnetic field which is different from the current magnetic field.

4.1.2. Magnetization of crustal rocks

A rock is a mixture of different minerals. The main components are silicates or carbonates that are diamagnetic with a small negative magnetic susceptibility ($\kappa \approx -10^{-6}$ SI). Paramagnetic minerals such as clay are present to a lesser extent with very low and positive magnetic susceptibility ($\kappa \approx 10^{-5} - 10^{-4}$ SI). The bulk magnetic susceptibility of a rock is dependent largely on the concentration of dispersed (1) ferrimagnetic minerals ($\kappa \approx 10^{-3} - 10$ SI, such as magnetite, pyrrhotite, hematite, pyrite), and (2) ferromagnetic minerals (such as pure iron and nickel), and (3) antiferromagnetic minerals (such as hematite). Rocks with a higher magnetic susceptibility will produce a larger induced magnetization. On the other hand, ferrimagnetization, ferromagnetization and antiferromagnetization disappear when the temperature of a rock is higher than the Curie temperature. This is because the thermal energy disrupts the alignment of magnetic ordering and the bulk magnetization becomes zero. The Curie temperature of magnetite is 575 ˚C.

Magnetite is the most important ferrimagnetic mineral in the magnetization of the crustal rocks because of its high magnetic susceptibility ($\kappa \approx 1 - 10$ SI). It can produce a high induced magnetization and preserve a remnant magnetization. However, if the grain size of the magnetite is large enough (larger than a few micrometers), multi-domain magnetization will be formed. The multi-domain magnetization is less stable than a single-domain magnetization. For example, magnetite from continental crustal rocks has coarse grain size and carries multi-domain magnetizations that are not stable over time. Nevertheless, the susceptibility of magnetite is the highest among all the naturally occurring minerals; therefore, strong magnetization of magnetite can be induced by the

Earth's magnetic field. Generally speaking, strong positive magnetic anomalies in continental crustal rocks can be considered as totally induced magnetization of magnetite.

An example for remnant magnetization is fine grained titanomagnetite in oceanic basalts. In oceanic basalts, the ancient magnetic field is preserved in the titanomagnetite grains by thermoremanent magnetization. The total magnetization is dominated by the remnant component and the induced component is negligible. The direction of an oceanic magnetic anomaly is essentially parallel to the ancient magnetic field. This has been widely used in paleomagnetic studies which led to many discoveries that were important to verify the theory of plate tectonics since the 1960s (Lowrie, 2007). On the other hand, remnant magnetization can disappear when the temperature of the rock is higher than the Curie temperature.

4.1.3. Previous magnetic studies of Alberta

The majority of aeromagnetic data collected in Canada were acquired for mineral exploration and geological mapping by the Geological Survey of Canada and other agencies (Ross et al., 1991; Plint and Ross, 1993; Villeneuve et al., 1993). Currently, compilations of aeromagnetic data can be downloaded from the Natural Resources Canada website (Natural Resources Canada, 2017). The aeromagnetic map of Alberta (Figure 4.1) is composed of discrete domains marked by their magnetic intensity and textural characteristics and their relations to adjacent domains. Moreover, many curvilinear magnetic features mapped in the Canadian Shield continue into the platform area of Alberta. These include the complex magnetic features of the Great Slave Lake shear zone,

the magnetic high of the Taltson Magmatic Arc, and the magnetic low of the Snowbird Tectonic Zone (Ross et al., 1994).

It is believed that the magnetic anomalies in Alberta mainly originate in the Precambrian basement rocks, rather than within the overlying sedimentary rocks of the WCSB. This is supported by the fact that the wave number distribution of aeromagnetic data of the Alberta sedimentary basin is similar to that of the shield with the near-surface high-frequency components removed (Villeneuve et al., 1993). Anomalies within the sedimentary basin are considered hard to distinguish and insignificant because of the data density and the acquisition elevation of aeromagnetic surveys (Ross et al., 1994).

The interpretation of aeromagnetic expression of the Alberta basement was based on the study of the aeromagnetic anomalies in the Canadian Shield because of their continuity and similarity (Ross et al., 1994). It was supposed that the aeromagnetic expression is largely controlled by lithological structures with some contribution from remanent-magnetization and dipole effects. The Nova, Wabamun, Rimbey, Loverna domains and Medicine Hat block are moderately magnetic which suggests the presence of ferrimagnetic basic and granitoids rocks (Pilkington et al., 2000).

Most aeromagnetic highs in Alberta are interpreted as magmatic belts with magnetite as the main contributor to the high magnetic susceptibility. These include the Ksituan, Buffalo Head, Matzhiwin and Taltson domains which are mainly characterized by positive magnetic anomalies. Drill-core samples in most areas have confirmed this interpretation (Villeneuve et al., 1993). An exception of the magmatic belt interpretation is

the Eyehill aeromagnetic high, where a high-grade metamorphic origin was suggested according to drill-core samples (Ross et al., 1994).

Aeromagnetic lows in Alberta include the Hottah, Kiskatinaw, Chinchaga, Thorsby, and Vulcan domains which are characterized as weakly magnetic and interpreted as due to induced magnetism with paramagnetic sources comprised of low-susceptibility silicate minerals (Villeneuve et al. 1993). It was interpreted that the narrow curvilinear aeromagnetic lows of the Thorsby, Vulcan and Kiskatinaw domains were caused by demagnetization during shearing. Phase changes during regional metamorphism or shearing could have transformed ferrimagnetic Fe-oxides into anti-ferrimagnetic Fe-silicates and/or magnetite (of high magnetic susceptibility) into hematite (of low magnetic susceptibility) (Pilkington et al., 2000). As a result of the phase change, the bulk susceptibility of the crustal rocks is reduced. In regards to the more extensive magnetic lows observed in the Chinchaga and Hottah terranes, demagnetization due to phase change may have occurred at the terrane boundaries during terrane assembly. Moreover, a lower magnetite content of crustal lithologies in these two terranes was proposed to explain the broad extent of the magnetic lows (Pilkington et al., 2000). Remanent magnetization that has an opposite direction to the present geomagnetic field was excluded as a possible reason for the aeromagnetic lows in Alberta, because coherent remanence directions are unlikely to exist over domain-sized areas (10-100 km; Pilkington et al., 2000). Incoherent remanent magnetization would cancel each other out and the bulk magnetization should be close to zero.

The internal structures of some magnetic domains may provide information about the deformation history. For example, the striated aeromagnetic features of the Taltson

magmatic belt were interpreted as a result of ductile deformation of the magmatic rocks (Villeneuve et al. 1993). The small subcircular aeromagnetic highs in the Taltson magmatic belt were suggested to represent relatively undeformed plutons (Ross et al., 1994). Another interesting feature is the finely striated magnetic high fabric observed in the Lacombe domain. Rock deformation was proposed to account for this feature. Moreover, the subcircular aeromagnetic highs in the northeast Lacombe domain may represent the undeformed Willingdon volcanic center suggested by Gailand and Burwash (1959) based on drill-core samples (Ross et al., 1994).

In summary, aeromagnetic data of Alberta demonstrate the complex geological structure of Alberta basement. Aeromagnetic anomalies were believed to originate from the basement and sedimentary rocks at the surface have little effect on the aeromagnetic features. It was suggested that the aeromagnetic features are largely depending on the lithology of the basement rocks (Pilkington et al., 2000).

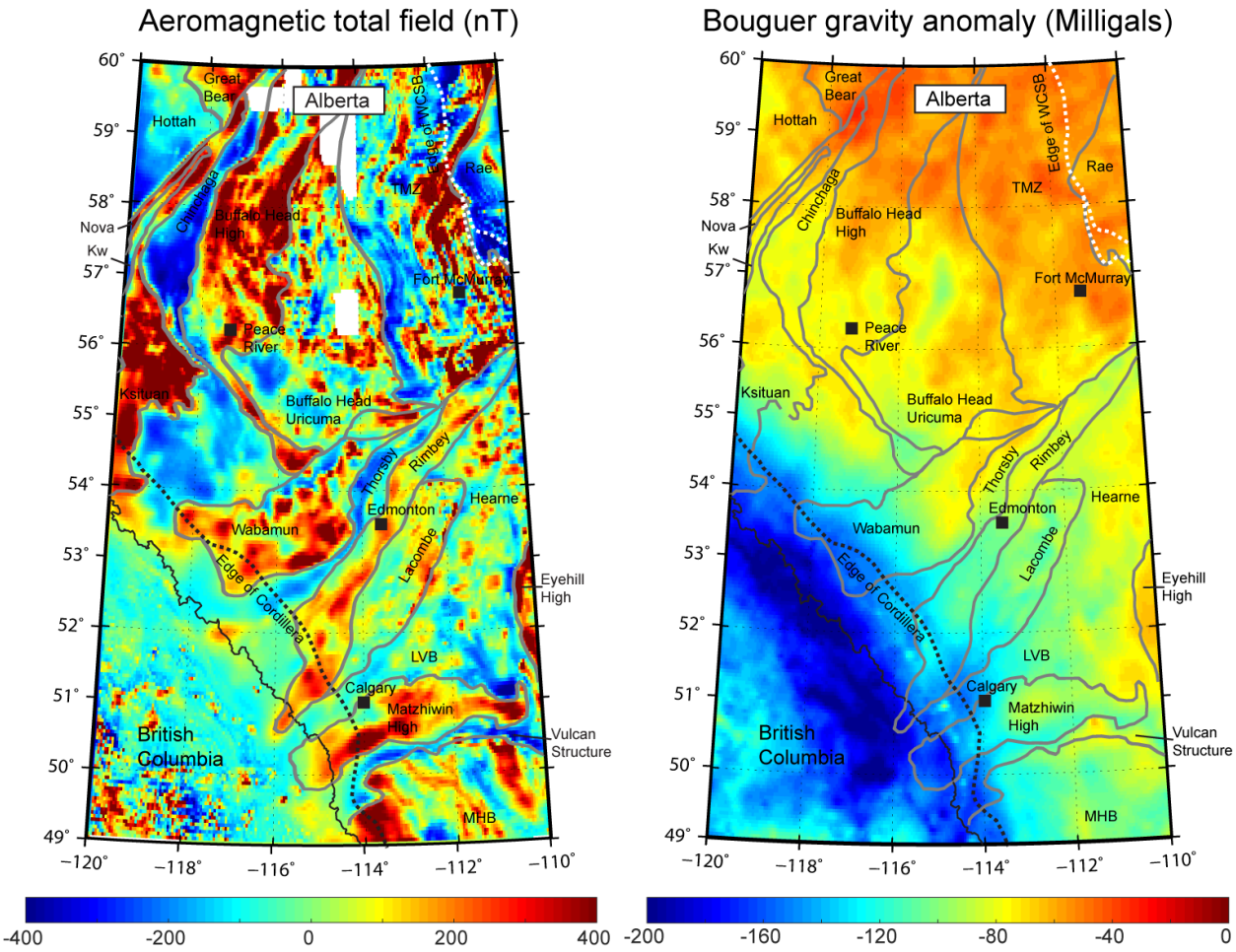

Figure 4.1: (a) Map of the total residual aeromagnetic field of Alberta (Geological Survey of Canada, 2017). (b) Bouguer anomaly map of Alberta (Geological Survey of Canada, 2017). The gray solid lines mark the Precambrian terrane boundaries which were defined by aeromagnetic data and isotopic dating by Pilkington et al. (2000).

4.2. Gravity studies

Gravity exploration is based on the law of universal gravitation which was proposed by Sir Isaac Newton. The law of universal gravitation describes that a particle attracts every other particle in the universe. The force of attraction is proportional to the product of the two particles' masses and the inverse square of the distance between them. The Earth's gravity field is the gravitational force exerted on a unit mass in the vicinity of Earth. Gravity

exploration uses the measurements of the Earth's gravity field to determine the subsurface density structure because the gravitational force is dependent on the mass (Lowrie, 2007).

Gravity measurements can be made in two ways to find either the absolute gravity or relative gravity. To find the absolute value of gravity, methods such as the classic pendulum method or the free-fall method are used. However, it is difficult to make instruments that can measure the absolute gravity accurately enough and which are portable for field work. Therefore, most gravimeters are designed to measure the relative change in gravity compared to a reference location. The sensitivity of a gravimeter is required to be in the order of 0.01 milligal. The absolute value of the gravity can be determined by using the relative values and referencing to a location where absolute gravity measurements are available (Lowrie, 2007).

4.2.1. Gravity anomalies

Raw gravity measurements are the combination of the subsurface gravity anomalies and other influencing factors such as the elevation, topography, and position on a rotating, non-spherical Earth. In order to account for the influencing factors, corrections need to be made. A gravity anomaly is the difference between the corrected gravity measurements with the predicted gravity that is calculated based on the reference ellipsoid.

The correction of the gravity measurements generally includes latitude correction, terrain correction, Bouguer plate correction, Free-air correction, and tidal correction. A generally used gravity anomaly is called the Bouguer gravity anomaly. It is defined by applying all the corrections mentioned above. Another gravity anomaly is referred to as the Free-air gravity anomaly. With the exception of the Bouguer correction, all the corrections

applied in the Bouguer gravity anomaly are applied in the Free-air gravity anomaly (Lowrie, 2007).

A Bouguer gravity anomaly reflects the inhomogeneous distribution of density in the Earth. More specifically, a positive Bouguer gravity anomaly indicates higher density of the region while a negative Bouguer gravity anomaly represents for lower density rocks.

The wavelength of a gravity anomaly is related to the horizontal extent of the anomaly and depth. Long wavelength anomalies result from deeper bodies and have broader, low amplitude features. The long wavelength anomalies are also called regional anomalies and represent deeper density contrasts. In contrast, short wavelength anomalies arise from a smaller and shallower source body and have narrow, sharp features. The short wavelength anomalies are also referred as residual anomalies that are due to shallow structures. Separation of the regional and residual anomalies is an important step in the interpretation of a gravity map.

4.2.2. Gravity anomalies in Alberta

Gravity data across Canada was collected by the Canadian Geodetic Survey and compilations of gravity data of Canada can be downloaded from the Natural Resources Canada website (Natural Resources Canada, 2017). The local detail of the gravity field in Alberta is partially masked by the strong regional gradient caused by the crustal thickening in the Canadian Cordillera and the thickness of the WCSB (Ross et al., 1994). Despite this, several significant features can be observed (Figure 4.1). In the Bouguer gravity map of Alberta, there are significant gravity lows (-120 milligal) coincident with the Vulcan structure which is ~40 milligals lower than the neighboring area. The Snowbird Tectonic

Zone (Thorsby domain) is at the boundary of gravity high to the north (~-60 milligals) and gravity low to the south (~-80 milligals). The Wabamun domain has higher values of Bouguer anomaly than the domains to the south of the STZ (Villeneuve et al., 1993).

To reduce the strong regional effects of the hot Canadian Cordillera, maps of horizontal gravity gradient and gravity isostatic residual can be constructed (Natural Resources Canada, 2017). The horizontal gravity gradient map represents the density structures of the upper ca. 15 km of crust. The strike directions of the gravity gradients in Alberta are mostly north-northwest (Figure 4.2). In contrast, the strike directions of the gravity gradients in southeast British Columbia, which is part of the Cordillera, are mostly northwest. The STZ and the Vulcan structure account for the most dramatic gradients of Alberta. High amplitude curvilinear gravity gradients are mapped inside the Lacombe domain as well. Moderate gravity gradients are observed along the southern boundary of the Wabamun domain, the western edge of the Eyehill High, and inside of the Matzhiwin domain.

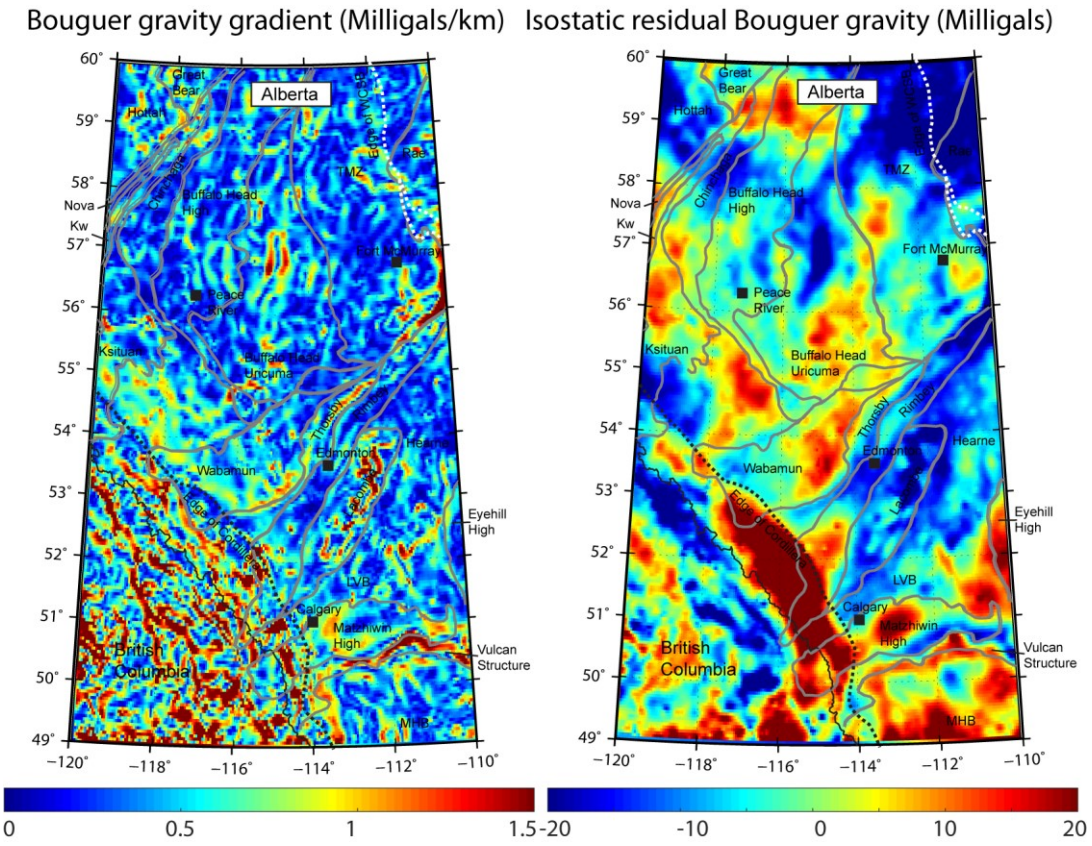

Figure 4.2: Bouguer gravity gradient map (left) and isostatic residual Bouguer gravity map (right) of Alberta and southeast British Columbia. The gray solid lines are the terrane boundary defined by Pilkington et al. (2000).

Isostatic residual Bouguer gravity anomaly maps emphasize short wavelength signals in the gravity field that arise from near surface density and/or thickness anomalies. The long wavelength features are removed by eliminating the effects of the isostatically compensated topography such as the crustal roots to the Cordillera. The isostatic residual gravity map of Canada represents variations in the gravity field caused by lateral variations in the density and thickness of Earth's crust and upper mantle (Jobin et al., 2017).

The isostatic residual of Alberta are mostly positive in contrast to the negative isostatic residual observed in most of the Canadian Shield. The highest amplitude, positive

isostatic anomaly is observed at the boundary of the Cordillera with the craton in southern Alberta. Large continuous regional isostatic lows are observed in the Thorsby, Rimbey, Lacombe, and northern Hearne in Alberta. The southern Hearn, Matzhiwin domain, and Eyehill High are characterized with positive, high amplitude isostatic anomalies. The Vulcan structure is marked by dramatic isostatic lows. The domains to the north of the Thorsby domain in Alberta are characterized by moderate high isostatic anomalies with the exception of the northern-central Buffalo Head domain and the northern Taltson domain.

4.3. 2-D Inversions of potential field data

To interpret the potential (magnetic and gravity) field data quantitatively, several 2-D profiles with density/magnetic susceptibility parameters have been published for major potential field features (such as the Red Deer High, Vulcan structure, etc.) in Alberta. Three north-south-striking 2-D gravity density profiles (-110.8˚W, -111.6˚W, 112.9˚W) across the Vulcan structure were proposed by Eaton et al. (1999; Figure 4.3). The Vulcan structure was modeled as result of a mid-crustal mass deficiency. Two gravity highs flanking the Vulcan gravity low were modeled as lower crustal material imbricated to shallower crustal depth.

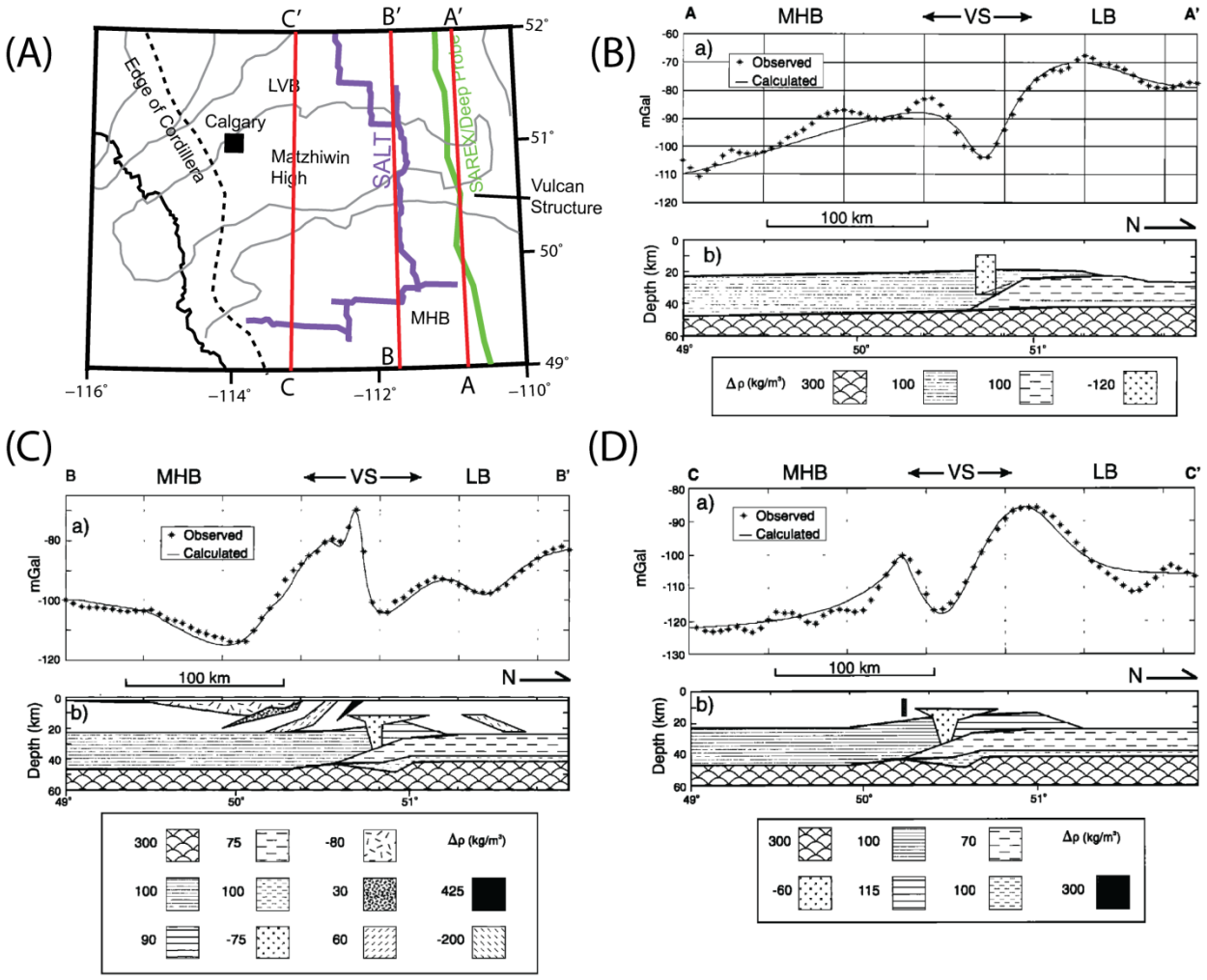

Figure 4.3: 2-D interpreted gravity profiles across the Vulcan structure. The locations of the profiles are indicated with red lines in figure A. The gray solid lines in figure A mark the Precambrian terrane boundaries which were defined by aeromagnetic data and isotopic dating by Pilkington et al. (2000). Figures B, C, and D are the density model of the three profiles A-A', B-B', and C-C'. Abbreviations: LVB, Loverna block; MHB, Medicine Hat block; SALT, southern Alberta Lithospheric Transect; VS, Vulcan structure; SAREX, southern Alberta Refraction Experiment. Figure B, C, and D are from Eaton et al. (1999).

Five 2-D potential field models across the Kimiwan magnetic high, Thorsby low, Red Deer magnetic high, Eyehill magnetic high, and Vulcan structure were presented by Hope and Eaton (2002; Figure 4.4). The Kimiwan magnetic high was modeled as either moderate positive susceptibility zone in the hanging wall or steeply dipping zone of high

susceptibility in the footwall. The Thorsby magnetic low and gravity gradient was associated with density and magnetic susceptibility contrasts between the Wabamun domain and domains to the south at mid- and lower-crustal depths. The 10 km Moho offset observed in seismic reflection studies is consistent with the gravity model across the Thorsby domain but was not required by the gravity model. The Red Deer High was modeled as a shallow body in the basement with an eastward dip which is consistent with magnetotelluric and seismic reflection studies. The Eyehill High was modeled to be at the western edge of a large block of dense material in the lower crust and associate with a sub-vertical dyke-shape body with high magnetic susceptibility. The Vulcan structure was explained by a low-density body at mid-crustal depth with remanent magnetization that is oriented antiparallel to the present-day field (Hope and Eaton, 2002).

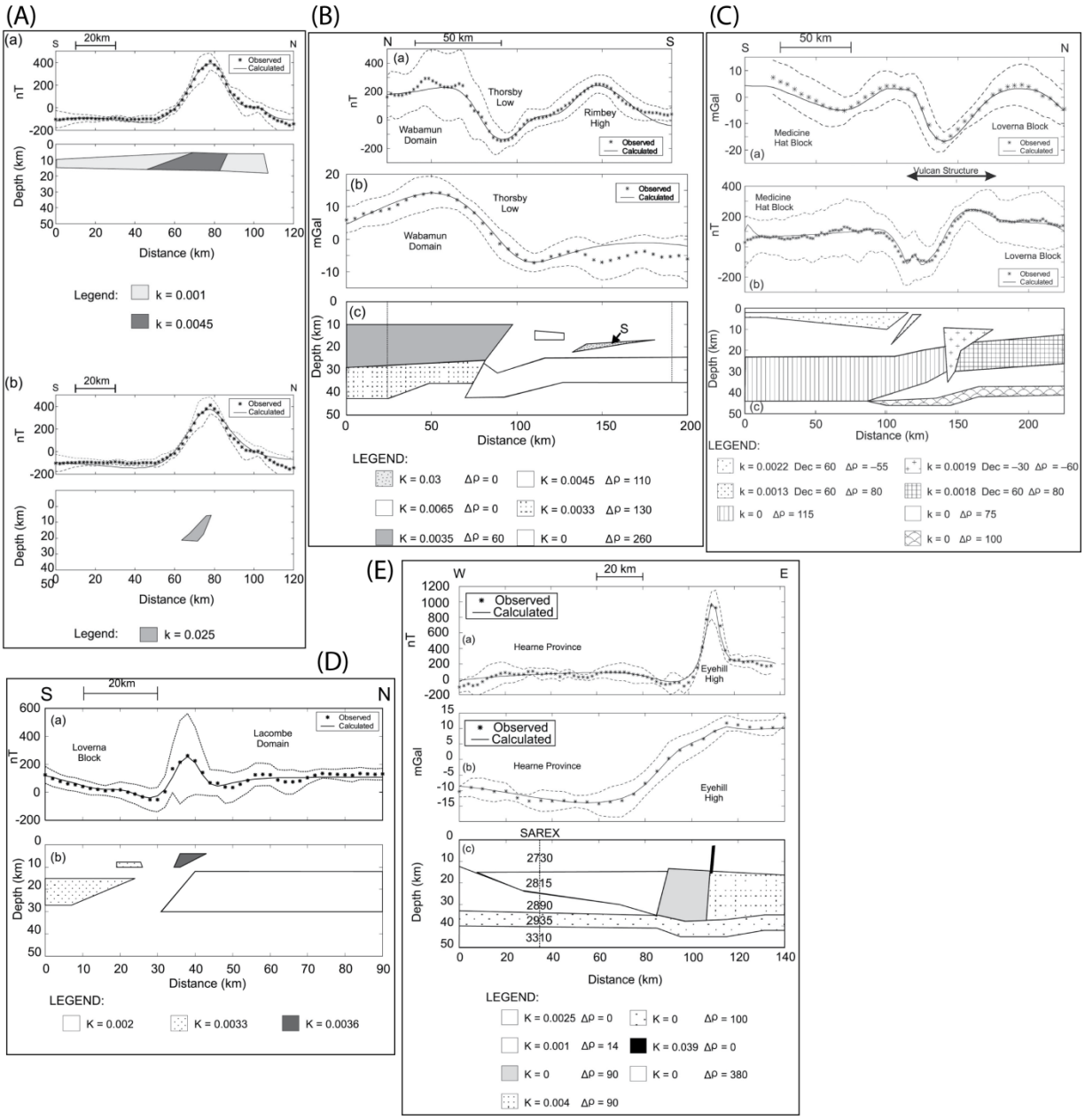

Figure 4.4: The potential field models across the Kimiwan High (A), Thorsby low (B), Red Deer High (D), Eyehill High (E), and Vulcan structure (C). Parameter K and $\Delta\rho$ represent the magnetic susceptibility (SI units) and the density (kg/m^3). Figure from Hope and Eaton (2002).

Gravity modelling of the MHB was conducted near the Lithoprobe seismic lines 29-31 (Lemieux et al., 2000; Figure 4.5). The gravity model was characterized with presence of a high density lower crustal layer and a geometric ramp in the upper and middle crustal

depth in the east. Moreover, the westward thickening of the low-density sedimentary layers of the WCSB was also modeled.

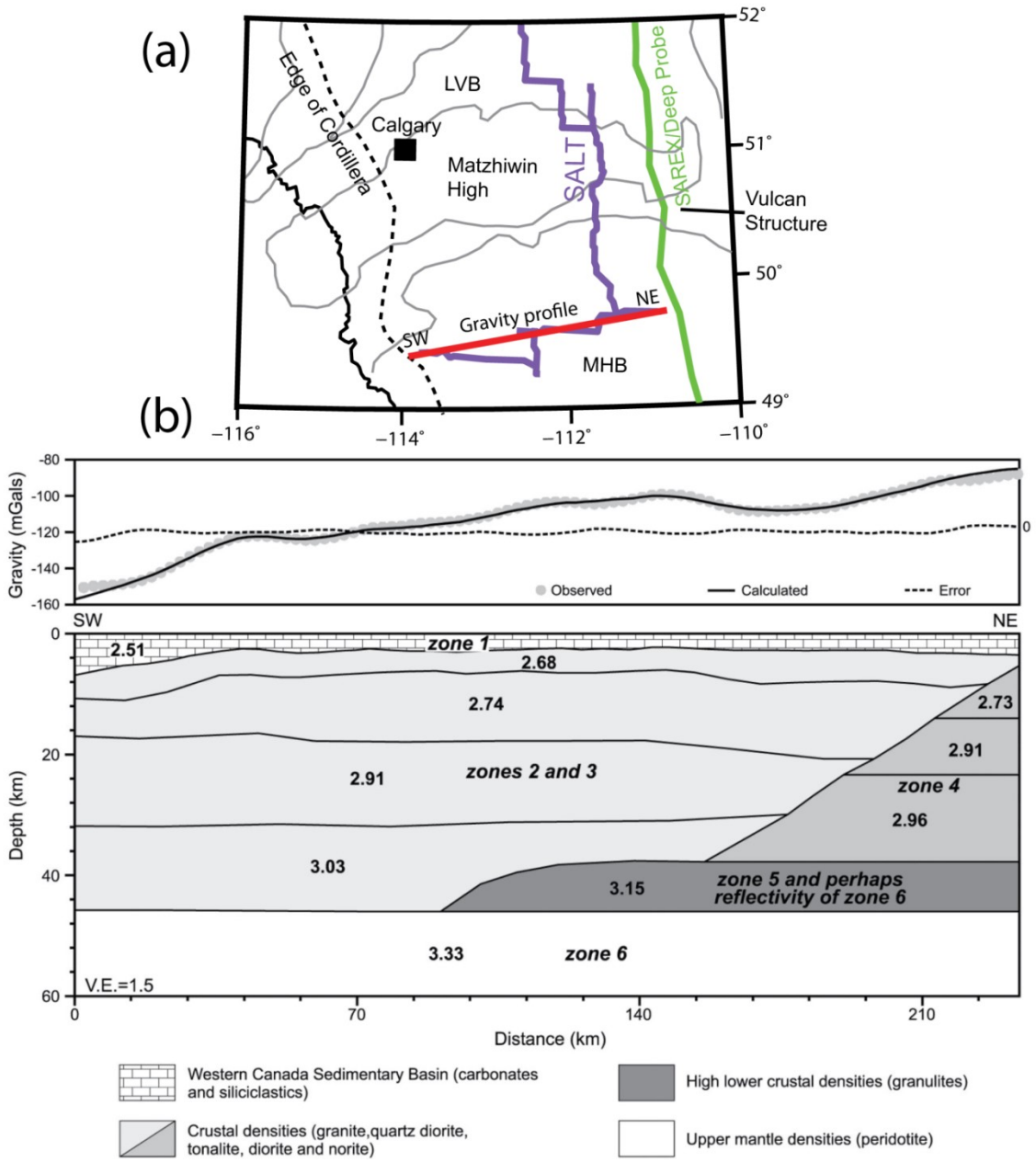

Figure 4.5: The 2-D density model of the Medicine Hat block shown in figure (b). The Figure (a) shows the location of the gravity profile with the red line. Abbreviations: LVB, Loverna block; MHB, Medicine Hat block; SALT, southern Alberta Lithospheric Transect; SAREX, southern Alberta Refraction Experiment. Figure b is from Lemieux et al. (2000). The gray solid lines in figure (a) mark the Precambrian terrane boundaries which were defined by aeromagnetic data and isotopic dating by Pilkington et al. (2000).

4.4. Geothermic studies

4.4.1. Introduction

The generation and transfer of heat inside the Earth accounts for a number of geological phenomena, such as volcanoes, intrusions, earthquakes, mountain building and metamorphism. Thus, understanding the geothermal regime can help to interpret the origin of many geological processes.

It is impossible to directly measure the temperature deep in the Earth, and temperatures and temperature gradients can only be measured in boreholes (Lowrie, 2007). The deeper thermal structure of the Earth can be extrapolated from surface measurements using thermal modelling and knowledge of rock properties at depth (such as the thermal conductivity, specific heat capacity, and radioactive heat generation). Specific heat capacity is defined as the amount of heat necessary to increase the temperature of 1 kg of the material by 1 ˚C. Crustal and upper mantle temperatures can also be inferred from seismic data because the seismic velocity is dependent on the temperature.

Radioactive heat generation is caused by the decay of radioactive isotopes. The heat generating elements (uranium, thorium and potassium) are present in very small quantities in the crust. In the mantle, the concentrations are two orders of magnitude less than in the crust. Nevertheless, most of the radioactive heat generated in the Earth is from the mantle because of the greater size of the mantle. The heat generation varies significantly in different rocks. For example, granite (~2.5 μWm^{-3}) has a greater radioactive heat generation than the mafic igneous rocks (~0.08-0.5 μWm^{-3}). The heat generation of

peridotite is very low (~0.006 μWm^{-3}). Furthermore, the continental upper crust (~1.8 μWm^{-3}) has the highest heat generation in the Earth.

Surface heat flow is a measure of heat loss from the Earth. The total present-day heat loss by the Earth is approximately (4.2-4.4) $\times 10^{13}$ W (Lowrie, 2007). In the ocean, most of the heat is lost during the creation and cooling of the oceanic lithosphere. More than 70% of the Earth's total heat loss occurs in the ocean and the oceanic heat flow generally decreases with the age of the oceanic crust. In the continent, the highest heat flows are observed in regions of the most recent tectonic activity.

Surface heat flow can be related to the thermal conductivity and geothermal gradient. For a solid rock in a plate shape that is infinitely long and wide, the surface heat flow can be expressed as:

$$Q = -k\frac{\partial T}{\partial z} \tag{4.1}$$

where Q is the surface heat flow per unit area of the rock, ∂T is the temperature difference on the two sides of the plate, ∂z is the thickness of the rock plate, and k is the thermal conductivity. The term $\partial T/\partial z$ is also referred as geothermal gradient and represents the rate of change of the Earth's temperature with depth. It can be measured in boreholes.

4.4.2. Geothermal regime in Alberta

Most of Alberta is covered by the rocks of Western Canada Sedimentary Basin (WCSB). The sedimentary layer acts as a thermal blanket due to its low thermal conductivity. Because of the sedimentary cover, only thermal properties of drill core samples on the top of the Precambrian basement can be accessed.

It has been found that the heat generation at the top of the Precambrian basement is related to the content of the radioactive elements (uranium, thorium, and potassium; Bachu and Burwash, 1994). This study used an analysis of unweathered core samples recovered from the upper few meters of the crystalline basement below the WCSB (Figure 4.6a). Heat generation is higher in northern Alberta than in the southern Alberta (Bachu and Burwash, 1994). Large spatial variation of heat generation (~1-8 μWm^{-3}) is observed in the Peace River region because of more closely spaced drill core samples. One major anomalous high heat generation region (~8 μWm^{-3}) is aligned with the Thorsby domain to the northeast of Edmonton (Bachu and Burwash, 1994; Majorowicz et al., 2016).

The geothermal gradients of the WCSB (Figure 4.6b) were calculated using well-log temperature measurements and found to be in the range 20-50 ˚C/km with trend that shows an increase to the north, which is similar to the trend in heat generation of the basement rocks (Bachu and Burwash, 1994; Majorowicz et al., 2016).

The heat flow with depth can be calculated using measurements of thermal conductivity and heat production from drill core samples. The heat flow at the top of the Precambrian basement in Alberta (Figure 4.6c) has a similar pattern to the geothermal gradient map. It is on average 20 mWm^{-2} higher than in the Canadian Shield (Majorowicz et al., 2016).

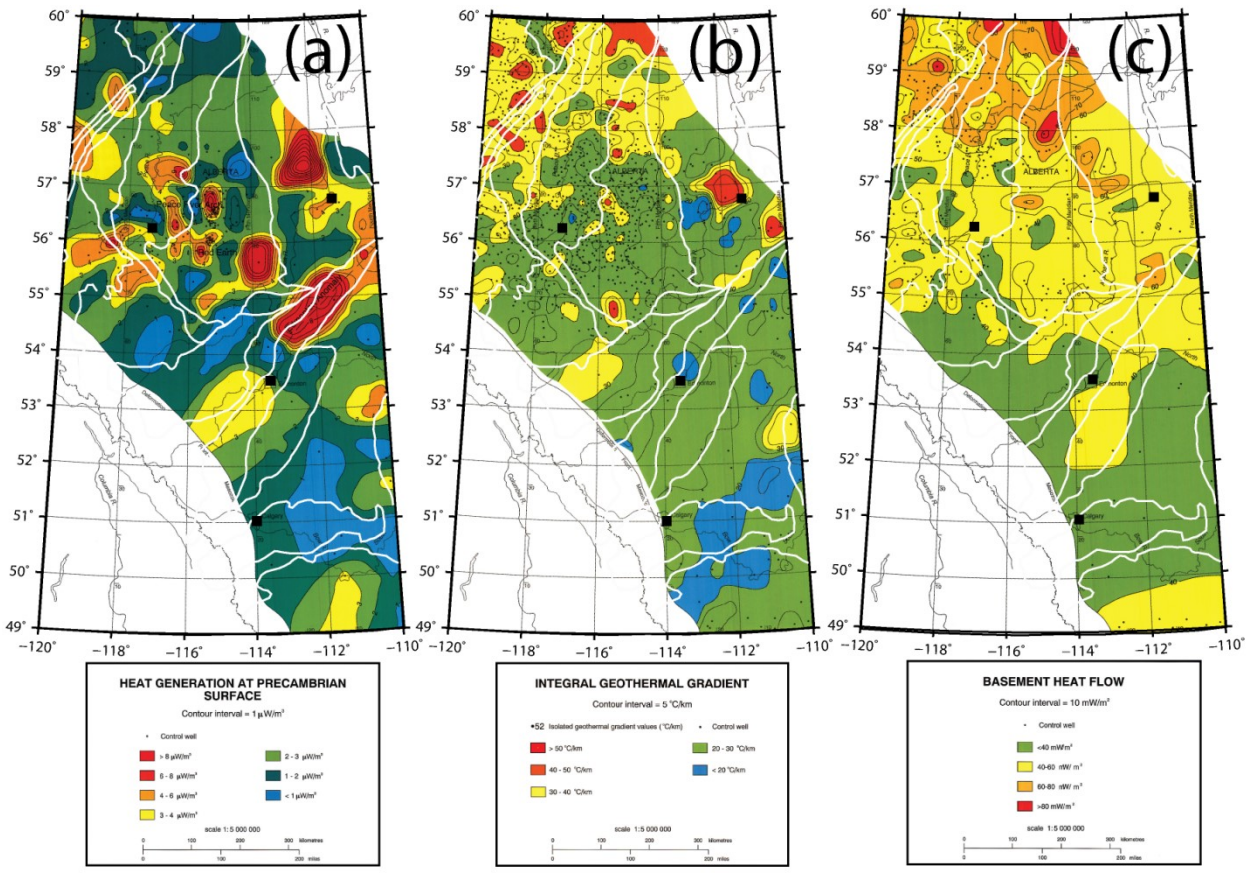

Figure 4.6: Geothermal maps of Alberta (modified from Bachu and Burwash, 1994). The white lines mark the boundary of tectonic domains (Pilkington et al., 2000). The black squares represent the locations of major cities.

4.4.3. Geothermal explorations

Geothermal exploration searches for regions where geothermal energy development could be viable. Majorowicz et al., (2014) found that the highest temperature at 5 km depth was 200 ˚C and located in northwest Alberta. Nieuwenhuis et al., (2015) mapped the highest temperature at 2 km depth of 100 ˚C at the same location. Both studies suggested there is geothermal potential in northwest Alberta. An Enhanced Geothermal System (EGS) would be required (Majorowicz et al., 2014) because: (a) this area is covered by sedimentary rock of ~2 km thickness and the high temperature reservoir is within the

Precambrian basement; (b) this area is close to the Great Slave Lake Shear Zone which may provide some natural fractures to be utilized or avoided in EGS.

4.5. Seismic studies

Seismic exploration uses the propagation of elastic waves to determine Earth structure and can measure the acoustic wave velocity and related parameters of the subsurface rocks (Lowrie, 2007). The variation in seismic wave velocity indicates rocks with different composition.

There are two kinds of seismic waves: body waves and surface waves.

- Seismic body waves propagate through the body of a medium. Body waves can be classified as the primary wave (P-wave) and secondary/shear wave (S-wave).
- The P-wave is a longitudinal wave and is the fastest of all seismic waves.
- The S-wave is a transverse/shear wave and is slower than the P-wave.
- Seismic surface waves travel along the free surface of a medium. They can be subdivided into Rayleigh waves and Love waves according to the styles of particle motion.

Seismic waves are recorded with seismographs which can convert ground vibrations into digital records. The seismograph is composed of a seismometer (geophone in exploration seismology) as a receiver and a seismogram as a recorder. Seismometers are capable of detecting motion of the Earth in vertical/horizontal direction or both directions (Lowrie, 2007).

The sources of the seismic signals can be either natural earthquakes or controlled sources. Seismic reflection and refraction studies use artificial sources of seismic waves such as the ones generated with vibroseis or dynamite and can image crustal structures. Seismic tomography can image the subsurface structure using natural or man-made sources. Teleseismic tomography uses waves from distant earthquakes to study structures down to the mantle and core (Lowrie, 2007).

4.5.1. Reflection seismology

The seismic reflection method is sensitive to velocity contrasts where seismic waves are reflected. A number of seismic reflection profiles using Vibroseis as energy sources were collected in Alberta during the Lithoprobe project as shown in Figure 4.7 (Hope et al., 1999). These include the Peace River Arch Industry Seismic Experiment (PRAISE) in northern Alberta, the Central Alberta Transect (CAT) in central Alberta, and the southern Alberta Lithospheric Transect (SALT) in southern Alberta. These seismic reflection profiles were designed to image the crustal structure and the total length of these seismic transects is nearly 2000 km (Hope et al., 1999). Another seismic reflection survey was named the Vibroseis Augmented Listen Time (VAuLT) experiment. It was designed to image the structure to the upper mantle depth of the Rocky Mountain foreland in southwest Alberta (Eaton et al., 2000).

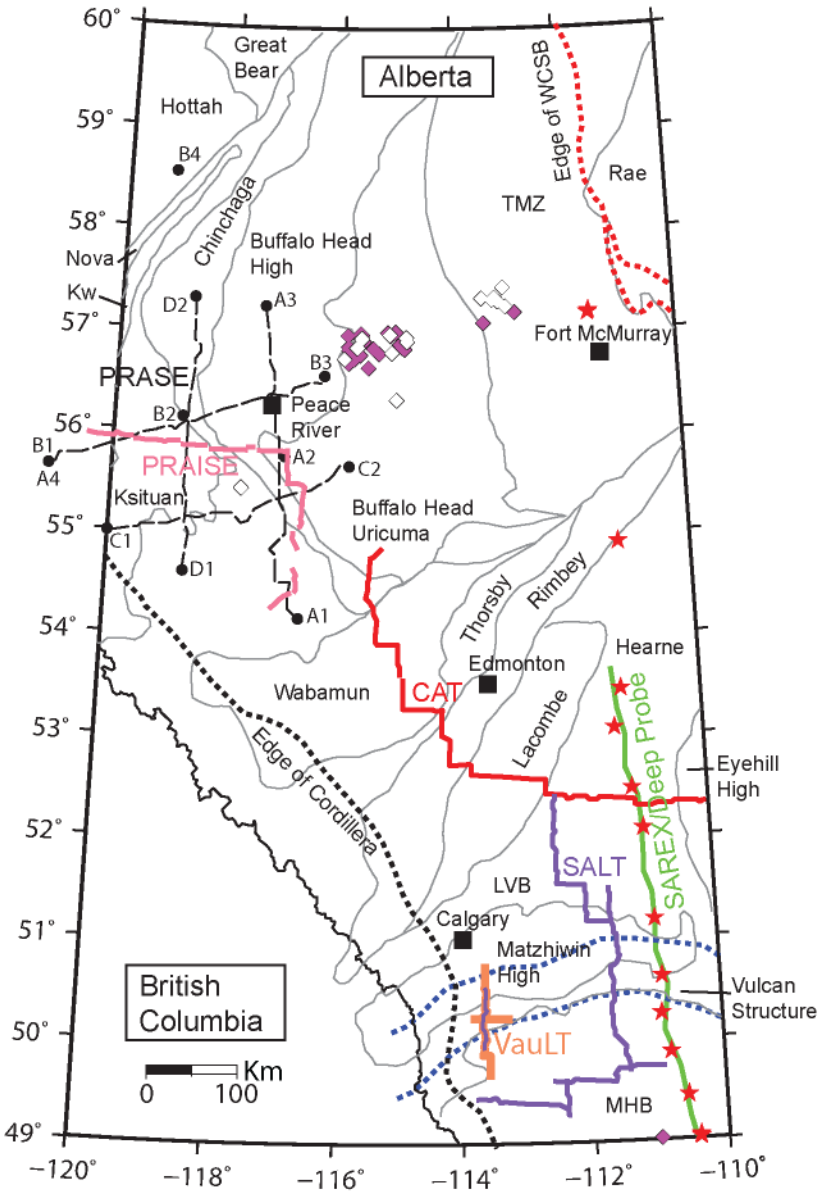

Figure 4.7: Map of Alberta with locations of various seismic reflection and refraction studies. The gray lines indicate the terrane boundaries. The star signs are shot point of the Deep Probe and southern Alberta Refraction Experiment (SAREX). Red dots mark the shot point locations of the PRASE project. The dashed blue lines mark the location of the Vulcan structure defined by Eaton et al. (1999). The diamond signs are locations of kimberlite or ultramafic intrusions. Abbreviations: PRAISE, Peace River Arch Industry Seismic Experiment; PRASE, Peace River Arch Seismic Experiment; CAT, Central Alberta Transect; SALT, southern Alberta Lithospheric Transect. VAuLT, Vibroseis Augmented Listen Time; TMZ, Taltson magmatic zone; LVB, Loverna Block; MHB, Medicine Hat Block.

4.5.1.1. General features of the seismic reflection profiles

The reflectivity features of the WCSB and the underlying crystalline basement in the Lithoprobe seismic lines were summarized in Hope et al. (1999). The sedimentary layers of the WCSB were imaged as prominent, laterally-continuous horizontal to sub-horizontal reflectors on the Lithoprobe seismic sections. In contrast to the sedimentary reflectors, the reflectivity of the Precambrian crystalline basement is characterized by lower signal to noise ratio and few laterally coherent reflections (Hope et al., 1999). Basement reflection amplitudes of the Lithoprobe seismic reflection lines are generally smaller in Archean-aged domains than the others. Anomalous high basement reflection amplitudes are observed in the Lacombe domain, which may account for the low-grade volcanic and sedimentary rocks in this region (Hope et al., 1999).

The Moho structure defined from the Lithoprobe reflection lines is summarized by Bouzidi et al. (2002) and Ross (2002). The Moho was recognized as the abrupt transition (with a vertical extent of 1-2 km) from reflective crust to non-reflective mantle in most of Alberta. The depth range of the Moho in Alberta was found to be 35-48 km. A localized shallow Moho was observed near the Kimiwan isotopic anomaly in the Peace River region (imaged on lines 11-12, Figure 4.9). A jump of 7-10 km in Moho depth across the STZ (Figure 4.8) and an increase of Moho depth across the Vulcan structure were defined (Figure 4.10) in the Lithoprobe profiles.

4.5.1.2. Central Alberta transect (CAT)

The CAT project included the Lithoprobe lines 1-10, and it covered the Wabamun domain at the northwest, and Thorsby, Rimbey, Lacombe domains, the Loverna block and

Eyehill high at the southeast (Figure 4.8). A shallow Moho was imaged at the southern boundary of the Wabamun domain. In contrast to that, the Moho of the Thorsby domain was imaged to be anomalously deep. The structural offset of the Moho depth was interpreted to be 7-10 km. The Loverna block was characterized with southeast-dipping reflections throughout the crust which was considered to be representative of the northwest sense vergence of crustal–scale imbrication. This feature was also observed in the Lacombe and Rimbey domains (Ross, 2002). These extensive dipping features were proposed to be result of Paleoproterozoic subduction along the northern edge of the Hearne province.

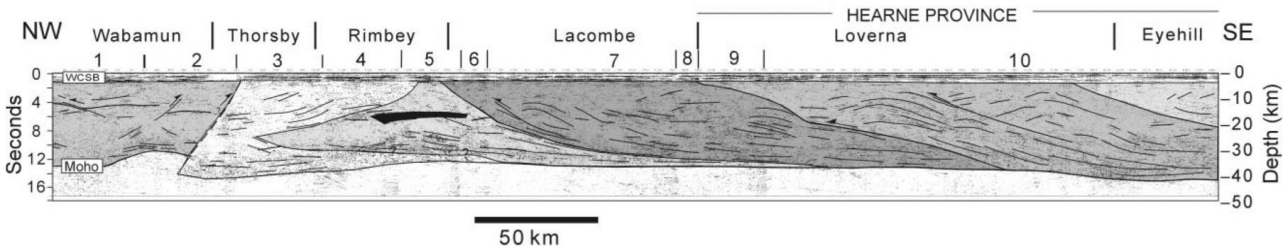

Figure 4.8: Interpreted CAT (Central Alberta Transect) of lines 1-10. The solid black lines are prominent reflections. Arrows indicate thrust movements. WCSB, Western Canada Sedimentary Basin. The black zone was recognized as a low-velocity zone interpreted as serpentinized material (Eaton and Cassidy, 1996). Figure from Ross (2002).

4.5.1.3. Peace River Arch Industry Seismic Experiment (PRAISE)

The seismic data of PRAISE project, including Lithoprobe lines 11-20, were interpreted by Ross and Eaton (2002; Figure 4.9). The Moho was well defined in the reflection profiles and was found to be at a depth of 37-42 km.

The lines 11-12 were oriented west-east and crossed the Kiskatinaw, Ksituan, Chinchaga, and Buffalo Head domains (Ross and Eaton, 2002). The Kiskatinaw domain was

characterized with east-dipping reflections from 10 km depth down to the Moho. The Ksituan domain was found to be only marginally reflective which suggested that the center of the Ksituan domain was less deformed than the Kiskatinaw domain. The Chinchaga domain was imaged with coherent reflectivity at various depth extent of the crust. The boundaries of the Ksituan domain were interpreted to be in fault contact with the two adjacent domains according to reflectivity cut-off relationships. No apparent seismic expression was observed at the boundary of the Chinchaga and Buffalo Head domains.

The lines 13, 14, and 20 were oriented in a north-south direction and crossed the Buffalo Head and Chinchaga domains. Crustal reflectivity of these segments was characterized by prominent Winagami reflection sequence (WRS). The WRS is a series of large, sub-horizontal, continuous reflections imaged at the upper and middle crustal depth in the PRAISE. It was found to be continuous across domain boundaries and therefore was interpreted as mafic intrusive sheets that were emplaced after the terrane assembly (Ross and Eaton, 1997). There was a lens-shaped region in the northern line 13. It was interpreted to indicate that extensional faulting with possible strike-slip motion occurred in this region.

The Kimiwan aeromagnetic high anomaly is transverse to the line 14ABC. The reflectivity of the WRS was found to be significantly disturbed in this region (Ross and Eaton, 2002).Lines 15-19 were recorded in connection with the CAT line 1 and are oriented mostly north-south. The most significant features of these segments are the south-dipping reflections in the lower crust of the Buffalo Head terrane overlaid by the diffractive crust of the Wabamun domain. There is a coherent subhorizontal reflection in the Wabamun

domain which is similar to the WRS but with less vertical displacement (Ross and Eaton, 2002).

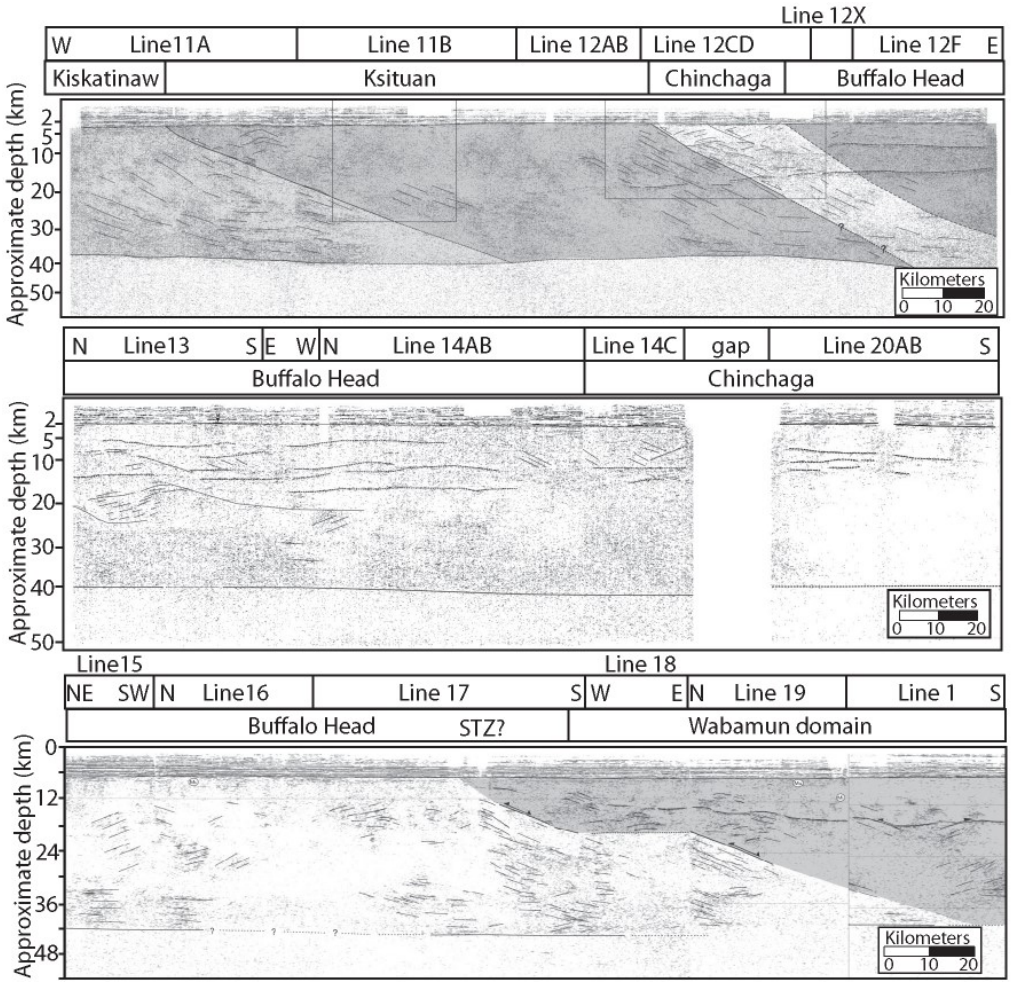

Figure 4.9: Interpreted PRAISE lines 11-20 from Ross and Eaton (2002). STZ, Snowbird Tectonic zone. The shading indicates the terrane boundaries in the crust.

4.5.1.4. Southern Alberta Lithospheric Transect (SALT)

The SALT data were acquired in 1995 and consisted of Lithoprobe lines 21-25 and lines 29-32 (Eaton et al., 1999).Lines 25 and 32 are north-south oriented profiles and crosscut the Vulcan structure. The crustal structure of lines 25 and 32 was interpreted in distinct zones according to their reflectivity characteristics (see details in Figure 4.10). The

lower crust of the Loverna block was imaged to extend southward below the upper crust of the Vulcan structure or the MHB. Mafic sill intrusions were imaged as subhorizontal high reflective zones in the MHB referred to as the Head-Smashed-In (HSI) reflection sequence (Figure 4.10; zone 5 of interpreted line 32; Mandler and Clowes, 1998). The Moho of the MHB was imaged deeper than the Loverna block.

In line 25 (Figure 4.10), zone 1 represents the Western Canada Sedimentary Basin (Eaton et al., 1999). Zone 2 is poorly imaged basement of multiple contaminations. Zones 3 and 8 are interpreted to be the upper and lower crust of the Loverna block. Zone 4 has strong diffractions. Zone 5 represents the Vulcan structure. Zones 6A and 6B are characterized with strong and weak south-dipping reflections, respectively. Zone 7 is interpreted to be the unreflective upper crust of Medicine Hat block (MHB). Zone 9A and 9B are interpreted to be the lower crust of the MHB with strong and weak reflectivity. Zone 10 represents the upper mantle. R1 is a sub-horizontal reflection in mid-crust depth. R2 is a dipping lower crustal reflection.

In the line 32, zone 1 and 2 are interpreted the same as in line 25. Zone 3 was interpreted to be the upper crust of the MHB or the Vulcan structure. Zone 4 is characterized with high attenuation. Zone 5 was inferred as the Head-Smashed-In reflection sequence. Zone 6 was inferred as the lower crust of the Loverna block. Zone 7A and 7B were interpreted as the lower crust of the MHB with strong and weak reflectivity. Zone 8 represents the upper mantle (Eaton et al., 1999).

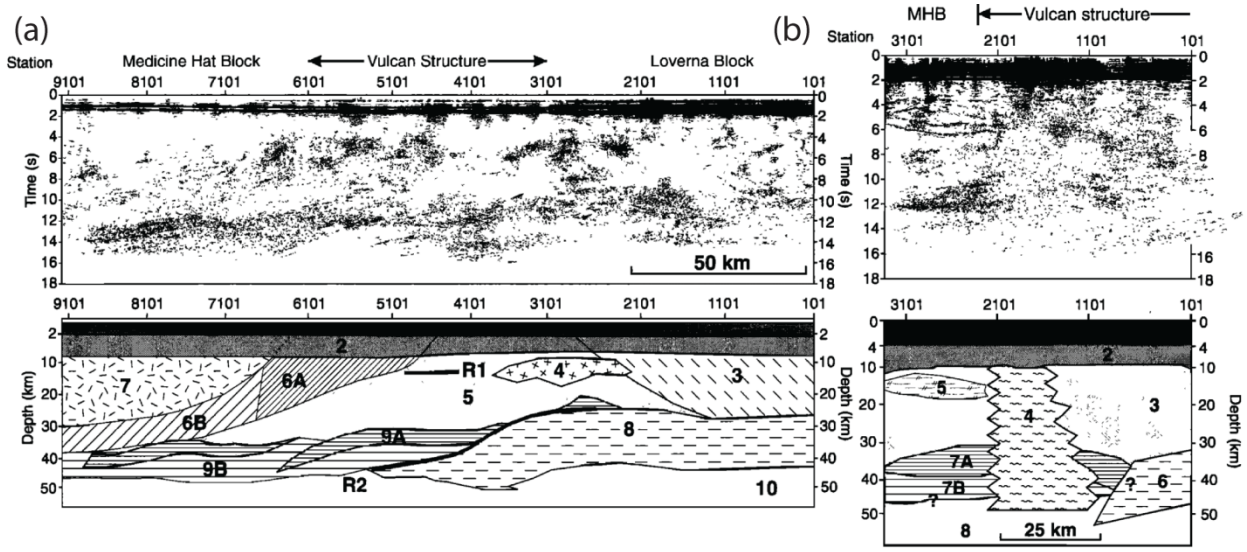

Figure 4.10: The migrated and coherency filtered seismic section along SALT lines 25 and 32 (top a and b, respectively) and its corresponding subdivision of zones with distinct reflectivity (bottom a and b, respectively). The conversion from time to depth uses the Phanerozoic isopach of 2.0-2.2 km from Wright et al. (1994), an average velocity of 6.6 km/s for the crust (Burianyk et al., 1997) and an upper mantle velocity of 8.1 km/s. Figure modified from Eaton et al. (1999).

The SALT line 29-31 crossed the MHB from the west to the east over a 200 km profile (Lemieux et al. 2000). The WCSB was found to thicken from ~3.2 km in the east to ~5.9 km to the west of the lines (Zone 1 in Figure 4.11). The crust of the MHB was imaged with west- and southwest-dipping reflectivity (Zone 3 in Figure 4.11). High-amplitude sub-horizontal reflections (named as HIS: Head-Smashed-In reflections) were imaged in the western part of the lines at upper crustal depth (Zone 2 in Figure 4.11). A layered lower crust was imaged in the MHB and interpreted as the delaminated Hearne crust (Zone 4 in Figure 4.11) with later stage mafic injections (Zone 5 in Figure 4.11). Furthermore, xenolith studies suggested that the lower crustal mafic injection of Zone 5 was a significant Paleoproterozoic thermal event happened coeval with the Tran-Hudson Orogen (Lemieux et al. 2000).

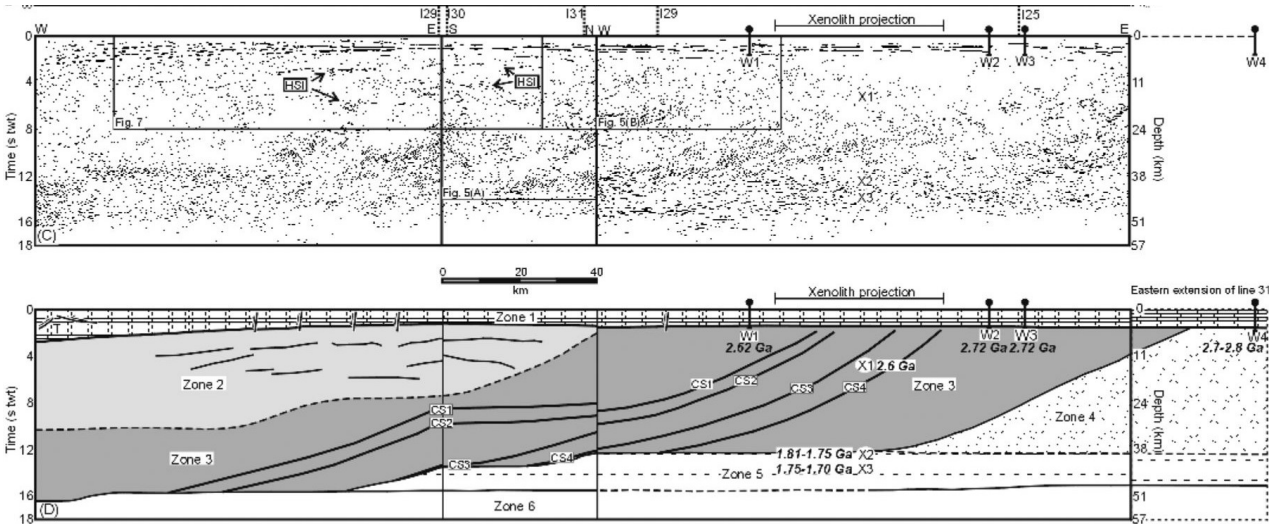

Figure 4.11: Migrated (top) and interpreted (bottom) SALT line 29-31. HIS: Head-Smashed-In reflections. Figure from Lemieux et al. (2000).

The SALT lines 21-24 were located in the Loverna block of southern Hearne (Figure 4.12). There is a deep Moho imaged in line 22 at a depth of ~45 km (Bouzidi et al., 2002).

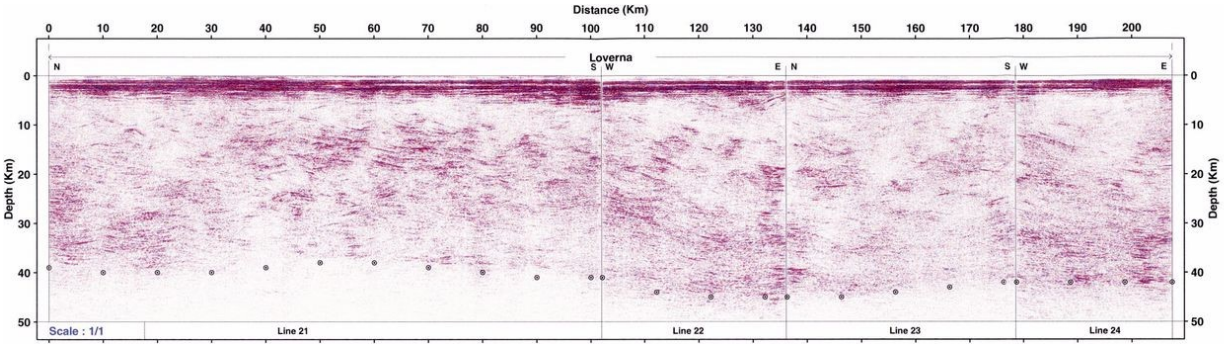

Figure 4.12: Migrated SALT lines 21-24 in Loverna block. The dots mark the locations of Moho according to the reflectivity features. Figure from Bouzidi et al. (2002).

4.5.1.5. Vibroseis Augmented Listen Time (VauLT)

The data of the VAuLT (Vibroseis Augmented Listen Time) experiment was interpreted by Eaton et al. (2000; Figure 4.13) which revealed the fine-scale structure of the upper mantle in the western Vulcan structure. The Moho was found to be indistinct in

the study area. A south-dipping band of high reflectivity with ~25 km thickness was imaged in the lower crust of the Vulcan structure and extends into the Medicine Hat block to a depth of ~60 km. Metamorphic transformation of mafic material into eclogite was proposed to explain this reflective band. Non-reflective zone observed within the Vulcan structure was interpreted as an intrusive complex that destructed the original structure of the crust. The only mantle reflective segment was located at a depth of ~120 km in the Vulcan structure and dips to the north.

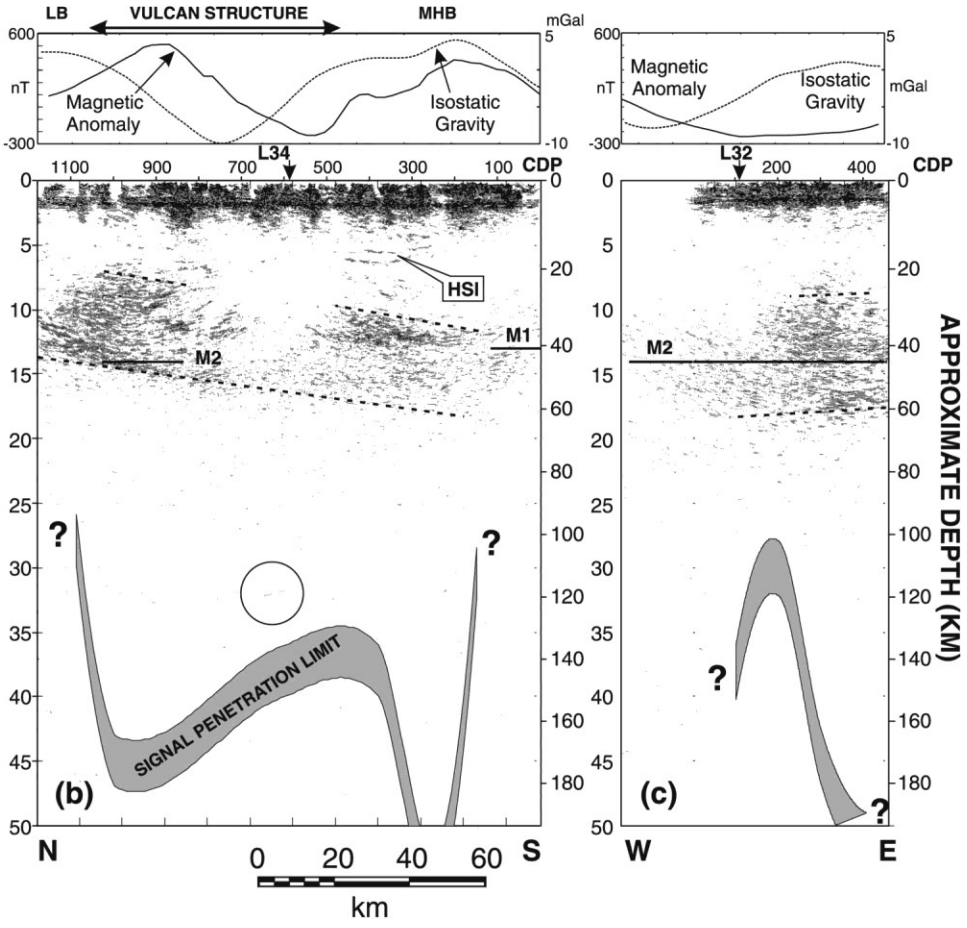

Figure 4.13: Left: migrated seismic section of line 32E; right: migrated seismic section of line 34E. The top two panels show the isostatic gravity and aeromagnetic field of the profile. The round circle marks the location of mantle reflective segment. M1 and M2 are Moho depth calculated from seismic refraction studies (Zelt and White, 1995). The dashed lines indicate the band of south-dipping reflectivity. Figure from Eaton et al. (2000).

4.5.2. Refraction seismology

The seismic refraction method uses refracted waves to determine the structure and seismic velocity of the subsurface. It is widely used to map the velocity structure of the crust and upper mantle and to determine the depth of the Moho (Lowrie, 2007). A number of refraction studies have been carried out in Alberta (Figure 4.7). The Lithoprobe's Southern Alberta Refraction Experiment (SAREX; Clowes et al., 2002) was designed to image the velocity structure of Archean domains in southern Alberta. The data of SAREX was combined with the data from Lithoprobe Deep Probe project to give a seismic velocity model of southern Alberta and Montana (Gorman et al., 2002). Several previous refraction studies in Alberta includes Chandra and Cumming (1972), Zelt and Ellis (1989; PRASE, Peace River Arch Seismic Experiment), Zelt and White (1995; SCORD 9, Southern Cordillera Refraction Experiment line 9).

4.5.2.1. Southern Alberta Refraction Experiment and Deep Probe

The most significant feature in the interpreted velocity model of the SAREX (Southern Alberta Refraction Experiment and Deep Probe) data is a thick (10-25 km), lower crustal layer with high velocity (7.5-7.9 km/s; Figure 4.14). It is imaged in the MHB and Wyoming block where the crust thickens to almost 60 km in comparison to ~40 km thickness in the Loverna block (Clowes et al., 2002). This layer was interpreted to be related with Paleoproterzoic magmatic underplating events based on lower crustal xenolith studies. Wavy structure was imaged in the Loverna block which was attributed to the crustal deformation history (Clowes et al., 2002).

The data of the Deep Probe project was combined with the SAREX data to give a velocity model of southern Alberta to a depth of ~150 km (Figure 4.14; Gorman et al., 2002). The velocity model suggested that the MHB was formed as an independent Archean crustal block. The most prominent features are two north-dipping reflectors imaged in the lithospheric mantle. They were interpreted as relic subduction zones associated with the assembly of the Archean blocks (Wyoming, MHB, and Hearne).

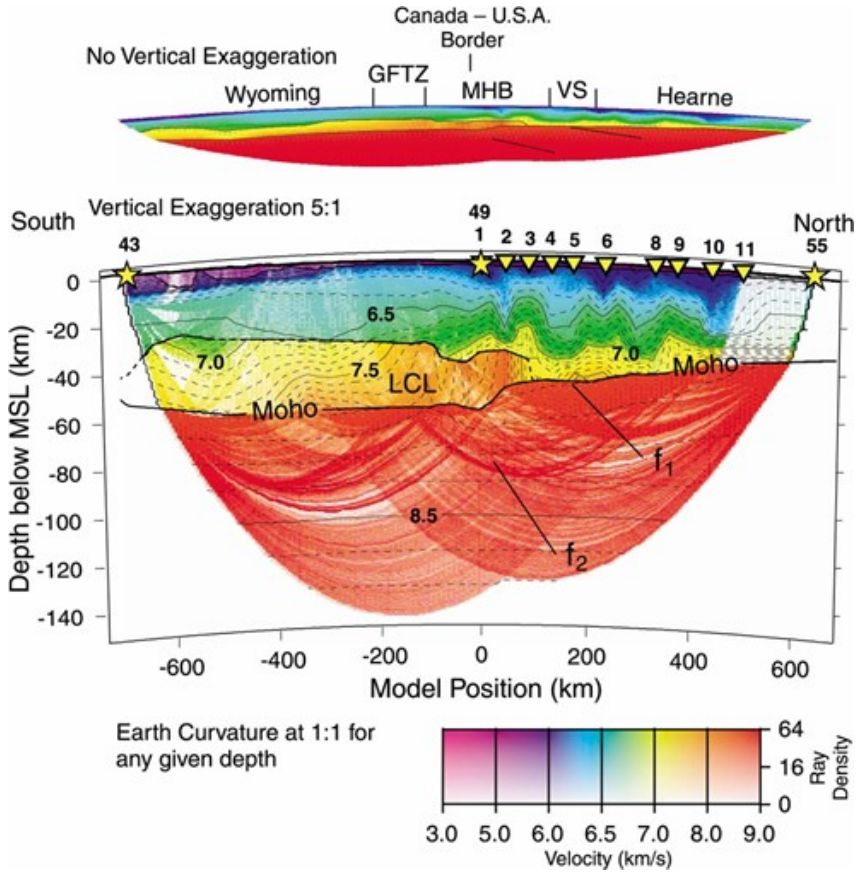

Figure 4.14: Interpreted Deep Probe Velocity model. Shot points of Deep Probe and SAREX (Southern Alberta Refraction Experiment and Deep Probe) are indicated as stars and triangle, respectively. LCL, Lower crustal layer; f_1 and f_2, upper mantle reflectors; GFTZ, Great Falls tectonic zone; MHB, Medicine Hat block; VS, Vulcan structure; MSL, mean sea level. Figure from Gorman et al. (2002).

4.5.2.2. Peace River Arch Seismic Experiment (PRASE)

The PRASE project was designed to image crustal structure of the Peace River Arch region in northern Alberta (Zelt and Ellis, 1989; Figure 4.15). It was done before the seismic reflection project – PRAISE. The crustal structure was found to be correlated with the tectonic terranes. It is laterally consistent without significant layering or thick low-velocity zones. The average Moho depth was about 40 km with its maximum and minimum values observed in the east and west, respectively. Furthermore, the average crustal velocity of the crystalline basement was found to be 6.6 km/s and the velocity of the underlay upper mantle was 8.25 km/s.

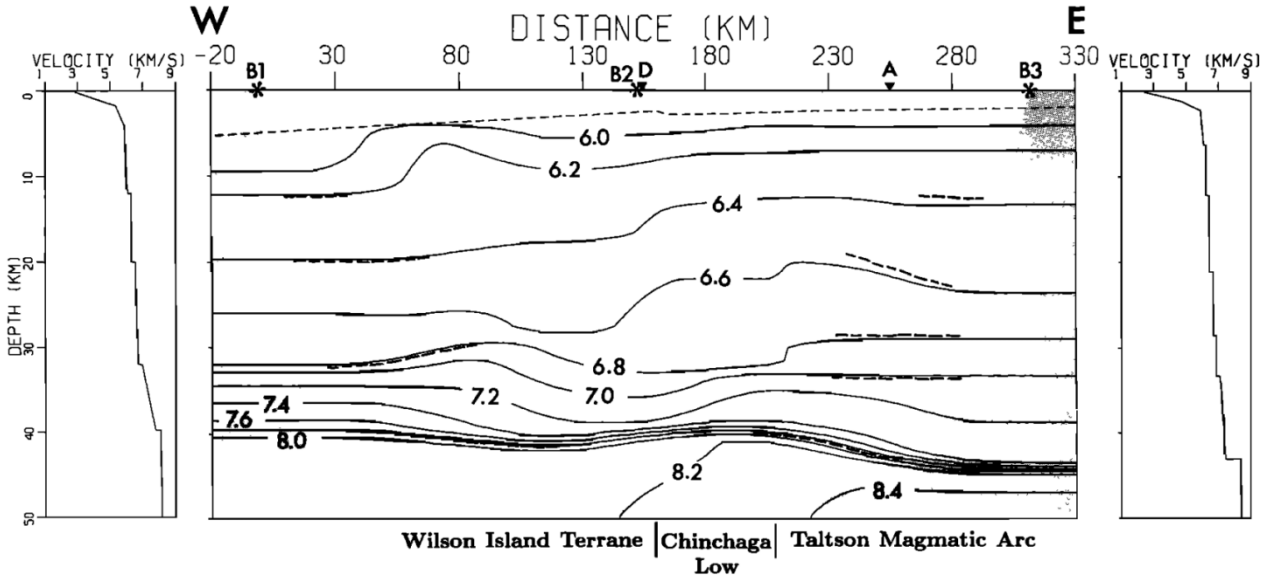

Figure 4.15: P-velocity model of the B profile in the Peace River Arch Seismic Experiment (PRASE; Zelt and Ellis, 1989). The two 1-D velocity models at the sides are corresponding to the velocity of two ends of the 2-D profile. B1, B2, and B3 are shot points in this profile. Letter A and D indicate the crossing points of profile B with profile A and D. Figure from Zelt and Ellis (1989).

4.5.3. Teleseismic studies

Several regional and global seismic P- / S- velocity models have been published for this region using receiver function analysis, teleseismic tomography and ambient noise correlation tomography methods. The energy sources of these studies are natural occurring earthquakes, and the man-made signals required in reflection and refraction seismology as described in section 4.5.1 and 4.5.2 are not used. The signals are recorded with permanent or temporary seismic stations. The advantage of the teleseismic studies are they have stronger sources with longer wavelength and can image the Earth deep to the mantle (Liu and Gu, 2012).

4.5.3.1. Regional broadband data receiver function analysis

Receiver functions are time series calculated from three-component seismograms. The sources of signals are teleseismic earthquakes which sample the Earth along the travel path. The response of the Earth just beneath the stations can be extracted by cancelling the common features of different components. The estimated receiver functions are used in an inversion scheme to find a velocity-depth model of the study area.

Maps of the Moho depth and crustal V_p/V_s ratio of Alberta were presented by Gu et al. (2018) using receiver functions analysis (Figure 4.16). Broadband seismic data with the most extensive regional coverage thus far has been used in this study. The Moho depth and Vp/Vs ratio were determined using the receiver function method based on P-to-S conversion at the Moho.

The average Moho depth in Alberta was determined to be ~40 km (Gu et al., 2018). A region of significant change (about 10 km) of Moho depth was observed near the STZ

which is consistent with Bouzidi et al. (2002). The Moho of the VS was observed to be anomalous deep and ~47 km at the west end and ~44 km at the east end. A sharp transition from a thick Moho at the foothills of Rocky Mountains to a shallow (~35 km) Moho in Alberta was observed in the latitude range of 49-51˚ N.

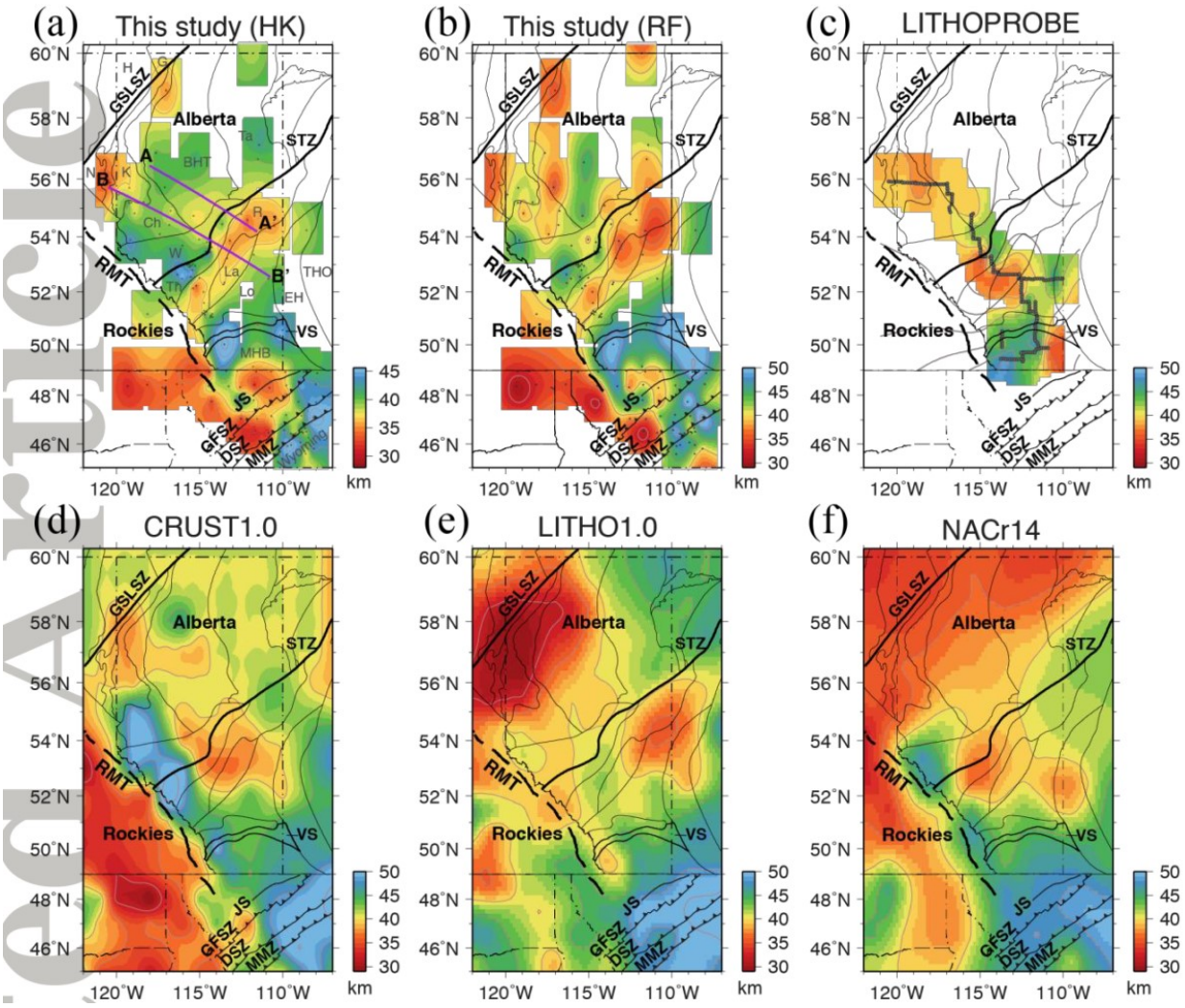

Figure 4.16: The depth of Moho in Alberta summarized in Gu et al. (2018). Maps (a) and (b) are results of Gu et al. (2018). Map (c) is from Bouzidi et al. (2002). Map (d) is CRUST1.0 from Laske et al. (2013). Map (e) and (f) are Litho1.0 and NACr14 from Masters et al. (2010) and Tesauro et al. (2014), respectively. RMT, Rocky Mountain Trench. GSLSZ, Great Slave Lake shear zone. STZ, Snowbird Tectonic zone. VS, Vulcan Structure. Figure from Gu et al. (2018).

A consistent low Vp/Vs ratio was mapped in the Taltson Magmatic Zone that was associated with possible intra-continental origin (Gu et al., 2018; Figure 4.17). Enhanced Vp/Vs ratios were mapped in the Wabamun domain and BHT which was linked to the WRS (Winagami reflection sequence). The STZ was classified into two segments according to the signature of crustal Vp/Vs ratios: the northeastern segment with low Vp/Vs ratios (<1.73) and the central-southwestern segment with clusters of high Vp/Vs ratios (>1.82).

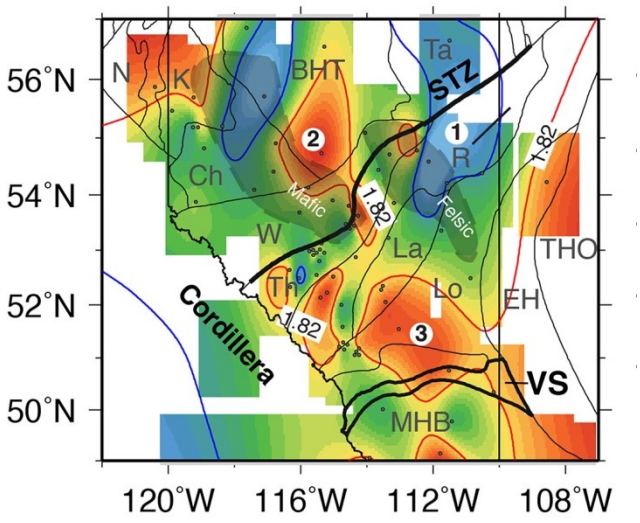

Figure 4.17: Map of Vp/Vs ratios in Alberta. The major anomalies are highlighted with labels 1-3. The shaded area show the locations of mafic and felsic magmatic intrusions from previous studies. Figure from Gu et al. (2018).

The low velocity zone was imaged in a previous study as well using receiver-function analysis of the seismic broadband station EDM. The low velocity zone was imaged at depths between 13 and 16 km near Edmonton (Eaton and Cassidy, 1996; Cassidy, 1995). This anomalous velocity zone was interpreted as a piece of ancient oceanic lithosphere with serpentinized material and relate with Proterozoic subduction happened along the STZ in Alberta.

This crustal low-velocity feature was described in detail with a shear-wave velocity inversion model using P-to-S receiver functions beneath eastern-central Alberta (Figure 4.18; Chen et al., 2015). The low velocity zone is about 200 km wide, over 10 km thick and at 10-20 km depth and spatially correlates with a high heat flow anomaly. The low-velocity anomalies were interpreted to be comprised of granitic rocks and may be related to the crystallization from the molten state during the Paleoproterozoic. Higher S-velocities in the depth range of 8-15 km were also observed. Some of these high velocity anomalies are coincident with the Winagami reflection sequences (WRS). All these observations were interpreted to support that distinct episodes of magmatism and crustal modification have occurred in the central Alberta.

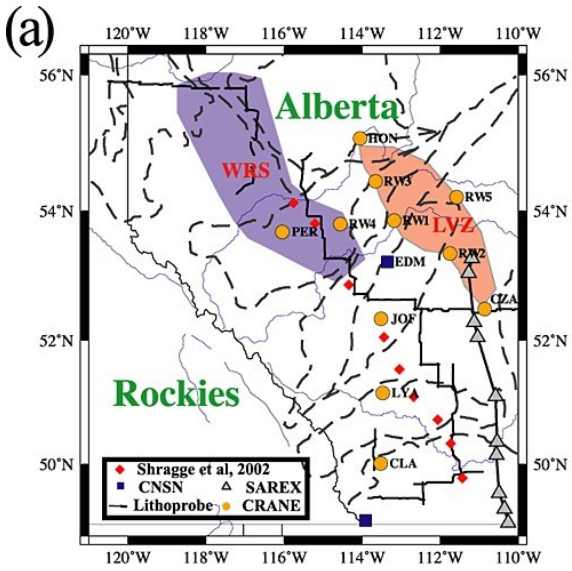

Figure 4.18: A map showing the high velocity anomaly associated with the Winagami reflection sequences (WRS) and the mid-crustal low velocity zone (LVZ). The symbols on the map indicate the locations of seismic stations. Black solid lines represent locations of previous seismic profiles. Black dashed lines marks the tectonic boundaries. Figure from Chen et al. (2015).

4.5.3.2. Regional teleseismic tomography

Seismic tomography methods utilize the seismic records to constrain the 2-D or 3-D velocity structure of the Earth. It is generally done via searching for an inversion solution with seismic velocity model that agrees with the observations (Liu and Gu, 2012). Seismic tomography can be based on different kinds of seismic data such as traveltime, waveform, surface waves, and ambient noise signals. The ray-based traveltime tomography is theoretically simple and had been widely used as a classic method. Another classic method is the waveform tomography which can be divided into ray path based or finite frequency tomography methods. The finite frequency tomography method has the advantage of higher resolution than the ray path method based one because it accounts for the effect of the wave near the ray path but far from the study area. The surface wave tomography methods cannot resolve the crustal structures well because the long wave length of the surface waves. Ambient noise tomography does not require an earthquake to generate seismic waves but use the random waves caused by oceanic and atmospheric disturbances.

P-wave traveltime tomography of broadband seismic data at 11 stations revealed that the Loverna block is characterized with the highest lithospheric velocity in south and central Alberta (Shragge et al., 2002). This feature was interpreted to indicate that the Loverna block is relatively intact and has the thickest lithosphere. The Vulcan structure was interpreted as a structural suture based on the distinct velocity properties observed in the Loverna block (high velocity) and MHB (low velocity).

A P-velocity model of Alberta for upper mantle depths was constructed using finite-frequency tomography by Chen et al. (2017; Figure 4.19). It showed that the lithospheric

structure of the craton is in sharp contrast to that of the Canadian Cordillera. The lithospheric depth of the MHB, southern Hearne (i.e. Loverna block), Lacombe domain, and Buffalo Head domain were determined to be 230 km, 350 km, 220 km, and 185 km, respectively. The lithosphere is thickest in the Hearne craton even though anomalous low P-velocities exist at the shallow depths.

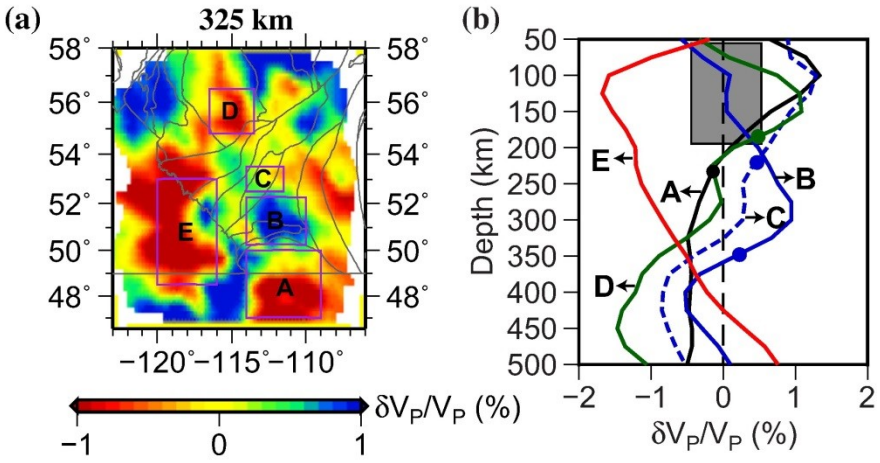

Figure 4.19: (a) P-wave velocity perturbations at 325 km depth. The boxes with letters A-E indicate regions with distinct velocity features. (b) Average 1-D velocities calculated with respect to each region in (a). The lithosphere-asthenosphere boundaries (LAB) are indicated with circles on the curves. The gray box marks the upper-lithospheric low velocity anomaly in region B. Figure from Chen et al. (2017).

The result of Chen et al. (2017) was updated by Chen et al. (2018) in which both S- and P- velocity models of Alberta were presented (Figure 4.20). Similar features were observed with a few new discoveries. A cylindrical low velocity anomaly at depths of 75-300 km was imaged in northern Alberta that was interpreted to indicate tectonothermal modifications have occurred in the region.

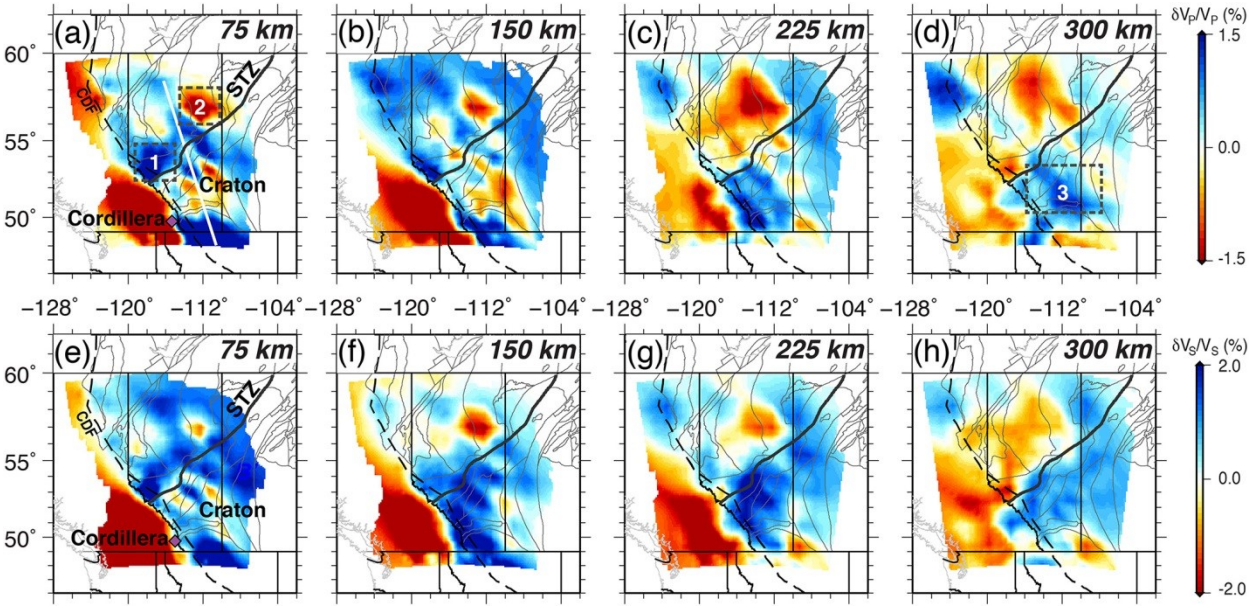

Figure 4.20: The P- and S- velocity model of Chen et al. (2018). Abbreviations: STZ, Snowbird tectonic zone; CDF, Cordillera deformation front.

Rayleigh-wave data were analyzed by Bao and Eaton (2015) and Bao et al. (2014) using seismic broadband data and shear velocity model of the western Canada was presented accordingly. The Loverna block of Hearne province and the Buffalo Head domain were imaged with high-velocity anomalies to depths up to 260 km (Figure 4.21). This feature was interpreted as ancient thick cratonic roots. In contrast, thinner lithosphere was imaged beneath the Wabamun domain and MHB (Bao and Eaton, 2015). Furthermore, the boundary of the North America craton and Cordillera was marked by an abrupt change in the lithosphere thickness (Bao et al., 2014). The lithosphere of the Cordillera was observed to be ~150 km less thick than that of the craton and the asthenosphere of the Cordillera lies 20-30 km beneath the crust. A high velocity anomaly was imaged below the Canadian Cordillera and was proposed as the delaminated part of the Cordillera lithosphere.

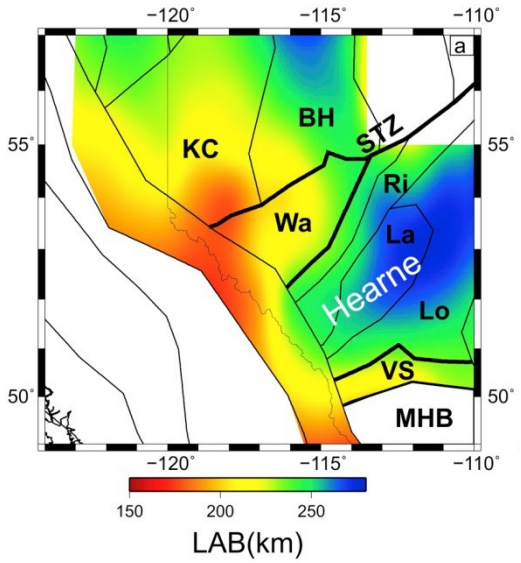

Figure 4.21: Map of the estimated lithosphere thickness. Figure from Bao et al. (2015).

Ambient noise correlation tomography of central and southern Alberta showed the S-velocity structure of the region (Gu and Shen, 2015). Anomalous low velocity bodies in the Wabamun and Buffalo Head domains were imaged at mid- and upper-crustal depth. This was explained by crustal melting in the Proterozoic eon result from crustal convergence. The lower crust of the southern Hearne province in Alberta is characterized by 10% higher S-velocity than the regional average. This was interpreted as evidence for relic, potentially undeformed part of the Hearne province.

4.5.3.3. Global and continental-scale teleseismic tomography

Many global and continental-scale seismic velocity models have been presented. Out of the many models, the shear velocity models SL2013NA and SEMum_NA14 have more detailed structure in Alberta (Figure 4.22). The SL2013NA is a global shear velocity of the North America presented by Schaeffer and Lebedev (2014). The model was constructed using waveform inversion of seismic broadband data. Perturbations in P and S velocity and

azimuthally anisotropy were all considered in the inversion scheme. The resolution of the SL2013NA was significantly improved because of the better data coverage.

The SEMum_NA14 is another high-resolution isotropic and radially anisotropic shear velocity model presented by Yuan et al. (2011) using the long-period full waveform inversion method. Other continental scale seismic velocity models includes: the NA07, which is a shear wave velocity model for the upper mantle based on Rayleigh wave and S-wave inversion for North America (Bedle and van der Lee, 2009). The model LLNL_G3Dv3 is a global P wave tomography model developed by Simmons et al. (2012). The velocity structures from the shallow sediments to the depth of Moho and low mantle are all included in this model. However, the model was constructed with 1˚ lateral spacing which results in low resolution in the Alberta area.

The general features of interest from the SEMum_NA14 and SL2013NA models are (a) the change from thin lithosphere beneath the Cordillera (<80 km) to thick lithosphere beneath the craton (>200 km), which follows the Rocky Mountain Front (Schaeffer and Lebedev, 2014; Yuan et al., 2014). (b) The craton root of the North American retracts to the center of the continent at the west side of the craton (Yuan et al., 2014). This is consistent with the observation of the lack of deep cratonic roots that was imaged in the Archean MHB and Wyoming Province (Schaeffer and Lebedev, 2014).

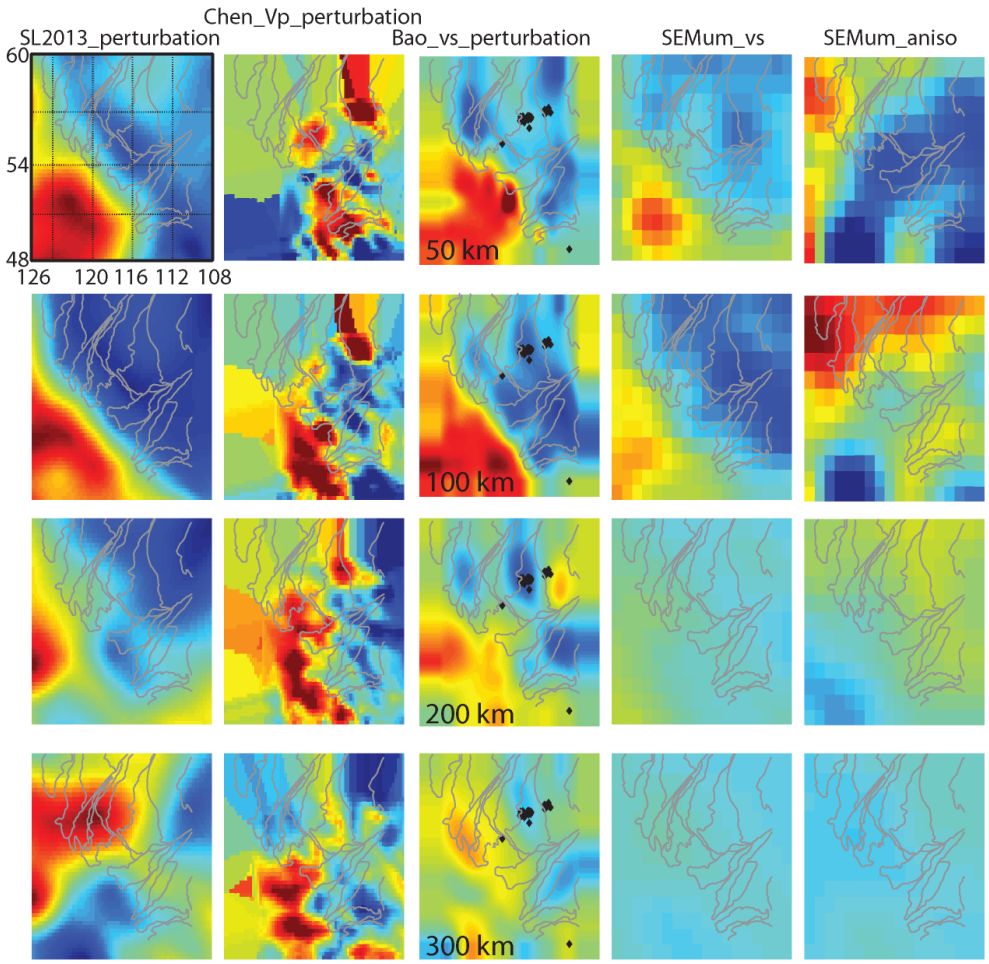

Figure 4.22: Seismic velocity maps of Alberta and surrounding areas at depths 50-300 km. The gray lines are tectonic terranes defined from aeromagnetic field. Each column represents depth slices from a specific seismic model. SL2013_perturbation is the shear velocity perturbation model of the SL2013NA (Schaeffer and Lebedev, 2014). Chen_Vp_perturbation represents the p-wave velocity model of Chen et al. (2017). Bao_vs_perturbation is the shear perturbation velocity model of Bao et al. (2016). SEMum_vs and SEMum_aniso are the shear velocity model and azimuthal anisotropy model from Yuan et al. (2014).

4.5.3.4. Seismic anisotropic features

Seismic anisotropy can be caused by anisotropic shape distribution of isotropic materials, or by the lattice preferred orientation of minerals. Shear wave splitting (SKS splitting) is an important observation for learning about seismic anisotropy. The SKS

splitting was analyzed to show the nature of lithosphere anisotropy in Alberta by Shragge et al. (2002). It was found that the anisotropy splitting is fairly uniform and similar to the geoelectric strike directions from Boerner et al. (2000).

Clear evidence of shear wave splitting in Alberta was also observed by Gu et al. (2011) and Wu et al. (2019). The fast axes of seismic measurements along the Rocky Mountain foothills were found to orient to NE-SW. This is consistent with the result of Shragge et al. (2002). This was interpreted to reflect (1) the "fossil" strain field within the lithosphere caused by the past NW-SE plate convergence history, and (2) the current absolute plate-motion which is also NW-SE (Gu et al., 2011). In comparison, seismic measurements in eastern-central Alberta showed that the fast axes are tangential to a N-S trending ellipse which is centered at 200-300 km northeast of Edmonton (Gu et al., 2011).

The seismic anisotropic velocity structure of central and southern Alberta and southeast British Columbia were also investigated using Rayleigh-wave analysis (Bao et al., 2016; Figure 4.23). As a surface wave, the Rayleigh wave can give better vertical resolution than shear wave splitting, which uses body waves to study seismic anisotropy. The key observations are consistent with Gu et al. (2011) and include: (a) Orogen-parallel fast direction at lower crustal depth in the study area; (b) increase of anisotropy in the Alberta at the lower lithosphere than upper lithosphere; (c) anisotropic layering in Alberta from N-S direction at the lithospheric depth to NE-SW direction at the uppermost asthenosphere depth. The upper N-S anisotropic layer was estimated to be ~220 km thick. This anisotropic direction was generally following the trend of the Trans-Hudson Orogen and was interpreted to be ancient anisotropy frozen after the tectonic assembly in

Paleoproterozoic. The lower NE-SW anisotropic layer was estimated to be ~208 km and caused by present-day mantle flow.

SEMum_NA14 is a high-resolution isotropic and radially anisotropic shear velocity model of North America presented by Yuan et al. (2014). It was concluded that in the craton, azimuthal anisotropy is weak at lithospheric depths but strong below the lithosphere. The fast axis direction of the sublithospheric azimuthal anisotropy was found to be consistent with the absolute plate motion direction (Yuan et al., 2014). This is consistent with the SKS anisotropy result of Bao et al. (2016).

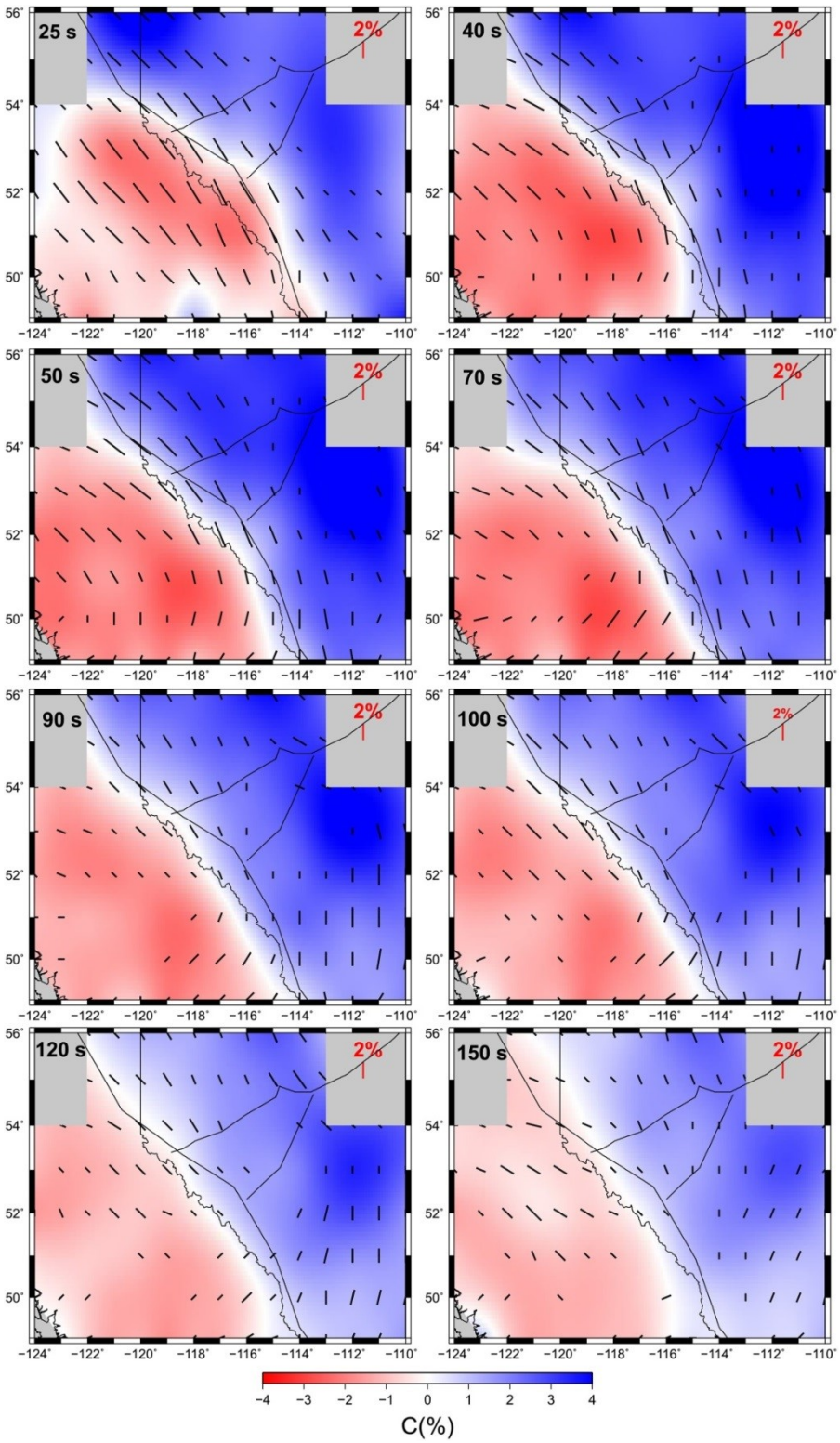

Figure 4.23: Maps of seismic azimuthal anisotropy with periods in western Canada. The seismic fast direction is indicated with black bars in the maps. The length of the bars is indicative of intensity of azimuthal anisotropy. Figure from Bao et al. (2016).

4.5.4. Summary of seismic studies

In summary, different seismic methods applied in Alberta gave consistent results about the Moho depth and crustal features. The Moho in Alberta is continuous with only a few abrupt discontinuities across the Thorsby domain (7-10 km offset; Ross, 2002) and Vulcan structure (~10 km offset; Clowes et al., 2002). The MHB is characterized with a lower crustal layer with higher velocity (Clowes et al., 2002). Receiver function analysis of broadband data has revealed a crustal low velocity zone to the northeast of Edmonton and a crustal high velocity zone associated with the Winagami reflection series (Gu et al., 2018). Teleseismic studies have shown that the Loverna block is characterized with fast velocities and a deep lithospheric root (Chen et al., 2017). Moreover, anisotropic modeling of seismic data has shown that the anisotropic feature of the lithospheric and sublithospheric mantle is quite different. The lithospheric mantle anisotropy was suggested to be caused by ancient tectonic activities and the sublithospheric anisotropy was suggested to be related with the mantle flow (Bao et al., 2016).

4.6. Previous magnetotelluric (MT) studies

Electromagnetic (EM) exploration uses low frequency radio waves to image subsurface electrical resistivity. The signals can be either naturally occurring or man-made. Increasing porosity, higher water content, partial melt, graphite phases and sulfide minerals can lower the bulk resistivity substantially and can be observed by EM methods (Chave and Jones, 2012). Details about the MT theory and method are presented in Chapter 2 of this thesis.

There is a long history of MT studies in Alberta. The first MT studies were made in Alberta in the 1960s (Niblett and Wittgenstein, 1960). A large amount of MT data was collected during the Lithoprobe Alberta Basement Transect project in the 1990s (Boerner et al., 2000). MT data have also continued to be collected by the University of Alberta during various projects (e.g. Nieuwenhuis et al., 2014). Moreover, magnetovatiational data were collected to map the resistivity structures in Alberta utilizing three-component magnetometers (Gough, 1986). Several significant crustal and upper mantle conductors were mapped during these studies.

4.6.1. Conductance of the WCSB

The sedimentary rocks of the WCSB act like a conductive layer above the Precambrian crystalline rocks. This feature was imaged with MT data inversions in Boerner et al. (2000) and Nieuwenhuis et al. (2014). The low resistivity of the WCSB is caused by the presence of aqueous pore fluids and clay minerals.

The conductance (product of conductivity and thickness) of the sedimentary rocks in central Alberta were calculated with MT data and compared to industrial well log estimations (Figure 4.24; Boerner et al., 2000). The conductance values range from about 200 to 800 Siemens. These two methods gave similar values of the conductance in the study area. The two results also follow the same trend of increasing to the east which is in contrary to the fact that the sediment layers are thicker in the west. Boerner et al. (2000) interpreted this observation as indicative of that not all sections of the sedimentary layers contribute to the bulk conductance of the WCSB.

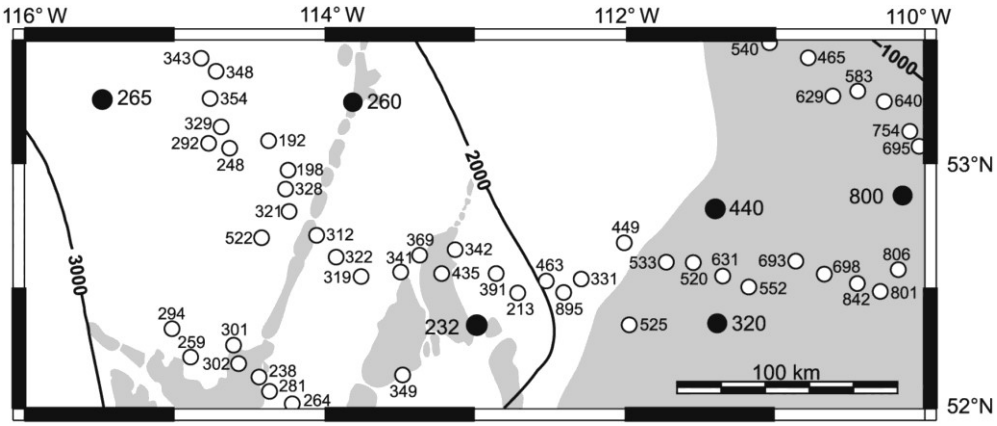

Figure 4.24: Map showing the conductance of the WCSB (product of conductivity and thickness of the WCSB in Siemens) marked with numbers and circles. The numbers with open circles were estimated from TM mode inversions of the Lithoprobe MT data. The numbers with solid circles were determined from industrial well logs. Contour lines represent the thickness of the WCSB in meters. Shaded zones indicate Leduc Formation reef complexes. Figure from Boerner et al. (2000).

4.6.2. Southern Alberta and British Columbia conductor

The southern Alberta and British Columbia resistivity anomaly (SABC, Figure 4.25) was recognized as a nearly linear, highly conductive body that strikes northeast-southwest across southern Alberta and the southeastern corner of British Columbia.

The SABC was first defined by Gough (1986) using magnetovariational data. The magnetovatiational data are essentially equivalent to the vertical component of magnetic field in MT studies. They are sensitive to lateral changes in electrical resistivity, but less sensitive to the resistivity change with depth. This characterization of the SABC is in agreement with several previous MT studies (Reddy and Rankin, 1972). The SABC was interpreted to support that the North American craton extends westerly to the Kootenay Lake in the British Columbia at lower crustal depth (Gough, 1986). Further studies of the magnetovariational data by Wang (1988a; 1988b) modelled the SABC in the shape of either

current sheets or a line current, and with 70-80 km width and 30-120 km depth of burial. More specifically, the southwest segment of the SABC was proposed to be in the depth range of 30-90 km while the northeast segment was proposed to be in the depth range of 70-120 km.

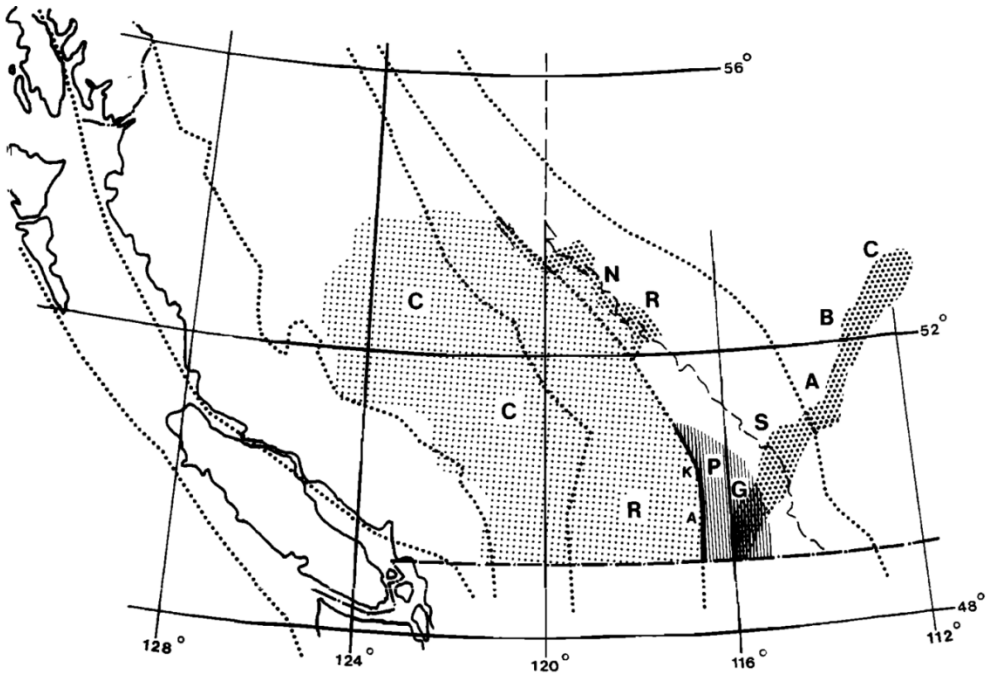

Figure 4.25: Map showing three major conductive structures (CCR, NR, and SABC) in western Canada. Figure from Gough (1986). Abbreviations: CCR, Canadian Cordilleran regional conductor; NR, Northern Rockies conductor; SABC, Southern Alberta and British Columbia conductor; PG, Purcell Geanticline; KA, Kootenay Arc.

4.6.3. Red Deer conductor

The Red Deer conductor (RDC; Figure 4.26) was first identified by Boerner et al. (1995) using the MT data collected during the Lithoprobe Alberta Basement Transect project. The RDC is a highly conductive, linear body that is coincident with the Red Deer aeromagnetic high. Two dimensional inversions of the MT data imaged the RDC just below the WCSB.

The RDC was proposed to be electrically thin because the TM responses of the MT sites near to the RDC are nearly identical to each other. Moreover, the structure of the RDC was interpreted to be roughly continuous but different along the strike. The southern segment was interpreted to be wider than the northern segment and reflect an oblique collisional history of the region (Boerner et al., 2000).

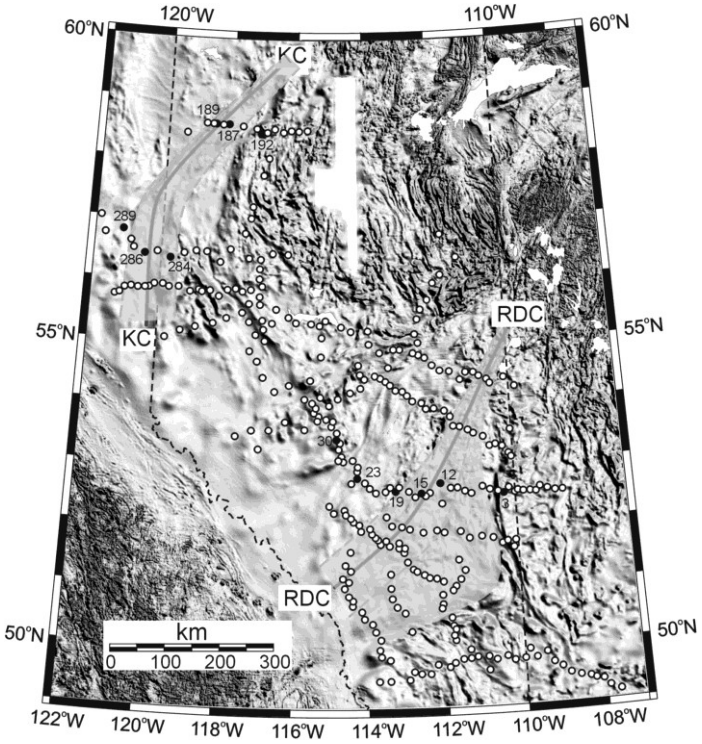

Figure 4.26: Schematic map showing the locations of the RDC (Red Deer conductor) and the KC (Kiskatinaw conductor) with grey shading. Dots mark the location of MT sites of the Alberta Basement Transect project. Figure from Boerner et al. (2000).

4.6.4. Kiskatinaw conductor

Kiskatinaw conductor (KC; Figure 4.26) was first imaged by (Boerner et al., 2000). It roughly follows the trend of the Kiskatinaw aeromagnetic low in the northwestern Alberta and northeastern British Columbia. Similar features of the MT responses observed in the RDC are associated with the KC except that the KC is less pronounced and narrower.

Turkoglu et al. (2009) published the first 3-D inversion of MT data collected in northwest Alberta in order to investigate the regional structural setting of the diamondiferous kimberlite found in the Buffalo Head Hills. In their 3-D inversion model, the most pronounced crustal resistivity anomaly was the Kiskatinaw Conductor (KC).

4.6.5. Loverna block conductor

The Loverna block conductor (LC; Figure 4.27) is a resistivity anomaly located in the southern Hearne province and south-central Alberta at upper mantle depth. It was first imaged and referred as Loverna Conductor (LC) by Nieuwenhuis et al. (2014) by 3-D inversions of MT data. The anomalous conductivity in the Loverna block was also discussed by Boerner et al. (1999; 2000). The origin of the LC was interpreted to be related to metasomatic enrichment of the lithospheric mantle during subduction process (Nieuwenhuis et al., 2014; Boerner et al., 1999).

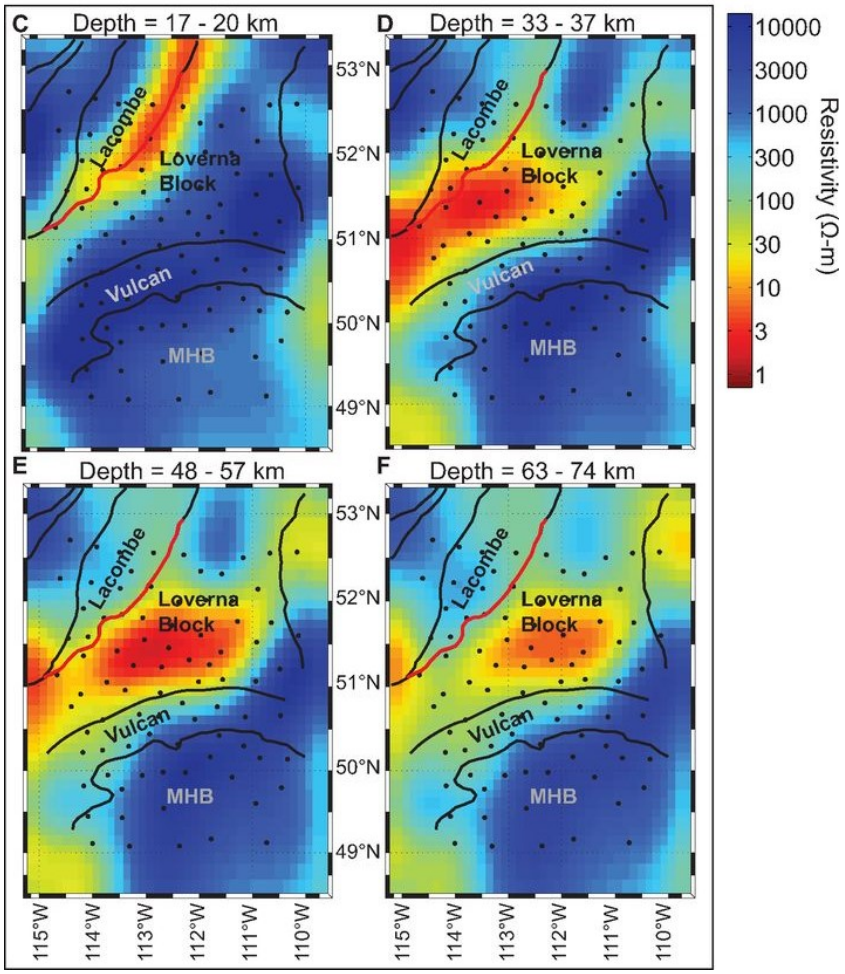

Figure 4.27: Maps of electrical resistivity of southern Alberta at various depths from the 3-D inversion model of Nieuwenhuis et al. (2014). Black lines are the boundary of the tectonic domains. The linear conductor along the southern edge of the Lacombe domain in the slice C was interpreted to be the RDC. The conductor imaged in slice D, E, and F was referred as the Loverna block conductor (LC). Figure from Nieuwenhuis et al. (2014).

4.6.6. Electrical anisotropy

Electrical anisotropy was proposed by Boerner et al. (2000), Yin et al. (2015), and Liddell et al. (2016) to explain some aspects of the MT data collected in Alberta.

Boerner et al. (2000) interpreted the Lithoprobe data to be anisotropic near the Kimiwan isostatic anomaly and the RDC in central and southern Alberta. This is because of

large phase splits observed in the MT data and that 2-D inversions could not resolve discrete bodies. The same dataset was studied by Nieuwenhuis et al. (2014). It was proved that 3-D electrical models were sufficient to fit the Lithoprobe dataset in southern Alberta and electrical anisotropy may exist but not necessary required to interpret the data.

Yin et al. (2014) suggested anisotropic structures in northwest Alberta due to conductive material in fractures. Liddell et al. (2016) fit the broadband MT data collected near to Fort McMurray in northeast Alberta to 2-D electrical anisotropic inversion models. The anisotropic inversion model successfully fit the out-of-quadrant phases, large phase splits, and phase tensors observed in the MT data. Interconnected graphite films within the metamorphic basement rocks were inferred as the cause of the electrical anisotropy (Liddell et al., 2016).

Chapter 5 : Magnetotelluric data collection and processing in Alberta

5.1. Introduction

MT studies in Alberta started in the 1960's and one of the first publications was that of Niblett and Sayn-Wittgenstein (1960). This study was significant because it was one of the first field tests of the theory of MT that had been proposed by Cagniard (1953). Subsequently, additional MT studies were undertaken by Srivastava et al. (1963), Vozoff et al. (1963), Vozoff and Ellis (1966), Rankin and Reddy (1969), and Reddy and Rankin (1972). These early studies used instruments that measured in the frequency band 0.001-0.1 Hz and the resulting data were analyzed with a 1-D approach. This clearly has some limitations, but in the relatively 1-D environment found in the Alberta Basin it gave generally robust results.

Studies in the 1970's showed that some of the data contained 2-D effects, e.g. Reddy and Rankin (1972) in central Alberta and Peeples and Rankin (1973) in southern Alberta. However, only 1-D inversions were completed at that time because 2-D inversion algorithms were not available.

By the early 1990's, many advances had been made in MT instrumentation such as the equipment developed by the GSC (Geological Survey of Canada) and named LIMS (Long-period Intelligent Magnetotelluric System), which was needed for deep sounding. Moreover, 2-D MT inversion algorithms such as Jupp and Vozoff (1977), Jiracek et al.

(1987), Madden and Mackie (1989), deGroot-Hedlin and Constable (1990), Smith and Booker (1991), and Mackie and Madden (1993) were becoming available. A set of 323 long-period MT (LMT) data composed of many profiles across Alberta was collected during the Lithoprobe Alberta Transect (ABT) project (Figure 5.1). These LMT data were presented and interpreted by Boerner et al. (2000). The ABT data were collected with the LIMS instruments. It can record LMT data in a period range of 20-10,000 seconds. After the ABT project was completed, many more LMT stations were collected by the University of Alberta using the NIMS (Narod Intelligent Magnetotelluric System; Narod et al., 2001) during 2002-2017.

In this research, two sets of MT data were collected. Firstly, a broadband MT (BBMT) dataset in northern Alberta was collected during the summer of 2014. This dataset was collected to get a better understanding of the crustal structure across the Hay River Fault (Chapter 6). Secondly, LMT stations were deployed during 2013-2017. These LMT data were combined with previously collected LMT data mentioned above to establish a grid of LMT stations covering the whole of Alberta for 3-D inversions with the best coverage in central Alberta.

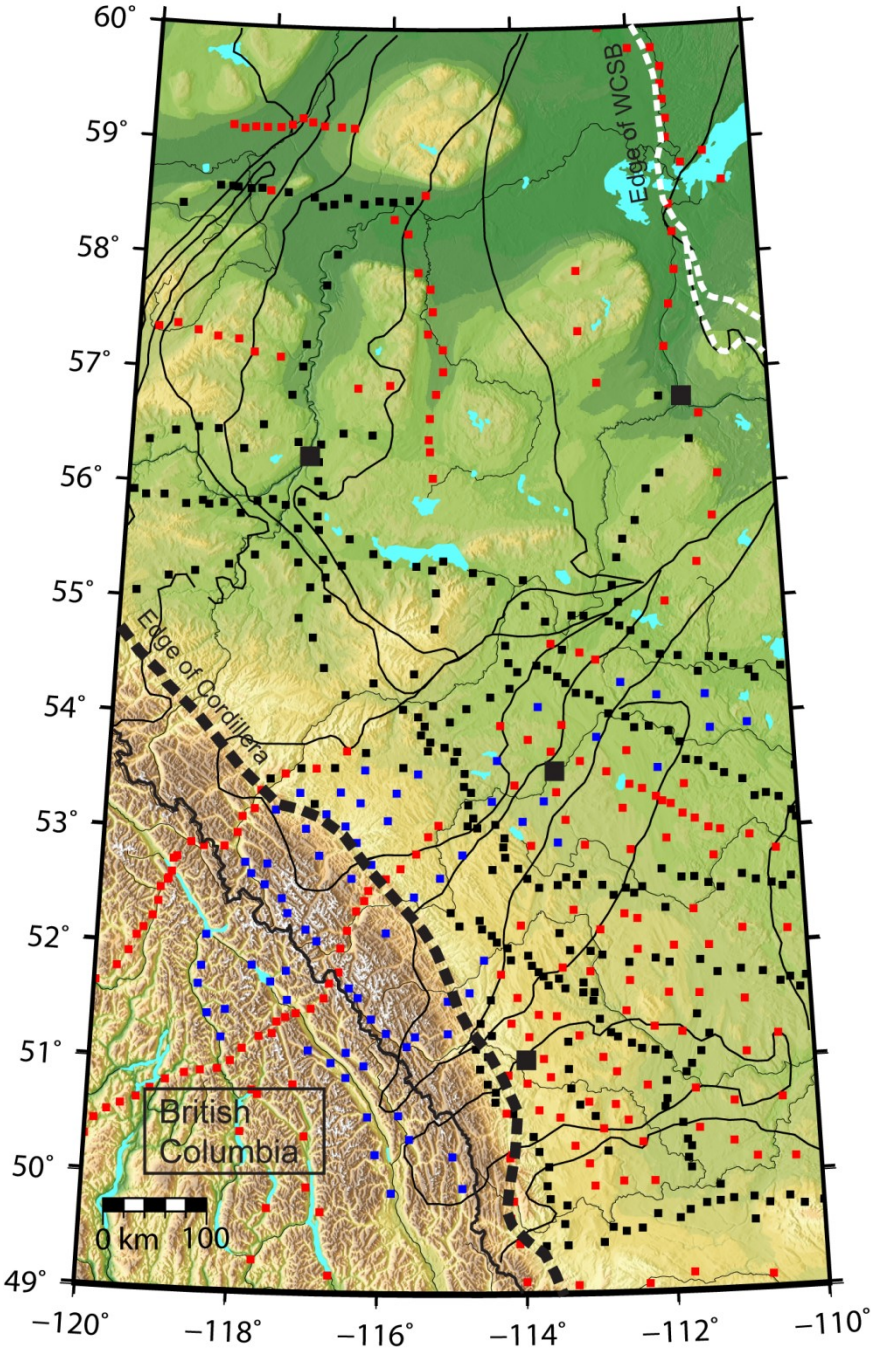

Figure 5.1: LMT data coverage in Alberta. The background is a topographic map and black lines mark the terrane boundaries defined from aeromagnetic field and isotopic studies of drill-core samples (Villeneuve et al. 1993). The black squares represent the LMT stations collected during the Lithoprobe ABT (Alberta Transect) project in the 1990's. The red squares represent the LMT stations collected by the University of Alberta during 2002-2017. The blue squares represent the LMT stations collected by the University of Alberta during this study between 2013 and 2017. Black squares are locations of major cities. The black dash line shows the edge of Cordillera deformation front. The white dash line shows the edge of the Western Canada Sedimentary Basin (WCSB).

The MT data collected in the field are time series of the magnetic and electric fields. In order to extract information about the Earth, reduce the amount of data, and eliminate noise and source factors, data processing needs to be done before interpretation. In this chapter, the MT data collection and processing methods used in this thesis will be presented. Moreover, characterization of the long-period dataset from Alberta used in this study will be presented and discussed in detail.

5.2. Overview of MT data collection and processing

Magnetotelluric time series data are a recording of the time variations of electric and magnetic fields at the surface of the Earth, either on land or seafloor. At a standard MT station, five field components are recorded as a function of time (Figure 5.2). These are typically the two horizontal electric field components ($E_x(t)$, $E_y(t)$) and all three components of the magnetic field ($H_x(t)$, $H_y(t)$, $H_z(t)$). The subscripts *x, y,* and *z* represent north-south, east-west, and vertical directions, respectively (Figure 5.2).

MT data processing aims to extract information about the electrical resistivity properties of the Earth from the time series by eliminating factors such as the amplitude of the EM signal and noise. Figure 5.2 summaries the basic steps of MT data processing:

- Firstly, because the propagation of EM signals is frequency dependent, the time series need to be transformed into the frequency domain.
- Secondly, the frequency domain spectra of electric and magnetic fields are used to calculate the apparent resistivity at specific frequencies.

This is a rough representation of time series processing. More details about the time series processing will be discussed in section 5.5.

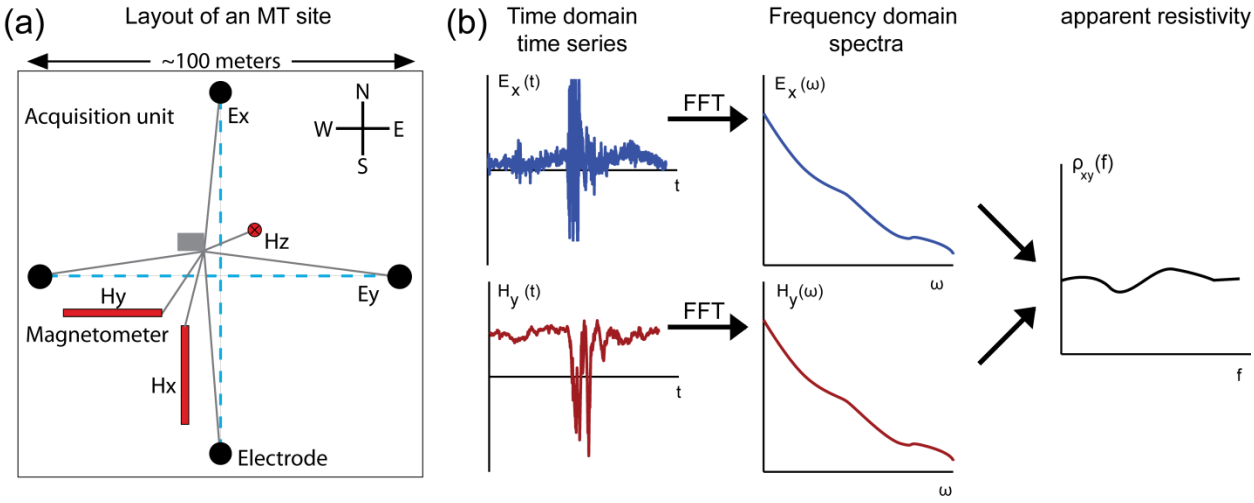

Figure 5.2: (a) The layout of an MT site. (b) Summary of data processing in Magnetotellurics. E_x and H_y are the electric field in north-south direction and magnetic field in east-west direction, respectively. The FFT represents the fast Fourier transform.

5.3. Magnetotelluric Instruments

The magnetotelluric instruments used in this study were the V5-2000 system (Fig. 5.3) for BBMT data recording and the Narod Intelligence Magnetotelluric System (NIMS, Fig. 5.4) for LMT data recording.

The V5-2000 system was developed by Phoenix Geophysics of Toronto (Figure 5.3). This system is comprised of a data logger, three induction coils, five electrodes, and a GPS antenna. Additionally, an external 12 volt battery is required to run the data logger. The V5-2000 system is set up with three sample rates named TS3 (2400 Hz), TS4 (150 Hz), and TS5 (15 Hz). The recording of the TS3 and TS4 signals is periodic (data is only recorded for a few seconds per minute) to reduce the amount of data while the recording of the TS5

signals is continuous. The V5-2000 systems are suitable for BBMT data collection in the period range of 0.001-1000 Hz. The typical recording time of the V5-2000 system for crustal-scale studies is 1-2 days.

Figure 5.3: The Phoenix Geophysics V5-2000 system[4].

The NIMS was originally developed by the University of Washington and Narod Geophysics Ltd (Figure 5.4). It has an 8-Hz sample rate and is used with a flux gate magnetometer. It is widely used to collect LMT data from 0.0001 to 0.1 Hz. The NIMS is usually kept in the field for several weeks to image crustal and mantle structures.

[4] Image from *http://www.phoenix-geophysics.com*

Figure 5.4: The Narod Intelligent Magnetotelluric System[5] (NIMS).

5.4. Data collection techniques

MT data collection requires that the electric and magnetic fields are measured with electrodes and magnetic sensors (Figure 5.2). All of the electrodes and magnetic sensors are connected to a data logger (recorder). The data logger records the electromagnetic field measurements from the electrodes and magnetic sensors, as well as the timing and location information from a GPS antenna.

The electric field is measured from the voltage across a pair of non-polarizing electrodes rather than polarizing metal stakes. This is because the data recording time is long in MT and non-polarizing electrodes can give better measurements than polarizing electrodes in this case. In MT, non-polarizing copper-copper sulphate (*Cu-CuSO₄*), lead-lead chloride (*Pb-PbCl*), or silver-silver chloride (*Ag-AgCl*) electrodes are used. In this study, lead-lead chloride electrodes were used.

[5] Image from *http://ngf.oregonstate.edu*

The electrodes are arranged in a cross, as shown in Figure 5.2. Two electrodes are spaced approximately 100 meters from each other and aligned in the direction of magnetic north. This pair of electrodes measures $E_x(t)$. The other two electrodes are placed in an orthogonal direction with a similar spacing to measure $E_y(t)$. The configuration of these two pairs of electrodes can be in "X" (preferred, shown in Figure 5.2) or "T" or even "L" shapes. The electrodes are buried underground at a depth of 30-50 centimeters to ensure good contact with the ground and minimize the thermal effects caused by temperature variations from day to night or sudden weather changes. Moreover, water and a clay mixture are usually used to improve the ground contact in the field.

The magnetic field components are measured with magnetic sensors oriented in three directions (Figure 5.2): magnetic north ($H_x(t)$), magnetic east ($H_y(t)$) and vertical ($H_z(t)$). Two kinds of sensors are used in BBMT and LMT data recording. Induction coils are used for BBMT data recording with instruments such as the Phoenix Geophysics V5-2000. Flux gate magnetometers are used for LMT data recoding with the NIMS. The magnetic sensors are buried to a depth of approximately 50 centimeters to reduce the thermal effects caused by surface temperature changes and to minimize motion.

Data collection using the V5-2000 system and NIMS is different in terms of the potential difference measured and the magnetometer used. Therefore, they will be discussed separately.

5.4.1 V5-2000 system

In a Phoenix Geophysics V5-2000 system deployment, a ground electrode is buried in the center of the site. The voltages recorded by a V5-2000 system are the potential differences between the center ground electrode and the other four electrodes.

Three induction coils are used for the measurement of magnetic fields in the three directions mentioned above. An induction coil is composed of a shock-resistant cylindrical casing containing a coil of copper wire wound onto a highly magnetically permeable core. Signals are measured as voltages because a voltage is induced when there is a change in the component of the magnetic field parallel to the axis of the coil. Therefore, induction coils are used to measure relative changes in magnetic field strength. Induction coils are only suitable for the acquisition of higher frequency data (above 0.001 Hz) because they can be insensitive to low frequency data when the rate of change of the magnetic field strength with time is too small.

5.4.2 NIMS

In a NIMS deployment, the voltages recorded are the potential differences between two dipole electrode pairs. There is a metal ground stake buried near the acquisition box to ground the system.

The magnetic sensors used in NIMS are three-component flux gate magnetometers. Flux gate sensors are composed of ring cores of a highly magnetically permeable alloy around which two coil windings (drive winding and sense winding) are wrapped in different shapes. When there is an external electromagnetic field, an alternating primary current can be generated in the drive coil winding. At the same time, a secondary induced

current is generated in the sense coil winding which is recorded and analyzed to give the absolute value of the external electromagnetic field. A three-component flux gate magnetometer can give the absolute measurements of the magnetic field in three orthogonal directions with a precision of 0.01 nT. There is no lowest frequency at which they work because the absolute values of the magnetic field components are measured.

5.5. Time series processing techniques

The MT data are recorded in the field as time variation of the electric and magnetic fields (Figure 5.5). The digital time series recording can be very large (hundreds of megabytes) and include redundant information. The redundant time series need to be transformed into the frequency domain to get the frequency dependent impedance and resistivity values, and to reduce the data to a smaller size for further analysis (Simpson and Bahr, 2005). This includes several steps as illustrated in Figure 5.2.

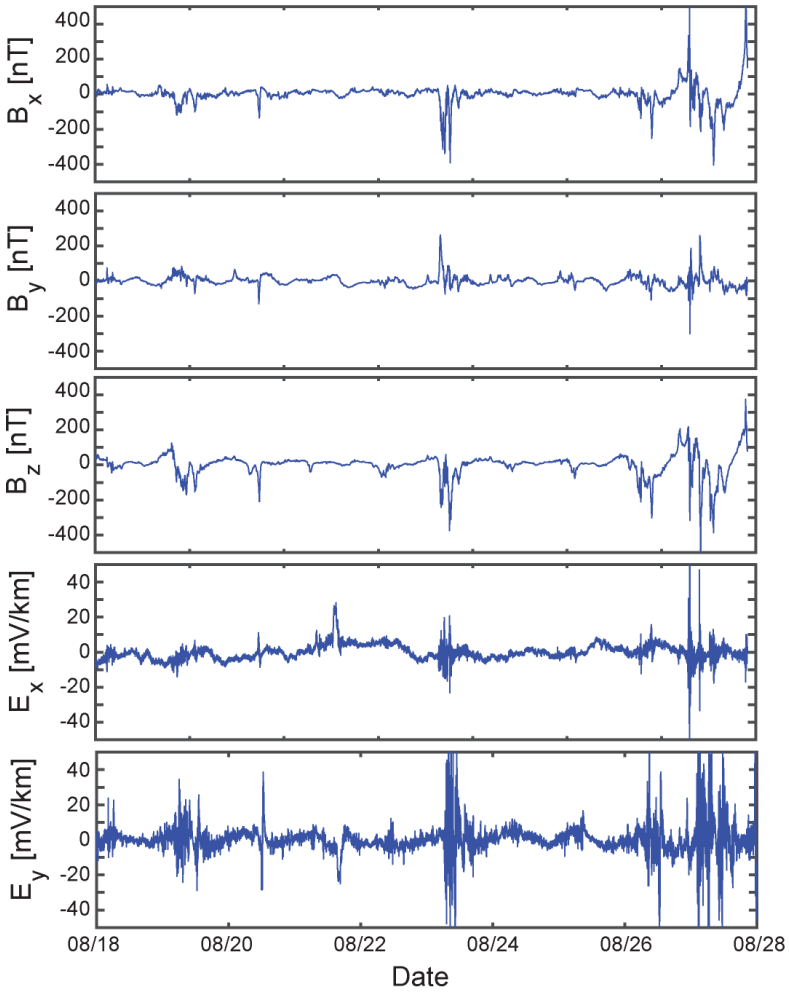

Figure 5.5: The 10-day time series of site JNP001.

5.5.1 Instrument Calibration

The MT equipment uses signal amplifiers while collecting data. Because the amplifiers can age and change their behavior over field seasons, the equipment needs to be recalibrated before the start of a field deployment. The calibration of NIMS is done on the instrument before the data collection. For a Phoenix Geophysics V5-2000 system, calibration files for the data-logger and three magnetic induction coils are generated. The

calibration files are used during the first step of data processing to get the true electromagnetic field measurements.

5.5.2 Fourier transform

The Fourier transform is needed to convert time series in the time domain into spectra in the frequency domain. This is done in several steps as discussed below.

5.5.2.1 Selecting the evaluation frequencies

Before transforming the data into the frequency domain, evaluation frequencies need to be chosen. When selecting these frequencies, these four rules should be followed:

1. The evaluation frequencies should be equally spaced on a logarithmic scale. A logarithmic scale is used based on the skin depth equation (Equation 2.20). When resistivities and frequencies are plotted on a log-log scale, they could be linearly related. See the equations 5.1 and 5.2 below for clarification.

$$\log_{10}\delta(f) = \log_{10}\sqrt{\frac{\rho}{\pi f \mu}} \tag{5.1}$$

$$\log_{10}\delta(f) = 0.5 * \log_{10}\frac{\rho}{\pi\mu} - 0.5 * \log_{10} f \tag{5.2}$$

where f is the frequency, μ is considered equal to the permeability of free space ($4\pi\times10^{-7}$ H/m), ρ represents the apparent resistivity, δ stands for the skin depth.

2. 6-10 evaluation frequencies for each decade are preferred.
3. The highest frequency possible is dependent on the sampling frequency according to the Nyquist theorem. For example, the NIMS has a sampling rate of 8 Hz, so the highest

frequency that could be measured is 4 Hz. However, in MT, it is preferred to have more samples for one frequency and the highest frequency is less than 4 Hz.

4. The lowest frequency is dependent on the length of the time series. Consequently, in order to find the Fourier coefficients for lower frequencies, longer time series are required.

5.5.2.2 Select time intervals of the time series

Because the entire time series can be very long, they are cut into many intervals prior to calculation of the Fourier coefficients at the selected evaluation frequencies. By doing this, the time series are used more efficiently. Another benefit of this step is that the Fourier coefficients at a specific frequency from all these intervals can be stacked together to enhance the signal and minimize the errors in the data. As mentioned above, longer time series are needed for calculating the Fourier coefficients at lower frequencies. Therefore, longer time intervals are required and fewer can be stacked for the lower frequencies.

5.5.2.3 Calculating the spectra matrix

After the evaluation frequencies have been chosen and the Fourier coefficients calculated, the spectral matrices at the specific frequencies are calculated. The single Fourier coefficients calculated form the raw spectra. An averaging scheme is used on the raw spectra to find the auto-power spectra and cross-power spectra for the selected evaluation frequencies. The auto-power spectra and cross-power spectra form the spectral matrix (Table 5.1) for the selected time series interval.

	E_x	E_y	H_x	H_y
E_x	$E_x^* E_x$	$E_x^* E_y$	$E_x^* H_x$	$E_x^* H_y$
E_y		$E_y^* E_y$	$E_y^* H_x$	$E_y^* H_y$
H_x			$H_x^* H_x$	$H_x^* H_y$
H_y				$H_y^* H_y$

Table 5.1: Spectral matrix of MT data

5.5.3 Computing impedance from spectra

After the spectra are calculated, the spectral matrices of the same frequency from all of the time series intervals are stacked to minimize the effects of noise. Then, the spectral matrices are used for the calculation of the impedance tensor using the equations below. These equations are generated by multiplying the linear expansion form of Equation 2.26 by the complex conjugate of the electric and magnetic spectra. Eight equations could be achieved in total. Below is one example of them.

$$\langle E_x^* E_x \rangle = Z_{xx} \langle E_x^* H_x \rangle + Z_{xy} \langle E_x^* H_y \rangle \tag{5.3}$$

where the * stands for the complex conjugate and the angle brackets represent the stacked result. $\langle E_x^* E_x \rangle$ is one example of an auto-power spectrum. $\langle E_x^* H_x \rangle$ and $\langle E_x^* H_y \rangle$ are examples of cross-power spectra. There are eight unknowns (real and imaginary part of the four components of the impedance tensor – Z_{xx}, Z_{xy}, Z_{yx}, and Z_{yy}) and eight equations, so the impedance tensor can be solved for.

Statistical procedures should be applied to minimize the effects of noise in the measured data. This is done during the stacking process mentioned above. Least-squares and robust least-squares methods are commonly used. Robust methods (Egbert and

Booker, 1986) and the remote referencing method are used in this study and described in the following sections.

5.5.3.1 Robust statistics

The robust least-squares method automatically down-weights the source contaminated outliers while searching for a least-squares solution. It was proved that a robust weighted-least-squares algorithm can improve the results (impedance tensor) substantially and give a better error estimation than the standard least-squares method. This process could also be integrated into the remote reference method, which is discussed in the next section.

5.5.3.2 Remote reference method

One problem in Equation 5.3 is that the auto-power spectra could amplify the noise in the corresponding channel (E_x in Equation 5.3, and likewise for the other channels). In order to suppress this effect, a remote reference method was introduced (Gamble et al., 1979; Clarke et al., 1983).

The remote reference method requires a remote site recording data simultaneously with the local site and deployed several to tens of kilometers away from the local site. The signals generated by the induced field should be coherent between the two sites whereas the noise is generally random and incoherent, so replacing the conjugate part in the auto-power spectra with the corresponding field of the remote reference site would minimize the noise. Figure 5.6 shows one example of the improvement in data quality after applying remote referencing.

In this case, the conjugate of the electric spectrum (E^*_x) in Equation 5.3 is replaced with the conjugate of the electric spectrum of the remote site (E^*_{xr}) and Equation 5.3 becomes

$$\langle E^*_{xr} E_x \rangle = Z_{xx} \langle E^*_{xr} H_x \rangle + Z_{xy} \langle E^*_{xr} H_y \rangle. \quad (5.4)$$

When the electric spectra are replaced with remote ones, it is a remote reference of the electric channel. The same thing can be done with the magnetic channels which is actually preferred because the magnetic signals are more coherent between the local and remote sites. This method is widely accepted and remote referencing of the magnetic channels is used in this study. One example is shown in Figure 5.6; the high frequency result is improved after applying the remote referencing method.

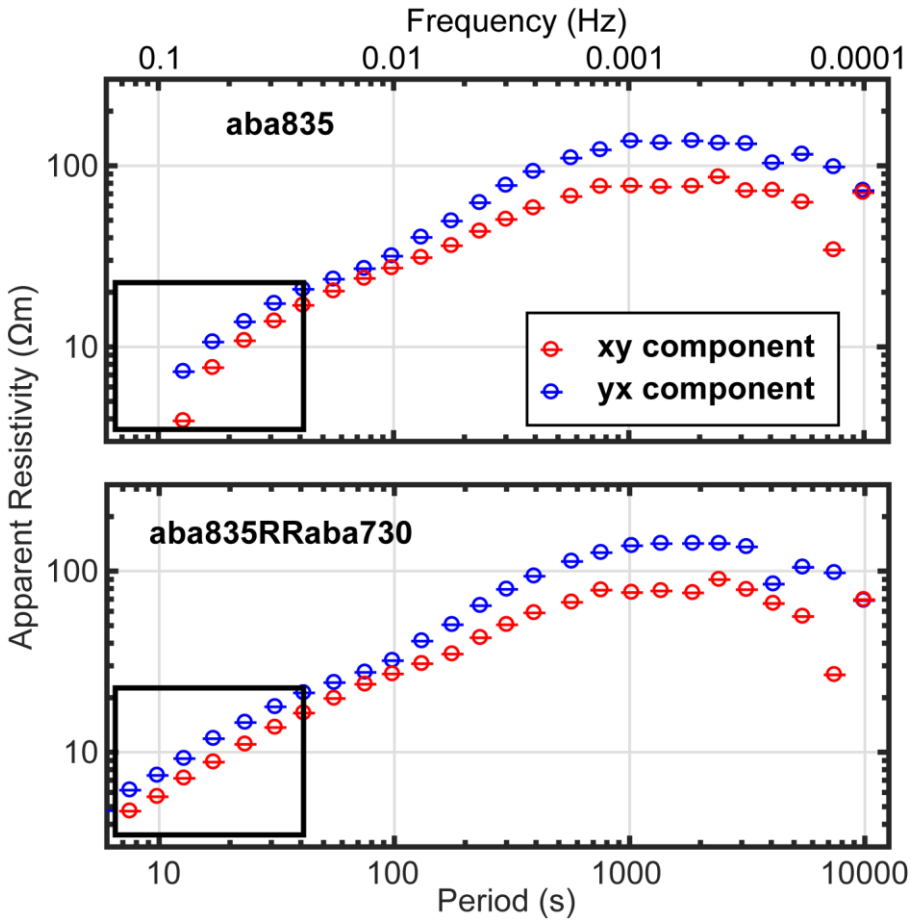

Figure 5.6: The comparison of the single site processing result (top) with the remote referencing result (bottom) of the site aba835. The remote referencing site used is aba730. The apparent resistivity associated with the Z_{xy} and Z_{yx} components are shown. The high frequency data are improved in this example (in the black square).

5.6. The Rainbow Lake profile: BBMT data collection and processing

The Rainbow Lake (RLK) project aimed to provide a better understanding of crustal structures. This region of Alberta is of interest because it is crossed by the Hay River Fault (HRF) (Hoffman, 1989) and it has been suggested that it has high geothermal potential (Majorowicz et al., 2014; Nieuwenhuis et al., 2015). The HRF is the southwestern brittle segment of the Great Slave Lake shear zone (Plint and Ross, 1993; Ootes et al., 2015). All

MT data previously collected in this region were LMT data (frequency range 0. 1-0.0001 Hz) which cannot resolve the shallow upper crustal resistivity structure.

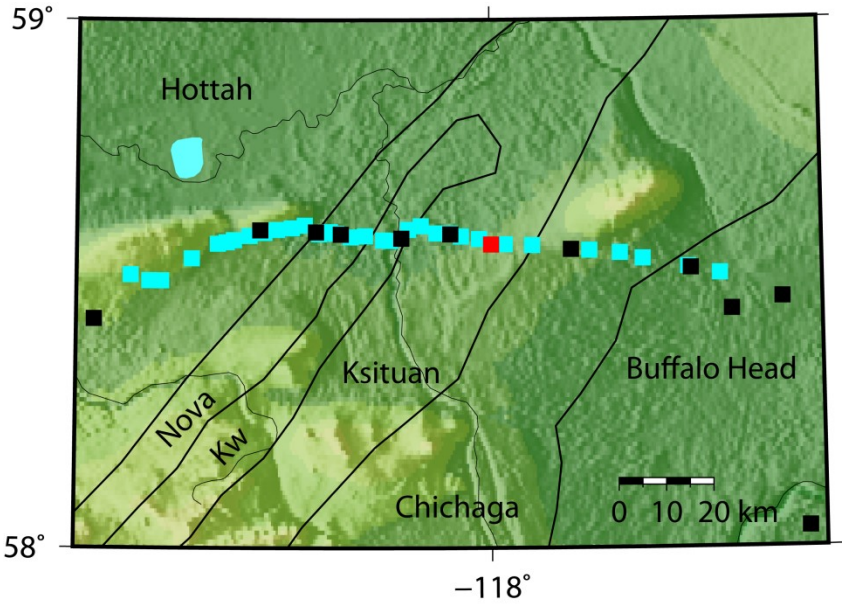

Figure 5.7: MT stations in the Rainbow Lake area. Background is a topographic map and black lines mark the terrane boundaries defined from aeromagnetic field and isotopic studies of drill-core samples (Villeneuve et al. 1993). The light blue squares represent the BBMT stations collected for this study. The red and black squares are LMT stations, color-coded the same as in Figure 5.1. Kw, Kiskatinaw terrane.

A profile of 35 new BBMT stations was deployed during this research project (Figure 5.7), which collected BBMT data in the frequency range 1000-0.001 Hz. The field work was undertaken in the summer of 2014 between the towns of High Level and Rainbow Lake. The instruments used were Phoenix V5-2000 systems as described above. The study area is covered by thick forest and MT stations were installed close to the highway connecting the two towns. Caution was taken to keep the MT instruments at least 200 meters away from the highway to avoid electromagnetic noise from vehicle traffic and power lines. Other possible sources of electromagnetic noise such as pipe lines or oil machines were also avoided.

The MT time series data were processed with two software packages: (a) the Phoenix SSMT 2000 and (b) the statistically robust technique of Egbert (1997). The remote reference method was applied to remove non-coherent noise in the magnetic fields. Estimates of the impedance and vertical magnetic field transfer functions were computed in a frequency range of 1000-0.001 Hz for most of the sites. However, there were three BBMT stations which recorded poor-quality MT data and were excluded from the following analysis (RLK025, RLK035, and RLK065). A detailed characterization of the RLK BBMT data is presented in Chapter 7.

As mentioned above, two software packages were used for data processing of the RLK time series. Before further MT data analysis and interpretation could be undertaken, the best processing results needed to be selected. The preferred result should have smaller error bars, exhibit smooth apparent resistivity and phase curves, and be consistent with neighboring BBMT stations since the spacing of the sites is only 3-5 km. Figure 5.8 shows the processing results obtained with the two software packages. At site RLK040, the SSMT package gives better single site processing result than the single site result of Egbert (1997). The Egbert result with a remote reference is much better than the remote reference result of the SSMT package. At site RLK030, the result of the Egbert software is better than the SSMT in both signal site processing and remote reference processing. Results of both SSMT and Egbert (1997) got better after applying the remote reference technique. However, the tipper result of the single-site Egbert is still better than that of the SSMT with remote reference applied. Thus, it is considered that for the Rainbow Lake dataset, the software of Egbert (1997) gives overall better results than the SSMT 2000. Therefore, the processing results of Egbert (1997) with or without remote reference

(depending on which one was better) were used in the following analysis and interpretations.

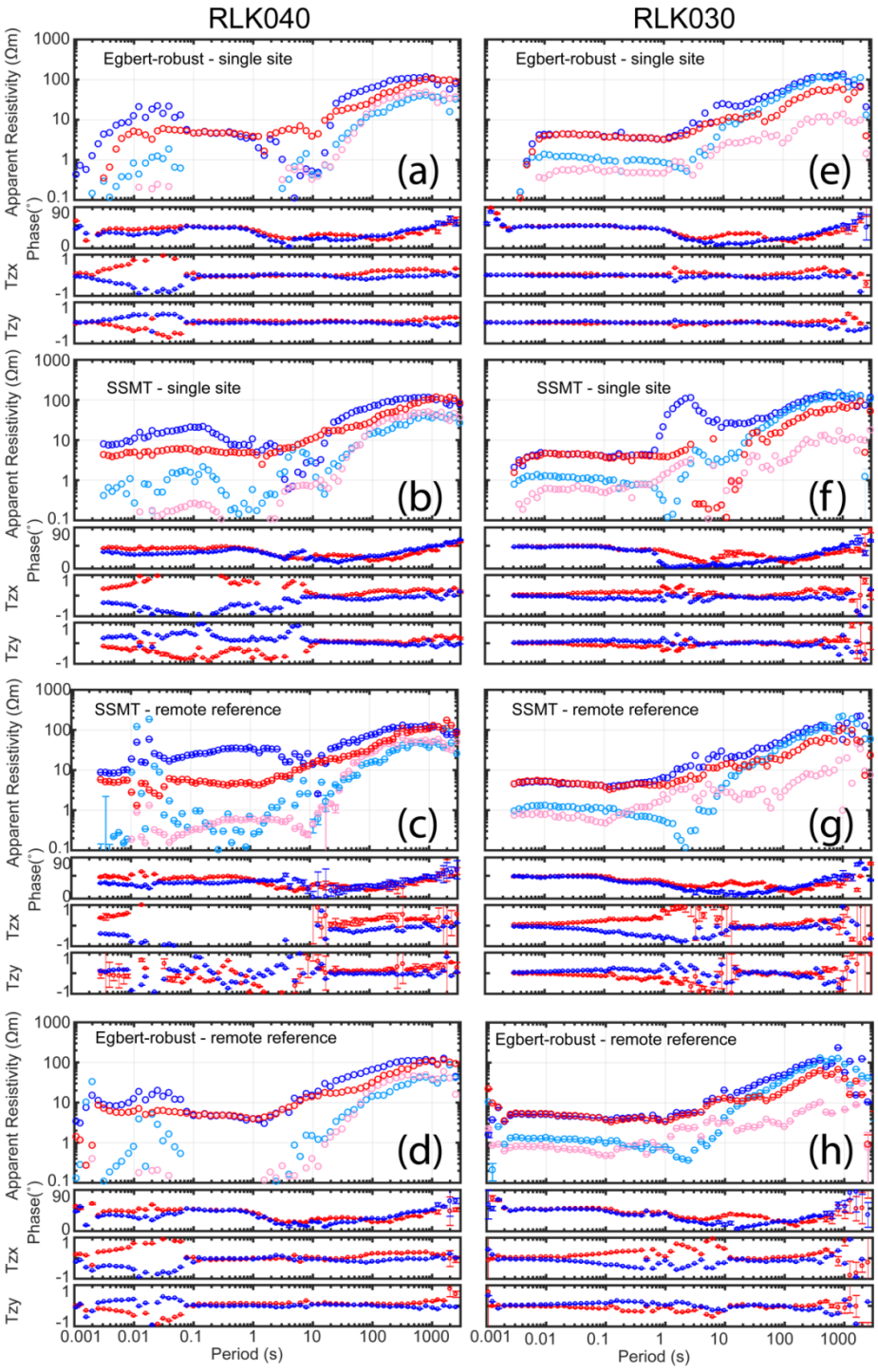

Figure 5.8: Plots of apparent resistivity, phase, and tipper after processing with two different software packages (Egbert, 1997 and SSMT 2000). Two sites (RLK030 and RLK040) were chosen to show. The top two rows (a, b, e, f) are all single site processing results with no remote reference applied. The bottom two rows (c, d, g, h) show remote reference results using the Egbert (1997) or SSMT 2000 software.

5.7. The Alberta dataset collection and processing

The dataset collected during the Lithoprobe project was intended for 2-D interpretation as was available at the time. For this reason, the LMT stations of the Lithoprobe were collected on profiles. In order to obtain a detailed 3-D electrical resistivity model of central Alberta, uniform inter-station spacing and better data coverage were needed. Therefore, LMT field work was undertaken in the summers of 2014, 2015, 2016, and 2017 to collect more LMT stations in central and southwest Alberta (Figure 5.1). A total of 72 LMT stations were recorded during this time period. The instruments used for this LMT data collection were the NIMS. The recording time for these instruments was typically between three and four weeks.

The LMT data were recorded as time series. The 10-day time series of the station JNP001 is shown in Figure 5.5. The daily variation of the magnetic field can be seen in the magnetic recordings. Moreover, the correlation of E_x with H_y and E_y with H_x can be observed. The data were processed with the statistically robust technique of Egbert (1997) and data in the frequency range of 0.1-0.0001 Hz were obtained. The remote reference method was applied to minimize the effect of noise in the magnetic fields. The single site result and remote reference result were compared and the better result was chosen for further analyses. The resultant apparent resistivity, phase, and tipper from station JNP001 are shown in Figure 5.9.

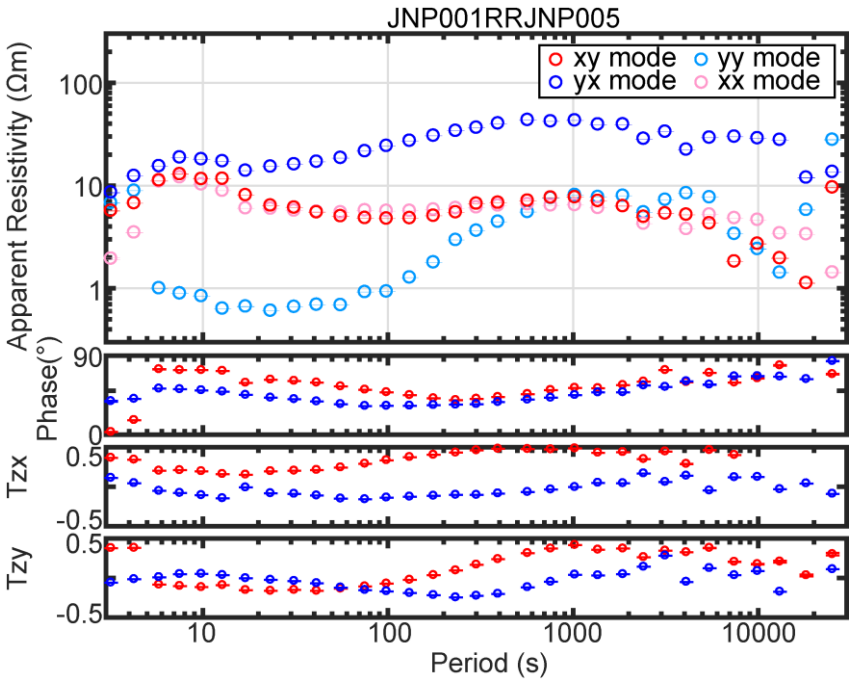

Figure 5.9: Plots of apparent resistivity, phase and tipper from MT station JNP001.

5.8. Characterization of the Alberta long-period magnetotelluric (LMT) dataset

5.8.1 Classification of typical data

When the original Lithoprobe data were combined with the new LMT data collected by the University of Alberta, this produced a dataset with a total of 656 LMT stations. According to the shapes of the apparent resistivity and phase curves, the LMT data can be divided into 14 groups (Figure 5.10). It is obvious that the LMT data show regional features. For example, the data similar to abt152 shown as blue triangles on the map are all along the Kiskatinaw terrane in which a conductor was suggested to exist and named as the Kiskatinaw conductor by Boerner et al. (2000). The LMT data outside of the WCSB are characterized by out of quadrant phases and very high or low resistivity values. In contrast,

out-of-quadrant phases are very rare at the LMT stations on top of the WCSB where the resistivity values start from 1-100 Ωm and stay in the range of 1-1000 Ωm.

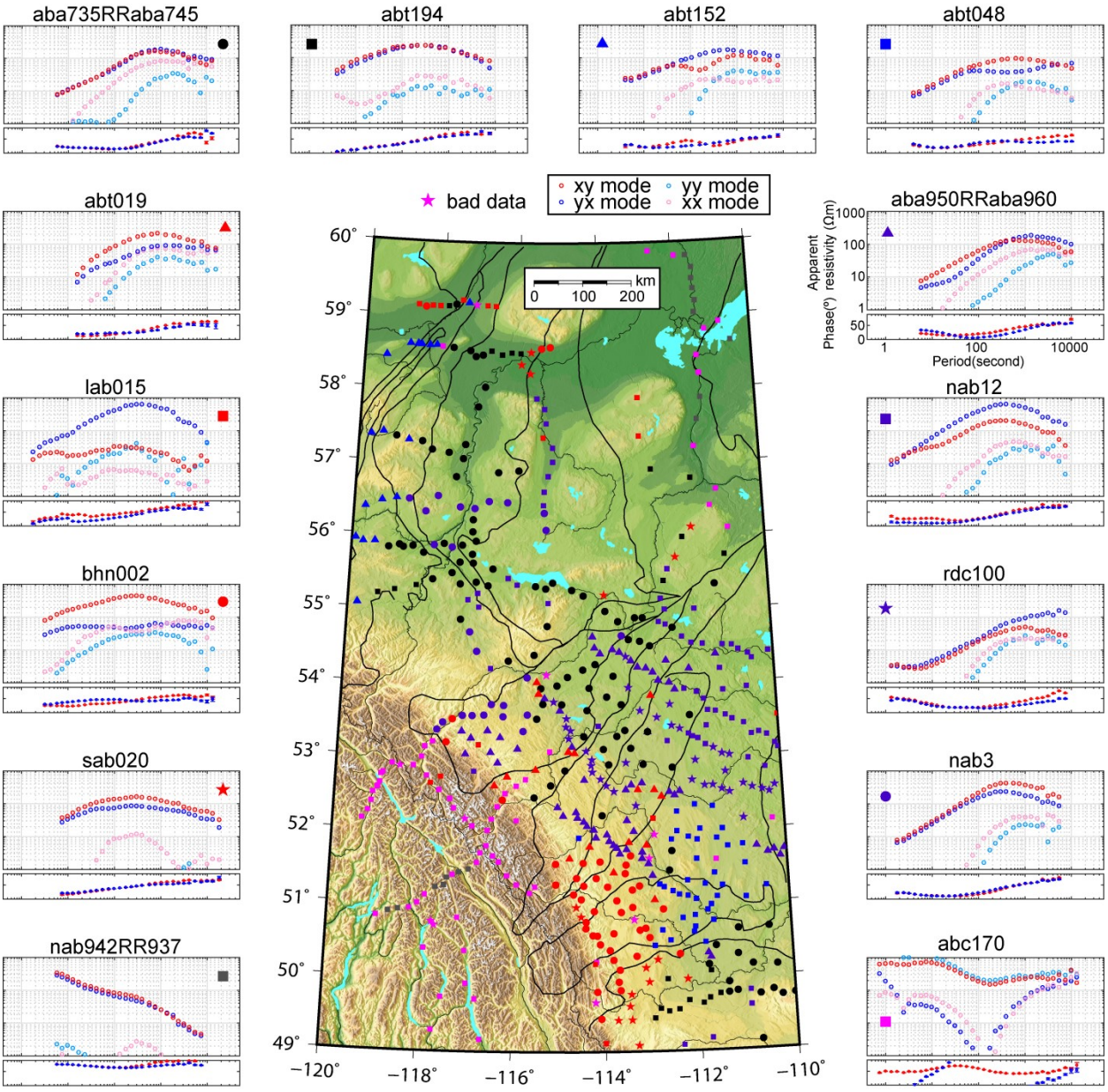

Figure 5.10: The typical LMT data curves and their distribution on the topographic map. Black lines mark the terrane boundaries defined from aeromagnetic field and isotopic studies of drill-core samples (Villeneuve et al. 1993).

5.8.2 Apparent resistivity and phase maps of the Alberta LMT data

The apparent resistivity and phase can reflect the electrical resistivity of the study area even though it is a rough representation as shown in Chapter 2. The average apparent resistivity and phase of the xy and yx components of the LMT data are shown as maps in Figure 5.11. The periods 9.8 s, 98 s, 1024 s, and 7447 s were chosen to illustrate aspects of the data. At low periods such as T = 9.8 s, the resistivity of the region outside of the WCSB is higher than the resistivity within the WCSB. This difference becomes smaller as the period increase. There is a low resistivity and large phase anomaly along the Red deer trend at periods of 98 s.

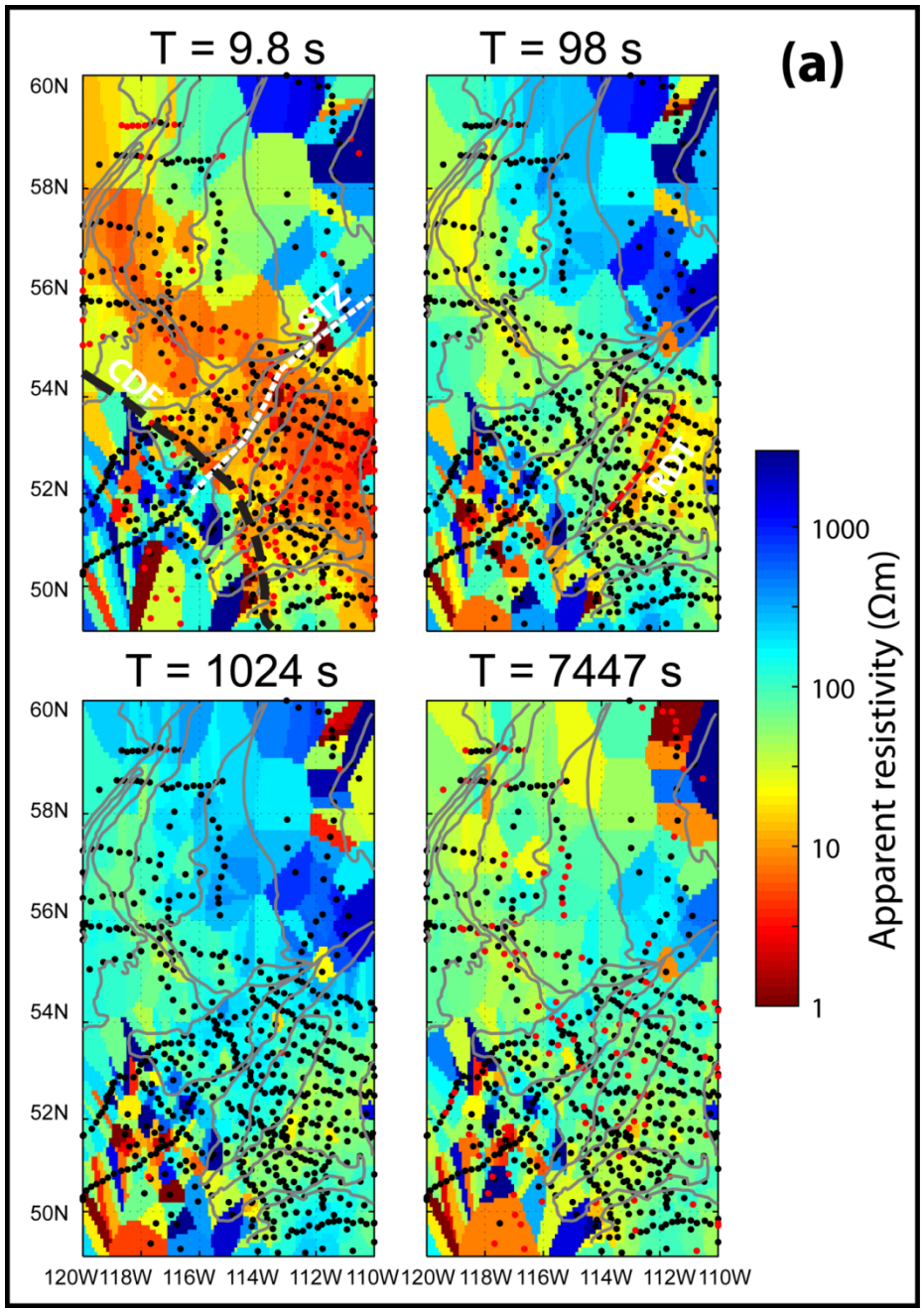

Figure 5.11(a): Maps of apparent resistivity calculated with the average impedance of the xy and yx components of the LMT dataset used in this study. The interpolation method used is the "nearest" method in MATLAB. The black dots in (a) are LMT stations with valid data at the specific period. The red dots in (a) are LMT stations with no data at the specific period. Gray lines mark the terrane boundaries defined from aeromagnetic field and isotopic studies of drill-core samples (Villeneuve et al. 1993). Black dashed line represents the location of the Cordillera deformation front (CDF). White dashed line shows the Snowbird tectonic zone (STZ). Red dashed line marks the location of the Red Deer Trend (RDT).

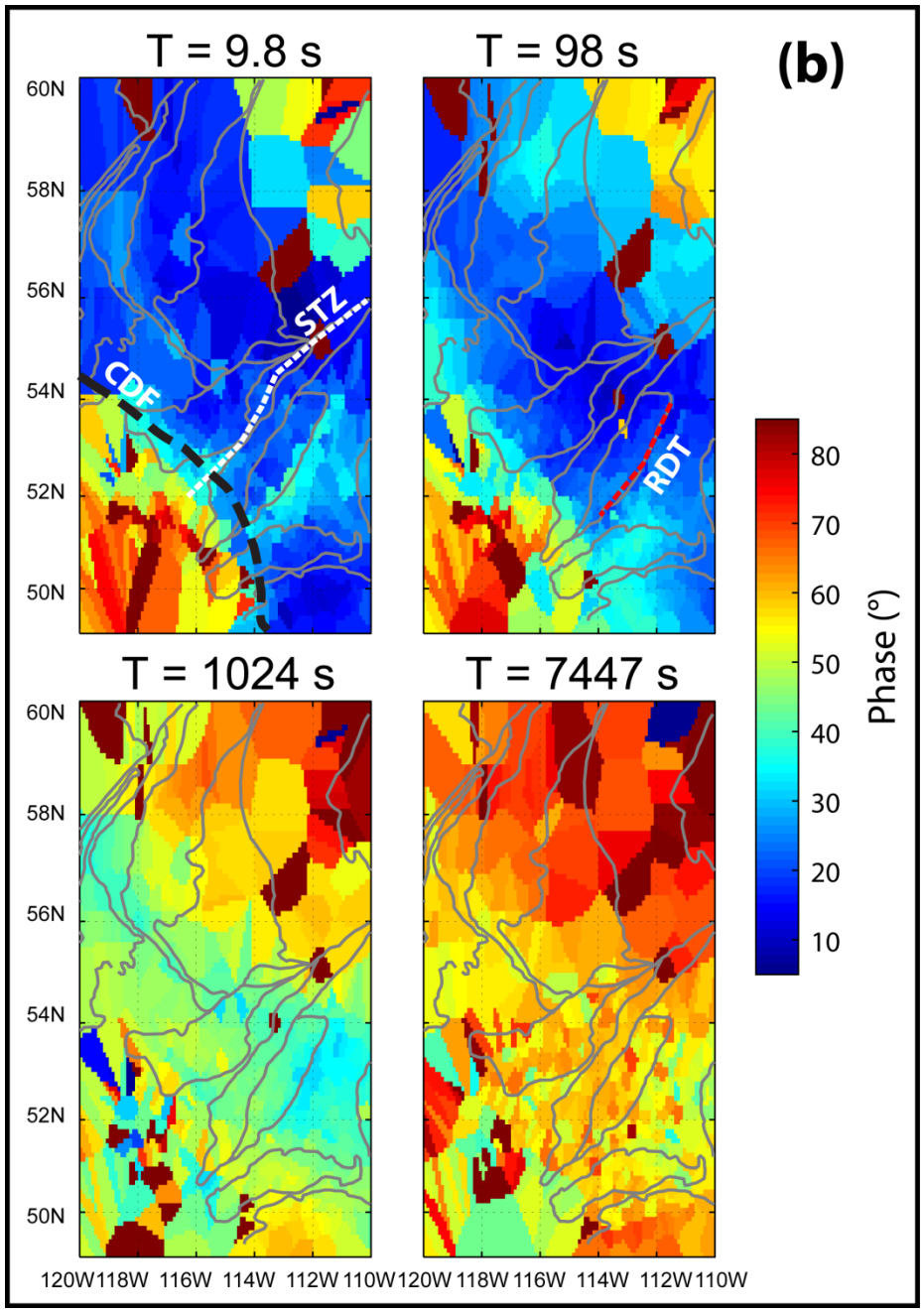

Figure 5.11(b): Maps of phase calculated with the average impedance of the xy and yx components of the LMT dataset used in this study. The interpolation method used is the "nearest" method in MATLAB. Gray lines mark the terrane boundaries defined from aeromagnetic field and isotopic studies of drill-core samples (Villeneuve et al. 1993). Black dashed line represents the location of the Cordillera deformation front (CDF). White dashed line shows the Snowbird tectonic zone (STZ). Red dashed line marks the location of the Red Deer Trend (RDT).

5.8.3 Induction vectors

Induction vectors are a good indicator of horizontal changes in subsurface resistivity (section 2.6.2) and shown in Figure 5.12. Since penetration depth increases with period, the increasing period can be considered a proxy for increasing depth.

At a short period (9.8 s) most of the induction vectors in the Alberta Basin are very small with lengths less than 0.1 (Figure 5.12). However, the induction vectors are large in southeast British Columbia and northeast Alberta (0.1-0.3). This indicates that the horizontal resistivity contrast at shallow depths is very small in the WCSB and large in other regions.

At a period of 98 s, systematic regional trends can be observed in the induction vectors. For example, the induction vectors in the Loverna block (LVB) at latitudes between 52˚ and 54˚ north (marked by a red polygon in Figure 5.12) are very small compared to the other parts of the study area. This also indicates less horizontal resistivity contrast in the area. Moreover, the induction vectors in southern Alberta point mostly to the south which indicates that the resistivity to the south is higher than to the north of the stations.

At a period of 7447 s, all of the induction vectors point to the northwest except for a few in southern Alberta. This may be due to the resistivity contrast between the North American craton and the Cordillera. A craton generally has a thick lithosphere whereas the Cordillera is considered to have a very thin lithosphere and hot asthenosphere (Currie et al., 2004). Therefore, at a similar investigation depth, the Cordillera should be less resistive than the North American craton.

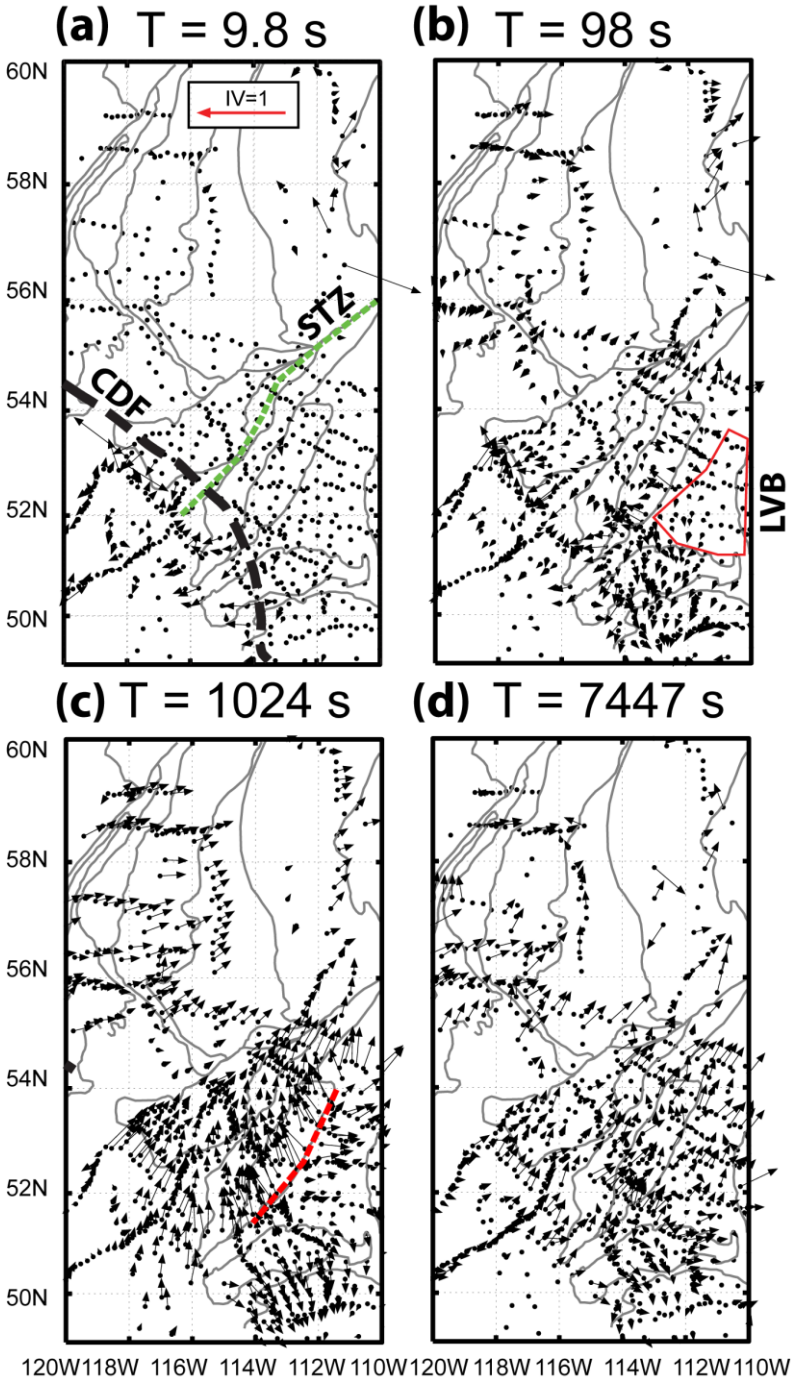

Figure 5.12: Induction vectors of the LMT data used at four periods, plotted to point away from conductors according to the Weise convention (Wiese, 1962). Gray lines mark the terrane boundaries defined from aeromagnetic field and isotopic studies of drill-core samples (Villeneuve et al. 1993). Black dashed line represents the location of the Cordillera deformation front (CDF). Green dashed line shows the Snowbird tectonic zone (STZ). Red dashed line marks the location of the Red Deer Trend (RDT). The red polygon marks the small induction vectors in the Loverna block (LVB).

5.8.4 Phase tensor

Phase tensors are indicative of the strike of the subsurface electrical structure and skew values are representative of the dimensionality of the electrical structure as shown in Chapter 2. The phase tensors of the LMT data used are shown in Figure 5.13. At a short period (T = 9.8 s) most of the phase tensor ellipses are roughly circular in shape and the skew values are generally smaller than three, indicative of a 1-D subsurface resistivity structure. A few exceptions are observed which can be associated with 2-D or 3-D resistivity structures. Firstly, the phase tensor ellipses are elongated along the Red Deer trend and the Rocky Mountain foothills. Secondly, elongated ellipses and high skew values are observed at the southwest and northeast corners of the study area (outside of the WCSB i.e. west of the Cordillera deformation front and east of the edge of the WCSB as shown in Figure 5.13).

At a period of 98 s, most of the phase tensor ellipses in the WCSB have major axes in a northwesterly direction, while the ones outside of the WCSB show more complicated features. Moreover, the phase tensors of the LMT stations in the Medicine Hat block show characteristics of 1-D resistivity structures.

At a period of 1024 s, the phase tensor ellipses in the southern Taltson domain and the middle of the Buffalo Head domain are circles, suggesting 1-D resistivity structure. The phase tensors in the northern Taltson domain, the Rocky Mountains in the southwest of the study area, and the Hearne domain show characteristics of 3-D resistivity structure. The phase tensors in the western and eastern MHB show different features, namely that the

western part has higher skew values than the eastern part. At a period of 7447 s, phase tensors indicative of 3-D features are dominant in the study area.

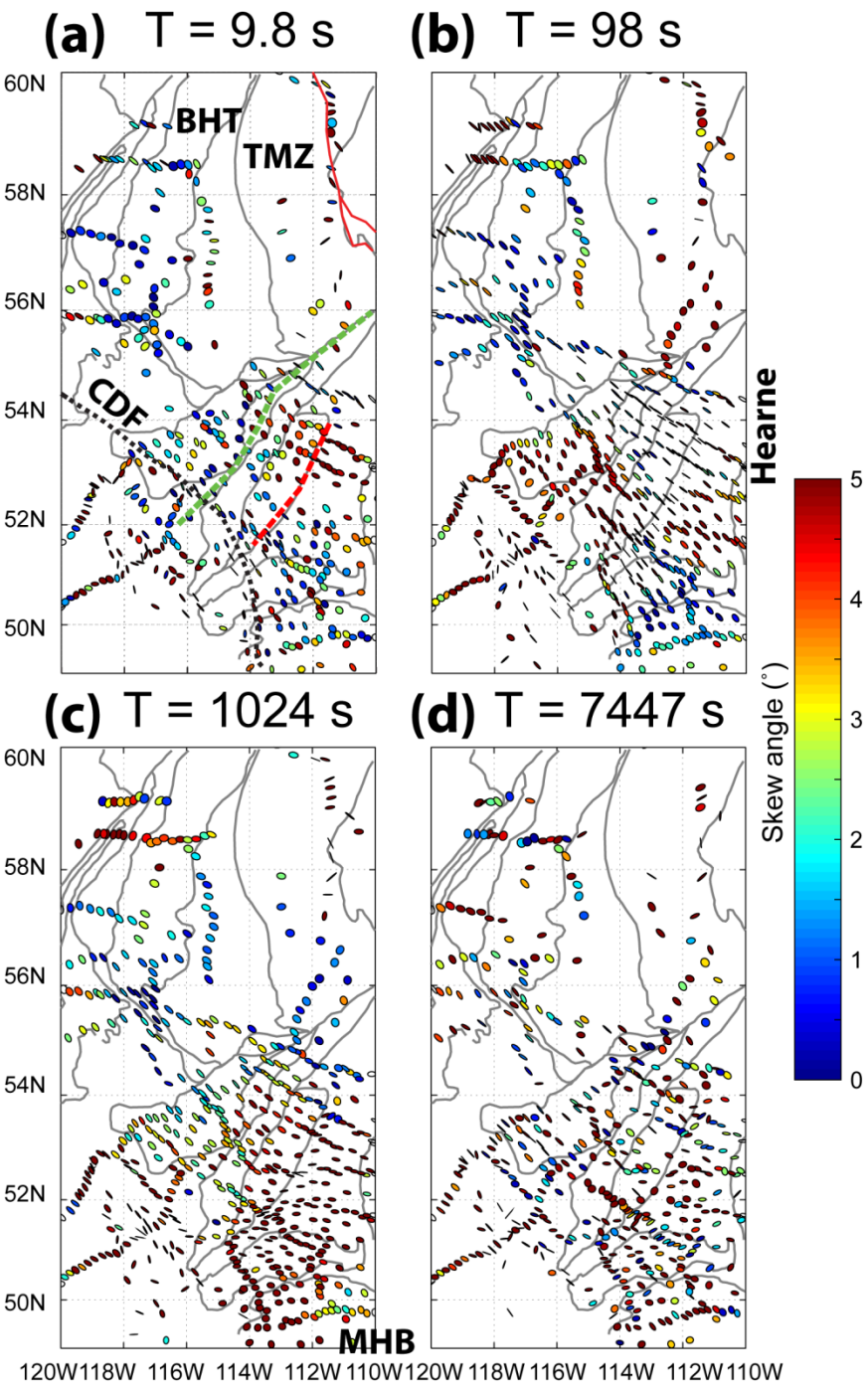

Figure 5.13: Phase tensor ellipses of the LMT data used at four periods. Gray lines mark the terrane boundaries defined from aeromagnetic field and isotopic studies of drill-core samples (Villeneuve et al. 1993). Black dashed line represents the location of the Cordillera deformation front (CDF). Green dashed line shows the Snowbird tectonic zone (STZ). Red dashed line marks the location of the Red Deer Trend (RDT). Red lines in the northeast corner show the edge of the WCSB (Western Canada sedimentary basin). Abbreviations: BHT, Buffalo Head terrane; TMZ, Taltson magmatic zone; MHB, Medicine Hat block.

5.9. Summary

In summary, MT data are collected in the field as time series which need to be processed to get impedance or apparent resistivity and phase for further analysis. Thirty five BBMT stations were collected in northwest Alberta during this study using the V5-2000 system. This dataset was used to generate a better model of the crustal resistivity structure across the Hay River Fault which will be shown in Chapter 6. Seventy two LMT stations were collected in central and southern Alberta during this study using the NIMS. These LMT stations are combined with previously collected LMT stations in Alberta to create a 3-D resistivity model of Alberta (Chapter 8).

Characterization of all LMT data in Alberta is shown in section 5.8. Regional similarities are observed by comparing the apparent resistivity curves (section 5.8.1). 1-D, 2-D, and 3-D features are all observed as shown by the apparent resistivity, phase, induction vectors, and phase tensors. For example, along the Red Deer Trend, low apparent resistivity and high elongated phase tensors imply a linear conductor. The LMT stations outside of the WCSB show more complex electrical structure than the ones above the WCSB. Although many valuable informative observations are made from the plots of apparent resistivity, phase, induction vectors, and phase tensors, the shape and depth of the conductors cannot be determined. Therefore, further inversions to get a resistivity model of Alberta are necessary and will be presented in the following chapters.

Chapter 6 : Geoelectric structure of the Great Slave Lake shear zone in northwest Alberta: implications for structure and tectonic history[6]

6.1. Introduction

The modern North American craton known as Laurentia has been assembled over the course of more than two billion years of Earth history and produced the crustal structure present today (Hoffman, 1989). Despite numerous studies (Chacko et al. 2000; Ross 2002; Ootes et al. 2015), there are still many aspects of the crustal structure which are not well defined and which need to be verified by multi-disciplinary methods. It is important to learn more about the crustal structure because (1) it allows us to understand if past tectonic processes were similar to those in operation today and (2) knowledge of the crustal structure and history is useful in understanding the present-day distribution of resources.

In this paper, the crustal structure and tectonic history of the Precambrian basement of northwest Alberta is investigated using an electromagnetic geophysical method called magnetotellurics (MT). The Alberta basement is located within Western Laurentia, the Precambrian core of the North America continent. It was assembled in the Paleoproterozoic by both convergent and strike-slip plate motions. The major strike-slip

[6] This chapter has been published by Wang et al. (2018) in the Canadian Journal of Earth Sciences. No change has been made from the published version.

features are the Hay River Fault (HRF; Figure 6.1) and the Great Slave Lake shear zone (GSLSZ).

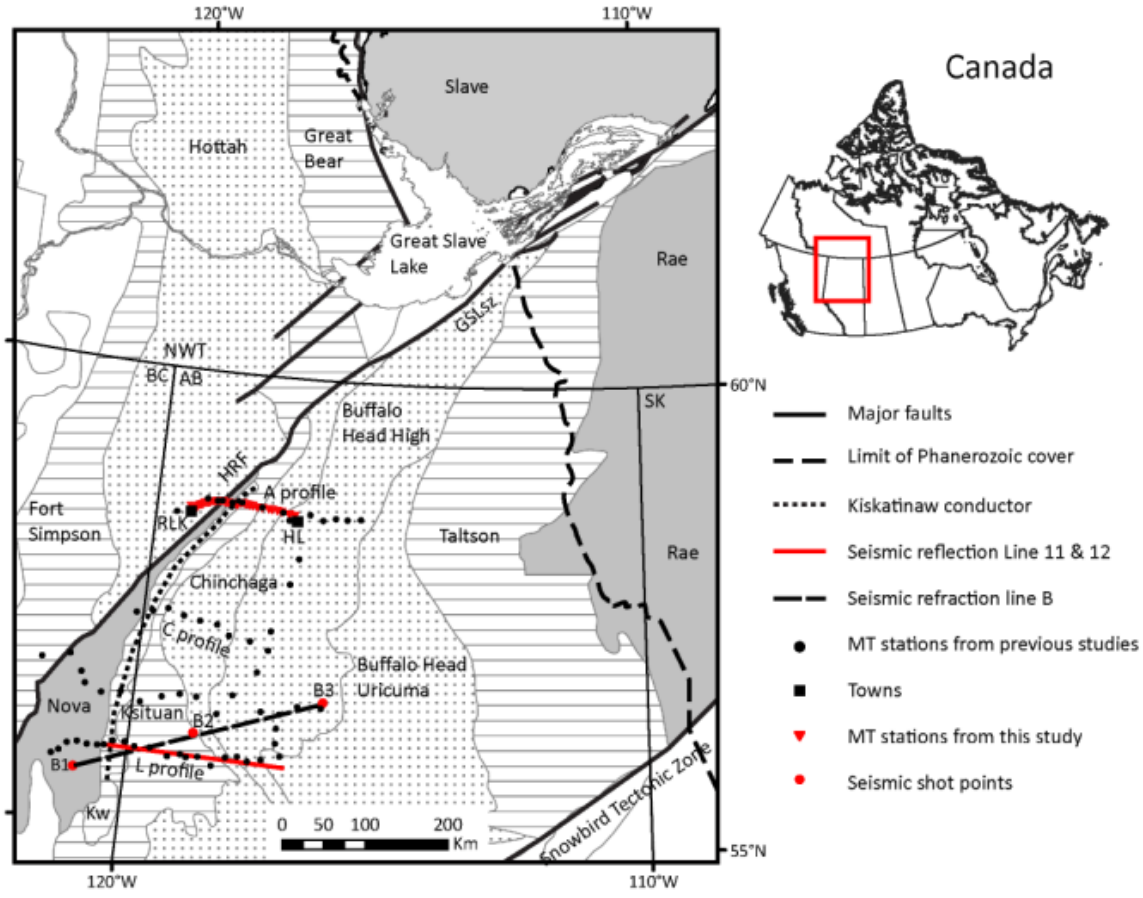

Figure 6.1: Generalized tectonic map of northern Alberta and southern Northwest Territories (modified after Hoffman 1989; Villeneuve et al. 1993; Ross 2002; Ootes et al. 2015). B1, B2, B3 are shot points for seismic refraction line B (Zelt et al. 1989). Profiles A, C and L are the MT profiles studied by Turkoglu et al. (2009). AB, Alberta; BC, British Columbia; GSLSZ, Great Slave Lake shear zone; HRF, Hay River fault; Kw, Kiskatinaw domain; NWT, Northwest Territories; SK, Saskatchewan; RLK, Rainbow Lake; HL, High Level. The MT profile for the current study runs from RLK to HL.

A number of major questions remain unresolved regarding the structure of this area, including (a) nature of deformation on the HRF and GSLSZ and (b) the polarity of subduction or under-thrusting that led to terrane assembly. A better understanding of the

basement structure is also important for a complete understanding of the development of the Western Canada Sedimentary Basin (WCSB; Ross 2002; Pană 2003). Furthermore, since the study area has the highest heat flow in Alberta, it is important to understand the crustal structure to determine how the geothermal energy potential of the area might be utilized (Majorowicz et al. 2014; Nieuwenhuis et al. 2015).

The study area is covered by sedimentary rocks of the WCSB (Wright et al. 1994), which means that geological studies of the basement rocks are limited to drill core samples. Geophysical exploration can also be used to understand the subsurface structure. While seismic exploration is one of the most widely used geophysical techniques, electromagnetic (EM) methods can also be used and produce images of electrical resistivity of the subsurface (Unsworth and Rondenay 2012). Magnetotellurics (MT) is the most suitable EM technique for studies of crustal and upper mantle structure because it is capable of deep exploration by using naturally occurring electromagnetic signals. Furthermore, MT is sensitive to the presence of low resistivity bodies which makes it a very useful tool to study both present day and ancient plate boundaries such as subduction zones and shear zones (Jones 1993; Unsworth and Bedrosian 2004).

Previous MT studies of the study area detected several low resistivity bodies in the crust and a mid-crustal layer that was inferred to be electrically anisotropic (Boerner et al. 2000; Turkoglu et al. 2009; Yin et al. 2014). However, the existing MT data have some limitations. Firstly, the large station spacing (10-20 km) limits the horizontal resolution. In other words, the lateral boundaries of anomalies could have uncertainties on the same scale as the station spacing. Secondly, the lack of high frequency data (0.2-1000 Hz) means the near surface structure cannot be well resolved (upper 4 km in the study region, see

details in Supplementary materials S1[7]). This could further introduce ambiguity in the deeper resistivity structure. Lastly, more data are needed to better constrain the anisotropic inversion results of Yin et al. (2014). Together these factors mean that the resistivity structure of the basement rocks in the study area is poorly defined. Unresolved questions include the geometry of terrane boundaries and their depth extent.

To better address these questions about the crustal structure of NW Alberta, additional broadband MT data were collected in 2014 at 35 stations with 3-5 km spacing along a 100 km profile in NW Alberta (Figure 6.1). The profile was chosen to provide a location where a geophysical transect could be made with road-based logistics. In this paper, the new broadband MT data are described and the inversion results are presented and interpreted.

6.2. Geological setting of study area

The Precambrian basement rocks in the area (Figure 6.1) are part of Laurentia and were assembled in the early Proterozoic (Hoffman, 1989). During the assembly of Laurentia, a number of small Archean crustal elements collided and were sutured together. At the same time, a set of Early Proterozoic orogenic belts and magmatic arcs were formed. A number of major basement terranes are found in the study area and are truncated by the Hay River Fault (Villeneuve et al. 1993).

[7] Listed as Appendix A1 in this thesis.

6.2.1. Hottah terrane

The Hottah terrane, which is a major component of the Wopmay Orogen, is older than 1.9 Ga but was largely overprinted by 1.89-1.85 Ga Great Bear magmatism (Ootes et al. 2015). Several models have been proposed for the evolution of the Hottah terrane: (a) an exotic microcontinent (Bowring and Grotzinger 1992), (b) an arc within the Slave craton (Reichenbach 1991), and (c) a rift-related terrane which formed to the south and was brought to its present location by dextral strike-slip faulting (Ootes et al. 2015).

6.2.2. Hay River Fault

The HRF is a major crustal-scale, right-lateral strike-slip fault that defines the boundary between the Hottah terrane and the Nova terrane. The HRF is continuous with the Great Slave Lake shear zone (GSLSZ). Together, these two deformation zones can be traced from the foothills of the Rocky Mountains to the Thelon Basin, giving a total length of 1300 km. They accommodate 300-700 km of horizontal offset between the coeval Thelon and Taltson zones (Hoffman 1987). The HRF and the GSLSZ were once considered to be a single fault system. However, the HRF is now known to be younger (ca. 1.84-1.75 Ga) than the GSLSZ (ca. 1.97-1.92 Ga; Plint and Ross 1993; Ootes, et al. 2015). Nevertheless, the HRF can be related to a brittle stage of deformation on the GSLSZ, which is also referred to as the McDonald Fault.

6.2.3. Terranes to the south of the Hay River Fault

The Nova terrane was once interpreted to be a crustal sliver of the Archean Slave craton (Ross et al. 1990). However, samples from the eastern Nova terrane yielded ages of

1.8 and 1.7-1.9 Ga, (Simandl and Davis 2005) and thus the Nova terrane is probably Proterozoic in age.

The Ksituan terrane is a magmatic arc of 1.98-1.90 Ga age. Similar ages were identified on samples from both the Kiskatinaw and Ksituan terranes. The Kiskatinaw terrane was interpreted as a deformed portion of the Ksituan magmatic arc (Villeneuve et al. 1993).

The Buffalo Head terrane is a complex magmatic belt with metaplutonic and subordinate felsic metavolcanic rocks dated 2.0-2.32 Ga, whereas the Chinchaga domain comprises metaplutonic and metasedimentary gneisses dated 2.09-2.18 Ga (Plint and Ross 1993).

6.3. Previous geophysical studies of the study area

Geophysical studies in the study area are limited to aeromagnetic, gravity, geothermic, and MT with limited spatial coverage (Boerner et al. 2000; Pilkington et al. 2000). About 400 km to the southwest, seismic refraction and reflection profiles crossed the same terranes found in the study area (Zelt et al. 1989; Ross and Eaton 2002).

6.3.1. Potential field data

The basement domains in Alberta have been largely defined from potential field data in combination with dating of drill core samples using U-Pb isotopic analyses of zircon and monazite (Figure 6.2; Ross et al. 1990; Villeneuve et al. 1993; Pilkington et al. 2000). The aeromagnetic anomaly data were used extensively to define the domain boundaries, while the gravity data played a minor role. This was because some crustal blocks with

dramatically different age are not associated with contrasts in the gravity data. The geochronology results were also used to confirm the division into domains (Villeneuve et al. 1993).

Gravity data available include isostatic anomaly data, Bouguer anomaly data and horizontal gravity gradient, and some of these are shown in Figure 6.2. The Bouguer anomaly data in Figure 6.2c shows long wavelength, regional trends and the details associated with crustal structures are relatively small (Villeneuve et al. 1993). The isostatic anomalies enhance the signals caused by crustal structures (Cook et al. 2005). However, they are very similar to the Bouguer anomalies in NW Alberta and are not plotted in Figure 6.2. The horizontal gravity gradient data suppress the long wavelength anomalies and emphasize density anomalies originating in the upper crust (Figure 6.2d). A high horizontal gradient is associated with the juxtaposition of crustal bodies of contrasting density or thickness. It can be seen that the whole MT profile is located in a region with low Bouguer anomaly (ca. -70 milligals). There are strong gravity horizontal gradients to the north and west of the profile, and moderate gravity gradients (0.3-1 milligals/km) in the region where the profile is located. There is limited correlation between the geologic terranes and the gravity anomalies in the study area. This implies that there are no major density changes along the profile in the upper crust.

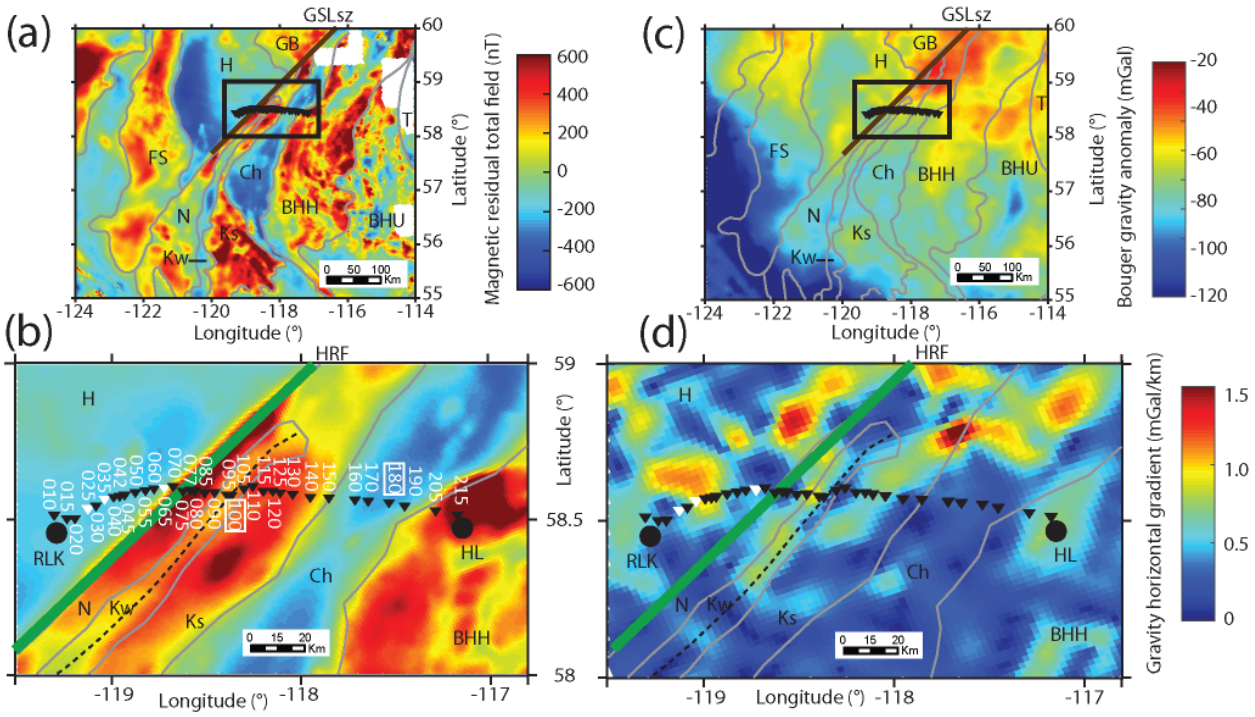

Figure 6.2: (a) Aeromagnetic map of the total residual field for northern Alberta and (b) in the study area. Data from the Geological Survey of Canada (2017). (c) Bouguer anomaly of northern Alberta and (d) gravity horizontal gradient of the study area. Data from Geomatics Canada (2017). The black rectangle in (a) and (c) shows the location of (b) and (d). The gray lines mark the Precambrian terrane boundaries from Pilkington et al. (2000). Broadband MT stations are shown by triangles. The white triangles in (b) represent stations not used in the 2-D inversion due to low data quality. The two white rectangles in (b) mark the stations with typical data shown in Figure S2 in the Supplementary Material[8]. The black circles mark the locations of nearby towns. The dashed line indicates the location of the trace of the Kiskatinaw conductor according to Boerner et al. (2000). H, Hottah; N, Nova; Kw, Kiskatinaw; Ks, Ksituan; Ch, Chinchaga; BHH, Buffalo Head High; BHU, Buffalo Head Uricuma; FS, Fort Simpson; GSLSZ, Great Slave Lake shear zone; HRF, Hay River fault; GB, Great Bear; T, Taltson; RLK, Rainbow Lake; HL, High Level.

In contrast, the total magnetic residual field is closely related to the terrane boundaries in the study area (Figure2). The amplitude of the magnetic anomalies is primarily controlled by the mineral assemblage of the rocks. Magnetite has the highest magnetic susceptibility of minerals commonly found in crustal rocks and is primarily

[8] Listed as Appendix in this thesis.

responsible for the high amplitude magnetic anomalies. Detailed description about the magnetic anomalies in the study area is discussed below.

(1) The Hottah terrane is weakly magnetic and characterized by paramagnetic sources originating in low-susceptibility silicate minerals (Pilkington et al. 2000). (2) The Buffalo Head terrane is characterized by sinuous aeromagnetic patterns and discrete subdomains. (3) The Chinchaga domain is a pronounced magnetic low. (4) The Ksituan terrane has a strong, positive aeromagnetic signature which is typical of calc-alkaline magmatic belts. (5) To the west of the Ksituan terrane are the Kiskatinaw magnetic low with a negative aeromagnetic anomaly and (6) the Nova Domain with a positive aeromagnetic anomaly (Ross et al. 1990; Villeneuve et al. 1993).

The HRF was identified from the sharp juxtaposition of aeromagnetic domains with distinct characteristics. In contrast to the sharp magnetic character of the HRF, the GSLSZ is characterized by striated positive and negative anomalies (Pană 2002). The width of the northeastern outcrop of the GSLSZ in the Canadian Shield was mapped geologically to be about 25 km (Hanmer et al. 1992). The width of the HRF is difficult to estimate from the aeromagnetic map only. If the HRF is an aeromagnetic high, it cannot be distinguished from the Nova terrane to the south; if it is an aeromagnetic low, it cannot be distinguished from the Hottah terrane to the north.

6.3.2. Seismic studies

No crustal-scale seismic data are available in the study area to date. Teleseismic tomographic models have limited resolution above the Moho (Schaeffer and Lebedev, 2014; Chen et al., 2017). The seismic receiver function analysis of Gu et al., (2011) and the seismic

reflection study of Bouzidi et al., (2002) only covered the southern end of the terranes found in the study area. The Moho depth defined by these studies was approximately 38 km. The closest crustal studies are the seismic refraction and reflection surveys in the Peace River Arch region (Figure 6.1; Zelt et al. 1989; Ross and Eaton 2002).

Lines 11 and 12 of the Peace River Arch Industry Seismic Experiment (PRAISE) were collected in 1994 and cross the same terranes as the MT profile in this paper (Figure 6.3; Ross and Eaton 2002). East-dipping reflections were observed in the Kiskatinaw terrane and can be traced from a depth of 10 km to the Moho at a depth of 40 km with an average dip of 25° (Ross and Eaton 2002). In contrast, the Ksituan terrane was only marginally reflective. In the western Ksituan domain, reflections are truncated against the dipping structures in the Kiskatinaw terrane (Ross and Eaton, 2002). The boundary of the Ksituan and Kiskatinaw terranes was defined by this cut-off relationship. At the eastern boundary of the Ksituan domain, an east-dipping reflection fabric can be traced from the top of the basement to the Moho. This dipping reflection appears to flatten out or intersect with more gently dipping reflections in the lower crust (Ross and Eaton 2002). In the Chinchaga domain, there are west-dipping reflections in the upper crust, which are cut off by east-dipping reflections at the eastern edge of the Ksituan domain. The middle crust of the Chinchaga domain features east-dipping reflections (Ross and Eaton, 2002) and sub-horizontal reflections are observed in the lower crust of the Chinchaga domain. There is no obvious change in the character of seismic reflections between the Chinchaga and Buffalo Head domains (Ross and Eaton 2002).

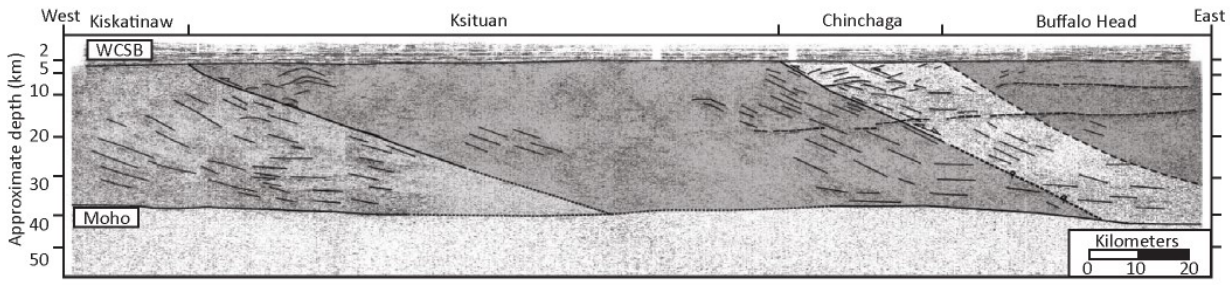

Figure 6.3: Interpreted seismic data of lines 11-12 from Peace River Arch Industry Seismic Experiment (PRAISE). Figure adapted from Figure 5 in Ross and Eaton (2002). The location of this profile is shown in Figure 6.1. WCSB, Western Canada Sedimentary Basin.

The Peace River Arch region was also studied by Zelt et al. (1989) using seismic refraction data in the PRASE (Peace River Arch Seismic Experiment) project. Line B of Zelt et al. (1989) crossed the same terranes as in the present paper (Figure 6.1). They observed that (a) there was a higher velocity in the basement 50-90 km away from shot B1. This anomalously high velocity zone is approximately located in the Kiskatinaw terrane (Figure 6.1). (b) It was not possible to pick intracrustal reflections for shot B2. This was interpreted to be the result of a reflective zone at the sediment-basement boundary. Note that the shot B2 was located at the boundary of the Ksituan and Chinchaga terranes (Figure 6.1). (c) The PmP (P-wave reflection from the Moho) character was diffuse for the shot B1 (located in the Nova terrane), whereas it appeared sharp for shot B3 and it is intermediate for the shot B2. This was proposed to be the product of a disturbed or transitional crust-mantle boundary at the west end of profile B whereas a sharp crust-mantle boundary occurs at the east end of the profile B (Zelt et al. 1989).

To sum up both seismic results, (a) the Kiskatinaw terrane is highly reflective and shows higher velocity in the crust than the Ksituan terrane. (b) At the boundary of the

Ksituan and Chinchaga terranes, there is a highly reflective zone at the sedimentary basin-basement boundary. (c) The Moho boundary is disturbed near the Kiskatinaw terrane because of the reflective features in the Kiskatinaw terrane.

6.3.3. Electromagnetic studies

The first extensive MT study of the Alberta basement rocks was made during the Alberta Basement Transect (ABT) of the Lithoprobe project (Boerner et al. 2000) when 320 long-period MT stations were recorded and these included ten of the long-period MT stations used in this study. A major low-resistivity anomaly was identified along the trend of the Kiskatinaw magnetic low and called the Kiskatinaw conductor (KC; Boerner et al. 2000).

The ABT data in northwestern Alberta were further analyzed by Turkoglu et al. (2009) who applied 3-D inversions to the data. The resulting 3-D inversion model imaged the KC which was found to follow the Kiskatinaw domain and dipped to the southeast. The KC was largest and dipped to the southeast at 20° on the 'L' profile (Figure 6.1). The KC was smaller and appeared as a vertical feature on the 'C' profile (Figure 6.1). On the profile 'A' which overlaps the profile in this study, the KC was not clearly imaged. Another conductor was found at the boundary between the Chinchaga and Ksituan domains but was deeper and more resistive than the KC by Turkoglu et al. (2009). The shallow electrical structure was not clearly imaged in the 3-D inversion model, due to the lack of high frequency MT data.

The ABT long-period data were supplemented with long-period MT stations collected as part of the GEM (Geo-Mapping for Energy and Minerals) project and published

by Yin et al. (2014). An east dipping anisotropic layer was found in the 2-D anisotropic inversion models. However, the resolution of the inversion models was not sufficient to locate the exact boundaries of the major conductors.

In conclusion, these prior MT studies have defined the general resistivity structure of the crust and upper mantle in the study area. However, new MT data, with closer station spacing, could resolve the crustal electrical structure in more detail than the previous data set.

6.3.4. Geothermics

The heat flow and the geothermal gradient near Rainbow Lake (RLK) and High Level (HL) are >76 mW/m^2 and 40-50 ˚C/km, respectively (Weides et al. 2014), which represent the highest values in Alberta. A temperature of almost 200˚C was inferred at a depth of 5 km around Rainbow Lake (Majorowicz et al. 2014). Nieuwenhuis et al. (2015) predicted the highest temperatures at depths of 1.5 and 2.0 km in Alberta (Figure 6.4; over 70 ˚C and over 90 ˚C, respectively). These depth ranges are within the low permeability Precambrian basement rocks. Therefore, an Enhanced Geothermal System (EGS) was suggested to utilize this heat (Majorowicz et al. 2014).

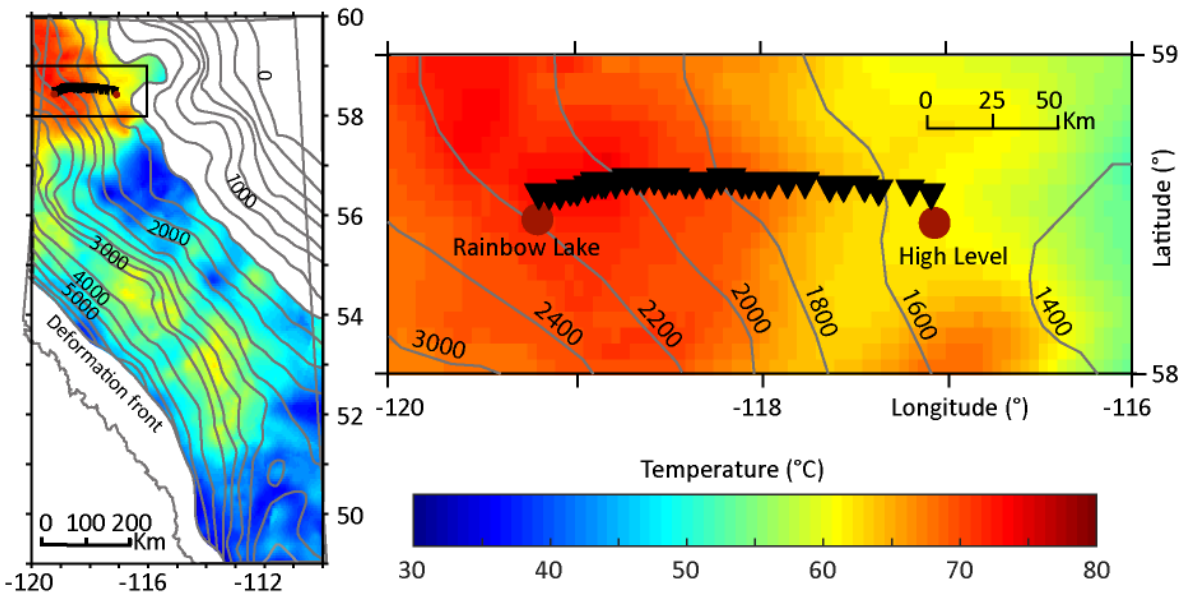

Figure 6.4: Temperature map at 1.5 km depth in Alberta (left) and the study area (right). The gray contour lines with numbers show the depth of the basement rocks. Temperature is not extrapolated in the basement rocks because there is little well control under the Western Canada Sedimentary Basin (WCSB, Nieuwenhuis et al. 2015). The black triangles represent the MT stations. The thickness of the WCSB is plotted according to the isopach map from Wright et al. (1994).

6.4. Magnetotelluric exploration in northwest Alberta

6.4.1. Brief introduction to the MT method

The magnetotelluric (MT) method is a geophysical technique that uses naturally occurring electromagnetic (EM) signals to determine the subsurface resistivity structure. The penetration depth of these signals is defined by the skin depth equation. For a homogenous earth with resistivity ρ, the skin depth can be expressed as:

$$\delta(f) = \sqrt{\rho/\pi f \mu} \tag{6.1}$$

where f is the frequency, μ is the magnetic the permeability, and generally taken to be the free space value ($4\pi\times10^{-7}$ H/m). Because of the wide range of frequencies present in the natural electromagnetic signal, the MT method is the only electromagnetic exploration technique that can provide resistivity information of the subsurface as deep as 400 km (Chave and Jones 2012).

6.4.2. MT data used

To overcome the limitations of the previously collected data, a profile of 35 broadband MT stations was collected with Phoenix MTU/MTU-A instruments in 2014 extending from Rainbow Lake to High Level (Figure 6.1). Two orthogonal electric field and three magnetic field components were measured as a function of time at each station. The locations of the stations were selected to be away from the highway and other sources of cultural noise. Details about how the new MT data improved the electrical resistivity model in the study area are included in the Supplementary Material (S1[9]).

6.4.3. Data processing, characterization and dimensionality analysis

The broadband MT data were processed to give estimates of the impedance tensor and magnetic field transfer functions in the frequency range of 1000-0.001 Hz. Details about data processing and some typical data are presented in the Supplementary Material (S2[10]).

Dimensionality analysis such as phase tensor plots, skew angles, strike analysis and induction vectors plots were applied to the MT data (details in the Supplementary Material

[9] Listed as Appendix A1 in this thesis.
[10] Listed as Appendix A2 in this thesis.

- S3[11]). Phase tensor analysis shows that the electrical structure is approximately 1-D at high frequency (near the surface) and 2-D at the intermediate frequency band (0.3-0.03 Hz) corresponding to greater depth. At low frequencies, high skew angles in the western part of the profile indicate 3-D or 2-D anisotropic electrical resistivity structure. The induction vectors show that the deep resistivity structure below the sedimentary layers is not 2-D. This is in contrast with the phase tensor analyses, which showed that the structure is 1-D/2-D except the lowest frequencies. This is probably because the induction vectors are sensitive to low resistivity bodies and current flow, whereas, they are less representative of the depth of the anomaly (Chave and Jones 2012). Therefore, 3-D low resistivity anomalies off the profile and anomalies deeper than the resolution of the MT data could contribute to the non-2-D behavior of the induction vectors. However, it should be noted that the induction vectors still contain the information about the local subsurface structure.

Strike analysis was done using the multi-site, multi-frequency distortion decomposition code of McNeice and Jones (2001; details in the Supplementary Material - S3). The most appropriate 2-D geoelectric strike direction found for all the data was N40˚E. Therefore, all the MT data were rotated to a geoelectric coordinate system with geoelectric strike direction (N40˚E) for further analysis.

6.4.4. Anisotropy

Electrical anisotropy means that the resistivity of the subsurface is directionally dependent. An anisotropic structure in the crust can be present if there is a preferred orientation of fluids, sulfide minerals or fractures (Wannamaker 2005, Liddell et al. 2016).

[11] Listed as Appendix A3 in this thesis.

An anisotropic dipping conductor was inferred to be present by Yin et al. (2014) in the depth range of 10-20 km. With the new MT stations, the anisotropy of this region can be rigorously reevaluated.

The dimensionality analysis in the Supplementary Material (S3[12]) gives information that can determine if the resistivity structure is anisotropic or isotropic. The large phase splits, large skew angle values, complex patterns of induction vectors in the MT data are indicative of anisotropic structure. However, it can be difficult to distinguish a 2-D anisotropic structure from 3-D heterogeneities in an isotropic structure (Heise and Pous 2001). Details about the characterization of the effects of anisotropy structure on the MT data are presented in the Supplementary Material (S4[13]).

6.5. Inversion of the MT data

From the dimensionality analysis, the subsurface resistivity structure appears to be generally 2-D. Therefore, 2-D inversions were used to invert the data and produce resistivity models. Anisotropic resistivity structure was suggested by Yin et al. (2014) and is also believed to exist in other ancient shear zones (Weckmann et al. 2003). Therefore, 2-D anisotropic inversions were also applied to the new MT data to check if electrical anisotropy is present. Because the data at low frequencies (0.03-0.003 Hz) on our profile show some 3-D features, a 3-D inversion could be useful to image deeper structure.

[12] Listed as Appendix A3 in this thesis.
[13] Listed as Appendix A4 in this thesis.

6.5.1. 2-D isotropic inversions

A profile was constructed perpendicular to the strike direction (N40˚E). Three stations (RLK025, RLK035, and RLK065) were excluded because of poor MT data quality, giving a total of 32 MT stations. In the geoelectric coordinate frame, the TE (transverse electric) mode is associated with the electric currents flowing in the strike direction while the TM (transverse magnetic) mode represents the electric currents flowing perpendicular to the strike direction. The data pseudo sections are shown in Figure S3 in the Supplementary Materia[14]l.

The NLCG inversion scheme of Rodi and Mackie (2001) was used for both the isotropic and anisotropic inversions. The mesh used in isotropic inversions has 122 vertical and 114 horizontal cells, giving a width of 480 km and a depth of 580 km for the total mesh area. The upper most row of cells had a vertical thickness of 16 meters, and the thickness increased geometrically with depth. The inversion started from a homogenous half space with a resistivity of 100 Ωm. For each inversion, 200 iterations were done to ensure the inversion had converged. A total of 55 frequencies from 300-0.0013 Hz were used in all inversions.

The first inversions investigated single modes (TE/TM/tipper only inversions) until the final r.m.s. misfit was lower than 2 and the data were considered to be well edited. Inversions of combinations of different modes were then undertaken. The final inversion model is the result of joint TE, TM and tipper inversion. Many inversions with different error floors were run as a test to determine the optimum values for the error floors. For the

[14] Listed as Appendix in this thesis.

inversion models presented here, the error floors for apparent resistivity and phase were set to 10% and 5%, respectively, for both the TE and TM modes. The error floor for the tipper was set as an absolute value of 0.04. A set of values were tested on the smoothness parameter τ varying from 0.01 – 100 for 2-D isotropic inversions. The model roughness and data fitting were plotted against each other (L-curve), in order to find the best tradeoff. According to the L-curve, the tau selected for the final inversion model was 3 for both the isotropic and anisotropic inversions. Additionally, the inversion was allowed to estimate static shift coefficients at just two stations (RLK150, RLK190) at the east end of the profile because they showed some distortion in the dimensionality analysis. However, there was no obvious change in the inversion model or r.m.s. misfit, so the final inversion did not consider static shift correction.

6.5.2. 2-D isotropic inversion results

The preferred 2-D isotropic inversion model is shown in Figure 6.5. It is evident that the shallow structure is better constrained with the addition of extra stations and high frequency data. The WCSB can be clearly seen and dipping gently to the west. The resolution of the major resistivity anomalies is better because of denser model mesh and closer stations. A final r.m.s. misfit of 2.3 is achieved in the preferred model. The comparison of the model response and the measured data are shown in pseudo-section format in Figure S3 in the Supplementary Material[15].

[15] Listed as Appendix in this thesis.

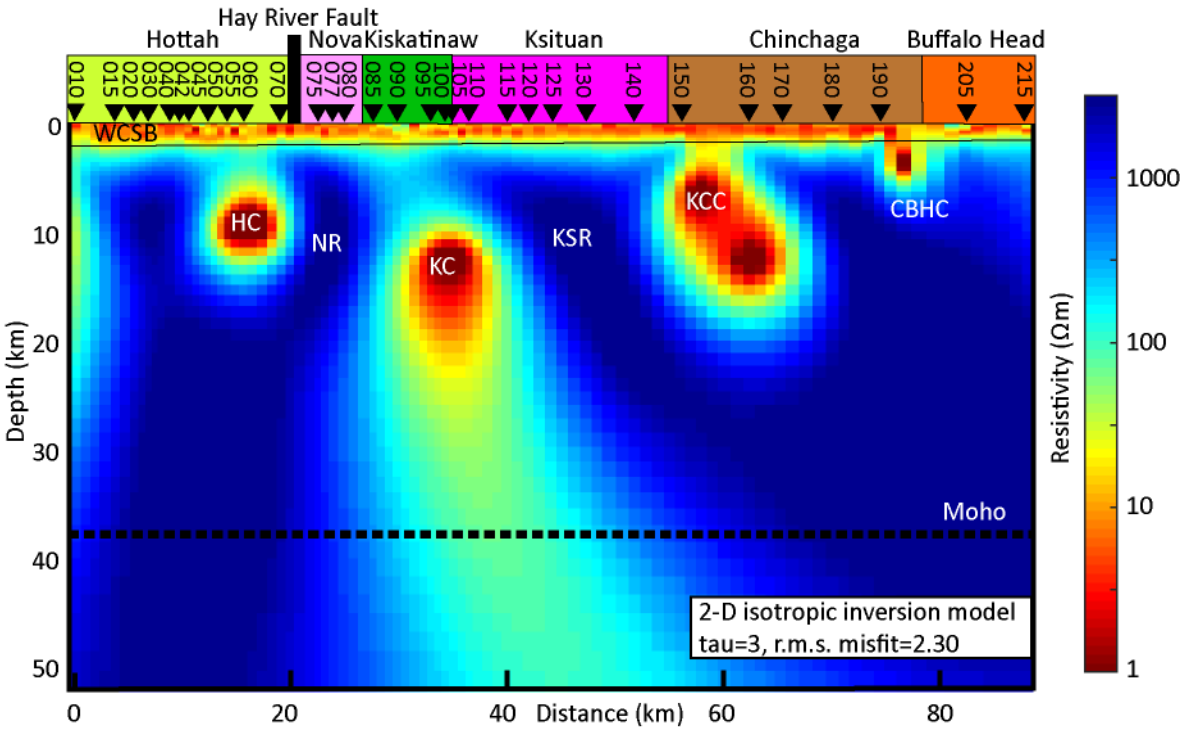

Figure 6.5: The preferred 2-D isotropic inversion model. CBHC, Chinchaga-Buffalo-Head conductor; HC, Hottah conductor; KC, Kiskatinaw conductor; KCC, Ksituan-Chinchaga conductor; NR, Nova resistor; KSR, Ksituan resistor; WCSB, Western Canada Sedimentary Basin. The dashed line shows the Moho according to Gu et al. (2011).

In the inversion model, several significant resistivity features can be observed. Firstly, the sedimentary layer near the surface is clearly imaged as a low resistivity layer (3-30 Ωm) that is continuous along the profile. One feature to note is the more resistive region (about 30 Ωm) between stations RLK085 and RLK100 in the 0-2 km depth range. Sedimentary rocks in this region are older than in other parts of the profile (Prior et al. 2013), making this observation consistent with the fact that older sedimentary rocks often have higher resistivity than younger sedimentary rocks (Haak and Hutton 1986) because of the reduction of porosity and clay content.

Secondly, the basement is generally imaged with resistivity greater than 3000 Ωm (e.g. Nova Resistor (NR) and Ksituan Resistor (KSR)), which is reasonable for old crystalline rocks. Finally, there are four distinct conductors in the basement with very low resistivity. The four conductors are described below in detail.

(1) Kiskatinaw conductor (KC): This is imaged from a depth of 10 km and extends to the Moho at a depth of 38 km (Gu et al. 2011). The KC dips steeply to the southeast with a very low resistivity (<1 Ωm) from 10-20 km. There is a less conductive tail (30-100 Ωm) from 20-40 km. The penetration depths of MT signal are 10 km and 140 km using a resistivity of 1 Ωm and 100 Ωm and the lowest frequency – 0.0013 Hz. Therefore, the magnetotelluric signal may not penetrate through the KC and the deeper tail could be an inversion artifact. Moreover, it should be noted that while the MT method can define the upper boundary of a conductor very well, the lower boundary can be poorly resolved. Only the conductance – the product of the conductivity and the thickness of the conductor is well resolved. This is further discussed in sensitivity tests and synthetic modeling and inversions in the Supplementary Material[16] (S5 and S1, respectively).

(2) Ksituan-Chinchaga conductor (KCC): This is located at the boundary of the Ksituan domain and Chinchaga domains. The KCC extends from the top of the basement at about 2 km to a depth of 18 km with a 45° dip to the southeast. Furthermore, there are two distinct smaller conductors in the KCC with resistivity <1 Ωm compared with the surrounding 3-10 Ωm resistivity. However, it is not clear if these features are resolved because the electromagnetic signals used in MT method are diffusive and are not sensitive to small structures. The resolution of this conductor is investigated by sensitivity tests and

[16] Listed as Appendix in this thesis.

synthetic modeling and inversions in the Supplementary Material[17] (S5 and S1, respectively).

(3) Hottah conductor (HC): The HC is under the Hottah terrane near the HRF, with resistivity <1 Ωm and depth of approximately 10 km.

(4) Chinchaga-Buffalo Head conductor (CBHC): The CBHC is a small conductor with resistivity <1 Ωm at the boundary of Chinchaga and Buffalo Head terranes. The top of the CBHC is just below the sedimentary layer (2 km) with a lower boundary at about 5 km depth.

6.5.3. 2-D anisotropic inversions

Two-dimensional anisotropic inversions were also applied to the data. The Supplementary Material (S6[18]) gives details and results of the 2-D anisotropic inversions. It was found that (a) a slightly lower r.m.s. misfit (about 2.1-2.2) could be achieved with the anisotropic inversions, compared to the isotropic inversion (about 2.3), (b) the r.m.s. misfit and the anisotropic inversion models do not change too much with the change of the anisotropic tau, and (c) the anisotropic inversion models are quite similar for three directions. These all may indicate that the electrical resistivity model does not need to be anisotropic to give an acceptable fit to the measured MT data. Therefore, it is concluded that the subsurface structure can, to a first approximation, be treated as electrically isotropic even though some anisotropy may be present. The large distortion of phase tensors, high skew angles and complex patterns of induction vectors observed in the MT

[17] Listed as Appendix in this thesis.
[18] Listed as Appendix A6 in this thesis.

data could be explained by along strike variations or 3-D effects instead. Details about this discussion are in the Supplementary Material (S6[19]).

6.6. Interpretation and discussion

It has been proposed that the crustal blocks in the area have been assembled by subduction processes, although the locations and geometry were poorly defined. Past subduction can produce major conductors that remain to the present day (Jones, 1993). In the following sections, the four conductors will be interpreted with regards to their location and cause of the low resistivity to determine the nature of these past tectonic events.

6.6.1. The Kiskatinaw conductor (KC)

The Kiskatinaw conductor (KC) was first described by Boerner et al. (2000) based on 2-D inversions of the Lithoprobe MT data. Turkoglu et al. (2009) presented 3-D inversion models which showed that the KC is a crustal-scale conductor following the surface trend of the Kiskatinaw terrane, with a dip and size that vary along strike.

The structure of the KC defined with MT can be compared to other geophysical studies. (a) The geometry of the KC in the 2-D inversion model is comparable to that obtained with the seismic reflection by Ross and Eaton (2002; Figure 6.6) who found that the crust of the Kiskatinaw terrane was highly reflective from 10 km depth to the Moho with east dipping features. (b) Seismic refraction showed that the Kiskatinaw terrane was characterized by higher velocities than neighbouring terranes and characterized by a

[19] Listed as Appendix A6 in this thesis.

disturbed Moho (Zelt et al. 1989). (c) The resistivity model shows that the Kiskatinaw terrane is much less resistive than the Ksituan terrane and the KC starts from a depth of 10 km, which is same as the top of the enhanced seismic reflectivity. The bottom of a low resistivity anomaly is hard to define with MT data, so it is inappropriate to compare the base of the KC to the seismic result. (d) Lastly, the Kiskatinaw terrane is an aeromagnetic low while the Ksituan terrane is an aeromagnetic high. (e) A moderate Bouguer gravity high is associated with the Kiskatinaw and Ksituan terranes in the study area.

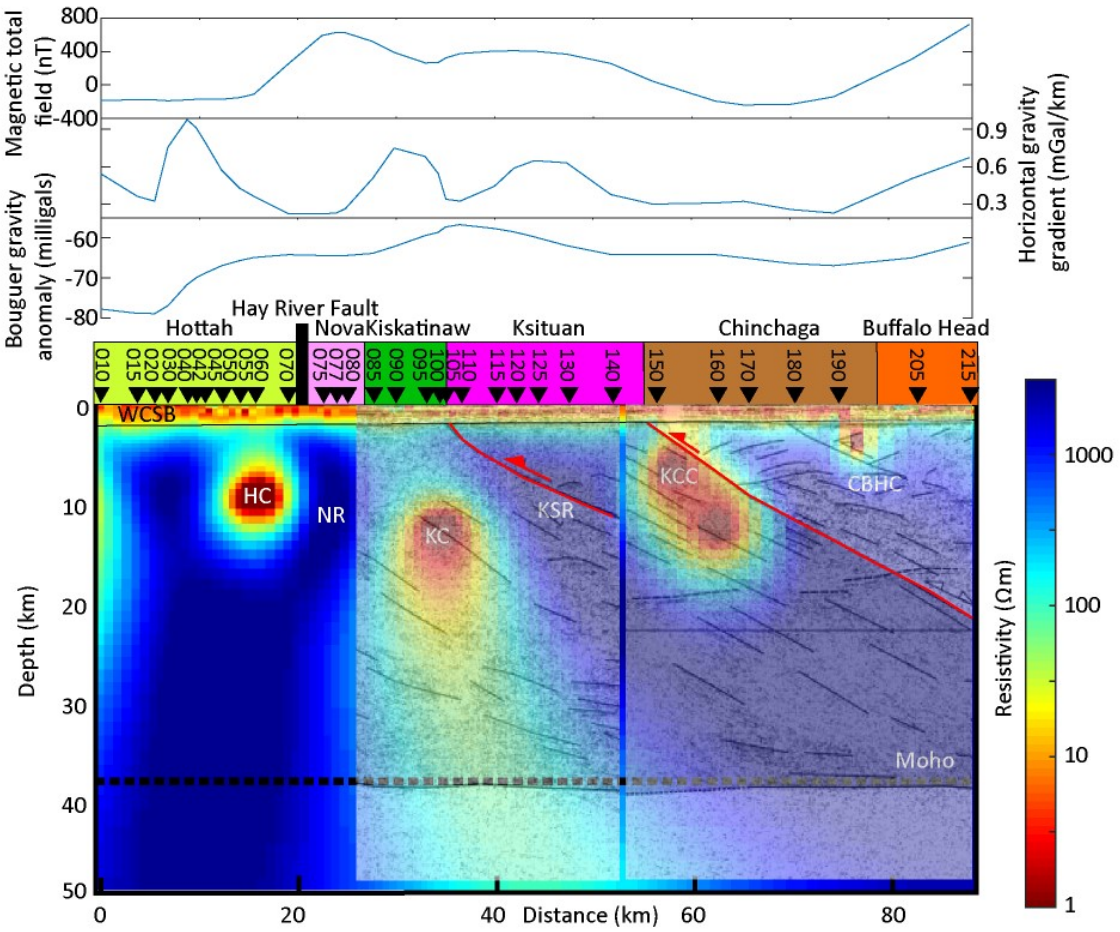

Figure 6.6: Comparison of the 2-D isotropic inversion model with the seismic reflection profile from Ross and Eaton (2002). The two seismic sections presented here are from the seismic profile shown in Figure 6.3. The top of the basement and the base of the crust (Moho) in the two results were aligned. No vertical exaggeration was applied. The red lines mark the terrane boundaries defined from the seismic reflection study. The red arrows indicate the direction of relative movements of crustal blocks. The three curves on the top show the magnetic total field, horizontal gravity gradient, and Bouguer anomaly data along the MT profile. The magnetic and gravity data sources are same as in Figure 6.2.

Along strike variation of the geometry of the KC may explain the difference between the MT and seismic results: the shallow part of the KC in the 2-D inversion model does not show the 25˚ dip angle observed in the seismic reflection data. The seismic profile crosses the southernmost part (at about 56˚N) of the Kiskatinaw terrane while the MT profile

presented in this paper crossed the northernmost part (at about 58.5˚N; Figure 6.1). These two profiles are located about 400 km apart. Furthermore, the MT profiles studied by Turkoglu et al. (2009) could link results of this study and the seismic study. The KC on profile 'L' shows a 20° dip which is close to the seismic result (25°). The 'C' profile from Turkoglu et al. (2009) imaged the KC, but it was weaker than in the profile 'L' and vertical. The KC was not imaged by Turkoglu et al. (2009) on profile 'A' at the expected shallow depth. However, a low resistivity anomaly was imaged in the depth slice at 41 km. This may be due to lack of high-frequency data and wide spacing between MT stations in the previous study. Consequently, the KC on the profile 'A' was imaged deeper than the actual location of the KC. Alternatively, another explanation is that the KC actually ends west of the profile 'A' and the KC imaged in this paper is a regional effect from the KC. In this case, the northern end of the KC should be less than 10 km from the profile, according to the skin depth equation.

Considering all results from these three studies, it can be concluded that the cross-sectional area of the KC is greatest at the southern end and decreases to the north i.e. the conductance of the KC decreases from the south to the north, and the dip of the KC changes from 25˚ in the south to vertical in the central and northern parts.

What is the cause of the low resistivity (1-3 ohm-m) of the KC? Possible explanations include fluid, partial melt, graphite, and sulfide minerals. Additional geological or geophysical information is needed to differentiate between the possibilities, which are considered below:

(a) Partial melt could not be the explanation for the low resistivity because the temperature of the crystalline rocks is far too low (300 ˚C at 10 km depth, Majorowicz et al. 2014).

(b) Aqueous fluids containing dissolved salts can produce a low resistivity and have been proposed as an explanation for crustal conductors observed in the stable continental crust (Wannamaker 2000). In this scenario, Archie's Law can be used to relate the low resistivity with rock porosity, fluid resistivity and interconnection of the pores quantitatively (Archie 1942; Supplementary Material - S7[20]).

Experimental results from Sinmyo and Keppler (2017) suggested that the resistivity of crustal fluids may be as low as 0.03 Ωm. To explain the observed resistivity of the KC (1 Ωm), and assuming the rock is fully saturated with a saline fluid of 0.03 Ωm resistivity, 3% and 17% porosity is required according to Archie's Law using cementation exponents of 1 and 2, respectively. This porosity range is high, which means it is unreasonable to explain the low resistivity of the KC by saline fluids alone. Another problem with this explanation is that even though water may have been present when the KC was formed, water is not likely to have been retained for almost 2 billion years without a source or a sealing mechanism to retain the water (Frost and Bucher 1994).

(c) Graphite films could also explain the low resistivity of the KC, and were suggested as the cause of the low resistivity of the North American Central Plains anomaly in the Paleoproterozoic Trans-Hudson Orogen (Jones et al. 1997). Boerner et al. (2000) interpreted the low resistivity of the KC to be associated with the concentration of carbonaceous material within euxinic basins that transformed into graphite. The carbon

[20] Listed as Appendix A7 in this thesis.

from the euxinic basins could be deposited as interconnected graphite by metamorphic processes. Another possible source of the carbon could be carbon-bearing metamorphic fluids. If this low resistivity is because of grain boundary graphite, and assuming that the pure graphite resistivity is 0.0001 Ωm, a volume fraction of 1% of well-connected graphite is needed to explain the 1 Ωm anomalies observed, according to Archie's Law (Archie 1942).

(d) It has also been suggested that the precipitation of sulfide minerals can be another way to lower the resistivity of the KC (Boerner et al. 2000). Sulfide minerals could precipitate during metamorphism, migrate with fluids and become disseminated within the rocks. The sources of sulfides could be subducted sediments or sulfur-bearing metamorphic fluids. It was shown that 3-7% of disseminated sulfide minerals could lower the bulk resistivity of rocks to 20-70 Ωm (Nelson and Van Voorhis, 1983). However, this value is higher than the resistivity of the KC and disseminated sulfide minerals alone cannot explain the low resistivity of the KC. Alternatively, sulfide minerals can be concentrated in the rocks to give lower resistivity values of 3-8 Ωm (Jones et al. 1997).

In summary, graphite and sulfide minerals are preferred explanation for the low resistivity of the KC. They could originate from metamorphic fluids or subducted sediments and transformed to conductive form during metamorphism and associated shear-related deformation.

6.6.2. The Ksituan-Chinchaga conductor (KCC)

The second major conductor is the Ksituan-Chinchaga conductor (KCC), which could be related to the conductor recognized by Turkoglu et al. (2009). However the conductors imaged in this study and by Turkoglu et al., (2009) are located at different depths (2-18 km

and 40-65 km, respectively). There are two solutions here: it is the same conductor, but imaged with different depth and conductance. The greater depth inferred by Turkoglu et al. (2009) could be the result of the lack of high frequency MT data. As mentioned above, only the conductance of a low resistivity body can be resolved with MT. The high conductance as a result of the KCC anomaly is represented as the shallow feature in this study while as a deeper feature in the model of Turkoglu et al. (2009). Alternatively, the KCC in the present paper is distinct from the conductor imaged by Turkoglu et al. (2009). However, in this case there should be another low resistive body at depth of around 40 km. The absence of a deeper conductor favors the first explanation i.e. both studies have imaged the same conductivity anomaly. Furthermore, the KCC was imaged to be continuous along the boundary of the Ksituan and Chinchaga terranes from the north to the south in the 3-D inversion model of Turkoglu et al. (2009).

The KCC can be correlated with the seismic reflective features at the boundary of the Ksituan and Chinchaga domains (Ross and Eaton 2002). The reflective feature was also identified in the seismic refraction survey (Zelt et al. 1989). The KCC detected in this study shows the dip angle (45°) and the depth range (2-18 km) that are consistent with the seismic results. Moreover, the KCC correlates with the boundary of the Ksituan (high) and Chinchaga (low) domain in the aeromagnetic data. However, because of its large width, it is hard to determine which side of the KCC corresponds to the boundary between the Ksituan and Chinchaga terranes.

The possible causes of low resistivity in the KCC are similar to those in the KC. Partial melt is an unlikely explanation. Is saline fluid possible explanation? Frost and Bucher (1994) concluded that in stable cratons, water could be gravitationally driven and

migrate to the upper 10 km of the crust. The KCC is imaged with an upper boundary just below the sedimentary basin at 2 km depth and with a lower boundary at about 16 km. Additionally, it was suggested that at this location, the Ksituan and Chinchaga domains have a thrust fault contact (Ross and Eaton 2002), which could represent a pathway for groundwater flow. Therefore, the low resistivity can be the result of saline fluid trapped in the fractures of the fault. As for the KC, a porosity of 3-17% of porosity is needed to explain the 1 Ωm resistivity of the KCC. However, the porosity range seems too high for crystalline rocks at 10 km depth, and another source of low resistivity is required. As discussed for the KC, graphite and sulfide minerals can be deposited with interconnection during metamorphic events. A volume fraction of a few percent of these conducting phases could lower the resistivity effectively. The low resistivity in the KCC may be caused by the combination of saline fluid, graphite and sulfide minerals.

6.6.3. The Hay River Fault (HRF) and the Hottah conductor (HC)

The Hay River Fault was originally identified from the boundary between contrasting aeromagnetic signatures in the Hottah and Nova terranes, although the exact location of the HRF is still somewhat uncertain. Is it possible that the fault zone itself has a magnetic anomaly? Villeneuve et al. (1993) proposed that shear zones could be magnetic lows since demagnetization could occur as a result of hydration and dynamic metamorphism such as occurred in the GSLSZ (Villeneuve et al. 1993) and the Kiskatinaw terrane (Ross and Eaton 2002). Shear deformation probably occurred at the HRF and if it was accompanied by fluid alteration and conversion of magnetite to hematite (Frost et al. 1989), the HRF should be a negative aeromagnetic anomaly. In this scenario, the location of the HRF is difficult to distinguish from the Hottah terrane to the north with aeromagnetic

data. Even if no demagnetization occurred as the HRF moved and it is a positive aeromagnetic anomaly, the location of the HRF is still hard to distinguish from the Nova terrane to the south with aeromagnetic data. No other geophysical data have been able to locate the HRF to date. Because the HRF is covered by Phanerozoic sedimentary rocks, geological studies cannot assist in this task.

Can the resistivity structure be used to locate the HRF? The HC is located close to the HRF and the HC is imaged within the negative aeromagnetic anomaly in the Hottah terrane. Unlike the KC and KCC, this resistivity feature does not have an obvious eastward dip. Modern-day strike-slip faults sometimes exhibit a low resistivity in the upper crust (0 -10 km), owing to a region of elevated porosity saturated with aqueous fluids (Unsworth and Bedrosian 1999). However, a zone of elevated porosity is unlikely to be present in ancient faults, as the fluid supply/connection would likely have been lost after 1.8 Ga. If the fluid flow in an active fault deposited graphite and/or sulfide minerals, then this could produce a low resistivity anomaly that would persist to the present day.

Another possibility is if the upper crustal part of the HRF was eroded and the rocks of the HRF currently exposed at the surface was formed in a mid-crustal environment. At such depths deformation in strike-slips faults will be ductile owing to the higher temperatures and pressures. While this can cause low resistivity when active, it will result in high resistivity when the shear zone becomes inactive and cools down. The GSLSZ in the Canadian Northwest Territories is an example of this phenomenon. It is believed that the upper crustal portion of the GSLSZ was eroded and the presently exposed part of the GSLSZ was developed under ductile conditions (Eaton and Hope, 2003). Wu et al. (2002) demonstrated that the GSLSZ was resistive in a 2-D inversion model based on MT data.

Given this background, there are three possible explanations for the observed resistivity pattern across the HRF. (1) The location of the HRF could be 5 km further northwest of the boundary of the negative and positive aeromagnetic signatures and the HC actually defines this fault, with the low resistivity due to graphite and/or sulfide minerals. (2) The HC is not related to the HRF and the high resistivity anomaly (NR) is either the unaltered basement, or the consequence of ductile shear deformation, similar to that observed on the GSLSZ to the northeast. (3) The HRF could be the resistive-conductive boundary between the Hottah and Nova terranes. This could occur if the HC was an internal feature of the Hottah or the Nova terrane and deformation associated with the HRF occurred in a localized belt.

6.6.4. The Chinchaga-Buffalo-Head conductor (CBHC)

The Chinchaga-Buffalo-Head conductor (CBHC) is the smallest and shallowest conductor detected in the study area, and no seismic structure was found in this location. The CBHC is located just below the sedimentary basin which indicates that groundwater from the sedimentary basin could be penetrating the basement rocks and causing the low resistivity. Since this conductor is located on the boundary of two terranes, explanations due to conducting phases such as graphite and sulfide minerals are also possible, as was the case for the KC and KCC.

6.6.5. Tectonic implications

According to the seismic reflection data and geochronology studies, a tectonic model was proposed by Ross (2002) for the study area. It suggested that the Chinchaga and Buffalo Head domains collided early in the assembly (Ross 2002; Ross and Eaton 2002).

This was followed by the westward subduction of the oceanic lithosphere between the Chinchaga and Nova domain which resulted in the formation of the Ksituan domain and Kiskatinaw domain as a magmatic arc during 1.90-1.98 Ga (Ross and Eaton 2002). It should be noted that the Kiskatinaw terrane was interpreted as a sheared equivalent of the Ksituan domain formed during the final stage of the collision between the Ksituan terrane and Nova terrane (Villeneuve et al. 1993; Ross and Eaton 2002).

The westward subduction direction was preferred because of the lack of coeval plutonic rocks within the Buffalo Head and Chinchaga domains. Ross and Eaton (2002) interpreted the apparent contradiction between the eastward dipping seismic reflections and the postulated westward subduction as a result of overprinting by a younger collision. This is possible and Van der Velden et al. (2005) argued that different vergence of the subduction zone and the crustal suture is relatively common and could be caused by lithospheric delamination.

Alternatively, geochemical and isotopic study of granitoids from the Taltson magmatic zone by Chacko et al. (2000) implied that eastward subduction occurred to the west of the Ksituan terrane, or perhaps even to the west of the Hottah terrane in the current coordinate system. This hypothesis is also consistent with the seismic reflection and the MT results. In this case, the suturing process has the same polarity as the subduction process.

The structure defined from the MT data generally correlates with the seismic reflection results. This study also compliments the aeromagnetic mapping by providing information about the subsurface geometry of the terrane boundaries. The change of the

gravity field in the study area is subtle and no obvious correlation between the gravity and resistivity anomalies is observed.

Combining the previous and new MT results, potential field data and the seismic reflection data, it is believed that there is a thrust fault between the Ksituan and Chinchaga domains from the top of the basement to a depth of about 18 km. This interpretation is consistent with (a) the cut-off reflections observed in the seismic reflection profile, (b) the reflective zone mapped in the seismic refraction profile, (c) the low resistive body imaged at the boundary of the Ksituan and Chinchaga terranes, (d) the contrasting aeromagnetic anomaly in the Ksituan (positive, high amplitude) and Chinchaga domain (negative, high amplitude) (e) No associated gravity anomaly is observed at the Ksituan-Chinchaga boundary which implies density and thickness of the basement rock are similar in the two terranes.

The properties of the Kiskatinaw domain can be explained if it is a shear-deformed part of the Ksituan domain, with faults on the eastern and western boundaries of the Kiskatinaw domain. This is consistent with geochronology results which show that the Ksituan and Kiskatinaw have the same age (1.98-1.90 Ga, Villeneuve et al 1993). Lithology studies also found that the rock samples from the Kiskatinaw terrane show foliated and gneissic features that indicate the Kiskatinaw terrane may be a deformed portion of the Ksituan terrane (Villeneuve et al 1993). It is speculated that the Kiskatinaw terrane and Ksituan terrane were the same unit before shear deformation of the Kiskatinaw terrane. As the terrane assembly progressed, the Kiskatinaw terrane was compressed by the Nova terrane and was sheared along the margin of the Ksituan domain. Possible demagnetization during the shearing process may have transformed the Kiskatinaw terrane from being a

high amplitude magnetic high to a low amplitude magnetic feature. The seismic reflections at the mid-crustal depths and the high velocity observed could also be a result of the deformation (i.e. compression and shearing). The low resistivity of the Kiskatinaw conductor can be explained by graphite or sulfide minerals formed through metamorphism. The short wavelength (ca. 20 km, trending N45˚E; Figure 6.2) Bouguer gravity high and gravity gradients observed along the Kiskatinaw and Ksituan terranes in the study area indicate lower density or thicker crustal rocks. Moreover, the Bouguer high does not appear to extend along strike. Therefore, the Bouguer high may be unrelated to the basement structure, but originated from the sedimentary layers.

Three different explanations were proposed for the structure and location of the HRF in the previous section. Constraints on the structure of the HRF were heavily dependent on the MT results because there is no seismic data in the study area.

Terrane accretion is believed to account for the assembly of the crust in the study area, even though it is impossible to decide which tectonic setting of the two discussed above is more reliable. The high correlation between the seismic reflection result and MT resistivity profile give indications about the terrane assembly process. (a) Although it is believed that the tectonic terranes in the study area have been attenuated to the northwest along the HRF, the major crustal features are preserved along strike in the process. (b) The strike-slip motion of the HRF occurred after the assembly of the tectonic terranes in northwest Alberta.

6.6.6. Geothermics

Studies of the fracture patterns in the Hay River fault zone could be a significant factor regarding the development of an EGS in this location (Majorowicz et al. 2014). Previous studies at EGS projects such as Soultz, France showed that (a) the movement of fluid between the two wells can be controlled by natural fracture structures and (b) it is possible that the fluid injected has been mixed with the natural brines (Genter et al. 2010). Moreover, (c) it was argued that while naturally occurring fractures could provide natural porosity, they could also represent a pathway for fluid loss or result in low heat transfer due to reduced contact between the fluid and the rocks (Fritz and Gerard, 2010). A better understanding of the subsurface structure can be important to evaluate these factors. The structural information listed in the tectonic implication section should be considered when exploring the geothermal energy in the area.

6.7. Conclusions

This MT study advances our knowledge about the structures of the crust in northwest Alberta. The sedimentary layer was imaged as a conductive feature on top of the resistive crystalline basement and four conductors are identified in the basement. Even though anisotropy was suggested by Yin et al. (2014), the present study suggests that electrical anisotropy is not required to explain the data.

The main conductor imaged in the study region is the Kiskatinaw conductor (KC) and may be traced as a continuous feature for over 400 km along the strike of the Kiskatinaw terrane. The location of the KC is coincident with a seismically reflective and high-velocity zone (Zelt et al. 1989; Ross and Eaton 2002). The low resistivity of the KC may be the result

of sulfide and graphite phases which were deposited during metamorphic event. The Kiskatinaw terrane was previously interpreted as a deformed and altered part of the Ksituan terrane (Ross and Eaton 2002) and this hypothesis is confirmed by this study. The second significant conductor is the Ksituan-Chinchaga conductor (KCC) which is also coincident with a zone of seismic reflectivity and the boundary of the Ksituan magnetic high and the Chinchaga magnetic low. The low resistivity of the KCC is most likely due to a combination of saline fluid, graphite film and sulfide minerals. The KCC may well be related to thrust movement at the boundary of the Ksituan and Chinchaga domains (Ross and Eaton, 2002). The Hottah conductor (HC) may be related to the Hay River Fault (HRF) if demagnetization occurred during shear deformation which transforms ferrimagnetic Fe-oxides into antiferromagnetic Fe-silicates (Villeneuve et al. 1993). In this scenario, graphite resulted from metamorphism could explain the low resistivity of the HC. If the HC is not related to the HRF, then the HRF could be associated with an aeromagnetic high anomaly and high resistivity. This could be explained by ductile deformation that resulted in the shear zone being depleted in volatiles after shearing, as is interpreted to have occurred in the GSLSZ (Wu et al. 2002). Another possibility is that very localized deformation occurred and the HRF behaves as an impermeable boundary between the HC and the adjacent crystalline rocks.

Aeromagnetic data can locate the terrane boundaries (Pilkington et al. 2000), and this MT study extends this analysis by imaging the geometry of these boundaries at depth. The resistivity anomalies imaged in this study generally correlate with terrane boundaries derived from aeromagnetic data.

The results complement previous studies of the tectonic evolution of the region by Ross and Eaton (2002) and Chacko et al. (2000). They both suggested that a combination of subduction and terrane accretion caused the amalgamation of the basement domains which is confirmed by this study.

Majorowicz et al. (2014) and Nieuwenhuis et al. (2015) suggested that an enhanced geothermal system (EGS) may be viable in the study area because of the high temperature at shallow depth. The results of this study supplement information about the subsurface structure that can be used for the evaluation and future development of an EGS.

Chapter 7 : Three-dimensional inversion tests on the Alberta long-period MT dataset

7.1. Introduction

It is known that the resistivity structure of the Earth varies in three dimensions (Chave and Jones, 2012). However, prior to the 1990s, MT data were generally interpreted with 2-D electrical resistivity models, because the available inversion programs were limited by computer speed and memory. Since the early 2000's, 3-D MT inversions have become more widely used because of:

(a) the development of efficient 3-D inversion algorithms. This includes the WSINV3DMT algorithm of Siripunvaraporn et al. (2005) and the ModEM algorithm of Kelbert et al. (2014), and

(b) the availability of powerful, massively parallel computer hardware, such as the computers operated by Westgrid and Compute Canada. These machines allow parallel computing to reduce the run time of the inversions, and provide large memory nodes (from 16 GB to more than 1000 GB per node). A typical MT inversion job needs at least 50 GB memory from multiple nodes and runs for about one week. If the same job ran on a non-parallel environment, it would take a few months to finish.

As the size of an MT dataset increases, the size of the resistivity model also increases and, more computing memory and time are required for a 3-D inversion. Therefore, only subsets of the MT data in Alberta can be used in an inversion. If the MT dataset is too big,

the memory required to run the 3-D inversion would exceed the available resources and the inversion could not run. Moreover, in the two inversion schemes used in this thesis (ModEM and WSINV3DMT), only one MT station is allowed in each model cell. This means a finer spatial grid is required to accommodate more MT stations which will result in a larger resistivity model size. The inversions were run on the Westgrid's computing facilities with high memory demand (about 100-1000 MB) for a time period ranging from a few days to a few weeks depending on the model and dataset sizes.

At the beginning of the research described in this thesis, the computing resources available limited the number of MT stations that could be inverted to be less than 200, and only inversions of subsets of the central Alberta dataset were achievable. More recently (from 2018) a more powerful machine – Cedar has become available and this has allowed us to undertake 3-D inversions that include more MT stations with a larger grid that covers the whole of Alberta.

Running these large 3-D MT inversions is an area of research that requires investigations of what data can be included. It is also essential to verify that if the resulting resistivity models can be considered stable. The 3-D MT inversion tests are described in this chapter. In the following chapter the inversion models of Alberta which will be interpreted in Chapter 9 are described.

7.2. Selection of the MT dataset to be inverted

MT inversion algorithms compute a resistivity model that fits a measured MT dataset to within a specified statistical tolerance. Therefore, selecting a reliable dataset is an essential first step to the success of inversions. The available MT data are a combination

of (1) legacy MT data previously collected in Alberta (Boerner et al., 2000; Nieuwenhuis et al., 2014) and (2) new MT data that were collected during this study and described in Chapter 5. Although an MT dataset with more stations will result in a more comprehensive resistivity model, it will also require more computer memory and computation time. Deciding which MT stations to use depends on several factors. The factors must be considered are listed below.

(a) Firstly, the main focus of the 3-D inversions in this thesis is the deep resistivity structures. Thus, only long-period magnetotelluric (LMT) data collected in Alberta and southwest British Columbia were used. There are a total of about 600 LMT stations available (Figure 7.1).

(b) Using all these LMT stations would be impractical for inversions because of the limited computational resources, and a subset must be chosen. Two LMT data subsets of 102 or 183 stations in the central Alberta were used to test the inversion strategy described in this Chapter (Figure 7.1). For the final inversion results of the central and whole Alberta described in the next Chapter, 409 and 405 LMT stations were used respectively. Moreover, some data at certain MT stations was found to be contaminated by noise and could not be fit with the inversion schemes at all. Thus these MT data were excluded from the dataset.

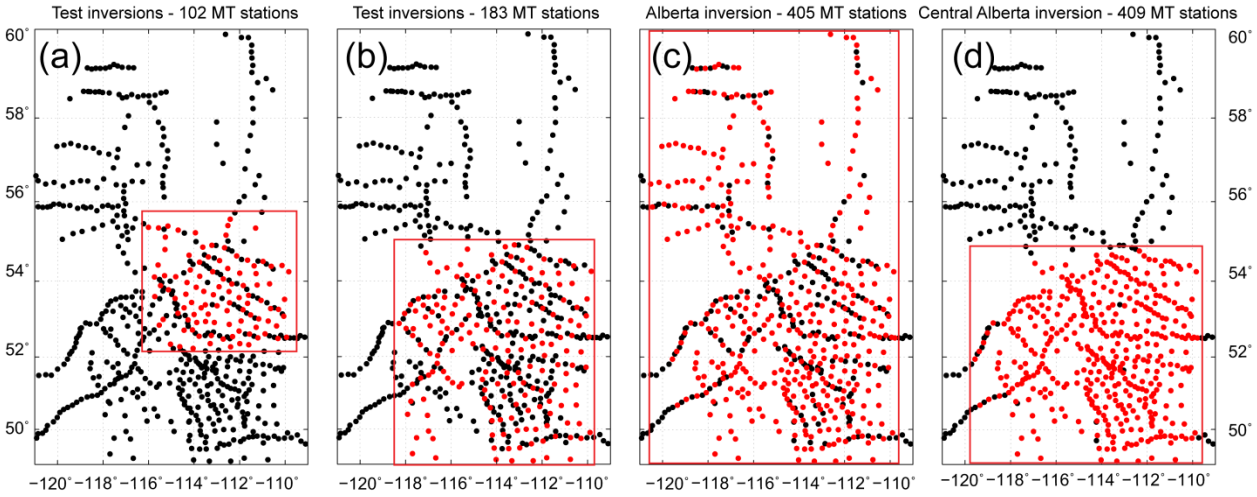

Figure 7.1: Data coverage of the test 3-D MT inversions using 102 stations (a) and 183 stations (b) and the inversions represented in the next chapter of the whole Alberta (c), the central Alberta (d). The red boxes show the core of the inversion models where the densest mesh is located. The black dots represent the locations of all of the LMT data available. The red dots overlay the black ones indicate the locations of the MT data selected for the inversions.

(c) The MT dataset is a compilation of MT data from different sources (see Chapter 5 for details) and with different types of instruments used to measure data (LIMS and NIMS). The frequency bands collected with LIMS and NIMS instruments are 20-10000 s and 0.25-10000 s respectively. Thus, the MT dataset contains a range of frequency sets. In order to eliminate redundant periods, all the MT data were interpolated onto a standard set of 31 logarithmically spaced periods from 2.16 to 13107 s. This interpolation minimizes the number of periods in the dataset and thus reduces the time and memory requirement of the inversions. The number of periods can be further reduced and the memory requirement can be thus reduced. It is done by selecting 1 in every two or three consecutive periods. In the 31 periods, 10 (a third of all) or 16 (half

of all) subsets of them can be acquired in this manner. Tests about MT dataset of reduced amount of periods are shown in section 7.4.1.

Not all the MT stations have data at every one of the 31 periods. Usually, the MT data at high and low frequencies tend to be noisier. The noise in high frequency data can be caused by the fluxgate magnetometer, and the noise in low frequency data are caused by limited number of cycles that can be utilized for data processing because the recording time is limited. Noisy data points were excluded from the dataset before inversion. It is valuable to confirm the data coverage for different periods. Figure 7.2 shows the data coverage of the available MT stations in map form for the periods (~10/100/1000/10000 s). It is reasonable to state that the LMT data coverage is good for the period range of 10-10000 s, especially in central Alberta.

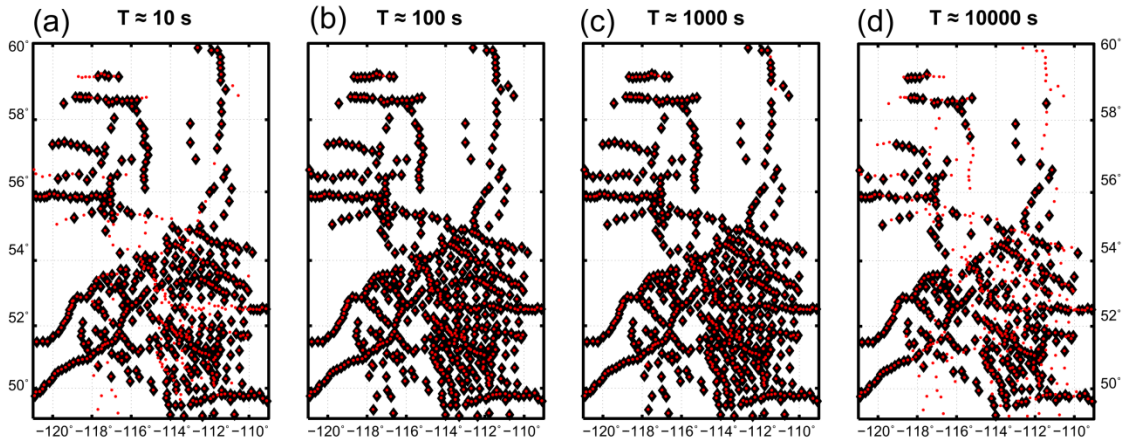

Figure 7.2: Maps showing the LMT data coverage for different periods in the range of 10-10000 s. The red dots represent the MT stations available in Alberta. The diamonds represents valid data at the specific period and the MT station. When there is only a red dot, it means that the MT station has no data at the specific period.

(d) Some of the MT data may have very small uncertainties (error bars) which makes it difficult for the inversion algorithm to fit. To avoid this, error floors are applied. For

data points with error values less than the error floor, the error is increased to the error floor value. The error floor of the dataset needs to be set to an appropriate value so that the inversion fits the dataset efficiently and the total r.m.s. misfit is reasonable.

(e) Finally, the MT dataset that is inverted can contain a combination of impedance and / or tipper data. If only impedances are inverted, then there are 8 responses at each frequency i.e. the real and imaginary components of the four impedance tensor components). If only tipper is inverted then there are 4 data components at each frequency. When both impedance and tipper are inverted, there will be 12 responses. While adding tipper can give more constraints on an inversion model, noisy tipper data can result in high r.m.s. misfit. Test inversions that illustrate this point are described in section 7.4.2.

7.3. Test Inversions on 102 LMT stations

When running a 3-D MT inversion, there are many parameters that control the inversion and which must be specified. These include:

- the MT data selected,
- the resistivity model from which the iterative inversion begins (referred to as the initial resistivity model),
- the reference model that is used for calculation of model covariance in ModEM and that is used for freezing known model features in WSINV3DMT, and
- smoothing parameters for model regularization which determine the degree to which the model is smoothed. A spectrum of models can be obtained, with rough

models generally having a lower r.m.s. misfit and smooth models having a higher r.m.s. misfit.

Many tests were performed to determine the optimal parameters. A small dataset of 102 MT stations in the central Alberta was used initially for the tests because this was technically achievable at the beginning of the research. Both ModEM and WSINV3DMT 3-D inversion algorithms mentioned above were used.

7.3.1. 3-D inversion tests with ModEM on 102 stations

7.3.1.1. The definition and setup of initial and reference resistivity models for ModEM

The initial resistivity model is used to start the iterative inversion. At each iteration, the model is modified to improve the fit between the forward response of the resistivity model and the measured MT data to within some statistical tolerance. A sensitivity matrix is calculated to direct the inversion. A Lagrange multiplier is used to impose spatial smoothing or other model regularization. This regularization is needed because MT inversion is non-unique, meaning that a range of resistivity models can be found that fit the MT data. The optimum smoothness is also an important criterion when searching for the solutions and will be discussed in the next section. The initial resistivity model is set to a homogenous model with 100 Ωm resistivity in this thesis unless indicated otherwise. The model space is made large enough to ignore the boundary conditions in MT inversions.

The initial resistivity model is three dimensional with the x, y, and z dimensions defined as the north-south, east-west, and vertical directions, respectively. The number of cells in each direction will be referred as *nx*, *ny*, and *nz* in this thesis. The core of the

horizontal grid is defined as a region where the cells have a uniform horizontal spacing in the *x* and *y* directions. The model cell size in the horizontal *x* (north-south) and *y* (east-west) directions for the inversions was always set to the same value. It was set to values between 6 and 20 km in this research. The inversion models looked smoother with more details when the model cell size was made smaller i.e. 6 km. However, smaller cell size means more model cells and larger model to cover the same area and requires more computer memory to run the inversion. Outside of the core region, the cell size increases outwards with a geometric factor in the range 1.1 – 1.3. This is reasonable considering the skin depth equation and electrical structure that is far from the MT sites cannot be imaged in detail. It also reduces the memory requirement of the inversion because less model cells are required.

The vertical height of the cells was defined to increase with a geometric factor between 1.1 and 1.3 with the shallowest row of cells having a height of 60-150 m. These values are defined from the fact that the smallest vertical grid size should be 1/3 of the smallest skin depth corresponding to the MT data with the shortest period. The shortest period in the MT dataset was 2.46 s. Using the skin depth equation with the average sedimentary rock resistivity (10 Ωm) observed in the Alberta Basin (Boerner et al., 2000), the smallest skin depth is about 2400 m. Therefore, the smallest vertical grid size should be less than 600 m. The extra fine shallow cells used in this thesis have another important purpose. Because in MT data, static shift can be caused by small-scale, near-surface conductive bodies, these extra fine cells allow the inversion algorithm to define the small-scale structure that causes the static shifts in the MT data. The distance that the grid extends from the core region should be sufficient for the lowest frequency signals to have

attenuated. This distance should exceed three times the largest skin depth. With the largest period 10000 s and an average resistivity of 100 Ωm, the largest skin depth is estimated to be 500 km. Therefore, the model should be more than 1500 km deep vertically and more than 3000 km wide horizontally. The model sizes used in this thesis all exceed these requirements for both the ModEM and WSINV3DMT inversions.

In regard to the reference model, it needs to be the same size as the initial resistivity model. The prior model is set as 100 Ωm half space unless indicated with other values in this thesis. In ModEM, it acts as a reference model when calculating the model covariance during the inversion process.

7.3.1.2. Model covariance characterization for ModEM

The inversion of MT data is non-unique i.e. many resistivity models can fit a single MT dataset to specified statistical tolerance. In order to reduce the non-uniqueness, a regularization factor was added to the inversion schemes. The regularization parameter controls the smoothness of the inversion model. There is a trade-off relationship between the r.m.s. misfit and the model smoothness. A rough model may fit the MT data better than a smooth model, however, the structure of the inversion model may be artefacts caused by the inversion scheme. A smooth model probably has a higher r.m.s. misfit than a rough model and may not extract all information in MT data. Thus, the r.m.s. misfit and the model smoothness need to be balanced by varying the regularization parameter. In ModEM, the model covariance (C_m) needs to be specified in order to control the smoothness of the inversion model.

In the ModEM algorithm, the model covariance is defined by calculating deviations from the reference model mentioned above. The smoothness of the model is controlled by three parameters α_x, α_y, and α_z. The α_x and α_y are specific to each layer and thus there are nz number of α_x and nz number of α_y. The parameter α_z controls smoothness in the vertical direction and only one single number is defined per model. The smoothing can be applied multiple times in the ModEM algorithm. Smoothing once and twice has been tested. The double smoothing made the model smoother but required ~50% more computing time. In order to save computation time, single smoothing was used for all the following inversions and other parameters were varied to achieve a smoother resistivity model.

There is a scaling factor (called 'initial search step in model units' in the inversion parameter file) that can be defined in the ModEM algorithm. It can account for cell size variations in grid. Values of 1, 5, and 10 were tested, and the final inversion models were similar, but the larger values of the search step gave more stable reduction in the r.m.s. misfit as the inversion proceeded.

Note that the smoothing of the resistivity model in the ModEM algorithm is applied according to the model units instead of the actual physical distance in meters. Therefore, if the model cell sizes are changed, the alpha values or the scaling factor should be adjusted also to keep the same smoothing in terms of actual physical distances in meters.

7.3.1.3. Preferred ModEM inversion model

The preferred result of the ModEM inversions with the 102-station dataset is shown in Figure 7.3. It is chosen based on that (1) the r.m.s. misfit is low (<3); (2) the model is smooth; (3) the model features are consistent with previous studies. In regards of the

initial model, the horizontal grid size was 8 km at the center of the model where the MT stations were located. The model size was *nx*=80, *ny*=80, *nz*=45. The reference model was the same as the initial model.

The dataset with 102 LMT stations was used with 31 periods ranging from 2-10000 s. Both impedance and tipper were used. The error floor used was 10% of $\sqrt{|Z_{xy} * Z_{yx}|}$for the diagonal impedance components – Z_{xx} and Z_{yy}, 5% of $\sqrt{|Z_{xy} * Z_{yx}|}$ for the off-diagonal impedance components – Z_{xy} and Z_{yx}, and 0.03 for the tippers. The covariance parameters α_x, α_y, and α_z were set to the same values – 0.3. The initial search step in model units was set to 1. The initial lambda was set to 100 and it was reduced as the inversion progressed and the final lambda was 1.

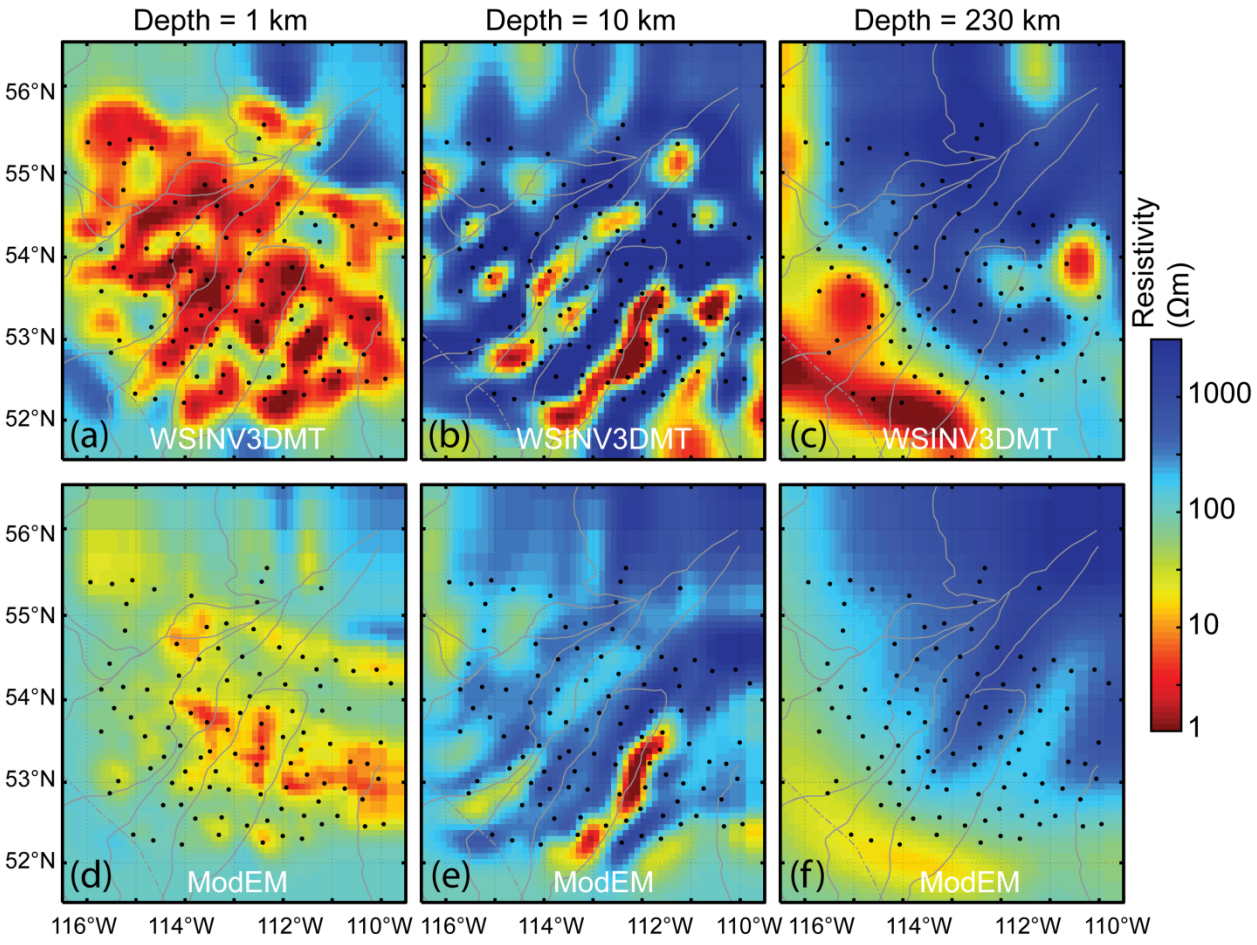

Figure 7.3: The inversion models of central Alberta using ModEM (figure (d), (e), (f)) and WSINV3DMT (figure (a), (b), (c)) algorithms shown as horizontal slices. The MT dataset (with 102 LMT stations) and initial model (100 Ωm half space) were the same for both inversions. The gray lines mark the boundaries of the basement terranes (Pilkington et al., 2000).

The final r.m.s. misfit achieved was 1.53 (Figure 7.4). It can be seen that the impedance is better fitted than the tipper and the data with smaller periods are fitted better than the data with large periods. The comparison of all the data components of the MT station aba950 with the one of the inversion model response shows that the data fit is overall good (Figure 7.5).

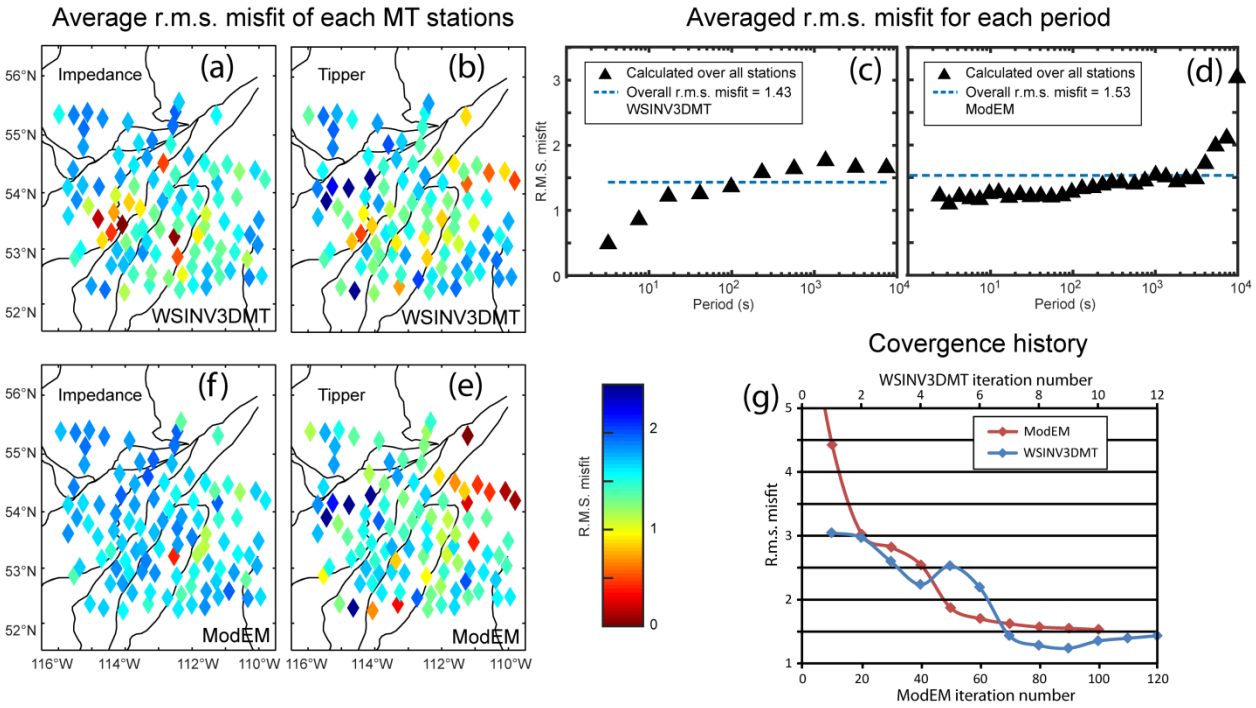

Figure 7.4: The r.m.s. misfit of the central Alberta inversion models computed using the WSINV3DMT (figure a, b, c) and ModEM (figure d, e, f) algorithms. The same dataset with 102 LMT stations was used for both methods. The black lines on the maps represent the geological boundaries (Pilkington et al., 2000). The diamonds show the locations of MT stations with color-filling to show the r.m.s. misfit. Figure (g) shows the convergence history of these two inversions.

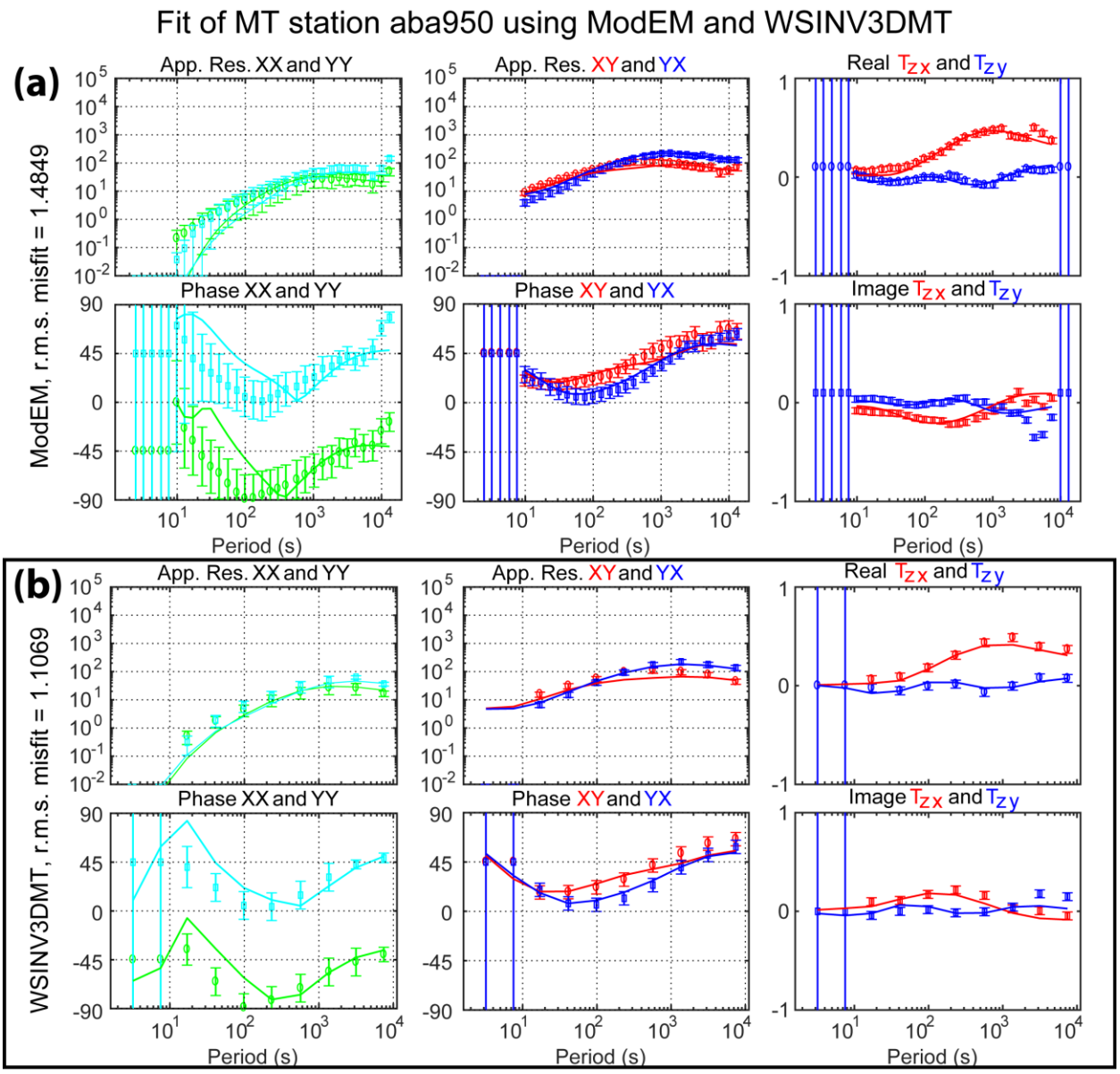

Figure 7.5: Typical fit of the response of the central Alberta inversion model (solid lines) to the measured MT data (circles with error bars). The MT station aba950 was chosen to show this. The top panel (a) shows the fit of the ModEM central Alberta inversion model and the bottom panel (b) shows the fit of the WSINV3DMT central Alberta inversion model. Note that the reversed signs of the imaginary components of tippers were due to the sign convention difference in the two inversion schemes.

7.3.2. 3-D inversions with WSINV3DMT on 102 stations

7.3.2.1. Definition and setup of initial and reference resistivity models for WSINV3DMT

The specification of the initial resistivity model for WSINV3DMT is the same as for ModEM. However, the purpose of the reference model is different in WSINV3DMT from ModEM. The reference model in WSINV3DMT is used in combination with a control model index file to freeze some known features of the model. For example, when the user knows the location of a nearby ocean, the resistivity of the ocean can be locked in the inversion model, and the WSINV3DMT algorithm will try to fit the dataset without changing the locked ocean. If no known features need to be set, then the prior model should be set the same as the initial model. In the ModEM algorithm, the similar freezing function and other model control functions are combined with the model covariance specifications and stored in the model covariance file.

7.3.2.2. Model covariance characterization for WSINV3DMT

In the WSINV3DMT algorithm, the model covariance is calculated from solving a diffusion equation. Smoothing parameters were set to control the characteristic of the model covariance. A time step (τ) and three scale values (δ_x, δ_y, and δ_z with respect to the three model dimensions x, y, and z) can be set. The decorrelation length scale for the diffusion equation is proportional to $\sqrt{4\delta\tau}$ of the local grid. A larger decorrelation length scale will result in a smoother model and require more computing time.

The time step needs to be an integer. The scale values need to be real numbers between 0 and 1. The time step value (τ) was set to 2, 3, 4, 5, 6, 8, and 10 as tests. The scale

values(δ_x, δ_y, and δ_z) were always kept the same for the three dimensions and were set to 0.09, 0.1, 0.11, 0.12, and 0.2 as tests. The best combination was found to be τ=10, δ_x=0.1, δ_y=0.1, δ_z=0.1 for the central Alberta inversions with 102 LMT stations.

7.3.2.3. Preferred WSINV3DMT inversion model

The preferred WSINV3DMT model is shown in Figure 7.3. The initial model parameters are exactly the same as the ModEM model described in section 7.3.1.3. The prior model is the same as the initial model. The smoothing parameters are set as τ=10, δ_x=0.1, δ_y=0.1, δ_z=0.1. The dataset used are with the same 102 LMT stations as described in section 7.3.1.3, however, only 10 periods were used instead of 31. The error floor used was 20% of $\sqrt{|Z_{xy} * Z_{yx}|}$for the diagonal impedance components – Z_{xx} and Z_{yy}, 10% of $\sqrt{|Z_{xy} * Z_{yx}|}$ for the off-diagonal impedance components – Z_{xy} and Z_{yx}, and 0.04 for the tippers. The final r.m.s. misfit was 1.43 (Figure 7.4). The fit of the inversion model is good overall and the data with lowest periods are fitted the best. In Figure 7.5, the resistivity, phase and tipper of the station aba950 is compared with the ones of the model response, it can be seen that the general trend of the curves are fitted well.

7.3.3. Comparison of ModEM and WSINV3DMT

Both the methods of Siripunvaraporn et al. (2005, WSINV3DMT software) and Kelbert et al. (2014, ModEM software) mentioned in Chapter 2 were used to find the best solutions in test inversions using the 102 LMT stations. To determine if both methods give consistent inversion results, the results were compared.

See Figure 7.3 to compare the two inversion models. When using proper parameters for the inversions, these two methods give similar dominant features in the inversion models. The spatial variation of resistivity is similar in the ModEM and WSINV3DMT inversions, but the absolute value of resistivity is quite different. For example, in the ModEM model the resistivity of the surface is around 3 Ωm, while in the WSINV model it is around 30 Ωm.

Another difference is that the ModEM model is smoother than the WSINV3DMT model. These differences may be caused by different model covariance parameters, which control the smoothness of the inversion model. The model covariance characterizations of the two algorithms have been explained in sections 7.3.1.2 and 7.3.2.2 and they are quite different.

In regard to the data fit (Figure 7.4), the ModEM central Alberta inversion model has a similar final averaged r.m.s. misfit as the WSINV3DMT. The ModEM inversion model has a final r.m.s. misfit of 1.53 and the WSINV3DMT model has a final r.m.s. misfit of 1.43. However, the ModEM model fits the impedance significantly better than the tipper while this is not the case for the WSINV3DMT. Moreover, the ModEM doesn't fit the data of longest periods as well as the WSINV3DMT. In Figure 7.5, the fitting of the apparent resistivity, phase and tipper is shown. Both inversion models can recover the general shape of the curves with minor discrepancies.

In summary, the WSINV3DMT and ModEM inversions can give similar results of the central Alberta inversion model with the 102-stations LMT dataset when the parameters are carefully setup. However, the ModEM inversion is less memory intensive than the

WSINV3DMT inversion. Therefore only small datasets such as the central Alberta dataset with 102 stations and small models with model size smaller than 80*80*45 (80 cells in the x and y direction, 45 cells in the z direction) were run with the WSINV3DMT software, and larger models with more stations were run with the ModEM software only. Another dataset of 183 LMT stations in the central Alberta was used to do more test about the ModEM inversion scheme as described below.

7.4. Test inversions on 183 LMT stations with ModEM

7.4.1. The preferred ModEM inversion model

The tests with the 183-station dataset were done to test about the number of periods and components to use in the dataset, and the covariance parameter in ModEM. In all these inversions, the preferred result of the ModEM inversions with the 183-station dataset is shown in Figure 7.6.

In regards of the initial model, the horizontal grid size was 12.5 km at the center of the model where the MT stations were located. The model size was *nx*=94, *ny*=88, *nz*=45. The reference model was the same as the initial model.

The dataset with 183 LMT stations was used with 31 periods ranging from 2-10000 s. Both impedance and tipper were used. The error floor used was 10% of $\sqrt{|Z_{xy} * Z_{yx}|}$for the diagonal impedance components – Z_{xx} and Z_{yy}, 5% of $\sqrt{|Z_{xy} * Z_{yx}|}$ for the off-diagonal impedance components – Z_{xy} and Z_{yx}, and 0.03 for the tippers. The covariance parameters α_x,

α_y, and α_z were set to the same values – 0.3. The initial search step in model units was set to 1. The initial lambda was set to 1.

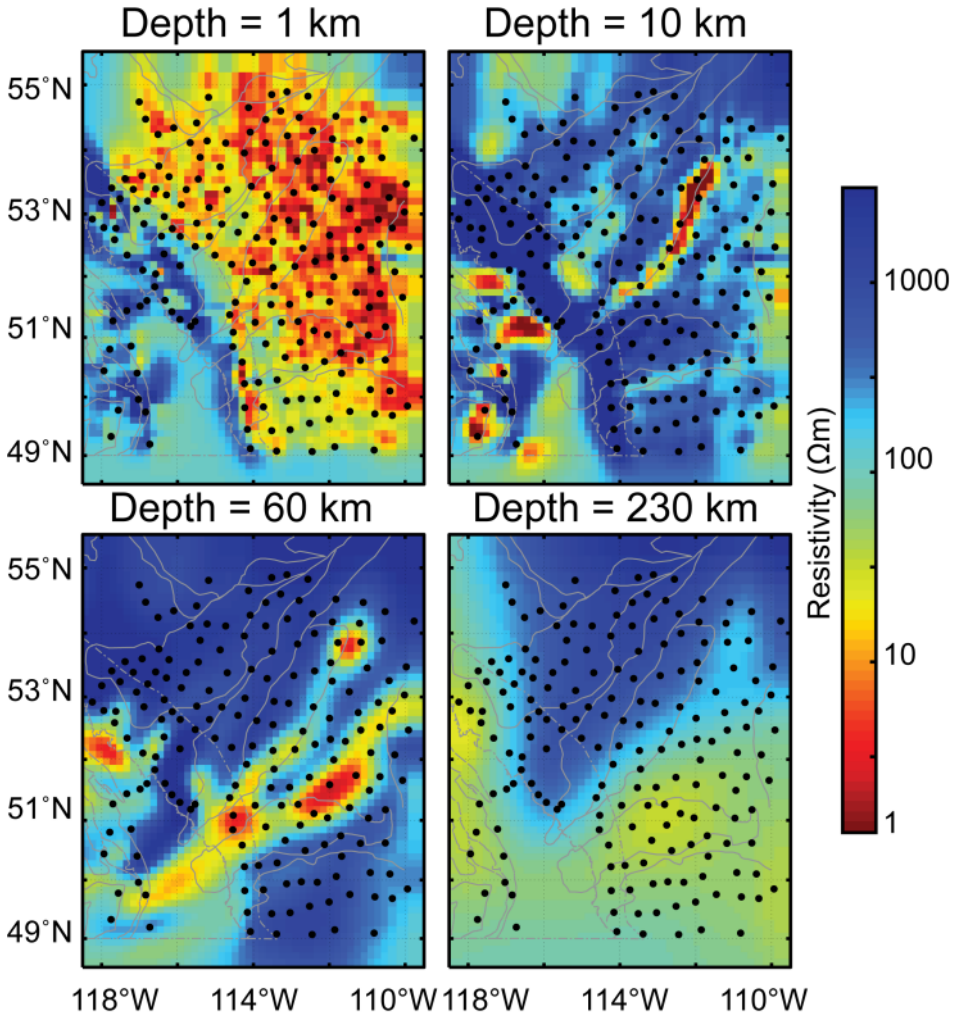

Figure 7.6: The preferred ModEM inversion model using the 183-station dataset shown as horizontal slices at varies depths. The gray lines mark the boundaries of the basement terranes (Pilkington et al., 2000).

The fit of the inversion model shown in Figure 7.6 is shown in Figure 7.7. The overall r.m.s. misfit is 2.3 (blue line in Figure 7.6b). The fit of each MT station show large spatial variations (Figure 7.6a) similar as the ModEM inversion of 102 stations (section 7.3.1.3). The MT stations at the southwest corner are fitted the worst. Moreover, the

impedance is fitted a lot better than the tipper. Comparison of the MT dataset with the inversion model responses are shown with the averaged apparent resistivity and phase of the xy and yx modes. Map views of the two are consistent mostly which means the data fit of the inversion model is good.

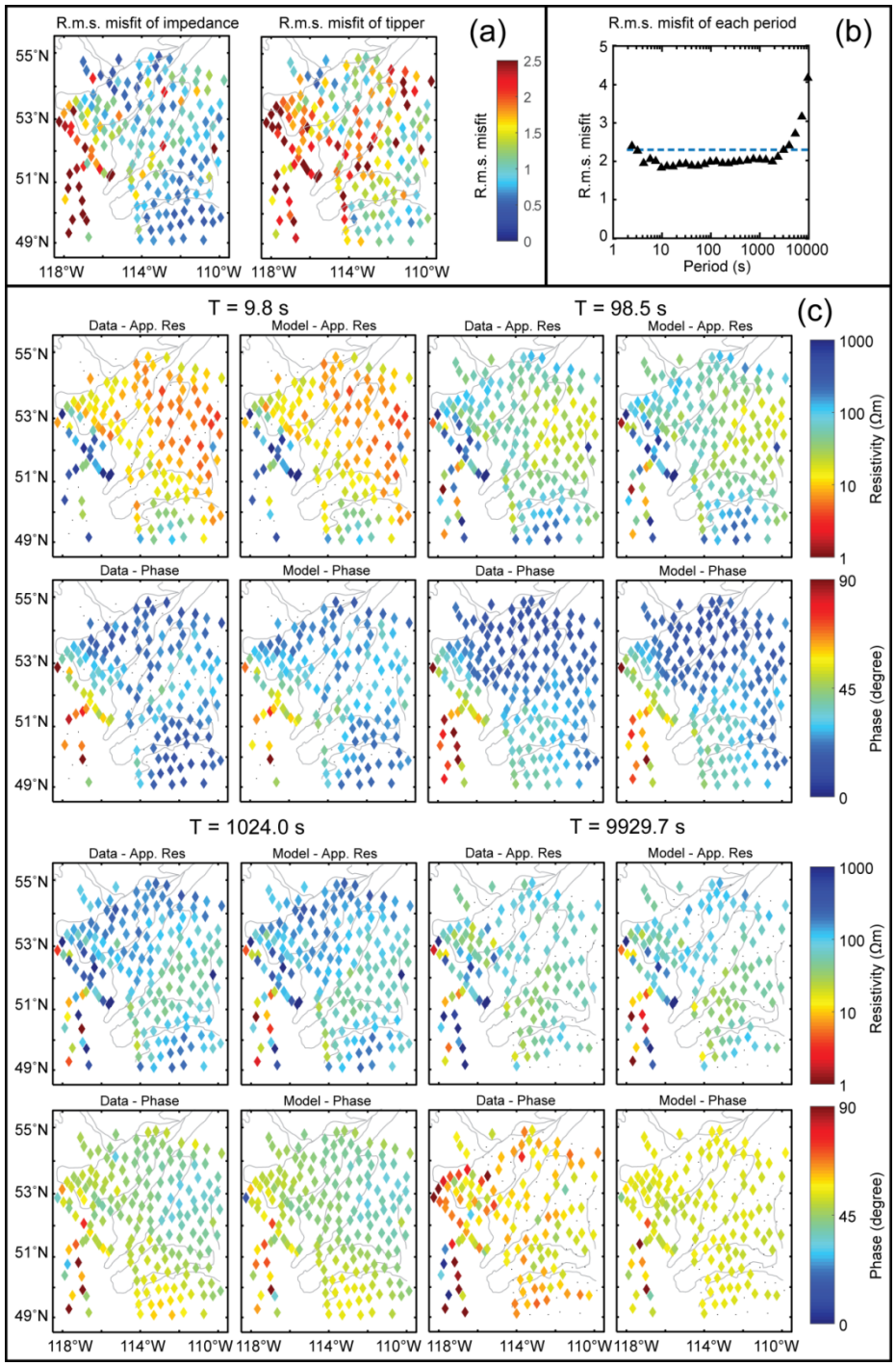

Figure 7.7: The fit of the ModEM inversion model of the 183-station dataset. (a) The r.m.s. misfit of impedance and tipper at each station shown as filling colors of the diamonds. (b)The r.m.s. misfit of each period (triangles) and the overall averaged r.m.s. misfit (blue line). (c) The comparison of the MT dataset with the model responses shown with the averaged apparent resistivity and phase of the *xy* and *yx* modes. The gray lines mark the boundaries of the basement terranes (Pilkington et al., 2000).

7.4.2. Tests with different number of periods

The LMT data used were interpolated to 31 periods as discussed in section 7.2. It is best to include all the periods in the dataset for inversions. However, smaller dataset with reduced amount of periods could potentially reduce the memory requirement of the inversions. Therefore, the 183-station dataset with 10, 16, and 31 periods were used in ModEM inversions while all the other parameters kept the same as the preferred inversion model in section 7.4.1.

The comparison in the data fit and inversion model is shown in Figure 7.8. As the number of periods in the dataset was reduced, the convergence of the inversion became slower. Note that the r.m.s. misfit map of the 10-period inversion is quite different than the other two inversion in Figure 7.8 and the 10-periods inversion converged a lot slower than the other two. In contrast, the r.m.s. misfit map of the 16-periods inversion is very similar to the 31-periods one. These observations demonstrated that keeping half of the periods (4-5 samples each decade) in the dataset is sufficient for the inversions to be considered stable. Nevertheless, the inversion with the dataset of 31 periods was the most stable and converged the fastest in the three.

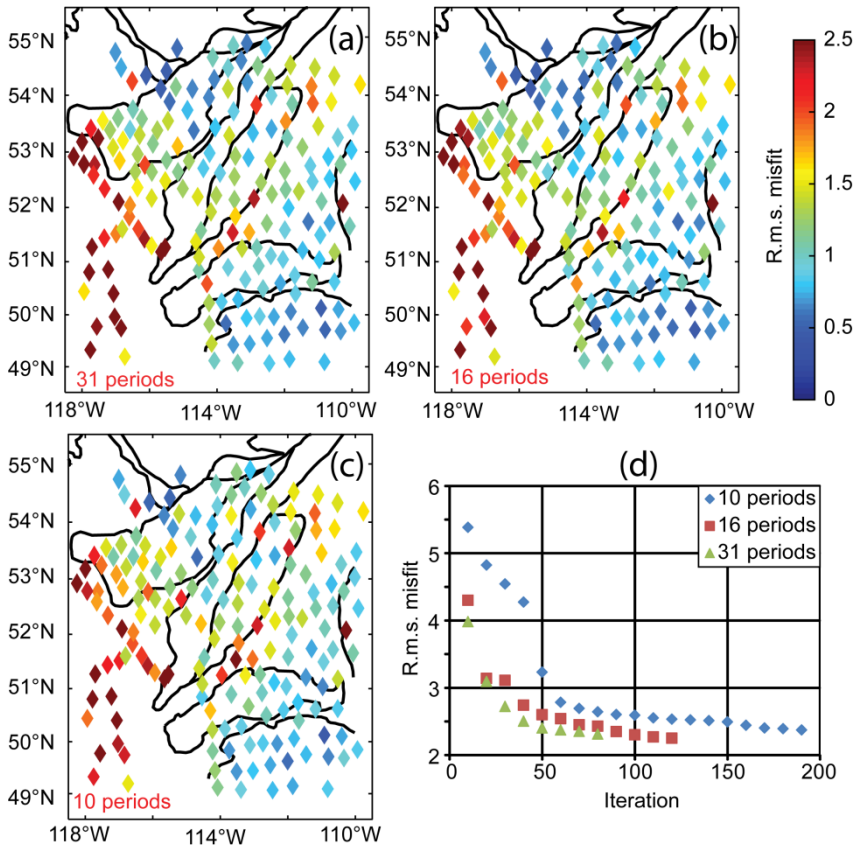

Figure 7.8: The comparison of data fit and convergence for ModEM inversions with the 183-station datasets using 31/16/10 periods in figure (a), (b), and (c), respectively. The r.m.s. misfit is the averaged value (averaged over all the periods and data components) for each station in the map. All of the inversions converged to a final r.m.s. misfit of ~2.3. The bottom right figure shows the r.m.s. reduction for the inversions as the inversion progressed in iterations. The grey lines mark the boundaries of the basement terranes (Pilkington et al., 2000).

7.4.3. Tests with datasets of 8/12 components

Campanya et al. (2016) demonstrated that the tipper information is important in 3-D inversions by conducting a synthetic case study about MT 3-D inversions. In order to find out whether to use the tipper or not, the 183-station dataset with and without tipper values were used in 3-D inversions and the results were compared. The other inversion parameters were the same as the preferred inversion model in section 7.4.1.

Figure 7.9 shows the difference of the MT inversion data fit. It is obvious that the tipper free dataset is fitted much better than the dataset with tipper. This is because the tipper is much noisier and thus difficult to fit. However, when considering the inversion model (Figure 7.9d), the inversion result with impedance and tipper dataset is more reasonable. Because it is expected to see conductors such as the RDC and the SABC in the resistivity model based previous studies (see Chapter 4 for details). The inversion model with impedance and tipper dataset imaged those conductors much closer to the previous studies. Therefore, datasets with impedance and tipper will be preferred to ones with impedance only

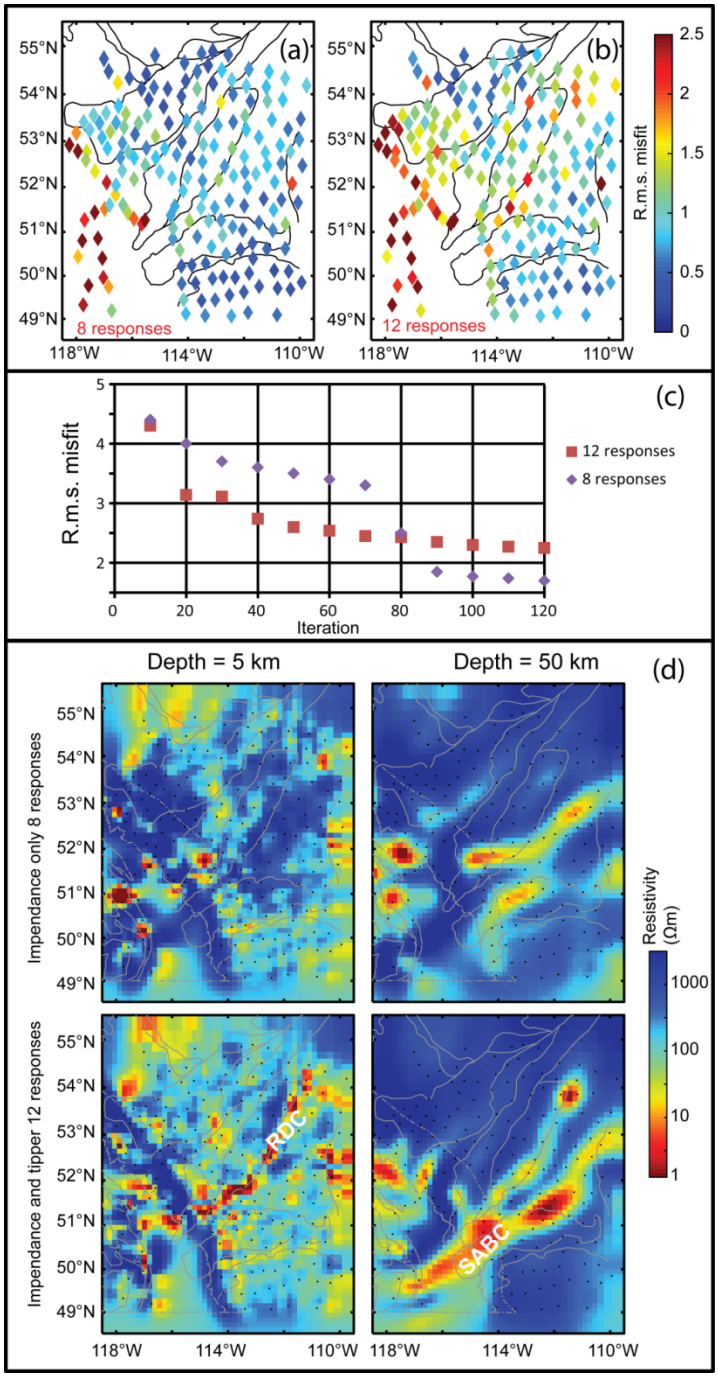

Figure 7.9: The r.m.s. misfit maps of ModEM inversions that used datasets with impedance only (8 responses, figure (a)) or with impedance and tipper (12 responses, figure (b)). Figure (c) shows the r.m.s. reduction for the two inversions as the inversion progressed in iterations. (d): Horizontal slices of the ModEM inversion models with datasets of impedance only (top) and datasets of impedance and tipper (bottom). The black dots represent the locations of MT stations. The grey lines in (a), (b), and (d) mark the boundaries of the basement terranes (Pilkington et al., 2000).RDC, Red Deer conductor. SABC, Southern Alberta British Columbia conductor.

7.4.4. Effect of varying smoothing of ModEM

The smoothing parameters defined in the covariance file are important for the smoothness of the inversion model. To figure out its effect on the inversion model, tests were done by varying the alpha (α) values using the 183-station dataset. Figure 7.10 shows the difference in the ModEM inversion models when all of the alpha (α) values in the x, y and z directions were set to 0.2, 0.3, and 0.4, respectively. All the other parameters were kept the same. The final r.m.s. misfits of the three inversions was very similar while the resistivity models look different in details. The higher the value of α, the smoother the model. For the depth slices of 1 km, higher alpha value results in a smoother sedimentary layer. For the depth slices of 60 km, lower alpha values of 0.2 and 0.3 result two parallel conductors which are imaged as one conductor with α=0.4. Moreover, there is a deep conductor imaged at depth = 350 km when α=0.4, which is not the case for the other two. This implies that deeper structures can be imaged better if α=0.4 than smaller values (α=0.2 or 0.3).

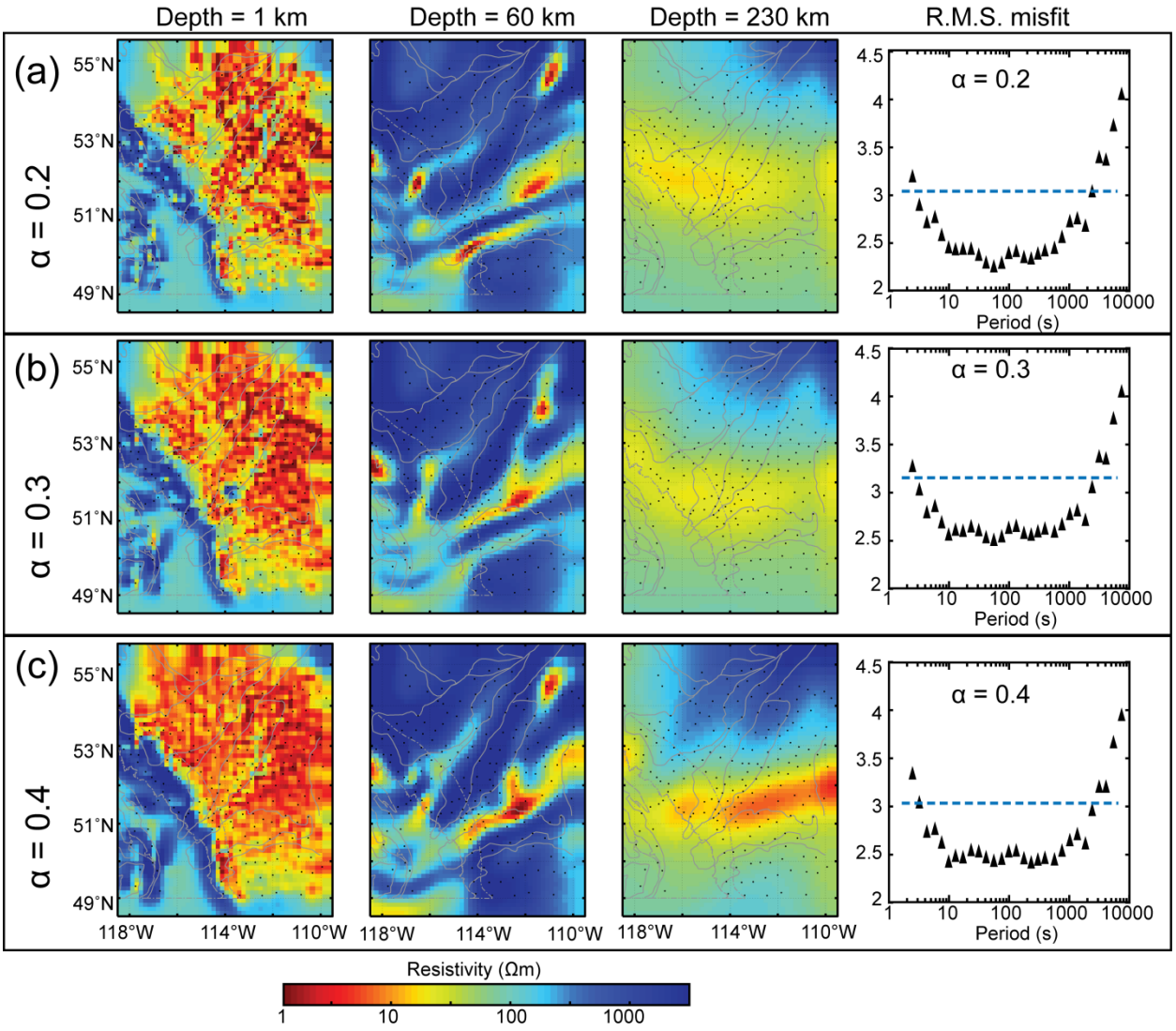

Figure 7.10: Horizontal slices to show the differences in the ModEM inversion models when all of the α values in three directions were set to 0.2 (a), 0.3 (b), and 0.4 (c). The right column represents the r.m.s. misfit for each period of the dataset averaged over all the stations. The blue dashed lines are average r.m.s. misfits for the inversions. The gray lines in the slices mark the boundaries of the basement terranes (Pilkington et al., 2000).

7.5. Conclusions based on tests with 102/183 stations

In conclusion, 3-D inversion schemes of Siripunvaraporn et al. (2005; WSINV3DMT) and Kelbert et al. (2014; ModEM) can give similar results in terms of major model features

and data fitting. However, due to the higher memory demand of WSINV3DMT than ModEM, inversions with larger datasets covering the whole Alberta will be done with ModEM only.

Tests runs also demonstrated that datasets with more periods and 12 components (including impedance and tipper) can result in better inversion results than the ones of fewer periods and with impedance only. It has also been shown that the higher the alpha value, the smoother the model features.

The final 3-D MT inversions of the whole Alberta and central Alberta datasets were done using lessons learned from these test inversions. The results are described in the following chapter and interpreted in Chapter 9.

Chapter 8 : Three-dimensional inversions of the Alberta LMT dataset

8.1. Introduction

Based on the insights derived from the inversion tests presented in Chapter 7, 3-D inversions using the ModEM algorithm were applied to the Alberta LMT dataset were done and the inversion results will be presented in this chapter. For the whole Alberta dataset (WAB), the 3-D ModEM inversion is applied to a grid of 405 LMT stations covering the entire province of Alberta (see the station distribution in Figure 7.1). Moreover, in Central Alberta (CAB), MT stations have relatively uniform spatial coverage and have the potential to yield an more reliable resistivity model compared to the WAB inversion. Therefore, 3-D ModEM inversions were applied to the CAB dataset of 409 LMT stations.

The model resolution is investigated with (1) synthetic inversions that tested how well the ModEM inversion could recover important model features. (2) More resolution tests were done by removing the low resistivity bodies in the whole Alberta inversion model and replacing them with higher resistivity values. If an increase of the r.m.s. misfit is observed, it means that the low resistivity body may be required by the MT data. (3) The WAB model will be compared with the CAB model also to see if both inversions give consistent results.

8.2. Inversion of MT data for the whole of Alberta

In the previous chapter we tested the inversion algorithms on a subset of the LMT data collected in Alberta. This allowed us to compare two established inversion algorithms and find the optimum control parameters. To extract the full value from the MT data, it is necessary to invert as many stations as possible. This is because more stations give better lateral coverage and would provide more details in the inversion model. This was only possible with the ModEM algorithm, owing to its lower computational resources requirement compared to WSINV3DMT.

The preferred model produced by the inversion of the 3-D whole Alberta data set (WAB model) is shown in Figure 8.1. This inversion began with a 100 Ωm half space model. The number of model cells was *nx* =200, *ny* =136, and *nz* =70. The width of central horizontal grids is 8 km. The thickness of the first vertical grid near the surface is 60 meters.

The dataset comprises 405 MT stations. The full impedance tensor and tipper were used, and all 31 periods were included in the dataset. The error floor was assigned to be 10% of $\sqrt{|Z_{xy} * Z_{yx}|}$ for the diagonal impedance components (Z_{xx} and Z_{yy}), 5% of $\sqrt{|Z_{xy} * Z_{yx}|}$ for the off-diagonal impedance components (Z_{xy} and Z_{yx}), and 0.03 for the tipper components. The inversion was run with the ModEM algorithm on the Cedar machine of Westgrid which took about three weeks with 126 processors (~ 4GB of memory per processor). The r.m.s. misfit started at 13.57 and was reduced to 2.22 after 326 iterations.

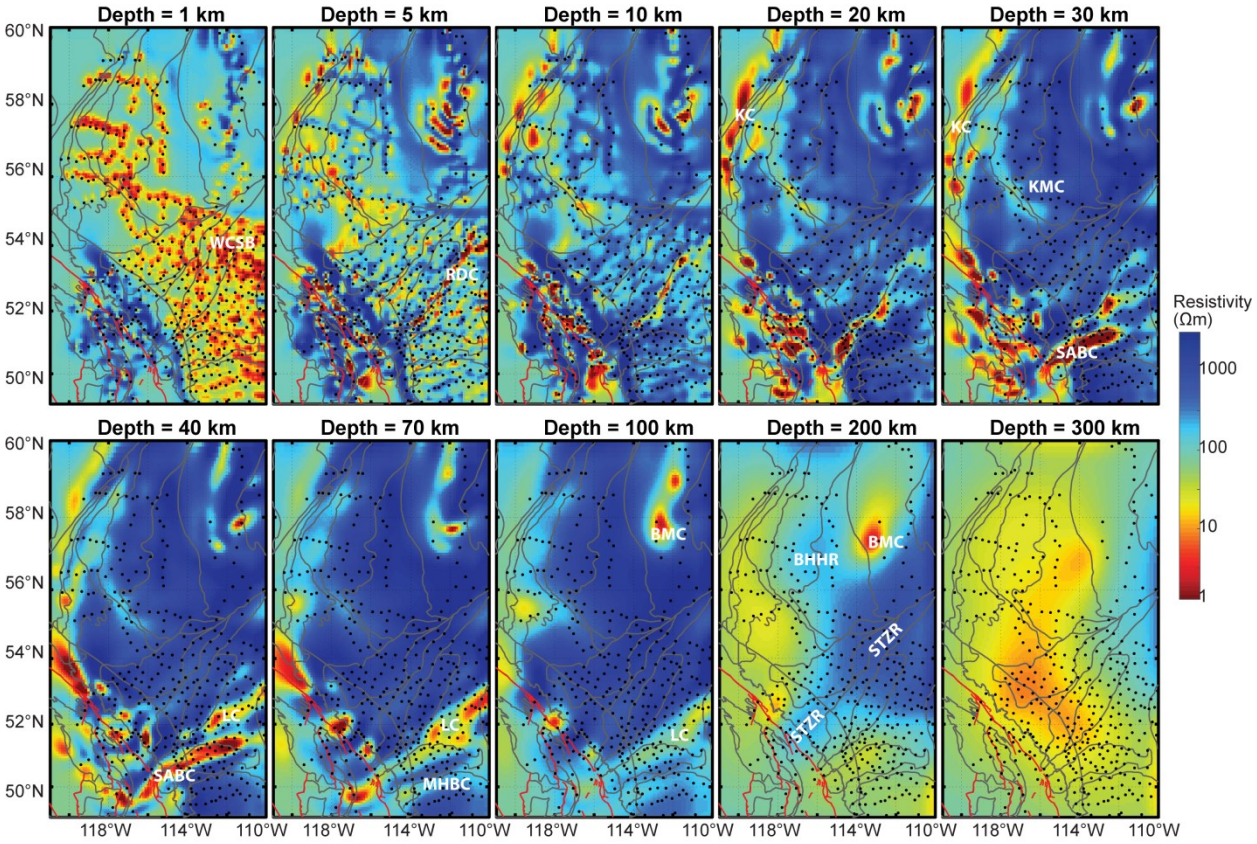

Figure 8.1: The 3-D resistivity model determined with a ModEM inversion of the whole Alberta shown as horizontal slices. The red and gray lines mark faults and boundaries of the basement terranes (Pilkington et al., 2000). The black dots represent the locations of the MT stations used in the inversion. Abbreviations: WCSB, Western Canada sedimentary basin; RDC, Red Deer conductor; KMC, Kimiwan conductor; SABC, Southern Alberta – British Columbia conductor; LC, Loverna block conductor; BMC, Birch Mountain field conductor; STZR, Snowbird Tectonic zone resistor; BHHR, Buffalo Head Hills resistor.

8.2.1. LMT Data fit of the whole Alberta resistivity model

It is important to confirm that the LMT dataset is fitted properly by the MT response of the 3-D resistivity model. Figure 8.2 shows the r.m.s. misfit distribution averaged over periods and MT stations. The r.m.s. misfit is a measure of the fit of the response of the inversion model to the MT dataset. A large r.m.s. misfit (>2 in this study) indicates a poor fit. The majority of the MT data were fit well. However, very large variations in the r.m.s. misfit

is observed. The MT data of longer periods (> 5000 s) and the MT stations at the northeast and southwest corners of the resistivity model were fit relatively poorly. The comparison between the MT data and the resistivity response (Figure 8.3) shows similar features to the r.m.s. misfit map. Generally, the response of the resistivity model and the MT data agrees well except for at the northeast and southwest corners.

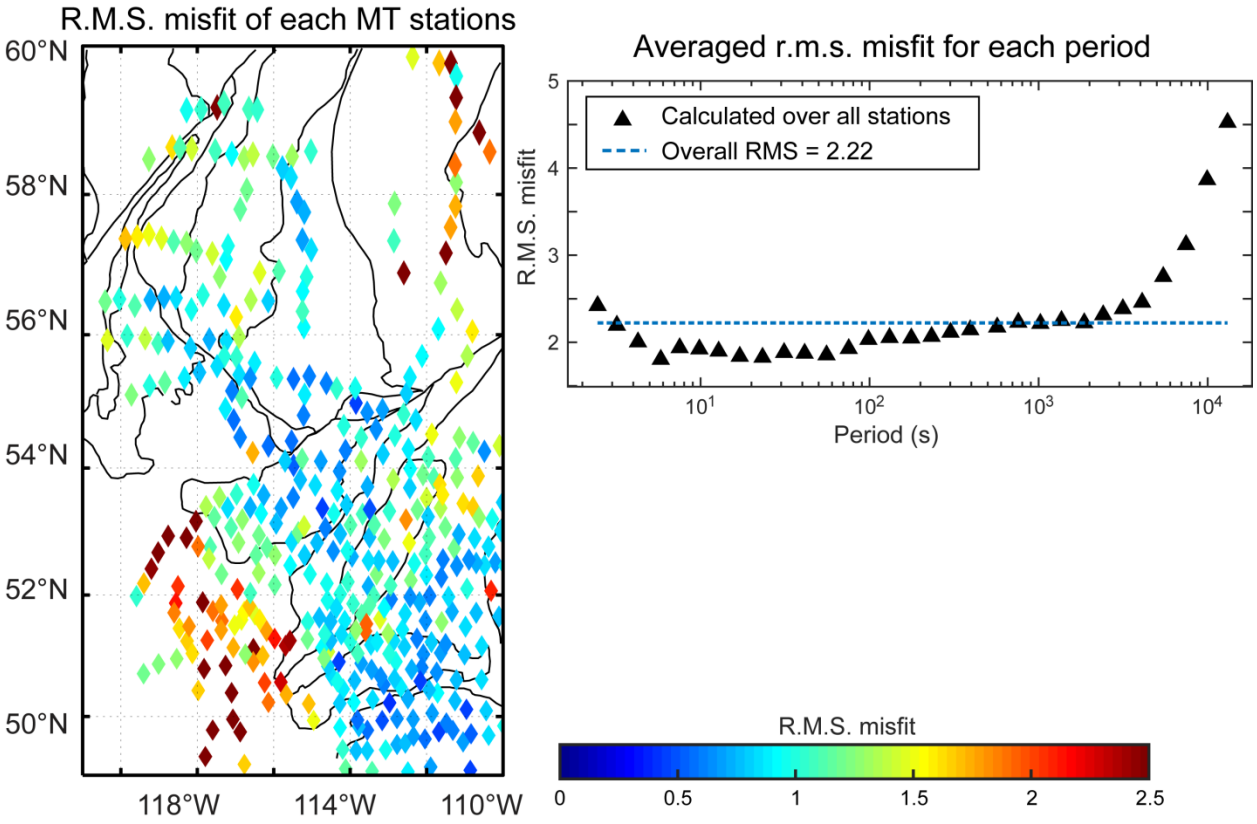

Figure 8.2: Right: the r.m.s. misfit for all periods averaged over all stations. Left: map view of the r.m.s. misfit for each station averaged over all periods. The gray lines show the boundaries of the basement terranes (Pilkington et al., 2000).

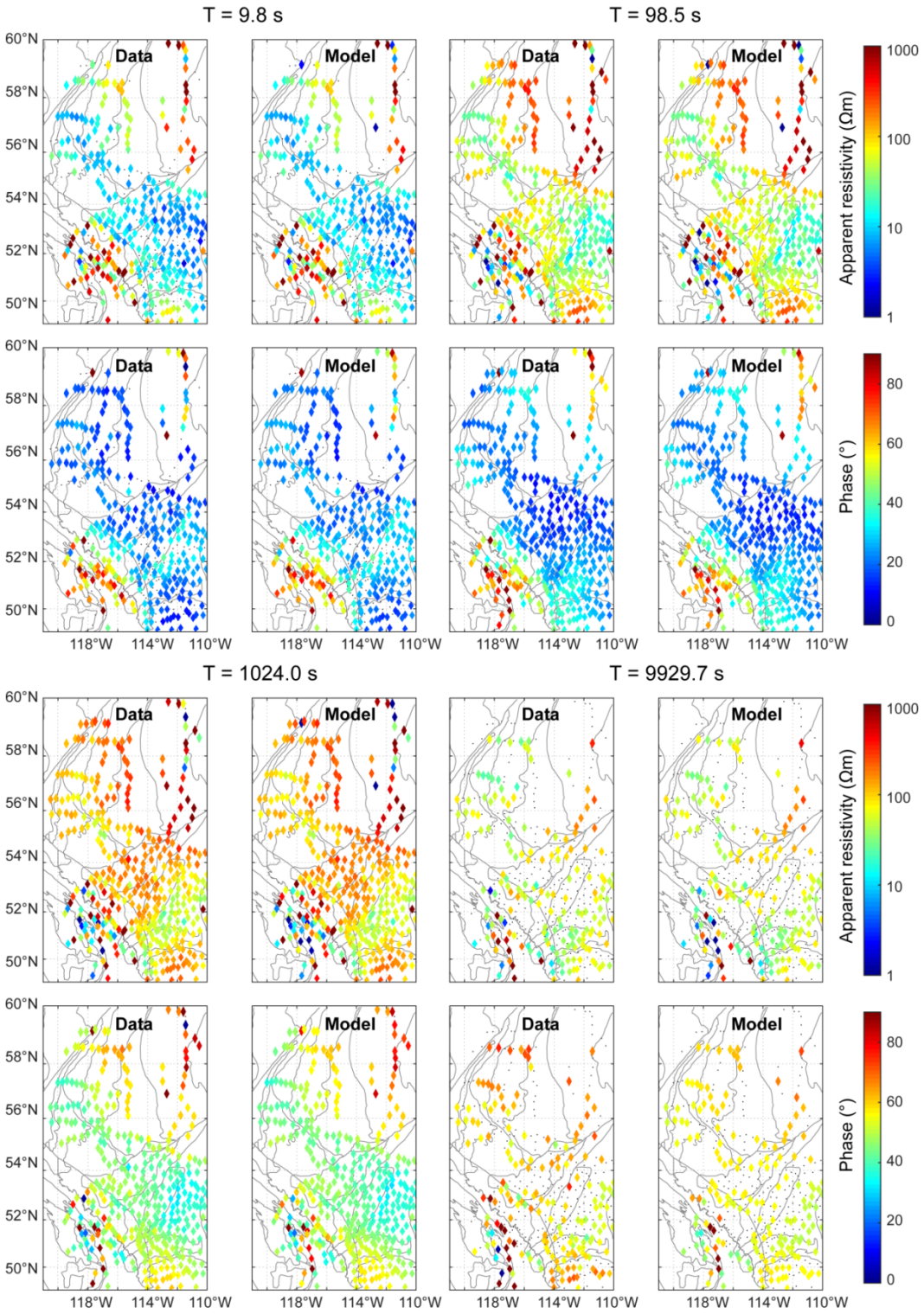

Figure 8.3: Comparison of the masured MT data and the inversion model response of the whole Alberta inversion model at four periods. The apparent resistivity and phase shown is the average of the off-diagonal components XY and YX. The gray lines mark the boundaries of the basement terranes (Pilkington et al., 2000).

8.2.2. Main features of the all Alberta resistivity model

In the WAB resistivity model (Figure 8.1), the station spacing is quite variable due to the logistics associated with MT deployments. In the south where road access was easy, a typical spacing is 20 km. In contrast, in the north, access was by helicopter or boat and the spacing was quite variable and in the range 10-200 km. Moreover, the data fit of these poorly sampled areas was not good. Therefore, only a few conductive features will be addressed in these areas.

The WAB model is generally very resistive (>1000 Ωm) at lithospheric depths (5-100 km), except at the surface (the WCSB), the northwest corner (near the Great Slave Lake shear zone), the southwest corner (Cordillera), and a few low resistivity anomalies. The Cordillera of southeast British Columbia is generally characterized with resistive upper crust and very conductive lower crust. The uppermost mantle of southeast British Columbia is quite resistive which may indicate the southwestward extension of the North American craton across the Cordillera deformation front at these depths. The detailed features of the WAB model will be discussed below by depth slices.

8.2.2.1. 1 km depth slice

The Western Canada Sedimentary Basin (WCSB) is imaged as a conductive layer at the surface with resistivity of 1-10 Ωm in southern and central Alberta. Note that where there is not enough station coverage (northern Alberta), the WCSB is not imaged as a horizontally continuous layer due to the skin depth equation (see the synthetic inversions

also described in section 8.3.1.1). The data fit in the Canadian Cordillera is poor as shown in Figure 8.2 and 8.3. Thus, features in this region will not be discussed.

8.2.2.2. 5 km and 10 km depth slices

Just below the WCSB conductor, there is a linear conductor imaged along the Red Deer aeromagnetic high at the depth of 5-10 km both in the WAB model. It will be referred to as the Red Deer conductor (RDC) as in Boerner et al. (2000). The resistivity of the RDC is very low and approximately 1 Ωm. It is worth noting that the RDC has some variations in resistivity structure along strike in the WAB model – this is discussed in more detail later. The northern segment of the RDC extends to greater depth than the southern segment.

8.2.2.3. 20 km depth slice

There is a linear low resistivity body (Referred to as KC) along the trend of the Kiskatinaw domain. This is consistent with previous studies (Boerner et al., 2000) and the 2-D resistivity model presented in this thesis (Chapter 6). Another upper-crustal conductor of interest is along the Kimiwan aeromagnetic high and isotope anomaly (referred as to KMC in this thesis). This conductor is characterized by a resistivity of 300 Ωm at depths of 20-35 km. Even though its resistivity is not very low, this feature is outstanding because the surrounding crust has a high resistivity of more than 1000 Ωm.

8.2.2.4. 30-70 km depth slices

The Moho beneath Alberta is expected to be in the depth range 35-50 km (Gu et al., 2018). In the WAB model, no corresponding resistivity feature can be found to correlate with the Moho. Instead, consistent resistive structure is observed across the Moho with the exception of a few conductors.

There are two southwest-northeast trending conductors imaged in the Hearne province at the lower crustal and upper mantle depths from 30 to 100 km. One conductor follows the northern boundary of the Matzhiwin aeromagnetic high and will be referred to as the Southern Alberta – British Columbia conductor (SABC) as named by Gough (1982). A second conductor is located in the center of the Loverna block and will be named the Loverna Block conductor (LC) following Nieuwenhuis et al. (2014). The SABC is more conductive (resistivity of 1 Ωm) and shallower than the LC. The LC is less conductive (resistivity of 10 Ωm) and separated from the SABC by a resistive band at the crustal depths in the WAB model. In the mantle, these two conductors merge together as the depth increases.

Moreover, there is a weak conductor (100 Ωm, referred to as MHBC) along the northern boundary of the MHB that separates the MHB and the Hearne province. This feature may be coincident with the internal conductor of the MHB mentioned by Nieuwenhuis et al. (2014).

8.2.2.5. 100-300 km depth slices

At depths greater than 100 km, there is a large conductive feature located in the northeast corner of the resistivity model in the Taltson terrane (57.5˚N, 113.5˚W). It is most significant at 100 km depth and extends to over 250 km. Because this conductor is closely located near to the Birch Mountain kimberlite field, it will be referred to as the Birch Mountain conductor (BMC). The resistivity of the BMC is approximately 10 Ωm.

It is also noteworthy that the most resistive part of the WAB model (as shown in the depth slice of 200 km) surrounds the STZ (considered as the Thorsby terrane in Alberta).

Because the depleted lithosphere is generally highly resistive (Selway, 2014), this indicates the lithosphere of the STZ may be more depleted than the other parts of Alberta. This resistor will be referred to as the STZR.

Another highly resistive region in the 200 km depth slice is in the center of the Buffalo Head terrane which is coincident with the Buffalo Head Hills kimberlite field. This is where the most diamondiferous kimberlites in Alberta were found (Eccles et al., 2004; Burwash et al., 2000) and the resistor will be referred to as the BHHR.

8.3. Resolution tests for the whole Alberta resistivity inversion model

Because the inversion of MT data is non-unique, it is important to test if the inversion model is imaging subsurface structures correctly and if the resistivity structures in the model are required by the MT data. Moreover, spatial aliasing may be present in the inversion model because the MT stations are not distributed uniformly, especially in northern Alberta (Figure 7.1). To address these issues, the resolution was tested in three ways: (1) synthetic MT inversions, (2) resistivity model editing, and (3) MT inversions with a closely spaced dataset of CAB.

8.3.1. Synthetic inversions with ModEM

In the WAB resistivity model in Figure 8.1, the electrical structure of the subsurface can be roughly divided into three layers – (1) the sedimentary basin (WCSB), (2) lithosphere containing a number of conductors, and (3) asthenosphere. In order to determine how well the ModEM inversion could recover these layers, two synthetic models were developed to represent the simplified three layer electrical resistivity structure of

Alberta. The two synthetic models comprise an upper layer that represents the Western Canada sedimentary basin as a 10 Ωm layer, which is underlain by a highly-resistive layer (1000 Ωm) that represents the lithosphere that extends to a depth of 200 km. The lowest layer is a conductor with 100 Ωm resistivity that represents the asthenosphere. The two synthetic resistivity models A and B are different in terms of the thickness of the WCSB (Figure 8.4). The thickness of the WCSB in synthetic model A is defined by the CRUST 1.0 model (Laske et al., 2013) while the one in synthetic model B is uniform and has a thickness of 3 km.

Both synthetic models have the same model geometry as the initial model used for the whole Alberta inversion as described in section 8.2. The numbers of cells are nx =200, ny =136, and nz =70. The actual locations of the MT sites used in the whole Alberta inversions were used in both synthetic inversions for model A and B. These factors make the synthetic MT dataset similar to the actual MT dataset described in this thesis in terms of station spacing for the investigation of spatial aliasing.

The synthetic inversions began by generating synthetic responses with forward modeling with the ModEM algorithm. Random Gaussian noise of 5% was added to the synthetic impedance dataset. The standard errors of the impedance dataset were defined as 10% of $\sqrt{|Z_{xy} * Z_{yx}|}$ for the diagonal impedance components (Z_{xx} and Z_{yy}), 5% of $\sqrt{|Z_{xy} * Z_{yx}|}$ for the off-diagonal impedance components (Z_{xy} and Z_{yx}), and 0.03 for the tippers. The synthetic dataset was then inverted with the ModEM inversion scheme. The covariance used was 0.3 for the horizontal and vertical directions. The initial lambda was

set to 100 so that it could be updated (by divided with 10) once the r.m.s. misfit change in two consecutive iterations was less than 0.001.

8.3.1.1. Synthetic inversion model A

In the synthetic model A, the depth of the sedimentary basin is defined from the CRUST 1.0 model (Laske et al., 2013) which is a seismic-based global crustal model. The thickness of the sedimentary layer is zero in the northeast corner of the Alberta and greatest in the Rocky Mountain Foothills (Figure 8.4a). The inverted model has a final r.m.s. misfit of 1.06. The initial synthetic and the inverted model A are shown in Figure 8.4.

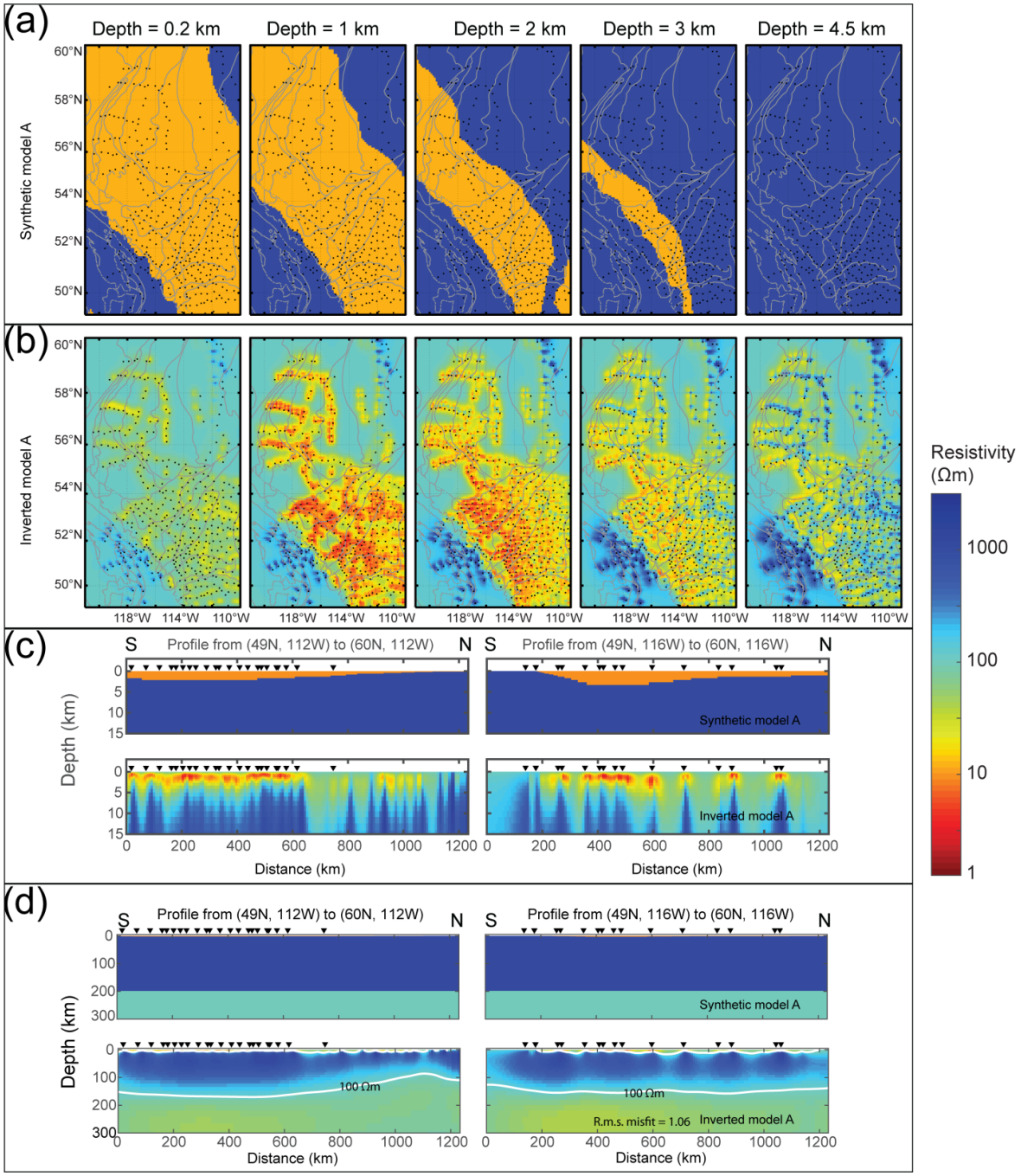

Figure 8.4: The three-layer synthetic model A used to test the ModEM inversion showing details of the WCSB as horizontal slices in the synthetic model (a) and the inverted model (b). Figure (c) shows the WCSB in two vertical profiles along longitude 112°W and 116°W. Figure (d) shows details of the lithosphere-asthenosphere boundary in the synthetic and inverted models. The white lines in figure (d) represent the 100 Ωm (the same as the resistivity of asthenosphere defined in the synthetic model A) contour in the inverted model A. The gray lines in (a) and (b) mark terrane boundaries (Pilkington et al., 2000).

By comparing the synthetic model A with the inverted model A in Figure 8.4, it is obvious that the WCSB can be imaged with the MT dataset; however, the thickness of the WCSB cannot be reliably recovered. Moreover, the horizontal extent of the WCSB in the inverted model A is similar to the synthetic model A in central and southern Alberta where there is good data coverage. This is not the case for regions of Alberta where there is not enough MT data coverage. In northern Alberta, the WCSB is not recovered as a continuous low resistivity layer.

It has been observed that the electrical LAB is characterized by a reduction in electrical resistivity that may be due to the presence of partial melts (Eaton et al., 2009). The 100 Ωm contour line in Figure 8.4d is the asthenosphere resistivity defined in the synthetic model and it is located close to the resistivity change. It will be used to represent the LAB here. The LAB defined from the 100 Ωm contour lines in the inverted model is about 50 km shallower than in the original model.

Moreover, it is interesting to note that the LAB shape changes from horizontal to bulging upward at the north end of the profile 112˚W (Figure 8.4). This may be related to spatial aliasing associated with the uneven MT station distribution or the coverage of the low resistivity surface of the WCSB. To determine which of these factors caused the incorrect depth estimate of the LAB, another synthetic model B with uniform thickness WCSB (3 km) was developed and tested (details in section 8.3.1.2). If no bulging feature could be imaged with synthetic model B, it implies that the uneven MT station distribution in northern Alberta is the cause of the bulging feature.

It is also important to note that the resistivity values of each layer are not imaged exactly the same as in the original synthetic model. All the three layers were imaged with lower resistivities than the synthetic model. (a) The sedimentary layer was defined with 10 Ωm resistivity but was imaged with minimum resistivity of 1 Ωm. (b) Only the core of the lithosphere was imaged with resistivity values close to the synthetic model (1000 Ωm). Specifically, the bulging part of the lithosphere is imaged with resistivity of ~100 Ωm, which is 10 times lower than the original synthetic model A. (c) The asthenosphere is imaged with slightly lower resistivity (~30 Ωm).

8.3.1.2. Synthetic model B

In the synthetic model B, the sedimentary layer has a uniform thickness of 3 km. Everything else, including inversion and model parameters, was the same as synthetic model A. The inverted model B achieved an r.m.s. misfit of 1.03. Details about the LAB are shown in Figure 8.5.

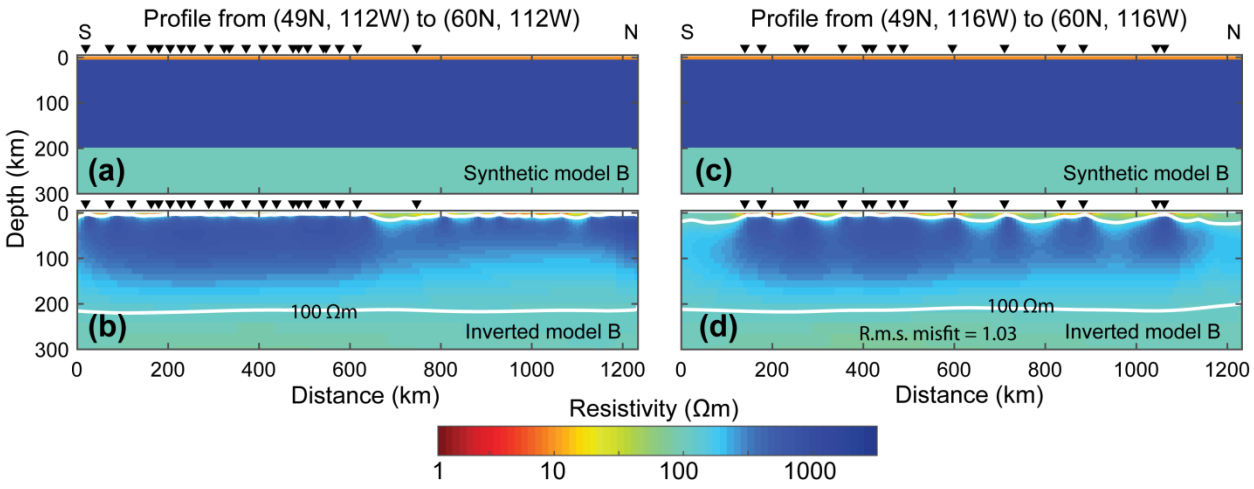

Figure 8.5: The three-layer synthetic model B used to test the ModEM inversion (a and c) and the inverted model (b and d). Two profiles along longitude 112°W and 116°W are shown. The white lines in figure (b and d) represent the 100 Ωm contour in the inverted model B.

In the inverted model B, the 100 Ωm contour lines are located closer to the LAB of the original model at 200 km depth than the synthetic model A. Nevertheless, a similar upward bulging feature is observed at the north end of the profile at 112˚W but to a lesser extent than in the inversion model A. This means that a uniform sedimentary layer cannot completely remove the bulging feature. Therefore, it is believed that both the shape of the sedimentary layer and the uneven distribution of MT stations attributes to the bulging feature in the synthetic modeling.

In summary, the synthetic ModEM inversions show that we can resolve the three layers of the electrical structure of Alberta in both synthetic models. However, (a) the resistivity of each layer was imaged with lower resistivity values than the true values. This could be partly due to the smoothing factor of the inversion scheme. On the other hand, a starting model with a half space of higher resistivity value than 100 Ωm may help with this issue. (b) The thickness of the sedimentary layer could not be imaged correctly. (c) The horizontal extent of the WCSB in northern Alberta could not be imaged correctly due to the large spacing between MT stations. (d) The depth of the LAB may be imaged at shallower depths than in the original model. (e) An upward-bulging LAB at the northern end of 112˚W with one-tenth the resistivity value of the original model could be expected. This is caused by the coverage of the sedimentary layer and the uneven distribution of MT stations. These observations should be considered when interpreting the 3-D inversion model of Alberta.

8.3.2. Model editing

Model editing is helpful and important to verify if the inverted resistivity model features are required by the MT data. Editing was done by (a) replacing the low resistivity anomalies of the inverted resistivity model with high resistivity values and (b) calculating the forward responses of the modified resistivity model. The r.m.s. misfit of the modified model was compared with the r.m.s. misfit of the inverted resistivity model. If the r.m.s. misfit of the modified model is greater than that of the inverted model, it indicates that the resistivity anomaly is required to be in the model to fit the MT data better and vice versa. The model editing tests were done for each anomalous resistivity feature of interest, including the KMC (Kimiwan conductor), SABC (Southern Alberta British Columbia conductor), LC (Loverna block conductor), BMC (Birch Mountain field conductor), and RDC (Red Deer conductor). Moreover, another test was done to find the effective investigation depth of the MT dataset.

8.3.2.1. Sensitivity test for the Red Deer conductor

The low resistivity RDC in the whole Alberta resistivity model was replaced with 100 Ωm resistivity in the depth range 3-11 km as shown in Figure 8.6. The 100 Ωm was chosen to be similar to the surrounding resistivity values in the inverted model. The r.m.s. misfit of the modified model is substantially larger than the original resistivity model for the MT stations surrounding the RDC. This demonstrates that the low resistivity of the RDC is required to fit the MT dataset properly.

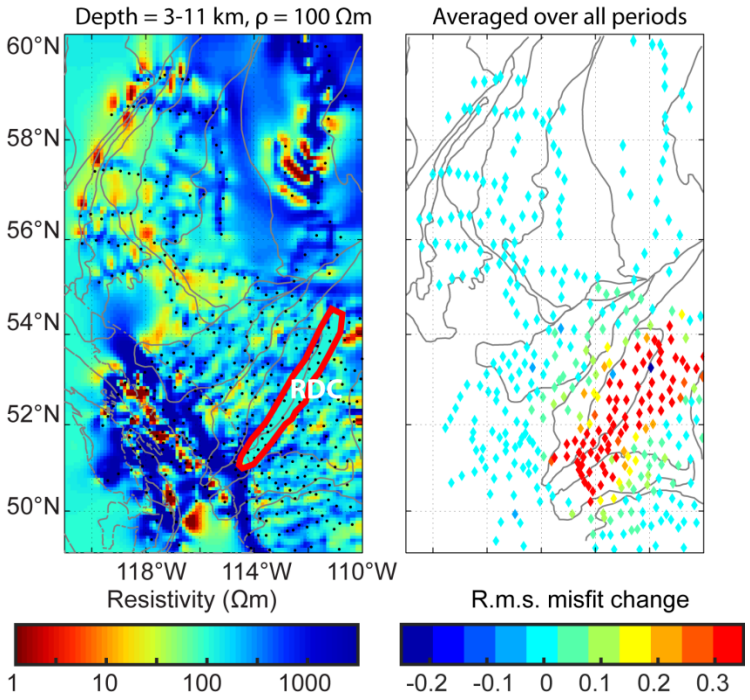

Figure 8.6: The sensitivity test for the Red Deer Conductor (RDC, whose boundary is marked with red lines) based on the whole Alberta resistivity model obtained using ModEM. The change of the r.m.s. misfit of the modified model from the inverted model for each MT station (diamonds) is shown on the right. The red color represents r.m.s. misfit increase after the model modification. The grey line represents the tectonic terrane boundaries (Pilkington et al., 2000).

8.3.2.2. Sensitivity test for the Kimiwan conductor

A sensitivity test was done for the KMC. The resistivity of the KMC was replaced with 300 Ωm in the depth range 10-20 km and 1000 Ωm in the depth range 20-35 km. These resistivity values were chosen to be closer to the resistivity values of the surrounding model cells. The averaged r.m.s. misfit of the MT stations near the KMC increase after this modification. This increase of r.m.s. misfit is most significant for the periods that are sensitive to the investigation depth corresponding to the KMC i.e. 1000 s (Figure 8.7). This test shows that the KMC is required by the MT dataset.

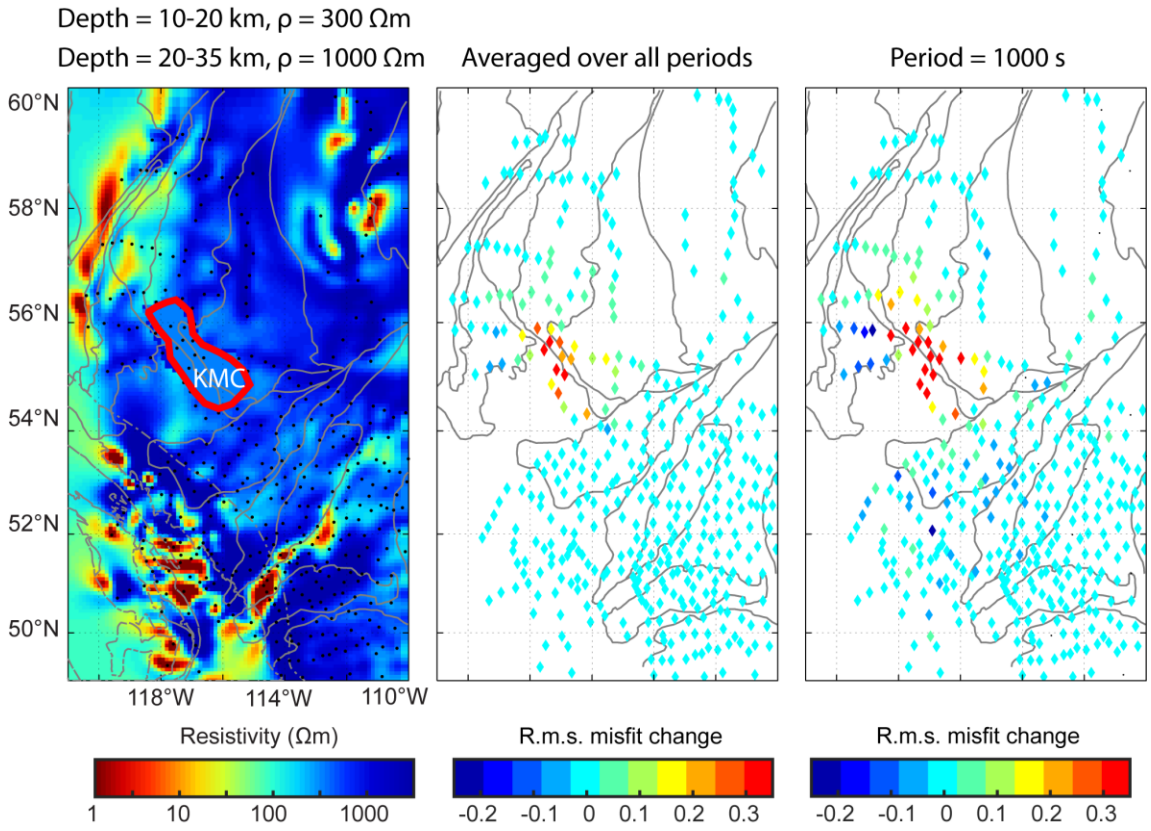

Figure 8.7: The sensitivity test for the Kimiwan conductor (KMC, whose boundary is marked with red lines) based on the whole Alberta resistivity model obtained using ModEM. The resistivity of the KMC was replaced with 300 Ωm and 1000 Ωm at depths 10-20 km and 20-35 km, respectively, shown in the figure at the left side. The change of the r.m.s. misfit of the modified model from the inverted model for each MT station (diamonds) is shown in the center. The change of the r.m.s. misfit of the modified model from the inverted model for each MT station at period = 1000 s is shown at the right side. The red color represents r.m.s. misfit increase after the model modification. The grey line represents the tectonic terrane boundaries (Pilkington et al., 2000).

8.3.2.3. Sensitivity test for the Loverna block conductor and the Southern Alberta – British Columbia conductor

Four separate sensitivity tests were carried out to check the SABC and LC at different depths. The LC is present at depths of 40-150 km and the SABC is at the depth range of 10-150 km. Three sensitivity tests were done to check the SABC at depths of 12-20

km, and 20-40 km, and 40-150 km separately. The resistivity of the SABC was replaced with 1000 Ωm at depths 12-20 km (Figure 8.8). The resistivity of the SABC was replaced with 3000 Ωm at depths 20-40 km. The resistivity of the SABC was replaced with 3000 Ωm at depths 40-150 km. One test was done to check the LC: the resistivity of the LC was replaced with 3000 Ωm at depths 40-150 km. The modified models all show larger r.m.s. misfit values for the MT stations surrounding the LC and SABC. These tests confirmed that the LC and SABC are required to be in the model by the MT data.

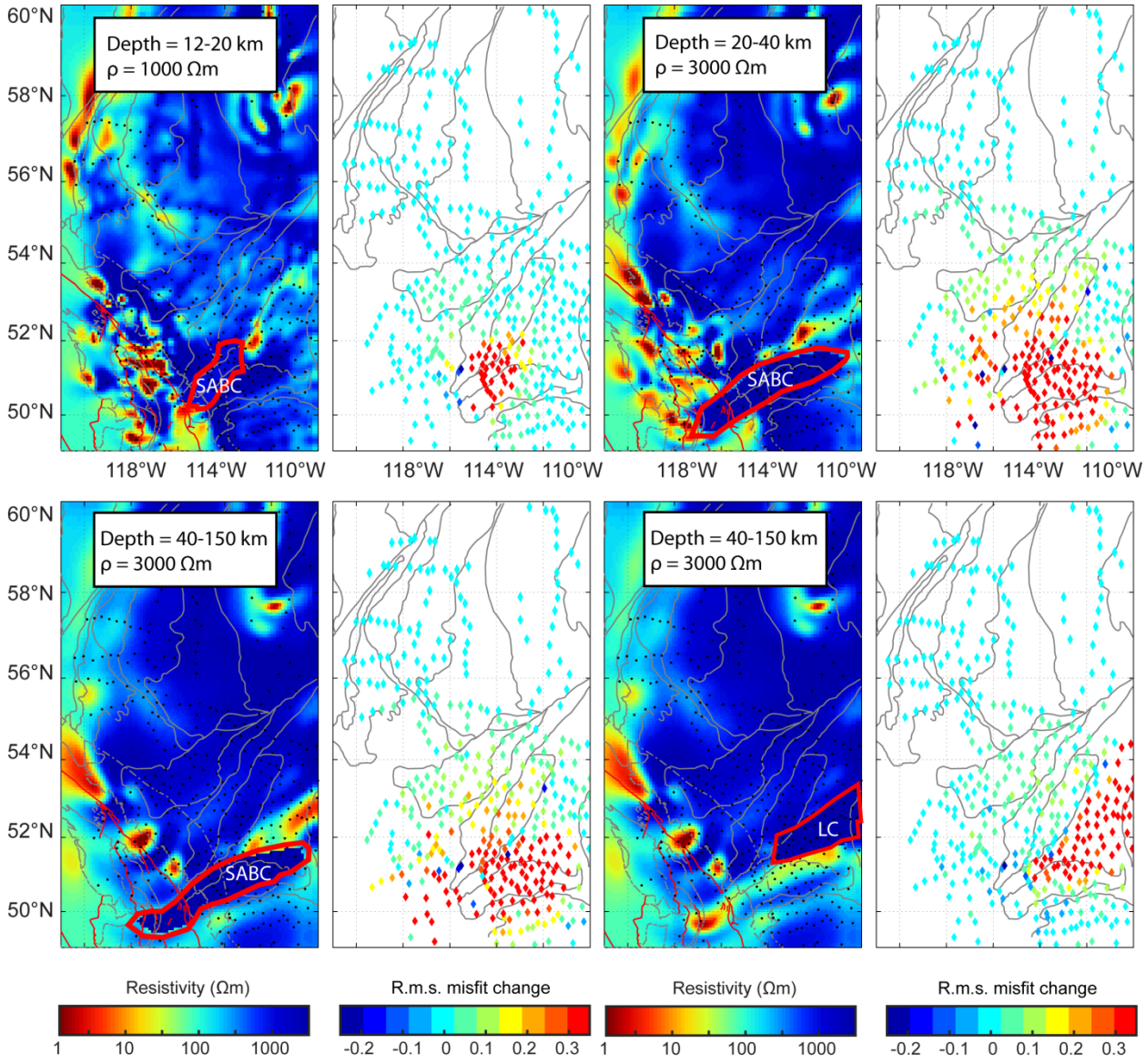

Figure 8.8: The sensitivity test for the Loverna block conductor and the southern Alberta – British Columbia conductor (LC and SABC, respectively) Their boundaries are marked with red lines based on the whole Alberta resistivity model obtained using ModEM. The change of the r.m.s. misfit of the modified model from the inverted model for each MT station (diamonds) is shown also. The red color represents r.m.s. misfit increase after the model modification. The grey line represents the tectonic terrane boundaries (Pilkington et al., 2000).

8.3.2.4. Sensitivity test for the Birch Mountain field conductor

The Birch Mountain conductor was replaced with resistivity values of 3000 Ωm in the depth range 100-200 km and 1000 Ωm in the depth range 200-300 km (Figure 8.9). Increased r.m.s. misfits were observed when comparing the edited resistivity model with the original inversion model. This shows that the BMC is required by the MT dataset.

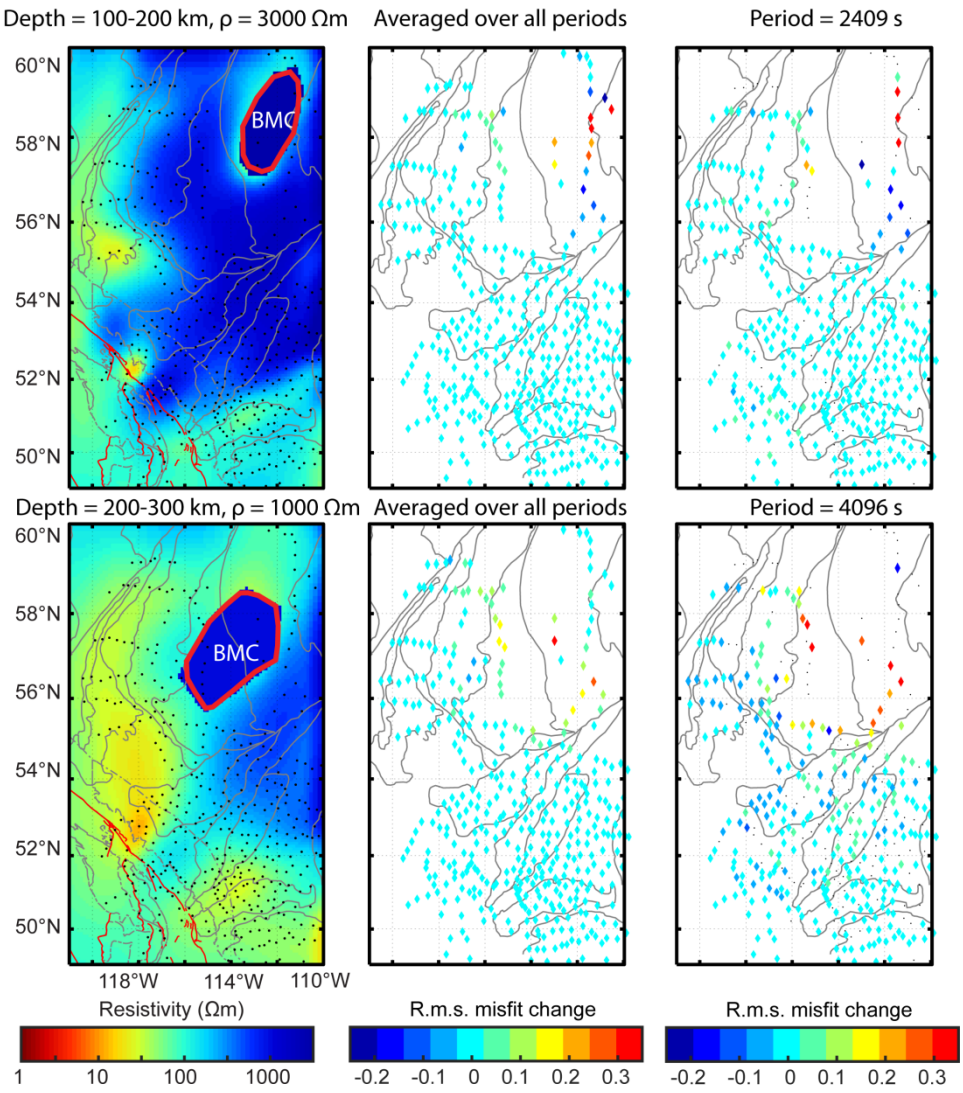

Figure 8.9: The sensitivity test for the Birch Mountain conductor based on the whole Alberta resistivity model obtained using ModEM. The resistivity of the BMC was replaced with 3000 Ωm at depths 100-200 km and 1000 Ωm at depths 200-300 km as shown in the left-side figures. The change of the r.m.s. misfit of the modified model from the inverted model for each MT station (diamonds) is shown in the middle figure. The right-side figure shows the change of the r.m.s. misfit for each MT station of the corresponding period. The red color represents r.m.s. misfit increase after the model modification. The grey line represents the tectonic terrane boundaries (Pilkington et al., 2000).

8.3.2.5. Sensitivity test of the effective investigation depth

It is important to know the effective investigation depth of the MT data before interpreting the resistivity models derived from inversion. The effective investigation depth depends on the longest period and the electrical resistivity of the subsurface according to the skin depth equation (Chapter 2). Five tests were performed to test the effective investigation depths of the MT data. In each test the resistivity model was edited to a value of 3000 Ωm below a specific depth: 300, 350, 400, 450, 500 km. An increase in r.m.s. misfit of the modified model would indicate that the MT data is affected by the change in electrical structure to that depth. As shown in Figure 8.10, more than 90% of the MT stations are sensitive to electrical resistivity structures to a depth of 350 km. The data of more than half of MT stations are affected by electrical structures to the depth of 400 km. Therefore, it is reasonable to discuss the electrical model of a depth < 350 km.

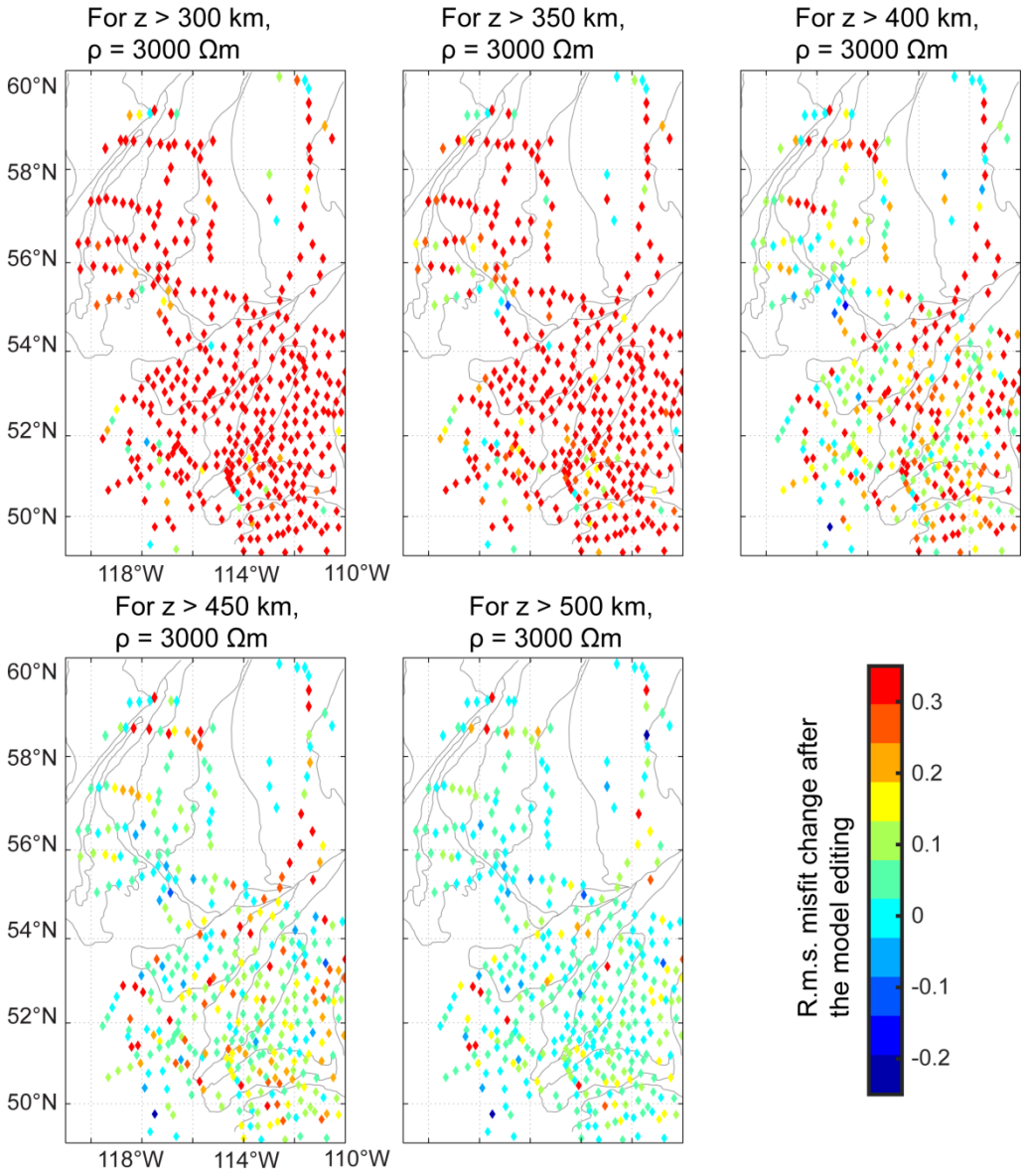

Figure 8.10: The sensitivity test of the effective investigation depths based on the whole Alberta resistivity model obtained using ModEM. The resistivity of the inverted model was replaced with 3000 Ωm at depths greater than 300/350/400/450/500 km. The change in the r.m.s. misfit of the modified model from the inverted model for each MT station (diamonds) is shown in the figure. The red color represents r.m.s. misfit increase after the model modification. This shows that the effective investigation depth is probably 350 km for most of the MT stations. The grey line represents the tectonic terrane boundaries (Pilkington et al., 2000).

In summary, the conductors KMC, SABC, LC, BMC, and RDC imaged in the WAB model are all required by the MT data as an increase of r.m.s. misfit was observed when they were edited with high resistivity values. Moreover, the effective investigation depth of the MT dataset is about 350 km and thus the maximum depth of the electrical model that should be discussed is 350 km.

8.3.3. Inversion of MT data for central Alberta

The whole Alberta inversion does not have a uniform MT station distribution and the grid size in the centre of the model was limited to 8 km due to the limitations of computer resources. More inversions with MT stations in central Alberta were run to test if a dataset with more uniform spaced MT stations and a model with smaller grid size would improve the inversion model.

The final central Alberta inversion result (CAB model) was run with 409 LMT stations and a half-space 100 Ωm initial and prior model with nx =148, ny =159, and nz =66. The central horizontal grid spacing is 6 km. The top vertical grid size is 133 meters. The horizontal covariance in the x and y directions were set to decrease from the surface to the bottom of the model from 0.6 to 0.2. The vertical covariance in the z direction was set to 0.5. This covariance setting is expected to reduce the model smoothing with depths and help to recover more features at depths. All the rest of the parameters were kept the same as the whole Alberta inversion.

8.3.3.1. Data fit of the central Alberta resistivity model

Figure 8.11 shows the data fit of the CAB resistivity model. The overall r.m.s. misfit is 2.29. The data fit of the CAB model is similar to that of the WAB model. Most of the MT

stations were fit with r.m.s. misfit smaller than one. The MT data in the southwest corner of the model and the longest periods (> 5000 s) had the highest misfit. Moreover, the MT stations along the Red Deer High and northeast of the Hearne province were poorly fitted also. The apparent resistivity and phase of (a) the MT data and (b) the response of the resistivity model are compared in the Figure 8.12. They are very similar for the MT stations in Alberta and large differences are observed in the southeast British Columbia.

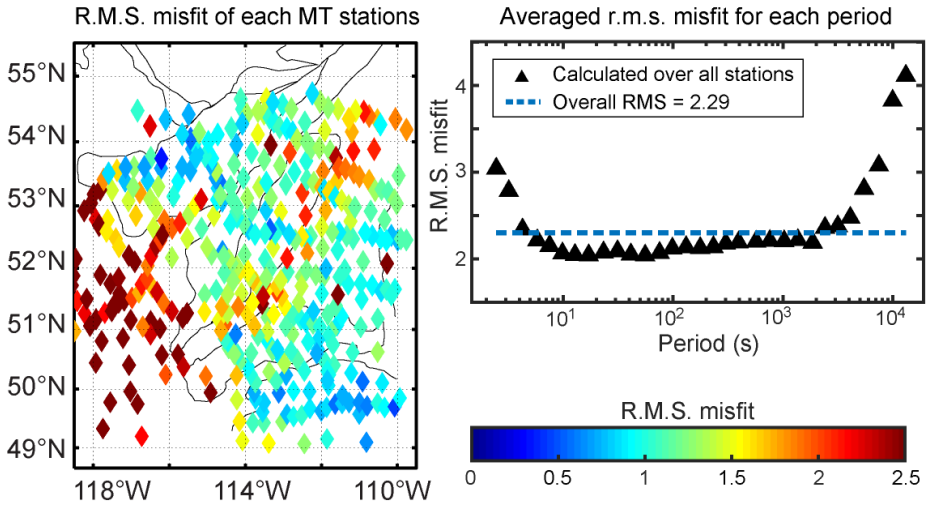

Figure 8.11: The r.m.s. misfit of the central Alberta inversion averaged over all the periods for each station (left) and over all the stations for each period (right). The gray lines in the map mark the boundaries of the basement terranes (Pilkington et al., 2000).

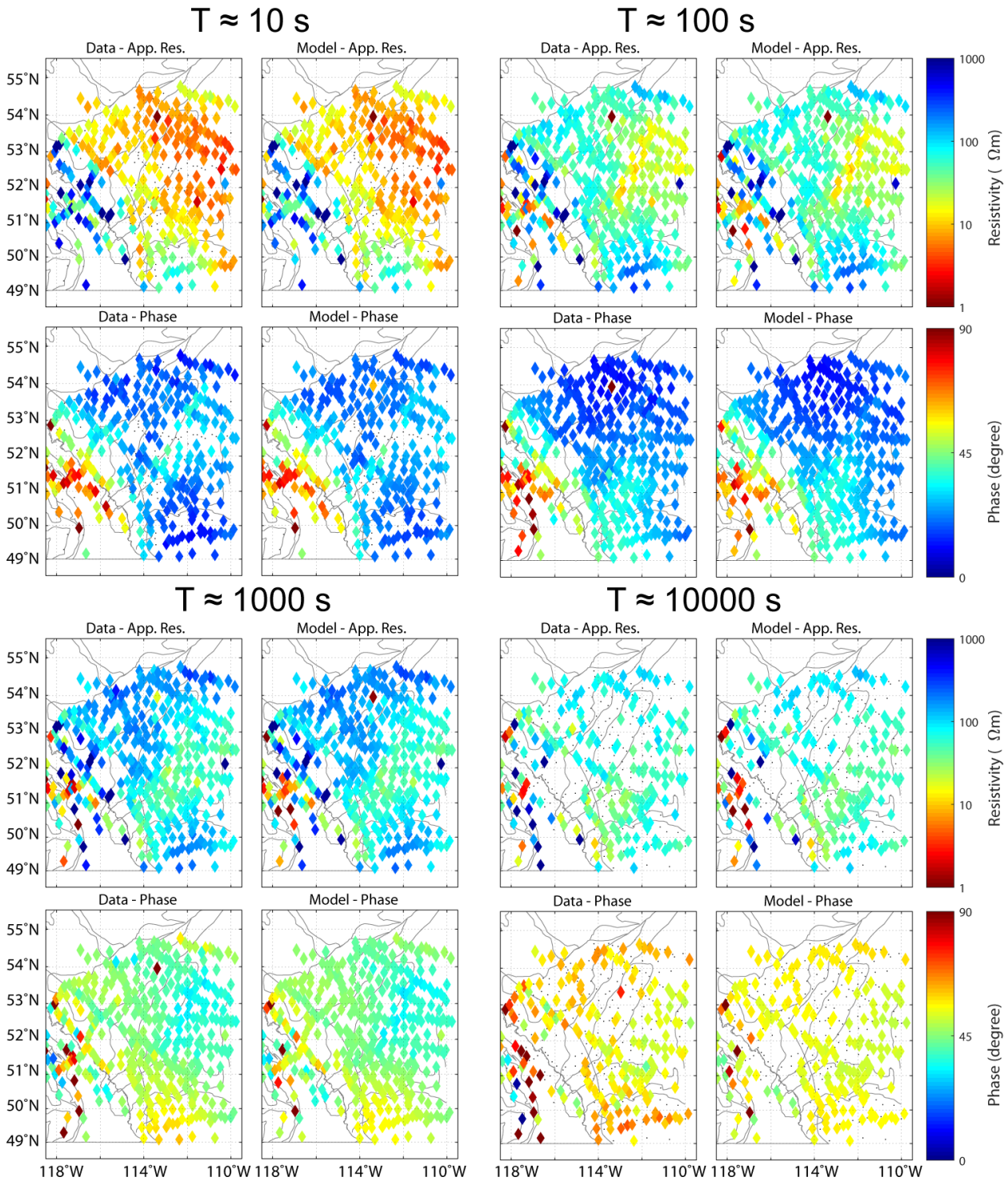

Figure 8.12: The comparison of the MT data and the resistivity model response at periods from 10-10000 s. The apparent resistivity and phase are calculated as an average from the XY and YX components. The grey lines represent the terrane boundaries (Pilkington et al., 2000).

8.3.3.2. Comparison with the whole Alberta resistivity model

The CAB model is shown in Figure 8.13. The general features of the CAB model are very similar to the corresponding parts of the WAB model. The WCSB is imaged as a smoother layer in the CAB model than in the WAB model probably due to the higher smoothing values used in the ModEM inversion at the top of the model than the whole Alberta inversion model. It can also be because of better lateral coverage since more stations are used in the CAB model than the WAB model. The RDC is imaged in both models except that it is imaged deeper in the CAB model at the northeast end of the conductor. The SABC and LC are imaged as well. However, the shape of the LC is somewhat different in the two models.

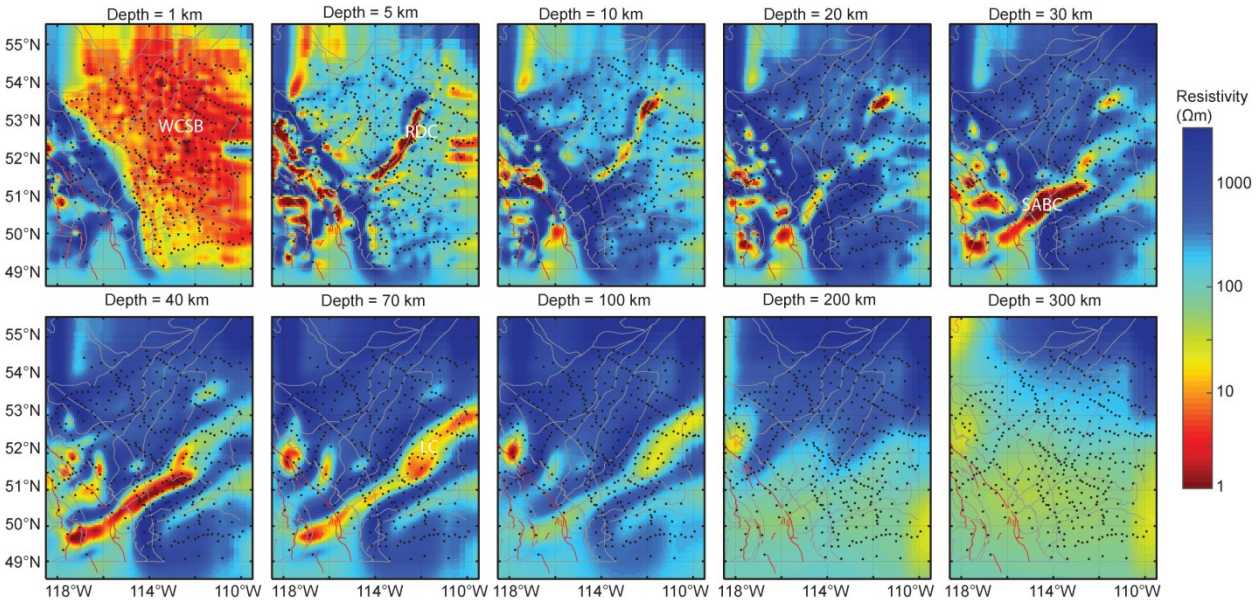

Figure 8.13: The 3-D resistivity model of the central Alberta shown with horizontal slices. The algorithm used is ModEM. The gray and red lines mark the terrane boundaries and faults, respectively (Pilkington et al., 2000). The black dots represent the locations of MT stations used for the inversion. Abbreviations: WCSB, Western Canada sedimentary basin; RDC, Red Deer conductor; SABC, Southern Alberta – British Columbia conductor; LC, Loverna block conductor.

These observations demonstrate that the WAB model is good enough to recover the electrical structures of Alberta even though coarser stations coverage and a larger grid were used than the CAB model. Nevertheless, since the CAB model has better lateral coverage and smaller mesh size than the WAB model, the interpretation of the conductive features of the central and southern Alberta will be based on the CAB model.

8.4. Conclusions

The ModEM three-dimensional inversion scheme has been applied to the dataset of 405 LMT stations covering all of Alberta. The 3-D resistivity model of Alberta shows many conductive features that are consistent with previous studies and can be correlated with

other geological and geophysical results. The conductors imaged include the WCSB, RDC, KMC, KC, SABC, LC, and BMC. The lithosphere of Alberta is generally highly resistive, out of which two resistive roots are imaged as the BHHR and STZR.

Tests have been performed to confirm that the 3-D WAB model is reliable. Synthetic modeling demonstrated that the three-layered Earth model could be resolved with the inversion scheme even though the specific resistivity values may be lower than the original model. Moreover, the LAB depth may be shallower than the original model as well. Secondly, the conductors have been edited with larger resistivity values, and increase of r.m.s. misfits were observed which showed that the conductors were required by the MT dataset. Lastly, an inversion model based on the closely-spaced central Alberta dataset of 409 LMT stations with a model of smaller grid size has been compared to the WAB model. It showed that the WAB and CAB models are consistent in terms of major resistivity features. All the tests demonstrated the WAB model should be trusted for interpretation. Moreover, the interpretation of the conductive features of the central and southern Alberta will be based on the CAB model because the CAB model has better lateral coverage and smaller mesh size than the WAB model.

Chapter 9 : Interpretation of resistivity models

The resistivity models derived from inversion of the Alberta MT dataset described in Chapter 8 contain a number of interesting features. Some of them are coincident with the other geophysical anomalies or geological boundaries summarized in Chapters 3 and 4. In this chapter, the structure and significance of these features will be interpreted systematically. Where possible, the physical properties, such as water content, melt fraction and composition of mantle materials, required to produce the observed resistivity will be determined using published laboratory experiments. In sections 9.1 – 9.8, the present-day resistivity structure will be defined and interpreted. A simplified list of the conductors in the MT inversion models and their interpretations are described in Table 9.1. The occurrence of diamondiferous kimberlites will be discussed based on the resistivity models in section 9.9. Finally, in section 9.10, the implications for the tectonic history of this region will be considered.

Conductor	Geophysical observations					Interpretations					
	Resistivity (Ωm)	depth (km)	Temperature (°C)	Seismic	aeromagnetic anomaly	Saline pore fluids	graphite films	sulfides	iron oxides	melts	hydrogen in NAM
Western Canada sedimentary basin conductor (WCSB)	1-30	0-5	N/A	high reflectivity	N/A	Y	N	N	N	N	N
Red Deer conductor (RDC)	1-10	5-30	N/A	faults imaged	positive	Y	Y	Y	Y	N	N
Kiskatinaw conductor (KC)	10-100	10-40	N/A	high reflectivity	negative	N	Y	Y	N	N	N
Kimiwan conductor (KMC)	10-30	0-35	N/A	faults imaged	positive	Y	Y	Y	Y	N	N
Loverna block conductor (LC)	3-30	45-120	400-700	low velocity	N/A	Y	Y	Y	N	Y	Y
Southern Alberta – British Columbia conductor (SABC)	1-10	30-90	300-500	N/A	N/A	Y	Y	Y	N	N	N
Birch Mountain field conductor (BMC)	3-10	100-250	800-1300	low velocity	N/A	Y	N	N	N	Y	Y

Table 9.1: A list of the crustal and upper mantle conductors imaged in Alberta in this thesis. NAM, nominally anhydrous minerals.

9.1. The Western Canada Sedimentary Basin (WCSB) conductor

9.1.1. Structure imaged in the WAB and CAB inversion models

A continuous low resistivity surface layer with resistivity in the range 1-30 Ωm is observed in both the whole Alberta (WAB) (Figure 9.1a) and the central Alberta 3-D inversion model (CAB) (Figure 9.1b) 3-D inversion models. This feature can be attributed to the WCSB because: (1) low resistivity is expected for clastic sedimentary rocks containing aqueous fluids in the pores; (2) this conductor is in the depth range of 0-5 km; (3) the western boundary of the WCSB conductor is located close to the Cordillera deformation front (CDF); and (4) the spatial extent of the WCSB conductor in the CAB model is similar to the WCSB defined in the seismic model CRUST 1.0 (Laske et al., 2013; Figure 9.1c). A localized high resistivity body can be observed at 110˚ W and 52˚ N with a resistivity greater than 100 Ωm. This feature is likely an artefact and caused by noisy MT data points at some nearby MT stations (see in Figure 8.3 for period = 9.8 s) and will not be discussed further in this chapter.

The WCSB conductor was imaged in both the CAB and WAB inversion models (Figure 9.1). However, the WCSB conductor in northern Alberta in the WAB model is not spatially continuous north of 54°N (Figure 9.1). This is because the distribution of MT stations in northern Alberta is sparse with an inter-station spacing up to 100 km. According to the skin depth equation, only the subsurface within the range of skin depths (δ = 4000 m, if ρ = 10 Ωm and T = 6 s) is sampled by an MT station. Therefore, it is impossible to image the WCSB as a continuous layer in northern Alberta with the current MT station distribution. Furthermore, as proved by the synthetic modeling in section 8.3.1, the base of

the WCSB is not well resolved in the MT inversion model because the LMT dataset used lacks the high frequency data that are sensitive to resistivity structure at shallow depths. Thus the thickness of the WCSB will not be discussed here. The thickness of the WCSB could be better resolved if a constrained inversion was undertaken because the thickness of the WCSB has been defined by seismic studies (Gu et al., 2018). This could be done in future research to improve the results.

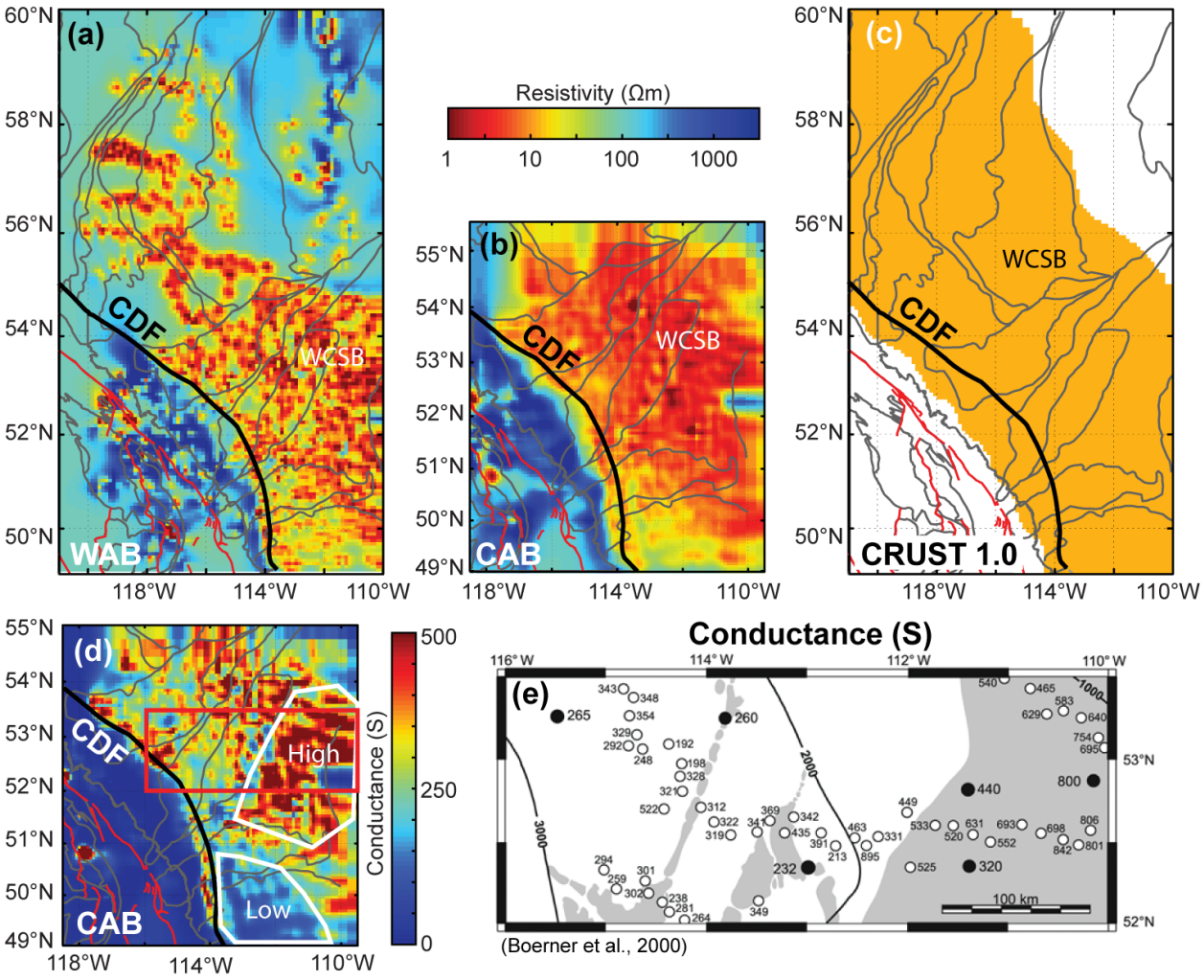

Figure 9.1: Depth slices of (a) the whole Alberta (WAB) inversion model and (b) the central Alberta (CAB) inversion model showing the Western Canada Sedimentary Basin conductor (WCSB). (c) shows the WCSB as defined in the seismic model – CRUST 1.0 (Laske et al., 2013). (d) shows the conductance in the depth range 0-5 km. The red box is the location of (e) which is marked with conductance values of the WCSB (from Boerner et al. (2000)). The thick black lines in figures (a-d) represent the location of the Cordillera deformation front (CDF). The black lines with numbers in (e) represent the depths of the WCSB. Shaded zones in (e) indicate Leduc Formation reef complexes. The grey lines are geological boundaries and the red lines are faults (Pilkington et al., 2000; Colpron and Nelson, 2011).

9.1.2. Interpretation

The low resistivity of the WCSB conductor is interpreted to be due to a combination of (a) the presence of saline fluids in the porous sedimentary rocks which is enhanced by (b)

clay minerals in shale units. Experimental results from Sinmyo and Keppler (2017) suggest that the resistivity of crustal fluids may be as low as 0.03 Ωm. According to Archie's Law, a concentration of 0.1-3 % of saline fluids with resistivity of 0.03 Ωm would result in bulk resistivities in the range 1-30 Ωm in the sedimentary rocks. Lithological studies have demonstrated that the porosity of three hydrocarbon-bearing formations of the WCSB is in the range 1-6% (Wüst et al., 2013). These formations are composed of shale, sandstone, siltstone, and carbonates. Moreover, clay contents between 4-21% have been widely observed in the WCSB (Wüst et al. 2013). The existence of clay minerals could further lower the bulk resistivity, which means that a concentration of less than 3% of saline pore fluid is required to explain the observed resistivity.

9.1.3. Conductance variations of the WCSB

Non-uniqueness is a problem in the interpretation of MT data; consequently, electrical resistivity at a certain depth cannot be well constrained. However, it has been shown that electrical conductance (product of conductivity and thickness) over a certain depth range can be reliably determined from MT data (section 2.10.3). Spatial variations in the conductance of the WCSB were investigated using the 2-D inversions of Boerner et al. (2000) whose results are shown in Figure 9.1e. The conductance was shown to be uncorrelated with the total thickness of the WCSB. Boerner et al. (2000) used 2-D MT modeling to estimate conductance but this method has limitations. The study described in this thesis allows us to use a 3-D approach to constrain the conductance of the WCSB with the 3-D CAB electrical resistivity models. The conductance for the depth range of 0-5 km of the CAB model is shown in Figure 9.1d. This provides a good estimate of the conductance of the WCSB because the highly resistive crystalline basement rocks in this depth range

should contribute very little to the total conductance. Large spatial variations in conductance values are observed in Figure 9.1e. The conductance of the WCSB ranges from 200 S to 800 S with an average value around 300 S. Similar spatial variations are observed in both our 3-D study and the 2-D study of Boerner et al. (2000).

There are two regions of the WCSB with anomalously high and low conductance. The high conductance regions (>500 S) are located in central Alberta (51.5-53.5˚N and 110-112˚W). The low conductance region (<150 S) is located in southern Alberta to the east of the Cordillera deformation front (49-51˚N and 111-114˚W). Boerner et al. (2000) attributed the lateral variation in the conductance of the WCSB to the fact that the resistivity values of individual strata of the WCSB vary greatly. In particular, they proposed that Devonian reef structures (shaded area in Figure 9.1e) were the major contributors to the high conductance anomaly in central Alberta. Reef structures are composed of carbonate minerals, and the electrical resistivity is controlled by the porosity and permeability and the nature of the fluid filling the pore spaces. It was stated that about half of the world's oil and gas is held in carbonates. Moreover, carbonates hold the majority of ground-water also (Ahr, 2011). A carbonate formation can be resistive if its pores are full of oil or the permeability is low, while it can be conductive if its pores are full of water and well-connected (Archie, 1952). On the other hand, shale can lower the electrical resistivity of a carbonate hydrocarbon reservoir since it is rich in clay minerals.

It is probable that the Devonian reef structures described by Boerner et al. (2000) have high clay content or porosity which enhances the conductivity substantially. The same explanation was given for the variations in resistivity measured in different well logs (Mossop and Shetsen, 1994). This observation supports the hypothesis that the

conductance of the WCSB is largely dependent on the porosity and clay content of the sedimentary rocks.

9.2. The Red Deer conductor (RDC)

9.2.1. Structure imaged in the CAB inversion model

The Red Deer conductor (RDC) is imaged in the CAB 3-D inversion model in Figure 9.2. The RDC is located on the boundary of the Lacombe and Loverna blocks, as was observed in the previous MT studies by Boerner et al. (2000) and Nieuwenhuis et al. (2014). The RDC is separated from the WCSB conductor by a resistive band in the depth range 3-5 km. It is also not connected with the SABC because the southern RDC terminates at the depth of 10 km while the SABC is imaged in the depth range 30-70 km. This observation is different from the 3-D model of Nieuwenhuis et al. (2014) and the 2-D model of Boerner et al. (2000). These previous studies imaged the RDC as being connected with the SABC/LC.

The RDC can be divided into (a) a long thin southern segment (latitude 51.5˚N – 53˚N) and (b) a deep broad northern segment (53˚N – 54˚N; Figure 9.2b). The southern segment of the RDC is imaged at depths of 5-10 km. The northern segment of the RDC is located at depths of 5-30 km. Both segments have low resistivity values in the range 1-10 Ωm.

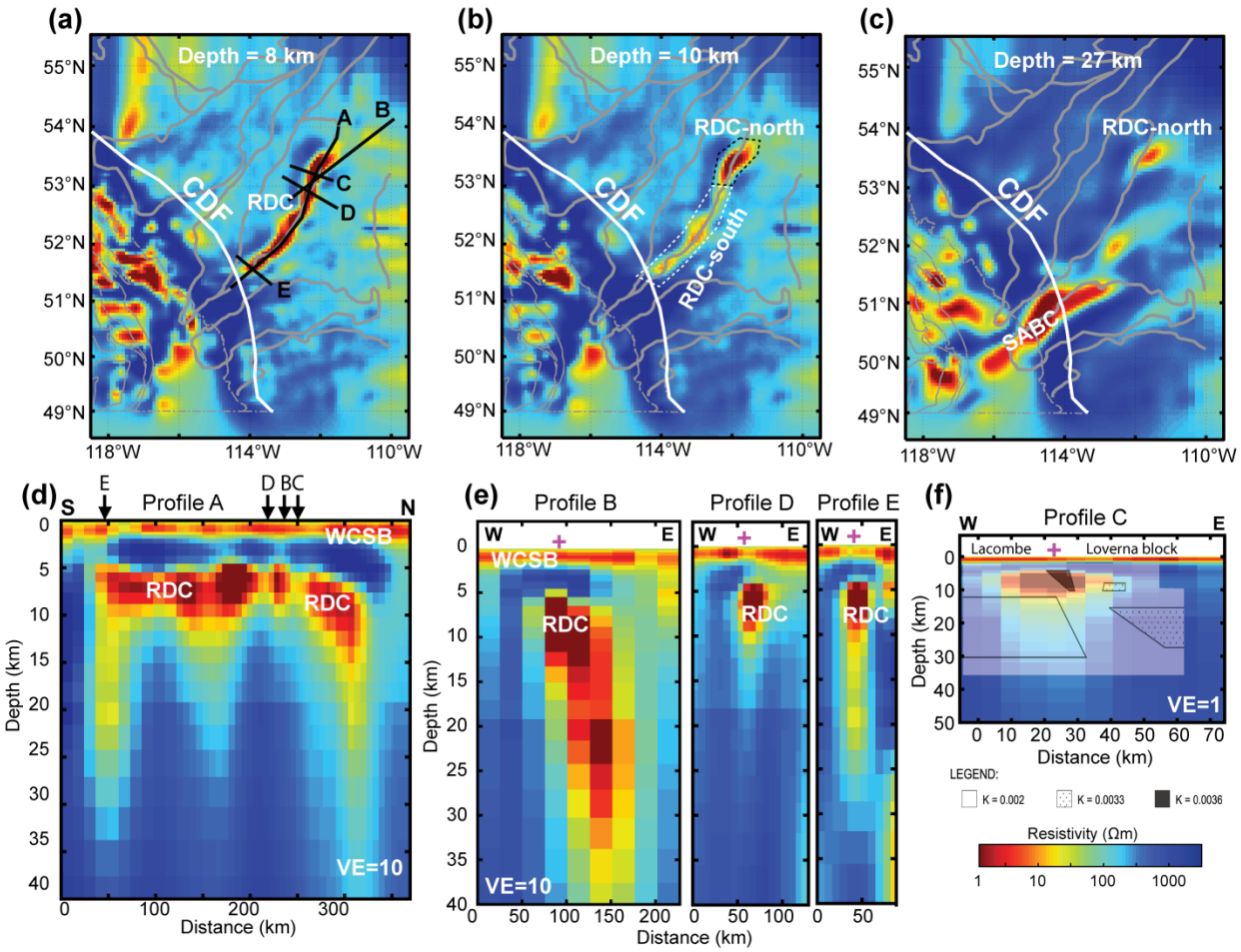

Figure 9.2: The Red Deer conductor (RDC) imaged in the CAB model in horizontal slice view at depths of 8/10/27 km (a/b/c) and profiles (A-E). Locations of profiles A-E are shown in the (a) with black solid lines. (d) shows the RDC parallel to the strike direction of the RDC. (e) shows the RDC as slices that are normal to the strike direction of the RDC on three profiles B, D, and E. (f) shows the RDC in a profile that is collocated with the 2-D magnetic model of Hope and Eaton, (2002). The grey lines in (a), (b), (c) mark the terrane boundaries (Pilkington et al., 2000; Colpron and Nelson, 2011). In panel (b), south and north segments of the RDC are marked with white and black dashed lines, respectively. Abbreviations: WCSB, Western Canada Sedimentary Basin; LC, Loverna block conductor; CDF, Cordillera deformation front; VE, vertical exaggeration.

9.2.2. Comparison with other geophysical models of RDC

The RDC is spatially coincident with the Red Deer aeromagnetic high trend (Figure 4.1). Previous 2-D potential field studies of the Red Deer aeromagnetic high have modelled

the measured data with (a) a small body of high magnetic susceptibility (0.0036 SI units) in the depth range 5-10 km along the Red Deer trend combined with (b) a southeast dipping boundary of two mid-crustal layers of different magnetic susceptibility values (Figure 9.2f; Hope and Eaton, 2002). The depth range and location of the southern RDC agree well with the potential field model anomaly described in (a) but no dipping structure was imaged in the mid-crust in the CAB model (Figure 9.2e).

It was proposed that the along-strike variation in the strength of the Red Deer aeromagnetic anomaly could be explained if the burial depth of the anomalous body associated with the Red Deer aeromagnetic anomaly varied along strike (Hope and Eaton, 2002). In this case, the northern segment of the Red Deer high was postulated to be shallower than the southern segment (Hope and Eaton, 2002). This variation in depth along strike is inconsistent with the CAB model, where the northern segment of the RDC is deeper than the southern segment (Figure 9.2e). Moreover, the RDC in the CAB model extends further north and west along the Red Deer trend than the Red Deer aeromagnetic high. This provides evidence that these two geophysical anomalies may not be caused by the same structure.

Furthermore, comparing the CAB resistivity model with seismic study of the Central Alberta Transect (CAT) reveals that the RDC is located close to the seismic-defined subsurface boundary of the Lacombe domain and the Loverna block (Ross, 2002; Figure 9.3). Based on the seismic studies of the CAT project, Ross et al. (1995) interpreted this boundary as a reverse fault that was active during the East Alberta Orogen and associated with southeastward subduction of the Wabamun domain along the northern boundary of the Hearne craton and part of substantial Paleoproterozoic imbrication in central Alberta.

It was also proposed to be coeval with the ~1.8 Ga Trans-Hudson Orogen. These two orogens were suggested to have acted as a tectonic vice that trapped the Hearne craton (Ross, 2002).

9.2.3. Interpretation of the RDC

Boerner et al., (2000) proposed that the low resistivity of the RDC was caused by grain-boundary graphite films. Carbonaceous sediments were proposed to have been deposited in a euxinic basin setting and subsequently imbricated and metamorphosed during the East Alberta Orogen. Assuming pure graphite has a resistivity of 0.0001 Ωm and are well interconnected (m=1; Appendix 7), then just 0.01% of grain-boundary graphite films can explain the 1 Ωm resistivity of the RDC using Archie's Law (Archie, 1942).

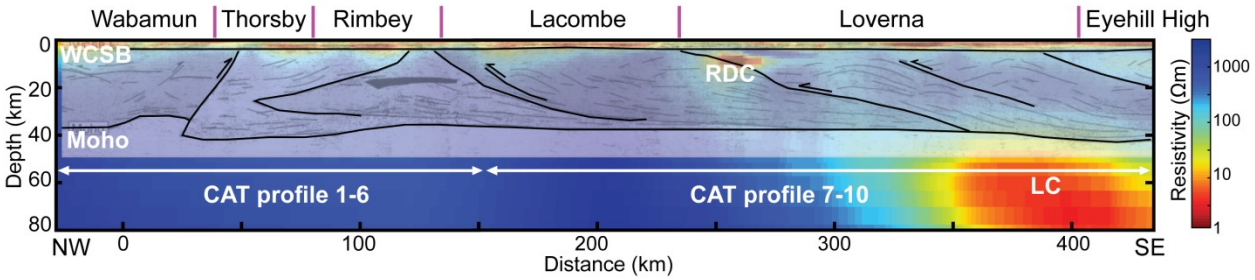

Figure 9.3: Comparison of the CAB resistivity model with the CAT seismic reflection profiles (Ross, 2002). The bottom of the WCSB and the crust are defined from the seismic profiles and marked with black lines. Major faults defined in the seismic profiles are marked with black lines. The terrane boundaries at the surface are marked with purple bars. Abbreviations: LC, Loverna block conductor; RDC, Red Deer conductor; CAT, Central Alberta Transect; WCSB, Western Canada Sedimentary Basin.

The strong aeromagnetic anomaly associated with the Red Deer trend was interpreted to be due to the presence of banded iron formations which can be associated with Paleoproterozoic foredeep basins (Hoffman, 1987; Boerner et al., 2000). The ferrous mineral associated with high magnetic susceptibility in the crust is magnetite and pure

magnetite can also have a very low electrical resistivity at room temperature (< 0.01 Ωm; Kakudate et al., 1979). Thus, the anomalous properties of the southern segment of the RDC and Red Deer aeromagnetic high anomaly could be jointly explained by inter-connected magnetite in the depth range of 5-10 km, considering their similar lateral and depth extent. According to Archie's Law, 1% of well-connected (m=1; Appendix 7) magnetite can produce the 1 Ωm resistivity of the RDC. Nevertheless, the magnetite may not be interconnected and in this case the southern RDC could be due to the presence of graphite or other interconnected non-magnetic ferrous minerals such as hematite.

On the other hand, the northern segment of the RDC is not spatially coincident with the structure causing the magnetic anomaly. If the magnetic anomaly at this location is also caused by interconnected magnetite, then a longer wavelength aeromagnetic high should be observed in the north compared to the south. This is not the case, so the origin of the northern RDC is unlikely to be magnetite. The northern RDC could be explained by graphite or non-magnetic ferrous minerals.

Other than the two conducting phases mentioned above, free porous fluids and sulfides have been suggested to be the cause of low resistivity zones in the upper crust such as the RDC. Water can be generated by (1) prograde metamorphism at depths, (2) subduction of wet rocks, or (3) fluid ex-solution from cooling magmas or partial melts (Hyndman et al., 1993). Water could be absorbed by retrograde hydration reactions, such as during cooling from granulite- to amphibolite-facies or from amphibolite- to greenschist-facies conditions (Hyndman et al., 1993; Yardley and Valley, 1997). The RDC is located within the Laurentia craton which has been cooling since the cessation of tectonic activities in Paleoproterozoic (Ross, 2002). Therefore, water generated from past tectonic

events would likely have escaped or been absorbed by retrograde hydration reactions in the RDC.

It has been shown that water does not often have a long residence time in the crust (Yardley and Valley, 1997), and may not be able to explain the low resistivity of an ancient feature such as the RDC. An alternative explanation is that the water causing the low resistivity originates at the surface of the Earth. It has been suggested that the depth extent of downward convective flow of meteoric water occurs at a depth where the pore-fluid pressure is equal to the hydrostatic pressure (Fournier, 1991). This occurs at depths greater than 10 km depth where crystalline rocks extend to the Earth's surface. Since the RDC is relatively shallow (less than 10 km), water could permeate through the WCSB and travel through the basement faults as shown in Figure 9.3. However, the resistivity of the RDC is 1 Ωm and the concentration of pore fluids required to produce the observed resistivity would be approximately 3-30% assuming the saline pore fluid has a resistivity value of 0.3-0.03 Ωm. This porosity is unreasonably high for old crystalline basement. Lithological studies have demonstrated that the porosity of three hydrocarbon-bearing formations of the WCSB is in the range 1-6% (Wüst et al., 2013). The porosity of the crystalline basement should be much lower than that of the WCSB. Therefore, saline pore fluid alone cannot produce the low resistivity of the RDC.

Sulfide minerals could also produce a region of low electrical resistivity such as the RDC. It was shown that 3-7% of disseminated sulfide minerals could lower the bulk resistivity of rocks to 20-70 Ωm (Nelson and Van Voorhis, 1983). Sulfide minerals were proposed to be the cause of the North American Central Plains anomaly and which has a resistivity of 3-8 Ωm (Jones et al., 1997). Pure sulfides have an electrical resistivity of 0.01

Ωm. Tectonic processes related to the Trans-Hudson Orogen were proposed to have been responsible for the concentration of the sulphides from folded sediments (Jones et al., 1997). This is similar to the tectonic environment of the RDC. The RDC was proposed to be related to a Paleoproterozoic foredeep basin (Boerner et al., 2000). Therefore, sulfides may also be a possible explanation for the low resistivity of the RDC.

In summary, the low resistivity of the RDC is most likely caused by some combination of graphite/sulfides/ferrous minerals at the southern end and by graphite/sulfides/non-magnetic ferrous minerals at the northern end. Saline pore fluids may contribute to the low resistivity at the shallow depths < 10 km.

9.3. The Loverna block conductor (LC) and Southern Alberta – British Columbia conductor (SABC)

9.3.1. Structure imaged in the CAB inversion model

The Loverna block conductor (LC; Nieuwenhuis et al., 2014) is well imaged in the CAB model and is connected to the Southern Alberta – British Columbia conductor (SABC) that was first described in Gough (1986). The region of the LC and SABC in the CAB model is shown in detail in Figure 9.4.

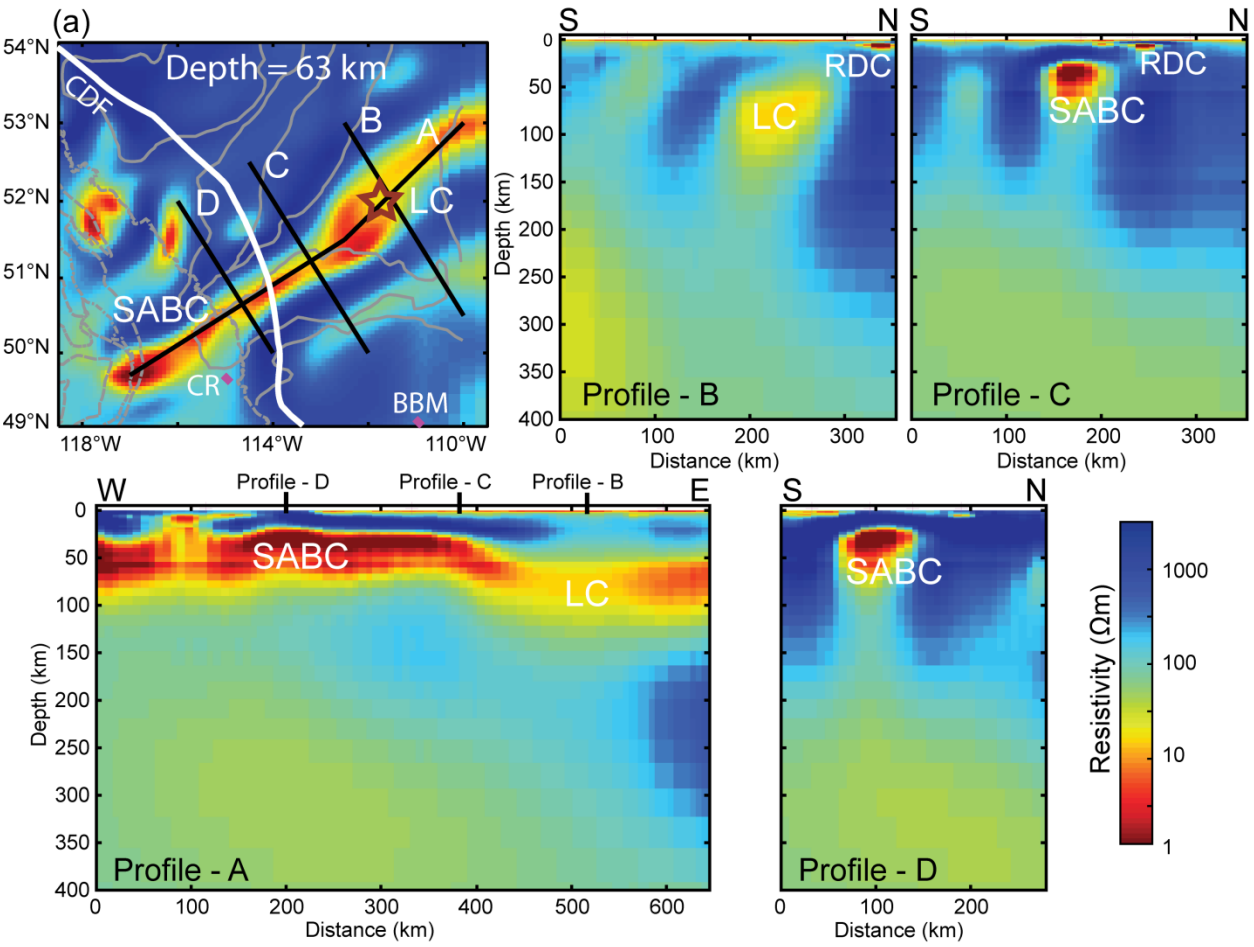

Figure 9.4: (a): horizontal slice of the CAB model at a depth of 63 km showing the shape of the LC and SABC and the locations of four profiles. Profile A is along the strike of the two conductors and profiles B, C, and D cross the two conductors. The star shows the location of MT station SAB225 whose resistivity profile was analysed in section 9.3.3. Gray lines are the terrane boundaries (Pilkington et al., 2000; Colpron and Nelson, 2011). Abbreviations: LC, Loverna block conductor; SABC, Southern Alberta – British Columbia conductor; RDC, Red Deer conductor; CDF, Cordillera deformation front; CR, Cross kimberlite field; BBM, Black Butte Minette field.

Profile A in Figure 9.4 is parallel to the strike of the LC and SABC. The SABC has a low resistivity in the range 1-10 Ωm with a depth range 30-90 km. The LC has a higher resistivity than the SABC in the range 3-30 Ωm and is deeper than the SABC (45-120 km). Figure 9.3 shows the Moho depth as determined from the CAT project. It can be seen that the LC is located beneath the Moho in the upper mantle. Profiles B, C, and D show the LC

and SABC in cross sections. The SABC has no obvious dip but the LC dips to the southeast. The horizontal slice at 63 km depth in Figure 9.4 shows the SABC is narrower than the LC (80 km and 120 km, respectively). Because of these significant differences in the two parts of this continuous conductor, they will be discussed as separate conductors in this thesis. The division of the SABC and LC is chosen to be at 51.5° N and 112.3°W.

9.3.2. Comparison with other geophysical studies of these features

The location of the SABC and LC as imaged in the CAB model is close to the location determined by the magnetovariational inversion of Wang (1988a, 1988b). This study modelled the SABC with a width of 70-80 km and in the depth range of 30-90 km to the west of the Rocky Mountain Foothills (details in section 4.6.2). For the part that is east of the Rocky Mountain foothills (coincident with LC in this study), it was imaged to be in the depth range of 70-120 km, i.e., in the mantle.

The location and geometry of the LC in the CAB model is similar to those in the 3-D model of Nieuwenhuis et al. (2014). However, small differences are observed. For example, (1) the RDC imaged in the CAB model is shallower than the one in the model of Nieuwenhuis et al. (2014). (2) The SABC was not imaged to be connected to the RDC in the CAB model. This is different to the model of Nieuwenhuis et al. (2014).

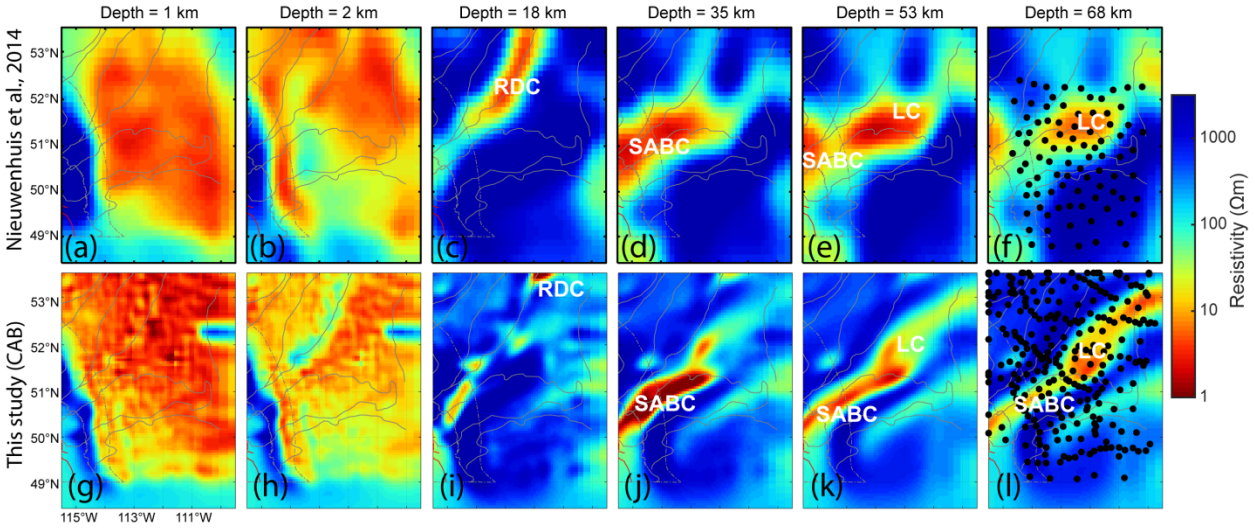

Figure 9.5: Comparison of the CAB model (bottom, g-l) from this study and the 3-D electrical resistivity model of Nieuwenhuis et al. (2014; top, a-f). The gray lines are basement terrane boundaries (Pilkington et al., 2000; Colpron and Nelson, 2011). Black dots in (f) and (l) represent the LMT stations used for the 3-D inversions of Nieuwenhuis et al. (2014) and this study, respectively. Abbreviations: WCSB, Western Canada Sedimentary Basin; SABC, Southern Alberta – British Columbia conductor; RDC, Red Deer conductor; LC, Loverna block conductor.

Moreover, the LC is coincident with a region of anomalous low seismic velocities at a similar depth range (50-150 km) in the Loverna block where the cratonic root was imaged to be more than 300 km thick (Chen et al., 2017; Figure 9.6). In terms of aeromagnetic signature, the Loverna block is moderately magnetic (-100 to 100 nT). The SABC is collocated with a moderately magnetic feature as well and bounded to the south by the Matzhiwin magnetic high anomaly (400 nT; Figure 4.1).

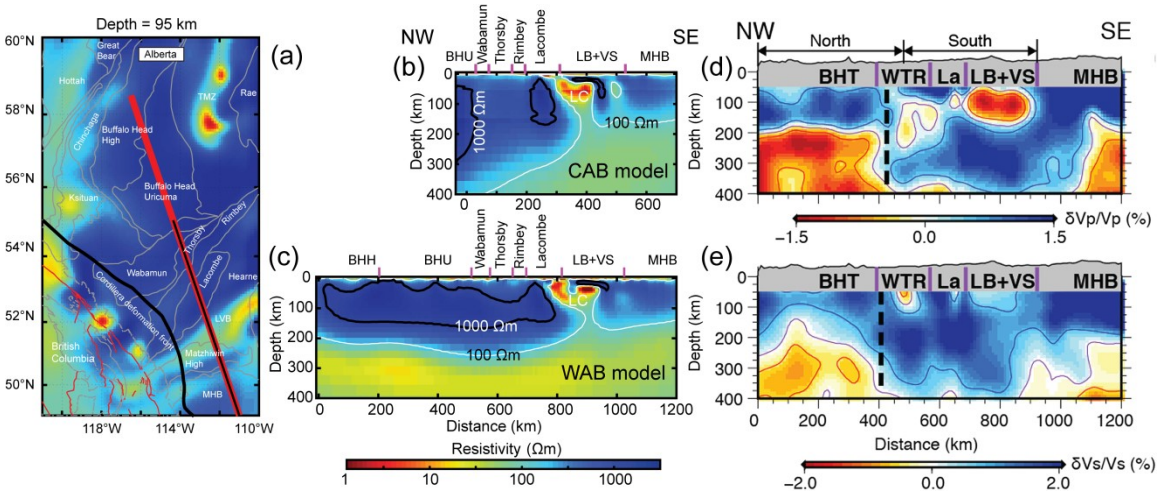

Figure 9.6: Comparison of the 3-D MT resistivity models and the seismic velocity models of Chen et al. (2018). (a) Horizontal slice of the Alberta model (WAB model) at a depth of 95 km. The thin black line shows the location of the profile in (b) as imaged in the CAB model. The red thick line represents the location of the profile shown in (c) as imaged in the WAB model. The red and gray lines are basement faults and terrane boundaries (Pilkington et al., 2000; Colpron and Nelson, 2011). (d) and (e) show the V_p- / V_s- velocity profiles from Chen et al. (2018). Abbreviations: BHH, Buffalo Head High; BHU, Buffalo Head Uricuma; BHT, Buffalo Head terrane (including BHH and BHU); WTR, Wabamun Thorsby Rimbey; La, Lacombe; LB, Loverna block; VS, Vulcan Structure; MHB, Medicine Hat block.

9.3.3. Interpretation of the Loverna block conductor

What is the cause of the low resistivity of the LC? To answer this question, it is necessary to develop a model of resistivity as a function of depth. Key parameters in this model are the temperature of the crust and mantle. A practical model is developed in this section, as outlined below. The geotherms of the LC and SABC were calculated using the method described in Appendix 9 (Figure 9.7b). It is close to the geotherm of Pollack and Chapman (1976) that was based on a surface heat flow of 35 mW/m^2. This is also consistent with the surface heat flow measurement in this region as well (< 40 mW/m^2; Figure 4.6).

To calculate the resistivity predicted for these temperatures, laboratory studies of mineral resistivity were used. If the mantle is assumed to be dry olivine then a resistivity greater than 1000 Ωm is predicted for temperatures in the range 700-1300 ˚C based on the model of Constable, (2006). This is shown in Figure 9.7a where it can be seen that the resistivity of the LC is much lower than the resistivity of dry olivine at mantle depths (Constable, 2006). It is obvious that the properties of the LC cannot be explained by the calculated geotherm and a lithology of just dry olivine. If the upper mantle contains a small fraction of conductive phases, then the resistivity could be much lower. Possible conductive phases include saline fluids, trace hydroxyl ion in nominally anhydrous minerals, partial melt, and interconnected graphite films or sulfides.

Saline pore fluids could be a possible reason for the low resistivity of the LC (Hyndman et al., 1993). However, as proposed for the RDC (section 9.2.3), ancient fluids produced by past tectonic events are unlikely to still be present, since they will be absorbed by metamorphic reactions. Nevertheless, in the case that the fluids are very saline, their thermodynamic water activity may be low enough to inhibit the formation of retrograde hydrous mineral from primary anhydrous minerals. This would potentially prevent all the free fluids from being consumed in hydration reactions. If the fluids have not been fully consumed, 0.1-1 % of porosity is required to produce a resistivity range of the LC (3-30 Ωm), assume the fluids are well-connected (Archie, 1942) and the resistivity of the pore fluids are 0.03 Ωm. On the other hand, it has been suggested that 1% concentration of fluids can reduce the seismic velocity by 10% (Hyndman et al., 1993). This is a little higher than the observation of Chen et al. (2018; 2-3% as shown in Figure 9.6). In summary, saline pore fluids could be a possible reason for the low resistivity of the LC.

Hydrogen (H+) in nominally anhydrous minerals (NAM) is another possible explanation for the low resistivity of the LC. It was suggested that a small amount of hydrogen (H+) can be dissociated and bounded as hydroxyl ions (OH) in nominally anhydrous minerals in the upper mantle (Bell and Rossman, 1992). In the lithospheric mantle, hydrogen can behave as proton and diffuse in mineral lattices. Experiments have concluded that hydrogen content is the most important factor that controls resistivity at lithospheric mantle temperatures and depths (Karato, 1990; Yoshino, 2010; Selway, 2014). On the other hand, high hydrogen content could lower the solidus of mantle minerals and cause partial melting (Hirschmann et al., 2009).

On the basis of data derived from laboratory studies (Karato, 1990; Lizarralde et al., 1995; Bell et al., 2003; Wang et al., 2006; Constable, 2006; Hirschmann et al., 2009; Yoshino et al., 2009), Rippe et al. (2013) developed a method to calculate upper mantle resistivity when hydrogen formed from dissociated water and silicic melt are both present. In order to apply this method, the resistivity profile beneath the LMT stations SAB225 was extracted from the CAB electrical resistivity model (Figure 9.7a).

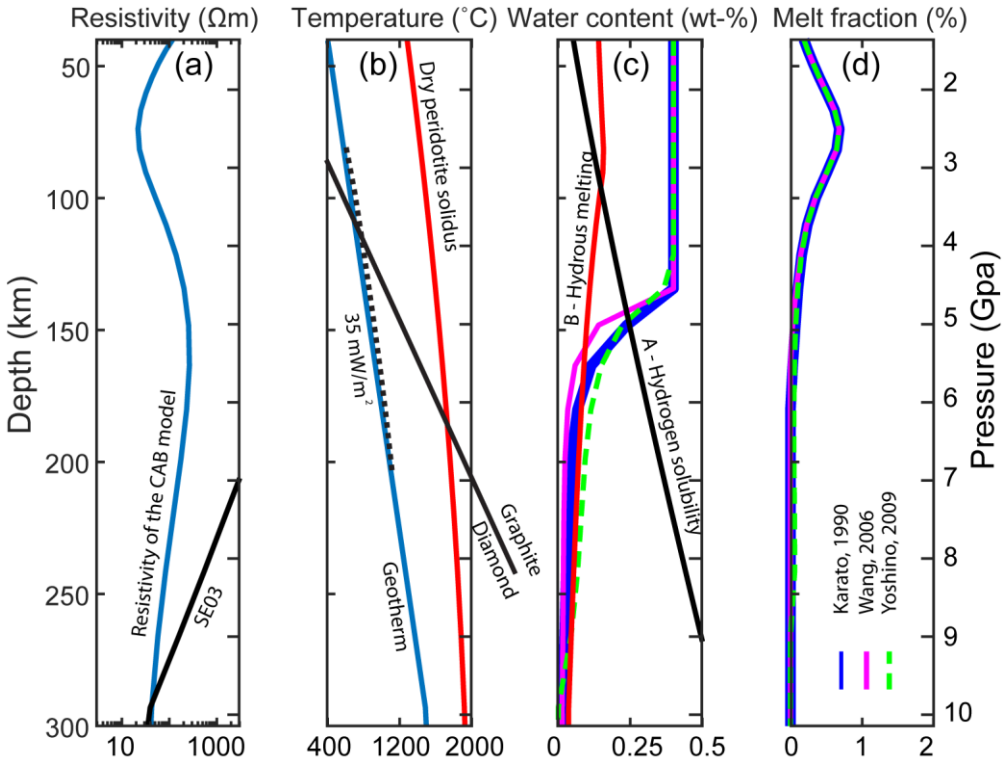

Figure 9.7: The analysis of water and melt content using the method of Rippe et al. (2013). (a): The resistivity profile imaged in the Alberta model beneath the MT station SAB225 (blue line; see the location of SAB225 in Figure 9.5) and the resistivity of dry olivine of model SEO3 (black line; Constable, 2006). The station SAB225 is located above the LC conductor. (b): simplified geotherm, as calculated in Appendix 9 (blue), dry peridotite solidus (red line; Hirschmann et al., 2009), and the 35 mW/m^2 geotherm defined by Pollack and Chapman (1976; dash black line). (c): water content calculated using the methods of Karato (1990, blue dashed line), Wang et al. (2006, magenta line) and Yoshino et al. (2009, green line). The black line (A) represents the hydrogen solubility (Lizarralde et al., 1995; Bell et al., 2003). The red line (B) shows the minimum amount of water required for hydrous melting. (d): the expected melt fraction using the methods of Karato (1990, blue dashed line), Wang et al. (2006, magenta line) and Yoshino et al. (2009, green line). The resistivity of melt used was 0.03 Ωm.

In the method of Rippe et al. (2013), the water content required to produce the low resistivity of the LC was calculated based on laboratory experiments (Figure 9.7c). It should be noted that the mantle mineral composition was assumed to be the same as the one of Proterozoic-age craton suggested by Griffin et al. (2003) and Griffin et al. (2008). This should be suitable considering the Proterozoic metamorphic and metasomatic history of

northern Alberta proposed by Burwash et al. (2000) and Eccles et al. (2010; 2011). Because of the discrepancy between different laboratory experiments, three calculations were done using the published results of Karato (1990), Wang et al. (2006), and Yoshino et al. (2009; Figure 9.7c). For the depth range of 50-150 km, the hydrogen content required is greater than the H+ solubility and thus water alone cannot explain the low resistivity of LC (Figure 9.7c). This is in agreement with the analysis of Nieuwenhuis et al. (2014). For depths greater than 150 km, water alone can explain the resistivity of the mantle of the Loverna block.

It is well established that water greatly reduces the melting point of peridotite (see review in Green et al., 2014 and references cited therein). It is possible that water and melt coexist in certain parts of the mantle. It is necessary to calculate the range of possible melt fractions that can explain the observed resistivity. Melt fraction can be calculated based on the resistivity, temperature, and water content (Figure 9.7d). The maximum hydrogen solubility (line (A) in Figure 9.7c) and the minimum amount of hydrogen required to induce hydrous melting of NAM (line (B) in Figure 9.7c) was plotted to facilitate interpretation (Lizarralde et al., 1995; Bell et al., 2003; Hirschmann et al., 2009). When the water content required is greater than (B) the minimum amount of hydrogen to induce hydrous melting and smaller than (A) the maximum hydrogen solubility, it is possible that hydrous melt is coexist with the water. In this case, the melt fraction was calculated using the modified Archie's Law of Glover et al. (2000) and assuming the water content of (B). The resistivity of the melt was assumed to be 0.03 Ωm as was used in Rippe et al. (2013). The melt fraction calculated should be the maximum amount required to produce the resistivity value observed (Rippe et al., 2013). Therefore, in the case when both water and

melts exist, two extreme scenarios can be expected: (1) the minimum amount of water required by the conductor should be same as (B) in Figure 9.7c and (2) the maximum amount of melt required by the conductor should be the ones shown in Figure 9.7d.

For the depth range of 50-100 km (Figure 9.7), the hydrogen concentration required to produce hydrous melting is higher than the hydrogen solubility. This means that no hydrous melting could occur for this depth range. For the depth range of 100-150 km, the hydrogen solubility is larger than the water content required hydrous melting, thus, hydrous melting could be possible. In this case, a combination of water and melt could explain the low resistivity of the LC. The minimum water content is same as the line (B) in Figure 9.7c (0.1-0.2 wt-%). The maximum melt fraction required is shown in Figure 9.7d (0.05-0.3%). For the depths greater than 150 km, no melt exists because the water content is less than the amount required to produce hydrous melting (line B).

The calculations described above demonstrate that neither H+ nor partial melt can explain the low resistivity of LC at the depth range 50-100 km. This is in agreement with previous studies that showed that the resistivity of the LC could not be explained by either melt or H+ (Boerner et al., 2000; Nieuwenhuis et al., 2014). They argued that if melt exists in the depth range of the LC, anomalous surface heat flow should be observed. However, the whole Loverna block is characterized by the lowest heat flow in Alberta (Figure 4.6).

Other conducting phases such as graphite or sulfide minerals should be considered to explain the low resistivity of the LC in the depth range 50-100 km. Boerner et al. (1999) suggested that hydrous minerals (phlogopite) or graphite could explain the low resistivity of the LC. The formation of hydrous minerals, sulfides and graphite could be related to

metasomatism of the upper mantle of the Churchill province caused by subduction during the Paleoproterozoic terrane assembly (details in section 3.3.3). It has been proposed that mantle conductors are strongly connected with episodes of mantle metasomatism and electrical resistivity of the mantle can be a proxy for the level of enrichment in incompatible elements of the lithosphere (Selway, 2014). The Hearne province was proposed to be trapped in a tectonic vice between two subduction zones ca. 1.85-1.78 Ga in a collisional plateau setting (Ross, 2002; Chen et al., 2017). It was proposed that in the northwest, southeastward-directed subduction occurred along the STZ while in the east, eastward subduction occurred along the Trans-Hudson Orogen. The SAREX seismic refraction project imaged two slabs beneath southern Alberta that were proposed to be subducted oceanic slabs of the Wyoming province and Medicine Hat block from the south in Neoarchean age (Figure 9.6; Gorman, 2002). All previous studies have demonstrated that the Hearne province has undergone episodes of mantle metasomatism which could have enriched the mantle with conducting phases and formed the LC.

Phlogopite veins were found in xenoliths from Eocene minettes of the Wyoming province in central Montana (Brien et al., 1995). Furthermore, phlogopite is also considered to be stable at upper mantle depths (0-180 km; Bell and Rossman, 1992). Chen et al. (2009) showed that regions of collocated low velocity and low electrical resistivity are observed at 100 km depth beneath the Slave craton with phlogopite and graphite. Therefore, similar explanations could be used in the Loverna Block because the LC is coincident with a region of low P-velocities in the depth range of 50-150 km (Chen et al., 2017).

Phlogopite is a type of mica. It has been shown by laboratory study that the electronic conduction of mica is via a hopping process (Dawy, 2002), which is the same the conduction mechanism as for H+ in NAM. The maximum H+ content in NAM is shown in Figure 9.6c. The hypothesis that phlogopite is an explanation for the low resistivity is supported by a range of laboratory studies that investigated the resistivity of phlogopite. Li et al. (2016) reported low resistivity for phlogopite with values of 1 Ωm at 900 ˚C. In contrast, Chen et al. (2009) claimed that experimental results showed that phlogopite could only produce a minimal reduction in resistivity. In agreement with Chen et al. (2009), Nieuwenhuis et al. (2014) suggested that graphite films and sulfide minerals were the preferred explanation for the low resistivity of LC, and suggested that phlogopite was unlikely as an explanation for the low resistivity of the LC. If there is phlogopite in the mantle of the Hearne craton, the maximum H+ content is around 0.2 weight % at depths < 180 km (Bell and Rossman, 1992). This amount of H+ is still less than the concentration required to produce the observed resistivity of the LC. Therefore, phlogopite may contribute to the low resistivity of the LC in the depth range 50-180 km. However other conducting phases such as graphite or sulfides are also required to produce the observed low resistivity.

Graphite films are unstable at a temperature > 700 ˚C (Yoshino and Noritake, 2011) corresponding to a depth of 120 km in the geotherm shown in Figure 9.6b. Therefore, graphite films could explain the low resistivity of the LC in the depth range 50-120 km. According to Archie's Law, a concentration of 0.01% of well-connected graphite films can explain the observed resistivity of 1 Ωm, assuming pure graphite has a resistivity of 0.0001 Ωm. Selway (2014) stated that low electrical resistivity anomalies due to sulfides should be

limited to discrete, small-scale features. This was because even though sulfides can exist in the mantle and crust, they are not volumetrically abundant and will not be inter-connected at depths greater than the uppermost mantle (Selway, 2014).

In summary, for the LC in the depth range of 50-100 km, graphite films can explain the low resistivity of the LC. Phlogopite may contribute to the low resistivity of LC but couldn't explain the LC by itself. For the depth range of 100-150 km, H+ alone cannot explain the LC and a small fraction of basaltic melt (< 0.3%) was needed as shown in Figure 9.6c&d. Low seismic velocities have been observed in the Loverna block at the depth range 50-150 km, which was interpreted to be caused by hydrous minerals and mantle enrichment (Chen et al., 2018). This seismic observation is consistent with the interpretation of the LC which suggests phlogopite and melt could exist at the depth range 50-150 km as described above. Moreover, graphite films are not stable at depths greater than 120 km and thus cannot explain the LC for this depth range. At greater depths (>150 km), H+ in NAM alone can explain the resistivity of the Hearne province.

9.3.4. Interpretation of the SABC

The SABC in Alberta in the CAB model is a narrower, shallower and more conductive (1-10 Ωm) feature than the LC, which suggests different origins for the two conductors. Saline pore fluids can be a reason for the low resistivity of the SABC as discussed for the LC. The SABC is more conductive than the LC, and thus the porosity required is higher (0.3-3 %). The porosity of 3% which would produce the resistivity value of 1 Ωm is too much high which means other conducting phases should be considered. Magnetite can be excluded to explain the low resistivity of the SABC since the SABC is only moderately

magnetic. However, other iron oxides (such as hematite) or sulfides may be the reason for the low resistivity of the SABC. Because they are electrically conductive (Pearce et al., 2006) and their magnetic susceptibility is low.

Hydrogen in nominally anhydrous minerals can also be excluded as the cause of the low resistivity. This is because the SABC is located very close to the LC and characterized with similar surface heat flow values which mean that the temperatures of the two should be similar. Thus, it is impossible to explain the low electrical resistivity of the SABC using hydrogen diffusion without exceeding the hydrogen solubility as discussed for the LC in the depth range 50-100 km. Phlogopite can produce low resistivity also as discussed for the LC. In this case, coincident anomalous seismic velocities should be observed because phlogopite is characterized by a low seismic velocity. However, in the seismic P-wave velocity of Chen et al. (2017), no anomalous low velocities were observed at the same location of the SABC. Therefore, phlogopite can probably be excluded as a possible reason for the low resistivity.

Partial melt can also be excluded as the reason for the SABC for the same reason as the LC in the depth range 50-100 km. The only remaining explanation for the low resistivity of the SABC in Alberta is grain-boundary graphite films. As calculated for the RDC in section 9.2, a volume fraction of 0.01% of grain-boundary graphite films can produce the bulk resistivity of 1 Ωm. The SABC in southeast British Columbia is within the region of Cordilleran deformation and therefore different mechanism may exist to cause the low resistivity. The focus of this thesis is about the Precambrian basement of Alberta and thus the part of the model relevant to the subsurface of British Columbia will not be discussed. However, the westward extension of the SABC suggests that the Precambrian basement

extends west of the Cordillera deformation front. This is supported by (1) a mantle xenolith study of the Cross kimberlite field (Canil, 2003; see location in Figure 9.9, 9.12 and 9.13). The thickness of the southwest Hearne lithosphere in the Cross kimberlite field is up to 200 km and is Proterozoic instead of Archean (Canil, 2003). (2) Exposed Laurentian basement rocks were observed by surface geology within the Omineca belt of the southern Canadian Cordillera which is at the location of 117˚W-118˚W and 51.5˚N-52.5˚N (Kuiper et al., 2014).

In summary, evidence from seismic and MT observations suggested extensive deformation and episodic metasomatic history of the uppermost mantle of the Hearne craton. Phlogopite, iron oxides, sulfides, or graphite films originated from metasomatism processes are possible phases that could lower the resistivity of the uppermost mantle of the Loverna block. The SABC in Alberta is connected to the LC. However, the preferred explanation for the low resistivity of the SABC in Alberta is graphite, iron oxides or sulfides.

9.4. The Kimiwan conductor (KMC)

9.4.1. Structure imaged in the WAB inversion model

The Kimiwan conductor (KMC) is imaged in the WAB inversion model with a resistivity in the range 10-30 Ωm and depth extent from just below the sedimentary basin to the lower crust at a depth of 35 km (Figure 9.8). It is located at the southern boundary of the Buffalo Head and Chinchaga terranes and extends for a total horizontal length of 200 km.

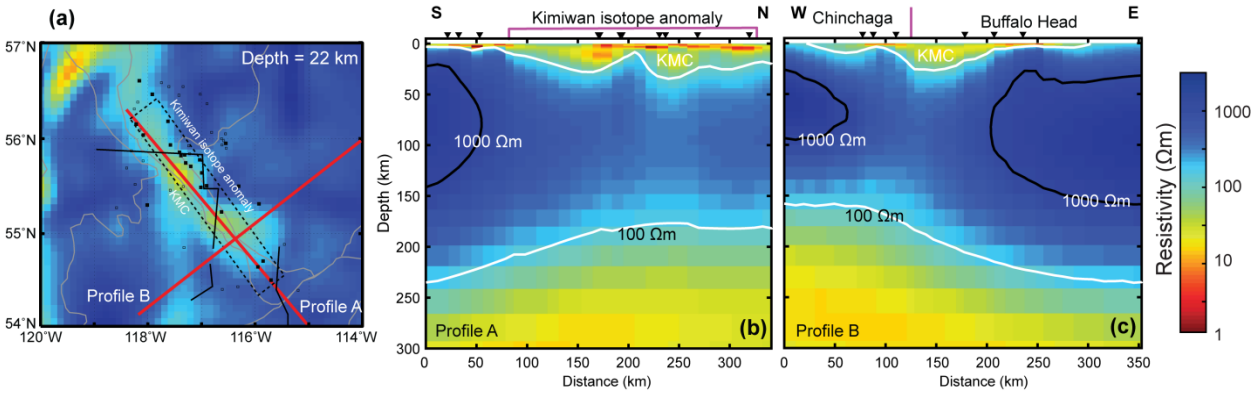

Figure 9.8: Plots of the Kimiwan conductor (KMC) as imaged in the WAB 3-D inversion model. (a): Horizontal slice of the WAB model at a depth of 22 km. The box with dashed lines shows the location of the Kimiwan oxygen isotope anomaly (Burwash et al., 2000). The black solid lines are the locations of Lithoprobe seismic reflection profiles (Bouzidi et al., 2002). The black open and filled squares are the location of the normal and anomalous $\delta^{18}O$ samples around the Kimiwan O-isotope anomaly, respectively. The gray lines are terrane boundaries (Pilkington et al., 2000). The red solid lines show the location of profiles A and B chosen to show the vertical extent of the Kimiwan conductor in figure (b) and (c).

9.4.2. Comparison with other geophysical data

The KMC is coincident with the Kimiwan oxygen isotope anomaly (KIA; Burwash et al., 2000; Figure 9.8), and the Kimiwan aeromagnetic high (Figure 4.1). Lithoprobe seismic reflection profiles crossed the Kimiwan isotope anomaly in several locations (Ross and Eaton, 2002; Figure 9.9). Fault structures at upper crustal depths imaged in the Lithoprobe profiles were associated with the Kimiwan isotope anomaly (Burwash et al., 2000; Figure 9.9).

9.4.3. Interpretation of the KMC

It has been proposed that the KIA was generated in an extensional tectonic setting. Fluids of meteoric origin interacted with rocks at relatively high-temperature (300-550 ˚C) at ~ 1.8 Ga to produce the O-isotope anomaly. This happened > 200 Myr after the original

crystallization of rocks of the Kimiwan area and before the deposition of rocks of the WCSB and the emplacement of the Winagami reflection sequences. The extension in the KIA was suggested to be related to regional tectonic events such as the closing of the Thorsby basin during the East Alberta Orogeny (Ross, 2002) and the Trans-Hudson Orogeny (Burwash et al., 2000; Corrigan et al., 2009).

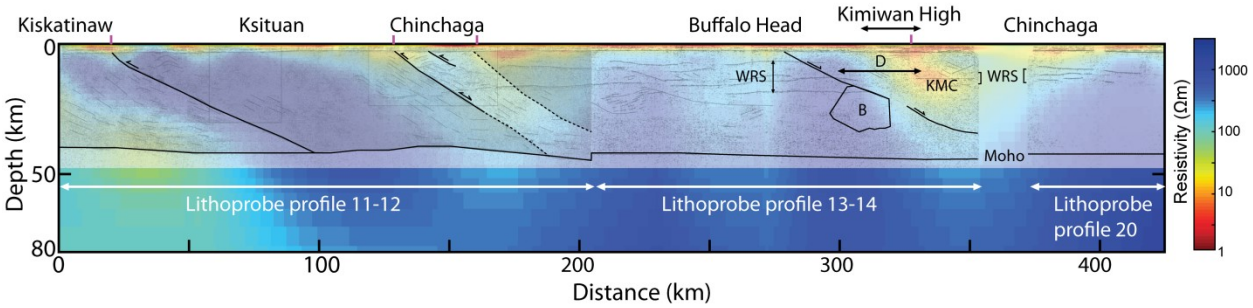

Figure 9.9: The Alberta 3-D inversion model compared with the Lithoprobe profiles 11-14 and 20. Black lines represent the major faults defined by (Ross and Eaton, 2002). Zone B and D were defined in Hope and Eaton (2002). D: a zone of disruption where the Winagami reflection sequence (WRS) is disturbed. B: a blank zone which may represent a plutonic body or a fault shadow zone. KMC represents the Kimiwan conductor.

The low resistivity of the KMC can be explained in the geological setting described above. The circulation of hot water in the KIA that generated the low $\delta^{18}O$ values of the rocks could have also deposited conducting minerals phases such as graphite, sulfides minerals or iron oxides such as magnetite or hematite. The mineral phases could be the by-product of retrograde metamorphism in KIA and moved along the fluid pathways, forming well-connected conductive films. Because the KMC is collocated with an aeromagnetic high anomaly, magnetite is the preferred candidate because of its high magnetic susceptibility and low electrical resistivity. Connected magnetite precipitated in mafic intrusions has been proposed to explain two low resistivity anomalies of the Vøring Plateau in Norway and the Exmouth Plateau in Australia (Myer et al., 2013). The resistivity of pure magnetite

can be as low as 10^{-4} Ωm (Myer et al., 2013). Using the Archie's Law, 0.001% of well-connected magnetite could explain the low resistivity of the KMC. However, this doesn't exclude the possibility of other conductive minerals. Without xenolith samples it is hard to determine if the magnetite is connected or not. Therefore, in the case that the magnetite is not connected, other conductive minerals (graphite, hematite, sulfides) could be responsible for the low resistivity of the KMC. It has been proposed by Frost et al. (1989) that magnetite and graphite can be formed during cooling by reduction of a CO_2-rich fluid. The resistivity of pure graphite is similar to magnetite and a concentration of 0.001% of grain-boundary graphite films can produce the low resistivity observed in the KMC.

On the other hand, the fault systems around the KMC could be the conduit that allows fluids originating at the surface to circulate at depth. A volume fraction of 0.1% - 0.3% well-connected saline fluids with 0.03 Ωm resistivity could explain the 10-30 Ωm resistivity of the KMC.

In summary, I attribute the existence of KMC to magnetite, grain-boundary graphite films, sulfides or saline pore fluids. High-temperature fluids circulation at ca. 1.8 Ga proposed to explain the KIA may have deposited magnetite/graphite along the grain boundaries at the same time. The well-connected magnetite/graphite/sulfides can explain the low resistivity of the KMC and the coincident Kimiwan aeromagnetic high. Moreover, saline fluids in the fault fractures observed on seismic profiles can be another possible reason for the KMC.

9.5. The Kiskatinaw conductor (KC)

9.5.1. Structure imaged in the WAB inversion model

The Kiskatinaw conductor (KC) is imaged in the 3-D WAB model close to the Kiskatinaw terrane at depths of 10-40 km (Figure 9.10). Its resistivity is in the range 10-100 Ωm. The KC was imaged in the 2-D inversion model described in Chapter 6. In the 3-D WAB model, it is not located exactly underneath the Kiskatinaw terrane as was the case in the 2-D model (Figure 9.10b&c). Moreover, its dip angle changes gradually from 45˚ to the east at the south end to almost vertical at the north end (Figure 9.15).

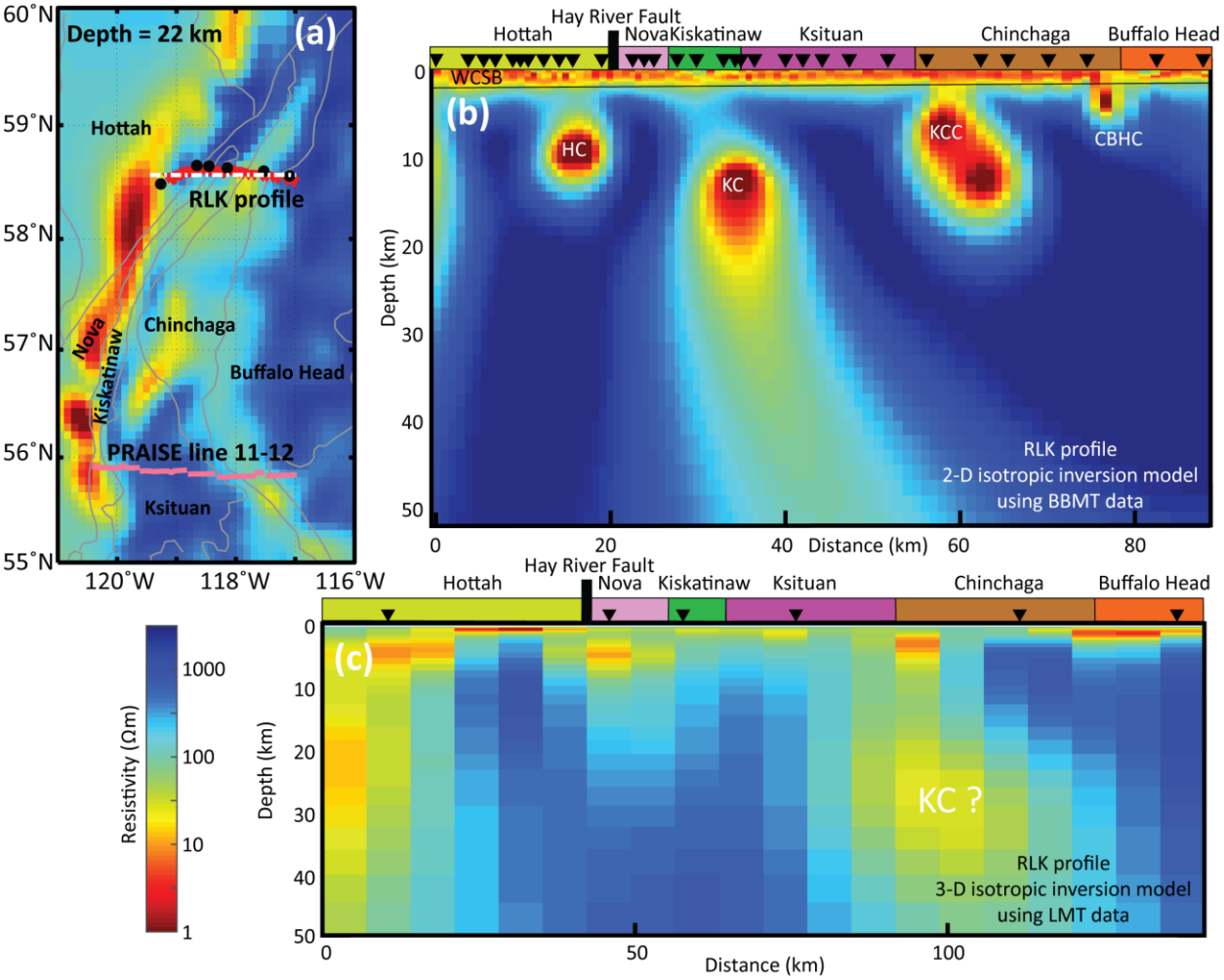

Figure 9.10: Plots of the Kiskatinaw conductor (KC) imaged in the Alberta 3-D inversion model and the 2-D inversion model of Chapter 6. (a): Horizontal slice of the Alberta 3-D inversion model at the depth of 22 km. The location of long-period MT stations (LMT) used in the 3-D inversion is shown with black dots. The red line represents the closely located broadband MT stations (BBMT) used in the 2-D inversion. The location of the Rainbow Lake (RLK) profile is indicated with the white dashed line. PRAISE lines 11-12 that crossed the KC at the south are also shown with pink lines. A profile subtracted from the Alberta 3-D inversion model along lines 11-12 is shown in Figure 9.9. The gray lines are terrane boundaries (Pilkington et al., 2000). (b): 2-D resistivity model along the RLK profile using BBMT. WCSB, Western Canada Sedimentary Basin; HC, Hottah conductor; KCC, Ksituan-Chinchaga conductor; CBHC, Chinchaga-Buffalo Head conductor. (c): Resistivity structure along the RLK profile subtracted from the Alberta 3-D inversion model using LMT.

9.5.2. Comparison with other geophysical data

A profile across the Kiskatinaw terrane was extracted from the 3-D WAB electrical resistivity model along the seismic PRAISE project line 11-12 (Figure 9.9). It can be seen that the dip angle of the conductive-resistive boundary near the Kiskatinaw terrane imaged in the MT model is similar to that of the subsurface boundary of the Kiskatinaw and Ksituan terranes imaged in the seismic reflection result, even though the location of the two boundaries do not exactly coincide.

Further to the north (58.5°N), a profile coincident with the broadband MT stations (RLK profile; Chapter 6) was extracted from the 3-D WAB model (Figure 9.10c). It can be seen that only one conductor is imaged in the 3-D WAB model while there are four distinct conductors imaged in the 2-D inversion model of the RLK profile. Nevertheless, both 2-D and 3-D models indicate that the conductor dips to the east.

This difference between the 2-D and 3-D MT inversion models is expected. Because sparsely-spaced long-period MT (LMT) data were used in the 3-D inversions while closely-spaced broadband MT (BBMT) data were used in the 2-D inversions of the RLK profile. It was shown in the 2-D synthetic inversion study of the RLK profile in Chapter 6 that only one conductor can be imaged when the location and period range of LMT data is used in the synthetic modeling. In contrast, when the location and period range of BBMT data was used in the synthetic modelling, four conductors could be identified. This is because the LMT data are not sensitive to shallow structures (depth < ~ 3 km according to skin depth equation) and the LMT stations in this region are quite widely spaced. The same reasons

could explain the difference between the MT and seismic results on the southern profile along the PRAISE lines 11-12.

9.5.3. Interpretation of the KC

It has been stated in Chapter 6 that the upper- and mid- crustal electrical resistivity structures beneath the profile of Project 1 are believed to be 2-D. The lower crust at this location shows some 3-D features. Therefore, the 2-D MT inversion model is considered to be valid for depths smaller than 30 km. The electrical structure of the KC is best imaged in the 2-D MT inversion model of the RLK profile and a detailed interpretation of the KC can be found in Chapter 6. However, the 3-D Alberta model complemented the 2-D inversion results and showed that the KC is a linear structure located close to the Kiskatinaw terrane. Moreover, the KC was imaged in seismic reflection study and 2-D and 3-D MT models to dip to the east. The comparison between the 2-D BBMT and 3-D LMT results also shows the importance of the period range and spatial coverage of MT data in the recovery of subsurface resistivity structures. The low resistivity of the KC can be explained by interconnected grain boundary graphite or sulfide phases deposited by metamorphic fluid migration as discussed in Chapter 6.

9.6. The Birch Mountain field conductor (BMC)

9.6.1. Structure imaged in the WAB inversion model

The Birch Mountain field conductor (BMC) is located in the Taltson magmatic zone in the depth range of 100-250 km (Figure 9.11). It dips towards the southwest and is characterized by resistivity values in the range 3-10 Ωm. A few small crustal low resistivity

anomalies can be observed above the BMC. However, because the MT station distribution in this area is very sparse, the shallow conductors are poorly constrained by the data and will not be discussed.

It has been demonstrated by synthetic modelling in section 8.3.1 and Figure 11.5 that a low resistivity body in the location of the BMC could be an artefact due to the irregular lateral distribution of the MT stations and geometry of the WCSB (section 8.3.1). However, the resistivity value of the BMC (<10 Ωm) in the WAB model is much lower than the one imaged in the synthetic modelling (<100 Ωm) of Figure 11.5. Moreover, the model editing test of the BMC showed that the BMC is required by the MT stations nearby (Figure 8.9). Therefore, the BMC may not be an artefact, but a required feature of the WAB model.

9.6.2. Comparison with other geophysical studies

The BMC is located close to the Birch Mountain kimberlite field (diamonds in Figure 9.11). Moreover, anomalously low P-/S- velocities (-2% perturbation) in the depth range of 75-300 km were observed at the same location of the BMC (Chen et al., 2018; Figure 9.11). No anomalous features in the potential field data and geothermal regime were observed at the same location.

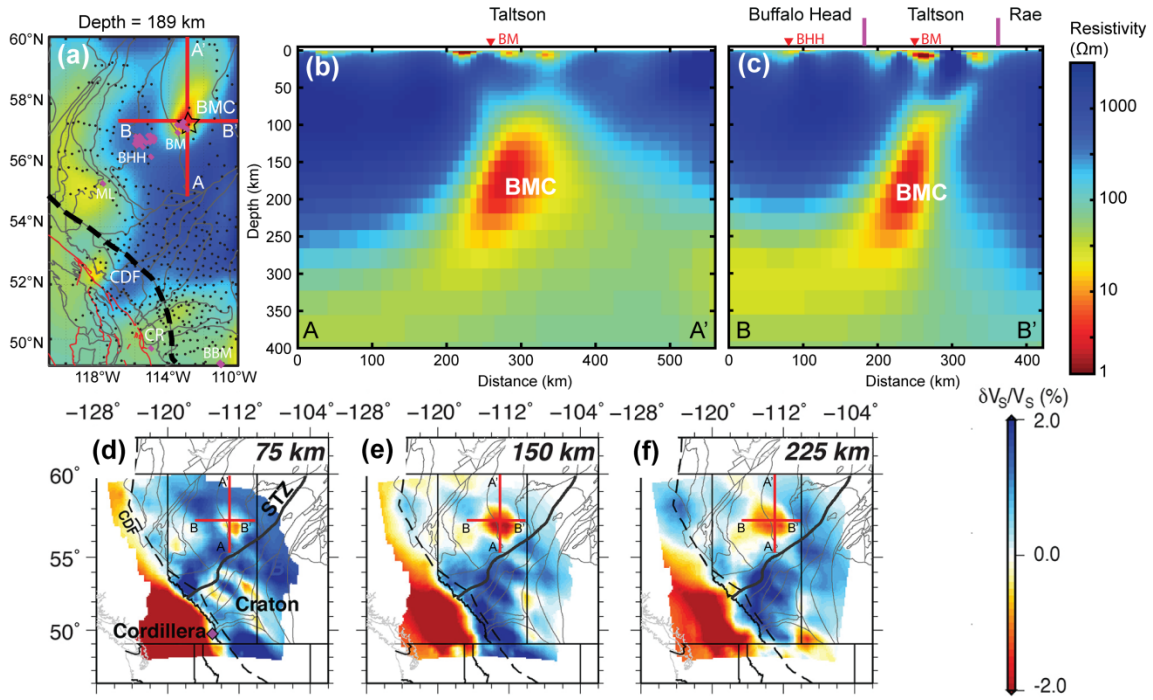

Figure 9.11: Details of the WAB model around the Birch Mountain field conductor (BMC). (a) Horizontal slice at 189 km depth. Purple and white diamonds represents the occurrence kimberlite pipes/ultrabasic rocks (Open Data Portal – Alberta Geological Survey, 2018). Black dots are the locations of MT stations used in the WAB inversion. Thick red lines are the location of the two profiles shown in panels (b) and (c). The gray lines are basement terrane boundaries (Pilkington et al., 2000; Colpron and Nelson, 2011). Red thin lines show the location of faults in southeast British Columbia. Thick black dashed line represents the Cordillera deformation front (CDF). The star marks the location of the MT station LAB010 whose resistivity profile is used in Figure 9.12. (b) Profile along latitude of 57.5˚N. The purple bars in (b) and (c) are the basement terrane boundaries. (c) Profile along longitude of 113˚W. Triangles on top of the profiles show the location of kimberlite fields near to the profile. Figure (d), (e), (f) show the shear velocity model of Chen et al. (2018) at various depth-slices. The low velocity anomaly is at the same location as the BMC. Abbreviations: BHH, Buffalo Head Hills kimberlite field; BM, Birch Mountains kimberlite field; ML, Mountain Lake kimberlite field; CR, Cross kimberlite field; BBM, Black Butte Minette fields; BMC, Birch Mountain field conductor; STZ, Snowbird tectonic zone.

9.6.3. Interpretation of the BMC

What could be the reason for the low resistivity of the BMC? Free saline pore fluids can be a possible reason. As have been discussed for the LC, 0.3-1 % of porosity is required to produce the low resistivity of the BMC (3-10 Ωm) according to Archie's Law. It has been

proposed that difference in iron content cannot produce significant electrical resistivity contrast in the mantle depths since the variation is very small (Selway, 2014). The large size of the BMC excludes the possibility of sulfides as a reason because sulfides were claimed to be small-scale features only (Selway, 2014).

In regards to graphite films, they are unstable at temperature > 700 ˚C (Yoshino and Noritake, 2011). In order to determine if graphite could be the cause of the low resistivity of the BMC, it is necessary to determine the local geotherm. The geotherm for northern Alberta have been derived from both geothermal studies in boreholes and from geothermobarometry studies of xenoliths and xenocrysts. The geothermal study of Majorowicz (2016) presented studies of temperatures in the Hunt well at Fort McMurray, located near to the BMC. Heat flow in the well was 55 mW/m2 which can be used to estimate a temperature of 700 ˚C at a depth of 100 km. Independent information comes from another geotherm defined from garnet thermobarometry in the Buffalo Head Hills kimberlite field yield 1000 ˚C at 4.8 GPa, corresponding to ~140 km depth (Aulbach et al., 2004). A heat flow of ~40 mW/m^2 was estimated for the mantle beneath the Buffalo Head Hills kimberlite field (Aulbach et al., 2004). This is in agreement with the thermobarometry result of Eccles et al. (2004), in which xenoliths and xenocrysts from the three kimberlite fields of north Alberta were studied (the Mountain Lake cluster, the Birch Mountain field, and the Buffalo Head Hills field). Therefore, graphite film will not be interconnected at depths greater than 100 km and not able to produce a low resistivity. Graphite may explain the low resistivity of the BMC for depths less than 100 km but cannot explain the low resistivity of the BMC at greater depths.

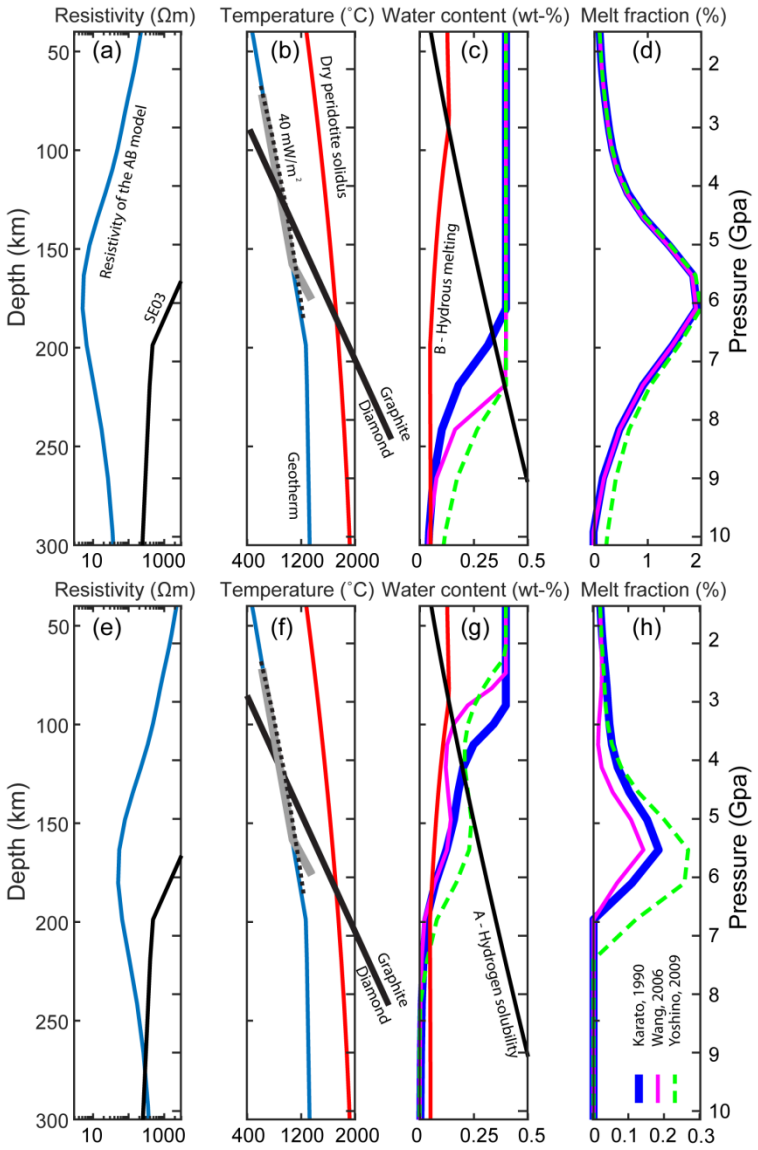

Figure 9.12: The analysis of water and melt content of the BMC using the method of Rippe et al. (2013). (a): The resistivity profile imaged in the Alberta model beneath the MT station LAB010 (blue line) and the resistivity of dry olivine of model SEO3 (black line; Constable, 2006). The station LAB010 is located on the top of the BMC conductor (see its location in Figure 9.11). (b): simplified geotherm calculated (blue), dry peridotite solidus (red line; Hirschmann et al., 2009), the geotherm defined from xenolith studies (gray line; Aulbach et al., 2004), the 40 mW/m^2 geotherm defined by Pollack and Chapman (1976; dash black line).(c): water content calculated using the methods of Karato (1990, blue dashed line), Wang et al. (2006, magenta line) and Yoshino et al. (2009, green line). The black line (A) represents the hydrogen solubility (Lizarralde et al., 1995; Bell et al., 2003). The red line (B) shows the minimum amount of water required for hydrous melting. (d): the expected melt fraction using the methods of Karato (1990, blue dashed line), Wang et al. (2006, magenta line) and Yoshino et al. (2009, green line). The resistivity of melt used was 0.03 Ωm. (e)-(h): the same calculations except that the resistivity profile of station LAB010 is multiplied by 10.

In order to apply the method of Rippe et al. (2013) to the BMC, the resistivity profile of MT station LAB010, which is located on the top of the BMC, was extracted from the WAB inversion model (Figure 9.12a). Moreover, because in the synthetic tests, the resistivity of the locality of the BMC was observed to be reduced by a factor of 10 due to the coverage of the WCSB and the uneven distribution of MT stations around the BMC. The resistivity profile of LAB010 was multiplied by 10 to accommodate the discrepancy (Figure 9.12b) and calculation based on this is shown along with the original result of the Alberta inversion model.

The geotherm for the BMC was calculated using the method described in Appendix 8 (Figure 9.12b). It is close to the 40 mW/m^2 geotherm of Aulbach et al. (2004) calculated from xenolith thermobarometry. Using the resistivity and temperature profile of LAB010, the expected water content was calculated (Figure 9.12c).

In Figure 9.12c, the H+ content exceeds the solubility limit in the depth range 50-90 km. This means that H+ alone cannot explain the BMC. Because the H+ content required to induce hydrous melting (B) is larger than the water solubility (A), there should be no melt at all in these depths. Therefore, for the depth range of 50-90 km, other conducting phases such as graphite are required (in addition to H+) to explain the low resistivity of the BMC. (2) The amount of H+ required in the depth range 90-200 km is greater than the solubility limit and thus H+ alone cannot explain the low resistivity of the BMC in this case. A maximum melt fraction of ~2% in the mantle was calculated to explain the low resistivity of the BMC (Figure 9.12d). This amount of melt is very high for an old, cold craton. The melt

fraction proposed for the explanation of the low resistivity in the tectonically active southern Canadian Cordillera was only 1.5 %. (3) In the depth range 200-300 km, water can explain the low resistivity of the BMC but partial melt could also be present.

In Figure 9.12g, (1) in the depth range 40-90 km, H+ and graphite could explain the low resistivity of the BMC as discussed for Figure 9.12g. (2) The concentration of H+ required at depths of 90-220 km is less than the H+ solubility (line (A) in Figure 9.12) and greater than the H+ content required to induce hydrous melting (line (B) in Figure 9.12). This means that H+ and melt could coexist. The minimum amount of H+ is equal to (line (B) in Figure 9.12; 0.1-0.25 wt-%) and the maximum amount of partial melt (< 0.3%) should be same as shown in Figure 9.12h. (3) For the depths range 220-270 km, the water required is less than the H+ content required to induce hydrous melting (line (b) in Figure 9.12), which means no hydrous melt can be present and H+ alone (< 0.5%) can explain the BMC. (4) For the depths of 270-300 km, the resistivity is smaller than the one of dry olivine as shown in Figure 9.12e; therefore, no H+ or melt is required.

Comparing the two results in Figure 9.12, it is believed that the result with increased resistivity is more reliable. Because (a) the synthetic modeling and inversion indicated lower resistivity imaged in this location than the original model; (b) lower melt fraction required in Figure 9.12h that is more plausible for Precambrian craton that has been stable for almost 1.8 Byr.

It should be noted that the melt composition was assumed to be basaltic in the method of Rippe et al. (2013). However, the solidus of nominally anhydrous, carbonated peridotite was proved to be much lower than the solidus of volatile free peridotite

(Dasgupta and Hirschmann, 2010). If there were carbonates in the depth range of the BMC, then carbonatite melts could be the reason for the observed low resistivity of the BMC. Carbonatites are believed to be derived from the mantle (Jones et al., 2013). It has been demonstrated that the electrical resistivities of molten carbonates are three orders of magnitude lower than molten silicates (Gaillard et al., 2008). Thus, much less carbonatitic melt will be required to produce the BMC than silicate melt as discussed using the method of Rippe et al. (2013). Therefore, carbonatite melts can be another candidate for the explanation of the BMC.

What could be the origin of water or melts predicted to be the cause of low resistivity in the BMC? Is there a genetic relationship between the kimberlite fields nearby and the BMC? Why is a conductor imaged underneath the Birch Mountain kimberlite field but not underneath the Buffalo Head Hills kimberlite field? In a cratonic setting, such as the western Laurentia, the lithosphere is generally characterized by olivine with a high Mg content and depleted in iron and water, which explains its longevity (Canil, 2008). It has been proposed that compositional variations due to metasomatism (such as hydrous or carbonate minerals) instead of variations in major-element composition could be the reason for seismic velocity changes of the mantle (Eeken et al., 2018). This idea can be applied to the BMC, which is coincident with low seismic S- and P- velocity anomalies (Chen et al., 2018). It was suggested that the low velocity anomalies are caused by enrichment of the mantle by subduction-related melt interaction. The consequent fertilization of the mantle lithosphere and increase of temperature caused by higher content of radioactive elements (such as potassium) could explain the observed seismic anomalies (Eccles, 2011; Chen et al., 2018).

Metasomatism during mantle enrichment can be the cause of mantle conductors because of the emplacement of incompatible elements such as hydrogen and carbon (Selway, 2014). It has been proposed that the mantle beneath northern Alberta had undergone significant metasomatic alterations and is relatively heterogeneous (Eccles et al., 2004; Burwash et al., 2000). The metasomatic events could have introduced more incompatible elements into the mantle beneath the Birch Mountains kimberlite field than beneath the Buffalo Head Hills kimberlite field.

In terms of the heterogeneity, it was demonstrated by the petrogenetic study of Eccles et al. (2004) that the Buffalo Head Hills kimberlite field is geochemically more depleted than the Birch Mountains kimberlite field. The latter is characterized by higher concentrations of incompatible-element-enriched minerals (such as carbonates and phlogopite). Specifically, it has been shown that the amount of phlogopite in the Birch Mountain kimberlite field pipes varies from zero to a maximum of 40 % by volume (Eccles et al., 2004). Phlogopite is a hydrous mineral that was suggested to be electrically conductive (Li et al., 2016) and stable at the depths of 0-200 km (Bell and Rossman, 1992). It can also reduce seismic velocity significantly (Rader et al., 2015). A volume fraction of 10-15% of phlogopite could reduce the seismic velocity by 5% as observed in the study of Chen et al. (2018). These lines of evidence show that the Birch Mountains kimberlite field is more enriched with water than the Buffalo Head Hills kimberlite field. The absence of mantle conductor beneath the Buffalo Head Hills kimberlite field could be caused by the depletion of incompatible elements.

9.7. The Snowbird Tectonic zone

The Snowbird tectonic zone (STZ) was defined by aeromagnetic and gravity anomalies and is a feature that extends for a distance of 2800 km from Hudson Bay to the Foothills of the Rocky Mountains in southwest Alberta (Ross, 2002). The STZ marks the boundary between the Rae and Hearne cratons of the Canadian Shield (Hoffman, 1988). In Alberta, the Thorsby domain is considered to be a splay of the STZ because its aeromagnetic low signature is continuous with the STZ to the east. The Thorsby domain is also coincident with a linear gravity gradient (Villeneuve et al., 1993). In Alberta, the STZ separates the Archean Hearne craton from the Proterozoic terranes to the north. The STZ in Alberta was interpreted to be a Paleoproterozoic subduction zone (Ross, 2002) while the STZ in the Canadian Shield was interpreted as Archean or Paleoproterozoic subduction zone or intra-continental shear zone (Hanmer, 1995; Jones et al., 2002; Mahan and Williams, 2005; details in section 3.3.1).

9.7.1. STZ structure imaged in the WAB inversion model

The STZ imaged in the WAB model is very resistive (300-3000 Ωm; Figure 9.13 & 8.1). A couple of moderately low resistivity anomalies of 300 Ωm are imaged at crustal depths; however, due to the limitations of the MT data coverage, they will not be discussed here. The STZ is imaged with a deep high resistivity root and extends westward into the Cordillera which makes it interesting to consider the lithospheric structure of the STZ.

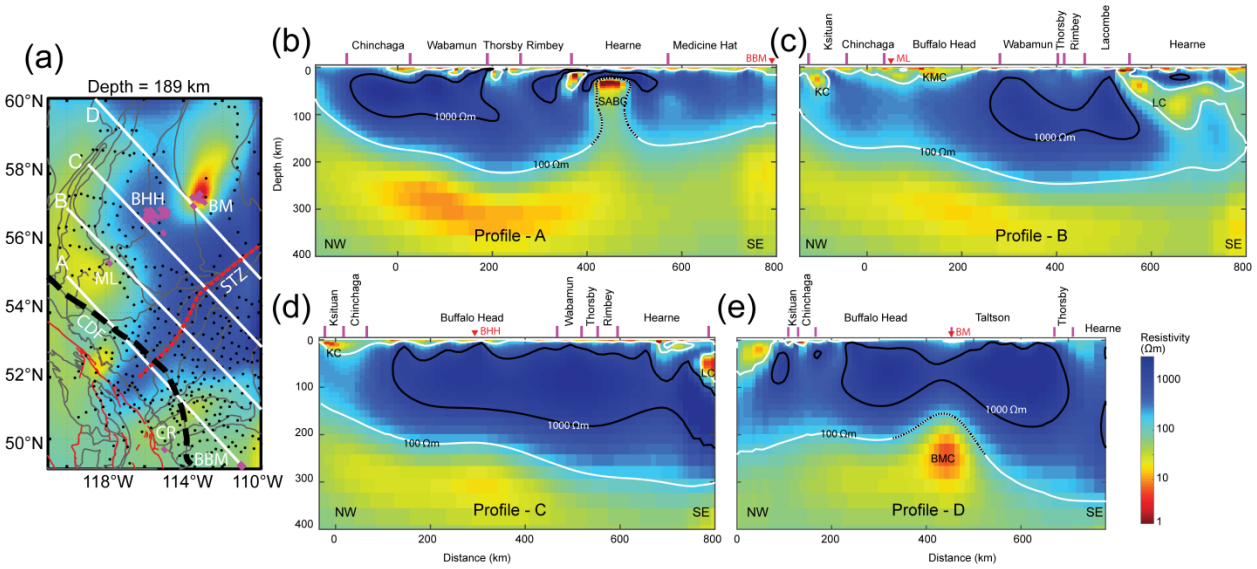

Figure 9.13: The Snowbird tectonic zone (red dash line) and lithospheric structure imaged in the Alberta inversion model shown with horizontal slice at 189 km depth (a) and vertical profiles in (b), (c), (d), and (e). The white lines in (a) are the location of the vertical profiles. Red and grey lines in figure (a) represent geological boundaries and faults (Pilkington et al., 2000; Colpron and Nelson, 2011). The thick black dash line shows the location of the Cordillera deformation front (CDF). The black and white contour lines in (b), (c), (d), and (e) are corresponding to 1000 Ωm and 100 Ωm, respectively. The black and white dashed lines represent where the 100 Ωm contour line should not be considered as the lithosphere-asthenosphere boundary (LAB). Abbreviations: BM, Birch Mountain kimberlite field; BHH, Buffalo Head Hills kimberlite field; ML, Mountain Lake kimberlite field; BBM, Black Butte Minette fields; SABC, Southern Alberta – British Columbia conductor; CR, Cross kimberlite field; KMC, Kimiwan conductor; LC, Loverna block conductor; KC, Kiskatinaw conductor.

The electrical LAB can be imaged with MT as a significant reduction in electrical conductivity across the LAB and the less resistive asthenosphere is often correlated with seismic low velocity zones (Eaton et al., 2009). This can be explained by the presence of partial melt in the asthenosphere and thus the conduction mechanism of minerals change from semiconductors in the lithosphere to ionic conduction in the asthenosphere (Jones and Craven, 2004; Eaton et al., 2009; Selway, 2014). Supporting experiments include the laboratory study of Schilling et al. (1997) that demonstrated the onset of partial melt in a sample of crystalline pyroxene granulite could reduce the electrical resistivity by almost

two orders. Moreover, the study of Gaillard et al. (2008) suggested 0.1 volume percent of carbonatite melts could explain the low resistivity of the oceanic asthenosphere.

In Figure 9.13, it is observed that the depth to the base of the resistive core delineated with the 100 Ωm contour line varies substantially across the STZ. In the seismic tomography models of Chen et al. (2018) and Bao and Eaton (2015), the thickest lithosphere in Alberta is 300 km and 275 km, respectively and was imaged in central Alberta around the STZ. Moreover, the lithosphere of the Buffalo Head terrane was reported to be only 200 km thick (Chen et al., 2018; Majorowicz, 2016; Aulbach et al., 2004). These results are consistent with the 100 Ωm contour line in the Alberta inversion model. Moreover, in the synthetic study described in section 7.4.1, the 100 Ωm contour line is located close to the LAB of the original model also. Furthermore, Nieuwenhuis et al. (2014) suggested using the 100 Ωm contour as the electrical LAB in the interpretation of a 3-D electrical resistivity model of southern Alberta. Therefore, the 100 Ωm contour line will be used to represent the LAB in the 3-D Alberta inversion models. However, it should be noted that the LAB depths in the WAB model should represent the minimum value as shown in the synthetic study (Figure 7.14). On the other hand, the resistivity structure beneath a shallow conductor cannot be resolved properly due to the attenuation of MT signal in the low resistivity body. Therefore, the LAB depth beneath the large mantle conductors (SABC, LC, KC, and BMC) is not as well imaged as the LAB where mantle conductors are absent.

The region of the STZ and neighboring Proterozoic terranes (Wabamun, Thorsby, Rimbey, Lacombe and the northern Hearne in Alberta; referred as RSTZ) are characterized by a thick and electrical resistive lithosphere that extends more southwestward to the Cordillera than all the other Precambrian terranes in Alberta (see the 189 km depth-slice in

Figure 9.13a). Vertical profiles across the RSTZ (Figure 9.13) show that the RSTZ is characterized with a LAB depth of 200-300 km from southwest to northeast.

9.7.2. Interpretation of the STZ

The highly resistive lithosphere of the RSTZ indicates mantle rocks that do not contain significant amounts of water, melt, or graphite / sulfide minerals. It was suggested that the resistivity of the sub-continental lithosphere can be a proxy for the state of enrichment in incompatible elements (such as Fe, Al, C, H; Selway, 2014). High resistivities imply the lithosphere of the RSTZ is more depleted in terms of these incompatible elements. The highly depleted lithosphere to a depth beneath the STZ that extends to a depth of 300 km is consistent with previous seismic studies mentioned above which imaged thick lithosphere at the same region (Bao and Eaton, 2015; Chen et al., 2018).

Moreover, the RSTZ is coincident with anomalous isostatic residual Bouguer gravity low, with the exception of the Wabamun domain (Figure 4.2). Chen et al. (2018) interpreted this coincidence as a result of deep cratonic root. Moreover, it has been observed that increasing the Mg and decreasing the Fe content will decrease density (Lee, 2003). The Mg content is quantified by the magnesium number defined as Mg# (= Mg / [Mg+Fe]) which is an important factor in determining the degree of depletion (Deschamps et al., 2002). The higher Mg# indicates a higher level of depletion. Thus, the RSTZ represents one portion of lithosphere in Alberta that is thick and highly depleted with greater Mg # according to the gravity isostatic residual Bouguer gravity data.

It should be noted that the isostatic residual gravity anomaly doesn't extend west of the Cordillera deformation front. This could be due to the isostatic residual gravity high

anomaly observed along the Cordillera deformation front. It was proposed to represent an uncompensated load in the crust that corresponds to an area of tectonically thickened supracrustal rocks (Jobin et al., 2017). This gravity high anomaly is originated shallower in depth and could have masked the deeper mantle gravity low anomaly to the west of the Cordillera deformation front. On the other hand, the isostatic gravity high anomaly can be genetically related to the isostatic low of the RSTZ. It has been suggested that the greater lithospheric strength (as a result of the thick and cold lithosphere) of the RSTZ could have resulted the greater flexural rigidity and provided isostatic support of the thickened supracrustal rocks of the isostatic high anomaly (Bao and Eaton, 2015).

The gradual change in the lithospheric thickness from southwest to northeast in the Alberta model indicates different lithospheric structure along the STZ. This is consistent with seismic observations that imaged the STZ as a boundary of mantle seismic wave-speed at the southwest and as a boundary of crustal structure and mantle seismic anisotropy at the northeast (Thompson et al., 2010; Bastow et al., 2014; Bao and Eaton, 2015). The STZ was classified into two segments according to the signature of crustal Vp/Vs ratios: the northeastern segment with low V_p/V_s ratios (<1.73) and the central-southwestern segment with clusters of high V_p/V_s ratios (>1.82; Gu et al., 2018). These consistent observations confirm that the STZ in Alberta is significantly different to the STZ to the northeast (relatively deep electrical LAB, low V_p/V_s ratios) and southwest (relatively shallow electrical LAB, high V_p/V_s ratios).

In summary, consistent evidence from seismic, isostatic residual Bouguer gravity data, and MT studies shows that the STZ and neighboring Proterozoic terranes are characterized by a thick lithosphere (~200-300 km) that extends westward into the

Canadian Cordillera. Moreover, the structure of the STZ in Alberta is different at the northeast and southwest.

9.8. Lithospheric structure of Alberta

Profiles of the 3-D Alberta electrical resistivity model are shown in Figure 9.14 and 9.15. The 100 Ωm resistivity contour line is chosen to represent the LAB as discussed in section 9.7. According to the lithospheric structure of Alberta observed in the WAB model, the lithospheric mantle of Alberta can be divided into several regions.

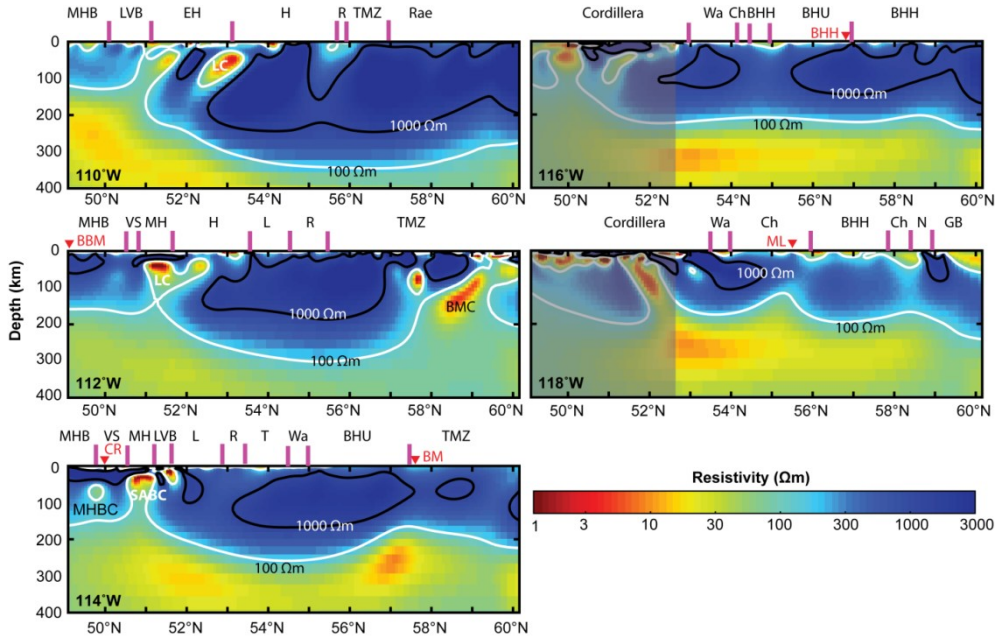

Figure 9.14: North-south profiles of the WAB electrical resistivity model. White and black lines represent the contour of resistivity values of 100 and 1000 Ωm, respectively. Purple bars are the terrane boundaries defined from Pilkington et al. (2000). Red triangles show the location of kimberlite and ultramafic intrusions. Abbreviations: GB, Great Bear; TMZ, Taltson; BHH, Buffalo Head High; BHU, Buffalo Head Uricuma; Ch, Chinchaga; Wa, Wabamun; R, Rimbey; T, Thorsby; L, Lacombe; LVB, Loverna Block; MH, Matzhiwin high; EH, Eyehill high; VS, Vulcan structure; MHB, Medicine Hat Block; BM, Birch Mountain kimberlite field; BHH, Buffalo Head Hills kimberlite field; ML, Mountain Lake kimberlite field; BBM, Black Butte Minette fields; CR, Cross kimberlite field.

(1) The Buffalo Head and Chinchaga terranes in northern Alberta are characterized by an LAB depth of ~ 200 km. This is consistent with the seismic body-wave tomography result of Chen et al. (2018; 200 km), geothermal study of Majorowicz (2016; 200 km), and the xenolith study of Aulbach et al. (2004; >180 km). The surface wave tomography result of Bao and Eaton (2015) imaged the LAB of the Buffalo Head terrane at a depth of 260 km. This may be caused by reduced data coverage north of 55˚N in their study.

(2) The LAB depth of the Proterozoic Taltson magmatic belt, Archean Rae province and the northern half of the Hearne province is ~ 300 km which is the thickest in Alberta.

(3) The LAB depth of the Proterozoic terranes in central Alberta surrounding the STZ is 200-300 km. Interestingly, the LAB of the STZ dips to the northeast, i.e., the lithosphere of the STZ is thinnest at the southwest and thickest at the northeast.

(4) The MHB is characterized with a relatively shallow LAB depth of 150-180 km although its crustal signature is Archean age. Moreover, the eastern part of the crust of the MHB between longitude 110˚W-111˚W is less resistive (<1000 Ωm) than the western part (>1000 Ωm; see profiles along 49˚N and 50˚N in Figure 9.15). There is a moderate mantle conductor (MHBC) imaged in the western MHB (see profiles along 50˚N in Figure 9.15 and along 114˚W in Figure 9.14).

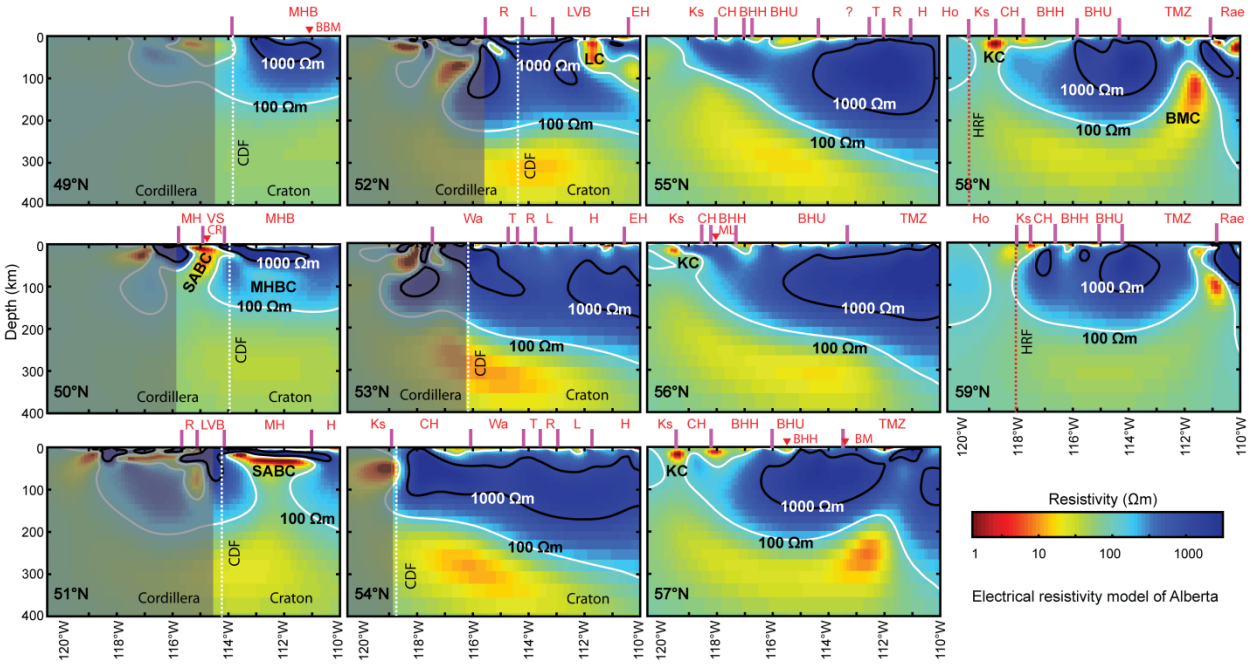

Figure 9.15: East-west profiles of the WAB 3-D electrical resistivity model. White and black lines represent resistivity contours of 100 and 1000 Ωm, respectively. Purple bars are the basement terrane boundaries (Pilkington et al., 2000). White dash lines represent the location of the Cordillera deformation front. Red dash lines represent the location of the Hay River Fault. Abbreviations: Ho, Hottah; GB, Great Bear; TMZ, Taltson; BHH, Buffalo Head High; BHU, Buffalo Head Uricuma; Ch, Chinchaga; Wa, Wabamun; R, Rimbey; T, Thorsby; L, Lacombe; LVB, Loverna Block; MH, Matzhiwin high; EH, Eyehill high; VS, Vulcan structure; MHB, Medicine Hat Block; Ks, Ksituan; MHB, Medicine Hat block; EH, Eyehill high; VS, Vulcan structure; BM, Birch Mountain kimberlite field; BHH, Buffalo Head Hills kimberlite field; ML, Mountain Lake field; BBM, Black Butte Minette fields; CR, Cross kimberlite field.

(5) Another interesting feature to note is the LAB of northern Alberta at 54 -57°N shows an eastward dip angle which flattens out further north. This may indicate extensive marginal deformation along the western edge of the Chinchaga terrane.

(6) The southern Hearne craton in Alberta (49-53°N) is dominated by several mantle conductors (SABC and LC). Thus it is difficult to determine the LAB depth from the WAB model because the mantle conductors make it difficult to image the deeper conductor associated with the LAB. This is a well know limitation of the MT method. The 3-D

inversion in this situation can make the LAB shallower than the true depth. However, where it is not covered by the shallow conductors, the LAB of the Vulcan structure and south Hearn in Alberta is imaged at a depth of 150-200 km (Figure 9.15). A xenolith study of the Cross kimberlite field showed that the base of the southwest Hearne lithosphere extends to 200 km and is Proterozoic instead of Archean (Canil, 2003; see location in Figure 9.11, 9.14 and 9.15). The LAB depth determined from the MT model should be a minimum value and thus the southern Hearne province in Alberta is believed to have an LAB depth of 200 km. This is much shallower than the LAB of the northern part of Hearne province in Alberta (300 km).

In summary, the LAB depth in Alberta inferred from the 3-D WAB model shows large spatial variations. In Figure 9.14 and 9.15, it can be seen that the LAB is deeper in the east than in the west. The depth of the LAB is not necessarily related to their age determined from crustal rocks. Instead, locations farthest from the craton edge appear to preserve the deepest lithospheric roots found in Alberta. This indicates that marginal deformation (1) along the western edge of the Laurentia craton and (2) along the southern edge of the Hearne province in Alberta is significant.

9.9. Diamondiferous kimberlite formation

There are four kimberlite/ultramafic intrusion fields in Alberta that have been described in section 3.4. The electrical structure of Alberta in the WAB model shows the LAB depth across Alberta and also the mantle composition in terms of incompatible elements and water/melt. With the lithospheric structure of Alberta defined from the WAB

model, the lithospheric structure beneath the kimberlite/ultramafic intrusion fields can be defined (Figure 9.13, 9.14, 9.15).

The Buffalo Head Hills and Birch Mountains kimberlite fields were found to host diamonds (Eccles, 2011), which are observed in the WAB model to have a deep LAB at ~ 200 km depth. In contrast, the Mountain Lake and Black Butte Minette fields, which are non-archetypal kimberlite and diamond poor, were observed to have a shallow LAB at 150-180 km. This shows the importance of a thick lithosphere in the diamond content of kimberlite fields. It has been proposed that 99% of diamonds found at the surface originated in the sub-continental lithospheric mantle (Stachel and Luth, 2015). Diamonds are believed to be formed during the cooling of C-O-H fluids and can be stable in the deep and cold lithospheric mantle with high pressure and relative low temperature (Stachel and Luth, 2015). The Buffalo Head Hills and Birch Mountains kimberlite fields are located within the Buffalo Head terrane and the Taltson magmatic zone, respectively, which were formed and/or modified in the Paleoproterozoic and have subsequently undergone conductive cooling (Ross, 2002). The Buffalo Head Hills diamondiferous kimberlite field was considered as a special case for diamond formation because its age is Proterozoic while the other diamondiferous kimberlite fields found were mostly located within an Archean craton (Eccles, 2011). The observation of a thick lithosphere of the diamondiferous kimberlites in the Buffalo Head Hills and Birch Mountains kimberlite fields proved that a thick, cold, and depleted lithosphere is a universal requirement for diamond formation/storage regardless of the age being Proterozoic or Archean.

The Buffalo Head Hills field is the most diamondiferous kimberlite field in Alberta and it is associated with a deep resistive root (BHHR) with no lithospheric mantle

conductor in the WAB model as shown in Figure 8.1. This is in agreement with the study of Turkoglu et al. (2009). In contrast, the Birch Mountains kimberlite field is characterized with a mantle conductor (BMC) at depth of 100-250 km. This means the Buffalo Head Hills lithosphere is more depleted in incompatible elements including carbon at comparative depths than the Birch Mountains kimberlite field. This is in agreement with the xenolith study of Eccles et al. (2004). This comparison shows that it is not necessary for the carbon content of the lithospheric mantle to be uniformly high for that lithosphere to be diamondiferous.

In summary, the contrasting lithospheric structures associated with the kimberlite / ultramafic rocks in Alberta demonstrate that diamondiferous kimberlite most commonly occurs where the lithosphere is a cold, thick and highly depleted. The carbon content in the lithosphere is not strongly correlated with the diamond formation or storage. MT study can be helpful to determine the depth of LAB and depletion of the lithosphere and thus help in the diamond exploration.

9.10. Tectonic implications

The new 3-D electrical resistivity model of Alberta provides constraints for the interpretation of the tectonic assembly history of the Alberta basement. In this section, tectonic implications of the MT models will be discussed by answering the questions asked in Chapter 3. Based on the electrical resistivity structures of the lithosphere of Alberta observed in the 3-D WAB model, the lithosphere of Alberta can be divided into four sections.

(1) Northern Alberta is characterized with an eastward-dipping LAB and a crustal-scale conductor (KC) and an upper mantle conductor (BMC).

(2) Proterozoic terranes in central Alberta surrounding the STZ are highly resistive at lithospheric mantle depths with no low resistivity anomalies.

(3) The MHB is characterized by a very shallow LAB and east to west variations in resistivity structure.

(4) The southern Hearne craton in Alberta has a thick lithosphere and three low resistivity anomalies in the crust and upper mantle (RDC, SABC and LC).

The contrasting lithospheric structures of different sections suggest that their origins may be different and thus each section will be discussed separately.

9.10.1. Northern Alberta

The eastward-dipping LAB of northern Alberta can be tentatively explained by the eastward subduction that occurred in this area during the Proterozoic. Extensive deformation along the cratonic edge during subduction could have resulted in the eastward-dipping LAB. Previous studies have also suggested this possibility as follows: (1) it was proposed that the Taltson magmatic zone was formed in an intra-continental setting, a far-field effect of eastward-dipping subduction event occurring further to the west (Chacko et al., 2000; De et al., 2000). (2) Early subduction events were also suggested to explain diamonds of the Buffalo Head terrane formed under sub-lithospheric conditions (Banas et al., 2006). (3) Previous study of Turkoglu et al. (2009) suggested eastward subduction that generated the Kiskatinaw conductor has supplement carbon to the diamonds of the Buffalo Head Hills kimberlites.

Ross and Eaton (2002) suggested that westward subduction has occurred on the western boundary of the Chinchaga domain, and coeval eastward subduction occurred on the eastern boundary of the Buffalo Head terrane. This arrangement could explain the formation of the Ksituan and Taltson magmatic belts. However, this model is not supported by (1) more detailed geochemical and isotopic studies of granitic rocks of the Taltson terrane (Chacko et al., 2000; De et al., 2000). (2) The electrical resistivity model of Alberta shows a gradual shallowing of the LAB towards the west. This indicates more extensive deformation to the west of the Chinchaga and Buffalo Head domains. (3) If subduction of oceanic lithosphere occurred to the east of the Buffalo Head terrane, a linear crustal electrical resistivity anomaly may exist such as the KC and RDC. The BMC is a mantle conductor and a localized feature in the center of the Taltson terrane. The absence of linear crustal/lithospheric electrical structures on the boundary of the Buffalo Head and Taltson terranes supports the tectonic model of Chacko et al. (2000) and De et al. (2000).

It was proposed that the Chinchaga and Buffalo Head terranes and the Rae and Hearne craton were sutured together prior to 2.0 Ga (Chacko et al., 2000; De et al., 2000). This is supported by the continuous LAB of the region observed in the 3-D WAB electrical resistivity model, ignoring the masking of the LAB beneath the BMC. The Taltson magmatic zone rocks were suggested to have been formed in an intra-continental setting between 1.9-2.0 Ga. Magmatic rocks of the Ksituan terrane (~2.0 Ga; Ross et al., 1991; Villeneuve et al., 1993) predate the Taltson magmatic belt (1.93-19.9 Ga) and were proposed to be the magmatic materials generated at the west margin of the cratonic nuclei (Chacko et al., 2000; De et al., 2000). In this case, the Nova terrane may be the surviving portion of the subducted plate at the convergent boundary. Alternatively, it could be a block that was

attached to the Ksituan terrane after subduction (<1.9 Ga) and before the Wopmay Orogen (>1.86 Ga), considering that this terrane is highly attenuated near the HRF.

The BMC could also be related to the magmatic rocks of the Taltson domain by referring to Cenozoic tectonism observed in Asia (Chacko et al., 2000; De et al., 2000). It was suggested that present-day crustal thickening in Tian Shan is due to far-field stresses caused by the India-Asia collision. It was also proposed that high-grade metamorphism and partial melting could be present in the lower crust of the Tian Shan by Windley (1997). If the BMC is a feature formed before the subduction along the Chinchaga terrane, it provides a tectonic weak zone for the development of concentrated lithospheric scale deformation far from the convergent boundary similar to Tian Shan. The granitoids of the TMZ were suggested to be associated with intra-crustal melting (Chacko et al., 2000; De et al., 2000). The heat from the modification of the lithosphere of the Taltson domain could have induced crustal melting and generated the magmatic rocks observed today.

Alternatively, the BMC could be a product of the far-field deformation. Hot materials from the asthenosphere may have migrated upward as a result of the far-field stress of the subduction. They will increase the crustal temperature and induce crustal melts and fertilize the lithosphere of the BMC that is preserved to date after the cessation of the tectonic shortening.

The KC was explained as the sheared portion of the Ksituan terrane (Ross and Eaton, 2002). The low resistivity was caused by conducting phases (graphite, sulfides) that were formed/inter-connected during deformation of the Kiskatinaw terrane (Chapter 6). The mechanism of shearing could be related to (1) the crustal shortening following the

eastward subduction along the Ksituan terrane or (2) the Hay River Fault during the Wopmay Orogen (Hoffman, 1987; Ootes et al., 2015).

Moreover, (1) the dip angle of the KC imaged in the WAB model changes from eastward at the southern end to almost vertical at the north and (2) the northern part of the KC is less resistive than the southern part (Figure 9.15). These differences could be used to relate the KC to the Hay River Fault. The northern part of the KC is the part that was sheared and attenuated the most. This means more extensive deformation occurred at the northern part than at the southern part of the Kiskatinaw terrane which could lead to the change of the dip angle and result in better connected conducting phases than the southern part. Therefore, it is believed that the KC was formed as a product of the crustal shortening following subduction or the formation of the Hay River Fault and the Wopmay Orogen. The impact of the Hay River Fault on the Kiskatinaw terrane can be demonstrated by the along-strike variation of the KC.

On the other hand, the northern segment of the KC may have been formed by a different mechanism from the southern segment of the KC. The southern segment of the KC can be explained as a product of the crustal shortening following subduction as stated above. However, the northern segment of the KC is close to the HRF, which is considered to be part of the Great Slave Lake shear zone. Even though the HRF was proposed to be a later-stage brittle deformation of the Great Slave Lake shear zone, which is dominated with ductile deformation in the Canadian Shield. It is possible that what is shown in the aeromagnetic data is only the shallow structure of the HRF. Based on the Sibson-Schultz models of faults (Sibson, 1977; Scholz, 1988), brittle deformation occurs at shallow depths of a fault and ductile deformation could happen at lower crustal depths. This is also

observed in the San Andreas Fault by MT studies of Unsworth et al. (1998) and Unsworth and Bedrosian (2004). If there is ductile deformation in the low crust of the HRF, the KC could be caused by the ductile deformation of the HRF instead of caused by crustal shortening following the eastward-subduction proposed above.

9.10.2. Central Alberta

Central Alberta is characterized by (1) relatively fast mantle seismic velocities, (2) a resistive lithosphere with no low resistivity anomalies and (3) gravity isostatic residual low anomaly. These all indicate highly depleted lithospheric mantle of this region. Central Alberta was proposed to be assembled during a Proterozoic orogeny – the East Alberta Orogen by Ross et al. (1995) based on seismic studies of the CAT project. This is the preferred interpretation of the assemblage history of central Alberta in this thesis. Moreover, some tentative relationships of the coeval and nearby Orogen are added.

It was suggested that the Thorsby domain was in an extensional setting during the early Proterozoic (Ross, 2002). It has accommodated the crustal escape block from the Taltson terrane at ca. 1.92-1.85 Ga. The crustal escape block of the Taltson may have been caused by the eastward subduction as suggested in section 9.9.1. This was followed by convergence process of oceanic crust assumption and terminal collision of the Wabamun domain and the Hearne (Ross, 2002).

The Rimbey terrane was proposed as a magmatic belt caused by the subduction formed at ca. 1.85-1.78 Ga. This time is subsequent to the Great Bear magmatism of the Wopmay Orogen (1.88-1.85 Ga). It is coeval with (1) the eastward indentation of the Fort Simpson terrane to the Hottah terrane and (2) the dextral movement of the McDonald fault

which is a continuous brittle fault to the northeast of the HRF (1.84-1.75 Ga; Ootes, et al., 2015; Ross, 2002). The Rimbey magmatism was also recognized to be coeval with the Tran-Hudson Orogen (1.88-1.79 Ga; Ross et al., 1994). Compressional forces from the two far collisions of the Wopmay Orogen and Trans-Hudson Orogen may have ended the opening of the Thorsby basin and initiated the subduction process of the East Alberta Orogen. Furthermore, the East Alberta Orogen and Tran-Hudson Orogen were proposed to comprise a tectonic vice that trapped the Hearne (Ross et al., 2000).

The Wabamun domain was suggested to represent mylonitic rocks of the STZ similar to the Tantato domain in the Canadian Shield (Ross et al., 1991). This can lead to the tentative suggestion that the Hearne craton was separated from the northern Alberta Proterozoic terranes by the Wabamun, and these three blocks were connected at ca. >1.92 Ga. During that time, the STZ could represent an intra-continental lithospheric weak zone that allowed the southward crustal escape of the Taltson terrane. The lithospheric weakness may be (1) a syngenetic feature related to the assembly of the Hearne and Rae provinces (i.e. Churchill province) as suggested by previous studies (Jones et al., 2002) or (2) a late-stage feature developed after the assembly of the Hearne and Rae provinces (Mahan and Williams, 2005). Explanation (1) is preferred considering the length of the STZ (~2800 km) but explanation (2) cannot be excluded.

9.10.3. The Medicine Hat block (MHB)

The eastern part of the MHB between 110°W and 111°W is less resistive than the western part. Moreover, the relative resistive part of the MHB to the west is underlain by a weak mantle conductor – the MHBC. This heterogeneity in lithospheric structure can be

related to the tectonic events occurred to the MHB. (1) Firstly, it has been suggested that sheet-like intrusions (referred to as the Head-Smashed-In sills) occurred over an area of 6000 km^2 and were confined to the northwestern portion of the MHB (Lemieux et al., 2000; Figure 4.11). The age of the emplacement of these sills was suggested to be Paleoproterozoic or Archean (>1.8 Ga; Lemieux et al., 2000). The MHBC may be related to the emplacement of the sills because they are coincident in location. The relatively resistive western part of the crust of the MHB may be caused by the injection of the sills. (2) Moreover, the western part of the MHB is coincident with southwest- or west-dipping crustal seismic reflections that were interpreted to be crustal-scale ramp (Lemieux et al., 2000; Figure 4.11). The crustal-scale ramp was proposed to be associated with the assembly of two Archean domains that formed the MHB and were sutured together by westward subduction at ca >2.6 Ga (Lemieux et al., 2000; Clowes et al., 2002). The crustal ramp is absent in the MHB east of 110˚W and the eastern MHB was proposed to be relatively undeformed Archean crust. Therefore, the different electrical resistivity in the east and west crust of the MHB may indicate the difference in composition of the two Archean domains.

The shallow LAB of the MHB may be caused by Proterozoic thermal events. The MHB was proposed to be an Archean microcontinent and subduction events have sutured the MHB with the Wyoming and Hearne craton (Gorman, 2002; Figure 3.11). However, interestingly, the MHB was suggested to have an Archean upper crust (2.6 Ga) and a Proterozoic lower crust (1.81-1.70 Ga) according to ages defined from drill core samples and xenolith studies (Davis et al., 1995; Lemieux et al., 2000). It is believed that the lower crust rocks of the MHB were modified extensively and mafic materials were injected to the

low crust at ca 1.85-1.70 Ga (Davis et al., 1995; Lemieux et al., 2000). This time is coeval with the Tran-Hudson Orogen and the East Alberta Orogen. This injection of mafic material may have modified the lithosphere of the MHB and caused the shallow LAB of the MHB observed today.

9.10.4. Southern Hearne province in Alberta

The southern Hearne province was proposed to have been modified due to tectonic events that occurred from late Archean to Paleozoic time. These include: (1) northward or southward subduction along the Vulcan structure (VS); (2) the Tran-Hudson Orogen to the east; (3) the East Alberta Orogen to the northwest. The southern Hearne is characterized with the RDC, LC and SABC in the WAB model. The RDC was interpreted to be related to the southeastward subduction along the northwest boundary of the Hearn province (section 9.2). This is electrical resistivity evidence for the proposed subduction process of the East Alberta Orogen (Ross et al., 1995; Boerner et al., 2000). Considering the geographic extent of the LC and SABC, it is suggested here that the SABC may be related to the subduction along the VS while the LC is probably associated with all the tectonic events mentioned above.

The VS was proposed by Hoffman (1990) to be an intra-continental collision zone. However, seismic observations did not favor such explanation (Ross et al., 1991; Eaton et al., 1990; Gorman et al., 2002; Chen et al., 2017, 2018). The contrasting LAB depths of the MHB and the Hearne province observed in the CAB model suggest that the MHB was formed as an individual block that was sutured to the Hearne. The VS was proposed to be a southward subduction zone between the Hearne and MHB by Eaton et al., (1999, 2000).

This is based on crustal-scale seismic studies (SALT and VauLT projects) of reflection features. The CAB model is compared to the seismic reflection result of the SALT and Vault projects (Figure 9.16 and Figure 9.17, respectively). No corresponding low resistivity anomaly can be correlated with the lower crustal reflections imaged by Eaton et al. (1999, 2000).

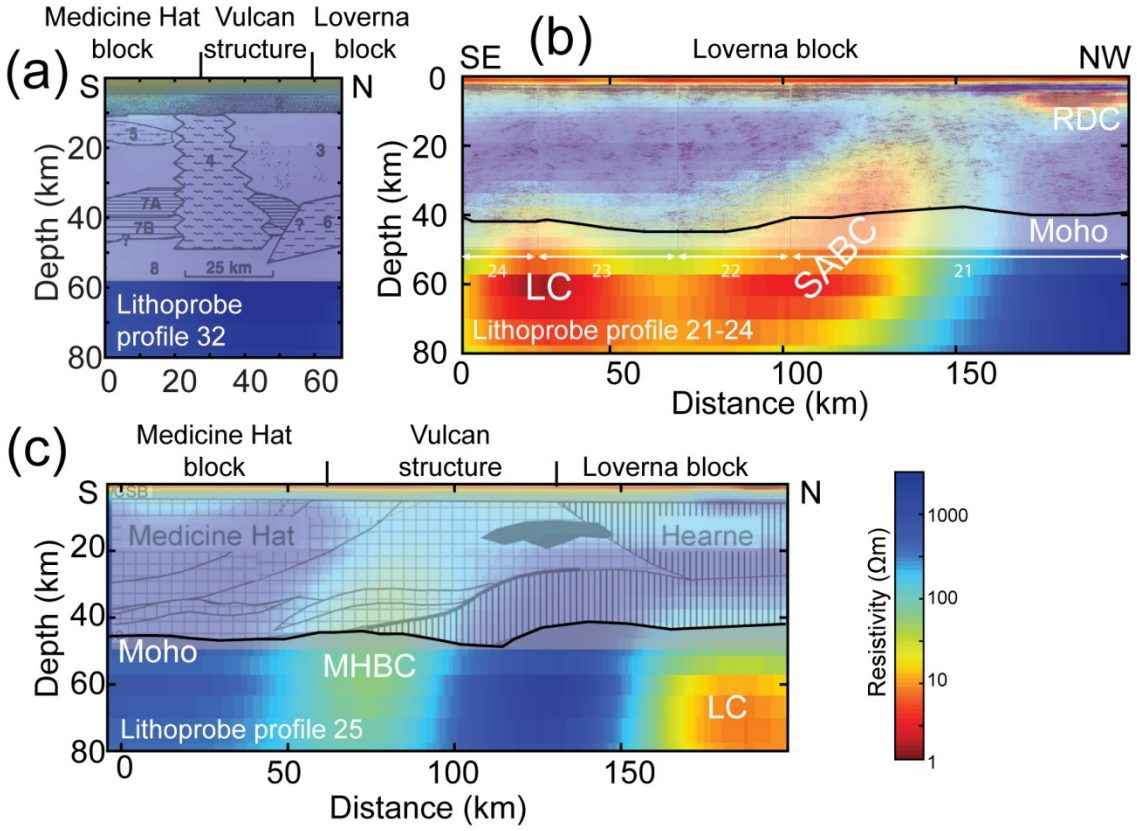

Figure 9.16: Comparison of the CAB model with the SALT profiles. The interpreted profile 25 and 32 is from (Eaton et al., 1999). The seismic section of profiles 21-24 is from Bouzidi et al. (2002). LC, Loverna block conductor; SABC, Southern Alberta British Columbia conductor; MHBC, Medicine Hat block conductor.

In contrast, for the lithospheric-scale seismic study of the SAREX, two northward-dipping reflectors were imaged in the subcrustal lithosphere underneath the MHB and VS (section 3.3). Thus, northward-dipping subduction was proposed by Gorman et al. (2002).

The northward subduction model was agreed by Nieuwenhuis et al., (2014) and Chen et al. (2017).

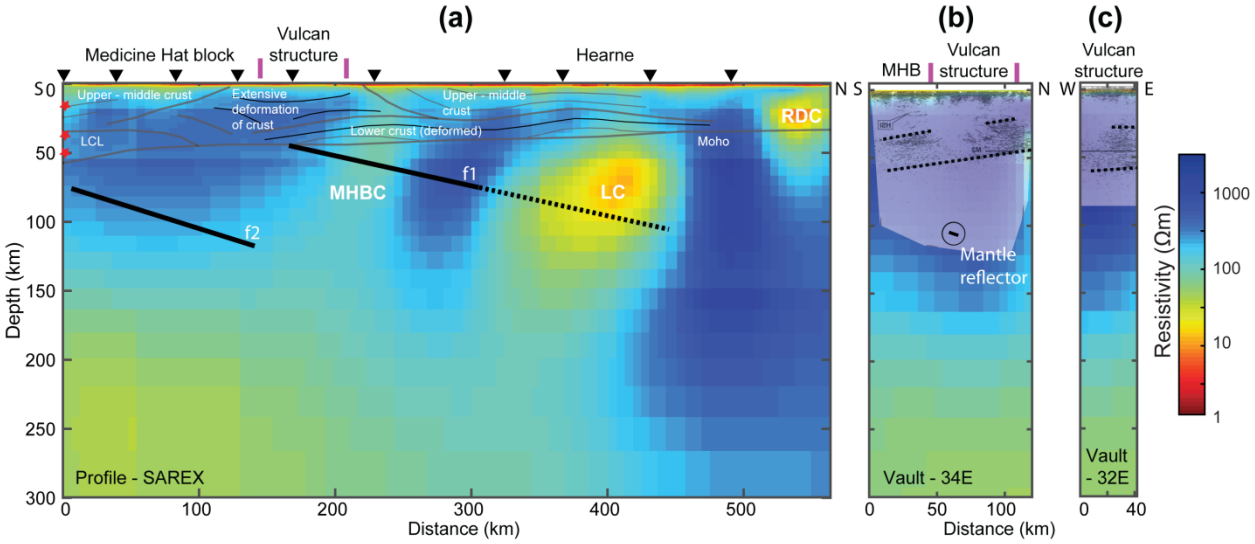

Figure 9.17: (a): The CAB model compared with the SAREX (Southern Alberta Refraction Experiment and Deep Probe) result from Clowes et al. (2002) and Gorman et al. (2002). Thin solid lines are major reflectors observed including Moho. Thick solid lines named f1 and f2 are the mantle reflectors. The dashed line underneath LC is extended from f1. (b) and (c): The CAB model compared with the Vibroseis Augmented Listen Time (VAuLT) profile 34E and 32E (Eaton et al., 2000). Dashed lines are the imaged reflectors. Abbreviations: RDC, Red Deer conductor; LC, Loverna block conductor; SABC, Southern Alberta – British Columbia conductor; MHB, Medicine Hat block.

The SAREX profile is compared with the CAB model (Figure 9.17a). It was suggested that the LC could be related to metasomatism caused by the subducting slabs f1 imaged in the SAREX by Nieuwenhuis et al., (2014). However, the reflector f1 cuts through the conductors (MHBC and LC) imaged in the CAB model. If the reflector f1 represents the subducting slab, then the electrical structure across it should not be continuous as observed in the CAB model, unless, the MHBC and LC are resultant from younger tectonic events than the subduction of f1. In the latter case, the tectonic "vice" associated with the

Proterozoic East Alberta Orogen and the Tran-Hudson Orogen could be related to the formation of the LC and MHBC.

The SABC may provide information about the proposed Archean subduction along the VS. The SABC is located to the north of and parallel to the positive aeromagnetic anomalies of the Matzhiwin block of the Hearne province. The Matzhiwin high was tentatively interpreted to be a magmatic belt with a crystallization age of 2.6 Ga (Villeneuve et al., 1993). In the northward subduction model, the Matzhiwin magmatic high can represent the magmatic arc of the Neoarchean subduction system and the SABC can be a product of the north-south lithospheric-scale shortening.

In summary, the observation of multiple conductors confirms that the southern Hearne is significantly different from the northern Hearne in Alberta. This difference can be associated with metasomatic modification and enrichment of the southern Hearne's mantle due to the tectonic events i.e. the Tran-Hudson Orogen and the East Alberta Orogen. It can also be attributed to the assembly history of the MHB and the Hearne. The Vulcan structure is believed to be a suture between the two Archean blocks. The subduction along the Vulcan structure is preferred to be northward dipping and of Neoarchean age. The SABC is tentatively interpreted to be associated with the formation of the Matzhiwin magnetic high and possible lithospheric-scale shortening due to the Archean assembly of the MHB and the Hearne. The LC is interpreted to be related to Proterozoic tectonic events.

9.11. Summary

In this chapter, the conductors and the lithospheric-scale electrical resistivity structure of Alberta are interpreted based on the 3-D models of the WAB and CAB. It can be

concluded that the conductors are closely related to the previous geological processes (such as the KMC) or tectonic events (such as the BMC and LC). The electrical lithospheric structure of the WAB model is highly consistent with previous seismic, gravity, xenolith studies. It is demonstrated that the LAB depths (100 Ωm contour line in the resistivity models) vary across Alberta. It has been suggested that a thick and depleted lithosphere is necessary for the formation of diamondiferous kimberlite.

Chapter 10 : Conclusions

10.1. Introduction

The rocks of the Alberta basement are part of the North American craton, which is also known as Laurentia. It is composed of both Archean cratons, including the Hearne craton and the Medicine Hat block in southern Alberta, and Proterozoic terranes such as the Buffalo Head terrane, Taltson magmatic zone in northern Alberta, and Rimbey, Thorsby, Lacombe terranes in central Alberta. These terranes were joined together in the Archean and Proterozoic and have been stable since Paleoproterozoic time (Hoffman, 1988; Ross et al., 1991).

Each part of the Alberta basement has its unique geology and geophysical features and was interpreted based on previous studies. In northern Alberta, the Taltson magmatic zone was proposed to be a subduction-related magmatic zone (Ross and Eaton, 2002) or a intra-continental magmatic zone (Chacko et al., 2000; De et al., 2000). In central Alberta, the Proterozoic terranes surrounding the Snowbird tectonic zone were assembled during the Proterozoic East Alberta Orogen (Ross et al., 1995). In southern Alberta, the Hearne craton was proposed to have been modified extensively by tectonic processes that included the suturing of the Hearne and the Medicine Hat blocks, the East Alberta Orogen, and the Tran-Hudson orogeny (Ross, 2002; Gorman et al., 2002; Nieuwenhuis et al., 2014; Chen et al., 2018).

The complex tectonic history of the rocks of the Alberta basement means that additional geophysical study of the basement could provide vital information on how

tectonic processes operated in the past and how they affect the current crustal and lithospheric structure. The research described in this thesis was carried out to get a better understanding of the crustal and lithospheric structure of Alberta using the magnetotelluric (MT) method.

The MT method studies the Earth's electrical resistivity with depth by measuring the variation of electric and magnetic fields at the surface. It is non-invasive and has minimal environmental impact. The electrical resistivity of rocks is sensitive to the presence of saline fluids, melts, H+ in the mantle, or other conducting mineral phases such as graphite and sulfides (e.g., Unsworth and Rondenay, 2012). The penetration depths of MT signals are dependent on the frequency of the signal, which gives the depth resolution of MT. Low frequency signals are more sensitive to deeper electrical structures than high frequency signals.

10.2. Data collection

Two field campaigns for the two projects outlined in Chapter 1 were designed to collect MT data in northern and central Alberta.

1. Broadband MT data (BBMT) in the frequency range 0.001-1000 Hz were collected in northwest Alberta across the Hay River fault in 2014.
2. In central Alberta, long-period MT data (LMT) in the frequency range of 0.0001-1 Hz were collected in 2013-2017. It was an effort to supplement the legacy long-period MT dataset of Alberta and to form a uniformly spaced grid of MT station in central Alberta.

10.3. Results of Project 1

The BBMT data collected in northwest Alberta were analyzed and a 2-D resistivity model was presented in Chapter 6 (Wang et al., 2018). The Western Canada Sedimentary Basin (WCSB) was imaged as a low resistivity layer above the resistive crystalline basement. Four crustal basement conductors were defined: (1) the Kiskatinaw conductor, (2) a conductor on the boundary of the Ksituan and Chinchaga domains, (3) a conductor on the boundary of the Chinchaga and Buffalo Head domains and (4) a conductor near the Hay River Fault. Both (1) and (2) correspond to areas of high seismic reflectivity. The low resistivity can be explained by interconnected grain boundary graphite, or sulfide minerals, deposited by metamorphic fluid migration.

10.4. Results of Project 2

The LMT data collected in central Alberta were combined with legacy LMT of the Lithoprobe project (Boerner et al., 2000) and from the University of Alberta (Turkoglu et al., 2009; Nieuwenhuis et al., 2014) to form a grid of LMT stations covering the whole of Alberta. Data analysis presented in Chapter 5 showed that 1-D, 2-D, and 3-D electrical resistivity structures exist in the crust and upper mantle beneath Alberta. Two LMT datasets were inverted using the ModEM scheme of Kelbert et al. (2014): (1) a dataset of 405 LMT stations covering whole Alberta (WAB); and (2) a dataset of 409 LMT stations covering central Alberta (CAB). Both the inversions had a final r.m.s. misfit of ~2.2. These two models are mutually consistent. .

10.4.1. Resistivity anomalies

In the 3-D electrical resistivity models of the WAB and CAB inversions, many electrical resistivity features are observed and were interpreted in combination with other geophysical observations.

1. The WCSB was imaged as a low resistivity layer at the surface. This was interpreted to be caused by the saline pore fluids and clay minerals distributed in the clastic sedimentary rocks. Large spatial variations of conductance of the WCSB in Alberta were observed. This indicates that the porosity, permeability, or clay content vary horizontally and affect the conductance of the WCSB in Alberta.

2. A crustal conductor with resistivity values in the range 1-10 Ωm was identified along the Red Deer Trend and referred as Red Deer conductor (RDC) as in previous studies (Boerner et al., 2000; Nieuwenhuis et al., 2014). The RDC was imaged to be deeper at the northern end than at the southern end. The cause of the low resistivity of the RDC may be a combination of graphite films / sulfides / ferrous minerals / saline fluids. The RDC is believed to be a product of the East Alberta Orogen (Ross, 1995), which involved southeastward subduction of the Wabamun domain along the northern boundary of the Hearne craton. It was also proposed to be coeval with the ~1.8 Ga Tran-Hudson Orogen. These two orogens were suggested to have acted as a tectonic vice that trapped the Hearne craton (Ross, 2002).

3. A crustal conductor was imaged coincident with the Kimiwan oxygen isotope anomaly (KIA; Burwash et al., 2000) and named as Kimiwan conductor (KMC). Well-connected conductive phases such as magnetite, graphite, sulfides, or saline pore fluids may be the

reason for the low resistivity of the KMC. It was suggested that the KIA was generated in an extensional crustal setting and fluids of meteoric origin interacted with rocks at relatively high-temperature (300-550 ˚C) at ~ 1.8 Ga (Burwash et al., 2000). This tectonic setting could also explain the deposition of the conductive phases.

4. A crustal conductor imaged along the Kiskatinaw terrane in northwest Alberta was identified as the Kiskatinaw conductor (KC), which was also observed in the 2-D inversion model of the BBMT data. The low resistivity of the KC can be explained by interconnected grain boundary graphite or sulfide phases deposited by metamorphic fluid migration. The dip angle of the KC was found to change along strike, from a dip to the east at the southwest end to almost vertical at the northeast end. This change of geometry is believed to be associated with the deformation along the Hay River Fault.

5. A conductor was imaged along the northern boundary of the Matzhiwin positive aeromagnetic anomaly at the depth range 30-90 km and named SABC as in previous studies (Gough, 1986; Wang, 1988a; Wang, 1988b). The explanation of the low resistivity of the SABC was attributed to well-connected graphite, iron oxides or sulfides. The conductive phases were proposed to be related to crustal shortening associated with the suture of the Hearne craton and the Medicine Hat block. The continuation of the SABC to the west of the Cordillera deformation front (CDF) demonstrates that the Precambrian basement exists farther west than the CDF in uppermost mantle depths.

6. Another conductor was imaged in the upper mantle beneath the Loverna block in a depth range 45-120 km. It is referred as the Loverna block conductor (LC) as in previous studies (Boerner et al., 2000; Nieuwenhuis et al., 2014). Graphite, phlogopite,

H+ and a small fraction of basaltic or carbonatite melts were suggested to be the conducting phases that reduce the electrical resistivity of the LC. The LC was believed to be caused by the Proterozoic tectonic reworking related to the East Alberta Orogen and the Tran-Hudson Orogen.

7. The deepest (100-250 km) conductive body imaged in the WAB electrical resistivity model is located beneath the Birch Mountain kimberlite field and was named as the Birch Mountain conductor (BMC). Hydrogen or melts of basaltic or carbonatite composition were proposed to be the reason for the low resistivity of the BMC. It is proposed that more mantle enrichment occurred beneath the Birch Mountain kimberlite field than the Buffalo Head kimberlite field. This explanation was also used to explain observations of the xenolith study of Eccles et al. (2004) and the seismic study of Chen et al. (2018).
8. The Snowbird tectonic zone and surrounding terranes (Wabamun, Thorsby, Rimbey, Lacombe, and northern part of the Hearne craton in Alberta) was imaged to be the most resistive part in Alberta with a deep lithosphere-asthenosphere boundary (LAB) at a depth of 200-300 km. This indicates that the lithosphere of the STZ is highly depleted in incompatible elements. Moreover, the LAB of the STZ in Alberta is deeper at the east than the west.

All the anomalous resistivity features observed in Alberta could be related to past tectonic events, which showes that the MT method is very helpful in tectonic studies. On top of the anomalous resistivity features, the electrical lithosphere-asthenosphere boundary (LAB) was defined using the WAB model.

10.4.2. The electrical lithosphere-asthenosphere boundary of Alberta

The LAB depths defined in this thesis agree well with previous estimates derived from a range of techniques (Canil, 2003; Aulbach et al., 2004; Bao and Eaton, 2015; Majorowicz, 2016; Chen et al., 2018). Large spatial variations in the LAB depth are observed and it is not necessarily related to their age determined from crustal rocks. The Buffalo Head terrane, Chinchaga terrane, and the western segment of the STZ are characterized by a LAB depth of ~200 km. The LAB of the Taltson magmatic zone and the eastern STZ is located at a depth of 300 km. The Medicine Hat block is imaged with the shallowest LAB of 150-180 km depths. The southern part of the Hearne craton in Alberta is believed to have an LAB depth of 200 km. This is much shallower than the LAB depth of the northern part of Hearne craton in Alberta (300 km). Moreover, the LAB in northern Alberta at 54 -57˚N shows an eastward dip angle. This may indicate extensive marginal deformation along the western edge of the Chinchaga terrane.

10.4.3. Relationship with diamondiferous kimberlites

There are several occurrences of kimberlite / ultramafic rocks in Alberta, among which only the rocks of the Buffalo Head kimberlite field and the Birch Mountain kimberlite field can be classified as typical kimberlites (Eccles et al., 2004). This phenomenon can be related to the deeper LAB of these two kimberlite fields relative to other areas in Alberta. Moreover, although the Birch Mountain kimberlite field is believed to be more enriched in incompatible elements including carbon, its diamond content is lower than the Buffalo Head kimberlites. Therefore, the carbon content in the lithosphere is not strongly correlated with the diamond formation or storage. These observations suggest that the MT

method can be helpful to determine the depth of LAB and depletion of the lithosphere and thus help in the diamond exploration.

10.4.4. Preliminary tectonic implications

Preliminary tectonic implications of Alberta were suggested based on the MT inversion model. In northern Alberta, the east-dipping LAB indicates extensive deformation along the western edge of the Chinchaga domain. Therefore, Proterozoic eastward subduction along the western edge of the Chinchaga domain was suggested during 1.9-2.0 Ga. The Taltson magmatic zone is considered to be an intra-continental feature caused by the subduction occurred to the west in agreement with Chacko et al. (2000) and De et al. (2000).

In central Alberta, the MT model presented in this thesis supports the tectonic model of the East Alberta Orogen proposed by Ross et al. (1995). The Wabamun domain was suggested to be a part of the STZ during the Archean and separates the Buffalo Head terrane and the Hearne craton. The opening of the Thorsby basin could have been related to the crustal escape of the Taltson magmatic zone at ca. 1.92-1.85 Ga; the latter could have resulted from the far-field compression force of the continental collision following the subduction along the Chinchaga to the west. The initiation of (1) the eastward indentation of the Fort Simpson terrane to the Hottah terrane (1.84-1.75 Ga; Ootes, et al., 2015) and (2) the Tran-Hudson Orogen (1.88-1.79 Ga; Ross et al., 1994) could have reversed the opening of the Thorsby basin and started subduction which formed the Rimbey magmatic belt at ca. 1.85-1.78 Ga. The East Alberta Orogen and Tran-Hudson Orogen are believed to comprise a tectonic vice that trapped the Hearne as proposed by Ross et al. (2000).

In southern Alberta, the Vulcan structure is interpreted to be a suture zone between the Hearne craton and the Medicine Hat block because contrasting LAB depths are observed. The Medicine Hat block shows contrasting electrical resistivity features that give support to the hypothesis that the MHB was formed by two micro-continents (Lemieux et al., 2000; Clowes et al., 2002).

It should be note that these tectonic interpretations assume that the electrical resistivity structures were formed by past tectonic events because they are coincident at present. However, the electrical resistivity structure may have been caused by past tectonic events after formation of the structure. Without knowing the age of formation of the basement rocks, it is impossible to determine if these proposed tectonic events directly caused the electrical resistivity anomalies. Some geochronological studies of the basement rocks would be valuable to address these questions.

10.5. Suggested future work

A short list of tasks that could extend this research is listed below.

1. The 3-D inversion results could be improved if more LMT data were collected in northern Alberta. The resolution of the conductors such as the BMC, KMC, and KC could be improved by more deployments of LMT stations in the future.
2. Three-dimensional MT inversion algorithms can use constraints, such as fixing the resistivity of certain regions and allowing discontinuities. This technique could be applied in Alberta. For example, the base of the WCSB has been defined by seismic studies and this could be used in the 3-D inversions of MT data in Alberta.

3. For the crustal resistivity anomalies, more closely-spaced, high-frequency broadband MT data are needed to recover the full details as have been shown for the Kiskatinaw conductor in section 9.5.3. Therefore, collection of extra MT data near the crustal conductors such as the KC, RDC, and KMC would represent useful future work.

4. Joint inversions of the gravity / seismic velocity / MT data available in Alberta may result a better model that is consistent with all the observations.

5. There may be electrical anisotropic structures in Alberta as suggested by previous MT studies described in sections 6.4.4 and 4.6.6. Thus, future 3-D anisotropic inversions would be an important subject.

6. The suggested interpretations of the cause of the low resistivity anomalies are mostly based on lab measurements. These studies could be extended by studies of xenoliths or drill-core samples.

7. Further detailed 3-D seismic imaging of basement structures where the conductors are located in the 3-D model of the whole of Alberta could be helpful.

8. The current tectonic interpretations are based on previous studies and this research. However, this is not complete and more geological and geophysical studies are needed to verify the current interpretations.

References

Ahr, M, Wayne, 2011. Geology of carbonate reservoirs: the identification, description and characterization of hydrocarbon reservoirs in carbonate rocks. Published by John Wiley & Sons, 2011. ISBN: 1118210387, 9781118210383.

Ansdell, K. M., Lucas, S. B., Connors*, K., and Stern, R. A. 1995. Kisseynew metasedimentary gneiss belt, Trans-Hudson orogen (Canada): Back-arc origin and collisional inversion. *Geology*, *23*, 1039–1043. http://doi.org/10.1130/0091-7613(1997)025<0090:kmgbth>2.3.co;2

Archie, G. E. 1942. The Electrical Resistivity Log as an Aid in Determining Some Reservoir Characteristics. Transactions of the AIME, Society of Petroleum Engineers, 146: 54–62. http://dx.doi.org/10.2118/942054-G

Aulbach, S., Griffin, W. L., O'Reilly, S. Y., and McCandless, T. E. 2004. Genesis and evolution of the lithospheric mantle beneath the Buffalo Head Terrane, Alberta (Canada). *Lithos*, *77*(1–4 SPEC. ISS.), 413–451. http://doi.org/10.1016/j.lithos.2004.04.020

Avdeev, D. B. 2005. *3D EM modeling and inversion from theory to application*. *Surveys in geophysics*. http://doi.org/10.1007/s10712-005-1836-2

Bachu S. Burwash R.A. 1994. Geothermal Regime in the Western Canadian Sedimentary Basin. In Geological Atlas of the Western Canada Sedimentary Basin (edited by Mossop G.D. and Shetsen I.), pp. 447-54. Canadian Society of Petroleum Geologists and Alberta Research Council, Calgary, Alberta.

Baba, K., and Chave, A. D. 2005. Correction of seafloor magnetotelluric data for topographic effects during inversion. *Journal of Geophysical Research: Solid Earth*, *110*(12), 1–16. http://doi.org/10.1029/2004JB003463

Banas, A., Stachel, T., Muehlenbachs, K., and McCandless, T. E. 2007. Diamonds from the Buffalo Head Hills, Alberta: Formation in a non-conventional setting. *Lithos*, *93*(1–2), 199–213. http://doi.org/10.1016/j.lithos.2006.07.001

Bahr, K. 1988. Interpretation of the magnetotelluric impedance tensor: regional induction and local telluric distortion. *J. Geophys.*, *62*(1), 119–127.

Baker, W. G., and Martyn D. F. 1953. ELECTRIC CURRENTS IN THE IONOSPHERE I . THE CONDUCTIVITY. *Philosophical Transactions of the Royal Society of London. Series A, Mathematical and Physical Sciences*, *246*(913), 281–294.

Bao, X., Eaton, D. W., and Guest, B. 2014. Plateau uplift in western Canada caused by lithospheric delamination along a craton edge. *Nature Geoscience*, *7*(11), 830–833. http://doi.org/10.1038/ngeo2270

Bao, X., and Eaton, D. W. 2015. Large variations in lithospheric thickness of western Laurentia: Tectonic inheritance or collisional reworking? *Precambrian Research*, *266*, 579–586. http://doi.org/10.1016/j.precamres.2015.05.010

Bao, X., Eaton, D. W., and Gu, Y. J. 2016. Journal of Geophysical Research : Solid Earth, 1–14. http://doi.org/10.1002/2015JB012453.Received

Bastow, I. D., Eaton, D. W., Kendall, J.-M., Helffrich, G., Snyder, D. B., Thompson, D. A., Pawlak, A. E. 2014. The Hudson Bay Lithospheric Experiment (HuBLE): insights into Precambrian plate tectonics and the development of mantle keels. Contient Formation through Time, Geological Society, London, Special Publications, 389(1), 41–67. http://doi.org/10.1144/sp389.7

Bedle, H., and Van Der Lee, S. 2009. S velocity variations beneath North America. *Journal of Geophysical Research: Solid Earth*, *114*(7). http://doi.org/10.1029/2008JB005949

Bedrosian, P. A., Unsworth, M. J., Egbert, G. D., and Thurber, C. H. 2004. Geophysical images of the creeping segment of the San Andreas fault: Implications for the role of crustal fluids in the earthquake process. *Tectonophysics*, *385*(1–4), 137–158. http://doi.org/10.1016/j.tecto.2004.02.010

Bell, D. R., and Rossman, G. R. 1992. The Role of Earth's Mantle : Nominally Anhydrous Minerals. *Science*, *255*, 1391–1397.

Bell, D. R., Rauch, F., Rossman, G. R., Endisch, D., and Maldener, J. 2003. Hydroxide in olivine: A quantitative determination of the absolute amount and calibration of the IR spectrum. *Journal of Geophysical Research: Solid Earth*, *108*(B2), 1–9. http://doi.org/10.1029/2001jb000679

Bertrand, E., Unsworth, M., Chiang, C. W., Chen, C. S., Chen, C. C., Wu, F., … Hill, G. 2009. Magnetotelluric evidence for thick-skinned tectonics in central Taiwan. *Geology*, *37*(8), 711–714. http://doi.org/10.1130/G25755A.1

Berman, R. G., Davis, W. J., and Pehrsson, S. 2007. Collisional snowbird tectonic zone resurrected-growth of laurentia during the 1.9 Ga accretionary phase of the hudsonian orogeny. *Geology*, *35*(10), 911--14.

Boerner, D. E., Kurtz, R. D., Craven, J. A., Rondenay, S., and Qian, W. 1995. Buried Proterozoic foredeep under the Western Canada Sedimentary Basin? *Geology*, *23*(4), 297. http://doi.org/10.1130/0091-7613(1995)023<0297:bpfutw>2.3.co;2

Boerner, D. E., Kurtz, R. D., Craven, J. A., Ross, G. M., Jones, F. W., and Davis, W. J. 1999. Electrical Conductivity in the Precambrian Lithosphere of Western Canada. *Science*, *283*(5402), 668–670. http://doi.org/10.1126/science.283.5402.668

Boerner, D. E., Kurtz, R. D., Craven, J. A., Ross, G. M., and Jones, F. W. 2000. A synthesis of electromagnetic studies in the Lithoprobe Alberta Basement Transect: constraints on Paleoproterozoic indentation tectonics. Canadian Journal of Earth Sciences, 37: 1509–1534. http://doi.org/10.1139/e00-063

Booker, J. R. 2013. The Magnetotelluric Phase Tensor: A Critical Review. Surveys in Geophysics, 35(1): 7–40. http://doi.org/10.1007/s10712-013-9234-2

Bostick. F. X. 1977. A simple almost exact method of MT analysis. Workshop on Electrical Methods in Geothermal Exploration, U.S. Geological Survey. Contract No. 14080001-8-359.

Bowring, S. A., and Podosek, F. A. 1989. Nd isotopic evidence from Wopmay Orogen for 2.0-2.4 North America. *Earth and Planetary Science Letters*, *94*, 217–230.

Bowring, S. A. Housh, T. B. Isachsen, C. E. 1990. The Acasta gneisses: remnant of Earth's early crust. LPI Conference on the Origin of the Earth, p. 319-343

Bowring, S.A., Williams, I.S., 1999. Priscoan (4.00–4.03 Ga) orthogneisses from northwestern Canada. Contributions to Mineralogy and Petrology 134, 3–16.

Bowring, S. A., and Grotzinger, J. P. 1992. Implications of new chronostratigraphy for tectonic evolution of Wopmay Orogen, northwest Canadian Shield. American Journal of Science, 292: 1–20. http://doi.org/:10.2475/ajs.292.1.1

Bouzidi, Y., Schmitt, D. R., Burwash, R. a, and Kanasewich, E. R. 2002. Depth migration of deep seismic reflection profiles: crustal thickness variations in Alberta. Canadian Journal of Earth Sciences, 39(3), 331–350. http://doi.org/10.1139/e01-080

Burianyk, M. J. A., Kanasewich, E. R., and Udey, N. 2010. Broadside wide-angle seismic studies and three-dimensional structure of the crust in the southeast Canadian Cordillera.

Canadian Journal of Earth Sciences, *34*(8), 1156–1166. http://doi.org/10.1139/e17-093

Burwash, R. A., Krupicka, J., and Wijbrans, J. R. 2000. Metamorphic evolution of the Precambrian basement of Alberta. *Canadian Mineralogist*, *38*(2), 423–434. http://doi.org/10.2113/gscanmin.38.2.423

Burwash, R. A., Chacko, T., Muehlenbachs, K., and Bouzidi, Y. 2000. Oxygen isotope systematics of the Precambrian basement of Alberta: implications for Paleoproterozoic and Phanerozoic tectonics in northwestern Alberta. *Canadian Journal of Earth Sciences*, *37*(11), 1611–1628. http://doi.org/10.1139/e00-090

Cagniard, L. 1950. Basic Theory of the Magnetotelluric Method of Geophysical Prospecting. *Geophysics*, *18*, 605–635. http://doi.org/10.1190/1.1437915

Caldwell, T. G., Bibby, H. M., and Brown, C. 2004. The magnetotelluric phase tensor. Geophysical Journal International, 158(2): 457–469. http://doi.org/10.1111/j.1365-246X.2004.02281.x

Campanya, J., Ogaya, X., Jones, A. G., Rath, V., Vozar, J., and Meqbel, N. 2016. The advantages of complementing MT profiles in 3-D environments with geomagnetic transfer function and interstation horizontal magnetic transfer function data: Results from a synthetic case study. *Geophysical Journal International*, *207*(3), 1818–1836. http://doi.org/10.1093/gji/ggw357

Canil, D., Schulze, D. J., Hall, D., Hearn Jr., B. C., and Milliken, S. M. 2003. Lithospheric roots beneath western Laurentia: the geochemical signal in mantle garnets. *Canadian Journal of Earth Sciences*, *40*(8), 1027–1051. http://doi.org/10.1139/e03-003

Canil, D. 2008. Canada's craton: A bottoms-up view. *GSA Today*, *18*(6), 4–10. http://doi.org/10.1130/GSAT01806A.1

Card, C. 2016. A coming together : The juxtaposition of the Rae and Hearne cratons along the Virgin River shear zone (Snowbird tectonic zone), Saskatchewan , Canada , and the implications for proto-Laurentia. PhD thesis.

Cassidy, J. F. 2010. Review: Receiver function studies in the southern Canadian Cordillera. *Canadian Journal of Earth Sciences*, *32*(10), 1514–1519. http://doi.org/10.1139/e95-123

Chacko, T., De, S. K., Creaser, R. A., and Muehlenbachs, K. 2000. Tectonic setting of the Taltson magmatic zone at 1.9–2.0 Ga: a granitoid-based perspective. Canadian Journal of Earth Sciences, 37(11): 1597–1609. http://doi.org/10.1139/e00-029

Chave, A. D., and Jones, A. G., 2012. The Magnetotelluric Method, Theory and Practice. Cambridge university Press, Cambridge, U.K.

Chave, A. D., and Smith, J. T. 1994. On electric and magnetic galvanic distortion tensor decompositions complex factors controlled by two unknown real constants . equations describing the full electric and magnetic tion decomposition of the magnetotelluric response tensor and magnetic and me. *Journal of Geophysical Research*, *99*, 4669–4682.

Chandra, N. N., and Cumming, G. L. 2010. Seismic Refraction Studies in Western Canada. *Canadian Journal of Earth Sciences*, *9*(9), 1099–1109. http://doi.org/10.1139/e72-095

Chen, C.-W., Rondenay, Stephane, Evans, R. L., and Snyder, D. B. 2009. Geophysical Detection of relict metasomatism from an Archean (~3.5 Ga) subduction zone. *Science*, *326*, 1089–1092.

Chen, Y., Gu, Y. J., Dokht, R. M. H., and Sacchi, M. D. 2015. Crustal imprints of Precambrian orogenesis in western Laurentia. *Journal of Geophysical Research B: Solid Earth*, *120*(10), 6993–7012. http://doi.org/10.1002/2014JB011353

Chen, Y., Gu, Y. J., and Hung, S. H. 2018. A New Appraisal of Lithospheric Structures of the Cordillera-Craton Boundary Region in Western Canada. *Tectonics*, *37*(9), 3207–3228. http://doi.org/10.1029/2018TC004956

Chen, Y., Gu, Y. J., and Hung, S.-H. 2017. Finite-frequency P-wave tomography of the Western Canada Sedimentary Basin: Implications for the lithospheric evolution in Western Laurentia. *Tectonophysics*, *698*, 79–90. http://doi.org/10.1016/j.tecto.2017.01.006

Clowes, R. M., Burianyk, M. J., Gorman, A. R., and Kanasewich, E. R. 2002. Crustal velocity structure from SAREX, the Southern Alberta Refraction Experiment. *Canadian Journal of Earth Sciences*, *39*(3), 351–373. http://doi.org/10.1139/e01-070

Clowes, R. M. 2009. A New View of the Continent Beneath Our Feet - LITHOPROBE's Scientific, Economic and Social Contributions. CSEG Recorder, (March), 7–16.

Colpron, M. and Nelson, J.L., 2011: A Digital Atlas of Terranes for the Northern Cordillera; British Columbia Ministry of Energy and Mines, BCGS GeoFile 2011-11.

Constable, S. C., Parker, R. L., and Constable, C. G. 1987. Occam's inversion: a practical algorithm for generating smooth models from electromagnetic sounding data. *Geophysics*, *52*(3), 267–462.

Constable, S. 2006. SEO3: A new model of olivine electrical conductivity. *Geophysical Journal International*, *166*(1), 435–437. http://doi.org/10.1111/j.1365-246X.2006.03041.x

Cook, F. A., Hall, K. W., and Lynn, C. E. 2005. The edge of northwestern North America at ~1.8 Ga. Canadian Journal of Earth Sciences, 42(6), 983–997. http://doi.org/10.1139/e05-039

Corrigan, D., Pehrsson, S., Wodicka, N., and de Kemp, E. 2009. The Palaeoproterozoic Trans-Hudson Orogen: a prototype of modern accretionary processes. *Geological Society, London, Special Publications*, *327*(1), 457–479. http://doi.org/10.1144/SP327.19

Čuma, M., Gribenko, A., and Zhdanov, M. S. 2017. Inversion of magnetotelluric data using integral equation approach with variable sensitivity domain: Application to EarthScope MT data. *Physics of the Earth and Planetary Interiors*, *270*, 113–127. http://doi.org/10.1016/j.pepi.2017.06.003

Dasgupta, R., and Hirschmann, M. M. 2010. The deep carbon cycle and melting in Earth's interior. *Earth and Planetary Science Letters*, *298*(1–2), 1–13. http://doi.org/10.1016/j.epsl.2010.06.039

Davis, W.J., Berman, R., and Kjarsgaard, B. 1995. U–Pb geochron- ology and isotopic studies of crustal xenoliths from the Archean Medicine Hat block, northern Montana and southern Alberta: Paleoproterozoic reworking of the Archean crust. In 1995 Al- berta Basement Transects workshop. Edited by G.M. Ross. Lithoprobe Report 47, pp. 330–335.

Dawy, M. 2002. Electrical Properties and Infrared Studies of Heated Mica Sheets. *Egypt. J. Sol*, *25*(1), 137–152.

DeGroot-Hedlin, C., and Constable, S. 1990. Occam's inversion to generate smooth, two-dimensional models from magnetotelluric data. *Geophysics*, *55*(12), 1613–1624. http://doi.org/10.1190/1.1442813

Deschamps, F., Trampert, J., and Snieder, R. 2002. Anomalies of temperature and iron in the uppermost mantle inferred from gravity data and tomographic models. *Physics of the Earth and Planetary Interiors*, *129*(3–4), 245–264. http://doi.org/10.1016/S0031-9201(01)00294-1

De, S. K., Chacko, T., Creaser, R. A., and Muehlenbachs, K. 2000. Geochemical and Nd-Pb-O isotope systematics of granites from the Taltson Magmatic Zone, NE Alberta: Implications for early Proterozoic tectonics in western Laurentia. *Precambrian Research*, *102*(3–4), 221–249. http://doi.org/10.1016/S0301-9268(00)00068-1

Dmitriev, V. I., and Berdichevsky, M. N. 1979. The Fundamental Model of Magnetotelluric Sounding. *Proceedings of the IEEE*, *67*(7), 1034–1044. http://doi.org/10.1109/PROC.1979.11386

Eaton, W., and Cassidy, J. F. 1996. A relic Proterozoic subduction zone in western Canada: New evidence from seismic reflection and receiver function data, *23*(25), 3791–3794.

Eaton, D. W., Ross M., G., and Clowes, R. M. 1999. Seismic-reflection and potential-field studies of the {Vulcan} structure, western {Canada}: a {Paleoproterozoic} {Pyrenees}? *Journal of Geophysical Research*, *104*(B10Bisbal new,), 23,223-255,269.

Eaton, D. W., Ross, G. M., Cook, F. a, and VanderVelden, a. 2000. Seismic imaging of the upper mantle beneath the Rocky Mountain foreland, southwestern Alberta. *Canadian Journal of Earth Sciences*, *37*(11), 1493–1507. http://doi.org/10.1139/e00-068

Eaton, D. W., and Hope, J. 2003. Structure of the crust and upper mantle of the Great Slave Lake shear zone, northwestern Canada, from teleseismic analysis and gravity modeling. Canadian Journal of Earth Sciences, 40(9); 1203–1218. http://doi.org/10.1139/e03-038

Eaton, D. W., Darbyshire, F., Evans, R. L., Grütter, H., Jones, A. G., and Yuan, X. 2009. The elusive lithosphere-asthenosphere boundary (LAB) beneath cratons. *Lithos*, *109*(1–2), 1–22. http://doi.org/10.1016/j.lithos.2008.05.009

Eeken, T., Goes, S., Pedersen, H. A., Arndt, N. T., and Bouilhol, P. 2018. Seismic evidence for depth-dependent metasomatism in cratons. *Earth and Planetary Science Letters*, *491*, 148–159. http://doi.org/10.1016/j.epsl.2018.03.018

Eccles, D. R., Heaman, L. M., Luth, R. W., and Creaser, R. A. 2004. Petrogenesis of the Late Cretaceous northern Alberta kimberlite province. *Lithos*, *76*(1–4 SPEC. ISS.), 435–459. http://doi.org/10.1016/j.lithos.2004.03.046

Eccles, D. R., Simonetti, S. S., and Cox, R. 2010. Garnet pyroxenite and granulite xenoliths from northeastern Alberta: Evidence of ~1.5 Ga lower crust and mantle in western Laurentia. *Precambrian Research*, *177*(3–4), 339–354. http://doi.org/10.1016/j.precamres.2010.01.006

Eccles, D. R. 2011. Northern Alberta kimberlite province : the first 20 years. *Energy Resources Conservation Board, ERCB/AGS Bulletin 65*.

Egbert, G. D. 1997. Robust multiple-station magnetotelluric data processing. Geophysical Journal International, 130(2): 475–496. http://doi.org/10.1111/j.1365-246X.1997.tb05663.x

Egbert, G. D., and Kelbert, A. 2012. Computational recipes for electromagnetic inverse problems. *Geophysical Journal International*, *189*(1), 251–267. http://doi.org/10.1111/j.1365-246X.2011.05347.x

Farquharson Colin G. Oldenburg Douglas W. Haber Eldad. 2002. An algorithm for the three-dimensional inversion of magnetotelluric data. Society of Exploration Geophysics. http://doi.org/10.1190/1.1817336.

Fournier, R. O. 1991. The transition from hydrostatic to greater than hydrostatic fluid pressure in presently active continental hydrothermal systems in crystalline rock. *Geophysical Research Letters*, *18*(5), 955–958.

Fowler C.M.R., 2005. The solid Earth: an introduction to global geophysics, 2nd ed. 685p.

Fritz, B., and Gerard, A. 2010. On the way to the exploitation of deep geothermal resources in naturally fractured environments. Comptes Rendus Geoscience, 342: 493–501. http://doi.org/10.1016/j.crte.2010.03.002

Frost, B. R., and Bucher, K. 1994. Is water responsible for geophysical anomalies in the deep continental crust? A petrological perspective. Tectonophysics, 231(4): 293–309. http://doi.org/10.1016/0040-1951(94)90040-X

Frost, B. R., Fyfe, W. S., Tazaki, K., and Chan, T. 1989. Grain-boundary graphite in rocks and implications for high electrical conductivity in the lower crust. *Nature*, *340*, 134–136.Genter, A., Evans, K., Cuenot, N., Fritsch, D., and Sanjuan, B. 2010. Contribution of the exploration of deep crystalline fractured reservoir of Soultz to the knowledge of enhanced geothermal systems (EGS). Comptes Rendus - Geoscience, 342(7–8): 502–516. http://doi.org/10.1016/j.crte.2010.01.006

Gaillard, F., Malki, M., Iacono-Marziano, G., Pichavant, M., and Scaillet, B. 2008. Carbonatite melts and electrical conductivity in the asthenosphere. *Science*, *322*(5906), 1363–1365. http://doi.org/10.1126/science.1164446

Garland, G. D., and Burwash, R. A. 1959. Geophysical and Petrological Study of Precambrian of Central Alberta, Canada. *AAPG Bulletin*, *43*(4), 790–806. http://doi.org/10.1306/0bda5ce7-16bd-11d7-8645000102c1865d

Geological Survey of Canada. 2017. Canadian Aeromagnetic Data Base, Airborne Geophysics Section, GSC: Central Canada Division, Geological Survey of Canada, Earth Sciences Sector, Natural Resources Canada.

Geomatics Canada. 2017. Canadian Geodetic Information System, Gravity and Geodetic Networks Section, Geodetic Survey Division, Geomatics Canada, Earth Sciences Sector, Natural Resources Canada.

Glover, P. W. J., Hole, M. J., and Pous, J. 2000. A modified Archie's law for two conducting phases. Earth and Planetary Science Letters, 180(0012), 369–383.

Gorman, A. R., Clowes, R. M., Ellis, R. M., Henstock, T. J., Spence, G. D., Keller, G. R., … Miller, K. C. 2002. Deep Probe: imaging the roots of western North America. Canadian Journal of Earth Sciences, 39(3), 375–398. http://doi.org/10.1139/e01-064

Gough, D.I. 1986. Mantle upflow tectonics in the Canadian Cordillera. Journal of Geophysical Research, 91: 1909-1919.

Green, D. H., Hibberson, W. O., Rosenthal, A., Kovács, I., Yaxley, G. M., Falloon, T. J., and Brink, F. 2014. Experimental Study of the Influence of Water on Melting and Phase Assemblages in the Upper Mantle. *Journal of Petrology*, *55*(10), 2067–2096. http://doi.org/10.1093/petrology/egu050

Griffin, W. ., O'Reilly, S. ., Abe, N., Aulbach, S., Davies, R. ., Pearson, N. ., … Kivi, K. 2003. The origin and evolution of Archean lithospheric mantle. *Precambrian Research*, *127*(1–3), 19–41. http://doi.org/10.1016/s0301-9268(03)00180-3

Griffin, W. L., O'Reilly, S. Y., Afonso, J. C., and Begg, G. C. 2009. The composition and evolution of lithospheric mantle: A re-evaluation and its tectonic implications. *Journal of Petrology*, *50*(7), 1185–1204. http://doi.org/10.1093/petrology/egn033

Groom, R. W., and Bailey, R. C. 1989. Decomposition of Magnetotelluric Impedance Tensors in the Presence of Local Three-Dimensional Galvanic Distortion. Journal of Geophysical Research, 94(No. B2): 1913–1925. http://doi.org/10.1029/JB094iB02p01913

Gu, Y. J., Ahmet, O., Shen, L., and Sean, C. 2011. The Canadian Rockies and Alberta Network (CRANE): New Constraints on the Rockies and Western Canada Sedimentary Basin. Seismological Research Letters, 82(4): 575–588. http://doi.org/10.1785/gssrl

Gu, Y. J., and Shen, L. 2015. Noise correlation tomography of Southwest Western Canada Sedimentary Basin. *Geophysical Journal International*, *202*(1), 142–162. http://doi.org/10.1093/gji/ggv100

Gu, Y. J., Chen, Y., Dokht, R. M. H., and Wang, R. 2018. Precambrian Tectonic Discontinuities in Western Laurentia: Broadband Seismological Perspectives on the Snowbird and Great Falls Tectonic Zones. *Tectonics*, *37*(5), 1411–1434. http://doi.org/10.1029/2017TC004843

Hanmer, S., Bowring, S., van Breemen, O., and Parrish, R. 1992. Great Slave Lake shear zone, NW Canada : mylonitic record of Early Proterozoic continental convergence, collision and indentation. *Journal of Structural Geology*, *14*(7), 757–773. http://doi.org/10.1016/0191-8141(92)90039-Y

Hanmer, S., Williams, M., and Kopf, C. 1995. Striding-Athabasca mylonite zone: implications for the Archean and Early Proterozoic tectonics of the western Canadian Shield. *Canadian Journal of Earth Sciences*, *32*(2), 178–196. http://doi.org/10.1139/e95-015

Haak, V., and Hutton, R. 1986. Electrical resistivity in continental lower crust. Geological Society Special Publications, 24: 35–49. http://doi.org/10.1144/GSL.SP.1986.024.01.05

Hanmer, S., Bowring, S., van Breemen, O., and Parrish, R. 1992. Great Slave Lake shear zone, NW Canada : mylonitic record of Early Proterozoic continental convergence, collision and indentation. Journal of Structural Geology, 14(7): 757–773. http://doi.org/10.1016/0191-8141 (92)90039-Y

Hauff, P. L. 2001. Alteration Mineralogy of Alberta Kimberlites : PIMA TM Infrared Spectroscopic Analysis. *Eub*, 79.

Heise, W., and Pous, J. 2001. Effects of anisotropy on the two-dimensional inversion procedure. Geophysical Journal International, 147(3): 610–621. http://doi.org/10.1046/j.0956-540x.2001.01560.x

Heise, W., and Pous, J. 2003. Anomalous phases exceeding 90° in magnetotellurics: Anisotropic model studies and a field example. Geophysical Journal International, 155(1): 308–318. http://doi.org/10.1046/j.1365-246X.2003.02050.x

Heise, W., Caldwell, T. G., Bibby, H. M., and Brown, C. 2006. Anisotropy and phase splits in magnetotellurics. Physics of the Earth and Planetary Interiors, 158(2–4): 107–121. http://doi.org/10.1016/j.pepi.2006.03.021

Hildebrand, R. S., Hoffman, P. F., and Bowring, S. A. 1987. Tectono-magmatic evolution of the 1.9-Ga great bear magmatic zone, Wopmay orogen, northwestern Canada. *Journal of Volcanology and Geothermal Research*, *32*(1–3), 99–118. http://doi.org/10.1016/0377-0273(87)90039-4

Hirschmann, M. M., Tenner, T., Aubaud, C., and Withers, A. C. 2009. Dehydration melting of nominally anhydrous mantle: The primacy of partitioning. *Physics of the Earth and Planetary Interiors*, *176*(1–2), 54–68. http://doi.org/10.1016/j.pepi.2009.04.001

Hoffman, P. F. 1989. Precambrian geology and tectonic history of North America. *The Geology of North America - An Overview: Boulder, Colorado, Geological Society of America*.

Hoffman, P. F. 1988. United plates of American, the birth of a craton: early Proterozoic assembly and growth of Laurentia. *Annual Review of Earth and Planet Science*, *16*, 543–603.

Hoffman, P. F. 1987. Continental transform tectonics: Great Slave Lake shear zone (ca. 1.9 Ga), northwest Canada. *Geology*, *15*(9), 785–788.

Hope, J., Eaton, D. W., and Ross, G. M. 1999. Lithoprobe seismic transect of the Alberta Basin: Compilation and overview. *Bulletin of Canadian Petroleum Geology*, *47*(4), 331–345.

Hope, J., and Eaton, D. 2002. Crustal structure beneath the Western Canada Sedimentary Basin: constraints from gravity and magnetic modelling. *Canadian Journal of Earth Sciences*, *39*(3), 291–312. http://doi.org/10.1139/e01-060

Hyndman, R. D., Vanyan, L. L., Marquis, G., and Law, L. K. 1993. the Origin of Electrically Conductive Lower Continental-Crust - Saline Water or Graphite. *Physics of the Earth and Planetary Interiors*, *81*(1–4), 325–344.

Hyndman, R. D., and Currie, C. A. 2011. Why is the North America Cordillera high? Hot backarcs, thermal isostasy, and mountain belts. *Geology*, *39*(8), 783–786. http://doi.org/10.1130/G31998.1

Jaupart, C., and Mareschal, J. C. 2015. Heat Flow and Thermal Structure of the Lithosphere. *Treatise on Geophysics: Second Edition (Vol. 6). Elsevier B.V. http://doi.org/10.1016/B978-0-444-53802-4.00114-7*

Jiracek, G. R., Rodi, W. L., and Vanyan, L. L. 1987. Implications of magnetotelluric modeling for the deep crustal environment in the Rio Grande rift. *Physics of the Earth and Planetary Interiors, 45(2), 179–192. http://doi.org/10.1016/0031-9201(87)90052-5*

Jobin, D. M., Veronneau, M. and Miles, W., 2017. Isostatic residual gravity anomaly map, Canada / Geological Survey of Canada, Open File 8076; scale 1:7 500 000. Doi:10.4095/299556.

Jones, A. G. 1983. On the equivalence of the "Niblett"and "Bostick" transformation in the magnetotelluric method. *Journal of Geophysics*, *53*, 72–73.

Jones, A. G. 1983. The problem of current channelling: A critical review. *Geophysical Surveys*, *6*(1–2), 79–122. http://doi.org/10.1007/BF01453996

Jones, A. G. 1988. Static shift of magnetotelluric data and its removal in a sedimentary basin environment. *Geophysics*, *53*(7), 967. http://doi.org/10.1190/1.1442533

Jones, A. G. 1993. Electromagnetic images of modern and ancient subduction zones. Tectonophysics, 219(1–3): 29–45. http://doi.org/10.1016/0040-1951(93)90285-R

Jones, A. G., Katsube, T. J., and Schwann, P. 1997. The longest conductivity anomaly in the world explained: Sulphides in fold hinges causing very high electrical anisotropy. Journal of Geomagnetism and Geoelectricity, 49(11–12): 1619–1629. http://doi.org/10.5636/jgg.49.1619

Jones, A. G. 2002. Magnetotelluric and teleseismic study across the Snowbird Tectonic Zone, Canadian Shield: A Neoarchean mantle suture? *Geophysical Research Letters*, *29*(17), 17–20. http://doi.org/10.1029/2002GL015359

Jones, F. W., Munro, R. A., Craven, J. A., Boerner, D. E., Kurtz, R. D., and Sydora, R. D. 2002. Regional geoelectrical complexity of the Western Canada Basin from magnetotelluric tensor invariants. *Earth, Planets and Space*, *54*(9), 899–905. http://doi.org/10.1186/BF03352437

Jones, A. G., and Craven, J. A. 2004. Area selection for diamond exploration using deep-probing electromagnetic surveying. *Lithos*, *77*(1–4 SPEC. ISS.), 765–782. http://doi.org/10.1016/j.lithos.2004.03.057

Jones, A. G., Ledo, J., Ferguson, I. J., Craven, J. A., Unsworth, M. J., Chouteau, M., and Spratt, J. E. 2014. The electrical resistivity of Canada's lithosphere and correlation with other parameters: contributions from Lithoprobe and other programmes. *Canadian Journal of Earth Sciences/Revue Canadienne Des Sciences de La Terre*, *51*(6), 573–617. http://doi.org/10.1139/cjes-2013-0151

Jones, A. P., Genge, M., and Carmody, L. 2013. Carbonate Melts and Carbonatites. *Reviews in Mineralogy and Geochemistry*, *75*(1), 289–322. http://doi.org/10.2138/rmg.2013.75.10

Jupp. D. L. B. and Vozoff, K. 1975. Stable iterative methods for the inversion of geophysical data. Geophys. J. Roy. Astr. Soc. 42. 957-976.

Jupp, D. L. B., and Vozoff, K. 1977. Two-dimensional magnetotelluric inversion. *Geophysical Journal of the Royal Astronomical Society*, *50*(2), 333–352. http://doi.org/10.1111/j.1365-246X.1977.tb04177.x

Kanasewich, E., Clowes, R., and McCloughan, C. 1969. A buried Precambrian rift in western Canada. *Tectonophysics*, *8*(4–6), 513–527. http://doi.org/10.1016/0040-1951(69)90051-1

Kao, H., Behr, Y., Currie, C. A., Hyndman, R., Townend, J., Lin, F. C., … He, J. 2013. Ambient seismic noise tomography of Canada and adjacent regions: Part I. Crustal structures. *Journal of Geophysical Research: Solid Earth*, *118*(11), 5865–5887. http://doi.org/10.1002/2013JB010535

Karato, S. 1990. © 19 90 Nature Publishing Group. *Letter to Nature*, *347*, 272–273. http://doi.org/10.1016/0021-9797(80)90501-9

Kakudate, Y., Mori, N., and Kino, Y. 1979. Pressure effect on the anomalous electrical conductivity of magnetite. *Journal of Magnetism and Magnetic Materials*, *12*, 22–25.

Kelbert, A., Meqbel, N., Egbert, G. D., and Tandon, K. 2014. ModEM: A modular system for inversion of electromagnetic geophysical data. *Computers and Geosciences*, *66*, 40–53. http://doi.org/10.1016/j.cageo.2014.01.010

Kuiper, Y. D., Shields, C. D., Tubrett, M. N., Bennett, V., and Buchwaldt, R. 2014. Age and provenance of a Paleoproterozoic to Devonian Canadian Cordilleran sequence of metasedimentary rocks, Thor-Odin dome, southeastern British Columbia. *Bulletin of* the Geological Society of America, 126(9–10), 1259–1274. http://doi.org/10.1130/B31031.1

Lee, C. T., Yin, Q., Rudnick, R. L., and Jacobsen, S. B. 2001. Preservation of ancient and fertile lithospheric mantle beneath the southwestern United States. *Nature*, *411*(6833), 69–73. http://doi.org/10.1038/35075048

Lee, C. T. 2003. Compositional variation of density and seismic velocities in natural peridotites at STP conditions: Implications for seismic imaging of compositional

heterogeneities in the upper mantle. Journal of Geophysical Research: Solid Earth, 108(B9). http://doi.org/10.1029/2003jb002413

Lemieux, S., Ross, G. M., and Cook, F. a. 2000. Crustal geometry and tectonic evolution of the Archean crystalline basement beneath the southern Alberta Plains, from new seismic reflection and potential-field studies. *Canadian Journal of Earth Sciences*, *37*(11), 1473–1491. http://doi.org/10.1139/e00-065

Lewry, J. F., Hajnal, Z., Green, A., Lucas, S. B., White, D., Stauffer, M. R., … Clowes, R. 1994. Structure of a Paleoproterozoic continent-continent collision zone: a LITHOPROBE seismic reflection profile across the Trans-Hudson Orogen, Canada. *Tectonophysics*, *232*(1–4), 143–160. http://doi.org/10.1016/0040-1951(94)90081-7

Li, Y., Yang, X., Yu, J. H., and Cai, Y. F. 2016. Unusually high electrical conductivity of phlogopite: the possible role of fluorine and geophysical implications. Contributions to Mineralogy and Petrology, 171(4), 1–11. http://doi.org/10.1007/s00410-016-1252-x

Liddell, M., Unsworth, M., and Pek, J. 2016. Magnetotelluric imaging of anisotropic crust near Fort McMurray , Alberta : implications for engineered geothermal system development. Geophysical Journal International, 205: 1365–1381. http://doi.org/10.1093/gji/ggw089

Liu, Q., and Gu, Y. J. 2012. Seismic imaging: From classical to adjoint tomography. *Tectonophysics*, *566–567*, 31–66. http://doi.org/10.1016/j.tecto.2012.07.006

Lizarralde, D., Chave, A., Hirth, G., and Schultz, A. 2004. Northeastern Pacific mantle conductivity profile from long-period magnetotelluric sounding using Hawaii-to-California submarine cable data. *Journal of Geophysical Research: Solid Earth*, *100*(B9), *17837–17854. http://doi.org/10.1029/95jb01244*

Lowrie William, 2007. *Fundamentals of Geophysics; 2nd edition, Cambridge University Press, 390p.*

Lyell, Charles. 1830. Principles of geology, being an attempt to explain the former changes of the Earth's surface, by reference to causes now in operation. London: John Murray. Volume 1.

Mackie, R. L., Madden, T. R., and Wannamaker, P. E. 1993. *3-Dimensional Magnetotelluric Modeling Using Difference-Equations - Theory and Comparisons To Integral-Equation Solutions. Geophysics, 58(2), 215–226. http://doi.org/10.1190/1.1443407*

Mackie, R. L., and Madden, T. R. 1993. Three-dimensional magnetotelluric inversion using conjugate gradients. *Geophysical Journal International*, *115*, 215–229.

Madden. T., and P. Nelson. 1964. A denfense of Cagniard's magnetotelluric method, Project Report NR-371-401. Office of Naval Res. U.S.A.

Madden, T. R., and Mackie, R. L. 1989. Three-dimensional Magnetotelluric Modeling and Inversion. *Proceedings of the IEEE*, *77*(2), 318–333. http://doi.org/10.1109/5.18628

Mahan, K. H., and Williams, M. L. 2005. Reconstruction of a large deep-crustal terrane: Implications for the Snowbird tectonic zone and early growth of Laurentia. *Geology*, *33*(5), 385–388. http://doi.org/10.1130/G21273.1

Majorowicz, J., Nieuwenhuis, G., Unsworth, M., Phillips, J., and Verveda, R. 2014. High Temperatures Predicted in the Granitic Basement of Northwest Alberta -an Assessment of the EGS Energy Potential. *In* Proceedings of the 39th Workshop on Geothermal Reservoir Engineering, Stanford University, Stanford, California, February. pp. 24-26.

Majorowicz, J. A. 2016. Heat flow–heat production relationship not found: what drives heat flow variability of the Western Canadian foreland basin? *International Journal of Earth Sciences*, (Majorowicz 1996), 1–14. http://doi.org/10.1007/s00531-016-1352-x

Mandler, H. A. F., and Clowes, R. M. 1998. The HSI bright reflector: Further evidence for extensive magmatism in the Precambrian of western Canada. *Tectonophysics*, *288*(1–4), 71–81. http://doi.org/10.1016/S0040-1951(97)00284-9

Martí, A. 2014. The Role of Electrical Anisotropy in Magnetotelluric Responses: From Modelling and Dimensionality Analysis to Inversion and Interpretation. *Surveys in Geophysics*, *35*(1), 179–218. http://doi.org/10.1007/s10712-013-9233-3

Maxwell, James Clerk. 1865. "A dynamical theory of the electromagnetic field". Philosophical Transactions of the Royal Society of London. 155: 459–512.

McDonough, M. R., McNicoll, V. J., Schetselaar, E. M., and Grover, T. W. 2000. Geochronological and kinematic constraints on crustal shortening and escape in a two-sided oblique-slip collisional and magmatic orogen, Paleoproterozoic Taltson magmatic zone, northeastern Alberta. *Canadian Journal of Earth Sciences*, *37*(11), 1549–1573. http://doi.org/10.1139/e00-089

McNeice, G. W., and Jones, A. G. 2001. Multisite, multifrequency tensor decomposition of magnetotelluric data. Geophysics, 66(1): 158–173. http://doi.org/10.1190/1.1444891

Meert, J. G. 2012. What's in a name? The Columbia (Paleopangaea/Nuna) supercontinent. *Gondwana Research*, *21*(4), 987–993. http://doi.org/10.1016/j.gr.2011.12.002

Monroe James S. and Wicander Reed. 2014. The Changing Earth – Exploring Geology and Evolution. 7th edition. Published by: Brooks Cole..

Mossop, G.D. and Shetsen, I., comp. 1994: Geological atlas of the Western Canada Sedimentary Basin; Canadian Society of Petroleum Geologists and Alberta Research Council, URL <http://ags.aer.ca/reports/atlas-of-the-western-canada-sedimentary-basin.htm>

Müller, R. D., Sdrolias, M., Gaina, C., and Roest, W. R. 2008. Age, spreading rates, and spreading asymmetry of the world's ocean crust. Geochemistry, Geophysics, Geosystems, 9(4), 1–19. https://doi.org/10.1029/2007GC001743

Myer, D., Constable, S., and Key, K. 2013. Magnetotelluric evidence for layered mafic intrusions beneath the vøring and exmouth rifted margins. *Physics of the Earth and Planetary Interiors*, *220*, 1–10. http://doi.org/10.1016/j.pepi.2013.04.007

Narod, B. B., Bennest, J. R., and Booker, J. R. 2001. Low Power Long Period Magnetotelluric System. American Geophysical *Union, Fall Meeting 2001*.

Nelson, P. H., and Van Voorhis, G. D. 1983. Estimation of sulfide content from induced polarization data. Geophysics, 48(1): 62–75. http://doi.org/10.1190/1.1441408

Niblett, E. R., and Sayn-Wittgenstein, C. 1960. Variation of Electrical Conductivity with Depth by the Magneto-Telluric Method. *Geophysics*, *25*, 998–1008. http://doi.org/10.1190/1.1438799

Nieuwenhuis, G., Unsworth, M. J., Pana, D., Craven, J., and Bertrand, E. 2014. Three-dimensional resistivity structure of Southern Alberta, Canada: implications for Precambrian tectonics. *Geophysical Journal International* , *197*(2), 838–859. http://doi.org/10.1093/gji/ggu068

Nieuwenhuis, G., Lengyel, T., Majorowicz, J., Grobe, M., Rostron, B., Unsworth, M. J., and Weides, S. 2015. Regional-Scale Geothermal Exploration Using Heterogeneous Industrial Temperature Data ; a Case Study from the Western Canadian Sedimentary Basin. In Proceedings of the World Geothermal Congress, Melbourne, Australia, April. pp. 19–25.

O'Brien, H. E., Irving, A. J., McCallum, I. S., and Thirlwall, M. F. 1995. Strontium, neodymium, and lead isotopic evidence for the interaction of post-suhduction asthenospheric potassic mafic magmas of the Highwood Mountains, Montana, USA, with ancient

Wyoming craton lithospheric mantle. *Geochimica et Cosmochimica Acta*, *59*(21), 4539–4556. http://doi.org/10.1016/0016-7037(95)99266-J

Olson, R. A., Eccles, D. R., Dinu, P., Edward, D., Beaton A., and Maslowski, A. 2006. Summary of mineral exploration and coal activity in Alberta during 2005.

Ootes, L., Davis, W. J., Jackson, V. A., and Breemen, O. Van. 2015. Chronostratigraphy of the Hottah terrane and Great Bear magmatic zone of Wopmay Orogen, Canada, and exploration of a terrane translation model. Canadain Journal of Earth Sciences, 52(12): 1062–1092. http://doi.org/10.1139/cjes-2015-0026

Pană, D. I. 2003. Precambrian Basement of the Western Canada Sedimentary Basin in Northern Alberta. EUB/AGS Earth Sciences Report 2002-02, Alberta Energy and Utilities Board.

Parker, R. L. 1980. The Inverse Problem of Electromagnetic Induction: Existence and Construction of Solutions Based On Incomplete Data. *Journal of Geophysical Research*, *85*(80), 4421–4428. http://doi.org/10.1029/JB085iB08p04421

Parkinson, W. D. 1962. The influence of continents and oceans on geomagnetic variations. *Geophysical Journal International*, *6*(4), 441–449.

Pearce, C. I. 2006. Electrical and Magnetic Properties of Sulfides. *Reviews in Mineralogy and Geochemistry*, *61*(1), 127–180. http://doi.org/10.2138/rmg.2006.61.3

Peeples, W. J., and Rankin, D. 1973. A magnetotelluric study in the western Canadian sedimentary basin. *Pure and Applied Geophysics PAGEOPH*, *102*(1), 134–147. http://doi.org/10.1007/BF00876600

Pek, J., and Verner, T. 1997. Finite-difference modeling of magnetotelluric fields in two-dimensional anisotropic media. Geophysical Journal International, 128(3): 505–521. http://doi.org/10.1111/j.1365-246X.1997.tb05314.x

Perry, H. K. C., Jaupart, C., Mareschal, J.-C., and Shapiro, N. M. 2006. Upper mantle velocity-temperature conversion and composition determined from seismic refraction and heat flow. Journal of Geophysical Research, 111(B7), 1–14. http://doi.org/10.1029/2005jb003921

Pilkington, M., Miles, W. F., Ross, G. M., and Roest, W. R. 2000. Potential-field signatures of buried Precambrian basement in the Western Canada Sedimentary Basin. Canadian Journal of Earth Science, 37: 1453–1471. http://doi.org/10.1139/e00-020

Plint, Heather, E., and Ross, Gerald, M. 1993. ^{40}Ar-^{39}Ar geochronology of selected crystalline basement samples from the Alberta Basin: the timing of Proterozoic assembly of the subsurface of western Canada. Radiogenic Age and Isotopic Studies: Report 7, Geological Survey of Canada, Paper 93-2, p. 71-82.

Pollack, H. N., and Chapman, D. S. 1977. On the regional variation of heat flow, geotherms, and lithospheric thickness. *Tectonophysics*, *38*(3–4), 279–296. http://doi.org/10.1016/0040-1951(77)90215-3

Price, a. T. 1962. The theory of magnetotelluric methods when the source field is considered. *Journal of Geophysical Research*, *67*(5), 1907–1918. http://doi.org/10.1029/JZ067i005p01907

Prior, G.J. 2013. Notes to Accompany Map 600 : Bedrock Geology of Notes to Accompany Map 600 : Bedrock Geology of Alberta. AER/AGS Open File Report, Alberta Energy Regulator.

Rader, E., Emry, E., Schmerr, N., Frost, D., Cheng, C., Menard, J., … Geist, D. 2015. Characterization and Petrological Constraints of the Midlithospheric Discontinuity. *Geochemistry, Geophysics, Geosystems*, *16*(10), 3484–3504. http://doi.org/10.1002/2015GC005943

Rankin D. and Reddy I. K. 1969. Geophysics. Vol 34. Issue 3. 305-503. http://dx.doi.org/10.1190/1.1440021

Reichenbach, I. G. 1991. The Bell Island Bay Group, remnant of an Early Proterozoic ensialic marginal basin in Wopmay orogen, District of Mackenzie. Geological Survey of Canada, Paper, no. 88-28. Natural Resources Canada.

Reddy, I. K., and Rankin, D. 1972. Magnetotelluric Measurements in Central Alberta. *Geophysics*, *36*(4), 739–753. http://doi.org/10.1190/1.1440209

Rippe, D., Unsworth, M. J., and Currie, C. A. 2013. Magnetotelluric constraints on the fluid content in the upper mantle beneath the southern Canadian Cordillera: Implications for rheology. *Journal of Geophysical Research: Solid Earth*, *118*(10), 5601–5624. http://doi.org/10.1002/jgrb.50255

Rodi, W., and Mackie, R. L. 2001. Nonlinear conjugate gradients algorithm for 2-D magnetotelluric inversion. Geophysics, 66(1): 174–187. http://doi.org/10.1190/1.1444893

Ross, G. M. 1990. Deep crust and basement structure of the Peace River Arch region: constraints on mechanisms of formation. Bulletin of Canadian Petroleum Geology, 38A. pp. 25–35.

Ross, G. M., Parrish, R. R., Villeneuve, M. E., and Bowring, S. A. 1991. Geophysics and geochronology of the crystalline basement of the Alberta Basin, western Canada. Canadian Journal of Earth Sciences, 28(4): 512–522. http://doi.org/10.1139/e91-045

Ross, G. M., Broome, J., and Miles, W. 1994. Chapter 4 - Potential fields and basement structure - Western Canada Sedimentary Basin; in Geological Atlas of the Western Canada Sedimentary Basin, G.D. Mossop and I. Shetsen (comp.). *Canadian Society of Petroleum Geologists and Alberta Research Council*, 41–47. Retrieved from http://ags.aer.ca/publications/chapter-4-potential-fields-and-basement-structure

Ross, G. M., and Eaton, D. W. 1997. Winagami reflection sequence: Seismic evidence for postcollisiona magmatism in the Proterozoic of western Canada. Geology, 25(3), 199–202. http://doi.org/10.1130/0091-7613(1997)025<0199:WRSSEF>2.3.CO;2

Ross, G. M., Eaton, D. W., Boerner, D. E., and Miles, W. 2000. Tectonic entrapment and its role in the evolution of continental lithosphere: An example from the Precambrian of western Canada. Tectonics, 19(1), 116. http://doi.org/10.1029/1999TC900047

Ross, G. M., and Eaton, D. W. 2001. Basement reactivation in the Alberta Basin: Observational constraints and mechanical rationale. Canadian Society of Petroleum Geologists, 49(3). http://doi.org/10.2113/49.3.429

Ross, G. M. 2002. Evolution of Precambrian continental lithosphere in Western Canada: results from Lithoprobe studies in Alberta and beyond. Canadian Journal of Earth Sciences, 39(3): 413–437. http://doi.org/10.1139/e02-012

Ross, G. M., and Eaton, D. W. 2002. Proterozoic tectonic accretion and growth of western Laurentia: results from Lithoprobe studies in northern Alberta. Canadian Journal of Earth Sciences, 39(3): 313–329. http://doi.org/10.1139/e01-081

Schaeffer, A. J., and Lebedev, S. 2014. Imaging the North American continent using waveform inversion of global and USArray data. Earth and Planetary Science Letters, 402(C), 26–41. http://doi.org/10.1016/j.epsl.2014.05.014

Schultz, M. E. J., Chacko, T., Heaman, L. M., Sandeman, H. A., Simonetti, A., and Creaser, R. A. 2007. Queen Maud block: A newly recognized Paleoproterozoic (2.4–2.5 Ga) terrane in northwest Laurentia. *Geology*, *35*(8), 707. http://doi.org/10.1130/g23629a.1

Schaeffer, A. J., and Lebedev, S. 2013. Global shear speed structure of the upper mantle and transition zone. *Geophysical Journal International*, *194*(1), 417–449. http://doi.org/10.1093/gji/ggt095

Scholz, C., H. 1988. The brittle-plastic transition and the depth of seismic faulting. Geologische Rundschau, 77(1), 319–328.

Selway, K. 2014. On the Causes of Electrical Conductivity Anomalies in Tectonically Stable Lithosphere. Surveys in Geophysics, 35(1), 219–257. http://doi.org/10.1007/s10712-013-9235-1

Shragge, J., Bostock, M. G., Bank, C. G., and Ellis, R. M. 2002. Integrated teleseismic studies of the southern Alberta upper mantle. *Canadian Journal of Earth Sciences*, *39*(3), 399–411. http://doi.org/10.1139/e01-084

Sibson, R. H. 1977. Fault rocks and fault mechanisms. Journal of the Geological Society, 133(3), 191–213. https://doi.org/10.1144/gsjgs.133.3.0191

Sinmyo, R., and Keppler, H. 2017. Electrical conductivity of NaCl-bearing aqueous fluids to 600 °C and 1 GPa. Contributions to Mineralogy and Petrology, 172(1), 4. http://doi.org/10.1007/s00410-016-1323-z

Siripunvaraporn, W., and Egbert, G. 2000. An efficient data-subspace inversion method for 2-D magnetotelluric data. *Geophysics*, *65*(3), 791–803. http://doi.org/10.1190/1.1444778

Siripunvaraporn, W., Egbert, G., Lenbury, Y., and Uyeshima, M. 2005. Three-dimensional magnetotelluric inversion: Data-space method. *Physics of the Earth and Planetary Interiors*, *150*(1–3 SPEC. ISS.), 3–14. http://doi.org/10.1016/j.pepi.2004.08.023

Smith, J. T., and Booker, J. R. 1988. Magnetotelluric inversion for minimum structure. *Geophysics*, *53*(12), 1565–1576. http://doi.org/10.1190/1.1442438

Smith, J., and Booker, J. R. 1991. Rapid inversion of two- and three-dimensional magnetotelluric data. *Journal of Geophysical Research*, *96*(4), 3905–3922. http://doi.org/10.1029/90JB02416

Simandl, G., and Davis, W. 2005. Cratonic Basement in Northeastern British Columbia: New U-Pb Geochronological Results and their Significance for Diamond Exploration. Geological Fieldwork 2004, Paper 2005-1, pp. 337–346.

Simmons, N. A., Myers, S. C., Johannesson, G., and Matzel, E. 2012. LLNL-G3Dv3: Global P wave tomography model for improved regional and teleseismic travel time prediction.

Journal of Geophysical Research: Solid Earth, *117*(10), 1–28. http://doi.org/10.1029/2012JB009525

Simpson, Fiona, and Bahr Karsten. Practical magnetotellurics. 2005. Cambridge university Press, Cambridge, U.K.

Sinmyo, R., and Keppler, H. 2017. Electrical conductivity of NaCl-bearing aqueous fluids to 600 °C and 1 GPa. *Contributions to Mineralogy and Petrology*, *172*(1): 4. http://doi.org/10.1007/s00410-016-1323-z

Siripunvaraporn, W., Egbert, G., Lenbury, Y., and Uyeshima, M. 2005. Three-dimensional magnetotelluric inversion: Data-space method. *Physics of the Earth and Planetary Interiors*, *150*(1–3 SPEC. ISS.), 3–14. http://doi.org/10.1016/j.pepi.2004.08.023

Srivastava, S. P., Douglass, J. L., and Ward, S. H. 2002. the Application of the Magnetotelluric and Telluric Methods in Central Alberta. *Geophysics*, *28*(3), 426–446. http://doi.org/10.1190/1.1439194

Stachel, T., and Luth, R. W. 2015. Diamond formation - Where, when and how? *Lithos*, *220–223*, 200–220. http://doi.org/10.1016/j.lithos.2015.01.028

Stern, R., Bleeker, W., 1998. Age of the world's oldest rocks refined using Canada's SHRIMP: The Acasta Gneiss Complex, northwest territories, Geoscience Canada 25, 27–31.

Swift, C. M. 1967. A magnetotelluric investigation of an electrical conductivity anomaly in the south-western United States. *PhD Thesis, Massachusetts Institute of Technology, Cambridge*.

Thompson, D. A., Bastow, I. D., Helffrich, G., Kendall, J.-M., Wookey, J., Snyder, D. B., and Eaton, D. W. 2010. Precambrian crustal evolution: Seismic constraints from the Canadian Shield. Earth and Planetary Science Letters, 297(3–4), 655–666. http://doi.org/10.1016/j.epsl.2010.07.021

Tikhonov, A. 1950. On Determining Electrical Characteristics of the Deep Layers of the Earth's Crust. *Dokl. Akas. Nauk USSR*, *73*, 295–297.

Türkoğlu, E., Unsworth, M., and Pana, D. 2009. Deep electrical structure of northern Alberta (Canada): implications for diamond exploration. Canadian Journal of Earth Sciences, 46(2): 139–154. http://doi.org/10.1139/E09-009

Unsworth, Martyn, J., Malin, Peter, E., Egbert, Gary, D., and Booker, John, R. 1997. Internal structure of the San Andreas fault at Parkfield , California. Geology, 25(4), 359–362. https://doi.org/10.1130/0091-7613(1997)025<0359:ISOTSA>2.3.CO;2

Unsworth, M., and Bedrosian, P. A. 2004. On the geoelectric structure of major strike-slip faults and shear zones. Earth, Planets and Space, 56(12): 1177–1184. http://doi.org/10.1186/BF03353337

Unsworth, M. 2010. Magnetotelluric studies of active continent-continent collisions. Surveys in Geophysics, 31(2): 137–161. http://doi.org/10.1007/s10712-009-9086-y

Unsworth, M., and Rondenay, S. 2013. Mapping the distribution of fluids in the crust and lithospheric mantle utilizing geophysical methods. *In* Metasomatism and the Chemical Transformation of Rock. Edited by Harlov, D. and Austrheim, H. Springer-Verlag Berlin Heidelberg. pp 535-598. http://doi.org/10.1007/978-3-642-28394-9

Unsworth, M. J., Egbert, G. D., and Booker, J. R. 1999. High-resolution electromagnetic imaging of the San Andreas Fault in Central California. Journal of Geophysical Research, 104(B1): 1131–1150. http://doi.org/10.1029/98JB01755

Van der Velden, A. J., and Cook, F. A. 2005. Relict subduction zones in Canada. Journal of Geophysical Research B: Solid Earth, 110(8): 1–17. http://doi.org/10.1029/2004JB003333

Villeneuve, M. E., Ross, G. M., Theriault, R. J., Miles, W., Parrish, R. R., and Broome, J. 1993. *TECTONIC SUBDIVISION AND U-Pb GEOCHRONOLOGY OF THE CRYSTALLINE BASEMENT OF THE ALBERTA BASIN, WESTERN CANADA*.

Vozoff, K., Hasegawa, H., and Ellis, R. M. 1963. Results and Limitations of Magnetotelluric Surveys in Simple Geologic Situations. *Geophysics*, *28*(5), 778–792. http://doi.org/10.1190/1.1439272

Vozoff K. and Ellis Robert M. 1966. Geophysics, Vol 31. Issue 6. 1037-1180. https://doi.org/10.1190/1.1439846

Vozoff, K. 1991. Chapter 8. The magnetotelluric method. Electromagnetic methods in applied geophysics. Volume 2, Application, Parts A and B. Society of Exploration Geophysicists. https://doi.org/10.1190/1.9781560802686.ch8.

Wait, J. R. 1954. On the Relation Between Telluric Currents and the Earth's Magnetic Field. In *Geophysics*, *19*, 281. http://doi.org/10.1190/1.1437994

Wang, E., Unsworth, M., and Chacko, T. 2018. Geoelectric structure of the Great Slave Lake shear zone in northwest Alberta: implications for structure and tectonic history. *Canadian Journal of Earth Sciences*, *55*(3). http://doi.org/10.1139/cjes-2017-0067

Wannamaker, P. E. 2005. Anisotropy versus heterogeneity in continental solid earth electromagnetic studies: Fundamental response characteristics and implications for physicochemical state. Surveys in Geophysics, 26: 733. http://doi.org/10.1007/s10712-005-1832-1

Wannamaker, P. E. 2000. Comment on "The petrologic case for a dry lower crust" by Bruce W. D. Yardley and John W. Valley. Journal of Geophysical Research, 105(B3): 6057–6064. http://doi.org/10.1029/1999JB900324

Wang, X. 1988a. Inversion of magnetovariation event to causative current. I. Current sheet model. *Physics of The Earth and Planetary Interiors*, *53*(1–2), 46–54. http://doi.org/10.1016/0031-9201(88)90135-5

Wang, X. 1988b. Inversion of magnetovariation event to causative current. III. Test of channelled current model, SABC conductor inverted as chennelled currents and structure evaluation. *Physics of The Earth and Planetary Interiors*, *53*(1–2), 64–79. http://doi.org/10.1016/0031-9201(88)90137-9

Wang, D., Mookherjee, M., Xu, Y., and Karato, S. 2006. The effect of water on the electrical conductivity of olivine. *Nature*, *443*(7114), 977–980. http://doi.org/10.1038/nature05256

Warner, M. 1990. Basalts, water, or shear zones in the lower continental crust? Tectonophysics, 173: 163–174. http://doi.org/10.1016/0040-1951(90)90214-S

Weides, S. N., Moeck, I. S., Schmitt, D. R., and Majorowicz, J. A. 2014. An integrative geothermal resource assessment study for the siliciclastic Granite Wash Unit, northwestern Alberta (Canada). Environmental Earth Science, 72: 4141. http://doi.org/10.1007/s12665-014-3309-3

Weidelt, P. 1985. Construction of conductance bounds from magnetotelluric impedances. *Journal of Geophysics*, *57*, 191–206.

Weckmann, U., Ritter, O., and Haak, V. 2003. A magnetotelluric study of the Damara Belt in Namibia 2. MT phases over 90° reveal the internal structure of the Waterberg Fault/Omaruru Lineament. Physics of the Earth and Planetary Interiors, 138(2): 91–112. http://doi.org/10.1016/S0031-9201 (03)00079-7

B.F. Windley. 1997. The Evolving Continents, Wiley, Chichester. 526 pp.

Wiese, von H. 1962. Geomagnetische Tiefentellurik Teil II: Die Streichrichtung der untergrundstrukturen des elektrischen Widerstandes, erschlossen aus

geomagnetischen Variationen. Geofisica Pura E Applicata, 52(1): 83–103. http://doi.org/10.1007/BF01996002

Wright, G. N., McMechan, M. E., and Potter, D. E. G. 1994. Structure and Architecture of the Western Canada Sedimentary Basin, In Geological Atlas of the Western Canada Sedimentary Basin, *Edited by* G.D. Mossop and I. Shetsen. Canadian Society of Petroleum Geologists and Alberta Research Council. Available from http://ags.aer.ca/publications/chapter-3-structure-and-architecture.htm

Wu, F. T. 1968. The inverse problem of magnetotelluric sounding: Geophysics. 33. 972-979.

Wu, X., Ferguson, I. J., and Jones, A. G. 2002. Magnetotelluric response and geoelectric structure of the Great Slave Lake shear zone. Earth and Planetary Science Letters, 196(1–2): 35–50. http://doi.org/10.1016/S0012-821X (01)00594-5

Wu, L., Gu, Y. J., Chen, Y., and Liang, H. 2018. *Shear wave splitting discloses two episodes of collision-related convergence in western North America*. *Journal of Geophysical Research-Solid Earth*. http://doi.org/10.1029/2018JB016352

Wust, R. a J., Nassichuk, B. R., and Bustin, R. M. 2013. Porosity Characterization of Various Organic-rich Shales from the Western Canadian Sedimentary Basin, Alberta and British Columbia, Canada. *AAPG Memoir 102: Electron Microscopy of Shale Hydrocarbon Reservoirs*, 81–100. http://doi.org/10.1306/13391707M1023585

Yardley, B. W. D., and Valley, J. W. 1997. The petrologic case for a dry lower crust high that rise to a fluid pressure to the rock that is still hot and ductile , the fluid pressure. *Journal of Geophysical Research*, *102*(97), 12173–12185. http://doi.org/doi:10.1029/9; http://dx.doi.org/10.1029/97JB00508

Yin, Y., Unsworth, M., Liddell, M., Pana, D., and Craven, J. A. 2014. Electrical resistivity structure of the Great Slave Lake shear zone, northwest Canada: Implications for tectonic history. Geophysical Journal International, 199(1): 178–199. http://doi.org/10.1093/gji/ggu251

Yoshino, T., Laumonier, M., McIsaac, E., and Katsura, T. 2010. Electrical conductivity of basaltic and carbonatite melt-bearing peridotites at high pressures: Implications for melt distribution and melt fraction in the upper mantle. *Earth and Planetary Science Letters*, *295*(3–4), 593–602. http://doi.org/10.1016/j.epsl.2010.04.050

Yoshino, T., Matsuzaki, T., Shatskiy, A., and Katsura, T. 2009. The effect of water on the electrical conductivity of olivine aggregates and its implications for the electrical

structure of the upper mantle. *Earth and Planetary Science Letters*, *288*(1–2), 291–300. http://doi.org/10.1016/j.epsl.2009.09.032

Yoshino, T., and Noritake, F. 2011. Unstable graphite films on grain boundaries in crustal rocks. *Earth and Planetary Science Letters*, *306*(3–4), 186–192. http://doi.org/10.1016/j.epsl.2011.04.003

Yuan, H., Romanowicz, B., Fischer, K. M., and Abt, D. 2011. 3-D shear wave radially and azimuthally anisotropic velocity model of the North American upper mantle. *Geophysical Journal International*, *184*(3), 1237–1260. http://doi.org/10.1111/j.1365-246X.2010.04901.x

Zhdanov, M., and Hursan, G. 2000. 3D electromagnetic inversion based on quasi-analytical approximation. *Inverse Problems*, *16*(5), 1297–1322. http://doi.org/10.1088/0266-5611/16/5/311

Zelt, C. A., and Ellis, R. M. 1989. Seismic structure of the crust and upper mantle in the Peace River Arch Region, Canada. Journal of Geophysical Research, 94(B5): 5729–5744. http://doi.org/10.1029/JB094iB05p05729

Zelt, C. A., and White, D. 1995. crustal structure and tectonics of the southeastern Canadian Cordillera. *Journal of Geophysical Research*, *100*, 24,255-24,273.

Appendix

1. Two dimensional synthetic isotropic modeling and inversion

It was intended that the new broadband MT data would give an improved model of the electrical resistivity of the crust and uppermost mantle in the vicinity of the Hay River Fault zone. The MT data previously collected had a spacing of 10-20 km which was too coarse to resolve the crustal resistivity structure in detail. The new MT data were collected with a station spacing of 3-5 km. The previous MT data had a frequency range of 0.0001-0.2 Hz, which corresponds to a minimum skin depth of 3.7 km at the highest frequencies with 10 Ωm resistivity according to the skin depth equation (described in S7). The new MT data were collected with a frequency range of 0.001-1000 Hz, giving a minimum skin depth of 50 m with 10 Ωm resistivity. The reduced skin depth makes it easier to invert the shallow electrical structure (depth < 3.7 km) during 2-D inversion because the MT signals are diffusive.

In order to investigate how the new higher frequency broadband data give a better image of the crustal structure than the old long-period data, synthetic inversions were implemented, and the actual locations and frequency band of the field MT data were used. The synthetic model was developed from the preferred 2-D isotropic inversion model with the mesh of 112 columns and 62 layers extending 480 km horizontally and 580 km vertically. There are three layers in the synthetic model (a) a 2 km sedimentary basin (10 Ωm), (b) a 100 km highly resistive crystalline rocks (3000 Ωm), and (c) a 100 Ωm layer extending to the base of the mesh. Four conductors similar to the ones imaged in the

preferred 2-D isotropic inversion model were added also. Two sets of data were generated by forward modeling (Fig. S1a). (a) Synthetic data with frequency 1000-0.001 Hz were generated at the broadband MT stations. (b) Synthetic long-period MT data were generated at the long-period stations with a frequency range of 0.2-0.0001 Hz. Gaussian noise of 10% was added to each data set.

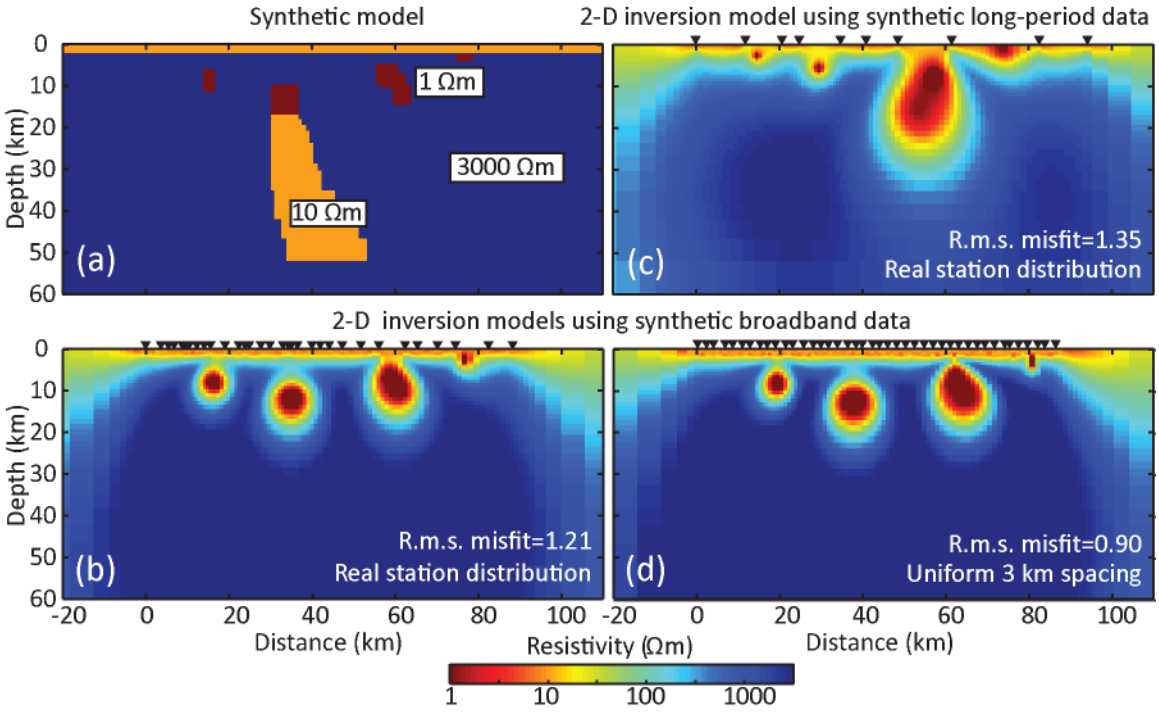

Fig. S1: Comparison of 2-D inversion models using synthetic data and actual distribution of broadband and long-period MT stations in the study area. (a) The forward model is made similar to the 2-D isotropic inversion result of the MT profile in this research. (b) The 2-D isotropic inversion model using broadband data generated from (a) with frequency range 327-0.0013 Hz and real MT station distribution. (c) The 2-D isotropic inversion model using long-period data generated from (a) with frequency range 0.0001-5 Hz. (d) The 2-D isotopic inversion model using broadband data generated from (a) with frequency range 327-0.0013 Hz and uniform 3 km inter-station spacing.

These two sets of synthetic data were inverted using the same mesh as the forward modeling and same inversion algorithm, mesh, error floor and tau value used to obtain the 2-D isotropic model. From these resistivity models (Fig. S1b&c), it is obvious that the new

MT data can resolve the crustal structures more reliably than the previously collected long-period MT data. The inversion model of the long-period synthetic data set can image the conductors but cannot tell the exact location or depth of the conductors while the broadband synthetic dataset can do it very well. Additionally, the long tail of the KC is not imaged by the broadband synthetic data, which means that it may be just an artifact of the inversion algorithm.

One more synthetic modeling study was implemented with a uniform station spacing (3 km) along the profile and broadband frequency range (1000-0.001 Hz) data were generated by forward modeling. The same procedure as described above was applied and the inversion model is shown in Fig. S1d. This model is very similar to the one with the actual station distribution and broadband frequency range. Therefore, it is confirmed that the actual station spacing used in this study is close enough to reliably determine the actual resistivity structure of the subsurface.

2. Data processing and analysis

1. Data processing

The broadband MT time series data were processed with both (a) the statistically robust technique of Egbert (1997) and (b) the Phoenix SSMT 2000 software to obtain estimates of the impedance and magnetic field transfer functions in the frequency range of 1000-0.001 Hz. Remote reference processing was applied to remove random non-coherent noise in the magnetic channels. The results for each MT station were evaluated based on the smoothness and mutual consistency of the apparent resistivity and phase curves. The final data used in the inversions were obtained with method (a), which gave better results

than method (b) for most of the sites. Using the same method for all sites also gave a consistent frequency set at stations. The selected MT data were edited to remove bad points which were obvious as outliers since the MT curves should always be smooth according to the theory of the MT impedance tensor (Chave and Jones 2012).

2. Characteristics of the MT data

MT data can be characterized quantitatively by impedance tensor, apparent resistivity and phase, and tipper or induction vectors, which are described below.

The magnetotelluric impedance is a tensor quantity which depends on the electric and magnetic field components and the angular frequency ω (ω=2πf, where f is the frequency in Hz). The xy component of the impedance is calculated from the north component of the electric field ($E_x(\omega)$) and the east component of the magnetic field ($H_y(\omega)$). Similarly, the yx component is derived from to the east component of the electric field ($E_y(\omega)$) and the north component of the magnetic field ($H_x(\omega)$). The relationship of the horizontal electric field and the impedance Z (ω) is defined as:

$$\begin{bmatrix} E_x(\omega) \\ E_y(\omega) \end{bmatrix} = \begin{bmatrix} Z_{xx}(\omega) & Z_{xy}(\omega) \\ Z_{yx}(\omega) & Z_{yy}(\omega) \end{bmatrix} \begin{bmatrix} H_x(\omega) \\ H_y(\omega) \end{bmatrix}$$

The impedance at each site is routinely plotted as a function of period, since this gives an impression of how the impedance varies with depth. It is convenient to plot these curves as apparent resistivity ($\rho_a(\omega)$) and phase ($\Phi(\omega)$), which are quantities that can be computed from the impedance.

$$\rho_a(\omega) = \frac{1}{\omega\mu}|Z(\omega)|^2 \; ; \; \phi(\omega) = tan^{-1}(Z(\omega))$$

where ω is the angular frequency, μ is the magnetic permeability, generally taken to be equal to the value of free space (Chave and Jones 2012).

Another quantity calculated from the data is the induction vector or tipper. The tipper (T_{zx}, T_{zy}) is defined as a transfer function of the horizontal and vertical magnetic field components (Chave and Jones 2012).

$$H_z(\omega) = T_{zx}(\omega)H_x(\omega) + T_{zy}(\omega)H_y(\omega)$$

The tipper is very sensitive to lateral resistivity changes since the vertical magnetic field H_z is generated by lateral variation of the resistivity (Chave and Jones 2012). The tipper can be projected onto the horizontal xy plane as the real and imaginary components of the induction vectors using the equation below,

$$\overrightarrow{T_{Real}(\omega)} = (Real\big(T_{zx}(\omega)\big), Real(T_{zy}(\omega)))$$

$$\overrightarrow{T_{Imag}(\omega)} = (Image\big(T_{zx}(\omega)\big), Image(T_{zy}(\omega))).$$

In this paper, the real components of the induction vectors are plotted to point away from conductors according to the Wiese convention (Wiese, 1962).

3. Typical MT data

All the curves collected in 2014 exhibit two kinds of features and corresponding typical examples (RLK100 and RLK180) are shown in Fig. S2. At high frequencies (> 1 Hz), the signals have a shallow penetration depth (about 1500 m) within the sedimentary basin. The apparent resistivity is about 10 Ωm and the phase angle is about 45° for both the TE and TM components. This shows that the electrical structure of the shallow part is 1-D. At

frequencies below 1 Hz, the apparent resistivity curves increase and the phase curves decrease because the MT signal passes through the sedimentary layer and starts to detect the more resistive crystalline basement rocks. At 0.1 Hz, the two modes start to diverge showing the structure of the subsurface is changing from 1-D to a more complicated structure (2-D or 3-D). A drop of resistivity curve is seen at station RLK100 at 0.01 Hz while the resistivity curve of the station RLK180 is quite flat.

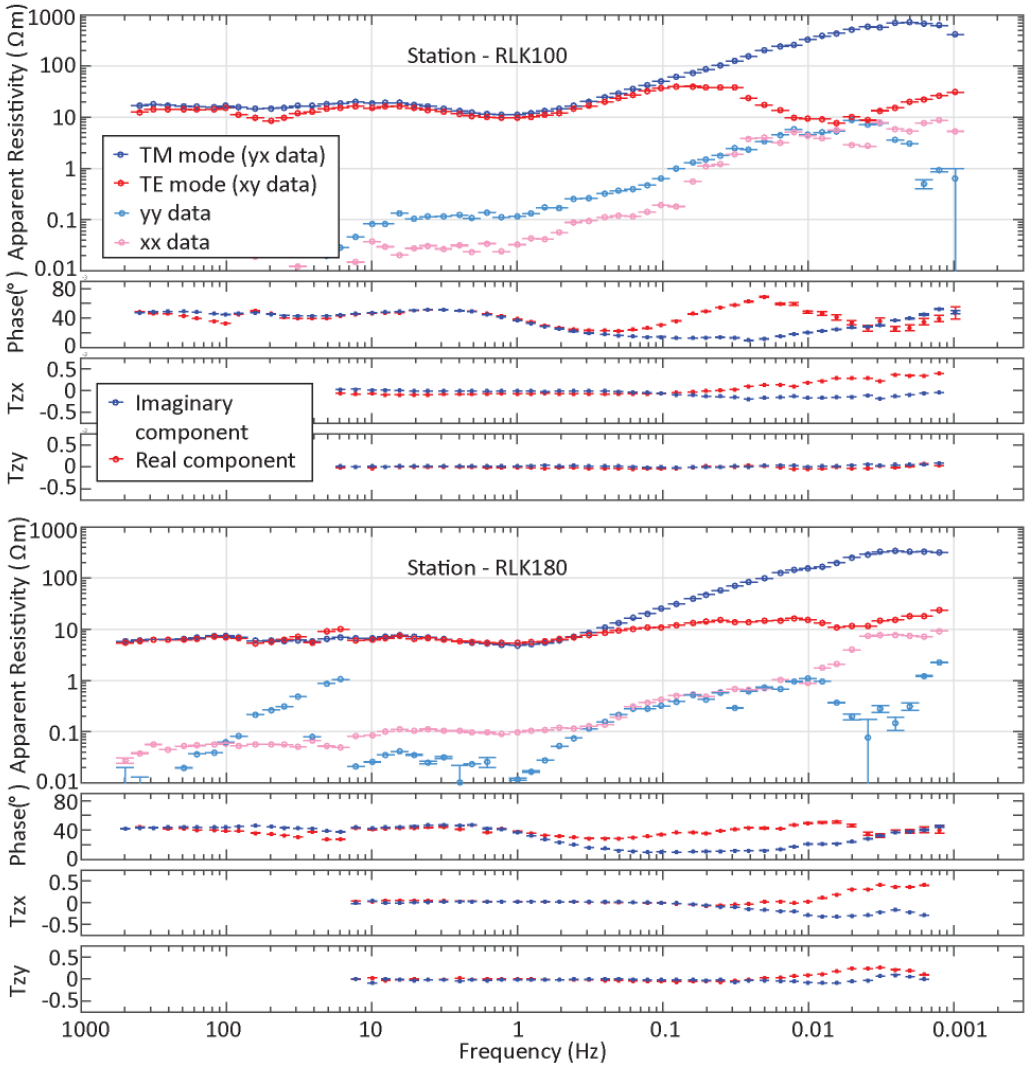

Fig. S2: MT data at two typical stations RLK100 and RLK180. Data shown are rotated to the geoelectric coordinate system (N40˚E).

There is a significant difference seen in the pseudo section of the TM and TE modes (Fig. S3). The TM mode pseudo section is quite consistent along the profile while there are variations seen in the TE mode pseudo section. The consistency of the TM mode was interpreted qualitatively as a result of very "thin" resistivity anomalies (Boerner, et al. 2000). The changing of features in the TE mode pseudo section indicates geoelectric structure change as pointed out by Boerner et al. (2000).

Theoretically, reversal of the sign of the T_{zy} should be expected across a 2-D low resistivity body. This is seen in the tipper pseudo section in Fig. S3. There are three sign reversals seen at stations RLK070, RLK090 and RLK150 in the pseudo section of the real component of H_z. This may indicate that there are three conductors at these sites where tipper reversal is seen.

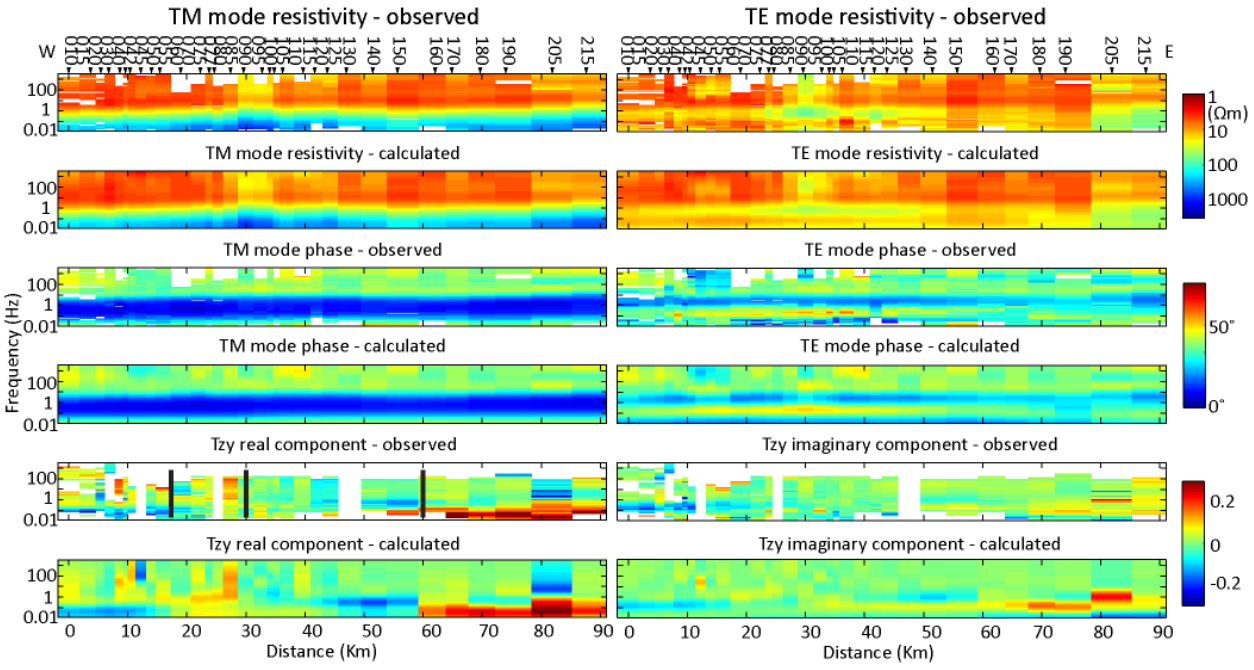

Fig. S3: Comparison of the pseudo sections of the responses calculated from the preferred 2-D inversion model and the observed data. The three black lines mark the reversal of the sign of the tipper real component which may indicate detection of conductors.

3. Dimensionality analyses

The dimensionality of the MT data should be analyzed to determine whether the subsurface structure is 1-D, 2-D or 3-D. The dimensionality analysis can also give some insights into the data set, such as the geoelectric strike direction, anisotropy, and the lateral resistivity distribution.

1. Phase tensor

Phase tensors are good indicator of the strike direction and the dimensionality of the subsurface resistivity structure. The method of Caldwell et al. (2004) was used to calculate the phase tensors. Two aspects of the phase tensors – the ellipticity and the skew (β) – need to be considered carefully. Theoretically, if the subsurface resistivity structure is 1-D then the phase tensor will plot as a circle and the skew will be zero. In the case of a 2-D isotropic structure the phase tensor will plot as an ellipse, with the major axis parallel or perpendicular to the strike direction and the skew equals to zero. Note that there is 90° ambiguity in the determination of the strike direction, and distinguishing between the two possible directions requires additional information (Chave and Jones 2012). In a 3-D or 2-D anisotropic case, the phase tensor will plot as an ellipse and the skew will be non-zero. Booker (2014) suggested a threshold of 3° although this is dependent on the impedance data quality.

Phase tensor ellipticity and the maximum phase angle of the data set are shown in Fig. S4. In the frequency band 100-0.3 Hz, the skew angles are consistently close to 0° and the ellipses are close to circular, indicating an approximately 1-D resistivity structure for the upper about 2000 m based on the skin depth equation (described in S7) with 10 Ωm

resistivity value and 1 Hz frequency. This is reasonable as the study region is covered by the 1.5-2 km thick layer of sedimentary rocks (Wright et al. 1994). In the frequency band 0.3-0.03 Hz, the skew angles are not too large (<2°) and the ellipticity of the ellipse is quite obvious, indicating a 2-D resistivity structure. In the frequency band 0.03-0.003 Hz, the phase tensors of the stations at the western side and eastern side show a different pattern: the skew angles of the western side stations are much higher than the eastern side stations, which means the western side maybe more 3-D or has some 2-D anisotropy structure.

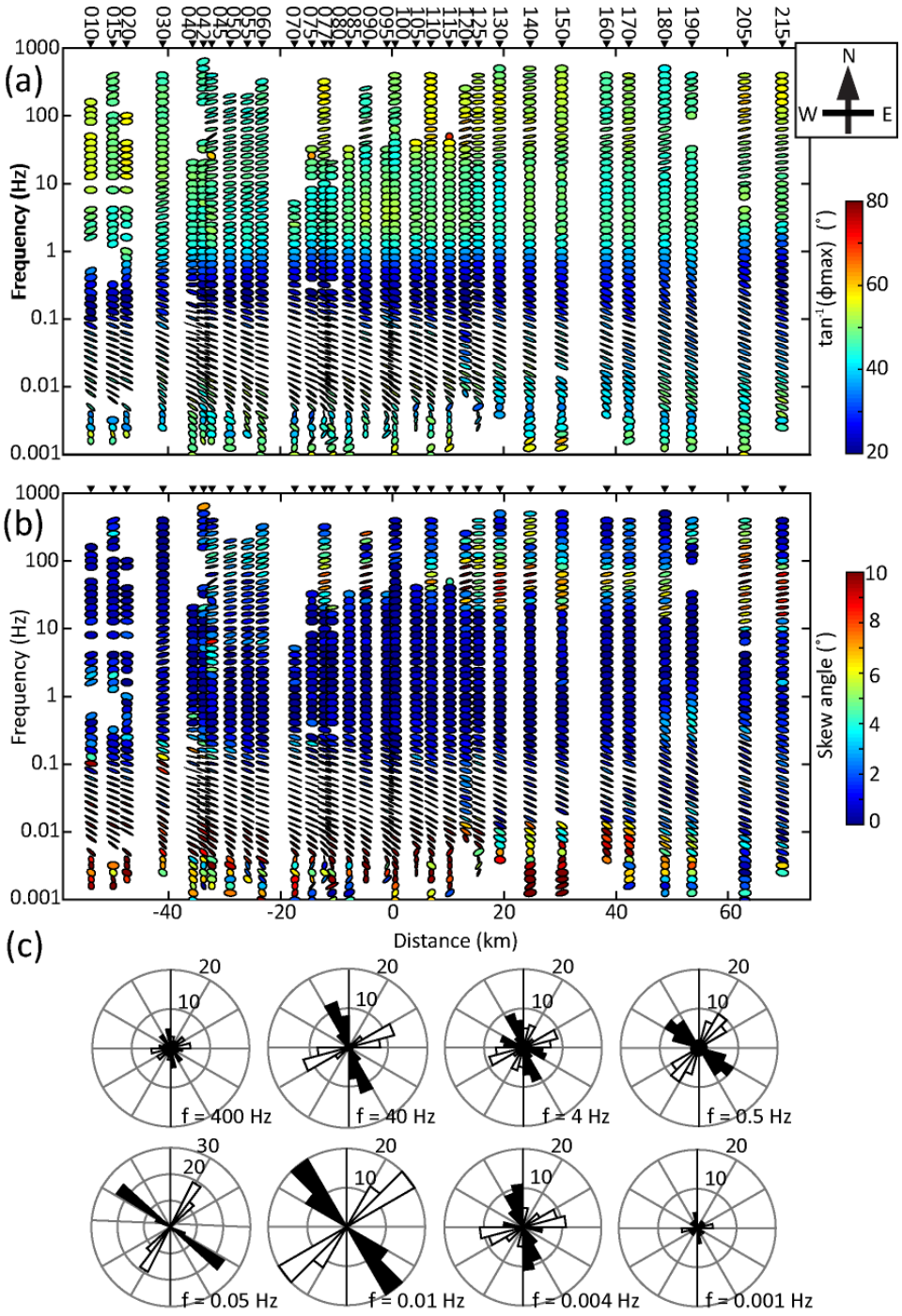

Fig. S4: (a) Scaled phase tensor (same length for the major axis) for the 32 MT stations used in the 2-D inversions. The colour fill shows the maximum principle value of the phase tensor. (b) Scaled phase tensor for the 32 MT stations used in the 2-D inversions. The colour fill shows the beta skew value of the phase tensor. (c) Rose diagram of the angle α-β which represents the geoelectric strike direction from the phase tensor analysis (Caldwell et al. 2004).

2. Strike analysis with tensor decomposition

Strike analysis was done using the McNeice-Jones multi-site, multi-frequency distortion decomposition code (McNeice and Jones 2001), which is based on the tensor decomposition method of Groom & Bailey (1989). The results are displayed as rose diagrams in Fig. S5. The white bars in the rose diagrams show the strike direction. This direction was chosen instead of the black bars because the terrane boundary defined by aeromagnetic mapping was found to be closer to the strike of the white bars and thus the inherent 90° ambiguity can be overcome. Based on these, it is clearly seen that the strike direction is about N70°E for the frequency band 10-1000 Hz which corresponds to depths of the sedimentary basin. This could be due to local variations in the structure of the WCSB in this location. In the intermediate frequency range (0.01-1 Hz) the strike direction is approximately N40°E. However for the frequency band 0.001-0.01 Hz, no specific strike direction can be found because of the deviation of the deep resistivity structure from the 2-D case. Another possible reason for inconsistent strike direction at this low frequency band is poor data quality because broadband instruments were used and the recording time is only about 20 hours at each station.

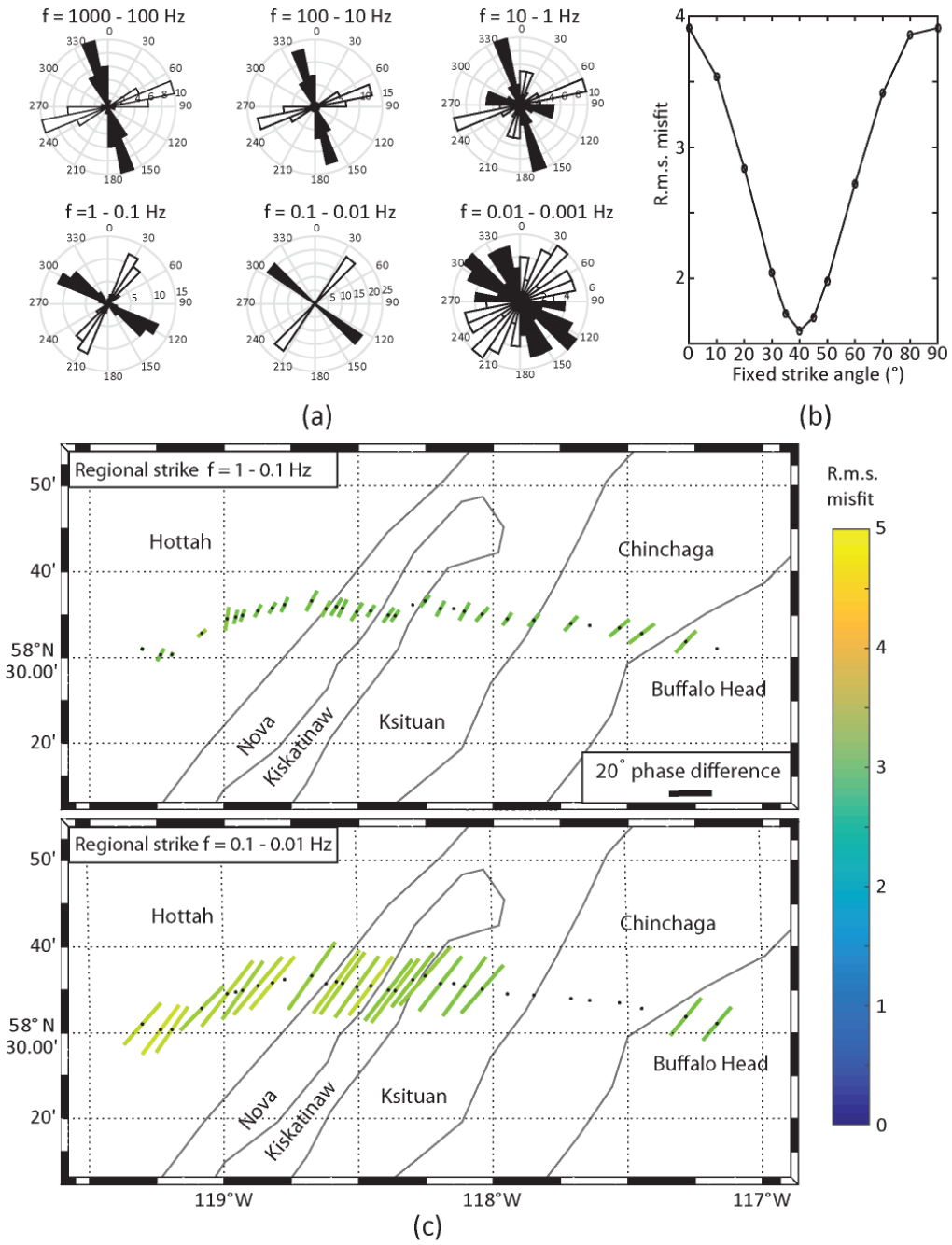

Fig. S5: Tensor decomposition using the method of McNeice and Jones (2001). (a) Tensor decomposition result for six decades allowing the strike angle to vary freely. (b) r.m.s. misfit of tensor decomposition of all decades and all stations with fixed strike angle varying from 0˚ to 90˚. (c) Maps showing the consistency of the calculated strike angle for each station along the MT profile for two different decades, 1-0.1 Hz and 0.1-0.01 Hz, which correspond to sedimentary layer and the basement, respectively. The length of the strike angle bars in (c) shows the value of phase split for each station at this decade.

Since different strike directions were found for different period bands, a second decomposition was made with the strike direction fixed. This direction was then fixed at various angles in the range 0°-90° and constrained, multi-station, tensor decompositions were implemented for the frequency band 0.001-1000 Hz. By analyzing the change of the r.m.s. (root mean square) misfit (Fig. S5b), it was found that the lowest r.m.s. misfit was achieved when the strike angle was fixed at N40°E.

3. Induction vectors

The real components of the induction vectors are an important indication of lateral changes in resistivity but are not good at determining the depth of a conductor (Chave and Jones 2012). Theoretically, in a 1-D isotropic situation, the vertical magnetic field should be zero as there is no lateral resistivity change. In a 2-D isotropic situation, the induction vectors should be orthogonal to the electrical strike direction while in a 3-D or 2-D anisotropic situation, patterns of induction vectors are more complicated.

The induction vectors for four periods are shown in Fig. S6. At high frequencies (2.05 Hz and 0.08 Hz), the induction vectors are very small and there is no consistency in their direction, indicating the shallow resistivity structure is 1-D which corresponds to the sedimentary rocks of the WCSB. At intermediate frequency (0.01 Hz), the induction vectors are longer (about 0.3) but don't all show the same direction with the western stations pointing north, the middle stations pointing northeast, and the eastern stations pointing east. This may indicate a 3-D or complicated 2-D resistivity structure in the Precambrian basement rocks. At low frequency (0.002 Hz), the induction vectors are longer (about 0.5) and point to the northeast but are not orthogonal to the strike direction derived above,

giving more evidence that the deep resistivity structure is not 2-D. In conclusion, the induction vectors are not consistent with the resistivity structure of the deep subsurface below the sedimentary layers having a simple 2-D structure. However, the non-2-D behavior of the induction vectors could be result of deeper (> 50 km) electrical structures because the induction vectors are not sensitive to depth. Another possibility is some conductors off the profile deflected the induction vectors. Yet, the induction vectors still contain the geoelectric information of the study area.

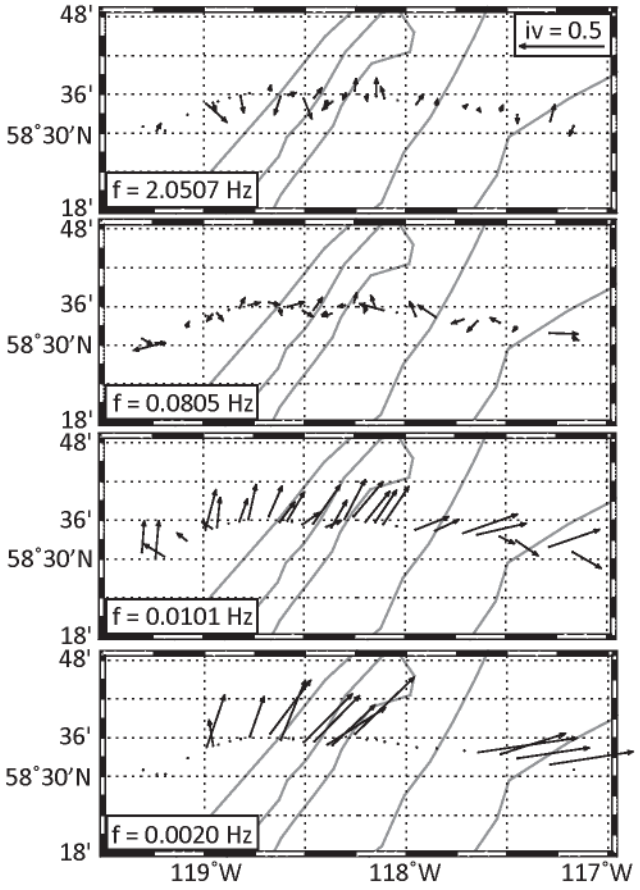

Fig. S6: Induction vector of selected periods of 32 MT stations used for 2-D inversions. The gray lines mark terrane boundaries. Vectors are plotted to point away from conductors according to Weise (1962).

4. Rotation of the data

In summary, dimensionality analysis indicates that the subsurface resistivity structure is overall 2-D. The induction vectors do not give useful information to determine the 2-D strike direction. The most appropriate 2-D geoelectric strike direction found for all stations and all period bands by strike analysis is N40˚E. Therefore, all the MT data are rotated from the geographic coordinate system to geoelectric coordinate system according to the geoelectric strike direction (N40˚E) for further analysis.

4. Effects of electrical anisotropy on MT data

There are several ways to identify the influence of electrical anisotropy in magnetotelluric data: (a) Phase splits can be an indicator of electrical anisotropy especially when this feature is observed over a large area or there is additional supportive information from geology, wells, other geophysical data (Heise and Pous 2001). (b) The phase tensor, which is another way to visualize phase splits, was studied by Heise et al. (2006) who demonstrated that the phase tensor shows ellipses instead of circle in a 1-D structure when there is an interface between and isotropic and anisotropic layer. Liddell et al., (2016) suggested that the phase tensor pseudo section is a key factor in identifying anisotropy. Large skew values may be caused by purely 2-D anisotropic structure as well as 3-D distortion. (c) Induction vectors can be deflected to the direction of the anisotropy when the geoelectric structure is 2-D anisotropic. Therefore, they are not perpendicular to either the 2-D strike direction or to the anisotropic strike direction (Wannamaker 2005). While in a 1-D anisotropic situation, induction vectors can be very small whereas there can be phase splits due to anisotropy (Heise and Pous 2001). (d) Out of quadrant phase can occur in case of anisotropy also which was discussed by Heise and Pous (2003) and Pek et al. (1997).

In this study, (a) large phase splits are observed at all the MT sites, with the exception of several eastern sites. (b) Very large skew angles are observed in the low frequency data on the phase tensor plot. (c) Induction vectors are not convincing to prove the subsurface resistivity structure is simply 2-D. (d) No out of quadrant phase angle was observed.

In conclusion, there may be electrical anisotropic structure. However, the observations could also be caused by a 3-D isotropic subsurface.

5. 2-D isotropic inversion sensitivity tests

Sensitivity tests were carried out to determine if the two major conductors (KC and KCC) in the 2-D isotropic inversion model are necessary to fit the data. This was done by editing the preferred 2-D isotropic inversion model. The resistivity of each conductor was replaced by the resistivity of the neighboring crystalline basement (3000 Ωm) and a forward modeling was performed to calculate the responses of the modified models. Furthermore, 2-D isotropic inversions were carried out with the resistivity of the KC and the KCC fixed at a value of 3000 Ωm. These inversions used the same parameters as the 2-D isotropic inversion mentioned above. The original data, the preferred 2-D isotropic inversion model response, the response of the modified model and the response of fixed inversion models of stations RLK090, RLK150 were compared in Fig. S7.

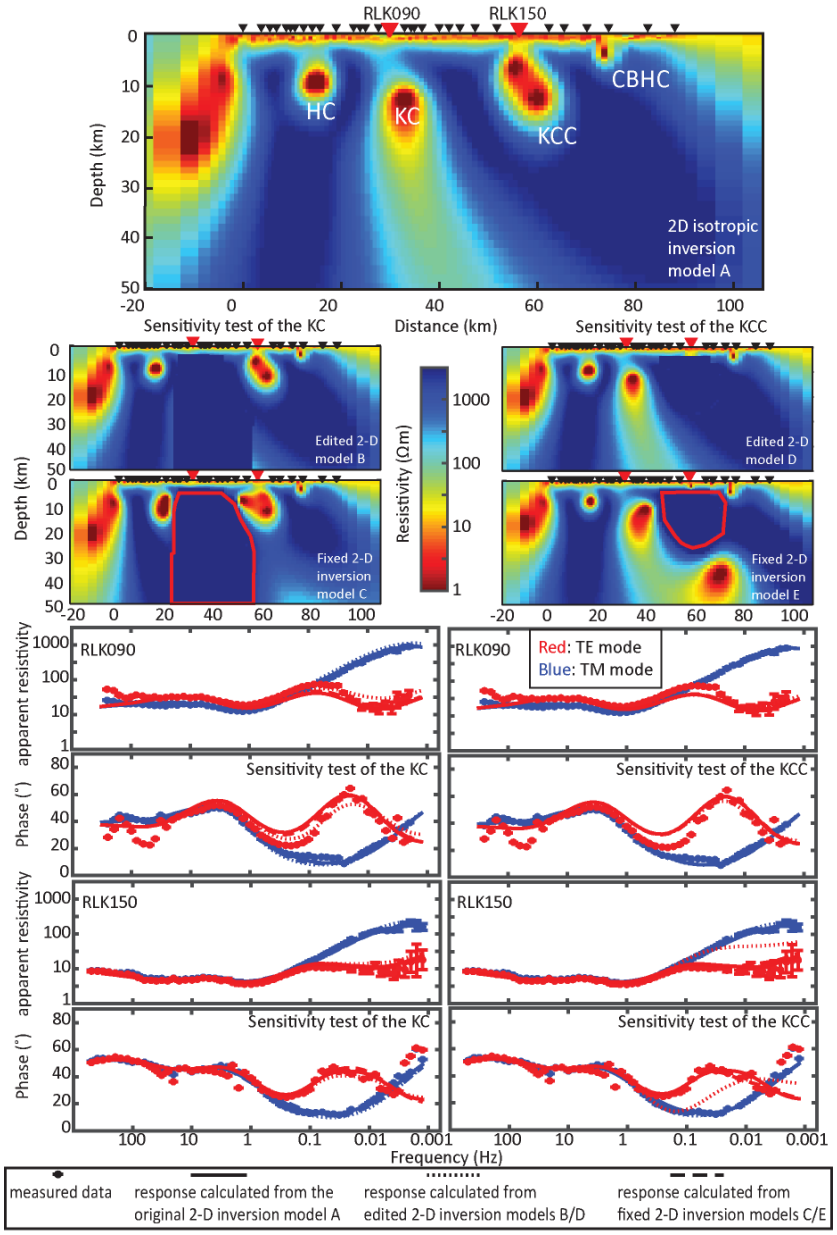

Fig. S7: Sensitivity test of the 2-D isotropic inversion model for the KC (left) and the KCC (right). In the edited 2-D inversion models, the KC and KCC are replaced with the resistivity of the highly resistive crystalline rocks (3000 Ωm). The third row figures are 2-D inversion models in which the KC and KCC are fixed to 3000 Ωm, respectively. Comparison of (a) measured data, (b) response calculated from the preferred 2-D inversion model A, (c) response of edited models B/C, and (d) response calculated from fixed models D/E on sites RLK090 and RLK150 are shown in the bottom.

When the KC is replaced with high resistivity (3000 Ωm), the response of the modified model does not agree with the measured MT data but shows higher resistivity and lower phase in the frequency range 0.1-0.001 Hz. This is very obvious at stations from RLK070 to RLK140, especially in the TE mode. When the KCC was replaced with high resistivity, the response of the modified model shows higher resistivity and lower phase especially in the TE mode in the frequency range 1-0.001 Hz which is different from the KC because the KCC is shallower than the KC. This is observed at all stations from RLK140 to RLK190. The fixed inversion models try to put conductors around the fixed area and the responses of these models are closer to the measured data than the responses of edited model. Overall, this sensitivity test confirms that the KC and KCC are necessary to get a good fit to the data and to explain the dataset.

6. 2-D anisotropic inversions

Two dimensional anisotropic inversions were also applied to the data because the existence of anisotropic resistivity structure in this area was suggested by Yin et al. (2014). The general parameters were the same as for both the 2-D isotropic and anisotropic inversions except the number of mesh layers. The anisotropic inversion used a mesh with 62 layers instead of the 114 layers used in the isotropic inversions. Because the anisotropic inversion code requires unfeasible memory of the computer if run with the 114-layers mesh.

There is another anisotropic τ to control the anisotropy of the inversion model. The larger the value of anisotropic τ, the more isotropic the inversion model will be. A set of value of anisotropic τ from 0.01 to 30 were given to 2-D anisotropic inversions. In order to

represent anisotropy in the electrical structure, the anisotropy inversion models have three resistivity values for each model cell in the strike direction (xx), perpendicular to the strike (yy) and vertical (zz). Note that this inversion only considers three conductivity values and assumes that the principal axes are aligned with the model co-ordinate system. In a general case the elements xy, xz, yz must be considered, but in this case they are assumed to be zero. The anisotropic 2-D inversion models are shown in Fig. S8. Based on the anisotropic inversion models and r.m.s. misfit, it is concluded that the subsurface structure can to a first approximation be treated as electrically isotropic even though some anisotropy may be present.

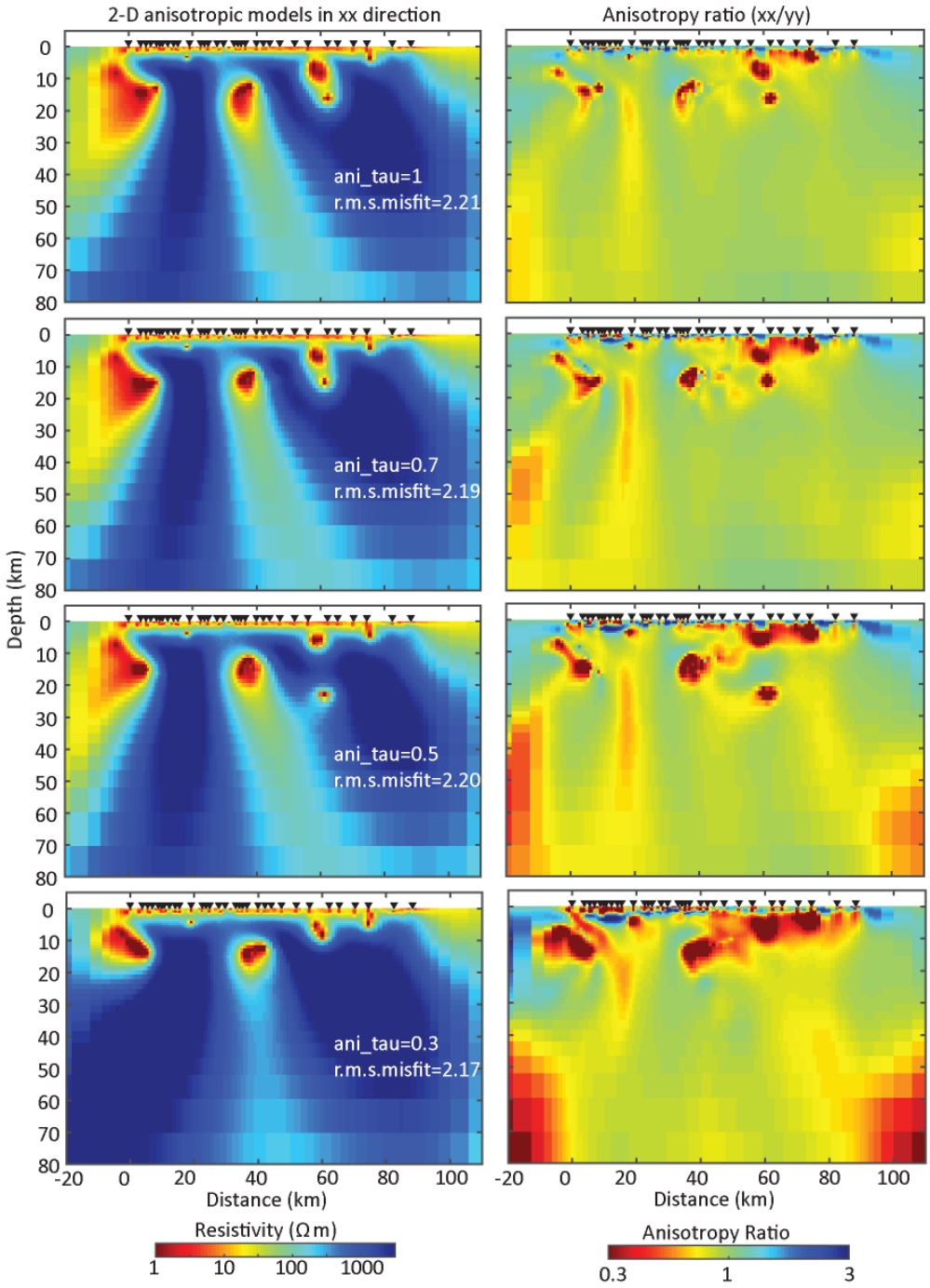

Fig. S8: 2-D anisotropic inversion models with tau=3 and different anisotropic tau values (0.3, 0.5, 0.7, 1). Left side figures show the models of xx direction with different anisotropic tau values; right side figures show the corresponding resistivity ratio of the models of the xx and yy directions.

Regarding the large distortion of phase tensors, high skew angles and patterns of along-strike induction vectors, Boerner et al. (2000) suggested that this could be the result of regional 3-D resistivity structures, such as a low resistivity body beneath the Canadian Cordillera to the SW. Turkoglu et al. (2009) gave an alternative explanation and suggested that non-plane wave source effects might be the reason for the distortion. However, the distortion may be explained by a 3-D effect from the conductors west of the profile or the along-strike variation of the KC. This explanation is consistent with that the high phase skew values are only observed at very low frequencies. According to the 2-D inversion results of profile A in the study of Boerner et al. (2000), there are large conductors beneath the Hottah terrane. Moreover, Turkoglu et al. (2009) showed that there is variation in the geometry of the KC in the strike direction which could also be a reason for the distortion. Therefore, it is reasonable that these out of profile conductors and along strike variation of the KC distort the phase tensors and induction vectors. In summary, electrical anisotropy is not necessary to explain phase tensors and induction vectors.

7. Archie's Law

Archie's Law can be used to relate the resistivity of a rock to the porosity, fluid resistivity, and interconnection of the pores (Archie, 1942). If the rock is saturated, Archie's Law can be expressed as:

$$\rho = \rho_w \emptyset^{-m}$$

where ρ is the resistivity of the rock, ρ_w is the resistivity of the pore fluid, $\emptyset$ is the porosity, m is the cementation exponent. If the pore space is well connected a value of m=1 is appropriate. If the pores are not well connected a value of m=2 is preferred.

Archie's Law assumes that there is no conduction within the rock matrix and it is not valid when the porosity is very low. For example, assuming a rock matrix with 1000 Ωm resistivity and a porosity of 0.0001 saturated with 1 Ωm saline water, The bulk resistivity of the rock calculated according to Archie's Law should be 10,000 Ωm when m=1 or 100,000,000 Ωm when m=2. These results are higher than the rock matrix's resistivity and are obviously not reasonable.

8. Calculation of the geotherm of the Birch Mountain conductor (BMC)

The geotherm for the BMC was calculated by assuming a mantle heat flow of $Q_m = 15\ mW/m^2$, and using the average surface heat flow of $Q_s = 45\ mW/m^2$ (Majorowicz et al., 2016). The thermal conductivity of the crustal rocks was assumed to be $K_c = 2.5\ W/mK$ (Jaupart and Mareschal, 2015; Perry et al., 2006). The temperature at the surface was assumed to be $0^{\circ}C$. The temperature in the crust (T_c *in* $^{\circ}C$) at the depth of d *(km)* was calculated using the method of Perry et al. (2006):

$$T_c = 0 + \frac{(Q_s + Q_m)}{(2 * K_c)} * d \qquad \text{(A.1)}$$

Assuming the thermal conductivity of the mantle to be $K_m = 3\ W/mK$ (Jaupart and Mareschal, 2015). The temperature of the lithospheric mantle (T_{lm}) can be calculated using the equation:

$$T_{lm} = T_{Moho} + \left(\frac{Q_m}{K_m}\right) * (d - D_{Moho}), \qquad \text{(A.2)}$$

where T_{Moho} is the temperature of Moho calculated using the Equation A.1. The depth of Moho (D_{Moho}) was assumed to be ~40 km (imaged by seismic methods; Gu et al., 2018). For the depths greater than the LAB, the temperature (T_a) is calculated using the equation:

$$T_a = T_{lab} + k_a * (d - d_{lab}) \quad \text{(A.3)}$$

where the T_{lab} is the temperature of the LAB calculated from Equation A.2. The adiabatic temperature gradient was assumed to be $k_a = 0.5\ ^{\circ}C/km$ (Lee et al., 2001). The depth of the LAB was assumed to be 200 km according to the xenolith study of Aulbach et al., (2004) and Chen et al., (2018). The calculated geotherm is shown in Figure 9.12, which is in agreement with the result of Aulbach et al., (2004).

9. Calculation of the geotherm for the Loverna block conductor (LC)

The geotherm for the LC was calculated using the same method as for the BMC but the specific values were varied according to geothermic and seismic studies. The surface temperature used was 0°C. The value of the mantle heat flow was assumed to be $Q_m = 15\ mW/m^2$ (Majorowicz et al., 2016). The average surface heat flow value used was $Q_s = 35\ mW/m^2$ (Bachu and Burwash, 1994). The thermal conductivity of the crustal rocks was assumed to be $K_c = 2.5\ W/mK$ (Jaupart and Mareschal, 2015; Perry et al., 2006). The thermal conductivity of the mantle rocks was assumed to be $K_m = 3.5\ W/mK$ (Jaupart and Mareschal, 2015). The adiabatic temperature gradient was assumed to be $k_a = 0.5\ ^{\circ}C/km$ (Lee et al., 2001). The depth of the Moho (D_{Moho}) was assumed to be ~40 km (imaged by seismic methods; Gu et al., 2018). The depth of the LAB was assumed to be 300 km according to the study of Chen et al. (2018). These values are chosen to produce a geotherm close to the geotherm of Pollack and Chapman (1976) that was based on a surface heat flow of 35 mW/m^2.